

Alma Mater Studiorum – Università di Bologna

DOTTORATO DI RICERCA IN

Ingegneria biomedica, elettrica e dei sistemi (IBES),
curriculum ingegneria elettrica

Ciclo XXX

Settore Concorsuale: 09/E2 Ingegneria dell'energia elettrica

Settore Scientifico Disciplinare: ING-IND 32 Convertitori, macchine e azionamenti elettrici

TITOLO TESI

MULTIPHASE ELECTRIC DRIVES FOR “MORE ELECTRIC AIRCRAFT” APPLICATIONS

Presentata da: Giacomo Sala

Coordinatore Dottorato

Prof. Daniele Vigo

Supervisore

Prof. Angelo Tani

Esame finale anno 2018

I want to thank a lot Angelo Tani for having taught me the research method and for his kind supervision.

Thanks to my colleagues from Bologna and Nottingham universities for helping me to solve everyday problems.

Last but not least, thanks to my family.

Index

Index.....	i
List of Figures	ix
List of Tables.....	xxi
Introduction	xxiii
CHAPTER 1.....	1
Multiphase Machines for More Electric Aircraft applications.....	1
1.1 Aircraft Industry and Market	1
1.2 The idea of More Electric Aircraft	3
1.3 The idea of More Electric Engine.....	5
Embedded starter/generator location.....	6
Embedded starter/generator machine topologies	7
1.4 State of the Art and Applications of Multiphase Drives	9
Performance	10
Fault tolerance and diagnosis	11
New control techniques	13
1.5 Multiphase Machines as a Fault-Tolerant solution for MEA applications.....	13
CHAPTER 2 Multi-Harmonic Generalised Model for Multiphase Machines	25
2.1 Space Vector Decomposition theory	26
Space Vectors Transformation (odd number of variables)	28
Space Vectors Transformation (even number of variables).....	29
2.2 General approach to Multiphase Machine Modelling: Stator Winding and Transformations	31
Armature field (one turn)	32
Armature field (multiphase winding).....	39
Space vectors analysis for modelling of multiphase machines	41
Space vectors analysis (the standard three-phase winding)	44
Space vectors analysis (12 phase asymmetrical winding)	48
Space vectors analysis (nine phase winding)	50
Space vectors analysis (multi-sectored triple three-phase winding)	53
2.3 Voltage Space Vector Equations	55

Voltage equation (single turn).....	56
Voltage equation (single phase)	57
Voltage equation (multiphase winding)	58
2.4 Linked Flux Space Vectors.....	61
Linked flux (single turn)	61
Linked flux (single phase).....	63
Linked flux (multiphase winding).....	64
Self inductance (single turn)	65
Self inductance (multiphase winding).....	66
2.5 Surface Permanent Magnet Machine Modelling	67
Single permanent magnet model and basic equations.....	67
Surface Permanent Magnet rotor.....	71
Voltage equation (single turn).....	73
Voltage equation (multiphase winding)	74
2.6 Squirrel Cage Modelling	75
Squirrel cage as an N_b -phase symmetrical winding	76
Voltage equation (single equivalent phase - between two bars)	77
Voltage equation (equivalent multiphase winding of the squirrel cage).....	78
Voltage equation (equivalent multiphase winding of a symmetrical cage)	81
Linked flux (general).....	82
Self inductance (equivalent multiphase winding of a squirrel cage - SVD)	83
Mutual flux (effect of a single turn on the squirrel cage).....	84
Mutual flux (effect of a multiphase winding on the squirrel cage).....	85
Voltage equation (effect of the cage on a single turn)	88
Voltage equation (effect of the cage on a multiphase winding).....	89
Voltage equations (summary)	91
2.7 Power, Torque and Force Equations.....	94
Power equation (single turn)	94
Power equation (multiphase winding).....	97
Power equation (squirrel cage).....	106
Airgap magnetic coenergy (alternative method for the torque evaluation)	113
Radial Force	119
2.8 Summary and Advantages of a Multi-Harmonic Model for Multiphase Machines	122
Advantages of a multi-harmonic SVD model	122

Multi-harmonic models (summary of the equations – simplified model).....	124
CHAPTER 3 Open Phase Faults and Fault Tolerant Controls in Multiphase Drives	129
Open Phase faults in Electrical Drives	129
3.1 Open Phase Faults in Inverter Fed Multiphase Machines	131
Terminal Box and Converter Connection Faults.....	131
Protections and Drives	131
Zero Current Control and Uncontrolled Generator Behaviour	134
3.2 Modelling and Fault Tolerant Control for Open Phase Faults	135
Model of and Open Phase Fault	135
Open Phase Fault Tolerant Control (FTC) Concept.....	136
Open Phase Fault in Three-Phase Electrical Drives.....	136
Open Phase Fault Tolerant Control in Multiphase Electrical Drives.....	137
Optimized FTC algorithm by means of the Lagrange multipliers method	139
3.3 Current Sharing and Fault Tolerant Control for Independently Star Connected Multi Three-Phase Machines under Open Phase Faults	142
Current Sharing for Independently Star Connected Three-Phase Subsystems	143
Current Sharing for Independently Star Connected Three-Phase Subsystems (d-q axis control enhancement)	146
Open Phase FTC Algorithm for Independently Star Connected Three-Phase Subsystems	147
3.4 Improved Fault Tolerant Control for Multiphase Machines under Open Phase Faults 149	
Optimized FTC Algorithm by means of the Lagrange Multipliers method for Multi Independently Star Connected n -Phase Subsystems (n odd)	149
Optimized FTC Algorithm by means of the Lagrange Multipliers method for Multi Three- Phase Subsystems Connected to a Single Star	150
Optimized FTC Algorithm by means of the Lagrange Multipliers method for Multi-Star Connected Three-Phase Subsystems	153
Optimized Open Phase FTC Algorithm for a dual three-phase winding (star connection constraints)	155
Optimized Open Phase FTC Algorithm for a triple three-phase winding (star connection constraints)	157
Optimized Open Phase FTC Algorithm for a quadruple three-phase winding (star connection constraints).....	161
3.5 Summary of the proposed Fault Tolerant Control for Open Phase Faults	168
3.6 Case study: 12-Phase Asymmetrical Machine	171
Analytical results.....	171

Control Schemes - Comparison.....	185
Numerical simulation results (Matlab-Simulink).....	188
Finite Element Results (Flux): Comparison of iron saturation and related torque reduction in case of two three-phase subsystem open phase fault (best double six-phase configuration for simplified six-phase FTC performance enhancement).....	199
Experimental results.....	203
3.7 Conclusions	213
CHAPTER 4 High Resistance and Interturn Short Circuit Faults.....	215
Introduction to High Resistance (HR) and Interturn Short Circuit (ISC) Faults	216
4.1 Equivalent circuit for High Resistance and Interturn Short Circuit Faults.....	217
Circuitual representation of HR and ISC faults	218
ISC faults – leakage inductances analysis.....	220
HR and ISC faults – resistances analysis	223
Circuitual phase voltage equations for HR and ISC faults.....	226
Linked fluxes equations for HR and ISC faults	230
4.2 Interturn Short Circuit Faults: Electromagnetic Analysis of the Short Circuit Loop 232	
Magnetic field generated by the ISC loop current	232
HR and ISC fault armature equations - Summary.....	233
Torque and radial force evaluation for ISC faults.....	235
4.3 Space Vector Model of a Multiphase Machine with a High Resistance or Interturn Short Circuit Fault.....	238
General Interturn Short Circuit with High Resistance Fault in Multiphase Electrical Machines	243
Summary of the complete Space Vector model for HR and ISC faults in multiphase machines.....	244
4.4 Principle for High Resistance and Interturn Short Circuit Faults Detection with Ideal Current Control (FOC) in distributed winding Induction Machines.....	246
Simplified model for distributed multiphase windings	247
Detection algorithm: concept	249
4.5 High Resistance Fault Detection Algorithm with Ideal Current Control (FOC).....	251
Advantages of redundant equations in the HR detection algorithm for improved accuracy	252
High Resistance Faults in Symmetrical Multiphase Machines (odd phases).....	256
High Resistance Fault in Asymmetrical Multi Three-Phase Machines (even phases) ..	259

4.6	Interturn Short Circuit Fault Detection with Ideal Current Control in Multiphase Machines	263
	Simplified model for distributed multiphase windings – space couplings caused by ISC fault in squirrel cage Induction Machines	264
	Simplified model for distributed multiphase windings – space couplings caused by ISC fault in SPM machines with sinusoidal MMF of the rotor magnets	265
4.7	Interturn Short Circuit Fault Detection Algorithm with Ideal Current Control in Three-Phase Squirrel Cage Induction Machines.....	267
	Simplified model for ISC fault detection in Three-Phase IMs.....	267
	Simplified model for ISC fault detection in Three-Phase IMs at steady state conditions	268
4.8	Analytical and Experimental Results: High Resistance and Interturn Short Circuits in Three-phase Induction Machines with V/f Control.....	274
	Test rig and prototype	275
	Healthy Machine	277
	High Resistance faults	281
	Interturn Short Circuit faults	283
	High Resistance and Interturn Short Circuit faults: Comparison with V/f control.....	287
4.9	Analytical Results of ISC fault detection for Three-phase IMs	289
4.10	Analytical and Experimental Results of High Resistance Detection in Nine-Phase Induction Machines	296
	High Resistance Fault Detection	297
4.11	Conclusion	303
CHAPTER 5 Modelling of Multi Three-Phase Sectored Machines for Radial Force Control		305
	Multi Sector Permanent Magnet machines (MSPM) as a possible multiphase machine solution for radial force control.....	306
5.1	Modelling of Multi Three-Phase Sectored Stator Windings	307
	General SVD model – additional transformation.....	307
	General SVD model – Voltage equations for MSPM machines	312
	MSPM particular SVD model – Voltage equations for MSPM machines.....	313
	General SVD model – Torque and Force for MSPM machines	315
5.2	Modelling of a Triple Three-Phase Sectored Machine (three pole pairs)	320
	SVD transformation – Current space vectors.....	320
	Triple Three-Phase MSPM machine – Voltage Equations by General Method (redundant)	322
	Triple Three-Phase MSPM machine – Voltage Equations by Particular Method	323

Triple Three-Phase MSPM machine – Torque and Force.....	325
5.3 Force and Torque Control of a Triple Three-Phase Secteded Machine.....	331
Control equations (multi synchronous reference frames)	331
Radial Force Control: F2/F ratio (F2pu)	332
Triple Three-Phase Inverse Transformation: From the multiphase space vectors to the three-phase ones	334
5.4 Force Control of a Triple Three-Phase Secteded Machine: optimised control for minimum stator copper Joule losses.....	336
5.5 Current Sharing Technique for Triple Three-Phase Machines (Radial Force Control and Compensation).....	339
Radial Force Evaluation in case of Current Sharing Control (standard method).....	339
Current Sharing advanced control of MSPM machines and Radial Force control	342
5.6 Radial Force FTC in case of Three-Phase Open Phase Fault.....	346
Radial Force Equation in case of Three-Phase Open Fault (independent 3 rd space control)	347
Radial Force Compensation in case of Three-Phase Open Fault (F=0).....	351
Radial Force FTC in case of Three-Phase Open Fault – optimised algorithm	351
5.7 Finite Element Simulation Results (Magnet software).....	354
Torque and Radial Force control parameters (K_T , $K_{PM(3,2)}$ and $K_{PM(3,4)}$)	355
Torque and Radial Force control (optimised control):.....	356
Radial Force Evaluation in case of Three-Phase Open Fault (standard torque control)	363
Radial Force Compensation at Rated Torque (id3=0 FTC)	364
Radial Force Fault Tolerant Control at Rated Torque (id3=0 FTC) – constant force....	366
Radial Force Fault Tolerant Control at Rated Torque (id3=0 FTC) – direction criticality	369
5.8 Numerical (Matlab-Simulink) Simulation Results	370
Radial Force Open Loop Control	372
Radial Force Open Loop Compensation (With detection delay)	374
Radial Force Open Loop Compensation (instantaneous).....	376
Bearingless Operation and FTC (early compensation) – rated torque and rated force ..	378
Bearingless Operation and optimised current sharing control – rated torque and rated force	381
Bearingless Operation with Optimised FTC – Minimum copper Joule losses	383
5.9 Experimental Results.....	386
Radial Force Open Loop Control	387

Radial Force Control in Bearingless Closed Loop Operation (stand still).....	390
Radial Force Control in Bearingless Closed Loop Operation (rated speed - 3000 rpm)	392
Radial Force Control in Bearingless Closed Loop Operation (transient up to 3000 rpm)	394
Radial Force Control in Bearingless Closed Loop Operation (bearingless control activation at 1000 rpm)	396
5.10 Conclusions.....	399
CHAPTER 6 Design and Control of Segmented Multi Three-Phase SPM Machines	403
Sectored and Segmented motor design - Concept.....	404
Summary of the Segmentation Design Degrees of Freedom	406
6.1 Field Analysis of a Triple Three-phase Sectored and Segmented SPM.....	407
General SV model of a segmented and sectored machine	408
SV Model of a Triple Three-Phase Segmented and Sectored SPM Machine	411
6.2 Machine Control and Winding Design.....	413
Torque Ripples in Segmented Machines.....	416
New Winding Design for Standard Current Control.....	418
Segmented Machine Control Technique for Standard Windings Designs.....	419
6.3 Coil Pitch, End Effect and Cogging Torque in Segmented Sectored Machines	420
Coil Pitch.....	420
End Effect and Cogging Torque.....	422
6.4 FEA Simulation Results	423
Performance - Healthy Machine Behaviour.....	423
6.5 Fault Tolerant Behaviour.....	430
6.6 Machine Prototype and Thermal Analysis	431
Machine Design.....	432
Thermal Analysis for Future Developments	434
6.7 Conclusion	438
Abstract	i
Academic activities	ii
Summary of the research activity.....	ii
Seminars	iii
Research period abroad	iii
Assistant Supervisor.....	iv
Publications	iv

List of Figures

Fig. 1.1– Power flow in a standard civil aircraft.....	3
Fig. 1.2 – Power flow in a civil MEA.	4
Fig. 1.3 – The MEA concept on Boeing 787.	5
Fig. 1.4 – Rolls-Royce electric starter/generator embedded in the gas turbine engine.....	6
Fig. 1.5 – Operating temperatures in a typical jet engine.	7
Fig. 1.6 – A typical MEE layout.	8
Fig. 1.7 - Multiphase system connected to a standard three-phase grid.....	9
Fig. 1.8 - Single channel electromechanical actuator fault-tree (probabilities given per hour flight).....	14
Fig. 1.9 - Dual-lane electromechanical actuator fault-tree (probabilities given per hour flight).	15
Fig. 1.10 - Method of flight control redundancy.....	15
Fig. 1.11 - Redundancies of multiphase machines.....	16
Fig. 2.1 – Space vector transformation and inverse transformation of an n variable system. .	26
Fig. 2.2 – Conventions of the proposed model.	34
Fig. 2.3 – Spatial location of a turn (turn k) in the airgap circumference.	34
Fig. 2.4 – Spatial location of a turn (turn k) in the airgap circumference.	35
Fig. 2.5 – Spatial distribution of the magnetic field produced by a turn (turn k) in the airgap.	39
Fig. 2.6 – Six slots distributed winding three-phase machine concept (example). The green vertical line (magnetic axis of the first phase) highlights the origin of the stator reference frame.	44
Fig. 2.7 – Six slots distributed winding three-phase machine with asymmetrical (left) and symmetrical (right) winding distribution (concept). With “x” are indicated the starting slots of the phases and with “o” the final ones.	45
Fig. 2.8 – 48 slots and 2 pole pairs distributed winding 12-phase machine. Asymmetrical winding (left) and quadruple three-phase winding (right). The magnetic axis and the starting of the phases are highlighted with coloured lines in the back iron and with crosses in the slots respectively.....	48
Fig. 2.9 – 36 slots and 2 pole pairs distributed winding 9-phase machine. Asymmetrical winding (left) and symmetrical winding (right). The magnetic axis and the starting of the phases are highlighted with coloured lines in the back iron and with crosses in the slots respectively. Note: the winding on the right is symmetrical in its electrical degrees representation.....	51
Fig. 2.10 – 18 slots and 3 pole pairs sectorized winding 9-phase machine. The magnetic axis and the starting of the phases in the first sector are highlighted with coloured lines in the back iron and with crosses in the slots respectively.	54
Fig. 2.11 – Simplified magnetic behaviour of the magnets.	67
Fig. 2.12 – Magnet with constant radial thickness with a general machine reluctance.	68
Fig. 2.13 - SPM rotor with three pole pairs.....	71
Fig. 2.14 - Squirrel cage and related model parameters.....	76
Fig. 2.15 – Equivalent phase of a squirrel cage.	77

Fig. 2.16 – Electrical circuit and parameters of the equivalent phase of a squirrel cage.	78
Fig. 2.17 - Example of B-H curve of a high power density hard magnetic material.	114
Fig. 2.18 - Coenergy of a hard magnetic material (concept).....	115
Fig. 3.1 – Open phase faults in a standard three-phase drive (most typical faults).....	130
Fig. 3.2 – Single switching open fault scheme in case of a top driver protections or missing signal from the DSP fault. Transient behaviour of the fault with a positive current (left) and steady state behaviour (right).	132
Fig. 3.3 – Single switching open fault scheme in case of a bottom driver protections or missing signal from the DSP fault. Transient behaviour of the fault with a positive current (left) and steady state behaviour (right).	134
Fig. 3.4 – Schematic draw of the three-phase subsystem FTC. a) and b) show example of not optimized current controls, while c) shows the solution with the phase of the inverter current contributions that minimizes the stator Joule losses to maintain the same \bar{i}_{S1} value for a quadruple three-phase systems ($N_T=4$).	144
Fig. 3.5 – Logic for the fault protection on a single leg.	147
Fig. 3.6 – Full three-phase fault protection logic.	148
Fig. 3.7 – Typical star configurations for a quadruple three-phase winding.	150
Fig. 3.8 – Double three-phase standard drive and relative magnetic axis directions.	155
Fig. 3.9 – Triple three-phase standard drive and relative magnetic axis directions.	158
Fig. 3.10 – Quadruple three-phase standard drive and relative magnetic axis directions.	162
Fig. 3.11 – Schematic of a standard quadruple three-phase drive and magnetic axis directions of the 12-phase machine.	171
Fig. 3.12 – Schematic of the basic idea of the three-phase FTC (purple) and the single-phase FTC (green) in case of single phase open fault for an independent star configuration of a multi three-phase machine.	172
Fig. 3.13 – Analytical Joule losses comparison of the healthy machine (blue) and the faulty machine (phase A1 open), with three-phase FTC (purple) and single-phase FTC (green). ..	173
Fig. 3.14 – Analytical maximum phase current comparison of the healthy machine (blue) and the faulty machine (phase A1 open), with three-phase FTC (purple) and single-phase FTC (green).	174
Fig. 3.15 – Analytical Joule losses comparison with healthy machine (blue) and the faulty machine (phase A1 open). Three-phase FTC (purple) and single-phase FTC: quadruple three-phase layout (green), double six-phase layouts (spotted) and twelve-phase layout (orange). The rated copper Joule losses are highlighted in red.	175
Fig. 3.16 – Analytical maximum phase current comparison with healthy machine (blue) and the faulty machine (phase A1 open). Three-phase FTC (purple) and single-phase FTC: quadruple three-phase layout (green), double six-phase layouts (spotted) and twelve-phase layout (orange). The maximum phase current is highlighted in red.	175
Fig. 3.17 – Analytical phase currents at rated value of the main current space vector. Healthy machine.	176
Fig. 3.18 – Analytical phase currents at rated value of the main current space vector. Three-phase FTC (phase A1 open).	177
Fig. 3.19 – Analytical phase currents at rated value of the main current space vector. Single-phase FTC (phase A1 open).	177

Fig. 3.20 – Analytical phase currents at rated value of the main current space vector. Double six-phase layout AB CD (phase A1 open).	178
Fig. 3.21 – Analytical phase currents at rated value of the main current space vector. Double six-phase layout AC BD (phase A1 open).	178
Fig. 3.22 – Analytical phase currents at rated value of the main current space vector. Double six-phase layout AD BC (phase A1 open).	179
Fig. 3.23 – Analytical phase currents at rated value of the main current space vector. Twelve-phase layout ABCD.....	179
Fig. 3.24 – Analytical Joule losses comparison with healthy machine (blue) and the faulty machine (phases A1, B1, B2, D1, D2 open). Three-phase FTC (purple) and single-phase FTC: quadruple three-phase layout (green), double six-phase layouts (spotted) and twelve-phase layout (orange). The rated copper Joule losses are highlighted in red.	180
Fig. 3.25 – Analytical maximum phase current comparison with healthy machine (blue) and the faulty machine (phases A1, B1, B2, D1, D2 open). Three-phase FTC (purple) and single-phase FTC: quadruple three-phase layout (green), double six-phase layouts (spotted) and twelve-phase layout (orange). The maximum phase current is highlighted in red.	181
Fig. 3.26 – Analytical phase currents at rated value of the main current space vector. Healthy machine.	181
Fig. 3.27 – Analytical phase currents at rated value of the main current space vector.	182
Fig. 3.28 – Analytical phase currents at rated value of the main current space vector.	182
Fig. 3.29 – Analytical phase currents at rated value of the main current space vector.	183
Fig. 3.30 – Analytical phase currents at rated value of the main current space vector.	183
Fig. 3.31 – Analytical phase currents at rated value of the main current space vector.	184
Fig. 3.32 – Analytical phase currents at rated value of the main current space vector.	184
Fig. 3.33 – Block diagram of the current sharing and three-phase FTC control scheme.	186
Fig. 3.34 – Block diagram of the single-phase and three-phase FTC control schemes.	187
Fig. 3.35 – Block diagram of the single-phase and three-phase FTC control schemes.	188
Fig. 3.36 – Simulation of a speed transient from 0 to 300 rpm, followed by the fault of phase A1 open ($t=1s$). From 1 to 1.25 s three-phase subsystem FTC, from 1.25 to 1.5 s single-phase FTC. The last subplot shows the α - β components of the main current space vector i_{S1} (blue) and of the auxiliary ones (red).....	189
Fig. 3.37 – Simulated phase currents. The machine is healthy (top left) and then has phase A1 opened, with the three-phase FTC (top right) and the single-phase FTC (centre and bottom). With colours are differentiated the 1 st phase (blue), the 2 nd (green) and the 3 rd (orange) of each inverter. The thickest lines refer to the phase currents of inverter A.	190
Fig. 3.38 – Simulated current space vectors trajectories. Trajectory of \hat{i}_{S1} (blue) and of the auxiliary vectors in case of single-phase FTC (green) and three-phase subsystem FTC (purple).	191
Fig. 3.39 – Three-phase homopolar currents in case of phase A1 open fault and single phase FTC. AB CD star connection (top), AC BD star connection (centre) and AD BC star connection (bottom).	193
Fig. 3.40 – Three-phase homopolar currents in case of phase A1 open fault and single phase FTC. Single-star layout.	196
Fig. 3.41 – B-H curve of the stator (NO 20) and rotor (VacoFlux 50) laminations.....	199

Fig. 3.42 – Flux view for the healthy machine (left), the machine working with a three-phase open fault without FTC (centre) and with three-phase FTC (right). Inverter D three-phase open fault.....	200
Fig. 3.43 – Flux view for the healthy machine (left), the machine working with a six-phase open fault without FTC (centre) and with six-phase FTC (right). Inverters C and D six-phase open fault.....	201
Fig. 3.44 – Flux view for the healthy machine (left), the machine working with a six-phase open fault without FTC (centre) and with six-phase FTC (right). Inverters B and D six-phase open fault.....	202
Fig. 3.45 – Test bench. From left to right: load (bidirectional drive) gearbox 9:1, torque meter, scaled prototype.....	203
Fig. 3.46 – Test bench. From the left to the right: DSP TMS320F28335, control board (with DSP), driver’s board for one three-phase winding, power board for one three-phase winding.	204
Fig. 3.47 – Quadruple three-phase inverter (left) and twelve phase starter/generator scaled prototype (right).	204
Fig. 3.48 – Matryoshka current sharing control with $K_A = 2K_B = 4K_C = 8K_D$, [10 A/div].	205
Fig. 3.49 – Simplified current sharing control with $K_A = -0.5$ and $K_B = K_C = K_D = 0.5$, [10 A/div].	205
Fig. 3.50 – Measured currents of the inverter-B, when the machine is healthy (top left) and then has phase A1 opened, with the three-phase subsystem FTC (top right). Then all the inverter currents with the single-phase FTC are shown: inverter-A (centre left), inverter-B (centre right), inverter-C (bottom left), inverter-D (bottom right). With colours are differentiated the 1 st phase (blue), the 2 nd (green) and the 3 rd (orange) of each inverter, [2A/div].	207
Fig. 3.51 – Measured current space vectors trajectories. Trajectory of \bar{i}_{s1} (left) and of the auxiliary vectors (5 th , 7 th and 11 th from the left to the right) in case of single-phase FTC (top) and three-phase subsystem FTC (bottom), [2A/div].	207
Fig. 3.52 – Total stator copper Joule losses in case of phase A1 open fault with three-phase FTC (left) and single-phase FTC (right), [20W/div].	208
Fig. 3.53 – Three-phase homopolar currents in case of phase A1 open fault and single-phase FTC. AB CD star layout, [2A/div].	208
Fig. 3.54 – Three-phase homopolar currents in case of phase A1 open fault and single-phase FTC. AC BD star layout, [2A/div].	209
Fig. 3.55 – Three-phase homopolar currents in case of phase A1 open fault and single-phase FTC. AD BC star layout, [2A/div].	209
Fig. 3.56 – Three-phase homopolar currents in case of phase A1 open fault and single phase FTC. Single-star layout, [2A/div].	211
Fig. 4.1 – High resistance (left) and Interturn short circuit (right) faults. Concept.	216
Fig. 4.2 – Ideal Interturn short circuit fault (left) and equivalent circuit (right). Concept.	217
Fig. 4.3 – High Resistance and Interturn Short Circuit concept and proposed nomenclature. Phase x (bottom) is healthy; phase y (centre) is affected by a HR condition; phase z (top) is affected by an ISC fault (with a resulting possible resistance variation).	218

Fig. 4.4 – Interturn Short Circuit concept and proposed nomenclature. Phase z is affected by an ISC fault (with a resulting possible resistance variation), and all the slot leakage effects are represented by their respective constants in case of a single slot pair per phase winding.	220
Fig. 4.5 – Interturn Short Circuit concept and proposed nomenclature for the leakage flux analysis. Phase x is healthy; phase z1 is affected by an ISC in the end winding; phase z2 is affected by a slot ISC fault.	221
Fig. 4.6 – Interturn Short Circuit concept and proposed nomenclature for the resistances analysis. Phase x is healthy; phase z1 is affected by an ISC in the end winding; phase z2 is affected by a slot ISC fault. With “Q” are highlighted the main radial thermal paths related to the short circuit current copper Joule losses (the axial path is implicit).	224
Fig. 4.7 – Three-phase IM BA 112 MB4 from M.G.M. Motori Elettrici S.p.A (left) and winding scheme (right).	275
Fig. 4.8 – Rewinding process from the original three-phase machine to the new customized winding.	276
Fig. 4.9 - New prototype of nine phase IM and test rig (left top), new winding scheme (right) and electrical winding scheme of the phase U1, where there are many additional terminals for interturn short circuit tests (left bottom).	276
Fig. 4.10 - Matlab-Simulink simulation V/f control with healthy machine. Phase currents (red, blue and green) and short circuit current (purple) at the top; current space vector trajectory at the bottom.	278
Fig. 4.11 - Drive used for the V/f experimental tests on the prototype in its three-phase winding configuration. Control board (left) and inverter (right). The DSP of the control board is a TMS320F2812.	279
Fig. 4.12 - Test setup scheme (top), terminal box connections for three-phase winding configuration and setup for the ISC and HR tests (bottom).	279
Fig. 4.13 - Experimental tests V/f control with healthy machine. Phase currents (red, blue and green) and short circuit current (purple) at the top; Current space vector trajectory at the bottom.	280
Fig. 4.14 - Matlab-Simulink simulation V/f control with High Resistance fault (1.85 Ohm additional) in the mentioned phases. Current space vector trajectories [2A/div].	281
Fig. 4.15 - Experimental results V/f control with High Resistance fault (1.85 Ohm additional) in the mentioned phases. Current space vector trajectories [2A/div].	282
Fig. 4.16 - Matlab-Simulink simulation V/f control with Interturn Short Circuit fault at no load (1.85 Ohm short circuit resistance) in the mentioned phases and coils. Current space vector trajectories [2A/div].	283
Fig. 4.17 - Matlab-Simulink simulation V/f control with Interturn Short Circuit fault on the U phase at no load (top), 10 Nm (centre) and 20 Nm (bottom) (1.85 Ohm short circuit resistance) in the mentioned phases and coils. Phase currents (red, blue and green) and short circuit current (purple).	284
Fig. 4.18 - Experimental results V/f control with Interturn Short Circuit fault at no load (1.85 Ohm short circuit resistance) in the mentioned phases and coils. Current space vector trajectories [2A/div].	285
Fig. 4.19 - Experimental results V/f control with Interturn Short Circuit fault on the U phase at no load (top), 10 Nm (centre) and 20 Nm (bottom) (1.85 Ohm short circuit resistance) in the mentioned phases and coils. Phase currents (red, blue and green) and short circuit current (purple).	286

Fig. 4.20 - Experimental results V/f control with Interturn Short Circuit fault on the U phase at no load varying the short circuit resistance from 14.3 to 1.85 Ohm. Phase currents (red, blue and green) and short circuit current (purple) on the top; current space vector trajectory on the bottom.....	288
Fig. 4.21 - Detection parameter \bar{x} at no load and rated frequency (50 Hz). HR connection up to about 1 Ohm and ISC detection with full short circuit of the central coil (28 turns) for each phase and short circuit resistance from 20 Ohm to 0 resistance (complete short circuit).....	291
Fig. 4.22 - Detection parameter \bar{x} at no load and rated frequency (50 Hz). HR connection up to about 1 Ohm and ISC detection with full short circuit of the different coils (28 turns) for each phase and short circuit resistance from 20 Ohm to 0 resistance (complete short circuit). The coils are identified with a different symbol only for the phase U.	292
Fig. 4.23 - Detection parameter \bar{x} at different slip values and rated frequency (50 Hz). ISC detection with full short circuit of the central coil (28 turns) of the U phase and short circuit resistance from 20 Ohm to 0 resistance (complete short circuit).....	293
Fig. 4.24 - Detection parameter \bar{x} at rated slip and rated frequency (50 Hz). ISC detection with a variable number of short circuited turns from 1 to 28 (one coil) of the U phase and short circuit resistance from 1 Ohm to 0 resistance (complete short circuit).....	293
Fig. 4.25 – Short circuit current at rated slip and rated frequency (50 Hz). The number of short circuited turns varies from 1 to 28 (one coil) of the U phase and short circuit resistance from 1 to 0 Ohm.....	294
Fig. 4.26 – Detection parameter \bar{x} at rated slip and rated frequency (50 Hz). The number of short circuited turns varies from 1 to 28 (one coil) of the U phase, the short circuit resistance is zero (full short circuit) and the short circuited turns have a resistance that increases from 1 to 2 times the normal value.	295
Fig. 4.27 – Short circuit current at rated slip and rated frequency (50 Hz). The number of short circuited turns varies from 1 to 28 (one coil) of the U phase, the short circuit resistance is zero (full short circuit) and the short circuited turns have a resistance that increases from 1 to 2 times the normal value.	295
Fig. 4.28 – Symmetrical triple three-phase machine concept (left) and magnetic axes (right). In blue, green and orange are highlighted the U, V and W phases of the three inverters (1, 2 and 3).....	296
Fig. 4.29 – Analytical results for the HR detection in the healthy machine matched with the prototype. Zero sequence (top left) 2 nd and 4 th space (top centre) and 6 th and 8 th spaces (top right) of the detection vectors. Evaluated Phase resistances for the U, V and W phases of each inverter (bottom). In blue, green and orange are highlighted the U, V and W phase resistances.	298
Fig. 4.30 – Experimental results at no load, 4A of magnetizing current and 300 rpm speed. HR detection in the healthy machine. Zero sequence (top left) 2 nd and 4 th space (top centre) and 6 th and 8 th spaces (top right) detection vectors. Evaluated phase resistances for the U, V and W phases of each inverter (bottom). In blue, green and orange are highlighted the U, V and W phase resistances. [1V=1Ohm].....	298
Fig. 4.31 – Analytical results for the HR detection of an HR fault of 0.345 Ohm in the phase U of the Inverter 1. Zero sequence (top left) 2 nd and 4 th space (top centre) and 6 th and 8 th spaces (top right) of the detection vectors. Evaluated Phase resistances for the U, V and W phases of	

each inverter (bottom). In blue, green and orange are highlighted the U, V and W phase resistances.....	300
Fig. 4.32 – Experimental results at no load, 4A of magnetizing current and 300 rpm speed. HR detection with 0.345 Ohm of additional resistance in series of phase U of inverter 1. Zero sequence (top left) 2 nd and 4 th space (top centre) and 6 th and 8 th spaces (top right) detection vectors. Evaluated phase resistances for the U, V and W phases of each inverter (bottom). In blue, green and orange are highlighted the U, V and W phase resistances. [1V=1Ohm]......	300
Fig. 4.33 – Analytical results for the HR detection of an HR fault of 0.345 Ohm in the phase V of the Inverter 1. Zero sequence (top left) 2 nd and 4 th space (top centre) and 6 th and 8 th spaces (top right) of the detection vectors. Evaluated Phase resistances for the U, V and W phases of each inverter (bottom). In blue, green and orange are highlighted the U, V and W phase resistances.....	301
Fig. 4.34 – Experimental results at no load, 4A of magnetizing current and 300 rpm speed. HR detection with 0.345 Ohm of additional resistance in series of phase V of inverter 1. Zero sequence (top left) 2 nd and 4 th space (top centre) and 6 th and 8 th spaces (top right) detection vectors. Evaluated phase resistances for the U, V and W phases of each inverter (bottom). In blue, green and orange are highlighted the U, V and W phase resistances. [1V=1Ohm]......	301
Fig. 4.35 – Analytical results for the HR detection of an HR fault of 0.345 Ohm in the phase W of the Inverter 1. Zero sequence (top left) 2 nd and 4 th space (top centre) and 6 th and 8 th spaces (top right) of the detection vectors. Evaluated Phase resistances for the U, V and W phases of each inverter (bottom). In blue, green and orange are highlighted the U, V and W phase resistances.....	302
Fig. 4.36 – Experimental results at no load, 4A of magnetizing current and 300 rpm speed. HR detection with 0.345 Ohm of additional resistance in series of phase W of inverter 1. Zero sequence (top left) 2 nd and 4 th space (top centre) and 6 th and 8 th spaces (top right) detection vectors. Evaluated phase resistances for the U, V and W phases of each inverter (bottom). In blue, green and orange are highlighted the U, V and W phase resistances. [1V=1Ohm]......	302
Fig. 5.1 – Triple three-phase sectored winding for a SPM machine. Machine drawing and winding layout.....	306
Fig. 5.2 – Force generation principle for a solid rotor machine in a dual-winding configuration. In black it is represented the magnetomotive force distribution of a 4-poles winding; in red it is represented the magnetomotive force distribution of a 2-poles winding. The two distributions represent the magnetomotive forces of typical three-phase star connected machines, defined by their α - β components.....	317
Fig. 5.3 – 18 slots and 3 pole pairs sectored winding 9-phase machine. The starting slots of the phases and their magnetic axes are highlighted with crosses in the slots and lines in the back iron respectively.	321
Fig. 5.4 – Triple three-phase MSPM machine control scheme for torque and radial force. ...	333
Fig. 5.5 – Flux and slot current density views. Rated torque at no force condition (left) and with 200N force control (right). The F2pu value is increased from zero to 1 (from left to right).	356
Fig. 5.6 – Stator copper Joule losses as function of the F2pu variable. Rated torque without force (blue), with 20 N (green) and with 200 N (red).	357
Fig. 5.7 – Stator copper Joule losses in the different three-phase subsystems as function of the F2pu variable. Rated torque with 200 N force.	357

Fig. 5.8 – Iron losses as function of the F2pu variable. Rated torque without force (black), with 20 N (brown asterisk) and with 200 N (red). Iron losses distribution (only for 200 N force t rated torque)	358
Fig. 5.9 – Efficiency as function of the F2pu variable. Rated torque without force (dashed), with 20 N (light blue asterisk) and with 200 N (continuous).....	359
Fig. 5.10 – Losses and efficiency as function of the F2pu variable. Rated torque without force (dashed), with 20 N (asterisk) and with 200 N (continuous). Iron losses (green), copper losses (red) and efficiency (blue).....	360
Fig. 5.11 – Machine radial force control at 5 [Nm] torque. The radial force control is 25 [N] static (a, b, c) and 25 [N] dynamic (d, e, f). The ratio F2pu is 0 (a, d), 0.5 (b, e) and 1 (c, f).	361
Fig. 5.12 – Radial force ripple at rated torque and speed with 200 N. F2pu varies from 0 (t = 0 s) to 1 (t = 0.02 s).	361
Fig. 5.13 – Machine torque when the reference is 5 Nm and the force is 25 N static (a, b, c) and dynamic (d, e, f). The F2pu value is 0 (a, d), 0.5 (b, e) and 1 (c, f).	362
Fig. 5.14 – Machine phase currents when the reference is 5 Nm and the force is 25 N static (a, b, c) and dynamic (d, e, f). The F2pu value is 0 (a, d), 0.5 (b, e) and 1 (c, f).	362
Fig. 5.15 – Currents in one sector open winding configurations with standard redundant symmetrical three-phase current control. The torque is 5 Nm.....	363
Fig. 5.16 – Simulated radial force (F) and analytical radial force evaluation (F E) in one sector open winding configurations with standard redundant three-phase current control. Force vector trajectory (a) and its x-y components (b). The torque is 5 Nm. In the legend, with A, B and C (red-purple, green-yellow and blue-black) the open winding conditions of the respective sectors are identified.....	364
Fig. 5.17 – Currents with 5 Nm torque and 0 N reference radial force. Healthy machine (a), standard open windings control (b), radial force compensation by fault tolerant control (c) and, radial force fault tolerant control at no load (d).	365
Fig. 5.18 – FE radial force values with 5 Nm torque and 0 N reference radial force. Healthy machine (a), standard open windings control (b), radial force compensation by fault tolerant control (c), radial force fault tolerant control at no load (d).	366
Fig. 5.19 – Currents with 5 Nm torque and 25 N reference radial force. Healthy machine (a), open phase behaviour with standard machine control (b), radial force fault tolerant control (c), fault tolerant radial force control at no load (d).	367
Fig. 5.20 – FE radial force values with 5 Nm torque and 25 N reference radial force. Healthy machine (a), standard open phase control (b), radial force compensation by fault tolerant control (c), radial force fault tolerant control at no load (d).....	368
Fig. 5.21 – Machine torque when the reference force is 25 N. The torque is 5 Nm (a,b,c) and 0 Nm (d). Healthy machine (a), faulty machine without fault tolerant control (b), radial force fault tolerant control (c), and radial force fault tolerant control at no load (d).....	368
Fig. 5.22 – FE currents values with 5 Nm torque and 25 N rotating reference radial force. Sector A open fault and FTC algorithm.	369
Fig. 5.23 – FE radial force values with 5 Nm torque and 25 N rotating reference radial force. Sector A open fault and FTC algorithm.	369
Fig. 5.24 – Control scheme of the prototype for two DoF bearingless operation.	371

Fig. 5.25 – Numerical simulation of a speed transient at no load from 0 to 3000 rpm, followed by a torque step of 5 Nm (at 0.5 s). The radial force is synchronous with the rotor as in a dynamic mass unbalance until 0.8 s, when the force is set to zero again. The speed, torque (a) and force (b), the d-q currents of each sector (c-e) and the d-q current space vector components (f-h) are plotted.....	373
Fig. 5.26 – Machine start up and rated torque step (t=0.05 s), followed by sector A open phase fault (t=0.15 s) and radial force open loop compensation (t=0.2 s).	374
Fig. 5.27 – Machine start up and rated torque step (t=0.05 s), followed by sector A open phase fault (t=0.15 s) and radial force open loop compensation (t=0.2 s). Three-phase d-q currents of the three sectors (top) and synchronised current space vector components (bottom).....	375
Fig. 5.28 – Machine start up and rated torque step (t=0.05 s), followed by sector A open phase fault with instantaneous radial force open loop compensation (t=0.15 s).....	376
Fig. 5.29 – Machine start up and rated torque step (t=0.05 s), followed by sector A open phase fault and instantaneous radial force open loop compensation (t=0.15 s). Three-phase d-q currents of the three sectors (top) and synchronised current space vector components (bottom).	377
Fig. 5.30 – Machine start up and rated torque step (t=0.05 s), followed by rated force step (t=0.1 s). FTC operation without fault for zeroing the sector A currents (t = 0.15 s) and open phase fault of sector A keeping the FTC active (t=0.2 s).....	378
Fig. 5.31 – Machine start up and rated torque step (t=0.05 s), followed by rated force step (t=0.1 s). FTC operation without fault for zeroing the sector A currents (t = 0.15 s) and open phase fault of sector A keeping the FTC active (t=0.2 s). Three-phase d-q currents of the three sectors (top) and synchronised current space vector components (bottom).....	379
Fig. 5.32 – x-y shaft position in a two DoF bearingless operation with rated force and rated force control at rated speed with sector A open phase fault with FTC (top) and without FTC (bottom).....	380
Fig. 5.33 – Start up and rated torque step (t=0.025 s), followed by rated force step (t=0.05 s). Advanced current sharing control: equal distribution (until t = 0.1 s); matryoshka current sharing (t=0.1-0.15 s); three-phase subsystem B generating (from t = 0.15 s).....	381
Fig. 5.34 – d-q components of the three-phase current space vectors (top) and the general ones (bottom). Start up and rated torque step (t=0.025 s), followed by rated force step (t=0.05 s). Advanced current sharing control: equal distribution (until t = 0.1 s); matryoshka current sharing (t=0.1-0.15 s); three-phase subsystem B generating (from t = 0.15 s).	382
Fig. 5.35 – Start up and rated torque step (t=0.025 s), followed by rated force step (t=0.2 s) with sector A open phase fault. Basic FTC (t=0-0.1 s and 0.2-0.3 s) and optimised FTC (t=0.1-0.2 s and 0.3-0.4 s).....	383
Fig. 5.36 – d-q components of the three-phase current space vectors (top) and the general ones (bottom). Start up and rated torque step (t=0.025 s), followed by rated force step (t=0.2 s) with sector A open phase fault. Basic FTC (t=0-0.1 s and 0.2-0.3 s) and optimised FTC (t=0.1-0.2 s and 0.3-0.4 s).....	384
Fig. 5.37 – Phase currents. Start up and rated torque step (t=0.025 s), followed by rated force step (t=0.2 s) with sector A open phase fault. Basic FTC (t=0-0.1 s and 0.2-0.3 s) and optimised FTC (t=0.1-0.2 s and 0.3-0.4 s).....	385
Fig. 5.38 – Experimental test setup. The three three-phase inverters (a), the control board (b), the machine MSPM prototype and test rig (c), and the rotor shaft with the displacement sensors (d).	386

Fig. 5.39 – Experimental results of a speed transient at no load from 0 to 600 rpm. The radial force is synchronous with the rotor as in a dynamic mass unbalance. The speed, torque (a) and force (b), the current space vector components (c-e) and the total stator copper losses are plotted.....	388
Fig. 5.40 – x-y shaft position. Experimental results of a speed transient at no load from 0 to 600 rpm. The radial force is synchronous with the rotor as in a dynamic mass unbalance. The x-y shaft position is only constrained by a backup bearing with 150 μ m radius.....	389
Fig. 5.41 – Phase currents in the three three-phase inverters. Experimental results of a speed transient at no load from 0 to 600 rpm. The radial force is synchronous with the rotor as in a dynamic mass unbalance. The steady state condition is at rated peak currents.	390
Fig. 5.42 – Stand still bearingless operation experimental results.	391
Fig. 5.43 – x-y shaft position: measured. Stand still bearingless experimental results.....	392
Fig. 5.44 – Bearingless operation at rated speed (3000 rpm): experimental results.	393
Fig. 5.45 – x-y shaft position: measured. Rated speed bearingless operation (3000 rpm). ...	394
Fig. 5.46 – Bearingless operation for a speed transient from 0 to 3000 rpm: experimental results.	395
Fig. 5.47 – x-y shaft position: measured. Speed transient from 0 to 3000 rpm in bearingless operation. The initial transient for centring the shaft at stand still is also shown.	396
Fig. 5.48 – Speed transient from 0 to 1000 rpm (t = 0.3 s), and bearingless control activation (t = 0.6 s). Experimental results.....	397
Fig. 5.49 – x-y shaft position: measured. Speed transient from 0 to 1000 rpm (t = 0.3 s) without position control, and bearingless control activation (t = 0.6 s). Experimental results.	398
Fig. 6.1 – Triple three-phase sectored designs with different segmentation layouts. The original not segmented design is the a) left top.	405
Fig. 6.2 – Triple three-phase sectored design and segmentation concept. The figure also shows the main segmentation parameters.	405
Fig. 6.3 – Triple three-phase sectored design: layout SDa, without segmentation. The turn number is N for each phase.	406
Fig. 6.4 – Zoom of the flux view of the SDc design in the segmentation arc.....	407
Fig. 6.5 – Permanent magnet flux density with and without slotting effect. FEA view. Machine with and without slots (left and right).	412
Fig. 6.6 – Permanent magnet flux density without slotting effect.	414
Fig. 6.7 – Permanent magnet flux density with slotting effect.	414
Fig. 6.8 – Control scheme of a triple three-phase segmented machine design.	420
Fig. 6.9 – Coil pitch effect as function of the external (or internal) segmentation thickness.	421
Fig. 6.10 – Coil pitch effect as function of the segmentation thickness. The internal and external segmentation thicknesses are equally increased of the angle shown in the x-axis.	422
Fig. 6.11 – Coil pitch effect caused by an external segmentation of 17 degrees. Maximum values.....	424
Fig. 6.12 – Coil pitch effect caused by an external segmentation of 17 degrees. Minimum values.....	424
Fig. 6.13 – Coil pitch effect as function of the external segmentation thickness with standard machine control. Maximum flux harmonic values (positive) and minimum flux harmonic values (negative).....	425

Fig. 6.14 – Coil pitch effect as function of the external segmentation thickness with proposed machine control. Maximum flux harmonic values (positive) and minimum flux harmonic values (negative).....	426
Fig. 6.15 – Cogging Torque (no load torque).	426
Fig. 6.16 – Flux view depending on the segmented area design moving from an SDb to an SDc design typology.	427
Fig. 6.17 – Torque with 10 A peak current and standard machine control.....	428
Fig. 6.18 – Torque with 10 A magnitude of the main current space vector (3 rd) and new machine control.....	428
Fig. 6.19 – Torque with 10 A magnitude of the main current space vector (3 rd). Comparison of the proposed control techniques and winding design.....	430
Fig. 6.20 – Manufactured stator prototype.....	433
Fig. 6.21 – 3D CAD of the prototype.....	433
Fig. 6.22 – Winding design for the segmented machine prototype.....	433
Fig. 6.23 – Evaluated thermal behaviour with Simscape. Healthy machine (left) and one sector open phase fault (right) at rated conditions.....	434
Fig. 6.24 – Evaluated thermal behaviour with MotorCad. Healthy machine.....	435
Fig. 6.25 – Thermocouples arrangement: FRONT. The thermocouples are highlighted with the signature [(TC)] in purple.	436
Fig. 6.26 – Thermocouples arrangement: REAR. The thermocouples are highlighted with the signature [(TC)] in purple.	436
Fig. 6.27 – Simscape simulated results. Healthy machine with 5Arms standard current control (about half the rated current), and with sector A, B and C three-phase open faults with standard fault compensation (the current is increased in the remaining healthy phases up to 7.5 Arms).	437
Fig. 6.28 – Experimental results. Healthy machine with 5Arms standard current control (about half the rated current), and with sector A, B and C three-phase open faults with standard fault compensation (the current is increased in the remaining healthy phases up to 7.5 Arms). ...	437
Fig. 6.29 – Exploitation of the empty slots for improving the machine cooling. Concept. ...	438

List of Tables

Table 3.1 – Main machine SVD control parameters.....	172
Table 3.2 – Maximum phase current in case of A1 open phase fault (in p.u. to the value of the healthy machine)	192
Table 3.3 – Comparison of the current space vector trajectories in respect to the healthy behaviour in case of A1 open phase fault. The scale is of 2A/div in all the figures.	194
Table 3.4 – Maximum phase current in case of A1 open phase fault (in p.u. of the value of the healthy machine).	195
Table 3.5 – Comparison of the current space vector trajectories in respect to the healthy behaviour in case of A1 open phase fault. The scale is of 2A/div in all the figures.	196
Table 3.6 – Maximum phase current in case of A1 open phase fault (in p.u. of the value of the healthy machine).	197
Table 3.7 – Comparison of the current space vector trajectories in respect to the healthy behaviour in case of A1, B1, B2, D1 and D2 open phases fault. The scale is 2A/div in all the figures.....	198
Table 3.8 – Maximum phase current in case of A1, B1, B2, D1 and D2 open phase faults (in p.u. of the value of the maximum peak current for the healthy machine).	198
Table 3.9 – Comparison of the current space vector trajectories in respect to the healthy behaviour in case of A1 open phase fault. The scale is of 2A/div in all the figures.	210
Table 3.10 – Comparison of the current space vector trajectories in respect to the healthy behaviour in case of A1 open phase fault. The scale is of 2A/div in all the figures.	212
Table 4.1 - Main machine parameters in its three-phase winding configuration.....	277
Table 4.2 – Simulation of a faulty three-phase IM. Results comparison.	287
Table 5.1 – Machine main parameters used in the model.....	321
Table 5.2 – Self inductance space parameters in μH	323
Table 5.3 – Matrix of the machine space vector inductances in μm (direct sequence interactions \bar{M}_{hp}^+ , and $\bar{M}_{hN_s/2}$)	324
Table 5.4 – Matrix of the machine space vector inductances in μH (inverse sequence interactions \bar{M}_{hp}^-).....	325
Table 5.5 – Table of the machine torque constants for the direct sequences of the armature field harmonics	327
Table 5.6 – Table of the current force constants	328
Table 5.7 – Table of the machine torque constants for the inverse sequences of the armature field harmonics.....	328
Table 5.8 – Table of the magnet force constants for the h-1 components of the armature field harmonics	329
Table 5.9 – Table of the magnet force constants for the h+1 components of the armature field harmonics	329
Table 5.10 – Table of the machine control parameters (FEA).....	355
Table 5.11 – Main machine parameters.	387

Table 6.1 - Main machine parameters of SDA design 421

Table 6.2 – Performance with 10 A magnitude of the main current space vector (3rd) with new control technique. 429

Table 6.3 – Inductance matrix components. Self and mutual inductances between phases of the same sector (highlighted) and of different sector (black). The mutual inductances with the phase UA and VA are shown in the top (yellow) and bottom (blue) respectively. The mutual inductances with the phases of the other sectors with UA and VA are shown in the other columns (black) 431

Table 6.4 – Three-phase open phase and short circuit fault (design comparison). In case of open phase fault, the FTC increases the currents in the healthy phases of 3/2 times the reference magnitude of the main current vector (3rd)..... 432

Introduction

This work shows the main activity carried out in my doctorate. I focused my research on the analysis of multiphase machines for More Electric Aircraft (MEA) applications.

A wide part of the PhD work looks at the methods to model multiphase electrical machines.

The models are firstly used to develop techniques for the on-line diagnosis and mitigation of faults, focusing on open phase, high resistance and inter-turn short circuit faults. In case of open phase faults, various fault tolerant control techniques for different multiphase machines are proposed, showing advantages and drawbacks of them. In particular, the multiphase and the multi three-phase layouts are compared for Induction Machines (IM).

A second part of the PhD is dedicated to the design and control of Multi Sector Permanent Magnet (MSPM) fault tolerant machines.

A radial force control for a MSPM machine is defined with the goal of controlling the radial force for a bearingless operation. Then, a fault tolerant control, that allows avoiding the radial force or also controlling it in case of open phase fault, is proposed. This idea is to aim for a fault tolerant bearingless machine or having the possibility to prevent and mitigating the effects of a bearing fault by the machine control.

The final part of the work is dedicated on a new design of MSPM machine, based on the stator segmentation idea. The proposed design aims to improve the fault tolerance of the machine without significantly affecting its performance in the healthy behaviour. This would reduce the difficulties on the monitoring and fault tolerant control of the standard topology.

Many efforts have been carried out in order to understand and properly control the analysed multiphase machines, allowing the development of accurate models and the realization of experimental tests.

Chapter 1 is an introduction on the MEA idea, highlighting the importance of the use of multiphase machines in the aeronautic field.

A generalized model of multiphase machine, based on the Space Vector Decomposition technique, is presented in Chapter 2. The chapter focuses on distributed winding IM and Surface Permanent Magnet (SPM) machines.

Chapter 3 describes and compares different fault tolerant control techniques for open phase faults in IMs.

Chapter 4 is related to interturn short circuits and high resistance connections.

In Chapter 5, a technique for the radial force control of a MSPM machine is presented, taking into account for different possible machine controls and fault conditions.

Chapter 6 focuses on a new idea of machine design for distributed winding MSPM machines based on the stator segmentation.

CHAPTER 1

Multiphase Machines for More Electric Aircraft applications

This chapter aims to introduce the reader to the process of aircraft electrification that is happening in this historical period, highlighting the importance of efficient and reliable drives for the future aircraft technologies. A focus on multiphase machines is given. Indeed, nowadays, multiphase machines are one of the main proposed solution to improve the performance and the fault tolerance of electrical machines, especially when the power of the system is as high that a standard three-phase drive is no more suitable to sustain it. This is the case of integrated starter-generators for aircrafts.

1.1 Aircraft Industry and Market

The aircraft market is continuously increasing, and because this is happening so fast, the industry must continue to seek opportunities for cost reduction and efficiency improvements to ensure a sustainable growth.

Aviation transported approximatively 3.8 billion passengers on commercial airlines in 2016, and this value is increasing with a rate higher than 7% in the last three years. Tab. 1.I reports the trend of the air passenger traffic [1].

Because most of the flights are between different countries, a key point for the success of the aircraft market is a proper coordination in terms of rules and standards.

The European air travel, for example, is actually responsible for an Air Traffic Management (ATM) of about 26,000 flights daily. In July 2017, the Network Manager has handled the record of one million flights across the EUROCONTROL network and in several occasions there were more than 35,000 flights in a single day [2]. In order to allow the sustainability of the future air transport in Europe, there are already new common rules and procedures (resulting by two

CHAPTER 1

Tab. 1.I – IATA: Statistic on commercial airline.

System-wide global commercial airlines	Passenger traffic (RPK), % Year-on-Year							Passenger capacity (ASK) % Year-on-Year						
	2011	2012	2013	2014	2015	2016	2017 F	2011	2012	2013	2014	2015	2016	2017 F
Global	6.3	5.3	5.2	5.7	7.3	7.4	7.4	6.6	4.0	4.8	5.5	6.7	7.5	7.0
Regions														
North America	2.9	1.0	2.3	2.7	5.3	4.2	4.0	2.8	0.0	2.0	2.5	5.0	4.6	4.4
Europe	8.4	4.6	3.9	5.7	6.0	5.4	7.0	8.9	2.6	2.7	5.1	4.8	5.7	6.9
Asia-Pacific	6.6	6.1	7.2	6.9	10.1	10.9	10.4	7.0	5.3	7.1	7.4	8.4	9.9	8.8
Middle East	10.0	14.7	11.6	12.1	10.4	11.3	7.0	9.8	12.0	12.3	10.9	12.9	13.1	6.9
Latin America	11.3	9.4	6.3	7.0	7.6	4.5	7.5	9.3	7.3	4.5	4.7	6.9	3.4	6.7
Africa	1.6	7.5	4.6	0.3	0.0	9.4	7.5	3.2	6.3	4.0	2.5	-0.2	8.2	7.9

Updated: 06/2017

Single European Sky, SES, legislative packages) for the establishment of the aircraft safety, capacity and efficiency standards.

The aircraft industry is also taking into account the emissions related to the global warming and the climate changes, as it is happening in the automotive sector too. The Advisory Council for Aeronautics Research in Europe (ACARE) has set that by 2020 the air transportation should achieve a 50% reduction of Co2 emissions, 80% reduction of NOx emissions, 50% reduction of external noise and a green design, manufacturing, maintenance and disposal product life cycle [3].

In terms of economic impact, the fuel is still responsible of about 18% of the operating costs, for a total fuel cost of about US\$130 billion every year. As can be seen in Tab. 1.II [4], the impact of the fuel cost is definitely important. Furthermore, the political and economic choices of the different countries of the world significantly affect the cost of the fuel of the total cost for the customers [5]. It results that many efforts aim to increase even more the efficiency of the propulsive and auxiliary systems.

Tab. 1.II – IATA: Fuel Impact on Operating Costs.

Year	% of Operating Costs	Average Price per Barrel of Crude (US\$)	Break-even Price per Barrel (US\$)	Total Fuel Cost
2004	17.3%	US\$38.3	US\$34.7	US\$65 billion
2005	22.0%	US\$54.5	US\$52.0	US\$91 billion
2006	27.2%	US\$65.1	US\$68.1	US\$127 billion
2007	28.6%	US\$73.0	US\$81.7	US\$146 billion
2008	35.7%	US\$99.0	US\$83.3	US\$203 billion
2009	28.2%	US\$62.0	US\$59.1	US\$134 billion
2010	26.9%	US\$79.4	US\$89.8	US\$151 billion
2011	29.8%	US\$111.2	US\$116.1	US\$191 billion
2012	32.3%	US\$111.8	US\$117.1	US\$228 billion
2013	32.0%	US\$108.8	US\$114.8	US\$231 billion
2014	29.3%	US\$99.9	US\$107.4	US\$224 billion
2015	24.3%	US\$53.9	US\$72.5	US\$175 billion
2016E	18.8%	US\$44.6	US\$61.7	US\$133 billion
2017F	17.4%	US\$54.0	US\$68.7	US\$129 billion

Updated: 06/2017

For the longer-term future aircrafts, it is estimated that the development of hybrid-electric and battery-powered aircrafts could contribute to meet the industry goal of reducing aviation’s global carbon footprint by 50% by 2050, compared to 2005. Indeed, the actual technology is already mature, and huge efforts will not result in equivalent improvements, while the aircraft electrification process seems to be a good possible solution. A study from Munich-based think tank Bauhaus Luftfahrt (“Ce-Liner”) finds that larger electrically powered commercial aircraft could be possible from around 2035, and could cover routes of up to 1600 km in the subsequent years, assuming continuing strong progress in battery technology [6]. Of course, the increase of the electrical power on-board makes the efficiency and reliability of the electrical grid, the power generators and the drives a central point in the research for the future technologies. That is why there is such a spread of projects related to the More Electric Aircraft (MEA), More Electric Engine (MEE) and All Electric Aircraft (AEA) applications in the universities and companies around the world. In terms of European research, the most important programme is Clean Sky, where the collaboration between industries and universities is resulting in new idea and a series of demonstrators that aim to reduce the “emission and noise footprints of the aircraft with new engine architectures, improved wing aerodynamics, tighter composite structures, smarter trajectories, and more electrical on-board energy” [7].

1.2 The idea of More Electric Aircraft

The aerospace industry challenges are similar to the automotive industry ones in terms of emissions, fuel economy and costs. As in the automotive market, the aerospace trend is to move toward the increasing use of More Electric drives.

The MEA concept provides for the utilization of electric power for all the non-propulsive systems of an aircraft. The traditional systems are also driven by hydraulic, pneumatic and mechanical sources. These non-electrical systems need a heavy and bulky infrastructure for the

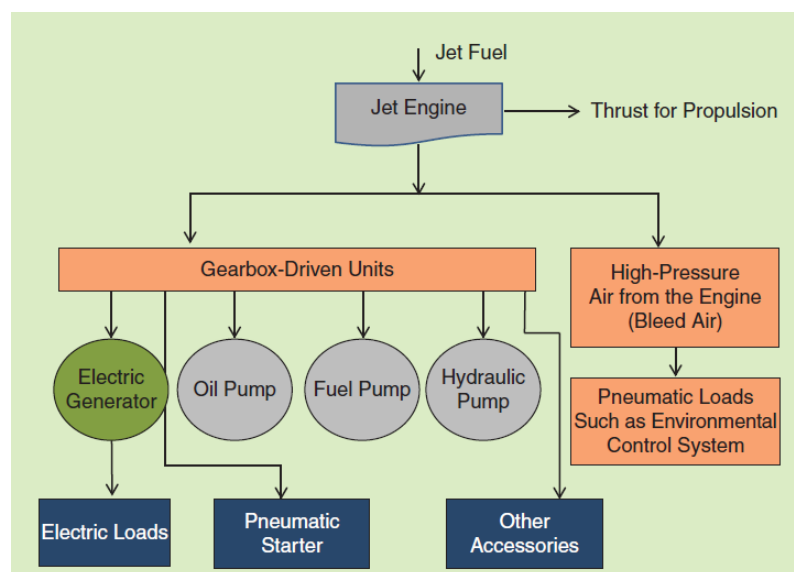


Fig. 1.1– Power flow in a standard civil aircraft.

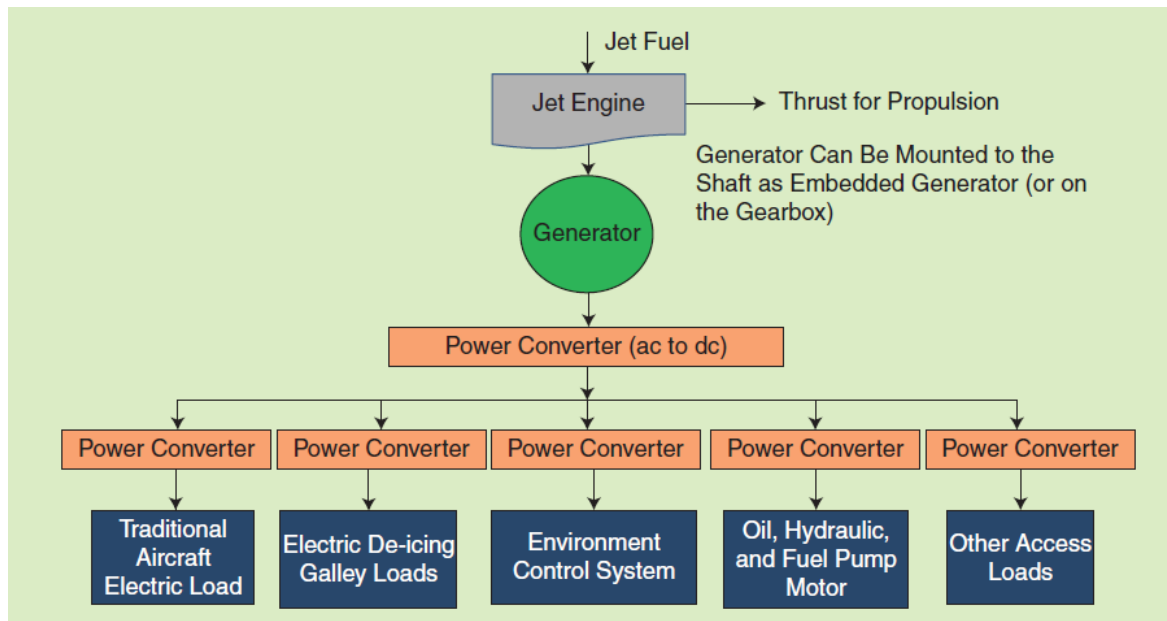


Fig. 1.2 – Power flow in a civil MEA.

power transmission, and the difficulties on the diagnosis and localization of the faults limit their availability. Fig. 1.1 [3] shows a standard power flow in a civil aircraft.

Instead, in a MEA design, the jet engine completely provides the aircraft trust, and an embedded generator provides the power required by all the electrical loads, as shown in Fig. 1.2 [3].

The Airbus Boeing 787 Dreamliner is an example that represents the recent industrial development of the MEA technology, and similar developments can be found on the other MEAs.

Boeing 787 Dreamliner was designed to be the first airliner with the use of composite as the primary material of its airframe and to move toward the idea of MEA, with the aim of increasing the efficiency of about 20% [8]. The advancements in engine technology, provided by GE and Rolls-Royce, are the biggest contributor to the airplane's overall full efficiency improvements [9]. To meet the requirements in terms of efficiency, reliability, availability, lightness and costs, one of the most important improvement on the design is that it includes mostly electrical flight systems, with a bleed-less architecture that allows extracting more efficiently power from the propulsive system, by two generators on each engine, and electrical brakes (rather hydraulically actuated brakes). The total electrical power (1 MVA) is subdivided in two 500 kVA channels, and two on the Auxiliary Power Units (APU), increasing the efficiency of the propulsion system. What has traditionally powered by bleed-air from the engine has been transitioned to an electric architecture. In particular, the only left bleed system on the Boeing 787 is the anti-ice system for the engine inlets [10, 11].

Furthermore, the 787 can be started without any ground power. To start the engine, the APU battery system is used to power the engine generators that start the engines in motoring mode [11]. Of course, owing to the starting profile, together with the emergency load profile, the sizing and the selection of the batteries have to be redesigned in MEA to meet the new power requirements, increasing the complexity of the new generation aircrafts [12].

787

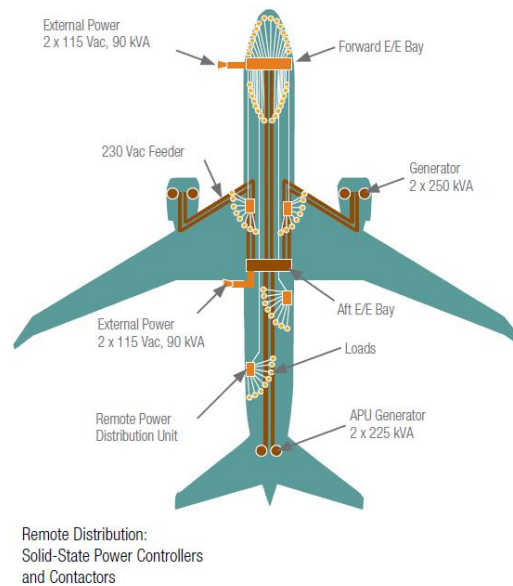


Fig. 1.3 – The MEA concept on Boeing 787.

Because of the essential reliability of the total system, moving to an electrification of the aircraft needs to introduce redundancies in the electrical system, and the final layout is as the one shown in Fig. 1.3 [11]. As example of this redundancy, Boeing 787 has demonstrated that it can fly for more than six hours with only one of the two engine (indeed it is a twin-engine aircraft) and one of the six generators working [13].

The no-bleed architecture of the Boeing 787 affects also its electrical systems, where a new 230 V ac at 360-800 Hz and ± 270 V dc voltage lines are added to the traditional 115 V ac at 400 Hz and 28 V dc. The ± 270 V dc voltage is reached by auto-transformer-rectifiers.

Gearboxes connect the generators to the engine, working at a variable frequency (360-800 Hz) proportional to the engine speed. This allows avoiding the constant speed drive of the Integrated Drive Generator (IDG), which is the most complex component. As a result, the IDG reliability increases using an easier and cheaper technology.

The Boeing 787 is a study example that shows the actual available technology for civil aircrafts and represents the efforts needed to introduce the MEA technology on-board.

1.3 The idea of More Electric Engine

The aviation industry has always pushed the boundaries of technology in order to create quieter and more efficient aircrafts, and even before the first light of the More Electric Boeing 787 Dreamliner, the main companies (as GE and Rolls-Royce) were looking on developing the next aircraft technology: the More Electric Engine. The idea of MEE is to replace all the accessories mechanically driven by the engine (oil, fuel and hydraulic pumps and the generators) with electrically driven ones, and produce the needed electrical power by embedded generators

directly attached on the engine shaft, rather than connect them by means of a mechanical gearbox [14, 15]. Furthermore, one of the key features needed to realize a MEA technology, is that the electrical generator can start the engine and can provide the electrical power to the loads with enough efficiency and reliability. Indeed, all the non-propulsive power comes from these embedded generators, and they must reach a level of availability and maturity that ensures a neglectable risk of failure for the system.

The MEE requirements need new architectures and technologies of electrical machines and drives. There are criticalities of having a high power and high power density electrical machine embedded on the shaft of the propulsive system that satisfies the requested reliability [16]. In particular, the machine might rotate at high speed (up to 10-50 krpm) in a harsh environment with high temperatures and vibrations. Furthermore, there are space and assembly limitations. That is why the research is focusing so much on the development of MEE solutions.

Fig. 1.4 [17] shows an example of embedded starter/generator.

To design a MEE it is essential to choose where to locate the starter/generators and the other generators, and the topology of the electrical machines.

Embedded starter/generator location

The generators could be placed on the Low Pressure shaft (LP) or on the High Pressure Shaft (HP) of the turbine engine. As can be seen from Fig. 1.5 [17], the two locations make the machine work at different pressures, temperatures and rotational speeds.

The rotational speed affects the size of the generator once its output power is fixed. The generators on the LP shaft will have a lower power density than the generators on the HP shaft (rotating at about 10000-20000 rpm). The temperature is lower on the LP side, since the HP

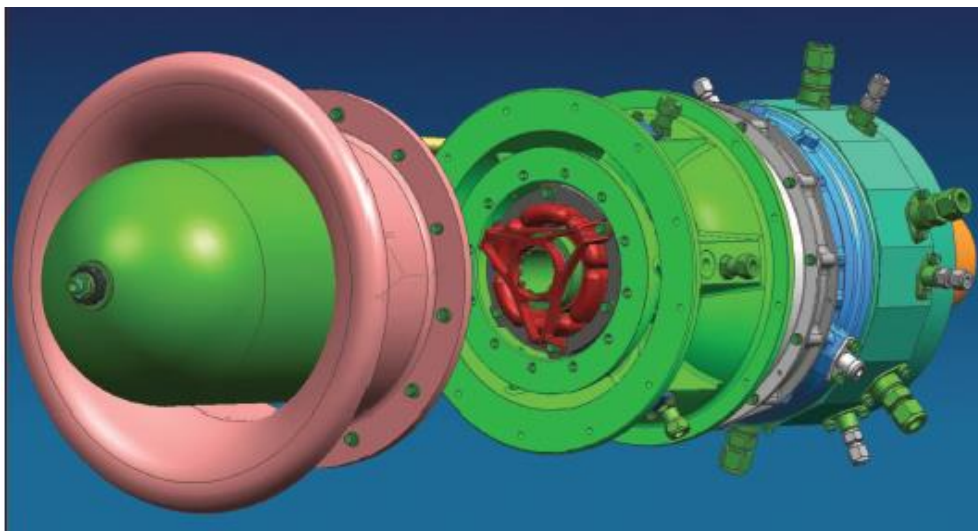


Fig. 1.4 – Rolls-Royce electric starter/generator embedded in the gas turbine engine.

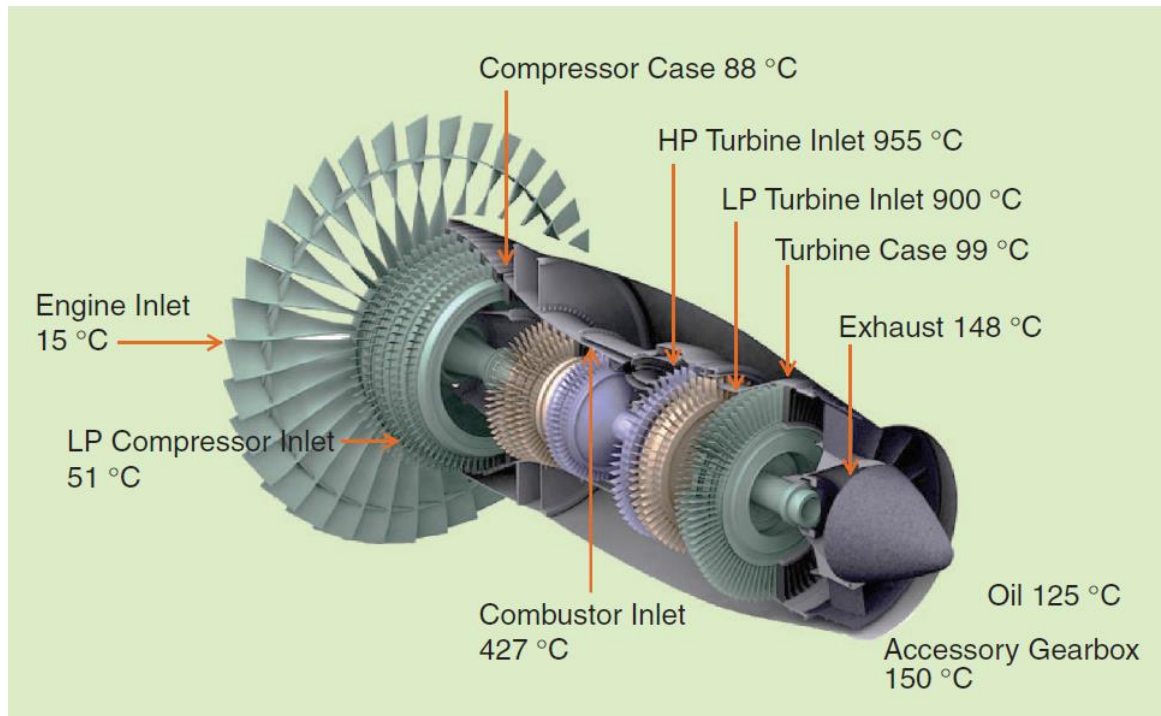


Fig. 1.5 – Operating temperatures in a typical jet engine.

generator would be near the exhausted air outlet (with an ambient operating temperature around 300-400 °C), but the lower pressure reduces the natural thermal cooling of the generator [18].

A typical MEE layout is shown in Fig. 1.6 [17]. As the starter/generator is placed on the HP shaft, it is one of the most stressed drives, because of the high temperature environment [19].

Embedded starter/generator machine topologies

According to [14], the main electrical machine topologies used for starter/generator application are:

- Switched Reluctance Machine (SRM)
- Permanent Magnet Brushless Machine (PMBM)
- Induction Machine (IM)

The main advantage of SRM is their robustness, reliability and availability in a harsh environment, owing to the absence of permanent magnets and windings on the rotor. However, its airgap must be larger than the other topologies in order to reduce the torque pulsations and acoustic noise produced by its double saliency. Furthermore, in high speed applications the fast pulsating fields might cause high rotor losses.

PMBM are preferred for their higher power density, torque density, power factor, efficiency and easy controllability when compared with SRM and IM. In case of fault, the PM machines are intrinsically less fault tolerant because of the presence of the induced back emf and the demagnetization issue [20].

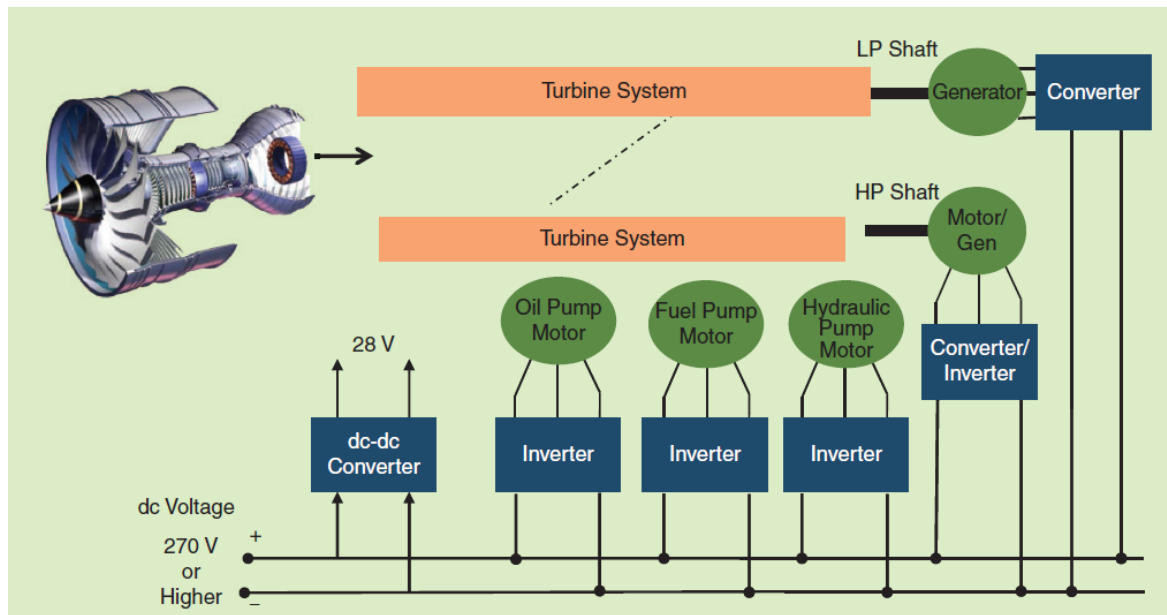


Fig. 1.6 – A typical MEE layout.

IM are robust, simple and cheap, but their power factor, power density and torque density are significantly reduced when compared with PMBM. Furthermore, the control of an IM is more complex and in case of short circuit fault, the rotor coupling makes the magnetic isolation of the healthy phases by the faulty ones almost impossible. Multiphase designs allow increasing the fault tolerance of IM, but they require complicated control techniques. The temperature tolerance and the easy sensorless control operation make IM still an interesting solution for MEE application.

Furthermore, the harsh environment and the ambient temperatures (possibly exceeding 250 °C) make the drive requires materials such as PMs and insulations close or beyond their operating limits. In [14] the HP S/G is a PMBM, while the generator on the LP is a geared SRM, and in [16] many type of PMBM S/G are compared in terms of fault tolerant solutions, highlighting the necessity of efficient cooling systems for its application, while in [18] a IM is preferred. Hence, new materials and cooling systems must be adopted for both the machine and the power electronic, and the choice of the best electrical machine for MEE applications are still to be defined.

The evaluation of the final drive reliability is a key point to allow introducing it on-board of an aircraft, because the safety of the system must be guaranteed over the performance and the efficiency. In the section CS-E 510 of the Certification Specifications for Engines (CS-E) of the European Aviation Safety Agency (EASA) it is reported that the probability of hazardous engine effects must be predicted to occur at a rate not in excess of 10^{-7} per engine flight hour for each engine. The probability that this event rises from a single failure cause must be predicted to be lower than 10^{-8} per engine flight hour. Major effects are constrained to 10^{-5} per engine flight hour. Indeed “it is recognized that the probability of Primary Failures of certain single elements cannot be sensibly estimated in numerical terms” [21]. These specifications show the importance of the research on reliable and fault tolerant drives for MEA applications. Section 1.5 focuses on the multiphase machine topology as a possible reliable solution.

1.4 State of the Art and Applications of Multiphase Drives

Since nowadays the electrical machines are no more directly connected to the grid, the number of phases can be arbitrary, becoming a potential design variable. A multiphase system differs from the standard single, double and three-phase ones, for having a number of phases (m) higher than 3. The high research interest on multiphase machines rises from the idea that for each new phase there is an additional degrees of freedom that can be exploited to implement more complex machine controls and designs. Of course, this complexity results in higher performance, reliability and control flexibility. The scheme of a multiphase drive connected to a standard three-phase grid is shown in Fig. 1.7 [22].

The advantages of a multiphase machine depend on the considered machine and winding topology, but some of them are intrinsic. In particular, multiphase machines allow splitting the total power of the system among an increased number of phases. Reducing the power on each phase results in a derating of the power electronic components needed for the converter that feed the machine. This can be explained taking as example a double layer three-phase winding machine with two series coils for each phase located in the same slots (U1-U2, V1-V2 and W1-W2). The two coils of each phase can be no more series connected and it is possible to consider them as two different phases, each connected to its new three-phase subsystem (U1-V1-W1 and U2-V2-W2). Two independent converters can feed the new three-phase windings, easily realizing a design of a six-phase drive. Feeding the new windings in order to control the machine with the same currents of the equivalent three-phase drive, the phase voltages that must be provided by each converter are half time the voltages required by the previous machine design. On the other hand, if the same voltage is kept, increasing the turns number the converter power switching can bear half of the current. This advantage is definitely important for high power drives, as in the electric ship propulsion [23-29], high power turbo compressors [30] and MEEs [18, 31-33], but it is also suitable for low voltage applications as in the automotive industry [34, 35]. Even if this PhD work is focused on multiphase electrical machines, it is worth to highlight that a similar approach, for reducing the switching device rating, can be adopted for power electronics, for example opting for a multilevel converter topology [36]; or even hybrid solutions of multilevel and multiphase systems can be proposed [37].

Moving toward multiphase drives means that the standard approach to the machine design must take into account also for the possibility to control the currents in the new phases with different control techniques than the one used for three-phase drives. That is why it is quite common to

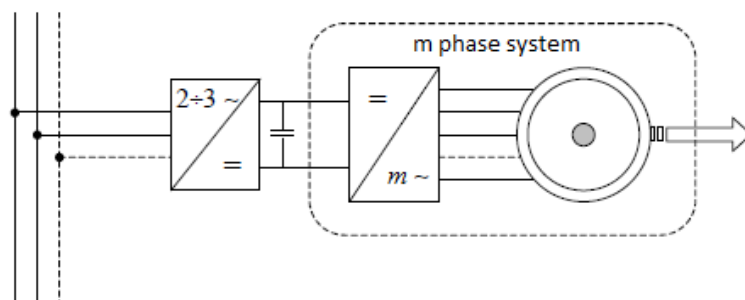


Fig. 1.7 - Multiphase system connected to a standard three-phase grid.

CHAPTER 1

place the new phases in different positions from the one of a three-phase machine, or even better to do a completely new winding design. This enable to:

- inject more independent currents in the phases;
- make possible the control of more harmonics of the magnetic field in the airgap.

As known, the constraint on the current control of a three-phase winding is related to its star connection. Owing to the star connection, the sum of the three currents must be equal to zero. This results on the possibility to independently control only two currents. While, in a multiphase machine with a single star connection the number of independent currents are $m - 1$; and in case of more stars (N_{star}), the independent currents are $(m - N_{star})$.

By the modelling of rotative electrical machines, it results that there is a direct relation between the armature magnetic field in the airgap and the stator currents. In many cases, the windings are placed in such a way that for each pair of added independent currents it is possible to completely control an additional harmonic of the armature field. Understanding and implementing these more complex control techniques needs a good experience on machine modelling, and many efforts have already been done in the past in order to clarify how to do this [38, 39].

The advantages of this improvement on multiphase electrical machine design and control can be summarized in:

- performance;
- fault tolerance and diagnosis;
- new control techniques.

Performance

A multiphase machine design and control can significantly increase the machine performance in terms of torque density. Indeed, the instantaneous magnetomotive force distribution depends on the position of each phase and on the value of the current passing into them. The position of the phases is generally constrained by the number of slots and the winding assembly feasibility, while the star connections are the only limit to the multiphase current control. Usually the design methods aim at maximizing the fundamental spatial harmonics of the magnetomotive force distribution, while minimizing the non-fundamental ones; that for a multiphase machine must be done taking into account of the phase shift control of the currents. Further improvements have been also proposed to increase the average torque exploiting the higher harmonics of the spatial distribution. These methods are named as current harmonic injection [40-45]. However, the use of higher order harmonics in the torque production must be investigated for each machine design and topology, because the order of the space harmonic significantly affects the efficiency of the torque production [43]. Furthermore, eliminating higher order harmonic fields in the airgap makes possible to mitigate the torque ripple and the machine noise. Multiphase machines allow reducing the torque ripples, because the harmonics that have the same order of the ones generated also by the rotor can be controlled to be deleted or minimized, reducing also their related losses [27, 46].

Fault tolerance and diagnosis

In case of aircraft applications, the most important goal of a drive is its reliability, and this is the main reason why multiphase machines are considered a suitable solution for MEA applications [20].

Faults in electrical machines can be mainly summarized in high resistance connections, open circuit and short circuit faults related to the winding deterioration. However, also eccentricities, bearing faults, rotor cage faults, permanent magnet demagnetization and sensor faults are related to the electromagnetic behaviour of the electrical machines, and suitable designs and controls can be proposed to detect or mitigate their effects.

In terms of fault tolerance, multiphase machines can be seen as a system with an internal redundancy: when one of the phases is opened, the others can help to compensate the missing power, minimizing the performance derating and avoiding a machine failure. However, the optimization of the fault tolerant control strategy is something that is not always easy to define because it depends on the machine topology [47-50] and the control strategy. One solution to compensate the open winding fault is to open all the legs of the inverter feeding the faulty system, and this is a choice often proposed for machines with three-phase inverters connected to three-phase star connected windings. However, it is also possible to keep suitable currents in the remaining healthy phases of the faulty subsystem in order to improve the fault tolerant performance [51]. Many works have already published to solve the problem of open circuit faults, and it seems that the methodologies on how to deal with this fault are quite mature. Instead, the compensation of the other faults seems more complex to manage and most of the works have been done for three-phase machines.

High resistance connections are easily compensated by the standard PI regulators, even if to obtain better performance additional inverse sequence or resonant regulators can be used in a fault tolerant control configuration, as in the diagnostic technique based on negative sequence regulators in [52], generalized in [53] and [54] for multiphase machines. Even if high resistances in one phase are not in general one of the most critical fault, their diagnosis is essential to detect a wrong connection or an undesired localized temperature increase in one phase in order to derate the machine and plan in advance the maintenance of the drive.

Many efforts are oriented on finding a suitable control technique that avoids the machine failure in case of short circuit faults. In [55] and [56] the fault tolerant control aims to maintain the machine performance as in the healthy behaviour significantly increasing the phase currents, in [57] the short circuit current is kept to zero compensating the back emf of the faulty phase by the remaining healthy ones. However, one of the main problem of the short circuits in electrical machines is that an on-line fault detection is needed, before putting into effect whatever fault tolerant algorithm.

The on-line detection of short circuit faults is a complex topic and it requires accurate models [58-60], electrical signature analysis [61, 62] or artificial intelligence techniques in order to allow discriminating this fault by the other topologies [63, 64]. As alternative solution, a specific wire design for the on-line detection of the fault is proposed in [65, 66], where the wires have a shelter used for the fault early detection. Because of the complexity of the short circuit

detection and compensation, other researches are also looking for solving the problem by fault tolerant designs, where the advantage of multiphase machines can be found in the possibility to place subsystems of phases in localized stator areas in order to make the various subsystems more independent [67-69].

Bearing faults are investigated by electrical signature analysis in [61, 70], while the eccentricities are detected by the back emf induced in additional windings in [71] and by electrical signature analysis in [72]. However, their compensation is possible only if there is a control on the machine radial forces, as discussed after in the part related to the new control techniques of multiphase machines.

Rotor faults depend on the analysed machine topology. In case of squirrel cage, for example, the most analysed rotor fault is the open fault of one bar. The cage faults is mainly analysed by electrical signature analysis [73], pendulous oscillation techniques [74] or by the monitoring of the external magnetic field [75]. Instead, in case of permanent magnet machines, the demagnetization fault is one of the most critical. The permanent magnet demagnetization is detected by sensing coils in [76], by the current signature analysis in [77, 78], by the back emf space vector harmonic content in [79], and by the back emf space vectors in [53] by means of the additional degrees of freedom of multiphase machines.

Solutions to reduce the effect of a rotor fault are presented in [80] for a squirrel cage broken bar, where a fuzzy logic controller is used, and in [81, 82] for the demagnetization of the PM, by means of a reluctance assisted design. However, most of the research on the rotor faults is still focused on the detection algorithms.

Finally, sensors fault are critical mainly for the current, voltage and speed-position sensors. The current sensor fault detection can be based on the average normalized value of the phase currents as in [83], or by more complex methods as Kalman filter or observer based as the works in [84, 85] that are generalized for also the other sensor faults. Considering the case of speed-position sensor fault, there are already many algorithms that allow controlling the electrical machines as what is called as a sensorless configuration. The techniques for the sensorless control of three-phase machines have been deeply studied and applied also in the industry. Alternative techniques for multiphase machines sensorless operation have been found for both induction and PM machines. In [86] the authors propose a sensorless technique that exploit the control of the third harmonic field of a seven phase machine in order to implement an alternative flux observer, while in [87] the sensorless technique based on the rotor slot harmonics is improved using the additional degrees of freedom of a five and a six phase machine. The control of higher harmonic fields is also proposed for the sensorless control of a nine phase IPM machines with high frequency signal injection techniques in [88].

To conclude, if a stop for unscheduled maintenance is very expensive or not accepted, the design and control of such more fault-tolerant complex drives may be justified, otherwise the advantages of multiphase machines must be evaluated in each application weighting the improved performance with the costs related to the increased number of devices.

New control techniques

In [89-91] an interesting multi-machine control is proposed. More machines are independently controlled even if their windings are series connected and fed by the same converter. This is possible because of phase transpositions. The phase transpositions change the sequences of the currents, or their relative shift angle. Each series machine, designed to interact only with the fundamental current sequence resulting in its winding, will have the additional losses related to the current sequences that are not useful for its torque production. This seems to be a really promising solution for applications in which the increased losses and the reduced efficiency of the machine is preferred in order to reduce the space and the costs required by the additional converters needed by each machine in the standard solution.

Another interesting control of a multiphase machine is the radial force control. Indeed, if the machine windings of an electrical machine are not symmetrical under each pole pair, also the even harmonic fields appear. These fields can be controlled in order to create a radial force that can compensate eccentricities, bearing faults or even levitate the rotor of the machine. This approach has been used to develop bearingless machines for both squirrel cage IM, as in [92, 93], and PM machines, as in [51, 94-96]. These solutions can be an alternative to the use of active magnetic bearings in high speed applications [97].

1.5 Multiphase Machines as a Fault-Tolerant solution for MEA applications

The reliability is essential in aeronautical applications, where many devices must be considered in the chain of faults that can result in the failure of the system. Generators, flaps actuators, aileron actuators and fuel pumps are some of the most critical drives, and they require being fault tolerant. Where the fault tolerant feature is used here after for MEA drives meaning that the analysed fault can be managed in order to not bring to its system failure even if at reduced performance. Indeed, in [98-100] the accepted probability of losing the control of the aircraft (for example by rudder jamming) is evaluated to be around 1×10^{-9} per hour flight.

However, the fault probabilities of three-phase drives can be evaluated as in Tab. 1.III [20].

Because of the strict regulations in aerospace applications, the critical components should not have a derating of torque or power in case of an electrical fault and the fault must not affect other components [20].

From Tab. 1.III it can be noticed that the faults in the electronic devices are more likely to happen. To mitigate these faults, it is quite common to have more dc grids with different dc bus. The control is also desired to have an on-line detection of the faults in order to detect and possibly mitigate the more probable faults: switching device breakage or open circuit and short circuit winding faults.

Tab. 1.III - Electric and electronic failure rates in three-phase drives.

Cause of failure	Failure rate/phase (per hour)
Open-circuit in windings	1.3×10^{-5}
Open-circuit in connections	1×10^{-6}
Open-circuit in others	0.4×10^{-6}
Short-circuit between phases	6.7×10^{-6}
Short-circuit in connections	1×10^{-6}
Short-circuit in others	0.4×10^{-6}
Total electrical failure	6.6×10^{-5}
Power supply	5.4×10^{-5}
Power electronic controller	8.5×10^{-5}
Control signal	1.3×10^{-5}
DSP failure	1×10^{-5}
Total electronic failure	1.5×10^{-4}

Having a precise evaluation of the fault probabilities of all the devices in an aircraft is really complex, however the authors in [99] give an interesting analysis of the fault probability of an electromechanical actuator, reported here as an example to understand how to meet the aircraft safety requirements. In Fig. 1.8 [99] there is a fault-tree analysis of a typical position-controlled electromechanical actuator.

The probability of the actuator failure (1.61×10^{-4} per hour flight) is too high, needing a fault-tolerant architecture, as the one of Fig. 1.9 [99], where a dual-lane solution for the electrical system is proposed.

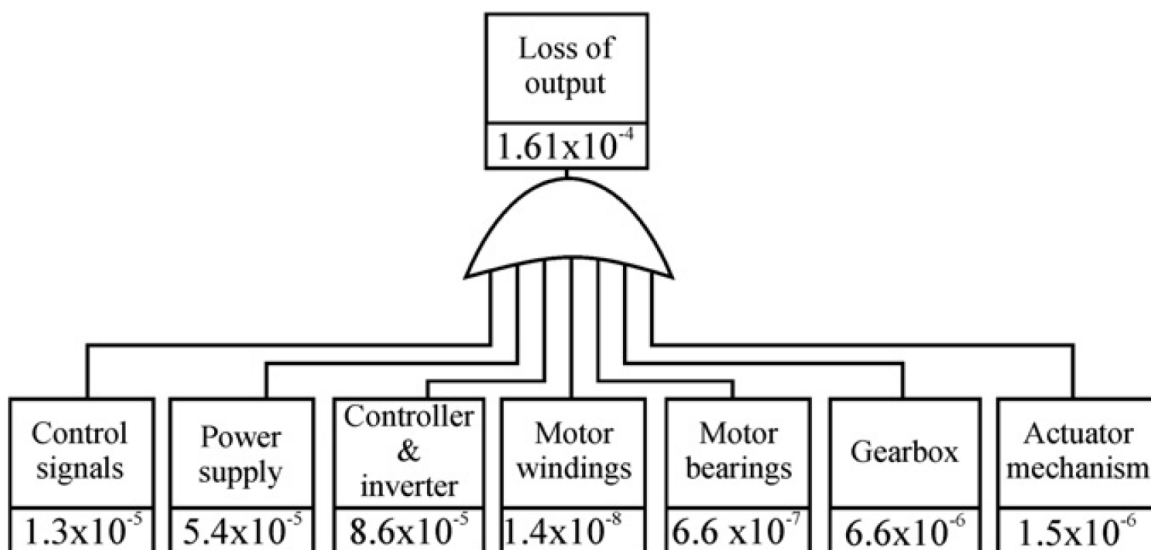


Fig. 1.8 - Single channel electromechanical actuator fault-tree (probabilities given per hour flight).

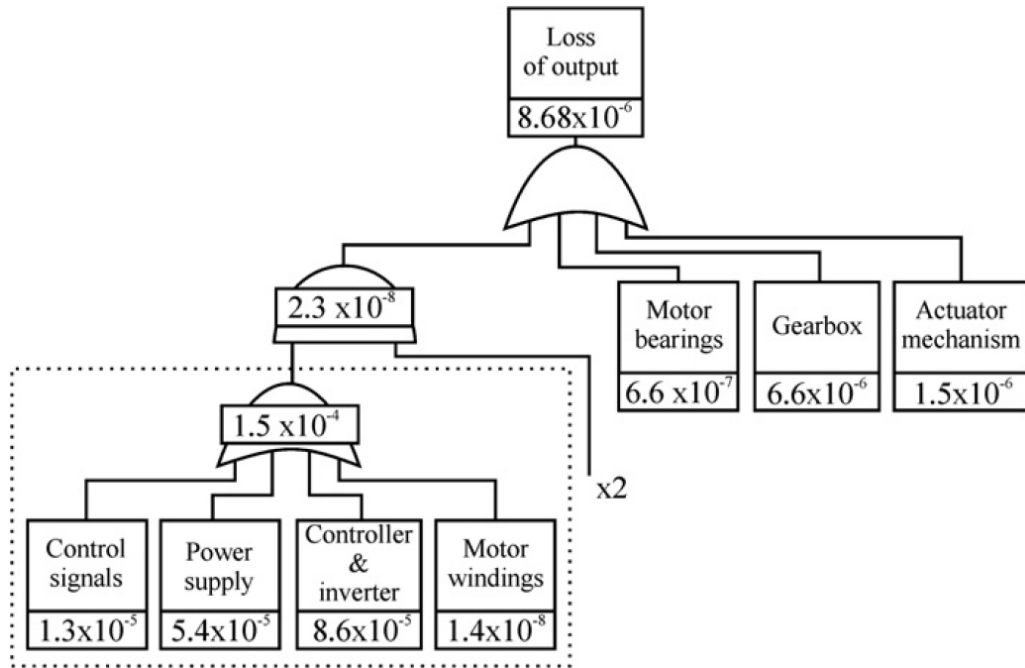


Fig. 1.9 - Dual-lane electromechanical actuator fault-tree (probabilities given per hour flight).

Having a dual-line solution allows increasing the reliability of the complete system up to 8.68×10^{-6} per hour flight. Finally, a further redundancy of the whole system must be adopted in order to reach a sufficient level of reliability ($<1 \times 10^{-9}$). This means that at least two redundant actuators are needed.

As previously mentioned, a different analysis must be carried out for each drive, in particular for the generators of MEE applications. Indeed, there are many additional criticalities (related to the harsh environment, vibrations and high power density requirements of these electrical machines) but the possibility to have them completely embedded with the turbine shaft allows avoiding the gearbox, one of the most critical mechanical components.

However, the example of the electromechanical actuator shows that, because by standard drives the required reliability and availability cannot be reached, the way to reach the fault

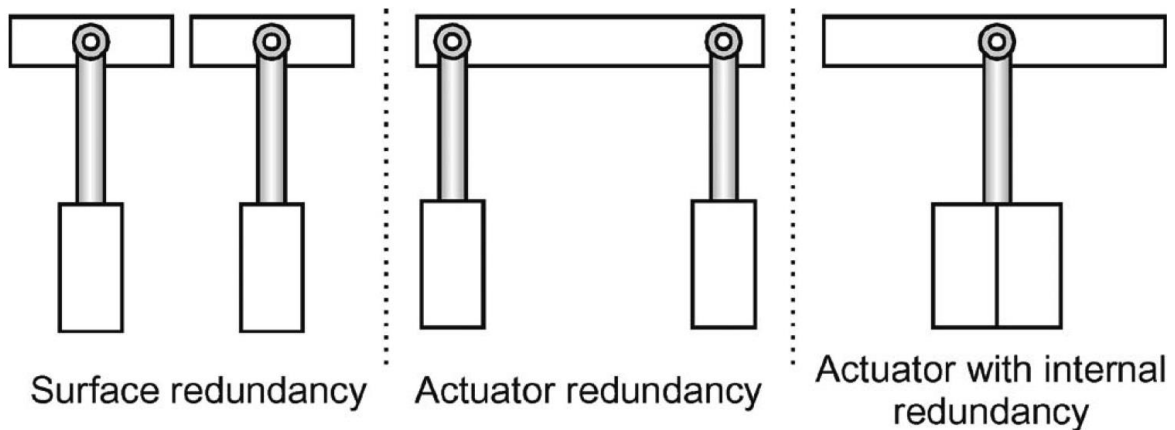


Fig. 1.10 - Method of flight control redundancy.

tolerance of a system is by means of redundancies. An easy way to explain the different redundancies can be done considering the flight control actuators, as in Fig. 1.10 [100].

The actuator can have a twin acting on two different surfaces (surface redundancy), having the drawback of a possible jam of the broken actuator in an undesired position. Other solutions are to have the two actuators on the same surface (actuator redundancy), or having an intrinsic redundant drive (internal redundancy). In addition, hybrid redundancies can be used. The goal of the research on multiphase machine fault tolerant drives is to give them an additional internal redundancy from the electrical point of view. The goal of this internal redundancy is to increase the reliability of the system as shown in the previous example of Fig. 1.9. In some cases, multiphase machines are also proposed for improving the drive performance in order to reduce the probability of the failure of the mechanical components (for example by low torque ripple and bearingless solutions).

As shown in Fig. 1.11 [100], once the machine design is defined, a first differentiation of the possible redundancies of a multiphase drive can be done considering only the electrical circuit. Many other and hybrid solutions can be adopted, but these are the more common in IM and PM ac drives. The layout mainly depends on the internal connection of the phases and on how they are connected to the power electronic devices. It is worth noticing that in reality there is also a magnetic coupling of the phases inside the machine, but with a proper control and design it is possible to make an easier comparison of the layouts neglecting the coupling. With this approximation, the multiphase drives can be summarized in [32, 99, 100]:

- Multiphase;
- Multi single-phase;
- Multi three-phase.

A multiphase layout consists of a single multiphase winding with all the phases connected to the same star. The machine has all the phases fed by a single converter. In a standard multiphase drive there are many critical faults that affect the complete system and can bring with high probability to a failure of the drive, as dc bus failure, short circuit fault of a switching device and short circuits in the winding. To avoid the failure of the system in these scenarios, one of the more reliable solution is the multi single-phase, where independent converters feed the phases. In this case, each phase affects the others only by the non-electrical couplings, significantly reducing the spread of the fault. However, this solution is more complex, expensive and less efficient. Furthermore, even if each fault is contained, the probability of having a fault is increased because of the higher number of switching devices. The multi three-

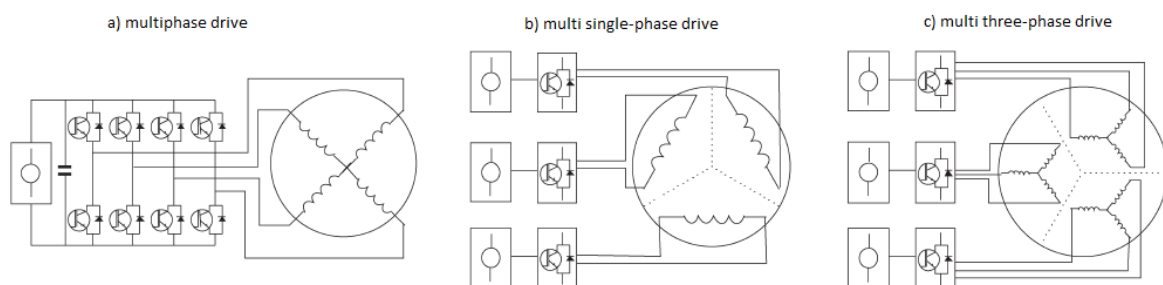


Fig. 1.11 - Redundancies of multiphase machines.

phase solution is an intermediate one. The additional components are only the dc buses. Of course, also multi-four phase, multi-five phase and so on can be adopted. However, the three-phase layout is interesting for the maturity of the three-phase technologies and because three is the minimum number of phases that allows having a vector control of the machine even if only one subsystem is healthy and all the others are open. Furthermore, increasing the number of the phases in each subsystem makes the control of the machine more complex (the idea of the redundant three-phase control, as in [101], must be abandoned) and the exploitation of the dc bus voltage is reduced, as can be seen in [102, 103].

To enhance the fault tolerance, the subsystem of phases may be also physically, magnetically and thermal isolated, but it is usually hard to meet the fault tolerant requests without affecting the system performance [68].

In this thesis, the focus is on standard machine design with multi three-phase winding solutions for fault tolerant controls. Only in some cases, the stars are connected together to realize a completely multiphase drive; in order to compare the proposed control techniques in the two configurations.

References:

- [1] IATA, *Fact Sheet: Industry Statistics*, 2017.
- [2] EUROCONTROL. (2017). *EUROCONTROL actual passenger traffic*. Available: <https://www.public.nm.eurocontrol.int/PUBPORTAL/gateway/spec/index.html>
- [3] K. Rajashekara, "Parallel between More Electric Aircraft and Electric/Hybrid Vehicle Power Conversion Technologies," *IEEE Electrification Magazine*, vol. 2, pp. 50-60, 2014.
- [4] IATA, *Fact Sheet: Fuel*, 2017.
- [5] IATA, *Fact Sheet: Aviation Charges, Fuel Fees and Taxes*, 2017.
- [6] IATA, *Fact Sheet: Thechnology Roadmap for Environmental Improvement*, 2017.
- [7] <http://www.cleansky.eu/>. (2017). *Clean Sky web site - Achievement Timeline*. Available: <http://www.cleansky.eu/achievements-timeline>
- [8] A. J. Timmis, A. Hodzic, L. Koh, M. Bonner, C. Soutis, A. W. Schäfer, *et al.*, "Environmental impact assessment of aviation emission reduction through the implementation of composite materials," *The International Journal of Life Cycle Assessment*, vol. 20, pp. 233-243, February 01 2015.
- [9] Boeing. (2012) 787 Propulsion System.
- [10] Boeing. (2006) Boeing 787 from the Ground Up.
- [11] Boeing. (2007) 787 No-Bleed System.
- [12] M. Tariq, A. I. Maswood, C. J. Gajanayake, and A. K. Gupta, "Aircraft batteries: current trend towards more electric aircraft," *IET Electrical Systems in Transportation*, vol. 7, pp. 93-103, 2017.
- [13] Boeing. *787 Electrical System*. Available: <http://787updates.newairplane.com/787-Electrical-Systems/787-electrical-system>
- [14] M. Hirst, A. Mcloughlin, P. J. Norman, and S. J. Galloway, "Demonstrating the more electric engine: a step towards the power optimised aircraft," *IET Electric Power Applications*, vol. 5, pp. 3-13, 2011.
- [15] E. Orr. (2013, June) More Electric Engines for More Electric Aircraft. *IET Transport Newsletter*.
- [16] Z. Zhang, J. Huang, Y. Jiang, W. Geng, and Y. Xu, "Overview and analysis of PM starter/generator for aircraft electrical power systems," *CES Transactions on Electrical Machines and Systems*, vol. 1, pp. 117-131, 2017.
- [17] B. S. Bhangu and K. Rajashekara, "Electric Starter Generators: Their Integration into Gas Turbine Engines," *IEEE Industry Applications Magazine*, vol. 20, pp. 14-22, 2014.
- [18] G. Rizzoli, G. Serra, P. Maggiore, and A. Tenconi, "Optimized design of a multiphase induction machine for an open rotor aero-engine shaft-line-embedded starter/generator," in *IECON 2013 - 39th Annual Conference of the IEEE Industrial Electronics Society*, 2013, pp. 5203-5208.
- [19] X. Ma, R. Su, J. Tseng King, S. Wang, X. Zhang, V. Vaiyapuri, *et al.*, "Review of high speed electrical machines in gas turbine electrical power generation," in *TENCON 2015 - 2015 IEEE Region 10 Conference*, 2015, pp. 1-9.
- [20] W. Cao, B. C. Mecrow, G. J. Atkinson, J. W. Bennett, and D. J. Atkinson, "Overview of Electric Motor Technologies Used for More Electric Aircraft (MEA)," *IEEE Transactions on Industrial Electronics*, vol. 59, pp. 3523-3531, 2012.
- [21] EASA, "Certification Specification for Engines," ed: EASA, 2007, p. 43.

- [22] G. Grandi and A. Tani, "Analisi dei circuiti multifase con il metodo dei vettori di spazio multipli," vol. ET06, ed. Torino: XXII Riunione Annuale dei Ricercatori di Elettrotecnica, 2006.
- [23] E. Levi, R. Bojoi, F. Profumo, H. A. Toliyat, and S. Williamson, "Multiphase induction motor drives - a technology status review," *IET Electric Power Applications*, vol. 1, pp. 489-516, 2007.
- [24] J. S. Thongam, M. Tarbouchi, A. F. Okou, D. Bouchard, and R. Beguenane, "Trends in naval ship propulsion drive motor technology," in *2013 IEEE Electrical Power & Energy Conference*, 2013, pp. 1-5.
- [25] L. Parsa and H. A. Toliyat, "Five-phase permanent magnet motor drives for ship propulsion applications," in *IEEE Electric Ship Technologies Symposium, 2005.*, 2005, pp. 371-378.
- [26] J. Dai, S. W. Nam, M. Pande, and G. Esmaili, "Medium-Voltage Current-Source Converter Drives for Marine Propulsion System Using a Dual-Winding Synchronous Machine," *IEEE Transactions on Industry Applications*, vol. 50, pp. 3971-3976, 2014.
- [27] F. Scuiller, J. F. Charpentier, and E. Semail, "Multi-star multi-phase winding for a high power naval propulsion machine with low ripple torques and high fault tolerant ability," in *2010 IEEE Vehicle Power and Propulsion Conference*, 2010, pp. 1-5.
- [28] C. Bassi, A. Tassarolo, R. Menis, and G. Sulligoi, "Analysis of different system design solutions for a high-power ship propulsion synchronous motor drive with multiple PWM converters," in *Electrical Systems for Aircraft, Railway and Ship Propulsion*, 2010, pp. 1-6.
- [29] B. Gamble, G. Snitchler, and T. MacDonald, "Full Power Test of a 36.5 MW HTS Propulsion Motor," *IEEE Transactions on Applied Superconductivity*, vol. 21, pp. 1083-1088, 2011.
- [30] A. Tassarolo, G. Zocco, and C. Tonello, "Design and Testing of a 45-MW 100-Hz Quadruple-Star Synchronous Motor for a Liquefied Natural Gas Turbo-Compressor Drive," *IEEE Transactions on Industry Applications*, vol. 47, pp. 1210-1219, 2011.
- [31] R. Bojoi, A. Cavagnino, A. Tenconi, A. Tassarolo, and S. Vaschetto, "Multiphase electrical machines and drives in the transportation electrification," in *2015 IEEE 1st International Forum on Research and Technologies for Society and Industry Leveraging a better tomorrow (RTSI)*, 2015, pp. 205-212.
- [32] R. Bojoi, A. Cavagnino, A. Tenconi, and S. Vaschetto, "Control of Shaft-Line-Embedded Multiphase Starter/Generator for Aero-Engine," *IEEE Transactions on Industrial Electronics*, vol. 63, pp. 641-652, 2016.
- [33] A. Cavagnino, Z. Li, A. Tenconi, and S. Vaschetto, "Integrated Generator for More Electric Engine: Design and Testing of a Scaled-Size Prototype," *IEEE Transactions on Industry Applications*, vol. 49, pp. 2034-2043, 2013.
- [34] M. Taha, J. Wale, and D. Greenwood, "Design of a high power-low voltage multiphase permanent magnet flux switching machine for automotive applications," in *2017 IEEE International Electric Machines and Drives Conference (IEMDC)*, 2017, pp. 1-8.
- [35] A. Cavagnino, A. Tenconi, and S. Vaschetto, "Experimental Characterization of a Belt-Driven Multiphase Induction Machine for 48-V Automotive Applications: Losses and Temperatures Assessments," *IEEE Transactions on Industry Applications*, vol. 52, pp. 1321-1330, 2016.
- [36] L. Ó, J. Alvarez, J. Doval-Gandoy, and F. D. Freijedo, "Multilevel Multiphase Space Vector PWM Algorithm," *IEEE Transactions on Industrial Electronics*, vol. 55, pp. 1933-1942, 2008.

- [37] E. Levi, I. N. W. Satiawan, N. Bodo, and M. Jones, "A Space-Vector Modulation Scheme for Multilevel Open-End Winding Five-Phase Drives," *IEEE Transactions on Energy Conversion*, vol. 27, pp. 1-10, 2012.
- [38] Z. Yifan and T. A. Lipo, "Space vector PWM control of dual three-phase induction machine using vector space decomposition," *IEEE Transactions on Industry Applications*, vol. 31, pp. 1100-1109, 1995.
- [39] H. A. Toliyat and T. A. Lipo, "Transient analysis of cage induction machines under stator, rotor bar and end ring faults," *IEEE Transactions on Energy Conversion*, vol. 10, pp. 241-247, 1995.
- [40] L. Parsa, "On advantages of multi-phase machines," in *31st Annual Conference of IEEE Industrial Electronics Society, 2005. IECON 2005.*, 2005, p. 6 pp.
- [41] M. Farshadnia, M. A. M. Cheema, A. Pouramin, R. Dutta, and J. E. Fletcher, "Design of Optimal Winding Configurations for Symmetrical Multiphase Concentrated-Wound Surface-Mount PMSMs to Achieve Maximum Torque Density under Current Harmonic Injection," *IEEE Transactions on Industrial Electronics*, vol. PP, pp. 1-1, 2017.
- [42] J. Wang, R. Qu, and L. Zhou, "Dual-Rotor Multiphase Permanent Magnet Machine With Harmonic Injection to Enhance Torque Density," *IEEE Transactions on Applied Superconductivity*, vol. 22, pp. 5202204-5202204, 2012.
- [43] R. O. C. Lyra and T. A. Lipo, "Torque density improvement in a six-phase induction motor with third harmonic current injection," *IEEE Transactions on Industry Applications*, vol. 38, pp. 1351-1360, 2002.
- [44] H. A. Toliyat, S. P. Waikar, and T. A. Lipo, "Analysis and simulation of five-phase synchronous reluctance machines including third harmonic of airgap MMF," *IEEE Transactions on Industry Applications*, vol. 34, pp. 332-339, 1998.
- [45] X. Huangsheng, H. A. Toliyat, and L. J. Petersen, "Five-phase induction motor drives with DSP-based control system," *IEEE Transactions on Power Electronics*, vol. 17, pp. 524-533, 2002.
- [46] J. K. Pandit, M. V. Aware, R. V. Nemade, and E. Levi, "Direct Torque Control Scheme for a Six-Phase Induction Motor With Reduced Torque Ripple," *IEEE Transactions on Power Electronics*, vol. 32, pp. 7118-7129, 2017.
- [47] A. Tani, M. Mengoni, L. Zarri, G. Serra, and D. Casadei, "Control of Multiphase Induction Motors With an Odd Number of Phases Under Open-Circuit Phase Faults," *IEEE Transactions on Power Electronics*, vol. 27, pp. 565-577, 2012.
- [48] R. Hyung-Min, K. Ji-Woong, and S. Seung-Ki, "Synchronous-frame current control of multiphase synchronous motor under asymmetric fault condition due to open phases," *IEEE Transactions on Industry Applications*, vol. 42, pp. 1062-1070, 2006.
- [49] H. S. Che, M. J. Duran, E. Levi, M. Jones, W. P. Hew, and N. A. Rahim, "Postfault Operation of an Asymmetrical Six-Phase Induction Machine With Single and Two Isolated Neutral Points," *IEEE Transactions on Power Electronics*, vol. 29, pp. 5406-5416, 2014.
- [50] M. Mengoni, G. Sala, L. Zarri, A. Tani, G. Serra, Y. Gritli, *et al.*, "Control of a fault-tolerant quadruple three-phase induction machine for More Electric Aircrafts," in *IECON 2016 - 42nd Annual Conference of the IEEE Industrial Electronics Society*, 2016, pp. 5747-5753.
- [51] G. Sala, G. Valente, A. Formentini, L. Papini, D. Gerada, P. Zanchetta, *et al.*, "Space Vectors and Pseudo Inverse Matrix Methods for the Radial Force Control in Bearingless Multi-Sector Permanent Magnet Machines," *IEEE Transactions on Industrial Electronics*, 2017.
- [52] M. Mengoni, L. Zarri, Y. Gritli, A. Tani, F. Filippetti, and S. B. Lee, "Online Detection of High-Resistance Connections With Negative-Sequence Regulators in Three-Phase

- Induction Motor Drives," *IEEE Transactions on Industry Applications*, vol. 51, pp. 1579-1586, 2015.
- [53] A. Tani, Y. Gritli, M. Mengoni, L. Zarri, G. Sala, A. Bellini, *et al.*, "Detection of magnet demagnetization and high-resistance connections in five-phase surface-mounted permanent magnet generators," in *2015 IEEE 10th International Symposium on Diagnostics for Electrical Machines, Power Electronics and Drives (SDEMPED)*, 2015, pp. 487-493.
- [54] A. Tani, L. Zarri, M. Mengoni, G. Serra, and D. Casadei, "Detection and localization of high resistance connections in quadruple three-phase induction motor drives," in *2014 International Conference on Electrical Machines (ICEM)*, 2014, pp. 2094-2100.
- [55] W. Zhao, C. Gu, Q. Chen, J. Ji, and D. Xu, "Remedial phase-angle control of a five-phase fault-tolerant permanent-magnet vernier machine with short-circuit fault," *CES Transactions on Electrical Machines and Systems*, vol. 1, pp. 83-88, 2017.
- [56] X. Wang, X. Ren, and J. Y. Zhang, "Short-circuit fault-tolerant control of bearingless permanent magnet slice machine," in *2013 IEEE Energy Conversion Congress and Exposition*, 2013, pp. 1148-1153.
- [57] S. Dwari and L. Parsa, "Optimum Fault-Tolerant Control of Multi-phase Permanent Magnet Machines for Open-Circuit and Short-Circuit Faults," in *APEC 07 - Twenty-Second Annual IEEE Applied Power Electronics Conference and Exposition*, 2007, pp. 1417-1422.
- [58] F. Wu, P. Zheng, and T. M. Jahns, "Analytical Modeling of Interturn Short Circuit for Multiphase Fault-Tolerant PM Machines With Fractional Slot Concentrated Windings," *IEEE Transactions on Industry Applications*, vol. 53, pp. 1994-2006, 2017.
- [59] D. C. Patel and M. C. Chandorkar, "Modeling and Analysis of Stator Interturn Fault Location Effects on Induction Machines," *IEEE Transactions on Industrial Electronics*, vol. 61, pp. 4552-4564, 2014.
- [60] J. Yun, K. Lee, K. W. Lee, S. B. Lee, and J. Y. Yoo, "Detection and Classification of Stator Turn Faults and High-Resistance Electrical Connections for Induction Machines," *IEEE Transactions on Industry Applications*, vol. 45, pp. 666-675, 2009.
- [61] J. H. Jung, J. J. Lee, and B. H. Kwon, "Online Diagnosis of Induction Motors Using MCSA," *IEEE Transactions on Industrial Electronics*, vol. 53, pp. 1842-1852, 2006.
- [62] F. Immovilli, C. Bianchini, E. Lorenzani, A. Bellini, and E. Fornasiero, "Evaluation of Combined Reference Frame Transformation for Interturn Fault Detection in Permanent-Magnet Multiphase Machines," *IEEE Transactions on Industrial Electronics*, vol. 62, pp. 1912-1920, 2015.
- [63] H. Henao, G. A. Capolino, M. Fernandez-Cabanas, F. Filippetti, C. Bruzzese, E. Strangas, *et al.*, "Trends in Fault Diagnosis for Electrical Machines: A Review of Diagnostic Techniques," *IEEE Industrial Electronics Magazine*, vol. 8, pp. 31-42, 2014.
- [64] B. Mirafzal, R. J. Povinelli, and N. A. O. Demerdash, "Interturn Fault Diagnosis in Induction Motors Using the Pendulous Oscillation Phenomenon," *IEEE Transactions on Energy Conversion*, vol. 21, pp. 871-882, 2006.
- [65] D. Barater, J. Arellano-Padilla, and C. Gerada, "Incipient Fault Diagnosis in Ultrareliable Electrical Machines," *IEEE Transactions on Industry Applications*, vol. 53, pp. 2906-2914, 2017.
- [66] D. Barater, G. Buticchi, C. Gerada, and J. Arellano-Padilla, "Diagnosis of incipient faults in PMSMs with coaxially insulated windings," in *IECON 2013 - 39th Annual Conference of the IEEE Industrial Electronics Society*, 2013, pp. 2756-2761.
- [67] L. Alberti and N. Bianchi, "Experimental Tests of Dual Three-Phase Induction Motor Under Faulty Operating Condition," *IEEE Transactions on Industrial Electronics*, vol. 59, pp. 2041-2048, 2012.

- [68] G. Sala, D. Gerada, C. Gerada, and A. Tani, "Design and control of segmented triple three-phase SPM machines for fault tolerant drives," in *2017 IEEE Workshop on Electrical Machines Design, Control and Diagnosis (WEMDCD)*, 2017, pp. 63-68.
- [69] P. Arumugam, T. Hamiti, and C. Gerada, "Modeling of Different Winding Configurations for Fault-Tolerant Permanent Magnet Machines to Restrain Interturn Short-Circuit Current," *IEEE Transactions on Energy Conversion*, vol. 27, pp. 351-361, 2012.
- [70] S. Singh and N. Kumar, "Detection of Bearing Faults in Mechanical Systems Using Stator Current Monitoring," *IEEE Transactions on Industrial Informatics*, vol. 13, pp. 1341-1349, 2017.
- [71] K. Kang, J. Song, C. Kang, S. Sung, and G. Jang, "Real-Time Detection of the Dynamic Eccentricity in Permanent-Magnet Synchronous Motors by Monitoring Speed and Back EMF Induced in an Additional Winding," *IEEE Transactions on Industrial Electronics*, vol. 64, pp. 7191-7200, 2017.
- [72] B. M. Ebrahimi, J. Faiz, and M. J. Roshtkhari, "Static-, Dynamic-, and Mixed-Eccentricity Fault Diagnoses in Permanent-Magnet Synchronous Motors," *IEEE Transactions on Industrial Electronics*, vol. 56, pp. 4727-4739, 2009.
- [73] A. Bellini, F. Filippetti, G. Franceschini, C. Tassoni, and G. B. Kliman, "Quantitative evaluation of induction motor broken bars by means of electrical signature analysis," *IEEE Transactions on Industry Applications*, vol. 37, pp. 1248-1255, 2001.
- [74] B. Mirafzal and N. A. O. Demerdash, "On innovative methods of induction motor interturn and broken-bar fault diagnostics," *IEEE Transactions on Industry Applications*, vol. 42, pp. 405-414, 2006.
- [75] A. Ceban, R. Pusca, and R. Romary, "Study of Rotor Faults in Induction Motors Using External Magnetic Field Analysis," *IEEE Transactions on Industrial Electronics*, vol. 59, pp. 2082-2093, 2012.
- [76] J. D. Bisschop, H. Vansompel, P. Sergeant, and L. Dupre, "Demagnetization Fault Detection in Axial Flux PM Machines by Using Sensing Coils and an Analytical Model," *IEEE Transactions on Magnetics*, vol. 53, pp. 1-4, 2017.
- [77] S. Rajagopalan, W. I. Roux, T. G. Habetler, and R. G. Harley, "Dynamic Eccentricity and Demagnetized Rotor Magnet Detection in Trapezoidal Flux (Brushless DC) Motors Operating Under Different Load Conditions," *IEEE Transactions on Power Electronics*, vol. 22, pp. 2061-2069, 2007.
- [78] J. R. R. Ruiz, J. A. Rosero, A. G. Espinosa, and L. Romeral, "Detection of Demagnetization Faults in Permanent-Magnet Synchronous Motors Under Nonstationary Conditions," *IEEE Transactions on Magnetics*, vol. 45, pp. 2961-2969, 2009.
- [79] D. Casadei, F. Filippetti, C. Rossi, and A. Stefani, "Magnets faults characterization for Permanent Magnet Synchronous Motors," in *2009 IEEE International Symposium on Diagnostics for Electric Machines, Power Electronics and Drives*, 2009, pp. 1-6.
- [80] M. N. Uddin, W. Wang, and Z. R. Huang, "Modeling and Minimization of Speed Ripple of a Faulty Induction Motor With Broken Rotor Bars," *IEEE Transactions on Industry Applications*, vol. 46, pp. 2243-2250, 2010.
- [81] Q. Chen, X. Fan, G. Liu, W. Zhao, J. Ji, L. Xu, *et al.*, "A new fault-tolerance motor with decoupled reluctance channel and PM channel," in *2017 IEEE 26th International Symposium on Industrial Electronics (ISIE)*, 2017, pp. 214-219.
- [82] L. Zhang, Y. Fan, C. Li, and C. Liu, "Design and Analysis of a New Six-Phase Fault-Tolerant Hybrid-Excitation Motor for Electric Vehicles," *IEEE Transactions on Magnetics*, vol. 51, pp. 1-4, 2015.

- [83] S. K. E. Khil, I. Jlassi, J. O. Estima, N. Mrabet-Bellaaj, and A. J. M. Cardoso, "Current sensor fault detection and isolation method for PMSM drives, using average normalised currents," *Electronics Letters*, vol. 52, pp. 1434-1436, 2016.
- [84] G. H. B. Foo, X. Zhang, and D. M. Vilathgamuwa, "A Sensor Fault Detection and Isolation Method in Interior Permanent-Magnet Synchronous Motor Drives Based on an Extended Kalman Filter," *IEEE Transactions on Industrial Electronics*, vol. 60, pp. 3485-3495, 2013.
- [85] T. A. Najafabadi, F. R. Salmasi, and P. Jabejdar-Maralani, "Detection and Isolation of Speed-, DC-Link Voltage-, and Current-Sensor Faults Based on an Adaptive Observer in Induction-Motor Drives," *IEEE Transactions on Industrial Electronics*, vol. 58, pp. 1662-1672, 2011.
- [86] M. Mengoni, L. Zarri, A. Tani, G. Serra, and D. Casadei, "Sensorless multiphase induction motor drive based on a speed observer operating with third-order field harmonics," in *2011 IEEE Energy Conversion Congress and Exposition*, 2011, pp. 68-74.
- [87] A. G. Yepes, F. Baneira, J. Malvar, A. Vidal, D. Pérez-Estévez, O. López, *et al.*, "Selection Criteria of Multiphase Induction Machines for Speed-Sensorless Drives Based on Rotor Slot Harmonics," *IEEE Transactions on Industrial Electronics*, vol. 63, pp. 4663-4673, 2016.
- [88] M. Ramezani and O. Ojo, "The Modeling and Position-Sensorless Estimation Technique for A Nine-Phase Interior Permanent-Magnet Machine Using High-Frequency Injections," *IEEE Transactions on Industry Applications*, vol. 52, pp. 1555-1565, 2016.
- [89] M. Mengoni, A. Tani, L. Zarri, G. Serra, and D. Casadei, "Position Control of a Multi-Motor Drive Based on Series-Connected Five-Phase Tubular PM Actuators," *IEEE Transactions on Industry Applications*, vol. 48, pp. 2048-2058, 2012.
- [90] E. Levi, M. Jones, S. N. Vukosavic, and H. A. Toliyat, "A novel concept of a multiphase, multimotor vector controlled drive system supplied from a single voltage source inverter," *IEEE Transactions on Power Electronics*, vol. 19, pp. 320-335, 2004.
- [91] E. Levi, M. Jones, S. N. Vukosavic, and H. A. Toliyat, "Operating principles of a novel multiphase multimotor vector-controlled drive," *IEEE Transactions on Energy Conversion*, vol. 19, pp. 508-517, 2004.
- [92] V. F. Victor, F. O. Quintaes, J. S. B. Lopes, L. d. S. Junior, A. S. Lock, and A. O. Salazar, "Analysis and Study of a Bearingless AC Motor Type Divided Winding, Based on a Conventional Squirrel Cage Induction Motor," *IEEE Transactions on Magnetics*, vol. 48, pp. 3571-3574, 2012.
- [93] M. Kang, J. Huang, J. q. Yang, and H. b. Jiang, "Analysis and experiment of a 6-phase bearingless induction motor," in *2008 International Conference on Electrical Machines and Systems*, 2008, pp. 990-994.
- [94] J. Huang, B. Li, H. Jiang, and M. Kang, "Analysis and Control of Multiphase Permanent-Magnet Bearingless Motor With a Single Set of Half-Coiled Winding," *IEEE Transactions on Industrial Electronics*, vol. 61, pp. 3137-3145, 2014.
- [95] G. Valente, L. Papini, A. Formentini, C. Gerada, and P. Zanchetta, "Radial force control of multi-sector permanent magnet machines," in *2016 XXII International Conference on Electrical Machines (ICEM)*, 2016, pp. 2595-2601.
- [96] S. Serri, A. Tani, and G. Serra, "Analytical model of radial forces considering mutual effects between torque and levitation current space vectors in 5-phase PM bearingless motors," in *IECON 2013 - 39th Annual Conference of the IEEE Industrial Electronics Society*, 2013, pp. 5142-5147.

CHAPTER 1

- [97] T. F. A. Chiba, O. Ichikawa, M. Oshima, M. Takemoto, and D. G. Dorrell, *Magnetic bearings and bearingless drives*: Elsevier, 2005.
- [98] B. Nystrom, L. Austrin, N. Ankarback, and E. Nilsson, "Fault Tree Analysis of an Aircraft Electric Power Supply System to Electrical Actuators," in *2006 International Conference on Probabilistic Methods Applied to Power Systems*, 2006, pp. 1-7.
- [99] J. W. Bennett, B. C. Mecrow, D. J. Atkinson, and G. J. Atkinson, "Safety-critical design of electromechanical actuation systems in commercial aircraft," *IET Electric Power Applications*, vol. 5, pp. 37-47, 2011.
- [100] J. W. Bennett, G. J. Atkinson, and B. C. Mecrow, "Fault-tolerant design considerations and control strategies for aerospace drives," vol. 59, ed: IEEE Trans. Ind. Electron., 2012, pp. 2049-2058.
- [101] A. Galassini, A. Costabeber, and C. Gerada, "Speed control for multi-three phase synchronous electrical motors in fault condition," in *IEEE EUROCON 2017 -17th International Conference on Smart Technologies*, 2017, pp. 698-703.
- [102] L. Zarri, M. Mengoni, A. Tani, G. Serra, and D. Casadei, "Minimization of the Power Losses in IGBT Multiphase Inverters with Carrier-Based Pulsewidth Modulation," *IEEE Transactions on Industrial Electronics*, vol. 57, pp. 3695-3706, 2010.
- [103] D. Casadei, D. Dujic, E. Levi, G. Serra, A. Tani, and L. Zarri, "General Modulation Strategy for Seven-Phase Inverters With Independent Control of Multiple Voltage Space Vectors," *IEEE Transactions on Industrial Electronics*, vol. 55, pp. 1921-1932, 2008.

CHAPTER 2

Multi-Harmonic Generalised Model for Multiphase Machines

For a multi three-phase machine with each three-phase subsystem having its own star connection, the easier way to control it is based on the approximation that it is possible to control each subsystem as an independent machine; and the three-phase machines are then connected to the same shaft [1]. A different approach must be used if the coupling between the different set of three-phase windings is likely to be taken into account for performance or control purposes. Furthermore, if there are multiphase machines with more than three phases connected to the same star point, the three-phase theory must be abandoned.

Nowadays, many improvements for the control of multiphase machines have been proposed and validated, and many of them are based on the theory of the multi Space Vector Decomposition (SVD) [2, 3]. The idea of the SVD approach is that the machine can still be thought as a sum of three-phase machines, each one described in terms of currents by a complex number (current space vector). The current space vector represents a harmonic of the armature field in the airgap rather than a physical three-phase subsystem. Furthermore, the current space vector equations are in general independent anymore; this happens in particular if there are reluctances, non-linearities or asymmetries caused by faults in the machine [3-5], or because of particular controls [6].

The next section introduces the space vector general transformations and inverse transformations needed to describe a multi-variable system. Then, the method is applied for the definition of a general model for multiphase machines based on the winding function approach.

The model is maintained as general as possible. Indeed, this chapter aims to present a unique machine model, which is general at least for all the machine topologies analysed in the next chapters. Due to the complexity of the equations, many steps are highlighted in the presentation of the model.

2.1 Space Vector Decomposition theory

The basis of the SVD theory comes from the idea of representing a “polyphase” system by a set of new “symmetrical co-ordinates”. In the late 1918, Fortescue wrote the first important publication on the multiphase space vectors, using them for the analysis of power networks [7]. As explained in this paper, asymmetrical systems can be represented by symmetrical systems with equal degrees of freedom. He also wrote: “I admit that the appearance of the equations is cumbersome, but that is almost impossible to overcome. The nature of the subject makes the equations cumbersome”. The development of this concept led to the definition of complex numbers that can be represented as vectors moving in different planes (generally named x - y , α - β or d - q) called space vectors [8].

A system of n variables of the x -th quantity ($x_k, k \in 1, 2, \dots, n$) can be fully represented by n complex numbers \bar{y}_h . Each complex numbers \bar{y}_h is referred to as the vector of the h -th space or h -th plane (h -th space vector).

Suitable transformations allow passing from the physical quantities x_k to the new ones \bar{y}_h . The general transformation, also called as Clarke transform, is as follows:

$$\bar{y}_h = \frac{C}{n} \sum_{k=1}^n x_k \bar{\alpha}^{h(k-1)}, \quad h = 0, 1, 2, \dots, n-1, \quad (2.1)$$

where C is an arbitrary constant and $\bar{\alpha} = e^{j\frac{2\pi}{n}}$.

The general inverse transformation of (2.1) is:

$$x_k = \frac{1}{C} \sum_{h=0}^{n-1} \bar{y}_h \bar{\alpha}^{-h(k-1)}, \quad k = 1, 2, \dots, n. \quad (2.2)$$

By means of (2.1) and (2.2) it is possible to pass from the physical domain of the system quantities to the new domain of the space vectors in their $\alpha_h - \beta_h$ (or $x_h - y_h$, or $d_h - q_h$) representation planes (or spaces) and vice versa. Fig. 2.1 shows schematically the concept of a transformation that brings to a new set of variables that fully represents the system.

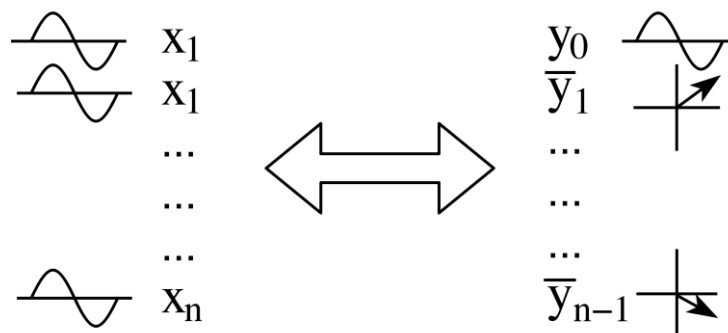


Fig. 2.1 – Space vector transformation and inverse transformation of an n variable system.

It is immediate to notice that the new system of variables is redundant. Indeed, the space vectors \bar{y}_h are in general complex numbers, while the physical variables are always real numbers (as the word “real” means). This results that there are more variables than the physical ones, and some additional relationship between the new variables must be found in order to identify an inverse transformation that considers the same number of input of the starting system. If the number of variables of the two models is the same, the number of constraints between the variables of each model and the number of independent variables (degrees of freedom of the system) is the same too. This allows developing a one-to-one transformation between the two domains.

It is worth noticing that (2.1) and (2.2) take into account for all the possible independent space vectors. Indeed, the transformation can also be written for all the values of h ($h \in [-\infty; \infty]$), as:

$$\bar{y}_h = \frac{C}{n} \sum_{k=1}^n x_k \bar{\alpha}^{h(k-1)}, \quad h = -\infty, \dots, \infty. \quad (2.3)$$

Moreover, introducing the total number of space vectors (z), the inverse transformation can be extended as:

$$x_k = \frac{n}{zC} \sum_{h=-\infty}^{\infty} \bar{y}_h \bar{\alpha}^{-h(k-1)}, \quad k = 1, 2, \dots, n. \quad (2.4)$$

However, all the additional vectors are redundant owing to the following relationship:

$$\begin{aligned} \bar{y}_{wn+h} &= \frac{C}{n} \sum_{k=1}^n x_k \bar{\alpha}^{(wn+h)(k-1)} = \\ &= \frac{C}{n} \sum_{k=1}^n x_k \bar{\alpha}^{wn(k-1)} \bar{\alpha}^{h(k-1)} = \\ &= \frac{C}{n} \sum_{k=1}^n x_k \bar{\alpha}^{h(k-1)} = \bar{y}_h. \end{aligned} \quad (2.5)$$

Indeed, $\bar{\alpha}^{wn(k-1)}$ is equal to 1 ($\bar{\alpha}^{wn(k-1)} = e^{j\frac{2\pi}{n}wn(k-1)} = e^{j2\pi w(k-1)} = 1$) for each h value (both positive and negative). This means that for each vector defined by (2.1) there are infinite others that are identic to it, and at the same time a vector that is different from all the one defined by (2.1) cannot exist. By the relation (2.5), it is possible to rewrite (2.4) as (2.2), making (2.2) completely general.

It is also important to highlight that the space vectors are a Hermitian function for their space (or plane or order). A Hermitian function is a complex function with the property that its complex conjugate is equal to the original function with the variable changed in sign. This means that, according to (2.2), the following relationship can be written:

$$\begin{aligned}
 \bar{y}_h^* &= \frac{C}{n} \sum_{k=1}^n x_k \bar{\alpha}^{-h(k-1)} = \\
 &= \frac{C}{n} \sum_{k=1}^n x_k \bar{\alpha}^{n-h(k-1)} = \\
 &= \frac{C}{n} \sum_{k=1}^n x_k \bar{\alpha}^{-h(k-1)} = \bar{y}_{-h}.
 \end{aligned} \tag{2.6}$$

By means of (2.6), it is easily possible to simplify (2.1) and (2.2) in order to reduce the number of independent space vector. However, the simplification depends on the number of variables; in particular, it changes if the variables are an odd or even number. The next two subsections show how the transformation and the inverse transformation can be simplified in case of an odd and an even number of symmetrical variables.

Space Vectors Transformation (odd number of variables)

If the variables of the system are odd, there is always one real space vector and all the others are complex. The real space vector is also called homopolar component, because it represents what is equal between all the variables (in other words, it is the average value when C is equal to 1), and it is defined as:

$$y_0 = \frac{C}{n} \sum_{k=1}^n x_k. \tag{2.7}$$

Note that it has been chosen to use as homopolar component the 0 -th one rather than the n -th space vector as it is usually done in literature. The advantage of this choice is that the order of the component is the same whatever the number of phases, making always clear what the homopolar sequence means.

All the other space vectors are complex numbers that respect the relationship (2.6). This allows rewriting (2.2) as:

$$x_k = \frac{y_0}{C} + \frac{1}{C} \sum_{h_{\text{odd}}=1,3,\dots}^{n-2} \bar{y}_h \bar{\alpha}^{-h(k-1)} + \frac{1}{C} \sum_{h_{\text{even}}=2,4,6,\dots}^{n-1} \bar{y}_h^* \bar{\alpha}^{-h(k-1)}, \quad k = 1, 2, \dots, n. \tag{2.8}$$

Because $\bar{\alpha}^{-h(k-1)} = \bar{\alpha}^{(n-h)(k-1)}$, the inverse transformations is:

$$x_k = \frac{y_0}{C} + \frac{1}{C} \sum_{h_{\text{odd}}=1,3,\dots}^{n-2} (\bar{y}_h \bar{\alpha}^{-h(k-1)} + \bar{y}_h^* \bar{\alpha}^{h(k-1)}), \quad k = 1, 2, \dots, n. \tag{2.9}$$

Introducing the real operator \Re , there is a useful relationship for complex numbers, which is:

$$\frac{\bar{y} + \bar{y}^*}{2} = \Re\{\bar{y}\}. \tag{2.10}$$

By means of (2.10), the inverse transformation (2.9) results in:

$$x_k = \frac{y_0}{C} + \frac{2}{C} \sum_{h_{\text{odd}}=1,3,\dots}^n \Re\{\bar{y}_{h_{\text{odd}}} \bar{\alpha}^{-h(k-1)}\}, \quad k = 1, 2, \dots, n. \quad (2.11)$$

Alternatively, by repeating the same passages considering only the even space vectors, the inverse transformation can be also rewritten as:

$$x_k = \frac{y_0}{C} + \frac{2}{C} \sum_{h_{\text{even}}=2,4,\dots}^{n-1} \Re\{\bar{y}_{h_{\text{even}}} \bar{\alpha}^{-h(k-1)}\}, \quad k = 1, 2, \dots, n. \quad (2.12)$$

A common choice on the modelling of three-phase electrical systems is to choose the C constant equal to 2 and using the inverse transformation (2.11). In this way, if the homopolar component y_0 is null, the only space vector needed to describe the system is the first one \bar{y}_1 , and all the variables of the system are described by the relation (2.11) as $x_k = \Re\{\bar{y}_1 \bar{\alpha}^{-(k-1)}\}$. This means that in case of symmetric and sinusoidal conditions, (waveforms, of the physical quantities in the time domain, with same frequency and amplitudes and shifted of the same angle in the time), the amplitude of each quantity is equal to the magnitude of the 1st space vector. That is why hereafter the C value is considered always equal to two.

The transformations and inverse transformations for a system with an odd number of variables (n odd) become:

$$\bar{y}_h = \frac{2}{n} \sum_{k=1}^n x_k \bar{\alpha}^{h(k-1)}, \quad (2.13)$$

and

$$x_k = \frac{y_0}{2} + \sum_{h_{\text{odd}}=1,3,\dots}^{n-2} \Re\{\bar{y}_{h_{\text{odd}}} \bar{\alpha}^{-h(k-1)}\}, \quad k = 1, 2, \dots, n, \quad (2.14)$$

or

$$x_k = \frac{y_0}{2} + \sum_{h_{\text{even}}=2,4,\dots}^{n-1} \Re\{\bar{y}_{h_{\text{even}}} \bar{\alpha}^{-h(k-1)}\}, \quad k = 1, 2, \dots, n. \quad (2.15)$$

Space Vectors Transformation (even number of variables)

In case of an even number of variables, it is less intuitive how to simplify the inverse transformation to a reduced number of independent space vectors. Indeed, to realize a one-to-one transformation the number of space vectors should be reduced in order to have a number of space variables equal to the equivalent number of degrees of freedom needed to fully describe the system.

In addition, there is a new space vector (the $n/2$ -th) which is always real:

$$y_{n/2} = \frac{C}{n} \sum_{k=1}^n x_k \bar{\alpha}^{-n/2(k-1)} = \frac{C}{n} \sum_{k=1}^n x_k e^{-j \frac{2\pi n}{n} \frac{k-1}{2}} = \frac{C}{n} \sum_{k=1}^n x_k (-1)^{(k-1)}. \quad (2.16)$$

This real component is no more homopolar, but if desired it can be seen as an evaluation of what has the same amplitude but opposite sign between half of the variables (x_1, x_3, x_5, \dots) and the other half (x_2, x_4, x_6, \dots).

Therefore, there are two real components and $n-2$ complex space vectors. Again, the relationship (2.6) allows rewriting (2.2) as:

$$x_k = \frac{y_0}{2} + \frac{y_{n/2}}{2} (-1)^{(k-1)} + \sum_{h=1,2,\dots}^{n/2-1} \Re\{\bar{y}_h \bar{\alpha}^{-h(k-1)}\}, \quad (2.17)$$

or

$$x_k = \frac{y_0}{2} + \frac{y_{n/2}}{2} (-1)^{(k-1)} + \sum_{h=n/2+1}^{n-1} \Re\{\bar{y}_h \bar{\alpha}^{-h(k-1)}\}. \quad (2.18)$$

The transformation with an even number of variables is quite important for the purpose of the generalisation of the model proposed in this chapter. Indeed, in many cases, the winding is asymmetrical, and a redundant transformation is needed. As explained in the next subsection, the redundant transformation often results to be symmetrical for an even number of redundant variables.

Redundant transformations for making symmetrical an asymmetrical transformation

In some cases, an asymmetrical transformation is used to describe some variables in order to represent them taking into account of the asymmetrical physic of the system (this happens for example in multiphase machines with an even number of phases asymmetrically distributed, as shown in the following section). In asymmetrical machines, often it is enough to introduce a double number of variables (half of them will be non-physical) in order to obtain a symmetrical transformation of the full set of variables. It results that the resulting symmetrical transformation must be with an even number of equivalent variables. It is possible to verify (numerically for example) that in some of these cases (2.17) can be simplified as:

$$x_k = \frac{y_0}{C} + \frac{y_{n/2}}{C} (-1)^{(k-1)} + \frac{4}{C} \sum_{h_{\text{even}}=2,4,6,\dots}^{n/2-2} \Re\{\bar{y}_h \bar{\alpha}^{-h(k-1)}\}, \quad k=1,2,\dots,n, \quad (2.19)$$

or

$$x_k = \frac{4}{C} \sum_{h_{\text{odd}}=1,3,\dots}^{n/2-1} \Re\{\bar{y}_h \bar{\alpha}^{-h(k-1)}\}, \quad k=1,2,\dots,n. \quad (2.20)$$

This result has been verified for distributed asymmetrical six-phase and twelve-phase windings, as mentioned in the next section.

The term n is the total number of variables used to define the symmetrical transformation. In the mentioned winding layouts (as the asymmetrical six-phase and twelve-phase ones), n is twice the variables of the system. Often, in order to define the transformation as for an odd number of symmetrical variables, the C constant is set equal to 4 rather than 2 in the transformation and inverse transformation. In general, C is set in order to keep the transformation shape as the one without redundant variables. Therefore, C results as twice the number of redundant and real variables divided by the number of real variables. Even if (2.19) and (2.20) are often used in the modelling of standard multiphase machines with asymmetrical windings, these inverse transformations are not general. The simplification of the inverse transformation must be verified for each machine, making an asymmetrical transformation of variable slightly more complex to use than a symmetrical one (the one generally used for multiphase machines with an odd number of phases symmetrically distributed). An example of asymmetrical winding that cannot be modelled with this approach (the multi sector winding) is presented in the next section and analysed in deep in Chapter 4.

Because the choice of the transformation to describe a multivariable system significantly affects the complexity of the model, the next subsection presents the proposed general approach to the transformations and inverse transformations of multiphase electrical machines. The transformations are defined on a winding function approach.

2.2 General approach to Multiphase Machine Modelling: Stator Winding and Transformations

The model of a multiphase machine differs from the one of an equivalent three-phase for the stator winding. The higher number of phases increases the number of independent currents and relative generated space harmonic fields that can be controlled.

In this section, the equations of the magnetic field produced by a winding are presented. The relationship between the currents and the magnetic field harmonics are defined in terms of current space vectors by means of the SVD theory.

Certainly, the SVD theory can be applied to whatever electrical machine, but the new variables (the space vectors) must be introduced in a suitable way for the control of the electromagnetic quantities (voltages, currents and fluxes). The proposed technique, to find a suitable transformation, is by means of a winding function approach. The idea is that each spatial harmonic of the magnetic field in the airgap can be directly related to a current space vector. In particular, the ρ -th space harmonic of the magnetic field (\bar{H}_ρ) can be related to the ρ -th space current vector (\bar{i}_ρ). Note that hereafter the term space is always used, when writing about the space vectors, for indicating the order of the considered vector, which is the plane where the vector is represented ($\alpha_\rho - \beta_\rho$, $x_\rho - y_\rho$ or $d_\rho - q_\rho$).

CHAPTER 2

Once the current space vector equations are determined, one of the most critical point of the machine model is to identify a suitable inverse transformation of the resulting space vectors. This is needed for example to evaluate the voltage reference values that define the modulating signals (voltage control).

The proposed method is based on the definition of a redundant multiphase transformation. Indeed, it is always possible to introduce additional variables to the system and then set them equal to zero. The idea rises from the desire of using symmetrical space vector transformations as (2.1) and (2.2).

The method used to model a stator winding is defined with the following hypothesis:

- The slotting effect, end-effect, saturations and all the others non-linearities of an electrical machine are neglected and the iron is considered to have an infinite magnetic permeability and zero losses.
- The magnetic field in the airgap is considered for only its radial component and the bending of the airgap is neglected (the radial component of the flux results in parallel flux lines), owing to define a mono dimensional model of the machine, where all the magnetic quantities depend only by the angular position (ϑ). In some analysis (squirrel cage and stator segmentation), also the axial dimension (z) is taken into account in the model for the evaluation of the skewing, but the field is still considered only radial.
- The first derivative of the electric displacement vector is supposed equal to zero :

$$\frac{d\bar{D}}{dt} = 0.$$

Note that the time dependence of the quantities in the model is not explicit if it is not needed for further explanations.

The next subsection defines the magnetic field in the airgap generated by the current flowing in a generic turn. Then, the analysis is extended to a multiphase winding. A suitable space vector transformation is defined from the equation of the overall magnetic field in the airgap produced by the stator currents. An in-deep analysis of this transformation is carried out in this section.

Armature field (one turn)

This subsection describes the relationship between the current flowing in one turn and the related field in the airgap.

It is well known that the airgap field produced by one turn, in the hypothesis of only radial flux, is described by a rectangular waveform until the reluctance (airgap thickness) is constant and the currents are supposed to be concentrated in points located in an angular position in the middle of the slots.

The basic equations needed to solve the problem of identifying the field distribution produced by a turn crossed by a current are:

- Gauss's law for magnetism

- Ampère's circuital law

Gauss's law for magnetism states that the flux density (B) has always divergence equal to zero, or (in its integral form) that the net flux exiting a closed surface is always zero:

$$\oint_{S_C} \bar{B} \cdot d\bar{S}_C = 0. \quad (2.21)$$

Ampère's circuital law states (in its integral form) that the magnetic field (H) around a closed path (integral line C) is equal to the total current passing to whatever surface (S_C) enclosed by this path. Separating the conduction current from the polarization current, it leads to the general Maxwell- Ampère's equation in its integral form:

$$\oint_C \bar{H} \cdot d\bar{l}_C = \int_{S_C} \left(\bar{J} + \frac{d\bar{D}}{dt} \right) \cdot d\bar{S}_C. \quad (2.22)$$

Under the hypotheses of the model (in particular, neglecting the effect of the electric displacement field \bar{D}) and replacing the second member with the current flowing in the considered turn, (2.22) can be simplified as:

$$\oint_C \bar{H} \cdot d\bar{l}_C = i_k. \quad (2.23)$$

There are two ways to use (2.21) and (2.23) for the definition of the field produced by a coil in the airgap. The first one is passing through the definition of the spatial distribution of the current density, and then applying the laws of the electromagnetism. The second is to simplify the model in order to apply directly the two equations based on the expected field distribution (rectangular distribution centred with the magnetic axis of the coil), going straight to the desired result. However, the second approach is only valid if the reluctance effects can be neglected. Instead, the first approach is more general and allows modelling also the machine reluctances (for example slotting effects and not isotropic rotor geometries, as in [4] for a five phase winding with an Internal Permanent Magnet, IPM, rotor). In the two next paragraphs, both the two methods are presented, in order to verify that they give the same result when the first method is simplified to an isotropic magnetic circuit, and to show how it is also possible to model machines taking into account for reluctance effects. Fig. 2.2 shows the conventions for the machine modelling, while Fig. 2.3 and Fig. 2.4 show the geometries and parameters used to model a general k -th turn of the stator winding.

The k -th turn has:

- its geometrical centre in the angular position ψ_k ;
- a pitch of $\Delta\psi_k$ radians ;
- a turn width of $\Delta\psi$ radians (meaning that, for the purposes of the model, the turn is simplified to rectangular shape).

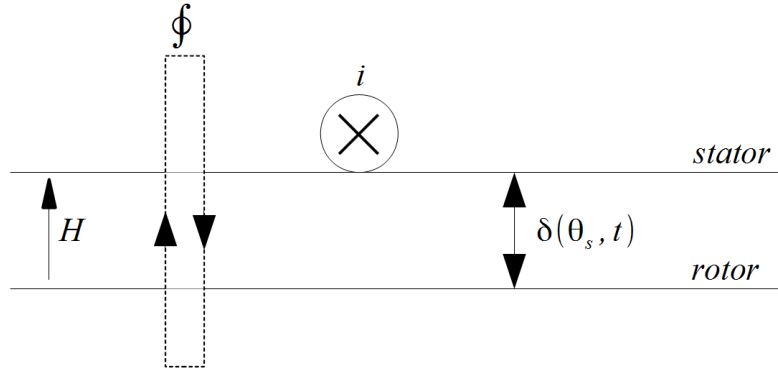


Fig. 2.2 – Conventions of the proposed model.

1st Method: current density distribution

This paragraph aims to define the magnetic field in the airgap generated by the current flowing in a generic turn by means of a general approach that is valid also in presence of a not isotropic magnetic circuit (reluctance).

The magnetic field produced by the k -th turn can be written as function of the spatial distribution of the linear current density.

Taking into account of an infinitesimal angle of the airgap ($d\vartheta_s$), the circuital law (2.23) can be written as:

$$H(\vartheta_s)\delta(\vartheta_s) - H(\vartheta_s + d\vartheta_s)\delta(\vartheta_s + d\vartheta_s) = \gamma_k(\vartheta_s)Rd\vartheta_s, \quad (2.24)$$

where $\gamma_k(\vartheta_s)$ is the linear current density of the k -th turn.

Introducing the inverse function of the airgap ($g = 1/\delta$), (2.23) can be also written as:

$$\frac{H(\vartheta_s)}{g(\vartheta_s)} - \frac{H(\vartheta_s + d\vartheta_s)}{g(\vartheta_s + d\vartheta_s)} = \gamma_k(\vartheta_s)Rd\vartheta_s. \quad (2.25)$$

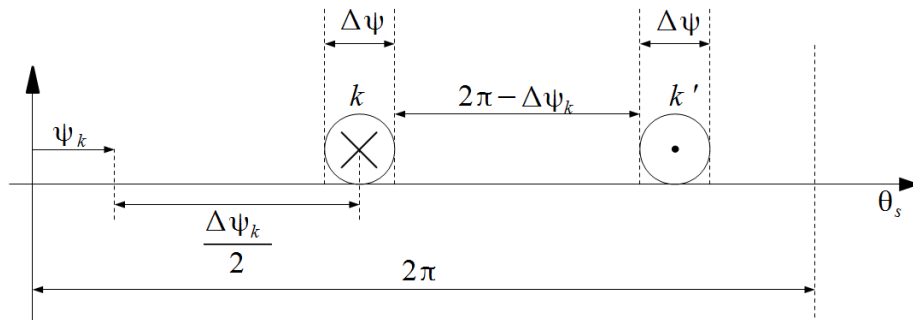


Fig. 2.3 – Spatial location of a turn (turn k) in the airgap circumference.

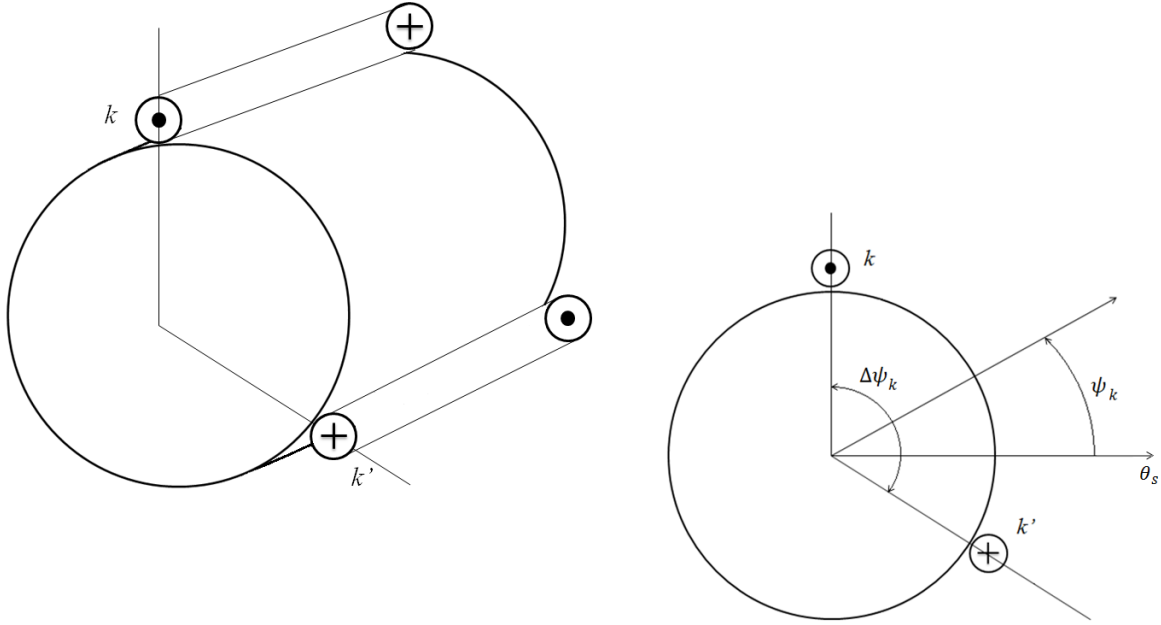


Fig. 2.4 – Spatial location of a turn (turn k) in the airgap circumference.

In terms of Taylor series, neglecting the higher order infinitesimal contributions, the following steps (where the angle dependence is implicit) can be done:

$$\begin{aligned} \frac{H(\vartheta_s)}{g(\vartheta_s)} - \frac{H(\vartheta_s + d\vartheta_s)}{g(\vartheta_s + d\vartheta_s)} &= \frac{H}{g} - \frac{H + \frac{dH}{d\vartheta_s} d\vartheta_s}{g + \frac{dg}{d\vartheta_s} d\vartheta_s} = \\ &= \frac{\frac{H}{g^2} \frac{dg}{d\vartheta_s} d\vartheta_s - \frac{1}{g} \frac{dH}{d\vartheta_s} d\vartheta_s}{1 + \frac{1}{g} \frac{dg}{d\vartheta_s} d\vartheta_s} = - \frac{\frac{d}{d\vartheta_s} \left(\frac{H}{g} \right) d\vartheta_s}{1 + \frac{1}{g} \frac{dg}{d\vartheta_s} d\vartheta_s}. \end{aligned} \quad (2.26)$$

Neglecting the higher order infinitesimal contributions, (2.26) becomes:

$$\lim_{d\vartheta_s \rightarrow 0} - \frac{\frac{d}{d\vartheta_s} \left(\frac{H}{g} \right) d\vartheta_s}{1 + \frac{1}{g} \frac{dg}{d\vartheta_s} d\vartheta_s} = - \frac{d}{d\vartheta_s} \left(\frac{H}{g} \right) d\vartheta_s. \quad (2.27)$$

The resulting circuital law (2.22) can be expressed for the infinitesimal angle of the airgap as:

$$- \frac{d}{d\vartheta_s} \left(\frac{H}{g} \right) d\vartheta_s = \gamma_k R d\vartheta_s. \quad (2.28)$$

That is:

$$\frac{d}{d\vartheta_s} \left(\frac{H}{g} \right) = \frac{dF}{d\vartheta_s} = -\gamma_k R, \quad (2.29)$$

with:

$$\frac{dF(\vartheta_s)}{d\vartheta_s} = -\gamma_k(\vartheta_s) R. \quad (2.30)$$

The term $F(\vartheta_s)$ represents the magnetomotive force distribution in the airgap related to the k -th turn, and can be evaluated once its linear current density (γ_k) is defined.

Once the magnetomotive force is defined, the magnetic field is simply calculated by the following equation (with ϑ_s explicit):

$$H(\vartheta_s) = g(\vartheta_s) F(\vartheta_s). \quad (2.31)$$

Equation (2.31) is general for whatever current distribution and reluctance circuit of the machine (slotting effects, reluctance of the rotor, etc.), until the approximation of radial field can be accepted. The advantage of this equation is that the magnetomotive force depends only from the current distribution (and not from the reluctance). Even if an analysis of the reluctance effects is not done in this thesis, it is worth to notice that rewriting (2.31) with all the quantities expressed in terms of their Fourier series allows evaluating which are the harmonics of the magnetomotive force and the reluctance that interact to produce each harmonic of the magnetic field.

Here below, the linear current density distribution is evaluated to define its representative magnetomotive force equation.

In case of a representation of the turns that neglects their radial thickness and with the hypothesis that the current density is the same in the turn width (rectangular wires), the linear current density of the generic k -th turn is described by the relationship:

$$\gamma_k(\vartheta_s) = \begin{cases} \pm \frac{i_k}{R\Delta\psi} & \text{if inside the turn width} \\ 0 & \text{if outside the turn width} \end{cases} \quad (2.32)$$

The linear current density of one turn can be expressed, in terms of Fourier series, by the following equation:

$$\gamma_k(\vartheta_s) = \Gamma_{k0} + \sum_{\rho=1}^{\infty} \Re \left\{ \bar{\Gamma}_{k\rho} e^{-j\rho\vartheta_s} \right\}, \quad (2.33)$$

where Γ_{k0} is the average value of the linear current density (always zero when considering a complete turn), and $\bar{\Gamma}_{k\rho}$ is the complex coefficient that represents the ρ -th order spatial harmonic of the linear current density distribution.

The complex coefficients of the Fourier series ($\bar{\Gamma}_{k\rho}$) are defined by the following Fourier transform:

$$\bar{\Gamma}_{k\rho} = \frac{1}{\pi} \int_{-\pi}^{\pi} \gamma_k(\vartheta_s) e^{j\rho\vartheta_s} d\vartheta_s. \quad (2.34)$$

The solution of (2.34) is quite straightforward with some expedients. Hereafter the solution steps are summarized:

$$\begin{aligned} \bar{\Gamma}_{k\rho} &= \frac{1}{\pi} \int_{\psi_k + \frac{\Delta\psi_k}{2} - \frac{\Delta\psi}{2}}^{\psi_k + \frac{\Delta\psi_k}{2} + \frac{\Delta\psi}{2}} \frac{i_k}{R\Delta\psi} e^{j\rho\vartheta_s} d\vartheta_s - \frac{1}{\pi} \int_{\psi_k - \frac{\Delta\psi_k}{2} - \frac{\Delta\psi}{2}}^{\psi_k - \frac{\Delta\psi_k}{2} + \frac{\Delta\psi}{2}} \frac{i_k}{R\Delta\psi} e^{j\rho\vartheta_s} d\vartheta_s = \\ &= \frac{i_k}{j\rho\pi R\Delta\psi} e^{j\rho\psi_k} \left(e^{j\rho\frac{\Delta\psi_k}{2}} - e^{-j\rho\frac{\Delta\psi_k}{2}} \right) \left(e^{j\rho\frac{\Delta\psi}{2}} + e^{j\rho\frac{\Delta\psi}{2}} \right) = \\ &= j \frac{4i_k}{\rho\pi R\Delta\psi} e^{j\rho\psi_k} \sin\left(\rho\frac{\Delta\psi_k}{2}\right) \sin\left(\rho\frac{\Delta\psi}{2}\right). \end{aligned}$$

When the width of the turn is negligible in the model, the following approximation is acceptable:

$$\begin{aligned} \bar{\Gamma}_{k\rho} &= \lim_{\Delta\psi \rightarrow 0} \left(j \frac{4i_k}{\rho\pi R\Delta\psi} e^{j\rho\psi_k} \sin\left(\rho\frac{\Delta\psi_k}{2}\right) \sin\left(\rho\frac{\Delta\psi}{2}\right) \right) = \\ &= j \frac{2i_k}{\pi R} e^{j\rho\psi_k} \sin\left(\rho\frac{\Delta\psi_k}{2}\right). \end{aligned} \quad (2.35)$$

The magnetomotive force distribution of the k -th turn can be now expressed by means of (2.30) introducing its Fourier transform:

$$\frac{d \sum_{\rho=1}^{\infty} \Re\{\bar{F}_{k\rho} e^{-j\rho\vartheta_s}\}}{d\vartheta_s} = - \sum_{\rho=1}^{\infty} \Re\{\bar{\Gamma}_{k\rho} e^{-j\rho\vartheta_s}\} \Re. \quad (2.36)$$

Solving the derivative and rearranging, the Fourier series components of the magnetomotive force can be expressed as:

$$\bar{F}_{k\rho} = -j \frac{R}{\rho} \bar{\Gamma}_{k\rho}. \quad (2.37)$$

The final expression of the magnetomotive spatial harmonics becomes:

$$\bar{F}_{k\rho} = \frac{2i_k}{\rho\pi} \sin\left(\rho\frac{\Delta\psi_k}{2}\right) e^{j\rho\psi_k}. \quad (2.38)$$

If the airgap is constant ($g(\vartheta_s) = \frac{1}{\delta}$), the magnetic field harmonics are directly related to the magnetomotive force distribution by (2.31), resulting in the equation:

$$\bar{H}_{k\rho} = \frac{\bar{F}_{k\rho}}{\delta} = \frac{2i_k}{\rho\pi\delta} \sin\left(\rho \frac{\Delta\psi_k}{2}\right) e^{j\rho\psi_k}. \quad (2.39)$$

The next paragraph aims to verify that (2.39) defines the magnetic field in the airgap generated by the current flowing in a generic turn in case of an isotropic magnetic circuit. This second method is less general, but much more simple.

2nd Method: point type currents for isotropic magnetic circuit

In case of an isotropic airgap ($\delta(\vartheta_s) = \delta$) and concentrated currents, it is possible to simplify the steps to reach the relationship between the harmonics of the armature magnetic field and the stator currents (2.39).

In this case, the two laws (2.21) and (2.23) can be simplified and directly used to find the desired equation. It can be done solving the following system of equations:

$$\begin{cases} \oint_C \bar{H} \cdot d\bar{l}_C = H_k^+ \delta + H_k^- \delta = i_k \\ \oint_{S_C} \bar{B} \cdot d\bar{S}_C = H_k^+ \Delta\psi_k - H_k^- (2\pi - \Delta\psi_k) = 0 \end{cases} \quad (2.40)$$

Resulting in:

$$\begin{cases} H_k^+ = \frac{i_k}{\delta} \frac{2\pi - \Delta\psi_k}{2\pi} \\ H_k^- = \frac{i_k}{\delta} \frac{\Delta\psi_k}{2\pi} \end{cases} \quad (2.41)$$

The space harmonics of the magnetic field can be directly derived by the Fourier transform of the spatial distribution given by (2.41) with the following steps:

$$\begin{aligned} \bar{H}_{k\rho} &= \frac{1}{\pi} \int_0^{2\pi} H_k e^{j\rho\vartheta_s} d\vartheta_s = \frac{1}{\pi} \int_{\psi_k - \frac{\Delta\psi_k}{2}}^{\psi_k + \frac{\Delta\psi_k}{2}} H_k^+ e^{j\rho\vartheta_s} d\vartheta_s - \frac{1}{\pi} \int_{\psi_k + \frac{\Delta\psi_k}{2}}^{\psi_k - \frac{\Delta\psi_k}{2}} H_k^- e^{j\rho\vartheta_s} d\vartheta_s = \\ &= \frac{1}{\pi} \int_{\psi_k - \frac{\Delta\psi_k}{2}}^{\psi_k + \frac{\Delta\psi_k}{2}} \frac{i_k}{\delta} \frac{2\pi - \Delta\psi_k}{2\pi} e^{j\rho\vartheta_s} d\vartheta_s - \frac{1}{\pi} \int_{\psi_k + \frac{\Delta\psi_k}{2}}^{\psi_k - \frac{\Delta\psi_k}{2}} \frac{i_k}{\delta} \frac{\Delta\psi_k}{2\pi} e^{j\rho\vartheta_s} d\vartheta_s = \\ &= \frac{i_k}{j\rho\pi\delta} \left(e^{j\rho \frac{\Delta\psi_k}{2}} - e^{-j\rho \frac{\Delta\psi_k}{2}} \right) e^{j\rho\psi_k} = \frac{2i_k}{\rho\pi\delta} \sin\left(\rho \frac{\Delta\psi_k}{2}\right) e^{j\rho\psi_k}. \end{aligned}$$

Exactly the same result of equation (2.39) is obtained. Fig. 2.5 shows the magnetic field in the airgap related to the analysed turn.

The next subsection defines the equation of total field in the airgap produced by a multiphase winding in an isotropic machine. Hereafter, the machine is considered as isotropic (the reluctance effects are neglected).

Armature field (multiphase winding)

This subsection aims to evaluate the field distribution produced by a multiphase winding.

Taking into account a single phase (x) with N_x coils (y), composed by N_{xy} turns each, the total armature field of the analysed phase can be written as:

$$\bar{H}_{x\rho} = \sum_{y=1}^{N_x} N_{xy} \bar{H}_{y\rho} = \sum_{y=1}^{N_x} N_{xy} \frac{2i_x}{\rho\pi\delta} \sin\left(\rho \frac{\Delta\psi_{xy}}{2}\right) e^{j\rho\psi_{xy}}. \quad (2.42)$$

Taking into account of all the m phases of the machine, the overall harmonics of the armature field can be written as:

$$\bar{H}_\rho = \sum_{x=1}^m \sum_{y=1}^{N_x} N_{xy} \bar{H}_{xy\rho} = \sum_{x=1}^m \sum_{y=1}^{N_x} N_{xy} \frac{2i_x}{\rho\pi\delta} \sin\left(\rho \frac{\Delta\psi_{xy}}{2}\right) e^{j\rho\psi_{xy}}. \quad (2.43)$$

If all the phases have the same coils geometry (in terms of winding in the slots) and are only placed in different stator areas, the pitch of the coils of each phase ($\Delta\psi_y$) is the same and also their relative positions (ψ_y), number (N_c) and turns number in each one (N). It follows that (2.43) becomes:

$$\bar{H}_\rho = \sum_{x=1}^m \sum_{y=1}^{N_x} N_{xy} \bar{H}_{xy\rho} = \frac{2N}{\rho\pi\delta} \sum_{x=1}^m i_x e^{j\rho\psi_x} \left(\sum_{y=1}^{N_c} \sin\left(\rho \frac{\Delta\psi_y}{2}\right) e^{j\rho\psi_y} \right), \quad (2.44)$$

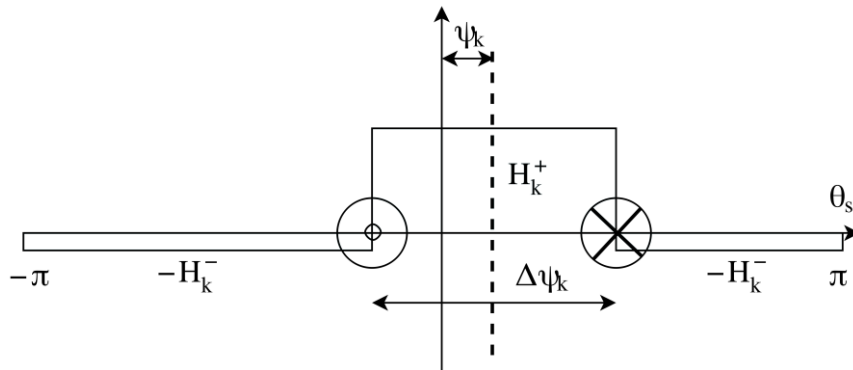


Fig. 2.5 – Spatial distribution of the magnetic field produced by a turn (turn k) in the airgap.

CHAPTER 2

where ψ_y is the angular shift from the magnetic axis of the y -th coil and the magnetic axis of the relative phase, while ψ_x is the magnetic axis of the x -th phase.

Owing to this choice of the angles in (2.44), it is possible to introduce a constant called winding factor and defined as:

$$K_{ap} = \frac{\sum_{y=1}^{N_c} \sin\left(\rho \frac{\Delta\psi_y}{2}\right) e^{j\rho\psi_y}}{pq}. \quad (2.45)$$

It is worth noticing that the winding factor K_{ap} might be, in general, a complex number. However, if the coils have the same number of turns and are symmetrically distributed around the magnetic axis of the relative phase (as it usually happens) it results in a real constant.

It results that the magnetic field harmonics can be written as:

$$\bar{H}_\rho = N \sum_{x=1}^m \sum_{y=1}^{N_c} \bar{H}_{xy\rho} = \frac{2NpqK_{ap}}{\rho\pi\delta} \sum_{x=1}^m i_x e^{j\rho\psi_x}. \quad (2.46)$$

It can be noticed that the only complex number in the last equation is related to the position of the stator phases. It follows that a new complex variable (\bar{i}_ρ , called current space vector) can be introduced in order to redefine (2.46) as:

$$\bar{H}_\rho = \frac{Nmpq}{\pi\delta} \frac{K_{ap}}{\rho} \bar{i}_\rho, \quad (2.47)$$

with the current space vector defined as:

$$\bar{i}_\rho = \frac{2}{m} \sum_{x=1}^m i_x e^{j\rho\psi_x}. \quad (2.48)$$

However, (2.48) is not always a symmetrical transformation of the m currents. A symmetrical transformation can be used, in order to generalize the machine model, as discussed in the previous subsection. In particular, the machine is considered having a number of phases equal to the slots number (N_s). The non-existing phases are not taken into account in the summation of the current space vector evaluation, while the existing phases are numbered with the position of their magnetic axis or with the first slot from which they appear with the same shape of the others. It results that (2.48) can be rewritten as:

$$\bar{i}_\rho = \frac{2}{m} \sum_{x=1}^{N_s} i_x e^{j\rho \frac{2\pi}{N_s}(x-1)}, \quad (2.49)$$

with x representing the x -th phase with its magnetic axis shifted of $\frac{2\pi}{N_s}(x-1)$ radians from the first phase of the winding (which defines the origin of the stator reference frame). The current i_x results to be equal to zero if there is not a phase with the magnetic axis in the x -th position. This concept is deeply investigated in the next section, and allows defining a symmetrical

transformation for the N_s redundant variables. Indeed, for a system of m phase, (2.49) is written for $N_s - m$ additional phases which not existing, can be taken into account just setting their currents to zero. These can be seen as searching phases (considering the searching coils idea) which are not fed by a voltage source and have zero current. However, for the purpose of this thesis, these phases are just needed for the generalisation of the model and do not have a physical meaning.

Often, it is possible to find a smaller symmetry in the winding of order n (all the existing phases have the magnetic axis centred in positions shifted of an angle multiple of $\frac{2\pi}{n}$ fro the first phase). In this case, a space vector symmetrical transformation with a reduced number of variables can be defined as:

$$\bar{i}_\rho = \frac{2}{m} \sum_{x=1}^n i_x e^{j\rho \frac{2\pi}{n}(x-1)}. \quad (2.50)$$

If the phases are symmetrically distributed (in the hypothesis of the model, this is possible only if the phases are an odd number), n is equal to the phase number m and:

$$\bar{i}_\rho = \frac{2}{m} \sum_{x=1}^m i_x e^{j\rho \frac{2\pi}{m}(x-1)}. \quad (2.51)$$

Finally, if $2mpq$ is equal to the slots number (N_s), (2.47) can be also represented as:

$$\bar{H}_\rho = \frac{NN_s}{2\pi\delta} \frac{K_{ap}}{\rho} \bar{i}_\rho. \quad (2.52)$$

The general equation needed to describe the harmonics of the magnetic field generated by a multiphase winding (2.47) (2.49) are analysed in the next subsection. In particular, it shows the current space vector transformation (2.49) explaining when and how the related inverse transformation can be simplified. In the following subsections, the approach is verified and for some common winding topologies.

Space vectors analysis for modelling of multiphase machines

The relationships between the phase currents and the space harmonics of the magnetic field are fully described by (2.47) or in many cases by (2.52). This equation allows introducing the complex numbers, already named current space vectors (\bar{i}_ρ). Because the final goal of the machine model is to define a proper control, a smart choice for representing the other variables of the system is by means of vectors defined in the same way.

The current space vectors are defined by (2.48) as:

$$\bar{i}_\rho = \frac{2}{m} \sum_{x=1}^m i_x e^{j\rho\psi_x}.$$

This transformation can be also used for all the other quantities of the system (voltages and linked fluxes), allowing to consider the machine as a sum of three-phase machines (each related to the considered space) interacting as described by the SVD model.

However, the identification of a suitable SVD inverse transformation is essential in order to evaluate the physical variables of the system and therefore to define the machine control (or in other words, calculating the reference phase voltages once the voltage space vectors are established). The proposed solution to define a general SVD inverse transformation is by means of a new symmetrical transformation that still keeps the same current space vector equations shape.

The idea is to settle a redundant multiphase transformation, introducing additional variables and set them equal to zero, in order to have a symmetrical transformation and inverse transformation (as (2.1) and (2.2)). The hypotheses are that:

- All the phases of the machine must be considered with the same geometry and just located in a different area of the stator (two different winding layouts are not taken into account). This assumption is the same used to define the magnetic field of the machine stator currents in (2.44).
- Each phase must be shifted from the others of a pitch that is a multiple of the same integer fraction of the total circumference. In particular, they must be shifted of an integer number of slots (assuming that the slots are symmetrically distributed around the stator circumference).

Because the analysed winding has equal coils (with pitch c_{pitch}) for each phase, and the phases are shifted at least from a slot pitch, the transformations (2.1) and (2.2) are written for a number of variables that is the same of the slot number (N_s), as for the currents in (2.49). The generalized transformation is defined as:

$$\bar{y}_h = \frac{2}{m} \sum_{k\mathfrak{R}=1}^{N_s} x_{k\mathfrak{R}} \bar{\alpha}^{h(k-1)}, \quad h = 0, 1, 2, \dots, N_s - 1, \quad (2.53)$$

with $\bar{\alpha} = e^{j\frac{2\pi}{N_s}}$ and $k\mathfrak{R}$ used to highlight that the summation keeps into account only once the quantities associated with the machine phases, under the hypothesis that the phases are geometrically equal, starting in the $k\mathfrak{R}$ -th slot, and wound in the same direction; otherwise the quantity $x_{k\mathfrak{R}}$ must be considered equal to zero.

The inverse transformation is still (2.2), adapted here below to the N_s quantities of the m -phase system.

$$x_k = \frac{m}{2N_s} \sum_{h=0}^{N_s-1} \bar{y}_h \bar{\alpha}^{-h(k-1)}, \quad k = 1, 2, \dots, N_s. \quad (2.54)$$

The inverse transformation can be simplified to take into account of the relationships that the different space vectors \bar{y}_h have, according to the considered winding layout. In particular, if it is possible to identify a symmetry in the phase positions, the angle that represent the symmetry can be redefined as $\bar{\alpha} = e^{j\frac{2\pi}{n_s}}$, where n_s is the new number of symmetrically distributed slots needed to place the starting coil of each phase. This approach allows simplifying the transformation and inverse transformation, using an equivalent number of slots n_s rather than the real one (N_s). The transformation results as:

$$\bar{y}_h = \frac{2}{m} \sum_{k\mathfrak{R}=1}^{n_s} x_{k\mathfrak{R}} \bar{\alpha}^{h(k-1)}, \quad h = 0, 1, 2, \dots, N_s - 1, \quad (2.55)$$

with $\bar{\alpha} = e^{j\frac{2\pi}{n_s}}$ and $k\mathfrak{R}$ used to highlight that the summation keeps into account only the phases starting in the $k\mathfrak{R}$ -th slot of the new reduced set of slots.

The inverse transformation becomes:

$$x_k = \frac{m}{2n_s} \sum_{h=0}^{n_s-1} \bar{y}_h \bar{\alpha}^{-h(k-1)}, \quad k = 1, 2, \dots, N_s. \quad (2.56)$$

It is worth to note that (2.53) is numerically identical to (2.48). It is just defined in a different way in order to realize that there is an inverse transformation that can always be used for all the machines that have a winding configuration in agreement with the hypothesis of the model described in this thesis.

These transformations and inverse transformations are the starting point of the proposed general machine model. They allow completely describing the full system and are coherent with the definition of a direct relationship between the current space vectors and the magnetic field in the airgap. Then, for each winding, the not existing variables (related to the not physical phases) are set to zero and the winding constraints are considered in order to find the final transformation and inverse transformation suitable for the analysed machine. The idea is to define a symmetrical transformation with the lowest number of variables (the equivalent number of reduced slots, n_s), in such a way the it is easier to find an inverse transformation that consider the same number of input variables as the degrees of freedom of the system.

The next subsections show the analysis of the space vector representation for some multiphase windings. The presented windings are the same of the machines analysed in the next chapters. For each of them more possible winding configurations and space vector transformations are considered, highlighting the differences.

Space vectors analysis (the standard three-phase winding)

This subsection shows the analysis of the simplest three-phase distributed winding machine in order to present the concept of symmetrical and asymmetrical winding and space vector transformation.

Fig. 2.6 shows a three-phase distributed winding machine with six slots. The origin of the stator reference frame is in the position of the magnetic axis of the first phase (in this case the first phase is the green one, wound from the slot 1 to the slot 4). This assumption is valid in the entire thesis, if not specified.

The relationship between the magnetic field harmonics and the generalized current space vector \bar{i}_ρ ($\bar{i}_\rho = \frac{2}{m} \sum_{x=1}^{N_s} i_x e^{j\rho \frac{2\pi}{N_s}(x-1)}$), is defined by (2.52) ($\bar{H}_\rho = \frac{NN_s}{2\pi\delta} \frac{K_{a\rho}}{\rho} \bar{i}_\rho$). For the analysed winding, the generalized current space vector is defined as:

$$\bar{i}_\rho = \frac{2}{3} \sum_{x=1}^3 i_x e^{j\rho \frac{2\pi}{6}(x-1)} \quad (2.57)$$

Taking into account for the convention of the positive currents, (the magnetic axis of the phase starting in the second coil is usually wound in the opposite direction of the others in order to create a suitable rotating field), the current space vector equation can be rewritten considering the phase starting in the 2nd slot as starting from the 5th. This can be done only because the geometry of the phase is the same if it is analysed as starting from one slot or from the other. This new solution leads to define the current space vectors as for an equivalent slots layout with only the odd slots (named y), as:

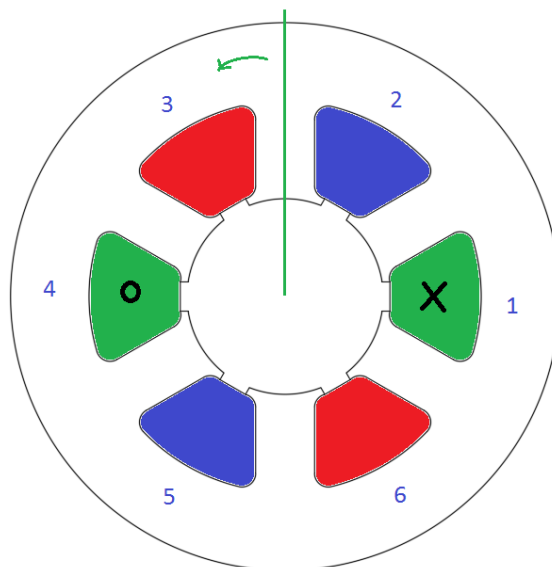


Fig. 2.6 – Six slots distributed winding three-phase machine concept (example). The green vertical line (magnetic axis of the first phase) highlights the origin of the stator reference frame.

$$\bar{i}_\rho = \frac{2}{3} \sum_{x=1,3,5} i_x e^{j\rho \frac{2\pi}{6}(x-1)} = \frac{2}{3} \sum_{y=1,2,3} i_y e^{j\rho \frac{2\pi}{3}(y-1)}. \quad (2.58)$$

Therefore, the generalized transformation of this machine can be defined in two significant ways:

- Asymmetrical winding
- Symmetrical winding

Asymmetrical winding (the standard three-phase winding) - example

If the phases are chosen as starting in the 1st, 2nd and 3rd slot respectively as in Fig. 2.7 (left), (2.53) can be written as:

$$\bar{y}_h = \frac{2}{3} (x_1 + x_2 \bar{\alpha}^h + x_3 \bar{\alpha}^{2h}) = \frac{2}{3} \left(x_1 + x_2 e^{j\frac{2\pi}{6}h} + x_3 e^{j\frac{2\pi}{6}2h} \right), \quad h = 0,1,2,3,4,5, \quad (2.59)$$

with $\bar{\alpha} = e^{j\frac{2\pi}{6}}$. It is worth to notice that this transformation is an asymmetrical one, and therefore it is considered as a redundant symmetrical transformation with six equivalent variables (twice the physical ones):

$$\bar{y}_h = \frac{2}{3} \left(x_1 + x_2 e^{j\frac{2\pi}{6}h} + x_3 e^{j\frac{2\pi}{6}2h} + x_4 e^{j\frac{2\pi}{6}3h} + x_5 e^{j\frac{2\pi}{6}4h} + x_6 e^{j\frac{2\pi}{6}5h} \right), \quad (2.60)$$

with $x_4 = x_5 = x_6 = 0$.

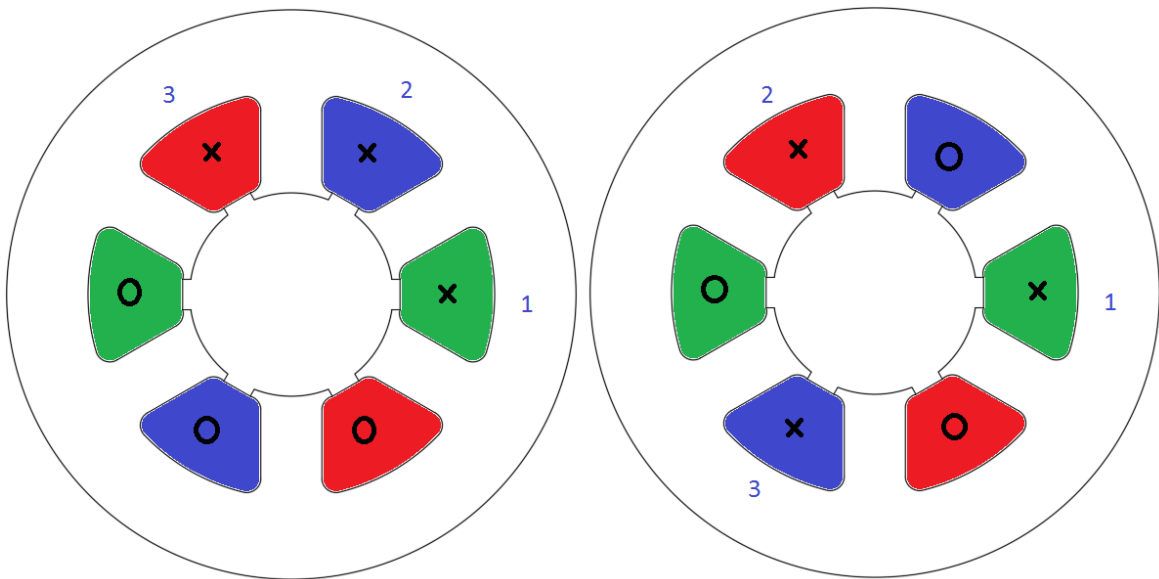


Fig. 2.7 – Six slots distributed winding three-phase machine with asymmetrical (left) and symmetrical (right) winding distribution (concept). With “x” are indicated the starting slots of the phases and with “o” the final ones.

CHAPTER 2

The generic inverse transformation is related to an equivalent system with six variables (an even number of variables), so it can be written as:

$$\begin{aligned} x_k &= \frac{m}{2N_s} \sum_{h=0}^{N_s-1} \bar{y}_h \bar{\alpha}^{-h(k-1)} = \frac{1}{4} \sum_{h=0}^5 \bar{y}_h \bar{\alpha}^{-h(k-1)} = \\ &= \frac{1}{4} \left(y_0 + \bar{y}_1 e^{-j\frac{2\pi}{6}(k-1)} + \bar{y}_2 e^{-j\frac{2\pi}{3}(k-1)} + y_3 e^{-j\pi(k-1)} + \bar{y}_4 e^{-j\frac{4\pi}{3}(k-1)} + \bar{y}_5 e^{-j\frac{2\pi}{6}5(k-1)} \right). \end{aligned} \quad (2.61)$$

As mentioned in the previous section, the inverse transformation for an even number of variables is defined also by (2.17) or, because the transformation is kept the same even for the redundant number of variables, as:

$$x_k = \frac{1}{4} y_0 + \frac{1}{4} y_3 e^{-j\pi(k-1)} + \frac{1}{2} \Re \left\{ \bar{y}_1 e^{-j\frac{2\pi}{6}(k-1)} \right\} + \frac{1}{2} \Re \left\{ \bar{y}_2 e^{-j\frac{2\pi}{3}(k-1)} \right\}. \quad (2.62)$$

It is straightforward to verify the relationship here below (for $k=1, 2$ and 3):

$$\frac{1}{4} y_0 + \frac{1}{2} \Re \left\{ \bar{y}_2 e^{-j\frac{2\pi}{3}(k-1)} \right\} = \frac{1}{4} y_3 e^{-j\pi(k-1)} + \frac{1}{2} \Re \left\{ \bar{y}_1 e^{-j\frac{2\pi}{6}(k-1)} \right\}.$$

Therefore, the inverse transform can be written also as:

$$x_k = \frac{1}{2} \sum_{h=0}^5 \bar{y}_h \bar{\alpha}^{-h(k-1)} = \frac{1}{2} y_0 + \Re \left\{ \bar{y}_2 e^{-j\frac{2\pi}{3}(k-1)} \right\} = \frac{1}{2} y_3 e^{-j\pi(k-1)} + \Re \left\{ \bar{y}_1 e^{-j\frac{2\pi}{6}(k-1)} \right\}. \quad (2.63)$$

This result is an example of the inverse transformation that can be used for asymmetrical systems modelled as symmetrical redundant ones, as shown in the equations (2.19) and (2.20).

It is immediate to define a new transformation for the analysed winding as:

$$\bar{z}_h = \bar{y}_{2h} = \frac{2}{3} (x_1 + x_2 \bar{\alpha}^{2h} + x_3 \bar{\alpha}^{4h}) = \frac{2}{3} \left(x_1 + x_2 e^{j\frac{2\pi}{3}h} + x_3 e^{j\frac{4\pi}{3}h} \right).$$

Which inverse transform is:

$$x_k = \frac{1}{2} z_0 + \Re \left\{ \bar{z}_1 e^{-j\frac{2\pi}{3}(k-1)} \right\}.$$

This means that a new symmetrical transformation can be defined, rather than the asymmetrical one. According to the model hypothesis, this is possible because the geometry of the second phase is the same if it is considered as starting in the slot 2 or 5 (only its magnetic axis is the opposite, but the magnetic axes of the phases depend on the winding connections and the proposed model is independent from the star connection constraints).

Symmetrical winding (the standard three-phase winding) - example

Owing to the result obtained by the asymmetrical winding of a standard three-phase machine, it seems that the transformation can be simplified to a symmetrical one. In order to avoid passing from the asymmetrical transformation, it is also possible to choose the starting of the winding phases considering them in the odd slots, knowing already that there are not phases starting in the even slots. In this way, the machine can be considered as an equivalent one with half the number of the slots for the starting of the phases (now the subscript of the variables, k , refers to the new set of symmetrical slots numeration as in Fig. 2.7, right):

$$\bar{y}_h = \frac{2}{3} (x_1 + x_2 \bar{\alpha}^{2h} + x_3 \bar{\alpha}^{4h}) = \frac{2}{3} \left(x_1 + x_2 e^{j\frac{2\pi}{3}h} + x_3 e^{j\frac{4\pi}{3}h} \right), \quad h = 0,1,2, \quad (2.64)$$

with $\bar{\alpha} = e^{j\frac{2\pi}{3}}$. This approach is always useful for machines with an odd number of phases symmetrically distributed.

The generic inverse transformation is as the one for a system with an odd number of variables, (2.14) and (2.15). The possible inverse transformations are rewritten here below for this specific case:

$$x_k = \frac{y_0}{2} + \Re \left\{ \bar{y}_1 \bar{\alpha}^{-(k-1)} \right\}, \quad k = 1,2,3, \quad (2.65)$$

and

$$x_k = \frac{y_0}{2} + \Re \left\{ \bar{y}_2 \bar{\alpha}^{-2(k-1)} \right\}, \quad k = 1,2,3. \quad (2.66)$$

The symmetrical winding model is usually preferred in the modelling of symmetrical machines because it reflects the winding conventions for the positive currents, and the star connection constraint results in having a null homopolar current space vector (i_0). Instead, in case of asymmetrical connection of the winding, the general transformation can be preferred for the same reason.

The analysis on a standard three-phase winding machine is useful to validate the effectiveness of the proposed transformation, and is one of the easier examples to show how the choice of a proper transformation is useful to simplify the machine model. The choice must be done taking into account of the star connection constraints and being aware of the complexity of an inverse transformation when the transformation is not the suitable one.

Hereafter, the concept is applied for almost all the multiphase winding layouts that are analysed in this thesis.

Space vectors analysis (12 phase asymmetrical winding)

A 12 phase asymmetrical winding with 2 pole pairs and 1 slot per pole and per phase, as the one in Fig. 2.8 (left) can be described by the following general transformation:

$$\bar{y}_h = \frac{2}{m} \sum_{k \Re=1}^{N_s} x_k \bar{\alpha}^{h(k-1)} = \frac{2}{m} \sum_{k \Re=1}^{48} x_k \bar{\alpha}^{h(k-1)}, \quad h = 0,1,2,\dots,N_s - 1, \quad (2.67)$$

with $\bar{\alpha} = e^{j\frac{2\pi}{N_s}} = e^{j\frac{2\pi}{48}}$, and the inverse transformation results in:

$$x_k = \frac{m}{2N_s} \sum_{h=0}^{N_s-1} \bar{y}_h \bar{\alpha}^{-h(k-1)} = \frac{1}{8} \sum_{h=0}^{48} \bar{y}_h \bar{\alpha}^{-h(k-1)}. \quad (2.68)$$

However, the phases under each pole pairs are the same and till there is a symmetry of the machine under the different pole pairs, the stator winding generates and interacts with only the harmonics of the magnetic field in the airgap multiple of the pole pairs number (p). Indeed the winding factor K_{ap} in (2.52) is zero for all the other harmonics. It means that the existence of a current space vector not multiple of p has not electromagnetic effects on the machine. Therefore, in the inverse transformation only the space vectors multiple of p are useful to determine the machine behaviour and define a machine control. The inverse transformation becomes:

$$x_k = \frac{mp}{2N_s} \sum_{h=0}^{N_s/p-1} \bar{y}_{ph} e^{-j\frac{2\pi}{N_s}ph(k-1)} = \frac{1}{4} \sum_{h=0}^{24} \bar{z}_h e^{-j\frac{2\pi}{24}h(k-1)}, \quad (2.69)$$

with the transformation:

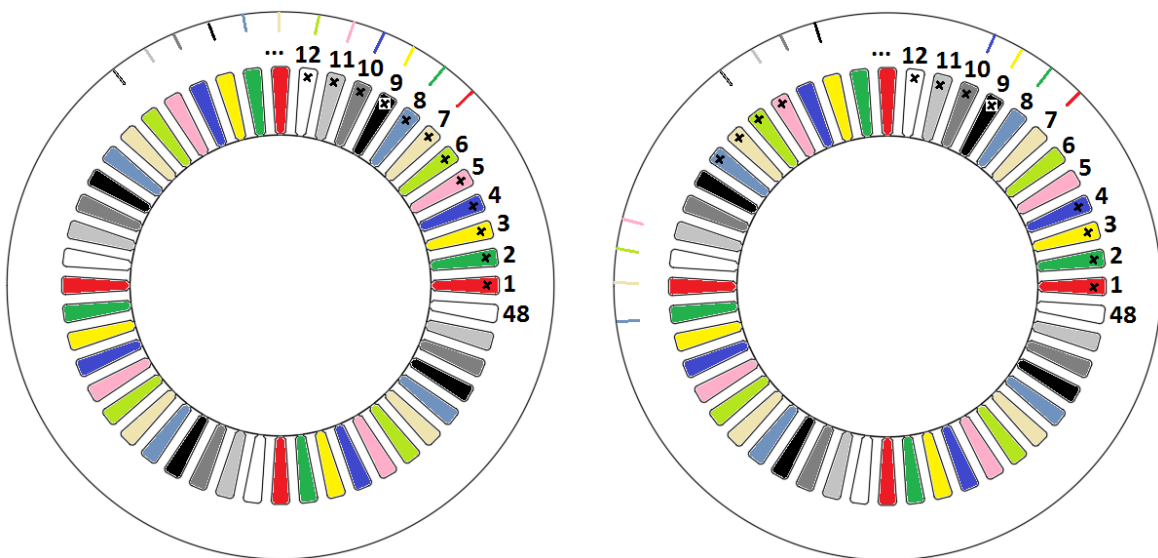


Fig. 2.8 – 48 slots and 2 pole pairs distributed winding 12-phase machine. Asymmetrical winding (left) and quadruple three-phase winding (right). The magnetic axis and the starting of the phases are highlighted with coloured lines in the back iron and with crosses in the slots respectively.

$$\bar{z}_h = \frac{2}{m} \sum_{n=1}^m x_n e^{j \frac{2\pi}{N_s} p h (n-1)} = \frac{2}{12} \sum_{n=1}^{12} x_n e^{j \frac{2\pi}{24} (n-1)}.$$

The following transformation can be introduced as done for the three-phase winding, recreating a symmetry in the transformation and inverse transformation neglecting the pole pairs. This approximation can be still done only because the field related to the currents (and linked with the winding) is always symmetrical under each pole pair, and so it is possible to define the space vectors without taking into account the current space vectors not multiple of p . With the new assumptions, the transformation for the analysed machine becomes:

$$\bar{y}_h = \frac{2}{12} \sum_{k=1}^{12} x_k \bar{\alpha}^{h(k-1)}, \quad h = 0, 1, 2, \dots, 23, \quad (2.70)$$

with the new $\bar{\alpha}$ value: $\bar{\alpha} = e^{j \frac{2\pi}{24}}$. In this case, the winding is asymmetrical, and it is not possible to find a reduced symmetry of the windings in order to simplify the transformation.

The inverse transformation results in:

$$x_k = \frac{1}{4} \sum_{h=0}^{23} \bar{y}_h \bar{\alpha}^{-h(k-1)}, \quad k = 1, 2, \dots, 12, \quad (2.71)$$

That can be also rewritten as:

$$x_k = \frac{1}{4} y_0 + \frac{1}{4} y_{12} e^{-j\pi(k-1)} + \frac{1}{2} \sum_{h=1}^{11} \Re\{\bar{y}_h \bar{\alpha}^{-h(k-1)}\}, \quad k = 1, 2, \dots, 12, \quad (2.72)$$

and it can be verified that for this winding a further simplification allows rewriting the inverse transformation as:

$$x_k = \sum_{h_{\text{odd}}=1}^{11} \Re\{\bar{y}_h \bar{\alpha}^{-h(k-1)}\}, \quad k = 1, 2, \dots, 12, \quad (2.73)$$

or

$$x_k = \frac{1}{2} y_0 + \frac{1}{2} y_{12} e^{-j\pi(k-1)} + \sum_{h_{\text{even}}=2}^{10} \Re\{\bar{y}_h \bar{\alpha}^{-h(k-1)}\}, \quad k = 1, 2, \dots, 12. \quad (2.74)$$

It is worth to notice that if the winding was not symmetrical under the pole pairs, all the current space vectors must be taken into account to analyse also the harmonics of the field not multiple of p . In this scenario, the general equations (2.67) and (2.68) must be considered in the model. How to better identify the relationships between the current space vectors in order to define a number of independent variable (among the current space vectors) equal to the degrees of freedom of the system remains an open question.

Quadruple three-phase configuration

The twelve-phase machine analysed in this thesis has another feature. The phases are gathered together in three groups of four phases. Each of this group has been wound thinking at its equivalent three-phase 4 slot per pole and per phase layout. It means that the second group of phases rather than starting in the 5-th slot (4+1) starts in the 9-th one (4*2+1), and the third group of phases starts in the 17-th one (4*4+1). Fig. 2.8 (right) shows the magnetic axis of the quadruple three-phase winding layout under the first pole pair.

However, the transformation remains the same, and just the phases are chosen with a different angle:

$$\bar{y}_h = \frac{2}{m} \sum_{k=1}^4 x_k \bar{\alpha}^{h(k-1)} + \frac{2}{m} \sum_{k=9}^{12} x_k \bar{\alpha}^{h(k-1)} + \frac{2}{m} \sum_{k=17}^{20} x_k \bar{\alpha}^{h(k-1)}, \quad h = 0,1,2,\dots,23, \quad (2.75)$$

with $\bar{\alpha} = e^{j\frac{2\pi}{24}}$, and the inverse transformation is still defined in the same way (considering the inverse transformation based on the odd space vectors) but for a different phase numeration:

$$x_k = \sum_{h_{\text{odd}}=1}^{11} \Re\{\bar{y}_h \bar{\alpha}^{-h(k-1)}\}, \quad k = 1,2,3,4,9,10,11,12,17,18,19,20. \quad (2.76)$$

The advantage of this choice is that in the equivalent three-phase configuration the machine can be described by a symmetrical three-phase transformation. Furthermore, if each phase of the four-phase subsystems is considered as part of a three-phase system with the respective phases of the two other subsystems, each of the resulting three-phase subsystems is a symmetrical one and the machine can be described as sum of four shifted three-phase subsystems. In particular, these four three-phase subsystem can be fed by independent converters, realising the so-called quadruple three-phase winding configuration.

The next two subsections present two completely different nine-phase windings. In the next, the nine phases are distributed in the same way in the different pole pairs with a series connection of the coils. Therefore, each phase is symmetrically wound around the stator circumference. In the following, the phases are wound only in some sectors of the stator, resulting in an asymmetrical coil distribution of each phase.

Space vectors analysis (nine phase winding)

In this subsection, a nine phase winding, as the one in Fig. 2.9, is considered. The winding is studied before as a three-phase winding to show how to take into account of the slot per pole and per phase number. Then, the nine-phase winding configuration is investigated.

Three-phase configuration

It is possible to consider the nine-phase winding as a three-phase winding if the phases are series connected. In Fig. 2.9, the equivalent three-phase winding can be identified by connecting the phases with the same colour (and different tone) in series. In this case the same assumption done for the 12-phase machine in terms of pole pairs can be done. The resulting transformation is:

$$\bar{y}_h = \frac{2}{3} \sum_{k \in \mathcal{R}=1}^{18} x_k \bar{\alpha}^{h(k-1)}, \quad h = 0, 1, 2, \dots, 17, \quad (2.77)$$

with $\bar{\alpha} = e^{j\frac{2\pi p}{N_s}} = e^{j\frac{2\pi}{18}}$, and the inverse transformation results in:

$$x_k = \frac{mp}{2N_s} \sum_{h=0}^{N_s/p-1} \bar{y}_h \bar{\alpha}^{-h(k-1)} = \frac{1}{4} \sum_{h=0}^{17} \bar{y}_h \bar{\alpha}^{-h(k-1)}. \quad (2.78)$$

In this example the slots per phase and per pole (q) is kept as a variable in order to generalize the method. The transformation can be investigated under the assumption that the phases are considered as starting from the same slot per pole and per phase, as in the steps below:

$$\bar{y}_h = \frac{2}{m} \sum_{k \in \mathcal{R}=1}^{N_s/p} x_k e^{j\frac{2\pi p}{N_s} h(k-1)} = \frac{2}{m} \sum_{n=1}^m x_n e^{j\frac{2\pi p}{N_s} hq(n-1)} = \frac{2}{m} \sum_{n=1}^m x_n e^{j\frac{2\pi}{2m} h(n-1)}.$$

This transformation is the same found for the asymmetrical three-phase winding (2.59). Again, the second phase can be considered as starting in the place of the 5th equivalent slot of the six phase equivalent stator. This allows defining a final transformation as the standard one:

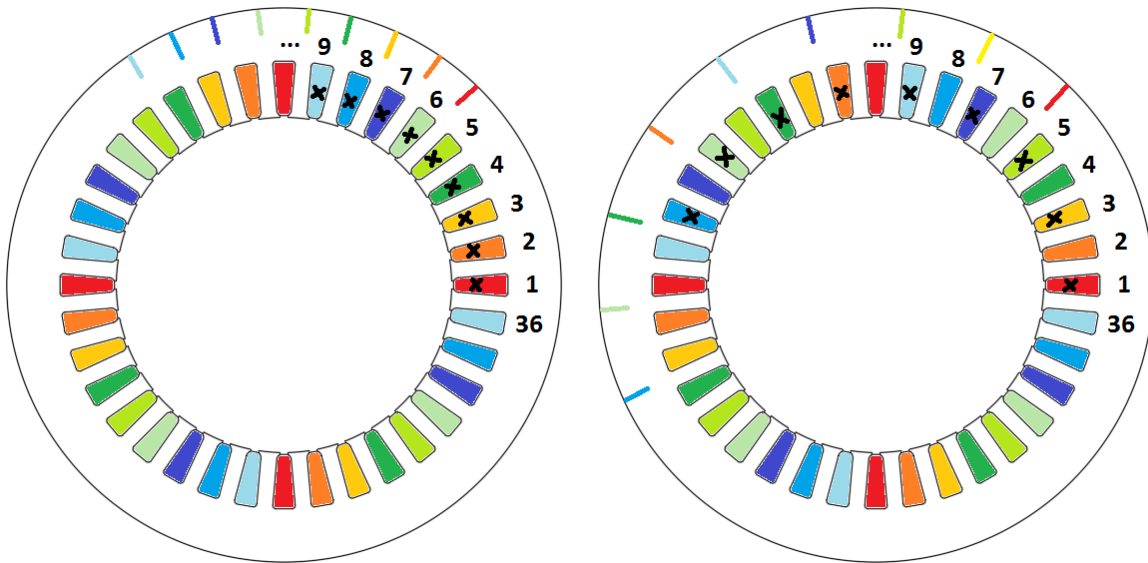


Fig. 2.9 – 36 slots and 2 pole pairs distributed winding 9-phase machine. Asymmetrical winding (left) and symmetrical winding (right). The magnetic axis and the starting of the phases are highlighted with coloured lines in the back iron and with crosses in the slots respectively. Note: the winding on the right is symmetrical in its electrical degrees representation.

$$\bar{y}_h = \frac{2}{m} \sum_{n=1}^m x_n e^{j \frac{2\pi}{m} h(n-1)} = \frac{2}{3} \sum_{n=1}^3 x_n e^{j \frac{2\pi}{3} h(n-1)},$$

with its inverse transformation given by:

$$x_k = \frac{2mpq}{2N_s} \sum_{h=0}^{N_s/(2pq)-1} \bar{y}_h \bar{\alpha}^{-h(k-1)} = \frac{1}{2} \sum_{h=0}^{m-1} \bar{y}_h \bar{\alpha}^{-h(k-1)} = \frac{1}{2} y_0 + \Re\{\bar{y}_1 \bar{\alpha}^{-(k-1)}\}, \quad (2.79)$$

with $\bar{\alpha} = e^{j \frac{2\pi}{m}} = e^{j \frac{2\pi}{3}}$.

Nine-phase configuration

Fig. 2.9 (left) shows the nine-phase winding configuration. The winding in its nine-phase configuration can be studied as an asymmetrical winding with the general transformation and inverse transformation as follows:

$$\bar{y}_h = \frac{2}{9} \sum_{k \in \mathbb{R}=1}^{36} x_k \bar{\alpha}^{h(k-1)} \quad \text{and} \quad x_k = \frac{1}{8} \sum_{h=0}^{35} \bar{y}_h \bar{\alpha}^{-h(k-1)}, \quad \text{with} \quad \bar{\alpha} = e^{j \frac{2\pi}{36}}.$$

If the analysis of the magnetic fields not multiple of p can be neglected in the model, it is possible to simplify the transformations taking into account of the pole pairs symmetry, resulting in:

$$\bar{y}_h = \frac{2}{9} \sum_{k \in \mathbb{R}=1}^{18} x_k \bar{\alpha}^{h(k-1)} \quad \text{and} \quad x_k = \frac{1}{4} \sum_{h=0}^{17} \bar{y}_h \bar{\alpha}^{-h(k-1)}, \quad \text{with} \quad \bar{\alpha} = e^{j \frac{2\pi}{18}}.$$

As done in the three-phase six slot machine, because the number of phases is odd, the starting of the phases can be chosen in a smart symmetrical way, resulting in the transformations:

$$\bar{y}_h = \frac{2}{9} \sum_{k=1}^9 x_k \bar{\alpha}^{h(k-1)}, \quad h = 0, 1, 2, \dots, 17, \quad (2.80)$$

with $\bar{\alpha} = e^{j \frac{2\pi}{9}}$, and:

$$x_k = \frac{1}{2} \sum_{h=0}^8 \bar{y}_h \bar{\alpha}^{-h(k-1)}. \quad (2.81)$$

Alternatively, in its common shape, as:

$$x_k = \frac{1}{2} y_0 + \sum_{h_{\text{odd}}=1}^7 \Re\{\bar{y}_h \bar{\alpha}^{-h(k-1)}\}. \quad (2.82)$$

The problem is similar to the one found for the three-phase machine modelled as an asymmetrical one, and again the solution is also simplified to recreate a symmetry in the transformation and inverse transformation neglecting the pole pairs. It must be noticed that in

most of the cases it is worth to connect the phases to the terminal box with the same assumption used for the transformation (the current that goes from the terminals into the phases must have the same direction in the starting of the phases according to their position in the transformation). This allows, in terms of current control and modelling, taking into account of the star connection just imposing the homopolar sequence equal to zero. It results that if the nine phase is wound and star connected in a symmetrical way also the symmetrical transformation is the suitable one. If the machine is asymmetrically wound, the asymmetrical transformation might be more likely used, as in an even-phase machine.

Triple Three-phase configurations

The nine-phase machine can be wound in a triple three-phase configuration, as in Fig. 2.9 (right), following the idea of the quadruple three-phase winding described in the previous subsection. In this case, the phases will start in the slots 1, 2, 3, 7, 8, 9, 13, 14 and 15. The resulting three-phase subsystems (1-7-13, 2-8-14 and 3-9-15) are symmetrical, and their transformations and inverse transformations are the standard symmetrical three-phase ones. However, the full transformation remains an asymmetrical one (asymmetrical triple three-phase machine). The problem can be solved choosing the same slots defined for the symmetrical nine-phase winding, realising a symmetrical triple three-phase machine (1-7-13, 3-9-15 and 5-11-17). In this way, the simplified symmetrical set of transformation and inverse transformation (2.82) can be adopted.

The next subsection presents the last multiphase winding topology analysed in this thesis, the sectored one.

Space vectors analysis (multi-sectored triple three-phase winding)

Another possible multiphase winding is the sectored one, shown for a nine-phase 3 pole pairs layout in Fig. 2.10. The nine-phase machine has three sets of three-phase windings (triple three-phase) located at 120 mechanical degrees in the stator area, and the phases are different under each pole pair.

Also in this case it is possible to connect in series the phases of the same colour topology in Fig. 2.10 (blue, red and green) in order to realize a standard three-phase winding with 3 pole pairs (modelled using the standard three-phase transformation, owing to the pole pairs number and the symmetry of the polar symmetry of the winding).

Instead, the nine-phase analysis is no more as the one discussed in the previous subsection (symmetrical or asymmetrical), because of the different pitch of the phases and the asymmetry under the pole pairs.

As example, let us assume that only the phases of the first sector are considered. In this case, the number of phases is still three, and they are symmetrically distributed under one pole pair, but the electromagnetic behaviour of the machine can hardly be represented by the analysis of

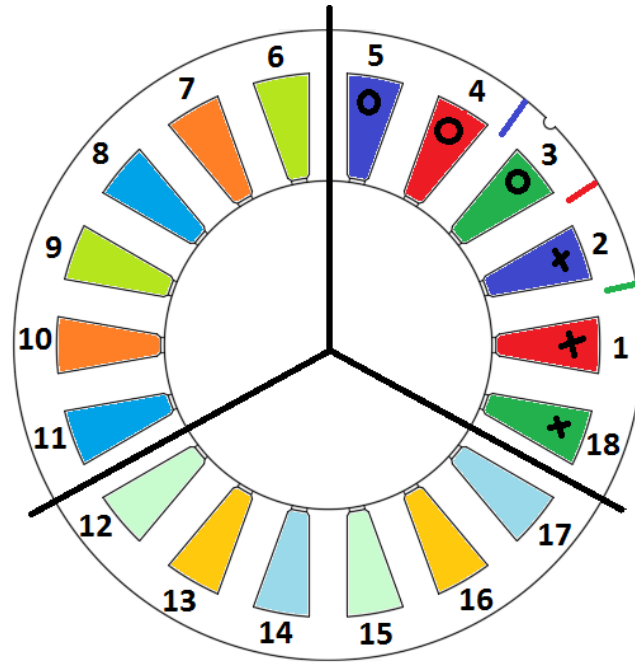


Fig. 2.10 – 18 slots and 3 pole pairs sectored winding 9-phase machine. The magnetic axis and the starting of the phases in the first sector are highlighted with coloured lines in the back iron and with crosses in the slots respectively.

only the harmonic fields multiple of p , because the winding factor related to the others field harmonics is no more zero. Therefore, the transformation must be evaluated for all the space vectors, otherwise critical effects caused by the unbalance of the machine would be neglected. The same happens if the nine phases are taken into account.

Not existing a reduced symmetry, the general transformation for the nine-phase machine remains the most general one, as below:

$$\bar{y}_h = \frac{2}{9} \sum_{k \in \mathbb{R}=1}^{18} x_k \bar{\alpha}^{h(k-1)}, \quad h = 0,1,2,\dots,17, \quad (2.83)$$

with $\bar{\alpha} = e^{j\frac{2\pi}{18}}$, and its inverse transformation is:

$$x_k = \frac{1}{4} \sum_{h=0}^{17} \bar{y}_h \bar{\alpha}^{-h(k-1)}, \quad (2.84)$$

simplifiable by the relationship of a symmetrical system with an even number of variables, as:

$$x_k = \frac{1}{4} y_0 + \frac{1}{4} y_9 e^{-j\pi(k-1)} + \frac{1}{2} \sum_{h=1,2,\dots}^8 \bar{y}_h e^{-j\frac{2\pi}{18}h(k-1)}. \quad (2.85)$$

For this winding layout, the inverse transformation is quite complex to be simplified to a reduced number of space vectors, and a customized transformation has been introduced in the 5th Chapter to analyse and control this machine topology by means of a SVD approach. This is true also for the multiphase winding presented in Chapter 6, segmented design. Indeed, it is

modelled with the same approach of the general transformation presented here. However, due to the complicated geometry of the winding, the analysis it is not presented in this chapter.

The next section shows the voltage space vector equations for a multiphase winding. The following sections focus on the evaluation of the analysis of the flux linked with the winding, which appears in the voltage equations.

2.3 Voltage Space Vector Equations

This section aims to present the voltage equations for a multiphase winding, starting from the voltage equation of one turn. Finally, the equations are written in terms of space vector representation in order to define a direct analysis (and eventually the control algorithm) of the field harmonics in the airgap. Indeed, the current space vectors are directly related to the spatial harmonics of the relative magnetomotive force distribution.

As it is usually done, in the modelling of star connected machines (as the one investigated in this work), the electrical equations are written in terms of phase voltages. Another possibility is writing the model in terms of terminal voltages. The advantage of a phase voltage model is that also the homopolar voltage (zero-space voltage space vector) is taken into account, while in the case of a terminal voltage model the homopolar voltage is neglected.

Having a phase voltage model allows evaluating the voltage of the neutral point of the star connection to detect faults and asymmetrical behaviours. Most of the time this information is not available by the measurements, but by the measured current and modulating voltages it is possible to predict its value if the source of the fault/asymmetry is known. In this thesis, the voltage of the neutral point is not measured for the purpose of the diagnosis, but its value is just evaluated in the model as an additional information for future investigations. Instead, in terms of current control the two models are equivalent, owing to the star connection constraint.

The SVD electrical equations of a multiphase machine can be directly derived from the space vector transformation of the phase voltages:

$$\bar{v}_h = \frac{2}{m} \sum_{x=1}^{N_s} v_x \bar{\alpha}^{h(x-1)}, \quad h = 0, 1, 2, \dots, N_s - 1, \quad (2.86)$$

where v_x is a phase considered as starting in the x -th slot.

The voltage inverse transformation is:

$$v_x = \frac{m}{2N_s} \sum_{h=0}^{N_s-1} \bar{v}_h \bar{\alpha}^{-h(x-1)}, \quad x = 1, 2, \dots, N_s,$$

where v_x is the voltage of the x -th phase of the m -phase machine, and $\bar{\alpha}$ is equal to $e^{j\frac{2\pi}{N_s}}$.

Each phase is composed by a series of turns wound around the stator. The next subsection shows the voltage equation for a single turn.

Voltage equation (single turn)

The voltage equation for the single k -th turn can be generally defined as:

$$v_k = r_k i_k + \frac{d\phi_{tot,k}}{dt}, \quad (2.87)$$

where r_k is the resistance of the turn and $\phi_{tot,k}$ is the total flux linked with it. The linked flux takes into account of the following components:

- Self leakage flux: flux that is produced by the turn, and therefore it is linked with it, but does not reach the airgap (in the hypothesis of the model it is the flux that does not reach the rotor iron)
- Mutual leakage flux: the leakage flux of the other stator turns that does not reach the airgap (the rotor) but it is linked with the analysed turn.
- Linked flux through the airgap: the sum of the flux produced by the turn (therefore linked) that reaches the airgap (rotor) plus the flux that is generated by the rotor and the other phases that reaches the airgap and is linked with the analysed turn.

$$\phi_{tot,k} = \phi_{LI,k} + \phi_{MI,k} + \phi_k.$$

These components can be expressed by the following relationships:

- Turn self leakage flux ($\phi_{LI,k}$): because this component is only related to the current flowing in the analysed turn, in the hypothesis of linear machine behaviour it can be evaluated as $\phi_{LI,k} = l_k i_k$. Where l_k is the self leakage inductance of the analysed turn.
- Turn mutual leakage flux ($\phi_{MI,k}$): being the sum of the leakage fluxes of the other $N_t - 1$ turns linked to the analysed one, its expression can be written as:

$$\phi_{MI,k} = \sum_{\substack{t=1 \\ t \neq k}}^{N_t} ml_{t,k} i_t,$$

where $ml_{t,k}$ is the mutual leakage inductance between the t -th and k -th turns.

Considering a turn of the x -th phase, the effect of the x -th phase turns can be distinguished by the effects of the turns of another y -th phase. Even the y -phase is defined as the one starting in the y -th slot and if it does not exist it means that the model can be simplified or the same model can be kept just imposing the variable related to the not existing phases equal to zero. The equation of the mutual leakage flux becomes:

$$\phi_{MI,k} = \sum_{\substack{tx=1 \\ tx \neq k}}^{N_{tx}} ml_{tx,k} i_x + \sum_{\substack{y=1 \\ y \neq x}}^m \sum_{\substack{ty=1 \\ ty \neq k}}^{N_{ty}} ml_{ty,k} i_y,$$

with $ml_{tx,k}$ the mutual leakage inductance of the tx -th turn of the phase x with the turn k and $ml_{ty,k}$ the mutual leakage inductance of the ty -th turn of the phase y with the turn k .

- Turn linked flux through the airgap (ϕ_k): this component is analysed in the next section, and it is responsible for machine electromagnetic power transferred to the rotor and for the mechanical power that results on the shaft.

The next subsection presents the voltage equation for one phase, starting from the considerations done for the single turn.

Voltage equation (single phase)

The voltage equation for the k-th turn of the x-th phase can be written as:

$$v_{kx} = r_{kx} i_x + ll_{kx} \frac{di_x}{dt} + \sum_{\substack{tx=1 \\ tx \neq k}}^{N_{tx}} ml_{tx,kx} \frac{di_x}{dt} + \sum_{\substack{y=1 \\ y \neq x}}^{N_s} \sum_{ty=1}^{N_{ty}} ml_{ty,kx} \frac{di_y}{dt} + \frac{d\phi_{kx}}{dt}. \quad (2.88)$$

The voltage equation of one phase, with all its series-connected turn, is evaluable by:

$$v_x = \sum_{kx=1}^{N_{tx}} v_{kx} = \left(\sum_{kx=1}^{N_{tx}} r_{kx} \right) i_x + \left(\sum_{kx=1}^{N_{tx}} ll_{kx} + \sum_{\substack{kx=1 \\ tx=1 \\ tx \neq k}}^{N_{tx}} \sum_{tx=1}^{N_{tx}} ml_{tx,kx} \right) \frac{di_x}{dt} + \sum_{\substack{y=1 \\ y \neq x}}^{N_s} \left(\sum_{ty=1}^{N_{ty}} \sum_{kx=1}^{N_{tx}} ml_{ty,kx} \right) \frac{di_y}{dt} + \sum_{kx=1}^{N_{tx}} \frac{d\phi_{kx}}{dt}. \quad (2.89)$$

The terms in the brackets can be identified as:

- Phase resistance (R_x): the total resistance of the series turns of the phase x. It is easily evaluated as:

$$R_x = \sum_{kx=1}^{N_{tx}} r_{kx}.$$

- Phase self leakage inductance (Ll_x): describing the flux that is produced by the phase x, and therefore it is linked with it, but does not reach the airgap (that in the hypothesis of the model is the same of saying that it is the flux that does not reach the rotor iron). It is evaluated as:

$$Ll_x = \sum_{kx=1}^{N_{tx}} ll_{kx} + \sum_{\substack{kx=1 \\ tx=1 \\ tx \neq k}}^{N_{tx}} \sum_{tx=1}^{N_{tx}} ml_{tx,kx}.$$

- Phase to phase mutual leakage inductance (Ml_{xy}): describing the leakage flux of the other stator phases that does not reach the airgap (the rotor) but it is linked with the analysed phase. It is evaluated as:

$$Ml_{xy} = \sum_{ty=1}^{N_{ty}} \sum_{kx=1}^{N_{tx}} ml_{ty,kx}.$$

Introducing the new constant and defining the total linked flux through the airgap of the phase

x as $\phi_x = \sum_{kx=1}^{N_{tx}} \phi_{kx}$, the phase voltage equation becomes:

$$v_x = R_x i_x + Ll_x \frac{di_x}{dt} + \sum_{\substack{y=1 \\ y \neq x}}^{N_s} Ml_{xy} \frac{di_y}{dt} + \frac{d\phi_x}{dt}. \quad (2.90)$$

The next subsection presents the voltage space vector equation for a general multiphase winding, highlighting how the leakage inductances might result in a more complicated model. Then, the equations are simplified neglecting the mutual leakage effects between different phases in order to simplify the equations for the machines analysed in the thesis.

Voltage equation (multiphase winding)

The space vector voltage equation becomes:

$$\bar{v}_h = \frac{2}{m} \sum_{x=1}^{N_s} R_x i_x \bar{\alpha}^{h(x-1)} + \frac{2}{m} \sum_{x=1}^{N_s} Ll_x \frac{di_x}{dt} \bar{\alpha}^{h(x-1)} + \frac{2}{m} \sum_{x=1}^{N_s} \sum_{\substack{y=1 \\ y \neq x}}^{N_s} Ml_{xy} \frac{di_y}{dt} \bar{\alpha}^{h(x-1)} + \frac{2}{m} \sum_{x=1}^{N_s} \frac{d\phi_x}{dt} \bar{\alpha}^{h(x-1)}. \quad (2.91)$$

If all the phases have the same phase resistance ($R_x = R_s$), the same phase self leakage inductance ($Ll_x = Ll$), and the space vector transformation are introduced, it is also possible to write the voltage space vector equation as:

$$\bar{v}_h = R_s \bar{i}_h + Ll \frac{d\bar{i}_h}{dt} + \frac{2}{m} \sum_{x=1}^{N_s} \sum_{\substack{y=1 \\ y \neq x}}^{N_s} Ml_{xy} \frac{di_y}{dt} \bar{\alpha}^{h(x-1)} + \frac{d\bar{\phi}_h}{dt}. \quad (2.92)$$

The inverse transformation of the currents is introduced to completely write the equation in terms of space vector components, resulting in:

$$\begin{aligned} \bar{v}_h &= R_s \bar{i}_h + Ll \frac{d\bar{i}_h}{dt} + \frac{1}{N_s} \sum_{x=1}^{N_s} \sum_{\substack{y=1 \\ y \neq x}}^{N_s} Ml_{xy} \sum_{\rho=0}^{N_s-1} \frac{d\bar{i}_\rho}{dt} \bar{\alpha}^{-\rho(y-1)} \bar{\alpha}^{h(x-1)} + \frac{d\bar{\phi}_h}{dt} = \\ &= R_s \bar{i}_h + Ll \frac{d\bar{i}_h}{dt} + \sum_{\rho=0}^{N_s-1} \left(\frac{1}{N_s} \sum_{x=1}^{N_s} \sum_{\substack{y=1 \\ y \neq x}}^{N_s} Ml_{xy} \bar{\alpha}^{h(x-1)} \bar{\alpha}^{-\rho(y-1)} \right) \frac{d\bar{i}_\rho}{dt} + \frac{d\bar{\phi}_h}{dt}. \end{aligned} \quad (2.93)$$

Introducing a new non-physical variable:

$$\bar{Ml}_{h\rho} = \frac{1}{N_s} \sum_{x=1}^{N_s} \sum_{\substack{y=1 \\ y \neq x}}^{N_s} Ml_{xy} \bar{\alpha}^{h(x-1)} \bar{\alpha}^{-\rho(y-1)},$$

the mutual leakage space vector between the space h and the space ρ , the general space vector voltage equation of a multiphase winding is:

$$\bar{v}_h = R_s \bar{i}_h + Ll \frac{d\bar{i}_h}{dt} + \sum_{\rho=0}^{N_s-1} \bar{M}l_{h\rho} \frac{d\bar{i}_\rho}{dt} + \frac{d\bar{\phi}_h}{dt}. \quad (2.94)$$

Mutual leakage inductances between different phases

It is interesting to notice that in a three-phase standard winding, as the one in Fig. 2.6, the mutual leakages between the phases can easily have all the same value, and the mutual leakage between the space h and the space ρ is:

$$\bar{M}l_{h\rho} = \frac{Ml}{N_s} \sum_{x=1}^{N_s} \bar{\alpha}^{h(x-1)} \sum_{\substack{y=1 \\ y \neq x}}^{N_s} \bar{\alpha}^{-\rho(y-1)}.$$

This parameter can be analysed as:

$$\bar{M}l_{h\rho} = \frac{Ml}{N_s} \sum_{x=1}^{N_s} \bar{\alpha}^{h(x-1)} \sum_{y=1}^{N_s} \bar{\alpha}^{-\rho(y-1)} - \frac{Ml}{N_s} \sum_{x=1}^{N_s} \bar{\alpha}^{(h-\rho)(x-1)},$$

which is equal to zero in all the cases but when h is equal to ρ , resulting in:

$$\bar{M}l_{hh} = \frac{Ml}{N_s} \sum_{x=1}^{N_s} \sum_{y=1}^{N_s} \bar{\alpha}^{h(x-y)} = Ml,$$

$$Ml_{00} = \frac{Ml}{N_s} \sum_{x=1}^{N_s} \sum_{y=1}^{N_s} 1 - \frac{Ml}{N_s} \sum_{x=1}^{N_s} 1 = Ml(N_s - 1).$$

It results that, if the mutual leakages between the phases have all the same value, the space vector voltage equations can be written as:

$$\begin{cases} v_0 = R_s i_0 + Ll \frac{di_0}{dt} + Ml_{00} \frac{di_0}{dt} + \frac{d\phi_0}{dt} \\ \bar{v}_h = R_s \bar{i}_h + (Ll + Ml) \frac{d\bar{i}_h}{dt} + \frac{d\bar{\phi}_h}{dt} \end{cases} \quad (2.95)$$

In case of a star connected symmetrical winding the system of equations is simplified as:

$$\begin{cases} v_0 = \frac{d\phi_0}{dt} \\ \bar{v}_h = R_s \bar{i}_h + (Ll + Ml) \frac{d\bar{i}_h}{dt} + \frac{d\bar{\phi}_h}{dt} \end{cases} \quad (2.96)$$

It can be concluded that in a star connected electrical machine, even if the mutual leakage inductances between the phases are significant, until their value is the same (as might happen in a symmetrical three-phase machine), they do not create additional interactions between the spaces of the space vector model. This is not true for a multiphase machine, where in general the mutual leakage inductances might have different values.

For example, it is possible to consider the triple three-phase sector winding of Fig. 2.10. Analysing its end-windings, there are two significant mutual leakage inductances: the mutual leakage between the central phase of each sector with the two other phases of the same (MI_{CL}) and the mutual leakage between the two external phase of each sector (MI_{LL}). Therefore, the mutual leakage space vectors are evaluated as:

$$\begin{aligned} \bar{M}I_{h\rho} = & \frac{1}{18} MI_{CL} \left(\sum_{x=1,7,13} \bar{\alpha}^{h(x-1)} \bar{\alpha}^{\rho(x-1)} (\bar{\alpha}^{-\rho} + \bar{\alpha}^{\rho}) + \sum_{x=1,7,13} \bar{\alpha}^{h(x-1)} (\bar{\alpha}^{-h} + \bar{\alpha}^h) \bar{\alpha}^{\rho(x-1)} \right) + \\ & + \frac{1}{18} MI_{LL} \left(\sum_{x=1,7,13} \bar{\alpha}^{h(x-1)} \bar{\alpha}^{-h} \bar{\alpha}^{\rho(x-1)} \bar{\alpha}^{\rho} + \sum_{x=1,7,13} \bar{\alpha}^{h(x-1)} \bar{\alpha}^h \bar{\alpha}^{\rho(x-1)} \bar{\alpha}^{-\rho} \right). \end{aligned}$$

It has been verified that in this winding topology, there are interactions between the spaces related to the mutual leakage space vectors also if MI_{LL} is equal to MI_{CL} .

Simplified voltage equation without mutual leakage inductances between different phases

The mutual leakage inductances depend on the winding configuration, the machine geometry and the end-winding layout. They are an important contribution especially if there are more phases wound inside same slots (as in a double layer winding configuration).

By the model, it results that in general all the space vector equations might be mutually coupled by the mutual leakages between the different phases. However, in case of single layer windings the mutual leakages can usually be neglected, simplifying the space vector voltage equation as:

$$\bar{v}_h = R_s \bar{i}_h + Ll \frac{d\bar{i}_h}{dt} + \frac{d\bar{\phi}_h}{dt}. \quad (2.97)$$

Because in this thesis all the analysed machines have single layer windings, the mutual leakage inductances are supposed to be zero. This allows identifying machine asymmetries by the space vector equations without carrying out an in-deep analysis of the mutual leakage effects.

The next section presents the analysis of the flux that passes through the airgap and links the phases of a multiphase winding. The overall effect of the flux to the phases of the winding is considered by a space vector representation of the system. The analysis is carried out starting from the flux linked with a single turn following the same approach used to define the voltage equations. The aim of this approach is to allow for the analysis of one fraction of the winding. This will be useful, in the next chapters, for representing an asymmetrical behaviour in case of a winding fault (open phase, high resistance and interturn short circuit faults) or a different number of turns in the different phases (as in Chapter 6).

2.4 Linked Flux Space Vectors

When not specified, hereafter the linked fluxes are the fluxes that pass through the airgap and are linked to the phases of the considered winding.

Under the assumptions of the model (in particular that the flux is only radial in the airgap), the linked flux contributions only depend on the geometry of the winding and on the distribution of the magnetic field in the airgap. This section analyses the flux linked with a single turn, a phase and finally a multiphase winding (by the space vector representation).

Linked flux (single turn)

The linked flux equation for a generic turn of the stator winding can be written as the integral through the surface of the turn of the normal component (to the considered surface) of the magnetic flux density. However, as done for the evaluation of the armature field, there are two ways to evaluate the linked fluxes. The first is valid for a general distribution of the conductors in the stator. The second method is based on the hypothesis of conductors concentrated in the centre of the slots.

1st Method: conductors density distribution

The flux linked with a generic k -th turn can be evaluated as:

$$\phi_k = - \int_{z=0}^L \left(\int_0^{2\pi} \left(\int_0^g \frac{\gamma_k(\vartheta)}{i_k} R d\vartheta \right) \mu_0 H(\vartheta, z) R d\vartheta \right) dz, \quad (2.98)$$

where H is the total magnetic field in the airgap, R is the average radius of the airgap, L is the active length of the machine, and $\int_0^g \frac{\gamma_k(\vartheta)}{i_k} R d\vartheta$ represents the conductor density of the k -th turn (considering that, as in the typical modelling approach, skin and proximity effects are neglected).

In terms of spatial harmonics of the distribution of the current density and total magnetic field, the linked flux can be written as:

$$\phi_k = -\mu_0 R^2 \int_{z=0}^L \left(\int_0^{2\pi} \left(\int_0^g \Re \sum_{\rho=0}^{\infty} \{ \bar{\Lambda}_{k\rho} e^{-j\rho\vartheta} \} d\vartheta \right) \sum_{h=1}^{\infty} \Re \{ \bar{H}_h(z) e^{-jh\vartheta} \} d\vartheta \right) dz, \quad (2.99)$$

where $\bar{\Lambda}_{k\rho}$ is the ρ -th harmonic of the conductor spatial distribution:

$$\bar{\Lambda}_{k\rho} = \frac{\bar{\Gamma}_{k\rho}}{i_k} = j \frac{4}{\rho\pi R \Delta\psi} \sin\left(\rho \frac{\Delta\psi_k}{2}\right) \sin\left(\rho \frac{\Delta\psi}{2}\right) e^{j\rho\psi_k}.$$

If the conductor width is not significant, the harmonics of the conductor distribution are simplified as:

$$\bar{\Lambda}_{k\rho} = j \frac{2}{\pi R} \sin\left(\rho \frac{\Delta\psi_k}{2}\right) e^{j\rho\psi_k}. \quad (2.100)$$

The following steps can evaluate the resulting linked flux:

$$\begin{aligned} \phi_k &= -\mu_0 R \int_{z=0}^L \left(\int_0^{2\pi} \left(\int_0^\infty \Re \left\{ j \frac{2}{\pi} \sin\left(\rho \frac{\Delta\psi_k}{2}\right) e^{j\rho\psi_k} e^{-j\rho\vartheta} \right\} d\vartheta \right) \sum_{h=1}^\infty \Re \left\{ \bar{H}_h(z) e^{-jh\vartheta} \right\} d\vartheta \right) dz = \\ &= - \int_{z=0}^L \left(\int_0^{2\pi} \sum_{\rho=0}^\infty \Re \left\{ -\frac{\mu_0 2R}{\rho\pi} \sin\left(\rho \frac{\Delta\psi_k}{2}\right) e^{j\rho\psi_k} (e^{-j\rho\vartheta} - 1) \right\} \sum_{h=1}^\infty \Re \left\{ \bar{H}_h(z) e^{-jh\vartheta} \right\} d\vartheta \right) dz = \\ &= \int_{z=0}^L \left(\int_0^{2\pi} \sum_{\rho=0}^\infty \Re \left\{ \frac{\mu_0 2R}{\rho\pi} \sin\left(\rho \frac{\Delta\psi_k}{2}\right) e^{j\rho\psi_k} e^{-j\rho\vartheta} \right\} \sum_{h=1}^\infty \Re \left\{ \bar{H}_h(z) e^{-jh\vartheta} \right\} d\vartheta \right) dz = \\ &= \int_{z=0}^L \left(\int_0^{2\pi} \sum_{\rho=0}^\infty \frac{\mu_0 R}{2\rho\pi} \sin\left(\rho \frac{\Delta\psi_k}{2}\right) (e^{j\rho\psi_k} e^{-j\rho\vartheta} + e^{-j\rho\psi_k} e^{+j\rho\vartheta}) \sum_{h=1}^\infty (\bar{H}_h(z) e^{-jh\vartheta} + \bar{H}_h^*(z) e^{jh\vartheta}) d\vartheta \right) dz = \\ &= \int_{z=0}^L \left(\int_0^{2\pi} \sum_{h=1}^\infty \frac{\mu_0 R}{2h\pi} \sin\left(h \frac{\Delta\psi_k}{2}\right) (\bar{H}_h^*(z) e^{jh\psi_k} + \bar{H}_h(z) e^{-jh\psi_k}) d\vartheta \right) dz = \\ &= \sum_{h=1}^\infty \frac{\mu_0 R}{h} \sin\left(h \frac{\Delta\psi_k}{2}\right) \left(\int_{z=0}^L \bar{H}_h^*(z) dz e^{jh\psi_k} + \int_{z=0}^L \bar{H}_h(z) dz e^{-jh\psi_k} \right). \end{aligned} \quad (2.101)$$

The same result can be obtained by assuming a negligible width of the conductors from the beginning, as shown in the next paragraph.

2nd Method: point type conductors

Assuming that the conductors are concentrated in points located in the central axes of the slots, the linked flux of the generic k-th turn can also be evaluated as:

$$\phi_k = \int_{z=0}^L \left(\int_{\psi_k - \Delta\psi_k}^{\psi_k + \Delta\psi_k} \mu_0 H(\vartheta, z) R d\vartheta \right) dz. \quad (2.102)$$

In terms of spatial harmonics of the distribution of the total magnetic field, the linked flux can be evaluated following the steps below:

$$\begin{aligned}
 \phi_k &= \mu_0 R \int_{z=0}^L \left(\int_{\psi_k - \frac{\Delta\psi_k}{2}}^{\psi_k + \frac{\Delta\psi_k}{2}} \Re \sum_{h=1}^{\infty} \left\{ \bar{H}_h(z) e^{-jh\vartheta} \right\} d\vartheta \right) dz = \\
 &= \mu_0 R \int_{z=0}^L \Re \sum_{h=1}^{\infty} \left\{ j \frac{\bar{H}_h(z)}{h} \left(e^{-jh\left(\psi_k + \frac{\Delta\psi_k}{2}\right)} - e^{-jh\left(\psi_k - \frac{\Delta\psi_k}{2}\right)} \right) \right\} dz = \\
 &= \mu_0 R \int_{z=0}^L \Re \sum_{h=1}^{\infty} \left\{ 2 \frac{\bar{H}_h(z)}{h} \sin\left(h \frac{\Delta\psi_k}{2}\right) e^{-jh\psi_k} \right\} dz = \tag{2.103} \\
 &= \int_{z=0}^L \sum_{h=1}^{\infty} \frac{\mu_0 R}{h} \sin\left(h \frac{\Delta\psi_k}{2}\right) \left(\bar{H}_h(z) e^{-jh\psi_k} + \bar{H}_h^*(z) e^{jh\psi_k} \right) dz = \\
 &= \sum_{h=1}^{\infty} \frac{\mu_0 R}{h} \sin\left(h \frac{\Delta\psi_k}{2}\right) \left(\int_{z=0}^L \bar{H}_h(z) dz e^{-jh\psi_k} + \int_{z=0}^L \bar{H}_h^*(z) dz e^{jh\psi_k} \right).
 \end{aligned}$$

As expected, the result is the same for the two methods and it is reported here below:

$$\phi_k = \sum_{h=1}^{\infty} \frac{\mu_0 R}{h} \sin\left(h \frac{\Delta\psi_k}{2}\right) \left(\int_{z=0}^L \bar{H}_h(z) dz e^{-jh\psi_k} + \int_{z=0}^L \bar{H}_h^*(z) dz e^{jh\psi_k} \right). \tag{2.104}$$

The dependence of the total magnetic field from the axial direction is need to take into account for the eventual skewing of the magnets of the squirrel cage, as will be investigated in the following sections.

The next subsection aims to present the evaluation of the linked flux for a single phase.

Linked flux (single phase)

If all the phases have the same coils geometry (in the slots, without considering the end-winding design) and are only placed in different stator areas, they have the same number of coils (N_C)

and turns (N). It follows that the linked flux of each phase ($\phi_x = \sum_{kx=1}^{N_{fx}} \phi_{kx}$) can be also written introducing the winding factor defined in (2.45), with the angle of the y-th coil ψ_y considered in respect of the magnetic axis of the considered phase ψ_x , as:

$$\phi_x = \sum_{h=1}^{\infty} \frac{\mu_0 R p q N K_{ah}}{h} \left(\int_{z=0}^L \bar{H}_h(z) dz e^{-jh\psi_x} + \int_{z=0}^L \bar{H}_h^*(z) dz e^{jh\psi_x} \right). \tag{2.105}$$

The next section defines the linked flux equations for a multiphase winding in terms of space vector representation.

Linked flux (multiphase winding)

The space vector of the flux linked with the various phases of a multiphase winding is:

$$\begin{aligned}
 \bar{\phi}_h &= \frac{2}{m} \sum_{x=1}^{N_s} \phi_x \bar{\alpha}^{h(x-1)} = \\
 &= \frac{2}{m} \sum_{x=1}^{N_s} \sum_{\rho=1}^{\infty} \frac{\mu_0 R p q N K_{a\rho}}{\rho} \left(\int_{z=0}^L \bar{H}_\rho(z) dz \bar{\alpha}^{-j\rho(x-1)} + \int_{z=0}^L \bar{H}_\rho^*(z) dz \bar{\alpha}^{j\rho(x-1)} \right) \bar{\alpha}^{h(x-1)} = \\
 &= \frac{2}{m} \sum_{\rho=1}^{\infty} \frac{\mu_0 R p q N K_{a\rho}}{\rho} \left(\int_{z=0}^L \bar{H}_\rho(z) dz \sum_{x=1}^{N_s} \bar{\alpha}^{-j(\rho-h)(x-1)} + \int_{z=0}^L \bar{H}_\rho^*(z) dz \sum_{x=1}^{N_s} \bar{\alpha}^{j(\rho+h)(x-1)} \right).
 \end{aligned} \tag{2.106}$$

Because considering a redundant symmetrical system of phases $\sum_{x=1}^{N_s} \bar{\alpha}^{j\nu(x-1)}$ is equal to N_s if ν is zero or a multiple of N_s , (2.106) can be rewritten as:

$$\bar{\phi}_h = \frac{2}{m} \mu_0 R p q N N_s \left[\sum_{y=0}^{\infty} \frac{K_{a(yN_s+h)}}{(yN_s+h)} \int_{z=0}^L \bar{H}_{(yN_s+h)}(z) dz + \sum_{y=\left(\frac{h}{N_s}\right)_{\text{int}}}^{\infty} \frac{K_{a(yN_s-h)}}{(yN_s-h)} \int_{z=0}^L \bar{H}_{(yN_s-h)}^*(z) dz \right]. \tag{2.107}$$

This equation results in having also equivalent linked fluxes with the not existing phases. However, these phases have zero currents. Therefore, their contributions to the power and the torque are zero. The not existing phases can be analysed as flux observer coils (coils used for the measurement of the linked fluxes).

If there is not a skew in the design of the machine, the simplified equation of the linked fluxes space vectors is:

$$\bar{\phi}_h = \frac{2}{m} \mu_0 L R p q N N_s \left[\sum_{y=0}^{\infty} \frac{K_{a(yN_s+h)}}{(yN_s+h)} \bar{H}_{(yN_s+h)} + \sum_{y=\left(\frac{h}{N_s}\right)_{\text{int}}}^{\infty} \frac{K_{a(yN_s-h)}}{(yN_s-h)} \bar{H}_{(yN_s-h)}^* \right], \tag{2.108}$$

with $K_{a\rho}$ the winding factor defined by (2.45).

The equations of the linked flux can be also used to evaluate the self inductance of the winding.

For the purposes of the thesis, the equation is written in the next subsection for the general single turn (k -th), and then the complete equation of the multiphase winding is given.

Self inductance (single turn)

The voltage equation for the k-th turn of the x-th phase (2.88) can be written, neglecting the mutual inductances with the other phases, as:

$$v_{kx} = r_{kx} i_x + l_{kx} \frac{di_x}{dt} + \sum_{\substack{tx=1 \\ tx \neq k}}^{N_{tx}} ml_{tx,kx} \frac{di_x}{dt} + \frac{d\phi_{kx}}{dt}. \quad (2.109)$$

The harmonics of the flux produced by the turn itself are described by (2.39) as:

$$\bar{H}_{kx\rho} = \frac{2i_{kx}}{\rho\pi\delta} \sin\left(\rho \frac{\Delta\psi_k}{2}\right) e^{j\rho\psi_{kx}}. \quad (2.110)$$

The linked flux with the turn can be written by (2.104) as:

$$\phi_{kx} = \sum_{h=1}^{\infty} \frac{\mu_0 R}{h} \sin\left(h \frac{\Delta\psi_k}{2}\right) \left(\int_{z=0}^L \bar{H}_h(z) dz e^{-jh\psi_{kx}} + \int_{z=0}^L \bar{H}_h^*(z) dz e^{jh\psi_{kx}} \right). \quad (2.111)$$

It follows that the linked flux produced by the turn itself can be written by (2.104) as:

$$\phi_{self,kx} = \sum_{h=1}^{\infty} \frac{\mu_0 RL}{h} \sin\left(h \frac{\Delta\psi_k}{2}\right) \left(\bar{H}_{kxh} e^{-jh\psi_{kx}} + \bar{H}_{kxh}^* e^{jh\psi_{kx}} \right). \quad (2.112)$$

Substituting (2.110), it can be rewritten as:

$$\begin{aligned} \phi_{self,kx} &= \sum_{h=1}^{\infty} \frac{\mu_0 RL}{h} \sin\left(h \frac{\Delta\psi_k}{2}\right) \left(\frac{2i_{kx}}{h\pi\delta} \sin\left(h \frac{\Delta\psi_k}{2}\right) e^{jh\psi_{kx}} e^{-jh\psi_{kx}} + \frac{2i_{kx}}{h\pi\delta} \sin\left(h \frac{\Delta\psi_k}{2}\right) e^{-jh\psi_{kx}} e^{jh\psi_{kx}} \right) = \\ &= \left(\sum_{h=1}^{\infty} \frac{4\mu_0 RL}{\pi\delta h^2} \sin\left(h \frac{\Delta\psi_k}{2}\right)^2 \right) i_{kx}. \end{aligned} \quad (2.113)$$

Introducing the single turn self inductance l_k defined as:

$$l_k = \sum_{h=1}^{\infty} \frac{4\mu_0 RL}{\pi\delta h^2} \sin\left(h \frac{\Delta\psi_k}{2}\right)^2,$$

it results in the final equation:

$$\phi_{self,kx} = l_k i_{kx}. \quad (2.114)$$

It results that the turn voltage equation can be written as:

$$v_{kx} = r_{kx} i_x + l_{kx} \frac{di_x}{dt} + \sum_{\substack{tx=1 \\ tx \neq k}}^{N_{tx}} ml_{tx,kx} \frac{di_x}{dt} + l_k \frac{di_x}{dt} + \frac{d\phi_{mutual,kx}}{dt}. \quad (2.115)$$

The next subsection presents the analysis of the self inductance effect for a multiphase winding in terms of space vector representation.

Self inductance (multiphase winding)

Considering the whole multiphase winding, analysing only the field produced by the winding itself (2.47), the linked fluxes space vector equation becomes:

$$\bar{\phi}_{self,h} = \frac{2}{m} \mu_0 L R p q N N_s \left[\sum_{y=0}^{\infty} \frac{K_{a(yN_s+h)}}{(yN_s+h)} \frac{Nmpq}{\pi\delta} \frac{K_{a(yN_s+h)}}{(yN_s+h)} \bar{i}_{(yn+h)} + \sum_{y=\left(\frac{h}{N_s}\right)_{int}}^{\infty} \frac{K_{a(yN_s-h)}}{(yN_s-h)} \frac{Nmpq}{\pi\delta} \frac{K_{a(yN_s-h)}}{(yN_s-h)} \bar{i}_{(yN_s-h)}^* \right]. \quad (2.116)$$

Taking into account that, owing to the symmetry of the transformation $\bar{i}_{(yN_s+h)}$ and $\bar{i}_{(yN_s-h)}^*$ are equal to \bar{i}_h , the equation can be simplified as:

$$\bar{\phi}_{self,h} = \frac{2}{m} \mu_0 L R p q N N_s \left[\sum_{y=0}^{\infty} \frac{K_{a(yN_s+h)}}{(yN_s+h)} \frac{Nmpq}{\pi\delta} \frac{K_{a(yN_s+h)}}{(yN_s+h)} + \sum_{y=\left(\frac{h}{N_s}\right)_{int}}^{\infty} \frac{K_{a(yN_s-h)}}{(yN_s-h)} \frac{Nmpq}{\pi\delta} \frac{K_{a(yN_s-h)}}{(yN_s-h)} \right] \bar{i}_h. \quad (2.117)$$

Introducing the non-physical h -space self inductance,

$$L_h = \frac{2}{m} \mu_0 L R p q N N_s \left[\sum_{y=0}^{\infty} \frac{K_{a(yN_s+h)}^2}{(yN_s+h)^2} \frac{Nmpq}{\pi\delta} + \sum_{y=\left(\frac{h}{N_s}\right)_{int}}^{\infty} \frac{K_{a(yN_s-h)}^2}{(yN_s-h)^2} \frac{Nmpq}{\pi\delta} \right],$$

the contribution of the linked flux produced by the winding itself is defined by:

$$\bar{\phi}_{self,h} = L_h \bar{i}_h, \quad (2.118)$$

and the total linked flux space vector results in:

$$\bar{\phi}_h = \bar{\phi}_{self,h} + \bar{\phi}_{mutual,h} = L_h \bar{i}_h + \bar{\phi}_{mutual,h}, \quad (2.119)$$

where $\bar{\phi}_{mutual,h}$ takes into account of the linked flux produced by the rotor or other sources of magnetic field (for example a short circuit loop in the winding itself, as it is shown in the next chapter).

The resulting space vector voltage equation results as:

$$\bar{v}_h = R_s \bar{i}_h + (Ll + L_h) \frac{d\bar{i}_h}{dt} + \frac{d\bar{\phi}_{mutual,h}}{dt}. \quad (2.120)$$

The eventual mutual coupling between the different spaces is considered in the term $\bar{\phi}_{mutual,h}$, also if in a standard machine design with negligible anisotropies of the magnetic circuit these mutual terms are not considered. If there are anisotropies or asymmetrical behaviours of the machine, also the mutual coupling between the armature spaces must be considered.

The next two sections aim to define the equations for the space vectors of the mutual flux $\bar{\phi}_{mutual,h}$, which takes into account for the coupling of the flux produced by the rotor and the considered multiphase winding. The next section considers for a SPM rotor, while the following one analyses the effect of a squirrel cage rotor.

2.5 Surface Permanent Magnet Machine Modelling

The electromagnetic behaviour of an electrical machine is defined by its interaction with the existing sources of magnetic field. The first source is the current distribution in the winding. The second one is related to the rotor. In case of a permanent magnet machine, the magnets are the only rotor source. This section presents the model of an SPM rotor and the effects of the magnet flux on a single turn and a multiphase winding.

Single permanent magnet model and basic equations

The method proposed to model the permanent magnet field is based on a fixed radial thickness of the magnets and radial magnetization. The magnets are supposed to be working in their linear behaviour, as in Fig. 2.11. The other hypothesis are the same used for the modelling of the armature field. The equation that describes the flux density can be considered differently in the air and in the magnets:

$$B = \begin{cases} \mu_0 H_{air} & \text{in the airgap} \\ B_r + \mu_M H_M & \text{in the magnets} \end{cases} \quad (2.121)$$

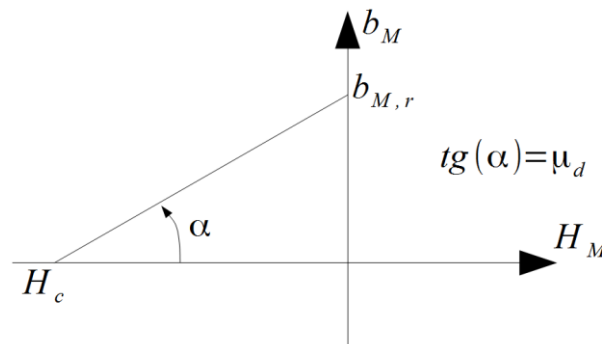


Fig. 2.11 – Simplified magnetic behaviour of the magnets.

The analysis of the magnetic field can be done taking into account a quite general geometry, as in Fig. 2.12. Under the model hypothesis, the radial position of the reluctance or of the magnet has not effect on the solution. An additional hypothesis that simplifies the problem is that the magnets relative permeability is considered equal to 1 ($\mu_M = \mu_0$).

The problem can still be easily solved by the Gauss's law for the electromagnetism (2.21) and the Ampère's circuital law (2.23), but this time the magnets internal equation must be taken into account.

The Gauss's law for the electromagnetism for the analysed problem is:

$$\int_0^{2\pi} B_{air}(\vartheta) d\vartheta = \int_{\psi_k - \frac{\Delta\psi_k}{2}}^{\psi_k + \frac{\Delta\psi_k}{2}} B_M(\vartheta) d\vartheta + \int_{\psi_k - \frac{\Delta\psi_k}{2}}^{\psi_k + \frac{\Delta\psi_k}{2}} B_{air}(\vartheta) d\vartheta = 0. \quad (2.122)$$

Because of the radial direction of the flux, the Gauss law expresses the continuity of the flux density in the radial direction. In presence of the magnets, this means that the following relationship is always true:

$$B_M(\vartheta) = B_{air}(\vartheta). \quad (2.123)$$

Including the magnet internal equation (2.121), it is possible to write:

$$B_r + \mu_M H_M(\vartheta) = \mu_0 H_{air}(\vartheta), \quad (2.124)$$

$$H_M(\vartheta) = \frac{\mu_0 H_{air}(\vartheta) - B_r}{\mu_M} \approx H_{air}(\vartheta) - \frac{B_r}{\mu_M}. \quad (2.125)$$

In Fig. 2.11 the closed loop where to integrate the magnetic field of the circuital law is dashed. The circuital law can be solved in three different scenarios (according to the selected closed loop):

1. Without passing through the magnet

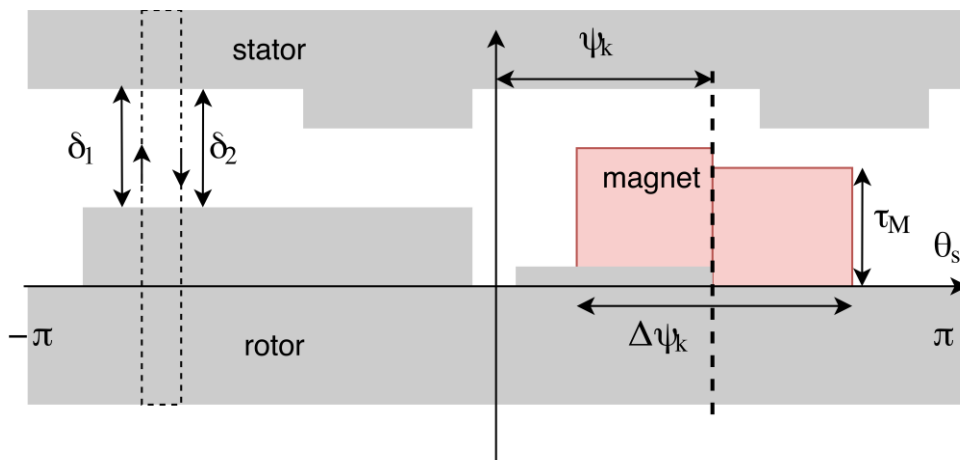


Fig. 2.12 – Magnet with constant radial thickness with a general machine reluctance.

2. Passing from one side through the magnet and coming back without doing it
3. Passing both times through the magnets

In the first scenario (outside the magnet), the circuital law results in the equation:

$$H_{1,air}\delta_1 - H_{2,air}\delta_2 = 0,$$

$$H_{1,air}\delta_1 = H_{2,air}\delta_2.$$

In the second scenario (half through the magnet), the circuital law results in the equation:

$$H_{1,M}\tau_M + H_{1,air}(\delta_1 - \tau_M) - H_{2,air}\delta_2 = 0.$$

Including the Gauss's law for the electromagnetism (2.125), it can be written that:

$$\frac{\mu_0 H_{1,air} - B_r}{\mu_M} \tau_M + H_{1,air}(\delta_1 - \tau_M) - H_2 \delta_2 = 0,$$

resulting in:

$$H_{1,air} \left[\frac{\mu_0}{\mu_M} \tau_M + \delta_1 - \tau_M \right] - \frac{B_r}{\mu_M} \tau_M = H_{2,air} \delta_2.$$

Doing the simplification that $\frac{\mu_0}{\mu_M}$ is almost equal to 1, allows writing the following approximated circuital law:

$$H_{1,air}\delta_1 - H_{2,air}\delta_2 \approx \frac{B_r}{\mu_M} \tau_M = i_{k,eq}. \quad (2.126)$$

This means that the magnetic behaviour is similar to the effect of a concentrated current at the border of the magnet with amplitude $\frac{B_r}{\mu_M} \tau_M$.

In the third scenario (completely through the magnet), the circuital law results in the equation:

$$H_{1,M}\tau_M + H_{1,air}(\delta_1 - \tau_M) - H_{2,M}\tau_M - H_{2,air}(\delta_2 - \tau_M) = 0.$$

Including the Gauss's law for the electromagnetism (2.125), it can be written that:

$$\frac{\mu_0 H_{1,air} - B_r}{\mu_M} \tau_M + H_{1,air}(\delta_1 - \tau_M) - \frac{\mu_0 H_{2,air} - B_r}{\mu_M} \tau_M - H_{2,air}(\delta_2 - \tau_M) = 0,$$

resulting in:

$$H_{1,air} \left[\frac{\mu_0}{\mu_M} \tau_M + \delta_1 - \tau_M \right] = H_{2,air} \left[\frac{\mu_0}{\mu_M} \tau_M + \delta_2 - \tau_M \right],$$

simplifiable, considering the magnet permeability similar to the air one, as:

$$H_{1,air} \delta_1 \approx H_{2,air} \delta_2.$$

By means of (2.126), the same approach used for the armature field is used here for the magnets: the magnet is considered as a turn centred in the angular position ψ_k with pitch $\Delta\psi_k$ and current equal to:

$$i_{k,eq} = \frac{B_r}{\mu_M} \tau_M.$$

As for the analysis of the field in the airgap produced by a single turn, also for the magnets it is possible to define two approaches. The first one, more general and presented in the next paragraph, defines the magnetomotive force of the magnets and evaluates the relative field distribution by means of the airgap geometry (it takes into account for reluctance effects). The second approach is based on the assumption of isotropic magnetic circuit (constant airgap and negligible slotting effect) and results in a simplified analysis. This second approach is not presented because is less general and leads to the same result as verified for the analysis of the field distribution produced by a single turn in Section 2.2.

Magnetomotive force method

The magnetomotive force of the equivalent turn representing a PM can be expressed in terms of spatial harmonics, substituting in (2.38) the equivalent current $i_{k,eq}$ given by (2.126), as:

$$\bar{F}_{k\rho} = \frac{2B_r \tau_M}{\mu_M \rho \pi} \sin\left(\rho \frac{\Delta\psi_k}{2}\right) e^{j\rho\psi_k}. \quad (2.127)$$

Note that now the angle of the magnet magnetic axis (ψ_k) depend on the relative position between the centre of rotor and the stator reference frames (\mathcal{G}_m), therefore also by the time: $\psi_k = \psi_k(\mathcal{G}_m) = \psi_k(t)$.

The magnetic field in the air of the airgap produced by one magnet can be evaluated by (2.31) as:

$$H(\mathcal{G}_s) = g(\mathcal{G}_s) F(\mathcal{G}_s). \quad (2.128)$$

Taking into account of the magnet material equation, it is also possible to write by (2.125) that:

$$H(\mathcal{G}_s) = \begin{cases} g(\mathcal{G}_s) F(\mathcal{G}_s) & \text{in the air} \\ \frac{\mu_0 g(\mathcal{G}_s) F(\mathcal{G}_s) - B_r}{\mu_M} \approx g(\mathcal{G}_s) F(\mathcal{G}_s) - \frac{B_r}{\mu_M} & \text{in the magnets} \end{cases} \quad (2.129)$$

In terms of flux density, (2.121) allows also verifying that the continuity of the flux density is verified:

$$B(\vartheta_s) = \begin{cases} \mu_0 g(\vartheta_s) F(\vartheta_s) & \text{in the air} \\ B_r + \mu_M \frac{\mu_0 g(\vartheta_s) F(\vartheta_s) - B_r}{\mu_M} = \mu_0 g(\vartheta_s) F(\vartheta_s) & \text{in the magnets} \end{cases}$$

The extension of the magnet field to a generic number and typology of surface mounted magnets is equivalent to the analysis done for the stator winding. The difference is only that the current in the equivalent coil is constant, its sign defines the polarity of the magnet, and the thickness can be seen as the amplitude of the current or the number of turns for a given current per turn.

For the purposes of the analysis shown in this thesis, a simplified case of surface permanent magnet rotor (with negligible pitch shortening magnets) is presented in the following subsection only to simplify the equations. However, in Chapter 5 and Chapter 6 the magnets shortening is considered as a design variable.

The next subsection presents the model of an overall SPM rotor.

Surface Permanent Magnet rotor

The idea of a standard surface permanent magnet rotor is shown in Fig. 2.13. According to the conventions used for the positive currents and the direction of the positive magnetic field, the amplitude of the permanent magnet field harmonics can be directly derived by (2.127). As in the modelling of the stator currents the origin of the stator reference frame has been chosen on the magnetic axis of the first phase of the machine, the origin of the rotor reference frame for an SPM machine is chosen in the centre of one north oriented magnet (for example the k -th in Fig. 2.13).

The equation of the harmonics of the equivalent magnetomotive force distribution for an SPM rotor with a general number of magnets symmetrically distributed as in Fig. 2.13 is:

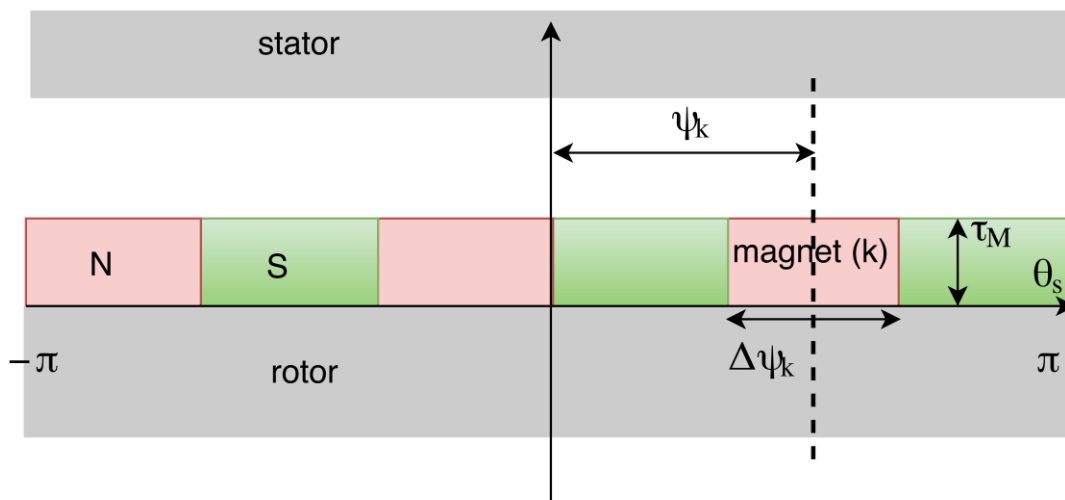


Fig. 2.13 - SPM rotor with three pole pairs.

$$\bar{F}_\rho = \frac{2B_r \tau_M}{\mu_M \rho \pi} \sin\left(\rho \frac{\Delta\psi_k}{2}\right) \sum_{z=1}^p \left(e^{j\rho \frac{\pi}{p}(2z-2)} - e^{j\rho \frac{\pi}{p}(2z-1)} \right) e^{j\rho\psi_k}, \quad (2.130)$$

simplified as:

$$\bar{F}_\rho = \frac{2B_r \tau_M}{\mu_M \rho \pi} \sin\left(\rho \frac{\pi}{2p}\right) \sum_{z=1}^p e^{j\rho \frac{\pi}{p} 2(z-1)} \left(1 - e^{j\rho \frac{\pi}{p}} \right) e^{j\rho\psi_k}. \quad (2.131)$$

Because (2.131) is different from zero only for the harmonic orders odd multiple of p , and in the not zero cases, it can be written that:

$$\sum_{z=1}^p e^{jh_{odd} 2\pi(z-1)} \left(1 - e^{jh_{odd}\pi} \right) = 2p,$$

the resulting equation for the harmonics of the magnets MMF is:

$$\bar{F}_\rho = \bar{F}_{ph} = \frac{4B_r \tau_M}{\mu_M h_{odd} \pi} \sin\left(h_{odd} \frac{\pi}{2}\right) e^{jph_{odd}\psi_k}. \quad (2.132)$$

Finally, if the rotor angular position is considered in the reference frame of the k -th magnet ($\psi_k = \vartheta_m$), the harmonics of magnet field in the air of the airgap are defined as:

$$\bar{H}_\rho = \bar{H}_{ph_{odd}} = \frac{4B_r \tau_M}{\mu_M h_{odd} \pi \delta} \sin\left(h_{odd} \frac{\pi}{2}\right) e^{jph_{odd}\vartheta_m}. \quad (2.133)$$

In many applications, the magnets are skewed in respect to the stator. Because of the manufacturing process of the permanent magnets, the skew is discrete. To obtain a continuous skew without an expensive design of the magnets it is possible to skew the stator lamination. However, in this case the winding process is more complicated. In this thesis, the stator skew is not considered, and the analysis is presented only for a discrete permanent magnet skew and a squirrel cage skew. The skew of the magnets can be represented, for a standard SPM rotor with symmetrically distributed magnets skewed by $\psi_{skew,w}$ radians in the w -th skew step (ΔL_w meter wide and centred in the axial position z_w), by the following relationship:

$$\bar{H}_\rho(z) = \bar{H}_{ph_{odd}}(z) = \frac{4B_r \tau_M}{\mu_M h_{odd} \pi \delta} \sin\left(h_{odd} \frac{\pi}{2}\right) e^{jph_{odd}\vartheta_m} e^{jph_{odd}\psi_{skew,w}}, \quad z \in \left[z_w - \frac{\Delta L_w}{2}; z_w + \frac{\Delta L_w}{2} \right]. \quad (2.134)$$

The next two subsections present the effect of an SPM rotor (in terms of linked flux) on a single turn and a multiphase winding respectively.

Voltage equation (single turn)

To complete the electromagnetic model of a multiphase machine with a SPM rotor (neglecting the reluctance of the magnetic circuit), hereafter the voltage equations of the stator winding are written taking into account of the electromotive force (*emf*) induced by the PM magnetic field. For the purposes of the thesis, the equation is written also for the general single stator turn (k -th), and then the complete space vector equation is given.

The linked flux with the k -th turn related to the PM field (named PM rather than mutual in order to distinguish it from the one produced by a wound or squirrel cage rotor) can be written by (2.111) as:

$$\phi_{PM,kx} = \sum_{h=1}^{\infty} \frac{\mu_0 R}{h} \sin\left(h \frac{\Delta\psi_k}{2}\right) \left(\int_{z=0}^L \bar{H}_h(z) dz e^{-jh\psi_{kx}} + \int_{z=0}^L \bar{H}_h^*(z) dz e^{jh\psi_{kx}} \right). \quad (2.135)$$

Substituting the harmonics of the PM field, it becomes:

$$\begin{aligned} \phi_{PM,kx} = & \sum_{h_{odd}=1}^{\infty} \frac{\mu_0 R}{ph} \sin\left(ph \frac{\Delta\psi_k}{2}\right) \left(\sum_{w=1}^{N_{skew}} \Delta L_w \frac{4B_r \tau_M}{\mu_M h \pi \delta} \sin\left(h \frac{\pi}{2}\right) e^{jph\vartheta_m} e^{jph\psi_{skew,w}} e^{-jph\psi_{kx}} \right) + \\ & + \sum_{h_{odd}=1}^{\infty} \frac{\mu_0 R}{ph} \sin\left(ph \frac{\Delta\psi_k}{2}\right) \left(\sum_{w=1}^{N_{skew}} \Delta L_w \frac{4B_r \tau_M}{\mu_M h \pi \delta} \sin\left(h \frac{\pi}{2}\right) e^{-jph\vartheta_m} e^{-jph\psi_{skew,w}} e^{jph\psi_{kx}} \right). \end{aligned} \quad (2.136)$$

A skew parameter can be identified as:

$$K_{skew,\rho} = \frac{1}{L} \sum_{w=1}^{N_{skew}} \Delta L_w e^{j\rho\psi_{skew,w}},$$

which is a real number if the skew angles $\psi_{skew,w}$ are chosen in relation to the magnetic axis of the considered series of magnets.

If the skew is constant along the axial length and the magnet pieces have the same length, the skew parameter can be simplified as:

$$K_{skew,\rho} = \frac{1}{N_{skew}} \sum_{w=1}^{N_{skew}} e^{j\rho \frac{\Delta\psi_{skew}(w - \frac{N_{skew}+1}{2})}{N_{skew}}}, \quad (2.137)$$

and the linked flux can be written as:

$$\phi_{PM,kx} = \sum_{h_{odd}=1}^{\infty} \frac{\mu_0 LR}{ph} \sin\left(ph \frac{\Delta\psi_k}{2}\right) K_{skew,ph} \frac{4B_r \tau_M}{\mu_M h \pi \delta} \sin\left(h \frac{\pi}{2}\right) \left(e^{jph\vartheta_m} e^{-jph\psi_{kx}} + e^{-jph\vartheta_m} e^{jph\psi_{kx}} \right), \quad (2.138)$$

simplifiable as:

$$\phi_{PM,kx} = \sum_{h_{odd}=1}^{\infty} \frac{2\mu_0 LR}{ph^2} \frac{4B_r \tau_M}{\mu_M \pi \delta} \sin\left(ph \frac{\Delta\psi_k}{2}\right) \sin\left(h \frac{\pi}{2}\right) K_{skew,ph} \Re\left\{e^{jph\vartheta_m} e^{-jph\psi_{kx}}\right\}. \quad (2.139)$$

The total voltage space vector equation of the analysed winding (2.97), introducing (2.119) and (2.139), results in:

$$v_{kx} = r_{kx} i_x + ll_{kx} \frac{di_x}{dt} + \sum_{\substack{lx=1 \\ lx \neq k}}^{N_{lx}} ml_{lx,kx} \frac{di_x}{dt} + l_k \frac{di_x}{dt} + \frac{d\phi_{PM,kx}}{dt}. \quad (2.140)$$

The next subsection extend the effect of an SPM rotor to a multiphase winding represented in terms of space vector equations.

Voltage equation (multiphase winding)

Considering the full stator winding, the mutual linked flux space vector $\bar{\phi}_{mutual,h}$ (named here $\bar{\phi}_{PM,h}$ in order to distinguish it from the one produced by a wound or squirrel cage rotor) with a non-skewed stator winding (2.106), taking into account that the magnets symmetry allows considering only for the harmonic orders odd multiple of p ($\rho = ph_{odd}$) of the PM magnetic field, becomes:

$$\begin{aligned} \bar{\phi}_{PM,h} = & \frac{2}{m} \mu_0 R L p q N N_s \left[\sum_{\substack{y=0 \\ \left(\frac{yN_s+h}{p}\right)_{odd,int}}}^{\infty} \frac{K_{a(yN_s+h)}}{(yN_s+h)} \sum_{w=1}^{N_{skew}} \Delta L_w \frac{4B_r \tau_M p}{\mu_M \pi \delta (yN_s+h)} \sin\left((yN_s+h) \frac{\pi}{2p}\right) e^{j(yN_s+h)\vartheta_m} e^{j(yN_s+h)\psi_{skew,w}} \right] + \\ & + \frac{2}{m} \mu_0 R L p q N N_s \left[\sum_{\substack{y=\left(\frac{h}{N_s}\right)_{int} \\ \left(\frac{yN_s-h}{p}\right)_{odd,int}}}^{\infty} \frac{K_{a(yN_s-h)}}{(yN_s-h)} \sum_{w=1}^{N_{skew}} \Delta L_w \frac{4B_r \tau_M p}{\mu_M \pi \delta (yN_s-h)} \sin\left((yN_s-h) \frac{\pi}{2p}\right) e^{-j(yN_s-h)\vartheta_m} e^{-j(yN_s-h)\psi_{skew,w}} \right]. \end{aligned} \quad (2.141)$$

Introducing the skew parameter $K_{skew,\rho}$, as before for the single turn analysis, the h -space linked flux space vector can be written as:

$$\begin{aligned}
 \bar{\phi}_{PM,h} = & \frac{2}{m} \mu_0 L R p q N N_s \frac{4 B_r \tau_M p}{\mu_M \pi \delta} \left[\sum_{\substack{y=0 \\ \left(\frac{yN_s+h}{p}\right)_{\text{odd.int}}}}^{\infty} \frac{K_{a(yN_s+h)} K_{skew,p(yN_s+h)}}{(yN_s+h)^2} \sin\left((yN_s+h) \frac{\pi}{2p}\right) e^{j(yN_s+h)\vartheta_m} \right] + \\
 & + \frac{2}{m} \mu_0 L R p q N N_s \frac{4 B_r \tau_M p}{\mu_M \pi \delta} \left[\sum_{\substack{y=\left(\frac{h}{N_s}\right)_{\text{int}} \\ \left(\frac{yN_s-h}{p}\right)_{\text{odd.int}}}}^{\infty} \frac{K_{a(yN_s-h)} K_{skew,p(yN_s-h)}}{(yN_s-h)^2} \sin\left((yN_s-h) \frac{\pi}{2p}\right) e^{-j(yN_s-h)\vartheta_m} \right].
 \end{aligned} \tag{2.142}$$

The total voltage space vector equation of the analysed winding (2.97), introducing (2.119) and (2.142), results in:

$$\bar{v}_h = R_s \bar{i}_h + (L_l + L_h) \frac{d\bar{i}_h}{dt} + \frac{d\bar{\phi}_{PM,h}}{dt}, \tag{2.143}$$

where the mutual coupling between the different spaces is not considered, knowing that, if there are anisotropies, also the mutual coupling between the armature spaces must be considered.

This subsection completes the electromagnetic model of a multiphase winding with an SPM rotor. The next section defines the model of squirrel cage. The model of the cage is based on the multiphase approach. In other words, the squirrel cage is represented by its equivalent multiphase winding. To complete the model of a general multiphase machine, the analysis of the power, the torque and the radial force for SPM and IMs is described in Section 2.7.

2.6 Squirrel Cage Modelling

This section aims to present a general model of a squirrel cage IM. In particular, the squirrel cage rotor is analysed in depth by a multiphase modelling approach. Initially, the squirrel cage is described taking into account also for the possible causes of asymmetries. Then, the effect of the cage on a multiphase winding is analysed starting from the analysis of a single turn.

The electromagnetic behaviour of an electrical machine is defined by its interaction with the existing sources of magnetic field. The first source is the current distribution in the winding. The second one is related to the rotor. In case of a squirrel cage machine, the bar and ring currents are the rotor source of magnetomotive force and relative magnetic field.

The next subsection shows how a squirrel cage rotor can be represented as a multiphase machine with Nb phases. The advantage of this representation is that the results obtained for a multiphase stator winding can be directly used for the modelling of the squirrel cage rotor.

Squirrel cage as an N_b -phase symmetrical winding

A squirrel cage is here analysed as an equivalent multiphase machine with N_b single-turn phases each starting in the relative rotor bar and ending in the next rotor bar. The transformation for the modelling of the quantities of this equivalent winding is quite easy because it is already a symmetrical system that in general cannot be simplified to a reduced symmetry. In case of a number of bars multiple of the pole pairs it can easier to consider for only the bars in one pole pair, but hereafter the bars number is taken as a general value without simplify according to the pole pairs number. A draft of a squirrel cage is presented in Fig. 2.14. As usually happens, the induction machine cages are twisted on their axial direction in order to reduce the interaction of the rotor with some field harmonics produced by the stator (skew of the rotor) and by the slotting effect. Therefore, the model takes into account also for the rotor skew.

Fig. 2.15 shows one of the N_b equivalent phases (the x -th) representing the squirrel cage.

The parameters r and l are the resistance and the self leakage inductance, while the subscripts of the squirrel cage model are referred to as in the following list:

- x refers to the equivalent non-physic phase between the b -th and the $(b-1)$ -th bars, renamed as $b_{(x)}$ and $b_{(x-1)}$ ($x = 1, 2, \dots, N_b$).
- $b_{(x)}$ refers to the bar where the equivalent x -th phase starts.
- $r_{(x)}$ refers to the ring of the circuit where the equivalent x -th phase is wound.
- R refers to the rear of the cage.
- F refers to the front of the cage.

According to the squirrel cage constraints, in addition to the standard relationships that can be derived analysing the electric scheme of Fig. 2.15, the currents must also respect the following relationships:

$$\sum_{x=1}^{N_b} i_{b(x)} = 0, \tag{2.144}$$

$$i_{rFb(x)} = -i_{(x)} + I_{rF0},$$

$$i_{rRb(x)} = i_{(x)} + I_{rR0},$$

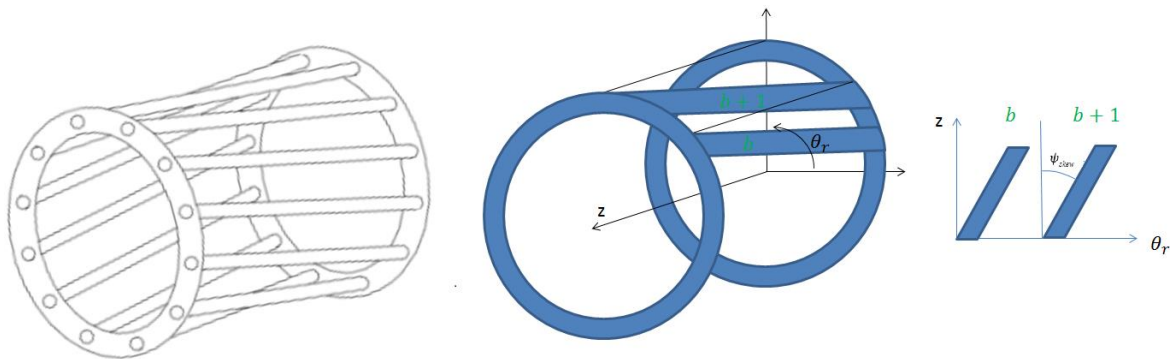


Fig. 2.14 - Squirrel cage and related model parameters.

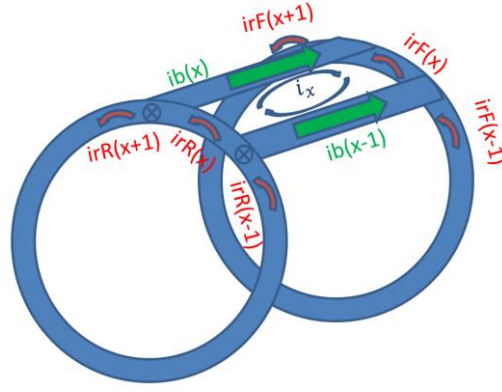


Fig. 2.15 – Equivalent phase of a squirrel cage.

where I_{rF0} and I_{rR0} are currents that can appear owing to axial fluxes. The mutual leakage inductances between different bars or different rings and between bars and rings are neglected in the analysis because considered not significant in a squirrel cage.

The next subsection shows the voltage equation of one of the equivalent phases representing the squirrel cage. The following one describes the overall equivalent multiphase winding of the squirrel cage in terms of space vector representation. Finally, the linked fluxes analysis is presented and the effect of the cage on the stator winding is defined.

Voltage equation (single equivalent phase - between two bars)

The voltage equation of the x -th equivalent phase shown in Fig. 2.16 is:

$$0 = R_{b(x)} i_{b(x)} + ll_{b(x)} \frac{di_{b(x)}}{dt} - R_{b(x-1)} i_{b(x-1)} - ll_{b(x-1)} \frac{di_{b(x-1)}}{dt} + \quad (2.145)$$

$$+ R_{rR(x)} i_{rR(x)} + ll_{rR(x)} \frac{di_{rR(x)}}{dt} - R_{rF(x)} i_{rF(x)} - ll_{rF(x)} \frac{di_{rF(x)}}{dt} + \frac{d\phi_x}{dt},$$

with ϕ_x is the linked flux with the x -th equivalent phase that passes through the airgap.

Equation (2.145) can be rewritten, considering that $i_{b(x)} = i_{(x)} - i_{(x+1)}$ and $i_{b(x-1)} = i_{(x-1)} - i_{(x)}$, as:

$$0 = R_{b(x)} (i_{(x)} - i_{(x+1)}) + ll_{b(x)} \frac{d(i_{(x)} - i_{(x+1)})}{dt} - R_{b(x-1)} (i_{(x-1)} - i_{(x)}) - ll_{b(x-1)} \frac{d(i_{(x-1)} - i_{(x)})}{dt} + \quad (2.146)$$

$$+ R_{rR(x)} (i_{(x)} + I_{rR0}) + ll_{rR(x)} \frac{d(i_{(x)} + I_{rR0})}{dt} - R_{rF(x)} (-i_{(x)} + I_{rF0}) - ll_{rF(x)} \frac{d(-i_{(x)} + I_{rF0})}{dt} + \frac{d\phi_x}{dt}.$$

Note that the constraint $\sum_{x=1}^{Nb} i_{b(x)} = 0$ result also in $\sum_{x=1}^{Nb} i_{(x)} = 0$. Indeed:

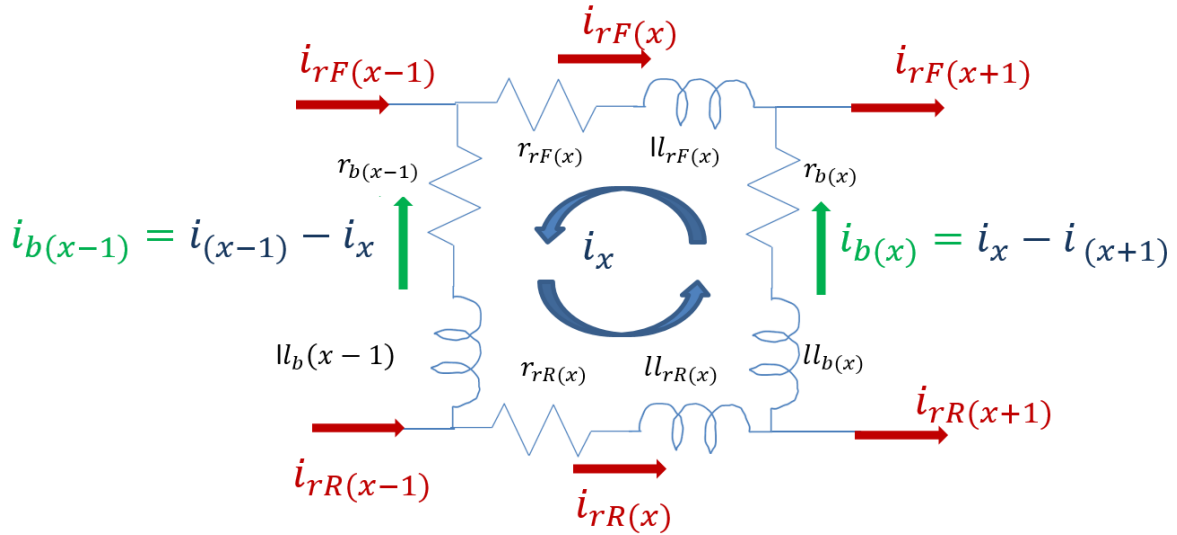


Fig. 2.16 – Electrical circuit and parameters of the equivalent phase of a squirrel cage.

$$\sum_{x=1}^{Nb} i_{b(x)} = \sum_{x=1}^{Nb} i_{(x)} - i_{(x-1)} = 2 \sum_{x=1}^{Nb} i_{(x)} = 0.$$

Simplifying (2.146) results in:

$$\begin{aligned} 0 = & (R_{b(x)} + R_{b(x-1)} + R_{rR(x)} + R_{rF(x)}) i_{(x)} - R_{b(x)} i_{(x+1)} - R_{b(x-1)} i_{(x-1)} + R_{rR(x)} I_{rR0} - R_{rF(x)} I_{rF0} + \\ & + (ll_{b(x)} + ll_{b(x-1)} + ll_{rR(x)} + ll_{rF(x)}) \frac{di_{(x)}}{dt} - ll_{b(x)} \frac{di_{(x+1)}}{dt} - ll_{b(x-1)} \frac{di_{(x-1)}}{dt} + ll_{rR(x)} \frac{dI_{rR0}}{dt} - ll_{rF(x)} \frac{dI_{rF0}}{dt} + \\ & + \frac{d\phi_x}{dt}. \end{aligned} \quad (2.147)$$

Equation (2.147) completely defines the behaviour of an equivalent phase of the squirrel cage. The next subsection presents the effect of all the equivalent phases of the cage rotor in terms of space vectors representation.

Voltage equation (equivalent multiphase winding of the squirrel cage)

Because the interaction of the rotor with the stator is by means of the field harmonics in the airgap and each of these harmonics can be related to the relative stator and rotor current space vectors, also the rotor voltage equation are written in terms of space vectors as follows:

$$\bar{v}_h = \frac{2}{N_b} \sum_{x=1}^{N_b} v_x \bar{\alpha}^{h(x-1)}, \quad (2.148)$$

with $\bar{\alpha} = e^{j\frac{2\pi}{N_b}}$. The cage equation becomes:

$$\begin{aligned}
 0 = \bar{v}_h = & \frac{2}{N_b} \sum_{x=1}^{N_b} (R_{b(x)} + R_{b(x-1)} + R_{rR(x)} + R_{rF(x)}) i_{(x)} \bar{\alpha}^{h(x-1)} + \frac{2}{N_b} \sum_{x=1}^{N_b} (-R_{b(x)}) i_{(x+1)} \bar{\alpha}^{h(x-1)} + \\
 & + \frac{2}{N_b} \sum_{x=1}^{N_b} (-R_{b(x-1)}) i_{(x-1)} \bar{\alpha}^{h(x-1)} + \frac{2}{N_b} \sum_{x=1}^{N_b} R_{rR(x)} \bar{\alpha}^{h(x-1)} I_{rR0} - \frac{2}{N_b} \sum_{x=1}^{N_b} R_{rF(x)} \bar{\alpha}^{h(x-1)} I_{rF0} + \\
 & + \frac{2}{N_b} \sum_{x=1}^{N_b} (l_{b(x)} + l_{b(x-1)} + l_{rR(x)} + l_{rF(x)}) \frac{di_{(x)}}{dt} \bar{\alpha}^{h(x-1)} + \frac{2}{N_b} \sum_{x=1}^{N_b} (-l_{b(x)}) \frac{di_{(x+1)}}{dt} \bar{\alpha}^{h(x-1)} + \quad (2.149) \\
 & + \frac{2}{N_b} \sum_{x=1}^{N_b} (-l_{b(x-1)}) \frac{di_{(x-1)}}{dt} \bar{\alpha}^{h(x-1)} + \frac{2}{N_b} \sum_{x=1}^{N_b} l_{rR(x)} \bar{\alpha}^{h(x-1)} \frac{dI_{rR0}}{dt} - \frac{2}{N_b} \sum_{x=1}^{N_b} l_{rF(x)} \bar{\alpha}^{h(x-1)} \frac{dI_{rF0}}{dt} + \\
 & + \frac{2}{N_b} \sum_{x=1}^{N_b} \frac{d\phi_x}{dt} \bar{\alpha}^{h(x-1)}.
 \end{aligned}$$

The following paragraph highlights the possibility to have axial fluxes and unbalanced rings. This thesis focus on faults on the stator winding. However, this brief analysis on possible asymmetries on the squirrel cage shows how the proposed model can be extended for the analysis of these phenomena.

Ring unbalances and axial fluxes

The contributions of the homopolar currents in the rings are not related to the considered space vector (harmonic), but they cause a voltage drop that can be analysed introducing the two axial equations of the cage:

$$0 = \sum_{x=1}^{N_b} R_{rF(x)} I_{rF0} + \sum_{x=1}^{N_b} l_{rF(x)} \frac{dI_{rF0}}{dt} - \sum_{x=1}^{N_b} R_{rF(x)} i_{(x)} - \sum_{x=1}^{N_b} l_{rF(x)} \frac{di_{(x)}}{dt} + \frac{d\phi_F}{dt}, \quad (2.150)$$

for the frontal ring, and

$$0 = \sum_{x=1}^{N_b} R_{rR(x)} I_{rR0} + \sum_{x=1}^{N_b} l_{rR(x)} \frac{dI_{rR0}}{dt} + \sum_{x=1}^{N_b} R_{rR(x)} i_{(x)} + \sum_{x=1}^{N_b} l_{rR(x)} \frac{di_{(x)}}{dt} + \frac{d\phi_R}{dt}, \quad (2.151)$$

for the rear ring. Note that the equations are independent from the bars parameters.

Furthermore, if the squirrel cage is symmetrical (there are not asymmetries in the resistances and inductances), the equation can be easily simplified as:

$$\begin{aligned}
 0 = N_b R_{rF} I_{rF0} + N_b l_{rF} \frac{dI_{rF0}}{dt} - \sum_{x=1}^{N_b} i_{(x)} R_{rF} - \sum_{x=1}^{N_b} \frac{di_{(x)}}{dt} l_{rF} + \frac{d\phi_F}{dt} = \\
 = N_b R_{rF} I_{rF0} + N_b l_{rF} \frac{dI_{rF0}}{dt} + \frac{d\phi_F}{dt}, \quad (2.152)
 \end{aligned}$$

for the frontal ring, and

$$\begin{aligned}
 0 &= N_b R_{rR} I_{rR0} + N_b l_{rR} \frac{dI_{rR0}}{dt} + \sum_{x=1}^{N_b} i_{(x)} R_{rR} + \sum_{x=1}^{N_b} \frac{di_{(x)}}{dt} l_{rR} + \frac{d\phi_R}{dt} = \\
 &= N_b R_{rR} I_{rR0} + N_b l_{rR} \frac{dI_{rR0}}{dt} + \frac{d\phi_R}{dt},
 \end{aligned} \tag{2.153}$$

for the rear ring. This allows considering that in a symmetrical squirrel cage the homopolar currents of the slices of rings related to the equivalent phases are only produced by axial fluxes in the machine.

Neglecting the axial fluxes allows writing:

$$0 = \sum_{x=1}^{N_b} R_{rF(x)} I_{rF0} + \sum_{x=1}^{N_b} l_{rF(x)} \frac{dI_{rF0}}{dt} - \sum_{x=1}^{N_b} R_{rF(x)} i_{(x)} - \sum_{x=1}^{N_b} l_{rF(x)} \frac{di_{(x)}}{dt}, \tag{2.154}$$

for the frontal ring, and

$$0 = \sum_{x=1}^{N_b} R_{rR(x)} I_{rR0} + \sum_{x=1}^{N_b} l_{rR(x)} \frac{dI_{rR0}}{dt} + \sum_{x=1}^{N_b} R_{rR(x)} i_{(x)} + \sum_{x=1}^{N_b} l_{rR(x)} \frac{di_{(x)}}{dt}, \tag{2.155}$$

for the rear ring.

This means that in case of an unbalance in the impedance in the slices of the rings there are homopolar currents (only in the unbalance ring) that might be taken into account in the cage equation.

Hereafter, the rings are supposed to be symmetrical and possible axial fluxes are neglected. Under this hypothesis, the equation of the squirrel cage can be simplified as in the next paragraph.

Balanced rings and negligible axial fluxes

If the impedances of the various ring slices are equal and there are no axial flux components linked with the rings, it results that the homopolar currents in the rings can be neglected. In this case, (symmetrical rings and no axial fluxes) the cage space vector equations can be written as:

$$\begin{aligned}
 0 &= \frac{2}{N_b} \sum_{x=1}^{N_b} (R_{b(x)} + R_{b(x-1)}) i_{(x)} \bar{\alpha}^{h(x-1)} + (R_{rR} + R_{rF}) \bar{i}_h + \\
 &+ \frac{2}{N_b} \sum_{x=1}^{N_b} (-R_{b(x)}) i_{(x+1)} \bar{\alpha}^{h(x-1)} + \frac{2}{N_b} \sum_{x=1}^{N_b} (-R_{b(x-1)}) i_{(x-1)} \bar{\alpha}^{h(x-1)} \\
 &+ \frac{2}{N_b} \sum_{x=1}^{N_b} (l_{b(x)} + l_{b(x-1)}) \frac{di_{(x)}}{dt} \bar{\alpha}^{h(x-1)} + (l_{rR} + l_{rF}) \frac{d\bar{i}_h}{dt} + \\
 &+ \frac{2}{N_b} \sum_{x=1}^{N_b} (-l_{b(x)}) \frac{di_{(x+1)}}{dt} \bar{\alpha}^{h(x-1)} + \frac{2}{N_b} \sum_{x=1}^{N_b} (-l_{b(x-1)}) \frac{di_{(x-1)}}{dt} \bar{\alpha}^{h(x-1)} + \bar{\phi}_h.
 \end{aligned} \tag{2.156}$$

From the next subsection, also the asymmetries of the bars of the squirrel cage are neglected in order to simplify the model of the overall machine.

Voltage equation (equivalent multiphase winding of a symmetrical cage)

If also the bars are symmetric, the equation of a symmetrical cage without axial fluxes is:

$$\begin{aligned}
 0 = & (2R_b + R_{rR} + R_{rF})\bar{i}_h - R_b \frac{2}{N_b} \sum_{x=1}^{N_b} i_{(x+1)} \bar{\alpha}^{h(x-1)} + \\
 & - R_b \frac{2}{N_b} \sum_{x=1}^{N_b} i_{(x-1)} \bar{\alpha}^{h(x-1)} + (2ll_b + ll_{rR} + ll_{rF}) \frac{d\bar{i}_h}{dt} + \\
 & - ll_b \frac{2}{N_b} \sum_{x=1}^{N_b} \frac{di_{(x+1)}}{dt} \bar{\alpha}^{h(x-1)} - ll_b \frac{2}{N_b} \sum_{x=1}^{N_b} \frac{di_{(x-1)}}{dt} \bar{\alpha}^{h(x-1)} + \bar{\phi}_h.
 \end{aligned} \tag{2.157}$$

It can be easily rewritten as:

$$0 = (R_b(2 - \bar{\alpha}^{-h} - \bar{\alpha}^h) + R_{rR} + R_{rF})\bar{i}_h + (ll_b(2 - \bar{\alpha}^{-h} - \bar{\alpha}^h) + ll_{rR} + ll_{rF}) \frac{d\bar{i}_h}{dt} + \bar{\phi}_h, \tag{2.158}$$

resulting in:

$$0 = \left(2R_b \left(1 - \cos\left(\frac{2\pi h}{N_b}\right) \right) + R_{rR} + R_{rF} \right) \bar{i}_h + \left(2ll_b \left(1 - \cos\left(\frac{2\pi h}{N_b}\right) \right) + ll_{rR} + ll_{rF} \right) \frac{d\bar{i}_h}{dt} + \bar{\phi}_h. \tag{2.159}$$

Introducing the non-physical rotor h -space resistance:

$$R_{rh} = 2R_b \left(1 - \cos\left(\frac{2\pi h}{N_b}\right) \right) + R_{rR} + R_{rF},$$

and rotor h -space leakage inductance:

$$Ll_{rh} = 2ll_b \left(1 - \cos\left(\frac{2\pi h}{N_b}\right) \right) + ll_{rR} + ll_{rF},$$

the final space vector equations of a symmetrical and squirrel cage rotor without axial fluxes can be written as:

$$0 = R_{rh}\bar{i}_h + Ll_{rh} \frac{d\bar{i}_h}{dt} + \bar{\phi}_h. \tag{2.160}$$

Equation , represents the voltage space vector equation of a squirrel cage rotor. The main difference from a short circuited multiphase winding is that also in case of a symmetrical

squirrel cage rotor the space resistance and space leakage inductance are function of the considered space.

The next subsection aims to define the analytical equation for the linked flux space vector $\bar{\phi}_h$. Instead, the following subsections present the couplings between a squirrel cage and a multiphase winding.

Linked flux (general)

The h -space linked flux space vector is as the one of an N_b -phase machine (2.108) with one turn per phase:

$$\bar{\phi}_h = 2\mu_0 R \left[\sum_{y=0}^{\infty} \frac{\sin\left((yN_b + h)\frac{\pi}{N_b}\right)}{(yN_b + h)} \int_{z=0}^L \bar{H}_{(yN_b+h)}(z) dz \right] + 2\mu_0 R \left[\sum_{y=\left(\frac{h}{N_b}\right)_{\text{int}}}^{\infty} \frac{\sin\left((yN_b - h)\frac{\pi}{N_b}\right)}{(yN_b - h)} \int_{z=0}^L \bar{H}_{(yN_b-h)}^*(z) dz \right], \quad (2.161)$$

with the equivalent winding factor equal to:

$$K_{ar,h} = \sin\left(h\frac{\pi}{N_b}\right). \quad (2.162)$$

If the winding is skewed, as in Fig. 2.1, with the z -axis starting from the middle of the axial length of the cage, , becomes:

$$\bar{\phi}_h = 2\mu_0 R \left[\sum_{y=0}^{\infty} \frac{\sin\left((yN_b + h)\frac{\pi}{N_b}\right)}{(yN_b + h)} \int_{z=0}^L \bar{H}_{(yN_b+h)}(z) e^{-j(yN_b+h)\left(z-\frac{L}{2}\right)\frac{\Delta\psi_{\text{skew}}}{L}} dz \right] + \quad (2.163)$$

$$+ 2\mu_0 R \left[\sum_{y=\left(\frac{h}{N_b}\right)_{\text{int}}}^{\infty} \frac{\sin\left((yN_b - h)\frac{\pi}{N_b}\right)}{(yN_b - h)} \int_{z=0}^L \bar{H}_{(yN_b-h)}^*(z) e^{j(yN_b-h)\left(z-\frac{L}{2}\right)\frac{\Delta\psi_{\text{skew}}}{L}} dz \right].$$

Note that the sign of the skewing changes, because the dependence by z of the magnetic field is internal to the harmonics, and integrating along a skewed path it is equal to shift all the harmonics in the airgap.

The harmonics of the magnetic field produced by the equivalent multiphase currents of a non-skewed cage are evaluable by (2.52) as:

$$\bar{H}_h = \frac{N_b}{\pi\delta} \frac{\sin\left(h \frac{\pi}{N_b}\right)}{h} \bar{i}_h. \quad (2.164)$$

If the skew is taken into account, the equation becomes:

$$\bar{H}_h(z) = \frac{N_b}{\pi\delta} \frac{\sin\left(h \frac{\pi}{N_b}\right)}{h} \bar{i}_h e^{jh\left(\frac{z-L}{2}\right) \frac{\Delta W_{skew}}{L}}. \quad (2.165)$$

It results that , can be considered sum of two terms (a self and a mutual effect with the other sources of magnetic field but the cage itself) as:

$$\bar{\phi}_h = \bar{\phi}_{self,h} + \bar{\phi}_{mutual,h}.$$

The next subsection defines the self linked flux space vector equation for a squirrel cage rotor.

Self inductance (equivalent multiphase winding of a squirrel cage - SVD)

The self contribution of the linked flux in a squirrel cage rotor modelled as a multiphase winding can be defined as:

$$\begin{aligned} \bar{\phi}_{self,h} = 2\mu_0 R & \left[\sum_{y=0}^{\infty} \frac{\sin\left(\left(yN_b+h\right) \frac{\pi}{N_b}\right)}{\left(yN_b+h\right)} \int_{z=0}^L \frac{N_b}{\pi\delta} \frac{\sin\left(\left(yN_b+h\right) \frac{\pi}{N_b}\right)}{\left(yN_b+h\right)} \bar{i}_{(yN_b+h)} dz \right] + \\ & + 2\mu_0 R \left[\sum_{y=\left(\frac{h}{N_b}\right)_{int}}^{\infty} \frac{\sin\left(\left(yN_b-h\right) \frac{\pi}{N_b}\right)}{\left(yN_b-h\right)} \int_{z=0}^L \frac{N_b}{\pi\delta} \frac{\sin\left(\left(yN_b-h\right) \frac{\pi}{N_b}\right)}{\left(yN_b-h\right)} \bar{i}_{(yN_b-h)}^* dz \right]. \end{aligned} \quad (2.166)$$

The equation does not depend by the z dimension anymore. Furthermore, the space vector relationships ($\bar{i}_{(yN_b+h)} = \bar{i}_{(yN_b-h)}^* = \bar{i}_h$) allows simplifying the self linked fluxes space vector equations as:

$$\bar{\phi}_{self,h} = 2 \frac{\mu_0 RL}{\pi\delta} N_b \left[\sum_{y=0}^{\infty} \frac{\sin\left(\left(yN_b+h\right) \frac{\pi}{N_b}\right)^2}{\left(yN_b+h\right)^2} + \sum_{y=\left(\frac{h}{N_b}\right)_{int}}^{\infty} \frac{\sin\left(\left(yN_b-h\right) \frac{\pi}{N_b}\right)^2}{\left(yN_b-h\right)^2} \right] \bar{i}_h. \quad (2.167)$$

Introducing the non-physical h-space self inductance of the cage equivalent multiphase winding:

$$L_{cage,h} = 2 \frac{\mu_0 R L N_b}{\pi \delta} \left[\sum_{y=0}^{\infty} \frac{\sin\left((yN_b + h)\frac{\pi}{N_b}\right)^2}{(yN_b + h)^2} + \sum_{y=\left(\frac{h}{N_b}\right)_{int}}^{\infty} \frac{\sin\left((yN_b - h)\frac{\pi}{N_b}\right)^2}{(yN_b - h)^2} \right],$$

the linked fluxes space vector equations result as:

$$\bar{\phi}_h = \bar{\phi}_{self,h} + \bar{\phi}_{mutual,h} = L_{cage,h} \bar{i}_h + \bar{\phi}_{mutual,h}, \quad (2.168)$$

and the squirrel cage voltage space vector equations are defined as:

$$0 = R_{rh} \bar{i}_h + (Ll_{rh} + L_{cage,h}) \frac{d\bar{i}_h}{dt} + \frac{d\bar{\phi}_{mutual,h}}{dt}. \quad (2.169)$$

Taking into account a general multiphase winding, the mutual effect of this winding of the cage is included in the term $\bar{\phi}_{mutual,h}$. This can be evaluated by (2.163), considering only the harmonics of the field produced by the stator winding. This analysis is done in the next two subsections for a single stator turn and for the overall stator multiphase winding respectively.

Mutual flux (effect of a single turn on the squirrel cage)

For the purposes of the thesis, before analysing the whole winding, the equation of the effect of the stator currents on the squirrel cage is written for the general single stator turn (k -th turn of the x -th phase in the position ψ_{kx} in the stator reference frame oriented with the magnetic axis of the first stator phase). The cage is considered with the centre of its first equivalent turn shifted by ϑ_m radians from the stator reference frame. The linked flux related to the k -th turn current i_{kx} is evaluated introducing (2.39) into (2.163) as follows:

$$\begin{aligned} \bar{\phi}_{mutual_{kx},h} = & 2\mu_0 R \left[\sum_{y=0}^{\infty} \frac{\sin\left((yN_b + h)\frac{\pi}{N_b}\right)}{(yN_b + h)^2} \int_{z=0}^L \frac{2i_{kx}}{\pi\delta} \sin\left((yN_b + h)\frac{\Delta\psi_k}{2}\right) e^{j(yN_b+h)(\psi_{kx}-\vartheta_m)} e^{-j(yN_b+h)\left(z-\frac{L}{2}\right)\frac{\Delta\psi_{skew}}{L}} dz \right] + \\ & + 2\mu_0 R \left[\sum_{y=\left(\frac{h}{N_b}\right)_{int}}^{\infty} \frac{\sin\left((yN_b - h)\frac{\pi}{N_b}\right)}{(yN_b - h)^2} \int_{z=0}^L \frac{2i_{kx}}{\pi\delta} \sin\left((yN_b - h)\frac{\Delta\psi_k}{2}\right) e^{-j(yN_b-h)(\psi_{kx}-\vartheta_m)} e^{j(yN_b-h)\left(z-\frac{L}{2}\right)\frac{\Delta\psi_{skew}}{L}} dz \right]. \end{aligned} \quad (2.170)$$

Simplifying, and replacing in $\int_{z=0}^L e^{j(yN_b-h)\left(z-\frac{L}{2}\right)\frac{\Delta\psi_{skew}}{L}} dz$ the skew constant defined as:

$$K_{skew,h} = \frac{1}{L} \int_{z=0}^L e^{jh\left(z-\frac{L}{2}\right)\frac{\Delta\psi_{skew}}{L}} dz = \frac{\sin\left(h\frac{\Delta\psi_{skew}}{2}\right)}{h\frac{\Delta\psi_{skew}}{2}}, \quad (2.171)$$

(2.170) becomes:

$$\begin{aligned} \bar{\phi}_{mutual_{kx},h} = & 4 \frac{\mu_0 RL}{\pi\delta} \left[\sum_{y=0}^{\infty} \frac{\sin\left((yN_b+h)\frac{\pi}{N_b}\right) \sin\left((yN_b+h)\frac{\Delta\psi_k}{2}\right)}{(yN_b+h)} K_{skew,(yN_b+h)} e^{j(yN_b+h)(\psi_{kx}-g_m)} \right] i_{kx} + \\ & + 4 \frac{\mu_0 RL}{\pi\delta} \left[\sum_{y=\left(\frac{h}{N_b}\right)_{int}}^{\infty} \frac{\sin\left((yN_b-h)\frac{\pi}{N_b}\right) \sin\left((yN_b-h)\frac{\Delta\psi_k}{2}\right)}{(yN_b-h)} K_{skew,(yN_b-h)} e^{-j(yN_b-h)(\psi_{kx}-g_m)} \right] i_{kx}. \end{aligned} \quad (2.172)$$

The equation can be simplified by introducing the new parameter $X_{ca_{kx},h}$, given by:

$$X_{ca_{kx},h} = \frac{\sin\left(\frac{h\pi}{N_b}\right) \sin\left(h\frac{\Delta\psi_k}{2}\right)}{(h)^2} K_{skew(h)}, \quad (2.173)$$

as:

$$\bar{\phi}_{mutual_{kx},h} = 4 \frac{\mu_0 RL}{\pi\delta} \left[\sum_{y=0}^{\infty} X_{ca_{kx},(yN_b+h)} e^{j(yN_b+h)(\psi_{kx}-g_m)} + \sum_{y=\left(\frac{h}{N_b}\right)_{int}}^{\infty} X_{ca_{kx},(yN_b-h)} e^{-j(yN_b-h)(\psi_{kx}-g_m)} \right] i_{kx}. \quad (2.174)$$

The next subsection defines the linked flux space vector on a squirrel cage rotor produced by a multiphase stator winding.

Mutual flux (effect of a multiphase winding on the squirrel cage)

In case of a full multiphase stator winding, the harmonics produced by the stator currents are defined by (2.47), with a symmetry of order n for the m -phase winding. The current space vector is defined by (2.48), resulting in:

$$\begin{aligned}
 \bar{\phi}_{mutual,h} = & 2\mu_0 R \left[\sum_{y=0}^{\infty} \frac{\sin\left((yN_b+h)\frac{\pi}{N_b}\right)}{(yN_b+h)} \int_{z=0}^L \frac{Nmpq}{\pi\delta} \frac{K_{a(yN_b+h)}}{(yN_b+h)} \bar{i}_{(yN_b+h)} e^{-j(yN_b+h)\left(z-\frac{L}{2}\right)\frac{\Delta\psi_{skew}}{L}} dz e^{-j(yN_b+h)\vartheta_m} \right] + \\
 & + 2\mu_0 R \left[\sum_{y=\left(\frac{h}{N_b}\right)_{int}}^{\infty} \frac{\sin\left((yN_b-h)\frac{\pi}{N_b}\right)}{(yN_b-h)} \int_{z=0}^L \frac{Nmpq}{\pi\delta} \frac{K_{a(yN_b-h)}}{(yN_b-h)} \bar{i}_{(yN_b-h)}^* e^{j(yN_b-h)\left(z-\frac{L}{2}\right)\frac{\Delta\psi_{skew}}{L}} dz e^{j(yN_b-h)\vartheta_m} \right].
 \end{aligned} \tag{2.175}$$

Replacing the skew constant $K_{skew,h}$, (2.175) becomes:

$$\begin{aligned}
 \bar{\phi}_{mutual,h} = & \frac{2Nmpq\mu_0 RL}{\pi\delta} \left[\sum_{y=0}^{\infty} \frac{\sin\left((yN_b+h)\frac{\pi}{N_b}\right) K_{a(yN_b+h)}}{(yN_b+h)^2} \bar{i}_{(yN_b+h)} K_{skew(yN_b+h)} e^{-j(yN_b+h)\vartheta_m} \right] + \\
 & + \frac{2Nmpq\mu_0 RL}{\pi\delta} \left[\sum_{y=\left(\frac{h}{N_b}\right)_{int}}^{\infty} \frac{\sin\left((yN_b-h)\frac{\pi}{N_b}\right) K_{a(yN_b-h)}}{(yN_b-h)^2} \bar{i}_{(yN_b-h)}^* K_{skew(yN_b-h)} e^{j(yN_b-h)\vartheta_m} \right].
 \end{aligned} \tag{2.176}$$

One of the more critical steps in the modelling of a multiphase induction machine with a squirrel cage is to relate the h -th space vector of the cage linked fluxes to the space vectors of the stator currents by taking into account the relationships of the N_s -th order symmetrical transformation

used to describe the stator quantities: $\bar{i}_\rho = \frac{2}{m} \sum_{x=1}^{N_s} i_x e^{j\rho \frac{2\pi}{N_s}(x-1)}$, with $\bar{i}_{zN_s+\rho} = \bar{i}_\rho$ and $\bar{i}_{zN_s-\rho} = \bar{i}_\rho^*$.

These relationships, and the introduction of the additional parameter $X_{ca,h}$ that relates the cage with the armature winding as in (2.174), allows rewriting the linked flux space vectors as:

$$\bar{\phi}_{mutual,h} = \frac{2Nmpq\mu_0 RL}{\pi\delta} \sum_{\rho=0}^{N_s-1} \left[\sum_{\substack{y=0 \\ \left(\frac{yN_b+h-\rho}{N_s}\right)_{int} \geq 0}}^{\infty} (X_{ca(yN_b+h)} e^{-j(yN_b+h)\vartheta_m}) \bar{i}_\rho + \sum_{\substack{y=0 \\ y \geq \left(\frac{h}{N_b}\right)_{int} \\ \left(\frac{yN_b-h-\rho}{N_s}\right)_{int} \geq 0}}^{\infty} (X_{ca(yN_b-h)} e^{j(yN_b-h)\vartheta_m}) \bar{i}_\rho^* \right]. \tag{2.177}$$

The next two paragraphs show how (2.177) results in case of multiphase windings with odd or even symmetries in their geometry.

Standard symmetrical winding (odd number of phases)

If the winding has a zero sequence of the current space vectors and an n -order symmetry with n odd (as the nine-phase in Fig. 2.9, right), (2.177) can be rearranged considering that $\bar{i}_{2N_s-\rho}^* = \bar{i}_\rho$ as:

$$\begin{aligned} \bar{\phi}_{mutual, \frac{N_s}{n}h} = & \frac{2Nmpq\mu_0RL}{\pi\delta} \sum_{\rho_{odd}=1}^{n-2} \left(\sum_{\substack{y=0 \\ \left(\frac{yN_b+h-\rho}{n}\right)_{int \geq 0}}}^{\infty} X_{ca(yN_b+h)} e^{-j(yN_b+h)g_m} + \sum_{\substack{y=0 \\ y \geq \left(\frac{h}{N_b}\right)_{int} \\ \left(\frac{yN_b-h+\rho}{n}\right)_{int \geq 1}}}^{\infty} X_{ca(yN_b-h)} e^{j(yN_b-h)g_m} \right) \bar{i}_{\frac{N_s}{n}\rho} + \\ & + \frac{2Nmpq\mu_0RL}{\pi\delta} \sum_{\rho_{odd}=1}^{n-2} \left(\sum_{\substack{y=0 \\ \left(\frac{yN_b+h+\rho}{n}\right)_{int \geq 1}}}^{\infty} X_{ca(yN_b+h)} e^{-j(yN_b+h)g_m} + \sum_{\substack{y=0 \\ y \geq \left(\frac{h}{N_b}\right)_{int} \\ \left(\frac{yN_b-h-\rho}{n}\right)_{int \geq 0}}}^{\infty} X_{ca(yN_b-h)} e^{j(yN_b-h)g_m} \right) \bar{i}_{\frac{N_s}{n}\rho}^* . \end{aligned} \quad (2.178)$$

Standard asymmetrical winding (even number of phases)

Instead, if the winding has a n -order symmetry with n even (as the twelve phase asymmetrical winding in Fig. 2.8), (2.177) can be rearranged as:

$$\begin{aligned} \bar{\phi}_{mutual, \frac{N_s}{n}h} = & \frac{2Nmpq\mu_0RL}{\pi\delta} \sum_{\rho_{odd}=1}^{n-1} \left(\sum_{\substack{y=0 \\ \left(\frac{yN_b+h-\rho}{n}\right)_{int \geq 0}}}^{\infty} X_{ca(yN_b+h)} e^{-j(yN_b+h)g_m} + \sum_{\substack{y=0 \\ y \geq \left(\frac{h}{N_b}\right)_{int} \\ \left(\frac{yN_b-h+\rho}{n}\right)_{int \geq 1}}}^{\infty} X_{ca(yN_b-h)} e^{j(yN_b-h)g_m} \right) \bar{i}_{\frac{N_s}{n}\rho} + \\ & + \frac{2Nmpq\mu_0RL}{\pi\delta} \sum_{\rho_{odd}=1}^{n-1} \left(\sum_{\substack{y=0 \\ \left(\frac{yN_b+h+\rho}{n}\right)_{int \geq 1}}}^{\infty} X_{ca(yN_b+h)} e^{-j(yN_b+h)g_m} + \sum_{\substack{y=0 \\ y \geq \left(\frac{h}{N_b}\right)_{int} \\ \left(\frac{yN_b-h-\rho}{n}\right)_{int \geq 0}}}^{\infty} X_{ca(yN_b-h)} e^{j(yN_b-h)g_m} \right) \bar{i}_{\frac{N_s}{n}\rho}^* + \\ & + \frac{2Nmpq\mu_0RL}{\pi\delta} \left(\sum_{\substack{y=0 \\ \left(\frac{yN_b+h-\frac{n}{2}}{n}\right)_{int \geq 0}}}^{\infty} X_{ca(yN_b+h)} e^{-j(yN_b+h)g_m} + \sum_{\substack{y=0 \\ y \geq \left(\frac{h}{N_b}\right)_{int} \\ \left(\frac{yN_b-h-\frac{n}{2}}{n}\right)_{int \geq 0}}}^{\infty} X_{ca(yN_b-h)} e^{j(yN_b-h)g_m} \right) \bar{i}_{\frac{N_s}{n}\frac{n}{2}} . \end{aligned} \quad (2.179)$$

This relationship represents the interaction between the h -th spaces of the cage with all the ρ -th spaces of the stator. In other words, once the current space vectors \bar{i}_ρ ($\rho=1, 2, \dots, n$) are known (they are always known if there is a current control or if all the currents are measured), (2.179) represents the effect (in terms of induced electromotive force, *emf*) of these current vectors on the rotor equation in the h -th space. Then, the h -th space equation determines the h -th cage

current space vector \bar{i}_h , and this current vector is related to the h -th harmonic of the spatial distribution of the magnetic field in the airgap (\bar{H}_h) and the higher order ones (\bar{H}_{kN_b-h} and \bar{H}_{kN_b+h}). Therefore if (2.179) results in an induced *emf* on the cage ($\bar{\phi}_{mutual,h}$) equal to zero, the rotor will not react generating the harmonics of the cage field of order $kN_b + h$ and $kN_b - h$ (with $k = 1, 2, \dots, \infty$).

The next two subsections aim to present the effect of the squirrel cage currents on the stator winding (starting from the analysis of a single stator turn).

Voltage equation (effect of the cage on a single turn)

To complete the electromagnetic model of a multiphase induction machine with a squirrel cage rotor, the voltage equations of the stator winding are written taking into account of the *emf* induced by the cage magnetic field. For the purposes of the thesis, the equations are written also for the general single stator turn (k -th), and then they are generalized to the full winding.

The linked flux with the k -th turn (related to the cage rotor field) are described by (2.111) considering the cage field described by (2.165), where the cage harmonics are shifted along the z direction in the stator reference frame. The linked flux equation is written as:

$$\begin{aligned} \phi_{cage,kx} = & \sum_{h=1}^{\infty} \frac{\mu_0 R}{h} \sin\left(h \frac{\Delta\psi_k}{2}\right) \left(\int_{z=0}^L \frac{N_b}{\pi\delta} \frac{\sin\left(h \frac{\pi}{N_b}\right)}{h} \bar{i}_h e^{jh\left(\frac{z-L}{2}\right)\frac{\Delta\psi_{skew}}{L}} e^{jh\vartheta_m} dz e^{-jh\psi_{kx}} \right) + \\ & + \sum_{h=1}^{\infty} \frac{\mu_0 R}{h} \sin\left(h \frac{\Delta\psi_k}{2}\right) \left(\int_{z=0}^L \frac{N_b}{\pi\delta} \frac{\sin\left(h \frac{\pi}{N_b}\right)}{h} \bar{i}_h^* e^{-jh\left(\frac{z-L}{2}\right)\frac{\Delta\psi_{skew}}{L}} e^{-jh\vartheta_m} dz e^{jh\psi_{kx}} \right). \end{aligned} \quad (2.180)$$

Introducing the skewing factor $K_{skew,h}$, (2.180) becomes:

$$\phi_{cage,kx} = \sum_{h=1}^{\infty} \frac{2\mu_0 R L N_b K_{skew,h}}{2\pi\delta h} \sin\left(h \frac{\Delta\psi_k}{2}\right) \frac{\sin\left(h \frac{\pi}{N_b}\right)}{h} \left(\bar{i}_h e^{-jh(\psi_{kx} - \vartheta_m)} + \bar{i}_h^* e^{jh(\psi_{kx} - \vartheta_m)} \right). \quad (2.181)$$

Introducing also the parameter $X_{ca_{kx},h}$, the final equation is:

$$\phi_{cage,kx} = \sum_{h=1}^{\infty} \frac{\mu_0 R L N_b}{\pi\delta} X_{ca_{kx},h} \left(\bar{i}_h e^{-jh(\psi_{kx} - \vartheta_m)} + \bar{i}_h^* e^{jh(\psi_{kx} - \vartheta_m)} \right). \quad (2.182)$$

The voltage equation of the generic k -th turn can be written as:

$$v_{kx} = r_{kx} i_x + l_{kx} \frac{di_x}{dt} + \sum_{\substack{tx=1 \\ tx \neq k}}^{N_{tx}} m l_{tx,kx} \frac{di_x}{dt} + l_k \frac{di_x}{dt} + \frac{d\phi_{cage,kx}}{dt}. \quad (2.183)$$

The next subsection extend the analysis of the effects of the rotor cage currents to a multiphase stator winding in terms of space vector representation.

Voltage equation (effect of the cage on a multiphase winding)

Considering the full stator winding, the mutual linked flux space vector $\bar{\phi}_{mutual,h}$ (named here $\bar{\phi}_{cage,h}$ in order to distinguish it from the one produced by a PM rotor) with a not skewed stator, is evaluated by (2.106) and (2.47) (adapted to the equivalent multiphase winding associated to the cage rotor) as:

$$\begin{aligned} \bar{\phi}_{cage,h} = & \frac{2}{m} \mu_0 R p q N N_s \left[\sum_{y=0}^{\infty} \frac{K_{a(yN_s+h)}}{(yN_s+h)} \int_{z=0}^L \frac{N_b}{\pi \delta} \frac{\sin\left(\frac{(yN_s+h)\pi}{N_b}\right)}{(yN_s+h)} \bar{i}_{(yN_s+h)} e^{j(yN_s+h)\left(z-\frac{L}{2}\right)\frac{\Delta\psi_{skew}}{L}} e^{j(yN_s+h)\vartheta_m} dz \right] + \\ & + \frac{2}{m} \mu_0 R p q N N_s \left[\sum_{y=\left(\frac{h}{N_s}\right)_{int}}^{\infty} \frac{K_{a(yN_s-h)}}{(yN_s-h)} \int_{z=0}^L \frac{N_b}{\pi \delta} \frac{\sin\left(\frac{(yN_s-h)\pi}{N_b}\right)}{(yN_s-h)} \bar{i}_{(yN_s-h)}^* e^{-j(yN_s-h)\left(z-\frac{L}{2}\right)\frac{\Delta\psi_{skew}}{L}} e^{-j(yN_s-h)\vartheta_m} dz \right]. \end{aligned} \quad (2.184)$$

Introducing the skew parameter $K_{skew,h}$, as done before for the single turn analysis, the h -space linked flux space vector can be rewritten as:

$$\begin{aligned} \bar{\phi}_{cage,h} = & \frac{2}{m} \mu_0 R L p q N N_s \frac{N_b}{\pi \delta} \left[\sum_{y=0}^{\infty} \frac{K_{a(yN_s+h)} K_{skew,(yN_s+h)}}{(yN_s+h)} \frac{\sin\left(\frac{(yN_s+h)\pi}{N_b}\right)}{(yN_s+h)} \bar{i}_{(yN_s+h)} e^{j(yN_s+h)\vartheta_m} \right] + \\ & + \frac{2}{m} \mu_0 R L p q N N_s \frac{N_b}{\pi \delta} \left[\sum_{y=\left(\frac{h}{N_s}\right)_{int}}^{\infty} \frac{K_{a(yN_s-h)} K_{skew,(yN_s-h)}}{(yN_s-h)} \frac{\sin\left(\frac{(yN_s-h)\pi}{N_b}\right)}{(yN_s-h)} \bar{i}_{(yN_s-h)}^* e^{-j(yN_s-h)\vartheta_m} \right]. \end{aligned} \quad (2.185)$$

The introduction of the parameter $X_{ca,h}$ already defined (that relates the cage with the armature space vectors), allows rewriting (2.185) as:

$$\bar{\phi}_{cage,h} = \frac{2}{m} \mu_0 R L p q N N_s \frac{N_b}{\pi \delta} \left[\sum_{y=0}^{\infty} X_{ca,(yN_s+h)} \bar{i}_{(yN_s+h)} e^{j(yN_s+h)g_m} + \sum_{y=\left(\frac{h}{N_s}\right)_{int}}^{\infty} X_{ca,(yN_s-h)} \bar{i}_{(yN_s-h)}^* e^{-j(yN_s-h)g_m} \right]. \quad (2.186)$$

One of the more critical steps in the modelling of a multiphase induction machine with a squirrel cage is to relate the h -space stator winding linked flux space vectors to the cage current space vectors by taking into account the relationships of the N_b -order symmetrical transformation used to describe the squirrel cage quantities:

$$\bar{i}_{\rho} = \frac{2}{N_b} \sum_{x=1}^{N_b} i_x e^{j\rho \frac{2\pi}{N_b}(x-1)},$$

with $\bar{i}_{zN_b+\rho} = \bar{i}_{\rho}$ and $\bar{i}_{zN_b-\rho} = \bar{i}_{\rho}^*$.

These relationships allows writing the following equation for the armature linked fluxes caused by the cage field:

$$\bar{\phi}_{cage,h} = \frac{2\mu_0 R L p q N N_s N_b}{\pi \delta m} \sum_{\rho=0}^{N_b-1} \left[\sum_{\substack{y=0 \\ \left(\frac{ym+h-\rho}{N_b}\right)_{int} \geq 0}}^{\infty} (X_{ca,(yN_s+h)} e^{j(yN_s+h)g_m}) \bar{i}_{\rho} + \sum_{\substack{y=0 \\ y \geq \left(\frac{h}{N_s}\right)_{int} \\ \left(\frac{ym-h-\rho}{N_b}\right)_{int} \geq 0}}^{\infty} (X_{ca,(yN_s-h)} e^{-j(yN_s-h)g_m}) \bar{i}_{\rho}^* \right]. \quad (2.187)$$

The next two paragraphs show how (2.187) results in case of a squirrel cage with an odd or an even number of bars.

Odd number of bars

In case of an odd number of bars, (2.187) is simplifiable as:

$$\begin{aligned} \bar{\phi}_{cage,h} = & \frac{2\mu_0 R L p q N N_s N_b}{\pi \delta m} \sum_{\rho_{odd}=1}^{N_b-2} \left(\sum_{\substack{y=0 \\ \left(\frac{yN_s+h-\rho}{N_b}\right)_{int} \geq 0}}^{\infty} X_{ca,(yN_s+h)} e^{j(yN_s+h)g_m} + \sum_{\substack{y=0 \\ y \geq \left(\frac{h}{N_s}\right)_{int} \\ \left(\frac{yN_s-h+\rho}{N_b}\right)_{int} \geq 0}}^{\infty} X_{ca,(yN_s-h)} e^{-j(yN_s-h)g_m} \right) \bar{i}_{\rho} + \\ & + \frac{2\mu_0 R L p q N N_s N_b}{\pi \delta m} \sum_{\rho_{odd}=1}^{N_b-2} \left(\sum_{\substack{y=0 \\ y \geq \left(\frac{h}{N_s}\right)_{int} \\ \left(\frac{yN_s-h-\rho}{N_b}\right)_{int} \geq 0}}^{\infty} X_{ca,(yN_s-h)} e^{-j(yN_s-h)g_m} + \sum_{\substack{y=0 \\ \left(\frac{yN_s+h+\rho}{N_b}\right)_{int} \geq 0}}^{\infty} X_{ca,(yN_s+h)} e^{j(yN_s+h)g_m} \right) \bar{i}_{\rho}^*. \end{aligned} \quad (2.188)$$

Even number of bars

Instead, in case of a squirrel cage with an even number of bars, (2.187) is simplifiable as:

$$\begin{aligned}
 \bar{\phi}_{cage,h} = & \frac{2\mu_0 R L p q N N_S N_b}{\pi \delta m} \sum_{\rho_{odd}=0}^{N_b-1} \left(\sum_{y=0}^{\infty} X_{ca,(yN_S+h)} e^{j(yN_S+h)g_m} + \sum_{y=0}^{\infty} X_{ca,(yN_S-h)} e^{-j(yN_S-h)g_m} \right) \bar{i}_{\rho} + \\
 & + \frac{2\mu_0 R L p q N N_S N_b}{\pi \delta m} \sum_{\rho_{odd}=0}^{N_b-1} \left(\sum_{y=0}^{\infty} X_{ca,(yN_S-h)} e^{-j(yN_S-h)g_m} + \sum_{y=0}^{\infty} X_{ca,(yN_S+h)} e^{j(yN_S+h)g_m} \right) \bar{i}_{\rho}^* + \\
 & + \frac{2\mu_0 R L p q N N_S N_b}{\pi \delta m} \left(\sum_{y=0}^{\infty} X_{ca,(yN_S+h)} e^{j(yN_S+h)g_m} + \sum_{y=0}^{\infty} X_{ca,(yN_S-h)} e^{-j(yN_S-h)g_m} \right) \bar{i}_{\frac{N_b}{2}}.
 \end{aligned} \tag{2.189}$$

The next subsection summarizes the space vector equations of a multiphase machine with a squirrel cage rotor.

Voltage equations (summary)

The total voltage space vector equation of the stator winding (2.97), introducing (2.119) and (2.142), results in:

$$\bar{v}_h = R_s \bar{i}_h + (L_l + L_h) \frac{d\bar{i}_h}{dt} + \frac{d\bar{\phi}_{cage,h}}{dt}, \tag{2.190}$$

while the cage voltage SVD equation (2.169) is reported below:

$$0 = R_r \bar{i}_h + (L_{l_r} + L_{cage,h}) \frac{d\bar{i}_h}{dt} + \frac{d\bar{\phi}_{mutual,h}}{dt},$$

aware that, if there are anisotropies also the mutual coupling between the armature spaces must be considered.

It is interesting to note that the cage parameters completely depend from the space, while the resistance and the leakage effects in a multiphase stator winding are independent from the space until there are not faults or asymmetries in the control or in the machine. In the assumption of healthy and symmetrical behaviour, the only effects of the mutual couplings between the stator and the rotor windings are described by the interaction between equations of the same space and by the relationships between the various spaces that limit the independent variables to the degrees of freedom of the machine quantities.

The general mutual flux space vectors (2.177) and (2.187) are reported here below.

The mutual flux produced by the stator winding and linked with the rotor cage is described as:

$$\bar{\phi}_{mutual,h} = \frac{2Nmpq\mu_0RL}{\pi\delta} \sum_{\rho=0}^{N_s-1} \left[\sum_{\substack{y=0 \\ \left(\frac{yN_b+h-\rho}{N_s}\right)_{int \geq 0}}}^{\infty} (X_{ca,(yN_b+h)} e^{-j(yN_b+h)\vartheta_m}) \bar{i}_{\rho} + \sum_{\substack{y=0 \\ y \geq \left(\frac{h}{N_b}\right)_{int} \\ \left(\frac{yN_b-h-\rho}{N_s}\right)_{int \geq 0}}}^{\infty} (X_{ca,(yN_b-h)} e^{j(yN_b-h)\vartheta_m}) \bar{i}_{\rho}^* \right].$$

The mutual flux produced by the rotor cage and linked with the stator winding is described as:

$$\bar{\phi}_{cage,h} = \frac{2\mu_0RLpqNN_sN_b}{\pi\delta m} \sum_{\rho=0}^{N_b-1} \left[\sum_{\substack{y=0 \\ \left(\frac{yN_s+h-\rho}{N_b}\right)_{int \geq 0}}}^{\infty} (X_{ca,(yN_s+h)} e^{j(yN_s+h)\vartheta_m}) \bar{i}_{\rho} + \sum_{\substack{y=0 \\ y \geq \left(\frac{h}{N_s}\right)_{int} \\ \left(\frac{yN_s-h-\rho}{N_b}\right)_{int \geq 0}}}^{\infty} (X_{ca,(yN_s-h)} e^{-j(yN_s-h)\vartheta_m}) \bar{i}_{\rho}^* \right].$$

The analysis of the mutual flux space vectors becomes complex when many harmonics of the magnetic field are considered. However, for most of the analysis it is possible to consider only the lowest order harmonics because their amplitude is generally significantly higher than the one of the higher order harmonics. Indeed, the coefficients of the mutual fluxes $X_{ca,h}$ decrease with the square value of the harmonic order according to (2.173), (2.171), (2.45) and (2.162):

$$X_{ca,h} = \frac{K_{ar,h} K_{a,h}}{h^2} K_{skew,h},$$

$$K_{skew,h} = \frac{\sin\left(h \frac{\Delta\psi_{skew}}{2}\right)}{h \frac{\Delta\psi_{skew}}{2}},$$

$$K_{a,h} = \frac{1}{pq} \sum_{y=1}^{N_c} \sin\left(h \frac{\Delta\psi_y}{2}\right) e^{jh\psi_y},$$

$$K_{ar,h} = \sin\left(h \frac{\pi}{N_b}\right).$$

Voltage equation (further considerations on the symmetries - SVD)

It is worth to notice that in case of a symmetrical transformation with a reduced symmetry, only some space vectors are evaluated for the inverse transformation and for the model. In particular, rather than the spaces $1, 2, \dots, N_s$, the only spaces evaluated in the inverse transformations and in the model are the ones multiple of $\frac{N_s}{n}$: $\frac{N_s}{n}, 2\frac{N_s}{n}, \dots, n\frac{N_s}{n}$. Therefore, all the equations are rewritten substituting n to N_s , as if the machine had n slots, and the transformations will be as (2.55) and (2.56).

Of course, attention must be used when the symmetry is reduced. If the symmetry is in terms of slot per pole and per phase, or because of a different choice of the starting slot of the phases, the new space vectors are still the same and are directly related to the relative harmonics of the magnetic field:

$$\bar{y}_h = \frac{2}{m} \sum_{k \in \mathbb{R}}^{n_s} x_{k \in \mathbb{R}} e^{j \frac{2\pi}{n_s} h(k-1)} = \frac{2}{m} \sum_{k \in \mathbb{R}}^{N_s} x_{k \in \mathbb{R}} e^{j \frac{2\pi}{N_s} h(k-1)},$$

with

$$x_k = \frac{m}{2n_s} \sum_{h=0}^{n_s-1} \bar{y}_h e^{-j \frac{2\pi}{n_s} h(k-1)} = \frac{m}{2N_s} \sum_{h=0}^{N_s-1} \bar{y}_h e^{-j \frac{2\pi}{N_s} h(k-1)}.$$

While, if the pole pairs are not considered in terms of possible asymmetrical behaviours (modelling in electrical degrees the machine considering it symmetrical under each pole pair), the model takes into account for only the electrical harmonics h -el:

$$\bar{y}_{h,el} = \frac{2}{m} \sum_{k \in \mathbb{R}}^{N_s} x_{k \in \mathbb{R}} e^{j \frac{2\pi}{N_s} p h(k-1)} \neq \frac{2}{m} \sum_{k \in \mathbb{R}}^{N_s} x_{k \in \mathbb{R}} e^{j \frac{2\pi}{N_s} h(k-1)} = \bar{y}_h,$$

with:

$$x_k = \frac{mp}{2N_s} \sum_{h=0}^{N_s/p-1} \bar{y}_{h,el} e^{-j \frac{2\pi}{N_s} h(k-1)} = \frac{m}{2N_s} \sum_{h=0}^{N_s-1} \bar{y}_h e^{-j \frac{2\pi}{N_s} h(k-1)},$$

only if the machine is symmetrical under each pole pairs, otherwise if in the space vector non-multiple of p there are additional information, these information are neglected in the electrical model. An example of this result is the one already mentioned of a multi-sector stator winding when only one sector three-phase subsystem is analysed. In this case, also not multiple of p harmonics are produced when the winding is fed.

Another example can be a standard star connected three-phase winding with two pole pairs with a 1st order field harmonic in the airgap, the winding will have opposite *emf* under its pole pairs. The total effect of the *emf* on the stator phases is eliminated by the series connection. Therefore, this harmonic will not affect the space equation of the machine. However, because of the interaction of the armature field (mainly a 2nd order harmonic) with this 1st order harmonic, there can be additional electromagnetic effects. For example, the radial force can appear and create eccentricities. In case of eccentric rotor, the magnetic circuit is unbalanced and the stator currents generate field harmonics not multiple of p by the interaction with the reluctance. The space vector can still be defined in electrical degrees, but knowing that the 1st electrical current space vector is related to the p -th harmonic of the armature field (and not the real 1st harmonic in mechanical degrees). This reason justify the assumption of writing the model without simplifying the pole pairs relationship in the space vector transformation, and only considering the space vectors multiple of p in the inverse transformation when the pole pairs symmetry is respected in the winding layout.

The next section analyses the power flows, the torque and the radial force in a multiphase electrical machine.

2.7 Power, Torque and Force Equations

Three analysis are proposed in this subsection. The first one is an analysis of the different components of the electrical power in input to the system. The second analysis is related to the evaluation of the magnetic coenergy of the machine. The last analysis refers to the introduction of the radial force principles in electrical machines.

The power analysis and the coenergy are also used to define the torque generated by the interactions between the various sources of magnetomotive force in the machine. However, the second method is more general and allows evaluating also the torque components not directly related to the input power to the stator winding, as the cogging and slotting effects.

The analysis of the power is also useful in order to highlight the various components. In particular, many control techniques presented in the next chapters are based on the optimisation of the stator copper losses in the control of the field harmonics in the airgap. Therefore, the copper Joule losses are highlighted in the proposed analysis.

The inputs of an electrical machine are the electrical power (in terms of terminals voltages and currents) and the external torque and force applied to the rotor (to the shaft) by the load. The instantaneous electrical power in input to an electrical machine is simply given by the sum of the power entering in each phase (sum of the power of its series turns).

The following analysis starts from the electrical power of a single turn following the approach presented in the previous sections.

Power equation (single turn)

The input electrical power of the single k -th turn of the x -th phase is defined as:

$$P_{kx} = v_{kx} i_x, \quad (2.191)$$

Introducing the voltage equation of the turn (2.115), the turn power equation becomes:

$$P_{kx} = v_{kx} i_x = r_{kx} i_x^2 + l_{kx} \frac{di_x}{dt} i_x + \sum_{\substack{tx=1 \\ tx \neq k}}^{N_{tx}} m l_{tx,kx} \frac{di_x}{dt} i_x + l_k \frac{di_x}{dt} i_x + \frac{d\phi_{mutual,kx}}{dt} i_x. \quad (2.192)$$

At steady state, considering only one frequency: $i_x = I \sin(\omega t + \varphi)$, the power equation can be analysed in its terms as:

- Turn copper Joule losses:

$$r_{kx} i_x^2 = r_{kx} I^2 \sin^2(\omega t + \varphi) = r_{kx} \frac{I^2}{2} (1 - \cos(2\omega t + 2\varphi)).$$

- Turn inductive power:

$$\left(l_{kx} + \sum_{\substack{tx=1 \\ tx \neq k}}^{N_{tx}} ml_{tx,kx} + l_k \right) \frac{di_x}{dt} i_x.$$

The inductive power of the electrical system at steady state conditions is completely considered as a reactive power (it has zero average value in one electrical period).

- Turn mutual power:

$$\frac{d\phi_{mutual,kx}}{dt} i_x.$$

This component represents the interaction of the turn with all the other systems of the machine. In particular, the contribution of the mutual power related to linked flux produced by the rotor represents the power transferred to the rotor. This power is partially related to the shaft torque (completely in case of a PM rotor).

Equation (2.111) describes the contribution of the rotor field to the mutual flux with the analysed turn, reported here below:

$$\phi_{kx} = \sum_{h=1}^{\infty} \frac{\mu_0 R}{h} \sin\left(h \frac{\Delta\psi_k}{2}\right) \left(\int_{z=0}^L \bar{H}_{h,rotor}(z) dz e^{-jh\psi_{kx}} + \int_{z=0}^L \bar{H}_{h,rotor}^*(z) dz e^{jh\psi_{kx}} \right).$$

Therefore, the related instantaneous electrical mutual power with the rotor is:

$$P_{mutual,kx} = \frac{d\phi_{mutual,kx}}{dt} i_x = \frac{d}{dt} \left[\sum_{h=1}^{\infty} \frac{\mu_0 R}{h} \sin\left(h \frac{\Delta\psi_k}{2}\right) \left(\int_{z=0}^L \bar{H}_{h,rotor}(z) dz e^{-jh\psi_{kx}} + \int_{z=0}^L \bar{H}_{h,rotor}^*(z) dz e^{jh\psi_{kx}} \right) \right] i_x. \quad (2.193)$$

SPM machine torque (single turn)

For a SPM rotor, by means of (2.139), the mutual power with the rotor results in:

$$P_{PM,kx} = \frac{d}{dt} \left[\sum_{h_{odd}=1}^{\infty} \frac{2\mu_0 LR}{ph^2} \frac{4B_r \tau_M}{\mu_M \pi \delta} \sin\left(ph \frac{\Delta\psi_k}{2}\right) \sin\left(h \frac{\pi}{2}\right) K_{skew,h} \Re\{e^{jph\vartheta_m} e^{-jph\psi_{kx}}\} \right] i_x. \quad (2.194)$$

Making the time derivative and dividing by the mechanical speed, the generated torque can be evaluated as:

$$T_{PM,kx} = \frac{P_{PM,kx}}{\frac{d\vartheta_m}{dt}} = \left[\sum_{h_{odd}=1}^{\infty} \frac{2\mu_0 LR}{h} \frac{4B_r \tau_M}{\mu_M \pi \delta} \sin\left(ph \frac{\Delta\psi_k}{2}\right) \sin\left(h \frac{\pi}{2}\right) K_{skew,h} \Re\{j e^{jph(\vartheta_m - \psi_{kx})}\} \right] i_x, \quad (2.195)$$

simplified as:

$$T_{PM,kx} = - \sum_{h_{odd}=1}^{\infty} K_{T,PM,kx,h} \sin(ph(\vartheta_m - \psi_{kx})) i_x, \quad (2.196)$$

CHAPTER 2

with $K_{T,PM,kx,h}$ the torque constant related to the h -th field harmonic equal to:

$$K_{T,PM,kx,h} = \frac{2\mu_0 LR}{h} \frac{4B_r \tau_M}{\mu_M \pi \delta} \sin\left(ph \frac{\Delta\psi_k}{2}\right) \sin\left(h \frac{\pi}{2}\right) K_{skew,h}.$$

It is interesting to note that in case of a single turn, in case of a dc current in the turn the torque has a zero average value and a sum of torque ripples at the frequencies of the permanent magnet field harmonics: $ph_{odd} \frac{d\vartheta_m}{dt}$. The only way to obtain a dc component of the torque is to have a current in the turn with an a.c. component at one of the frequencies of the rotor harmonics: $i_x = I_x \sin(ph_{odd}(\vartheta_m + \varphi_x))$. Indeed, in this case the following relationship occurs:

$$\sin(ph(\vartheta_m - \psi_{kx})) \sin(ph(\vartheta_m + \varphi_x)) = \frac{1}{2} [\cos(ph(\psi_{kx} - \varphi_x)) - \cos(ph(2\vartheta_m - \psi_{kx} + \varphi_x))].$$

It results that there is also a dc component of the torque for the h -th field harmonic.

Squirrel cage machine torque (single turn)

For a squirrel cage rotor, by means of (2.182), the mutual power with the rotor results in:

$$P_{cage,kx} = \frac{d}{dt} \left[\sum_{h=1}^{\infty} \frac{\mu_0 R L N_b}{\pi \delta} X_{ca_{kx},h} \left(\bar{i}_{cage,h} e^{-jh(\psi_{kx} - \vartheta_m)} + \bar{i}_{cage,h}^* e^{jh(\psi_{kx} - \vartheta_m)} \right) \right] i_x, \quad (2.197)$$

with $X_{ca_{kx},h}$ defined by (2.173).

Solving the time derivative, the power equation becomes:

$$P_{cage,kx} = \left[\sum_{h=1}^{\infty} \frac{2\mu_0 R L N_b}{\pi \delta} X_{ca_{kx},h} \Re \left\{ \frac{d\bar{i}_{cage,h}}{dt} e^{-jh(\psi_{kx} - \vartheta_m)} - jh \frac{d\vartheta_m}{dt} \bar{i}_{cage,h} e^{-jh(\psi_{kx} - \vartheta_m)} \right\} \right] i_x. \quad (2.198)$$

The terms that are not multiplied by the mechanical speed do not contribute to the mechanical power. The additional terms, that depend by the time derivative of the cage currents, represent the power transferred between the stator and the rotor that do not produce the mechanical power. Therefore, the generated torque can be evaluated by these terms divided by the mechanical speed as:

$$T_{cage,kx} = \frac{P_{cage,kx}}{\frac{d\vartheta_m}{dt}} \Bigg|_{\bar{i}_{cage,h} = \text{constant}} = \left[\sum_{h=1}^{\infty} \frac{2\mu_0 R L N_b}{\pi \delta} X_{ca_{kx},h} \left\{ -jh \bar{i}_{cage,h} e^{-jh(\psi_{kx} - \vartheta_m)} \right\} \right] i_x, \quad (2.199)$$

simplified as:

$$T_{cage,kx} = \left[\sum_{h=1}^{\infty} K_{T,cage,kx,h} \Re \left\{ -j \bar{i}_{cage,h} e^{-jh(\psi_{kx} - \vartheta_m)} \right\} \right] i_x, \quad (2.200)$$

with $K_{T,cage,kx,h}$ the torque constant related to the h -th field harmonic of the cage (in other words, to the h -th rotor current space vector $\bar{i}_{cage,h}$) defined as:

$$K_{T,cage,kx,h} = \frac{2\mu_0 R L N_b}{\pi \delta} \frac{\sin\left(\frac{h\pi}{N_b}\right) \sin\left(h \frac{\Delta\psi_k}{2}\right)}{h} K_{skew(h)}.$$

The analysis of the average torque and the torque ripples, produced by the interaction between the turn and the cage, depends on the currents in the two systems. Therefore, the analysis is much more complex than the one of a SPM machine because the cage currents must be evaluated by the machine behaviour.

The next subsection extends the analysis of a single turn to a multiphase winding represented in terms of space vector equations.

Power equation (multiphase winding)

The input electrical power for a multiphase winding is defined as:

$$P = \sum_{x=1}^m \left(\sum_{t=1}^{N_x} v_{tx} \right) i_x = \sum_{x=1}^m v_x i_x, \quad (2.201)$$

with tx used here to indicate the t -th series turn of each x -th phase. The equation can be investigated in terms of the voltage and current inverse transformations defined in a general way as:

$$x_k = \frac{m}{2N_S} \sum_{h=0}^{N_S-1} \bar{y}_h \bar{\alpha}^{-h(k-1)},$$

with $\bar{\alpha} = e^{j\frac{2\pi}{N_S}}$ and k used to indicate the starting slot of the machine phases. The power can be written in terms of space vectors as:

$$P = \sum_{x=1}^m v_x i_x = \sum_{\substack{k=1 \\ k=k\Re}}^{N_S} \frac{m}{2N_S} \sum_{h=0}^{N_S-1} \bar{v}_h \bar{\alpha}^{-h(k-1)} \frac{m}{2N_S} \sum_{\rho=0}^{N_S-1} \bar{i}_\rho \bar{\alpha}^{-\rho(k-1)}. \quad (2.202)$$

However, as the transformation is defined in its general shape, it is possible to effectively consider also the not existing phases in the power equation, because the transformation takes into account of the fact that the quantities related to the not existing phases are equal to zero. The used general transformation (2.52) is reported here below to highlight again that the not existing phases are not taken into account:

$$\bar{y}_h = \frac{2}{m} \sum_{k \in \mathfrak{R}}^{N_s} x_{k \in \mathfrak{R}} \bar{\alpha}^{h(k-1)}, \quad h = 0, 1, 2, \dots, N_s - 1.$$

In this case, the power of all the phases (existing and not) can be evaluated as:

$$P = \sum_{k=1}^{N_s} v_k i_k = \left(\frac{m}{2N_s} \right)^2 \sum_{k=1}^{N_s} \sum_{h=0}^{N_s-1} \sum_{\rho=0}^{N_s-1} \bar{i}_\rho \bar{v}_h e^{-j \frac{2\pi}{N_s} (h+\rho)(k-1)}. \quad (2.203)$$

Because in the general inverse transformation all the space vectors are used, for each k -th phase (starting in the k -th slot) it is possible to rewrite (2.203) as:

$$P = \sum_{k=1}^{N_s} v_k i_k = \left(\frac{m}{2N_s} \right)^2 \sum_{h=0}^{N_s-1} \sum_{\rho=0}^{N_s-1} \bar{i}_\rho \bar{v}_h \sum_{k=1}^{N_s} e^{-j \frac{2\pi}{N_s} (h+\rho)(k-1)}. \quad (2.204)$$

Because N_s equivalent phases (existing and not) are considered, $\sum_{k=1}^{N_s} e^{-j \frac{2\pi}{N_s} (h+\rho)(k-1)}$ is equal to zero for all the h and ρ values but the one for which $h + \rho = zN_s$. This happens only with $h + \rho = N_s$ or $h + \rho = 0$ if both h and ρ are zero). In these cases $\sum_{k=1}^{N_s} e^{-j \frac{2\pi}{N_s} (h+\rho)(k-1)}$ is equal to N_s . Therefore, the instantaneous input power equation can be rewritten in a general shape as:

$$P = \sum_{k=1}^{N_s} v_k i_k = \frac{m^2}{4N_s} \left[i_0 v_0 + i_{\frac{N_s}{2}} v_{\frac{N_s}{2}} + \sum_{\substack{h=1 \\ h \neq \frac{N_s}{2}}}^{N_s-1} \bar{v}_h \bar{i}_{N_s-h} \right], \quad (2.205)$$

with the term $i_{\frac{N_s}{2}} v_{\frac{N_s}{2}}$ existing only if N_s is an even number. According to the space vector transformation relationships \bar{i}_{N_s-h} is equal to \bar{i}_h^* , and the power equation can be rewritten as:

$$P = \sum_{k=1}^{N_s} v_k i_k = \frac{m^2}{4N_s} \left(i_0 v_0 + i_{\frac{N_s}{2}} v_{\frac{N_s}{2}} \right) + \frac{m^2}{4N_s} \sum_{\substack{h=1 \\ h \neq \frac{N_s}{2}}}^{N_s-1} (\bar{v}_h \bar{i}_h^*). \quad (2.206)$$

By the same relationship, the number of analysed vectors can be reduced as:

$$P = \sum_{k=1}^{N_s} v_k i_k = \frac{m^2}{4N_s} \left(i_0 v_0 + i_{\frac{N_s}{2}} v_{\frac{N_s}{2}} \right) + \frac{m^2}{2N_s} \Re \sum_{h=0}^{N_s/2-1} \{ \bar{v}_h \bar{i}_h^* \}. \quad (2.207)$$

This equation is completely general and because of this, it is a redundant expression. However, all the next analysis can be done also for the particular expression of the power for each machine, taking into account only for the needed space vectors.

The voltage space vector equation for a multiphase symmetrical winding (2.190) is reported here below:

$$\bar{v}_h = R_s \bar{i}_h + (Ll + L_h) \frac{d\bar{i}_h}{dt} + \frac{d\bar{\phi}_{mutual,h}}{dt}.$$

Introducing this expression in (2.207) allows writing the instantaneous power as:

$$\begin{aligned} P = & \frac{m^2}{4N_s} \left(R_s i_0 i_0 + (Ll + L_0) \frac{di_0}{dt} i_0 + \frac{d\phi_{mutual,0}}{dt} i_0 \right) + \\ & + \frac{m^2}{4N_s} \left(R_s i_{\frac{N_s}{2}} i_{\frac{N_s}{2}} + \left(Ll + L_{\frac{N_s}{2}} \right) \frac{di_{\frac{N_s}{2}}}{dt} i_{\frac{N_s}{2}} + \frac{d\phi_{mutual,\frac{N_s}{2}}}{dt} i_{\frac{N_s}{2}} \right) + \\ & + \frac{m^2}{2N_s} \Re \sum_{h=0}^{N_s/2-1} \left\{ R_s \bar{i}_h \bar{i}_h^* + (Ll + L_h) \frac{d\bar{i}_h}{dt} \bar{i}_h^* + \frac{d\bar{\phi}_{mutual,h}}{dt} \bar{i}_h^* \right\}. \end{aligned} \quad (2.208)$$

This equation can be simplified as:

$$\begin{aligned} P = & \frac{m^2}{4N_s} \left(R_s i_0^2 + (Ll + L_0) \frac{di_0}{dt} i_0 + \frac{d\phi_{mutual,0}}{dt} i_0 \right) + \\ & + \frac{m^2}{4N_s} \left(R_s i_{\frac{N_s}{2}}^2 + \left(Ll + L_{\frac{N_s}{2}} \right) \frac{di_{\frac{N_s}{2}}}{dt} i_{\frac{N_s}{2}} + \frac{d\phi_{mutual,\frac{N_s}{2}}}{dt} i_{\frac{N_s}{2}} \right) + \\ & + \frac{m^2}{2N_s} \Re \sum_{h=0}^{N_s/2-1} \left\{ R_s |\bar{i}_h|^2 + (Ll + L_h) \frac{d\bar{i}_h}{dt} \bar{i}_h^* + \frac{d\bar{\phi}_{mutual,h}}{dt} \bar{i}_h^* \right\}. \end{aligned} \quad (2.209)$$

Unfortunately, the zero and $\frac{N_s}{2}$ current space vector are not always zero, as discussed in the previous sections. Indeed, they are always equal to zero if the winding is completely symmetrical and star connected (odd phase symmetrical winding with all the phases star connected), otherwise their values depend by the winding distribution and star connections. For example, a three-phase winding layout without star connection and with each phase fed by its own H-bridge converter allows for the circulation of the zero space current (homopolar current).

However, the power contributions can still be analysed in their respective terms:

- Armature copper Joule losses:

$$P_J = \frac{m^2}{4N_s} \left(R_s i_0^2 + R_s i_{\frac{N_s}{2}}^2 \right) + \frac{m^2}{2N_s} \sum_{h=1}^{N_s/2-1} R_s |\bar{i}_h|^2.$$

It is interesting to note that in general some effects as the ripple of Joule losses in the various phases (or turns) at steady state operation is not present in the total instantaneous power of the system. For example, in a symmetrical three-phase winding (described by the general transformation (2.64)) the sum of the machine armature Joule losses is:

$$P_J = \frac{9}{12} R_s \left(|\bar{i}_1|^2 + |\bar{i}_2|^2 \right) = \frac{3}{2} R_s \left(|\bar{i}_1|^2 \right).$$

The first current space vector of the three-phase machine at steady state and in a standard control rotates at constant speed and magnitude, generating a constant sum of the Joule losses. Therefore, the analysis of the power of each phase can be useful to better analyse the local effects. For example, this can be done for a better evaluation of the thermal stress of the windings considering the electrical frequency of the machine in its working cycles.

- Armature inductive power:

$$P_L = \frac{m^2}{4N_s} \left((Ll + L_0) \frac{di_0}{dt} i_0 + \left(Ll + L_{\frac{N_s}{2}} \right) \frac{di_{\frac{N_s}{2}}}{dt} i_{\frac{N_s}{2}} \right) + \frac{m^2}{2N_s} \Re \sum_{h=1}^{N_s/2-1} \left\{ (Ll + L_h) \frac{d\bar{i}_h}{dt} \bar{i}_h^* \right\}.$$

The inductive power of the electrical system at steady state conditions is completely considered as a reactive power (it has zero average value in one electrical period whatever the frequency of the system). If the currents are all dc, this power component is zero because it is related to the variation of the magnetic energy of the system during the time.

- Armature mutual power:

$$P_{mutual} = \frac{m^2}{4N_s} \left(\frac{d\phi_{mutual,0}}{dt} i_0 + \frac{d\phi_{mutual,\frac{N_s}{2}}}{dt} i_{\frac{N_s}{2}} \right) + \frac{m^2}{2N_s} \Re \sum_{h=1}^{N_s/2-1} \left\{ \frac{d\bar{\phi}_{mutual,h}}{dt} \bar{i}_h^* \right\}.$$

This component represents the interaction of the stator winding with all the other systems of the machine. In particular, the contribution of the mutual power related to linked flux produced by the rotor represents the power transferred to the rotor. This power is partially related to the shaft torque (completely in case of a PM rotor).

Equation (2.107) is used to describe the contribution of the rotor field to the mutual flux linked with stator multiphase winding. It is reported here below considering only the mutual components:

$$\begin{aligned} \bar{\phi}_{mutual,h} &= \frac{2}{m} \mu_0 R p q N N_s \sum_{y=0}^{\infty} \frac{K_{a(yN_s+h)}}{(yN_s+h)} \int_{z=0}^L \bar{H}_{mutual(yN_s+h)}(z) dz + \\ &+ \frac{2}{m} \mu_0 R p q N N_s \sum_{y=\left(\frac{h}{N_s}\right)_{int}}^{\infty} \frac{K_{a(yN_s-h)}}{(yN_s-h)} \int_{z=0}^L \bar{H}_{mutual(yN_s-h)}^*(z) dz. \end{aligned} \quad (2.210)$$

Therefore, the related instantaneous electrical mutual power with the rotor can be considered as the sum of the contributions of the various space vectors, defined as:

$$\begin{aligned} P_{mutual} &= \frac{P_{mutual,0}}{2} + \frac{P_{mutual,\frac{N_s}{2}}}{2} + \sum_{h=1}^{N_s/2-1} P_{mutual,h} = \\ &= \frac{m^2}{4N_s} \left(\frac{d\phi_{mutual,0}}{dt} i_0 + \frac{d\phi_{mutual,\frac{N_s}{2}}}{dt} i_{\frac{N_s}{2}} \right) + \frac{m^2}{2N_s} \Re \sum_{h=1}^{N_s/2-1} \left\{ \frac{d\bar{\phi}_{mutual,h}}{dt} \bar{i}_h^* \right\}. \end{aligned} \quad (2.211)$$

Each space power contribution $P_{mutual,h}$ is defined as:

$$P_{mutual,h} = \frac{m^2}{2N_s} \Re \left\{ \frac{d\bar{\phi}_{mutual,h}}{dt} \bar{i}_h^* \right\}. \quad (2.212)$$

Substituting (2.210) in (2.212), it results that:

$$P_{mutual,h} = \frac{m^2}{2N_s} \Re \left\{ \frac{2}{m} \mu_0 R p q N N_s \frac{d}{dt} \left[\sum_{y=0}^{\infty} \frac{K_{a(yN_s+h)}}{(yN_s+h)} \int_{z=0}^L \bar{H}_{mutual(yN_s+h)}(z) dz \right] \bar{i}_h^* \right\} + \frac{m^2}{2N_s} \Re \left\{ \frac{2}{m} \mu_0 R p q N N_s \frac{d}{dt} \left[\sum_{y=\left(\frac{h}{N_s}\right)_{int}}^{\infty} \frac{K_{a(yN_s-h)}}{(yN_s-h)} \int_{z=0}^L \bar{H}_{mutual(yN_s-h)}^*(z) dz \right] \bar{i}_h^* \right\}. \quad (2.213)$$

In the next two paragraphs, the analysis of the mutual effects related to the rotor field are separately considered for the case of a SPM machine and a squirrel cage one, as done above for the analysis of a single turn.

SPM machine torque (multiphase winding)

Introducing the equation of the mutual flux space vector in case of a SPM rotor (2.142), the relative mutual power equation (named $P_{PM,h}$ here below) can be written as:

$$P_{PM,h} = \frac{m^2}{2N_s} \Re \left\{ \frac{2}{m} \mu_0 L R p q N N_s \frac{4B_r \tau_M p}{\mu_M \pi \delta} \frac{d}{dt} \left[\sum_{y=0}^{\infty} \frac{K_{a(yN_s+h)} K_{skew(yN_s+h)}}{(yN_s+h)^2} \sin\left((yN_s+h) \frac{\pi}{2p}\right) e^{j(yN_s+h)g_m} \right] \bar{i}_h^* \right\} + \frac{m^2}{2N_s} \Re \left\{ \frac{2}{m} \mu_0 L R p q N N_s \frac{4B_r \tau_M p}{\mu_M \pi \delta} \frac{d}{dt} \left[\sum_{y=\left(\frac{h}{N_s}\right)_{int}}^{\infty} \frac{K_{a(yN_s-h)} K_{skew(yN_s-h)}}{(yN_s-h)^2} \sin\left((yN_s-h) \frac{\pi}{2p}\right) e^{-j(yN_s-h)g_m} \right] \bar{i}_h^* \right\}. \quad (2.214)$$

The equation can be simplified as:

$$\begin{aligned}
 \frac{P_{PM,h}}{dt} = & \frac{m\mu_0 L R p^2 q N N_s}{N_s} \frac{4B_r \tau_M}{\mu_M \pi \delta} \Re \left\{ \left[\sum_{\substack{y=0 \\ \left(\frac{yN_s+h}{p}\right)_{\text{odd.int}}}}^{\infty} j(yN_s+h) \frac{K_{a(yN_s+h)} K_{skew(yN_s+h)}}{(yN_s+h)^2} \sin\left((yN_s+h) \frac{\pi}{2p}\right) e^{j(yN_s+h)g_m} \bar{i}_h^* \right] + \right. \\
 & \left. + \frac{m\mu_0 L R p^2 q N N_s}{N_s} \frac{4B_r \tau_M}{\mu_M \pi \delta} \Re \left\{ \left[\sum_{\substack{y=\left(\frac{h}{N_s}\right)_{\text{int}} \\ \left(\frac{yN_s-h}{p}\right)_{\text{odd.int}}}}^{\infty} -j(yN_s-h) \frac{K_{a(yN_s-h)} K_{skew(yN_s-h)}}{(yN_s-h)^2} \sin\left((yN_s-h) \frac{\pi}{2p}\right) e^{-j(yN_s-h)g_m} \bar{i}_h^* \right] \right\} \right\}.
 \end{aligned} \tag{2.215}$$

The resulting torque contribution related to the h -th armature current space vector is:

$$\begin{aligned}
 T_{PM,h} = & m\mu_0 L R p^2 q N \frac{4B_r \tau_M}{\mu_M \pi \delta} \Re \left\{ \left[\sum_{\substack{y=0 \\ \left(\frac{yN_s+h}{p}\right)_{\text{odd.int}}}}^{\infty} j(yN_s+h) \frac{K_{a(yN_s+h)} K_{skew(yN_s+h)}}{(yN_s+h)^2} \sin\left((yN_s+h) \frac{\pi}{2p}\right) e^{j(yN_s+h)g_m} \bar{i}_h^* \right] + \right. \\
 & \left. + m\mu_0 L R p^2 q N \frac{4B_r \tau_M}{\mu_M \pi \delta} \Re \left\{ \left[\sum_{\substack{y=\left(\frac{h}{N_s}\right)_{\text{int}} \\ \left(\frac{yN_s-h}{p}\right)_{\text{odd.int}}}}^{\infty} -j(yN_s-h) \frac{K_{a(yN_s-h)} K_{skew(yN_s-h)}}{(yN_s-h)^2} \sin\left((yN_s-h) \frac{\pi}{2p}\right) e^{-j(yN_s-h)g_m} \bar{i}_h^* \right] \right\} \right\},
 \end{aligned} \tag{2.216}$$

simplified as:

$$T_{PM,h} = \Re \left\{ \left[\sum_{\substack{y=0 \\ \left(\frac{yN_s+h}{p}\right)_{\text{odd.int}}}}^{\infty} j K_{T,PM,y,h}^+ e^{j(yN_s+h)g_m} \bar{i}_h^* \right] + \Re \left\{ \left[\sum_{\substack{y=\left(\frac{h}{N_s}\right)_{\text{int}} \\ \left(\frac{yN_s-h}{p}\right)_{\text{odd.int}}}}^{\infty} -j K_{T,PM,y,h}^- e^{-j(yN_s-h)g_m} \bar{i}_h^* \right] \right\} \right\}, \tag{2.217}$$

with:

$$K_{T,PM,y,h}^+ = m\mu_0 L R p^2 q N \frac{4B_r \tau_M}{\mu_M \pi \delta} \frac{K_{a(yN_s+h)} K_{skew(yN_s+h)}}{(yN_s+h)} \sin\left((yN_s+h) \frac{\pi}{2p}\right),$$

$$K_{T,PM,y,h}^- = m\mu_0 L R p^2 q N \frac{4B_r \tau_M}{\mu_M \pi \delta} \frac{K_{a(yN_s-h)} K_{skew(yN_s-h)}}{(yN_s-h)} \sin\left((yN_s-h) \frac{\pi}{2p}\right),$$

the torque constants related to the h -th armature current space vector.

The total torque for a SPM multiphase machine is:

$$T = \frac{T_0}{2} + \frac{T_{N_s}}{2} + \sum_{h=1}^{N_s/2-1} T_h. \quad (2.218)$$

It is interesting to note that in order to obtain a constant torque with one of the contributes of the first summation in (2.216), the h -th current space vector must rotate in the same direction of the rotor at speed equal to $\frac{d\theta_m}{dt}(yN_s + h)$. Usually only one y value is chosen to produce a constant torque and the other values will result in torque ripples. On the other hand, to create a constant torque with the contributions in the second summation, the current vector must rotate in the opposite direction of the rotor at speed $\frac{d\theta_m}{dt}(yN_s - h)$. In other words, in some cases the torque contributions can be used to increase the average torque of the machine by a direct sequence and in other cases by an inverse current sequence of the h -th current space vector.

For example, in a three-phase SPM machine, it is possible to generate a torque by the p -th current space vector (this is the common choice in the control of PM machines). However, this results in a torque ripple at $6p$ times the mechanical speed related to the interaction between the $5p$ -th field harmonic of the PM with the $5p$ -th field harmonic of the armature because \bar{i}_{5p} is equal to \bar{i}_p^* . However, it is also possible to control the only independent current space vector (\bar{i}_p) in order to create a torque control based on the interaction between the field harmonics of order $5p$. This can be done by controlling \bar{i}_p with an inverse sequence at 5 times the fundamental electrical frequency. This will usually result in a huge torque ripple related to the contribution of the uncontrolled main field harmonic and in a significantly reduced efficiency in the torque production (because of the inverse proportionality of the torque constants $K_{T,PM,y,h}^\pm$ with the field harmonic orders: $K_{T,PM,y,h}^\pm \propto \frac{1}{yN_s \pm h}$). Theoretically, this approach can be used to define an improved machine control that allows eliminating the torque ripples related to the higher order field harmonics.

Squirrel cage machine torque (multiphase winding)

Introducing the equation of the mutual flux space vector linked with the multiphase winding and produced by a squirrel cage rotor (2.187), the mutual power equation ($P_{cage,h}$) for the h -th armature space vector can be written as:

$$\begin{aligned}
 P_{cage,h} = & \frac{m^2}{2N_s} \Re \left\{ \frac{2\mu_0 R L p q N N_s N_b}{\pi \delta m} \sum_{\rho=0}^{N_b-1} \frac{d}{dt} \left[\sum_{\substack{y=0 \\ \left(\frac{yn+h-\rho}{N_b}\right)_{int \geq 0}}^{\infty} (X_{ca,(yN_s+h)} e^{j(yN_s+h)g_m}) \bar{i}_{cage,\rho} \right] \bar{i}_h^* \right\} + \\
 & + \frac{m^2}{2N_s} \Re \left\{ \frac{2\mu_0 R L p q N N_s N_b}{\pi \delta m} \sum_{\rho=0}^{N_b-1} \frac{d}{dt} \left[\sum_{\substack{y=0 \\ y \geq \left(\frac{h}{N_s}\right)_{int} \\ \left(\frac{yn-h-\rho}{N_b}\right)_{int \geq 0}}^{\infty} (X_{ca,(yN_s-h)} e^{-j(yN_s-h)g_m}) \bar{i}_{cage,\rho}^* \right] \bar{i}_h^* \right\}.
 \end{aligned} \tag{2.219}$$

The equation can be simplified as:

$$\begin{aligned}
 P_{cage,h} = & \frac{\mu_0 R L m p q N N_s N_b}{N_s \pi \delta} \Re \left\{ \sum_{\rho=0}^{N_b-1} \sum_{\substack{y=0 \\ \left(\frac{yn+h-\rho}{N_b}\right)_{int \geq 0}}^{\infty} (X_{ca,(yN_s+h)} e^{j(yN_s+h)g_m}) \frac{d}{dt} \bar{i}_{cage,\rho} \bar{i}_h^* \right\} + \\
 & + \frac{\mu_0 R L m p q N N_s N_b}{N_s \pi \delta} \Re \left\{ \sum_{\rho=0}^{N_b-1} \sum_{\substack{y=0 \\ y \geq \left(\frac{h}{N_s}\right)_{int} \\ \left(\frac{yn-h-\rho}{N_b}\right)_{int \geq 0}}^{\infty} (X_{ca,(yN_s-h)} e^{-j(yN_s-h)g_m}) \frac{d}{dt} \bar{i}_{cage,\rho}^* \bar{i}_h^* \right\} + \\
 & + \frac{\mu_0 R L m p q N N_s N_b}{N_s \pi \delta} \Re \left\{ \sum_{\rho=0}^{N_b-1} \frac{d g_m}{dt} \sum_{\substack{y=0 \\ \left(\frac{yn+h-\rho}{N_b}\right)_{int \geq 0}}^{\infty} (j(yN_s + h) X_{ca,(yN_s+h)} e^{j(yN_s+h)g_m}) \bar{i}_{cage,\rho} \bar{i}_h^* \right\} + \\
 & + \frac{\mu_0 R L m p q N N_s N_b}{N_s \pi \delta} \Re \left\{ \sum_{\rho=0}^{N_b-1} \frac{d g_m}{dt} \sum_{\substack{y=0 \\ y \geq \left(\frac{h}{N_s}\right)_{int} \\ \left(\frac{yn-h-\rho}{N_b}\right)_{int \geq 0}}^{\infty} (-j(yN_s - h) X_{ca,(yN_s-h)} e^{-j(yN_s-h)g_m}) \bar{i}_{cage,\rho}^* \bar{i}_h^* \right\}.
 \end{aligned} \tag{2.220}$$

Considering only the contributions proportional to the rotor speed, the torque related to the h -th armature space is evaluated as:

$$\begin{aligned}
 T_{cage,h} = & \frac{\mu_0 R L m p q N N_b}{\pi \delta} \Re \left\{ \sum_{\rho=0}^{N_b-1} \sum_{\substack{y=0 \\ \left(\frac{yn+h-\rho}{N_b}\right)_{int \geq 0}}}^{\infty} (j(yN_S + h) X_{ca,(yN_S+h)} e^{j(yN_S+h)g_m}) \bar{i}_{cage,\rho} \bar{i}_h^* \right\} + \\
 & + \frac{\mu_0 R L m p q N N_b}{\pi \delta} \Re \left\{ \sum_{\rho=0}^{N_b-1} \sum_{\substack{y=0 \\ y \geq \left(\frac{h}{N_S}\right)_{int} \\ \left(\frac{yn-h-\rho}{N_b}\right)_{int \geq 0}}}^{\infty} (-j(yN_S - h) X_{ca,(yN_S-h)} e^{-j(yN_S-h)g_m}) \bar{i}_{cage,\rho}^* \bar{i}_h^* \right\}, \quad (2.221)
 \end{aligned}$$

simplified as:

$$\begin{aligned}
 T_{cage,h} = & \Re \left\{ \sum_{\rho=0}^{N_b-1} \sum_{\substack{y=0 \\ \left(\frac{yn+h-\rho}{N_b}\right)_{int \geq 0}}}^{\infty} j K_{T,cage,y,h}^+ e^{j(yN_S+h)g_m} \bar{i}_{cage,\rho} \bar{i}_h^* \right\} + \Re \left\{ \sum_{\rho=0}^{N_b-1} \sum_{\substack{y=0 \\ y \geq \left(\frac{h}{N_S}\right)_{int} \\ \left(\frac{yn-h-\rho}{N_b}\right)_{int \geq 0}}}^{\infty} -j K_{T,cage,y,h}^- e^{-j(yN_S-h)g_m} \bar{i}_{cage,\rho}^* \bar{i}_h^* \right\}, \quad (2.222)
 \end{aligned}$$

with:

$$\begin{aligned}
 K_{T,cage,y,h}^+ &= \frac{\mu_0 R L m p q N N_b}{\pi \delta} (yN_S + h) X_{ca,(yN_S+h)}, \\
 K_{T,cage,y,h}^- &= \frac{\mu_0 R L m p q N N_b}{\pi \delta} (yN_S - h) X_{ca,(yN_S-h)},
 \end{aligned}$$

the torque constants related to the h -th armature current space vector.

The total torque of the squirrel cage multiphase machine is:

$$T = \frac{T_0}{2} + \frac{T_{N_S}}{2} + \sum_{h=1}^{N_S/2-1} T_h. \quad (2.223)$$

The analysis of the torque generated in a squirrel cage machine is quite complex because of the slip of the various rotor field harmonics related to the not constant rotor current space vectors. Indeed, in general all the rotor current space vectors rotate with a particular speed (related to their slip) in the rotor reference frame.

In order to clarify the power components in a squirrel cage IM, the power analysis is presented in the next subsection, considering the squirrel cage equivalent multiphase winding.

Power equation (squirrel cage)

A squirrel cage can be analysed as a multiphase machine with N_b symmetrical phases and without an external power source ($P = 0$), because there is not an external voltage source:

$$\bar{v}_h = 0.$$

The voltage space vector equation of the equivalent multiphase winding of a squirrel cage rotor (2.169) is reported here below:

$$0 = R_{rh} \bar{i}_h + (Ll_{rh} + L_{cage,h}) \frac{d\bar{i}_h}{dt} + \frac{d\bar{\phi}_{winding,h}}{dt}.$$

Introducing this expression in (2.207) allows writing the instantaneous input power as:

$$\begin{aligned} 0 = P = & \frac{N_b}{4} \left(R_{r0} i_0^2 + (Ll_{r0} + L_{cage,0}) \frac{di_0}{dt} i_0 + \frac{d\phi_{winding,0}}{dt} i_0 \right) + \\ & + \frac{N_b}{4} \left(R_{rh} i_{\frac{N_b}{2}}^2 + \left(Ll_{r\frac{N_b}{2}} + L_{cage,\frac{N_b}{2}} \right) \frac{di_{\frac{N_b}{2}}}{dt} i_{\frac{N_b}{2}} + \frac{d\phi_{winding,\frac{N_b}{2}}}{dt} i_{\frac{N_b}{2}} \right) + \\ & + \frac{N_b}{2} \Re \sum_{h=0}^{N_s/2-1} \left\{ R_{rh} |\bar{i}_h|^2 + (Ll_{rh} + L_{cage,h}) \frac{d\bar{i}_h}{dt} \bar{i}_h^* + \frac{d\bar{\phi}_{winding,h}}{dt} \bar{i}_h^* \right\}. \end{aligned} \quad (2.224)$$

The power contributions can be analysed in their respective terms:

- Cage copper Joule losses:

$$P_J = \frac{N_b}{4} \left(R_{r0} i_0^2 + R_{rh} i_{\frac{N_b}{2}}^2 \right) + \frac{N_b}{2} \Re \sum_{h=0}^{N_s/2-1} \left\{ R_{rh} |\bar{i}_h|^2 \right\};$$

- Cage inductive power:

$$\begin{aligned} P_L = & \frac{N_b}{4} \left((Ll_{r0} + L_{cage,0}) \frac{di_0}{dt} i_0 + \left(Ll_{r\frac{N_b}{2}} + L_{cage,\frac{N_b}{2}} \right) \frac{di_{\frac{N_b}{2}}}{dt} i_{\frac{N_b}{2}} \right) + \\ & + \frac{N_b}{2} \Re \sum_{h=0}^{N_s/2-1} \left\{ (Ll_{rh} + L_{cage,h}) \frac{d\bar{i}_h}{dt} \bar{i}_h^* \right\}; \end{aligned}$$

- Cage mutual power:

$$P_{winding} = \frac{N_b}{4} \left(\frac{d\phi_{winding,0}}{dt} i_0 + \frac{d\phi_{winding,\frac{N_b}{2}}}{dt} i_{\frac{N_b}{2}} \right) + \frac{N_b}{2} \Re \sum_{h=0}^{N_s/2-1} \left\{ \frac{d\bar{\phi}_{winding,h}}{dt} \bar{i}_h^* \right\}.$$

The contribution of the stator multiphase winding field to the mutual flux linked with the rotor cage is described by (2.177), reported here below:

$$\bar{\phi}_{winding,h} = \frac{2Nmpq\mu_0RL}{\pi\delta} \sum_{\rho=0}^{N_s-1} \left[\sum_{\substack{y=0 \\ \left(\frac{yN_b+h-\rho}{N_s}\right)_{int} \geq 0}}^{\infty} (X_{ca(yN_b+h)} e^{-j(yN_b+h)g_m}) \bar{i}_{\rho} + \sum_{\substack{y=0 \\ y \geq \left(\frac{h}{N_b}\right)_{int} \\ \left(\frac{yN_b-h-\rho}{N_s}\right)_{int} \geq 0}}^{\infty} (X_{ca(yN_b-h)} e^{j(yN_b-h)g_m}) \bar{i}_{\rho}^* \right].$$

Therefore, the related instantaneous electrical mutual power with the rotor can be considered as the sum of the contributions of the various space vectors, defined as:

$$\begin{aligned} P_{winding} &= \frac{P_{winding,0}}{2} + \frac{P_{winding,\frac{N_b}{2}}}{2} + \sum_{h=1}^{N_b/2-1} P_{winding,h} = \\ &= \frac{N_b}{4} \left(\frac{d\phi_{winding,0}}{dt} i_0 + \frac{d\phi_{winding,\frac{N_b}{2}}}{dt} i_{\frac{N_b}{2}} \right) + \frac{N_b}{2} \Re \sum_{h=0}^{N_b/2-1} \left\{ \frac{d\bar{\phi}_{winding,h}}{dt} \bar{i}_h^* \right\}. \end{aligned} \quad (2.225)$$

Each space power contribution $P_{winding,h}$ is defined as:

$$P_{winding,h} = \frac{N_b}{2} \Re \left\{ \frac{d\bar{\phi}_{winding,h}}{dt} \bar{i}_h^* \right\}. \quad (2.226)$$

Introducing the equation of the space vector of the mutual flux linked with a squirrel cage rotor and generated by a multiphase winding (2.177), the mutual power equation for the h -th armature space vector can be written making explicit which are the armature (*winding*) and cage related (*cage*) current space vectors, as:

$$\begin{aligned} P_{winding,h} &= \frac{N_b}{2} \Re \left\{ \frac{2Nmpq\mu_0RL}{\pi\delta} \sum_{\rho=0}^{N_s-1} \frac{d}{dt} \left[\sum_{\substack{y=0 \\ \left(\frac{yN_b+h-\rho}{N_s}\right)_{int} \geq 0}}^{\infty} (X_{ca(yN_b+h)} e^{-j(yN_b+h)g_m}) \bar{i}_{winding,\rho} \right] \bar{i}_{cage,h}^* \right\} + \\ &+ \frac{N_b}{2} \Re \left\{ \frac{2Nmpq\mu_0RL}{\pi\delta} \sum_{\rho=0}^{N_s-1} \frac{d}{dt} \left[\sum_{\substack{y=0 \\ y \geq \left(\frac{h}{N_b}\right)_{int} \\ \left(\frac{yN_b-h-\rho}{N_s}\right)_{int} \geq 0}}^{\infty} (X_{ca(yN_b-h)} e^{j(yN_b-h)g_m}) \bar{i}_{winding,\rho}^* \right] \bar{i}_{cage,h}^* \right\}. \end{aligned} \quad (2.227)$$

The equation can be simplified as:

CHAPTER 2

$$\begin{aligned}
P_{winding,h} &= \\
&= \frac{Nmpq\mu_0RLN_b}{\pi\delta} \Re \left\{ \sum_{\rho=0}^{N_s-1} \sum_{\substack{y=0 \\ \left(\frac{yN_b+h-\rho}{N_s}\right)_{int \geq 0}}}^{\infty} (-j(yN_b+h)X_{ca(yN_b+h)}e^{-j(yN_b+h)\vartheta_m}) \frac{d\mathcal{G}_m}{dt} \bar{i}_{winding,\rho} \bar{i}_{cage,h}^* \right\} + \\
&+ \frac{Nmpq\mu_0RLN_b}{\pi\delta} \Re \left\{ \sum_{\rho=0}^{N_s-1} \sum_{\substack{y=0 \\ \left(\frac{yN_b+h-\rho}{N_s}\right)_{int \geq 0}}}^{\infty} (X_{ca(yN_b+h)}e^{-j(yN_b+h)\vartheta_m}) \frac{d\bar{i}_{winding,\rho}}{dt} \bar{i}_{cage,h}^* \right\} + \\
&+ \frac{Nmpq\mu_0RLN_b}{\pi\delta} \Re \left\{ \sum_{\rho=0}^{N_s-1} \sum_{\substack{y=0 \\ y \geq \left(\frac{h}{N_b}\right)_{int} \\ \left(\frac{yN_b-h-\rho}{N_s}\right)_{int \geq 0}}}^{\infty} (j(yN_b-h)X_{ca(yN_b-h)}e^{j(yN_b-h)\vartheta_m}) \frac{d\mathcal{G}_m}{dt} \bar{i}_{winding,\rho}^* \bar{i}_{cage,h} \right\} + \\
&+ \frac{Nmpq\mu_0RLN_b}{\pi\delta} \Re \left\{ \sum_{\rho=0}^{N_s-1} \sum_{\substack{y=0 \\ y \geq \left(\frac{h}{N_b}\right)_{int} \\ \left(\frac{yN_b-h-\rho}{N_s}\right)_{int \geq 0}}}^{\infty} (X_{ca(yN_b-h)}e^{j(yN_b-h)\vartheta_m}) \frac{d\bar{i}_{winding,\rho}^*}{dt} \bar{i}_{cage,h} \right\}.
\end{aligned} \tag{2.228}$$

Considering only the contributions proportional to the rotor speed, the torque related to the h -th cage space is evaluated as:

$$\begin{aligned}
T_{winding,h} &= \frac{\mu_0RLmpqNN_b}{\pi\delta} \Re \left\{ \sum_{\rho=0}^{N_s-1} \sum_{\substack{y=0 \\ \left(\frac{yN_b+h-\rho}{N_s}\right)_{int \geq 0}}}^{\infty} (-j(yN_b+h)X_{ca(yN_b+h)}e^{-j(yN_b+h)\vartheta_m}) \bar{i}_{winding,\rho} \bar{i}_{cage,h}^* \right\} + \\
&+ \frac{\mu_0RLmpqNN_b}{\pi\delta} \Re \left\{ \sum_{\rho=0}^{N_s-1} \sum_{\substack{y=0 \\ y \geq \left(\frac{h}{N_b}\right)_{int} \\ \left(\frac{yN_b-h-\rho}{N_s}\right)_{int \geq 0}}}^{\infty} (j(yN_b-h)X_{ca(yN_b-h)}e^{j(yN_b-h)\vartheta_m}) \bar{i}_{winding,\rho}^* \bar{i}_{cage,h} \right\},
\end{aligned} \tag{2.229}$$

simplified as:

$$\begin{aligned}
 T_{winding,h} = & \Re \left\{ \sum_{\rho=0}^{N_s-1} \sum_{\substack{y=0 \\ \left(\frac{yN_b+h-\rho}{N_s}\right)_{int} \geq 0}}^{\infty} -jK_{T,winding,y,h}^+ e^{-j(yN_b+h)\vartheta_m} \bar{i}_{winding,\rho} \bar{i}_{cage,h}^* \right\} + \\
 & + \Re \left\{ \sum_{\rho=0}^{N_s-1} \sum_{\substack{y=0 \\ y \geq \left(\frac{h}{N_b}\right)_{int} \\ \left(\frac{yN_b-h-\rho}{N_s}\right)_{int} \geq 0}}^{\infty} jK_{T,winding,y,h}^- e^{j(yN_b-h)\vartheta_m} \bar{i}_{winding,\rho}^* \bar{i}_{cage,h} \right\}, \tag{2.230}
 \end{aligned}$$

with:

$$\begin{aligned}
 K_{T,winding,y,h}^+ &= \frac{\mu_0 R L m p q N N_b}{\pi \delta} (yN_b + h) X_{ca(yN_b+h)}, \\
 K_{T,winding,y,h}^- &= \frac{\mu_0 R L m p q N N_b}{\pi \delta} (yN_b - h) X_{ca(yN_b-h)},
 \end{aligned}$$

the torque constants related to the h -th cage current space vector.

The total torque of the squirrel cage multiphase machine is:

$$T = \frac{T_0}{2} + \frac{T_{N_b}}{2} + \sum_{h=1}^{N_b/2-1} T_h. \tag{2.231}$$

The analysis of the torque generated in a squirrel cage machine can be solved by the power analysis of the stator winding or of the cage. Indeed, comparing only the lower harmonic contribution of the h -th order current space vectors, the related torque can be defined by (2.230) as:

$$T_{winding,h} = K_{T,winding,0,h}^+ \Re \left\{ -j e^{-jh\vartheta_m} \bar{i}_{winding,h} \bar{i}_{cage,h}^* \right\},$$

with:

$$K_{T,winding,0,h}^+ = \frac{\mu_0 R L m p q N N_b}{\pi \delta} h X_{ca,h},$$

or by (2.222) as:

$$T_{cage,h} = K_{T,cage,0,h}^+ \Re \left\{ j e^{jh\vartheta_m} \bar{i}_{cage,h} \bar{i}_{winding,h}^* \right\},$$

with:

$$K_{T,cage,0,h}^+ = \frac{\mu_0 R L m p q N N_b}{\pi \delta} h X_{ca,h} = K_{T,winding,0,h}^+.$$

The two torque equations are equal, being $\Re\{\bar{x}^*\} = \Re\{\bar{x}\}$.

As expected, the torque given by the cage analysis is the same of the one given by the stator winding (indeed the torque is produced by both the armature and cage fields, and the equation validate the effectiveness of the model).

While in case of a SPM rotor, the torque equation (2.217) for only the p -th space is reported here below:

$$T_{PM,p} = \Re\left\{jK_{T,PM,0,p}^+ e^{jp\vartheta_m} \bar{i}_p^*\right\}.$$

Squirrel cage machine not-mechanical mutual power (multiphase winding)

Here below the second terms of the mutual power contribution of a squirrel cage machine are analysed in order to verify that these power contributions are related to the mutual power that is not mechanical. Therefore, these terms (named *transf*) represent the power transferred between the stator and the rotor that is not generated by the torque production.

The contribution in (2.220) referred to the power transferred to the stator by the rotor is:

$$P_{cage,transf,h} = \frac{\mu_0 R L m p q N N_s N_b}{N_s \pi \delta} \Re \left\{ \sum_{\rho=0}^{N_b-1} \sum_{\substack{y=0 \\ \left(\frac{ym+h-\rho}{N_b}\right)_{int \geq 0}}}^{\infty} (X_{ca,(yN_s+h)} e^{j(yN_s+h)\vartheta_m}) \frac{d}{dt} \bar{i}_{cage,\rho} \bar{i}_h^* \right\} +$$

$$+ \frac{\mu_0 R L m p q N N_s N_b}{N_s \pi \delta} \Re \left\{ \sum_{\rho=0}^{N_b-1} \sum_{\substack{y=0 \\ y \geq \left(\frac{h}{N_s}\right)_{int} \\ \left(\frac{ym-h-\rho}{N_b}\right)_{int \geq 0}}}^{\infty} (X_{ca,(yN_s-h)} e^{-j(yN_s-h)\vartheta_m}) \frac{d}{dt} \bar{i}_{cage,\rho}^* \bar{i}_h \right\}.$$

The contribution in (2.228) referred to the power transferred to the rotor by the stator is:

$$\begin{aligned}
 P_{winding,transf,h} = & \frac{Nmpq\mu_0RLN_b}{\pi\delta} \Re \left\{ \sum_{\rho=0}^{N_s-1} \sum_{\substack{y=0 \\ \left(\frac{yN_b+h-\rho}{N_s}\right)_{\text{int}} \geq 0}}^{\infty} (X_{ca(yN_b+h)} e^{-j(yN_b+h)\vartheta_m}) \frac{d\bar{i}_{winding,\rho}}{dt} \bar{i}_{cage,h}^* \right\} + \\
 & + \frac{Nmpq\mu_0RLN_b}{\pi\delta} \Re \left\{ \sum_{\rho=0}^{N_s-1} \sum_{\substack{y=0 \\ y \geq \left(\frac{h}{N_b}\right)_{\text{int}} \\ \left(\frac{yN_b-h-\rho}{N_s}\right)_{\text{int}} \geq 0}}^{\infty} (X_{ca(yN_b-h)} e^{j(yN_b-h)\vartheta_m}) \frac{d\bar{i}_{winding,\rho}^*}{dt} \bar{i}_{cage,h}^* \right\}.
 \end{aligned}$$

Considering only one harmonic of the magnetic field in the airgap and the relative space vector components, the two previous relationships can be rewritten as:

$$P_{cage,transf,h} = \frac{\mu_0RLmpqNN_b}{\pi\delta} \Re \left\{ X_{ca,(h)} e^{j(h)\vartheta_m} \frac{d\bar{i}_{cage,h}}{dt} \bar{i}_{winding,h}^* \right\},$$

and

$$P_{winding,transf,h} = \frac{\mu_0RLmpqNN_b}{\pi\delta} \Re \left\{ X_{ca,(h)} e^{-j(h)\vartheta_m} \frac{d\bar{i}_{winding,h}}{dt} \bar{i}_{cage,h}^* \right\}.$$

Considering a steady state condition, the equations can be written as:

$$P_{cage,transf,h} = \omega_{rh} \left[\frac{\mu_0RLmpqNN_b}{\pi\delta} \Re \left\{ X_{ca,(h)} e^{j(h)\vartheta_m} \bar{i}_{cage,h} \bar{i}_{winding,h}^* \right\} \right],$$

and

$$P_{winding,transf,h} = \omega_{sh} \left[\frac{\mu_0RLmpqNN_b}{\pi\delta} \Re \left\{ X_{ca,(h)} e^{-j(h)\vartheta_m} \bar{i}_{winding,h} \bar{i}_{cage,h}^* \right\} \right],$$

with ω_{rh} and ω_{sh} the rotor and stator electrical frequencies for the h -th space. As expected, with the stator and rotor current vectors having the same electrical frequency, the two equations give the same result. This is what happens for example in a transformer. Indeed, an induction machine at stand still operation can be seen as a transformer with the secondary winding in short circuit. Its mutual power is completely transferred between the stator and the rotor without producing a mechanical power (even if in this case there is a torque, the rotor is not moving and therefore there is not work and mechanical power).

Instead, if the rotor is moving, the difference between the power transferred from the stator to the rotor and the power transferred from the rotor to the stator is the mechanical power:

$$P_{mech,h} = P_{winding,transf,h} - P_{cage,transf,h} = (\omega_{sh} - \omega_{rh}) \left[\frac{\mu_0 RLmpqNN_b}{\pi\delta} \Re \left\{ X_{ca,(h)} e^{j(h)\vartheta_m} \bar{i}_{cage,h} \bar{i}_{winding,h}^* \right\} \right].$$

In order to produce a not zero average torque, the speed of the stator field (ω_{sh}) must be synchronous with the speed of the rotor field ($\omega_m + \omega_{rh}$), resulting (as expected) in:

$$T_{mech,h} = \frac{P_{winding,transf,h} - P_{cage,transf,h}}{\omega_m} = \left[\frac{\mu_0 RLmpqNN_b}{\pi\delta} \Re \left\{ X_{ca,(h)} e^{j(h)\vartheta_m} \bar{i}_{cage,h} \bar{i}_{winding,h}^* \right\} \right].$$

Introducing the variable K_{Ph} , with:

$$K_{Ph} = \frac{\mu_0 RLmpqNN_b}{\pi\delta} \Re \left\{ j e^{j(h)\vartheta_m} \bar{i}_{cage,h} \bar{i}_{winding,h}^* \right\},$$

the steady state power between the stator and the rotor can be written as:

$$\begin{aligned} P_{mutual,rotor,h} &= \frac{\mu_0 RLmpqNN_b}{\pi\delta} \Re \left\{ \frac{d}{dt} \left[X_{ca,(h)} e^{-j(h)\vartheta_m} \bar{i}_{winding,h} \right] \bar{i}_{cage,h}^* \right\} = \\ &= \frac{\mu_0 RLmpqNN_b}{\pi\delta} (\omega_{sh} - h\omega_m) \Re \left\{ j e^{-j(h)\vartheta_m} \bar{i}_{winding,h} \bar{i}_{cage,h}^* \right\} = \\ &= \frac{\mu_0 RLmpqNN_b}{\pi\delta} (-\omega_{sh} + h\omega_m) \Re \left\{ j e^{j(h)\vartheta_m} \bar{i}_{cage,h} \bar{i}_{winding,h}^* \right\} = \\ &= -K_{Ph}\omega_{sh} + K_{Ph}h\omega_m, \end{aligned}$$

and:

$$\begin{aligned} P_{mutual,stator,h} &= \frac{\mu_0 RLmpqNN_b}{\pi\delta} \Re \left\{ \frac{d}{dt} \left[X_{ca,(h)} e^{j(h)\vartheta_m} \bar{i}_{cage,h} \right] \bar{i}_{winding,h}^* \right\} = \\ &= \frac{\mu_0 RLmpqNN_b}{\pi\delta} (\omega_{rh} + h\omega_m) \Re \left\{ j e^{j(h)\vartheta_m} \bar{i}_{cage,h} \bar{i}_{winding,h}^* \right\} = \\ &= K_{Ph}\omega_{rh} + K_{Ph}h\omega_m. \end{aligned}$$

The previous relationships can be rewritten as:

$$P_{mutual,rotor,h} = P_{winding,transf,h} + P_{winding,h} = -K_{Ph}\omega_{sh} + K_{Ph}h\omega_m,$$

$$P_{mutual,stator,h} = P_{cage,transf,h} + P_{cage,h} = K_{Ph}\omega_{rh} + K_{Ph}h\omega_m.$$

Because to produce a not zero average torque at steady state conditions the rotor frequency must be $\omega_{rh} = \omega_{sh} - h\omega_m$, and $K_{Ph}h\omega_m$ represents the mechanical power, it results that:

$$P_{mutual,stator,h} = K_{Ph}\omega_{rh} + K_{Ph}h\omega_m = K_{Ph}(\omega_{sh} - h\omega_m) + K_{Ph}h\omega_m = K_{Ph}\omega_{sh},$$

$$P_{mutual,rotor,h} = -K_{Ph}\omega_{sh} + K_{Ph}h\omega_m = -P_{mutual,stator,h} + P_{mechanical,h}.$$

As expected, a component of the transferred mutual power from the stator to the rotor, $P_{mutual,stator,h}$, does not result in a mechanical power. The power component $P_{mutual,rotor,h}$ takes into account for the total active power that the cage needs in order to allow for the bar currents to

circulate. Indeed if the machine is working in motoring mode the stator absorbs from the grid/converter an active power equal to $P_{mutual, stator, h}$. Part of this power ($P_{mechanical, h}$) is transferred to the load, and the remaining is absorbed by the cage $P_{mutual, rotor, h}$ to sustain its losses.

If there is not mechanical power, as in a transformer ($\omega_m = 0$) or at no load ($K_{ph} = 0$), all the mutual active power flows from the stator to the rotor to sustain its losses (the iron losses, that are here neglected, and the Joule ones).

The next subsection aims to evaluate the torque equations by the analysis of the coenergy of the machine.

Airgap magnetic coenergy (alternative method for the torque evaluation)

Another method to define the torque of an electrical machine is by means of the derivative of the magnetic coenergy of the system with respect to the rotor position.

The magnetic coenergy of the system is:

$$W' = \int_0^H \int B dH dV, \quad (2.232)$$

where V is the volume of the system.

In an electrical machine, the coenergy in the iron can be neglected because the magnetic field (H) is much lower than the one in the airgap (the magnetic permeability of the iron μ_{Sheet} is significantly higher than the one of the air, μ_0). Furthermore, the hypothesis of the model is to have only radial flux in the machine. Therefore, the magnetic field in the air (only in its radial component) can be defined as: $H = \frac{B}{\mu_0}$.

Torque evaluation from the coenergy analysis

The coenergy of a system with hard magnetic materials, as the one in Fig. 2.17 [9], can be analysed substituting the permanent magnet volumes with a virtual airgap. The magnets are described only by their equivalent magnetomotive force, as in [10]. Indeed, if the magnet

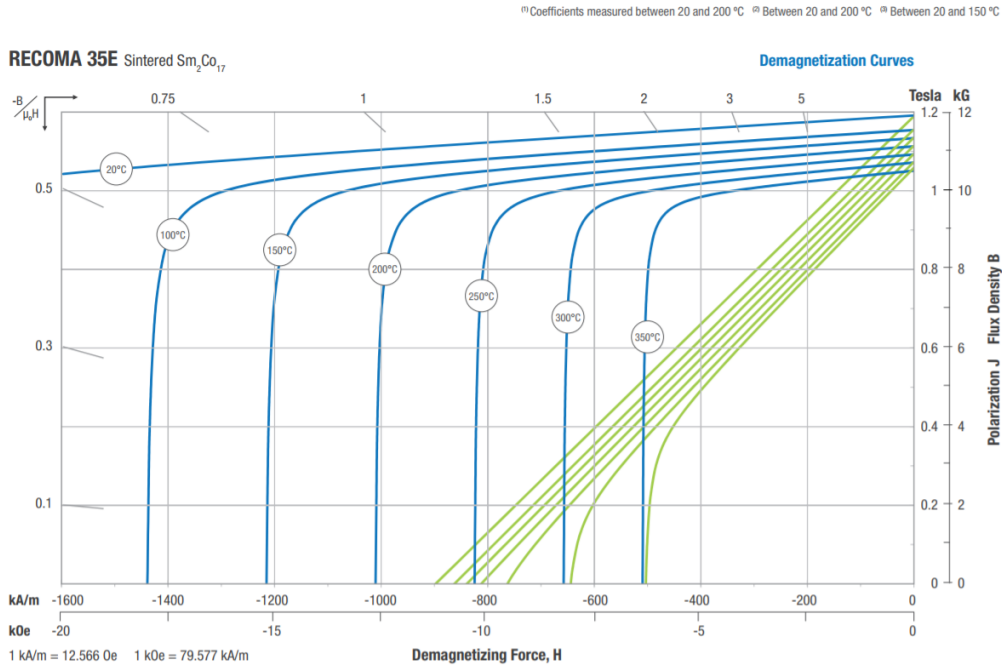


Fig. 2.17 - Example of B-H curve of a high power density hard magnetic material.

characteristic can be linearized in the working points (until the demagnetising field remains single-valued), the coenergy of the permanent magnet can be evaluated as in [11] (the graphical meaning of the equation is shown in Fig. 2.18):

$$W' = \int_0^{H_m} \int B_m dH dV_m. \tag{2.233}$$

This equation can be modified considering a linear magnet material behaviour as:

$$\begin{aligned} W' &= \int \left(B_m H_m + \frac{1}{2} (B_r - B_m) H_m \right) dV_m = \int \left(\frac{1}{2} B_m H_m + \frac{1}{2} B_r H_m \right) dV_m = \\ &= \int \left(\frac{1}{2} (B_m + B_r) H_m \right) dV_m = \int \left(\frac{1}{2\mu_m} (B_m + B_r)(B_m - B_r) \right) dV_m = \\ &= \frac{1}{2\mu_m} \int (B_m^2 - B_r^2) dV_m. \end{aligned} \tag{2.234}$$

Because the remanence depends only by the magnet magnetization, the component of the coenergy that depends by the rotor position and is related to the torque production is only:

$$W'' = \int \frac{B_m^2}{2\mu_m} dV_m. \tag{2.235}$$

Because the magnet permeability is almost as the one of the air, and the continuity of the flux makes the flux density be the same in the radial dimension for all the points in the airgap and magnets, the magnet regions can be considered as an equivalent air for the torque evaluation (virtual airgap).

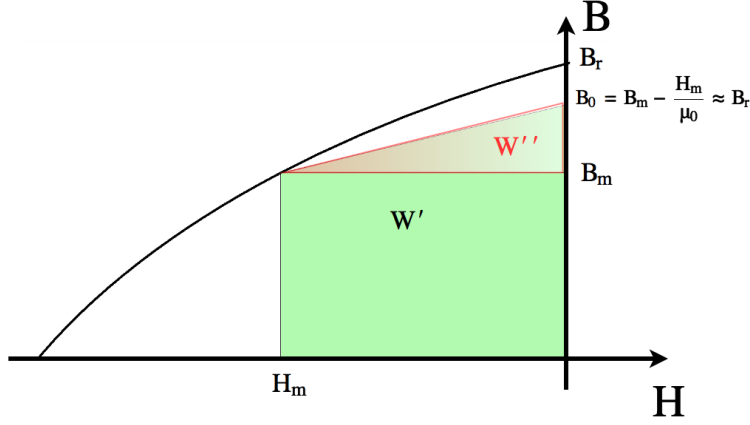


Fig. 2.18 - Coenergy of a hard magnetic material (concept).

Therefore, the component of the coenergy of the full system that affects the torque is evaluated as:

$$W' = \frac{1}{2} \int \frac{B^2}{\mu_0} dV = \frac{\mu_0}{2} \int H^2 dV. \quad (2.236)$$

The torque of the system can be approximately expressed as:

$$T = \frac{dW'}{d\vartheta_m} = \frac{1}{2\mu_0} \frac{d}{d\vartheta_m} \int B^2 dV = \frac{\mu_0}{2} \frac{d}{d\vartheta_m} \int H^2 dV, \quad (2.237)$$

where ϑ_m is the angular position of the rotor and B is the flux density in the air region of the airgap.

According to the model hypothesis, the torque general equation can be rewritten, keeping only the time as implicit, as:

$$T(\vartheta_m) = \frac{\mu_0}{2} \frac{d}{d\vartheta_m} \int H^2 dV = \frac{\mu_0}{2} \frac{d}{d\vartheta_m} \int_0^{2\pi L} \int_0^R H^2(\vartheta_s, \vartheta_m, z) \delta(\vartheta_s, \vartheta_m, z) R d\vartheta_s dz. \quad (2.238)$$

By this equation, it is also possible to evaluate reluctance torque components (cogging and slotting effects for example). Indeed, the magnetic field can be written as in (2.31), and can be rewritten in its general shape as:

$$H(\vartheta_s, \vartheta_m, z) = g(\vartheta_s, \vartheta_m, z) F(\vartheta_s, \vartheta_m, z), \quad (2.239)$$

where $g = 1/\delta$. Therefore, the general torque equation can be modified as below:

$$\begin{aligned}
 T(\mathcal{G}_m) &= \frac{\mu_0}{2} \frac{d}{d\mathcal{G}_m} \int_0^{2\pi L} \int_0^0 g^2(\mathcal{G}_s, \mathcal{G}_m, z) F^2(\mathcal{G}_s, \mathcal{G}_m, z) \frac{1}{g(\mathcal{G}_s, \mathcal{G}_m, z)} R d\mathcal{G}_s dz = \\
 &= \frac{\mu_0}{2} \int_0^{2\pi L} \int_0^0 \frac{d[g(\mathcal{G}_s, \mathcal{G}_m, z) F^2(\mathcal{G}_s, \mathcal{G}_m, z)]}{d\mathcal{G}_m} R d\mathcal{G}_s dz = \tag{2.240} \\
 &= \frac{\mu_0}{2} \int_0^{2\pi L} \int_0^0 \left[F^2(\mathcal{G}_s, \mathcal{G}_m, z) \frac{dg(\mathcal{G}_s, \mathcal{G}_m, z)}{d\mathcal{G}_m} + 2g(\mathcal{G}_s, \mathcal{G}_m, z) F(\mathcal{G}_s, \mathcal{G}_m, z) \frac{dF(\mathcal{G}_s, \mathcal{G}_m, z)}{d\mathcal{G}_m} \right] R d\mathcal{G}_s dz = \\
 &= T_{reluctance}(\mathcal{G}_m) + T_{mutual}(\mathcal{G}_m),
 \end{aligned}$$

where the contribution related to the interaction between the magnetomotive sources (currents and permanent magnets) and the reluctance of the magnetic circuit is:

$$T_{reluctance}(\mathcal{G}_m) = \frac{\mu_0}{2} \int_0^{2\pi L} \int_0^0 F^2(\mathcal{G}_s, \mathcal{G}_m, z) \frac{dg(\mathcal{G}_s, \mathcal{G}_m, z)}{d\mathcal{G}_m} R d\mathcal{G}_s dz.$$

Instead, the interaction between the magnetomotive sources taking into account of the modulation of the flux caused by the reluctance distribution is:

$$T_{mutual}(\mathcal{G}_m) = \mu_0 \int_0^{2\pi L} \int_0^0 \left[g(\mathcal{G}_s, \mathcal{G}_m, z) F(\mathcal{G}_s, \mathcal{G}_m, z) \frac{dF(\mathcal{G}_s, \mathcal{G}_m, z)}{d\mathcal{G}_m} \right] R d\mathcal{G}_s dz.$$

If the machine has negligible reluctance effects, as the machines investigated in this work of thesis, the first effect (reluctance torque) is zero, and the torque can be simplified as:

$$T(\mathcal{G}_m) = T_{mutual}(\mathcal{G}_m) = \mu_0 \int_0^{2\pi L} \int_0^0 \left[g F(\mathcal{G}_s, \mathcal{G}_m, z) \frac{dF(\mathcal{G}_s, \mathcal{G}_m, z)}{d\mathcal{G}_m} \right] R d\mathcal{G}_s dz. \tag{2.241}$$

If the airgap is constant, the following simplified torque equation is preferred:

$$T(\mathcal{G}_m) = \mu_0 R \delta \int_0^{2\pi L} \int_0^0 H(\mathcal{G}_s, \mathcal{G}_m, z) \frac{dH(\mathcal{G}_s, \mathcal{G}_m, z)}{d\mathcal{G}_m} d\mathcal{G}_s dz. \tag{2.242}$$

The magnetic field in the airgap can be substituted by its Fourier expansion in the angular dimension \mathcal{G}_s :

$$H(\mathcal{G}_s, \mathcal{G}_m, z) = \Re \left\{ \sum_{h=1}^{\infty} \bar{H}_h(\mathcal{G}_m, z) e^{-jh\mathcal{G}_s} \right\} = \sum_{h=1}^{\infty} \frac{\bar{H}_h(\mathcal{G}_m, z) e^{-jh\mathcal{G}_s} + \bar{H}_h^*(\mathcal{G}_m, z) e^{jh\mathcal{G}_s}}{2}. \tag{2.243}$$

Keeping implicit the dependences with the rotor position and the axial direction, the torque equation for an isotropic machine can be written as:

$$T(\mathcal{G}_m) = \mu_0 R \delta \int_0^{2\pi L} \int_0^0 \sum_{h=1}^{\infty} \frac{\bar{H}_h e^{-jh\mathcal{G}_s} + \bar{H}_h^* e^{jh\mathcal{G}_s}}{2} \sum_{\rho=1}^{\infty} \frac{d\bar{H}_\rho e^{-j\rho\mathcal{G}_s} + d\bar{H}_\rho^* e^{j\rho\mathcal{G}_s}}{2} d\mathcal{G}_s dz, \tag{2.244}$$

that is:

$$\begin{aligned}
 T(\mathcal{G}_m) = & \frac{\mu_0 R \delta}{4} \int_0^L \sum_{\rho=1}^{\infty} \sum_{h=1}^{\infty} \left[\bar{H}_h \frac{d\bar{H}_\rho}{d\mathcal{G}_m} \int_0^{2\pi} e^{-j(\rho+h)\mathcal{G}_s} d\mathcal{G}_s + \bar{H}_h^*(\mathcal{G}_m, z) \frac{d\bar{H}_\rho}{d\mathcal{G}_m} \int_0^{2\pi} e^{-j(\rho-h)\mathcal{G}_s} d\mathcal{G}_s \right] dz + \\
 & + \frac{\mu_0 R \delta}{4} \int_0^L \sum_{\rho=1}^{\infty} \sum_{h=1}^{\infty} \left[\bar{H}_h \frac{d\bar{H}_\rho^*}{d\mathcal{G}_m} \int_0^{2\pi} e^{j(\rho-h)\mathcal{G}_s} d\mathcal{G}_s + \bar{H}_h^* \frac{d\bar{H}_\rho}{d\mathcal{G}_m} \int_0^{2\pi} e^{j(\rho+h)\mathcal{G}_s} d\mathcal{G}_s \right] dz.
 \end{aligned} \tag{2.245}$$

The terms $\int_0^{2\pi} e^{jz\mathcal{G}_s} d\mathcal{G}_s$ are always zero but when z is equal to zero (in that case it is 2π).

Therefore, the only torque contribution is given by the interaction between space harmonics of the magnetic field of the same order (with the same angular periodicity), and the torque can be evaluated as:

$$T(\mathcal{G}_m) = \frac{2\pi\mu_0 R \delta}{4} \int_0^L \sum_{h=1}^{\infty} \left[\bar{H}_h^* \frac{d\bar{H}_h}{d\mathcal{G}_m} + \bar{H}_h \frac{d\bar{H}_h^*}{d\mathcal{G}_m} \right] dz. \tag{2.246}$$

The magnetic field is the sum of the stator and rotor components: $\bar{H}_h = \bar{H}_{stator,h} + \bar{H}_{rotor,h}$.

However, the armature field harmonics do not depend by the rotor position; therefore, the torque equation can be simplified as:

$$T(\mathcal{G}_m) = \frac{2\pi\mu_0 R \delta}{4} \int_0^L \sum_{h=1}^{\infty} \left[(\bar{H}_{stator,h}^* + \bar{H}_{rotor,h}^*) \frac{d\bar{H}_{rotor,h}}{d\mathcal{G}_m} + (\bar{H}_{stator,h} + \bar{H}_{rotor,h}) \frac{d\bar{H}_{rotor,h}^*}{d\mathcal{G}_m} \right] dz. \tag{2.247}$$

The torque equation can be rewritten as:

$$\begin{aligned}
 T(\mathcal{G}_m) = & \frac{2\pi\mu_0 R \delta}{4} \int_0^L \sum_{h=1}^{\infty} \left[\bar{H}_{stator,h}^* \frac{d\bar{H}_{rotor,h}}{d\mathcal{G}_m} + \bar{H}_{stator,h} \frac{d\bar{H}_{rotor,h}^*}{d\mathcal{G}_m} \right] dz + \\
 & + \frac{2\pi\mu_0 R \delta}{4} \int_0^L \sum_{h=1}^{\infty} \left[\bar{H}_{rotor,h}^* \frac{d\bar{H}_{rotor,h}}{d\mathcal{G}_m} + \bar{H}_{rotor,h} \frac{d\bar{H}_{rotor,h}^*}{d\mathcal{G}_m} \right] dz.
 \end{aligned} \tag{2.248}$$

Each harmonic of the rotor field depends by the rotor position by a function like $\bar{H}_{rotor,h} = \bar{H}_{rotor,h,(\mathcal{G}_m=0)} e^{jh\mathcal{G}_m} = \bar{H}_{rotor,h,0} e^{jh\mathcal{G}_m}$, while $\bar{H}_{rotor,h,(\mathcal{G}_m=0)}$ depends only by the magnets design or by the cage currents (note that the rotor sources of magnetic field, like permanent magnets or squirrel cage currents, are synchronous with the rotor, being part of it). Therefore, the term depending only by the rotor field is zero, as shown here below:

$$\begin{aligned}
 & \bar{H}_{rotor,h,0}^* e^{-jh\mathcal{G}_m} \bar{H}_{rotor,h,0} \frac{de^{jh\mathcal{G}_m}}{d\mathcal{G}_m} + \bar{H}_{rotor,h,0} e^{jh\mathcal{G}_m} \bar{H}_{rotor,h,0}^* \frac{de^{-jh\mathcal{G}_m}}{d\mathcal{G}_m} = \\
 & = jh\bar{H}_{rotor,h,0}^* \bar{H}_{rotor,h,0} e^{-jh\mathcal{G}_m} e^{jh\mathcal{G}_m} - jh\bar{H}_{rotor,h,0}^* \bar{H}_{rotor,h,0} e^{-jh\mathcal{G}_m} e^{jh\mathcal{G}_m} = 0.
 \end{aligned}$$

The torque equation remains described as:

$$\begin{aligned}
 T(\vartheta_m) &= \frac{2\pi\mu_0 R\delta}{4} \int_0^L \sum_{h=1}^{\infty} \left[jh\bar{H}_{stator,h}^* \bar{H}_{rotor,h,0} e^{jh\vartheta_m} - jh\bar{H}_{stator,h} \bar{H}_{rotor,h,0}^* e^{-jh\vartheta_m} \right] dz = \\
 &= \pi\mu_0 R\delta \int_0^L \sum_{h=1}^{\infty} \Re \left\{ jh\bar{H}_{stator,h}^* \bar{H}_{rotor,h,0} e^{jh\vartheta_m} \right\} dz.
 \end{aligned} \tag{2.249}$$

The harmonic of the magnetic field for a multiphase winding (2.52) is:

$$\bar{H}_\rho = \frac{Nmpq}{\pi\delta} \frac{K_{ap}}{\rho} \bar{i}_\rho.$$

For a SPM symmetrical rotor (2.132) it is:

$$\bar{H}_{ph_{odd}}(z) = \frac{4B_r\tau_M}{\mu_M h_{odd}\pi\delta} \sin\left(h_{odd} \frac{\pi}{2}\right) e^{jph_{odd}\vartheta_m} e^{jph_{odd}\psi_{skew,w}}, \quad z \in \left[z_w - \frac{\Delta L_w}{2}; z_w + \frac{\Delta L_w}{2} \right].$$

For a squirrel cage rotor (2.163) it is:

$$\bar{H}_h(z) = \frac{N_b}{\pi\delta} \frac{\sin\left(h \frac{\pi}{N_b}\right)}{h} \bar{i}_h e^{jh\left(z - \frac{L}{2}\right) \frac{\Delta\psi_{skew}}{L}} e^{jh\vartheta_m}.$$

By the presented equations, the evaluation of the torque is straightforward.

SPM machine: torque equation (energy method)

The torque of a SPM machine results (only for h odd and multiple of the pole pairs number) as:

$$\begin{aligned}
 T &= \pi\mu_0 R\delta \sum_{h=1}^{\infty} \Re \left\{ jph \frac{Nmpq}{\pi\delta} \frac{K_{aph}}{ph} \bar{i}_{ph}^* \frac{4B_r\tau_M}{\mu_M h\pi\delta} \sin\left(h \frac{\pi}{2}\right) e^{jph_{odd}\vartheta_m} \int_0^L e^{jph\psi_{skew,w}} dz \right\} = \\
 &= 4\mu_0 LRNmpq \frac{B_r\tau_M}{\mu_M\pi\delta} \sum_{h=1}^{\infty} \Re \left\{ j\bar{i}_{ph}^* \frac{K_{aph}}{h} \sin\left(h \frac{\pi}{2}\right) e^{jph\vartheta_m} K_{skew,ph} \right\},
 \end{aligned} \tag{2.250}$$

exactly as in the equation founded by the analysis of the instantaneous power.

Squirrel cage machine: torque equation (energy method)

The torque of a squirrel cage machine results as:

$$\begin{aligned}
 T(\vartheta_m) &= \pi\mu_0 R \delta \sum_{h=1}^{\infty} \Re \left\{ jh \frac{Nmpq}{\pi\delta} \frac{K_{ah}}{h} \bar{i}_{winding,h}^* \frac{N_b}{\pi\delta} \frac{\sin\left(h \frac{\pi}{N_b}\right)}{h} \bar{i}_{cage,h} \int_0^L e^{jh\left(z - \frac{L}{2}\right) \frac{\Delta W_{skew}}{L}} dz e^{jh\vartheta_m} \right\} = \\
 &= \pi\mu_0 LR \delta \sum_{h=1}^{\infty} \Re \left\{ jh \frac{Nmpq}{\pi\delta} \frac{K_{ah}}{h} \bar{i}_{winding,h}^* \frac{N_b}{\pi\delta} \frac{\sin\left(h \frac{\pi}{N_b}\right)}{h} \bar{i}_{cage,h} K_{skew,h} e^{jh\vartheta_m} \right\} = \\
 &= \mu_0 LR Nmpq \frac{N_b}{\pi\delta} \sum_{h=1}^{\infty} \Re \left\{ j \frac{K_{ah} K_{skew,h} \sin\left(h \frac{\pi}{N_b}\right)}{h} \bar{i}_{winding,h}^* \bar{i}_{cage,h} e^{jh\vartheta_m} \right\} = \\
 &= \mu_0 LR Nmpq \frac{N_b}{\pi\delta} \sum_{h=1}^{\infty} \Re \left\{ jh X_{ca,h} \bar{i}_{winding,h}^* \bar{i}_{cage,h} e^{jh\vartheta_m} \right\},
 \end{aligned} \tag{2.251}$$

exactly as in the equation founded by the analysis of the instantaneous power.

Radial Force

In case of asymmetries and faults, electrical machines might have a not zero resultant force. On the other hands, some designs of electrical machines allow for the control of the resultant radial force acting on the rotor.

In this thesis, the radial force is analysed for both the cases (faults and force control). In particular, this subsection deals with the identification of a radial force equation for a general electrical machine. Then, the equation is simplified considering the fundamental hypothesis of the model: only the radial component of the magnetic field is taken into account.

Magnetic force principle

According to the Maxwell tensor principle, the magnetic pressure in absence of electric field can be expressed as:

$$\bar{\sigma}_r = \frac{1}{2\mu_0} \left(2B_r B_t \bar{t} + \left(B_r^2 - B_t^2 \right) \bar{r} \right) = \sigma_t \bar{t} + \sigma_r \bar{r}, \tag{2.252}$$

where $\bar{\sigma}_r$ is the magnetic pressure, or Maxwell stress tensor, and the subscripts r and t are used to represent the radial and tangential components.

Considering only the radial component of the flux, (2.252) is simplified as:

$$\sigma_r = \frac{B_r^2}{2\mu_0}. \quad (2.253)$$

The magnetic field in the model is considered positive when it is directed from the rotor to the stator, the same convention is used for the radial unit vector \bar{r} in (2.252) (that is described as positive if it is an attractive force of the rotor to the stator), resulting in the following equation:

$$\frac{dF_r}{dS_r} = \sigma_r = \frac{B_r^2}{2\mu_0}. \quad (2.254)$$

The subscript that indicates the direction of the force component (r) is neglected hereafter, making implicit that only the radial component is analysed.

Equation (2.254) allows defining the radial force on a closed surface surrounding the rotor (acting on the centre of the airgap, with radius R). In case of linear magnetic circuit, the resulting radial force on the rotor results as:

$$\bar{F}(\mathcal{G}_m) = \int_0^L \int_0^{2\pi} \sigma(\mathcal{G}_s, z) e^{j\mathcal{G}_s} R d\mathcal{G}_s dz = \int_0^L \int_0^{2\pi} \frac{\mu_0 H^2(\mathcal{G}_s, z)}{2} e^{j\mathcal{G}_s} R d\mathcal{G}_s dz. \quad (2.255)$$

The magnetic field, H , depends by the sources of magnetomotive force and by the reluctance of the circuit, and its evaluation has already been presented. The magnetic field in the airgap can be substituted by its Fourier series, and the following relationship to be defined:

$$\begin{aligned} \bar{F}(\mathcal{G}_m) &= \frac{\mu_0 R}{2} \int_0^L \int_0^{2\pi} \left[\sum_{h=1}^{\infty} \frac{\bar{H}_h(\mathcal{G}_m, z) e^{-jh\mathcal{G}_s} + \bar{H}_h^*(\mathcal{G}_m, z) e^{jh\mathcal{G}_s}}{2} \right]^2 d\mathcal{G}_s dz = \\ &= \frac{\mu_0 R}{8} \int_0^L \int_0^{2\pi} \left[\sum_{h=1}^{\infty} (\bar{H}_h(\mathcal{G}_m, z) e^{-jh\mathcal{G}_s} + \bar{H}_h^*(\mathcal{G}_m, z) e^{jh\mathcal{G}_s}) \sum_{\rho=1}^{\infty} (\bar{H}_\rho(\mathcal{G}_m, z) e^{-j\rho\mathcal{G}_s} + \bar{H}_\rho^*(\mathcal{G}_m, z) e^{j\rho\mathcal{G}_s}) \right] e^{j\mathcal{G}_s} d\mathcal{G}_s dz = \\ &= \frac{\mu_0 R}{8} \int_0^L \int_0^{2\pi} \sum_{\rho=1}^{\infty} \sum_{h=1}^{\infty} \left[\bar{H}_h(\mathcal{G}_m, z) \bar{H}_\rho(\mathcal{G}_m, z) e^{-j(h+\rho-1)\mathcal{G}_s} + \bar{H}_h(\mathcal{G}_m, z) \bar{H}_\rho^*(\mathcal{G}_m, z) e^{-j(h-\rho-1)\mathcal{G}_s} \right] d\mathcal{G}_s dz + \\ &+ \frac{\mu_0 R}{8} \int_0^L \int_0^{2\pi} \sum_{\rho=1}^{\infty} \sum_{h=1}^{\infty} \left[\bar{H}_h^*(\mathcal{G}_m, z) \bar{H}_\rho(\mathcal{G}_m, z) e^{j(h-\rho+1)\mathcal{G}_s} + \bar{H}_\rho^*(\mathcal{G}_m, z) \bar{H}_h^*(\mathcal{G}_m, z) e^{j(h+\rho+1)\mathcal{G}_s} \right] d\mathcal{G}_s dz. \end{aligned} \quad (2.256)$$

The term $\int_0^{2\pi} e^{jz\mathcal{G}_s} d\mathcal{G}_s$ is null for all the cases in which z is different from zero, for which it results equal to 2π . Therefore, because $\pm(h+\rho)\pm 1$ is never equal to zero, the radial force equation can be written as:

$$\bar{F}(\mathcal{G}_m) = \frac{\pi\mu_0 R}{4} \int_0^L \sum_{h=1}^{\infty} \left[\bar{H}_h(\mathcal{G}_m, z) \bar{H}_{h-1}^*(\mathcal{G}_m, z) + \bar{H}_h^*(\mathcal{G}_m, z) \bar{H}_{h+1}(\mathcal{G}_m, z) \right] dz. \quad (2.257)$$

It results that, whatever are the sources of the magnetic field, the resultant force on the rotor is produced by the interaction between the generic h -th field harmonic with the field harmonics of order $h-1$ and $h+1$. This result can be used to explain the radial forces produced by reluctance design, eccentricities, or faults, and can be used to define a radial force control by the stator currents with or without considering the presence of a rotor source of magnetic field. It is quite easy to understand by (2.257) that a resulting radial force can exist only if there are both even and odd field harmonics.

Extended analysis for the tangential components of the magnetic field in the airgap

If all the Maxwell stress tensor components are considered, the general force equation is:

$$\bar{F}(\mathcal{G}_m) = \int_0^L \int_0^{2\pi} (\sigma_t \bar{t} + \sigma_r \bar{r}) R d\mathcal{G}_s dz = \int_0^L \int_0^{2\pi} (j\sigma_t e^{j\mathcal{G}_s} + \sigma_r e^{j\mathcal{G}_s}) R d\mathcal{G}_s dz, \quad (2.258)$$

resulting in the equation:

$$\bar{F}(\mathcal{G}_m) = \frac{R}{2\mu_0} \int_0^L \int_0^{2\pi} (j2B_r B_t e^{j\mathcal{G}_s} + (B_r^2 - B_t^2) e^{j\mathcal{G}_s}) d\mathcal{G}_s dz, \quad (2.259)$$

that becomes, in case of linear magnetic circuit, as:

$$\begin{aligned} \bar{F}(\mathcal{G}_m) &= \frac{\mu_0 R}{2} \int_0^L \int_0^{2\pi} (j2H_r H_t e^{j\mathcal{G}_s} + (H_r^2 - H_t^2) e^{j\mathcal{G}_s}) d\mathcal{G}_s dz = \\ &= \frac{\mu_0 R}{2} \int_0^L \int_0^{2\pi} j2 \left[\frac{\sum_{h=1}^{\infty} \bar{H}_{rh}(\mathcal{G}_m, z) e^{-jh\mathcal{G}_s} + \bar{H}_{rh}^*(\mathcal{G}_m, z) e^{jh\mathcal{G}_s}}{2} \right] \left[\frac{\sum_{h=1}^{\infty} \bar{H}_{th}(\mathcal{G}_m, z) e^{-jh\mathcal{G}_s} + \bar{H}_{th}^*(\mathcal{G}_m, z) e^{jh\mathcal{G}_s}}{2} \right] e^{j\mathcal{G}_s} d\mathcal{G}_s dz + \\ &+ \frac{\mu_0 R}{2} \int_0^L \int_0^{2\pi} \left(\left[\frac{\sum_{h=1}^{\infty} \bar{H}_{rh}(\mathcal{G}_m, z) e^{-jh\mathcal{G}_s} + \bar{H}_{rh}^*(\mathcal{G}_m, z) e^{jh\mathcal{G}_s}}{2} \right]^2 - \left[\frac{\sum_{h=1}^{\infty} \bar{H}_{th}(\mathcal{G}_m, z) e^{-jh\mathcal{G}_s} + \bar{H}_{th}^*(\mathcal{G}_m, z) e^{jh\mathcal{G}_s}}{2} \right]^2 \right) e^{j\mathcal{G}_s} d\mathcal{G}_s dz. \end{aligned} \quad (2.260)$$

Following the same steps done for the only radial component, it results:

$$\begin{aligned} \bar{F}(\mathcal{G}_m) &= \frac{\mu_0 R}{4} \int_0^L \int_0^{2\pi} j \left[\frac{\sum_{h=1}^{\infty} \bar{H}_{rh}(\mathcal{G}_m, z) e^{-jh\mathcal{G}_s} + \bar{H}_{rh}^*(\mathcal{G}_m, z) e^{jh\mathcal{G}_s}}{2} \right] \left[\frac{\sum_{h=1}^{\infty} \bar{H}_{th}(\mathcal{G}_m, z) e^{-jh\mathcal{G}_s} + \bar{H}_{th}^*(\mathcal{G}_m, z) e^{jh\mathcal{G}_s}}{2} \right] e^{j\mathcal{G}_s} d\mathcal{G}_s dz + \\ &+ \frac{\mu_0 R}{8} \int_0^L \int_0^{2\pi} \left(\left[\frac{\sum_{h=1}^{\infty} \bar{H}_{rh}(\mathcal{G}_m, z) e^{-jh\mathcal{G}_s} + \bar{H}_{rh}^*(\mathcal{G}_m, z) e^{jh\mathcal{G}_s}}{2} \right]^2 - \left[\frac{\sum_{h=1}^{\infty} \bar{H}_{th}(\mathcal{G}_m, z) e^{-jh\mathcal{G}_s} + \bar{H}_{th}^*(\mathcal{G}_m, z) e^{jh\mathcal{G}_s}}{2} \right]^2 \right) e^{j\mathcal{G}_s} d\mathcal{G}_s dz = \\ &= j \frac{\pi \mu_0 R}{2} \int_0^L \sum_{h=1}^{\infty} [\bar{H}_{r,h}(\mathcal{G}_m, z) \bar{H}_{t,h-1}^*(\mathcal{G}_m, z) + \bar{H}_{r,h}^*(\mathcal{G}_m, z) \bar{H}_{t,h+1}(\mathcal{G}_m, z)] dz + \\ &+ \frac{\pi \mu_0 R}{4} \int_0^L \sum_{h=1}^{\infty} [\bar{H}_{r,h}(\mathcal{G}_m, z) \bar{H}_{r,h-1}^*(\mathcal{G}_m, z) + \bar{H}_{r,h}^*(\mathcal{G}_m, z) \bar{H}_{r,h+1}(\mathcal{G}_m, z)] dz + \end{aligned}$$

$$-\frac{\pi\mu_0 R}{4} \int_0^L \sum_{h=1}^{\infty} [\bar{H}_{t,h}(\vartheta_m, z)\bar{H}_{t,h-1}^*(\vartheta_m, z) + \bar{H}_{t,h}^*(\vartheta_m, z)\bar{H}_{t,h+1}(\vartheta_m, z)] dz. \quad (2.261)$$

The Maxwell stress tensor analysis can be also used for evaluating the torque, which approximatively results from considering the average of the tangential component of the Maxwell stress tensor multiplied by the average airgap radius. In case of isotropic magnetic circuit, the torque can be expressed as:

$$\begin{aligned} T(\vartheta_m) &= \frac{R}{2\mu_0} \int_0^L \int_0^{2\pi} R \sigma_t d\vartheta_s dz = \frac{R}{2\mu_0} \int_0^L \int_0^{2\pi} R(2B_r B_t) d\vartheta_s dz = \\ &= \frac{\mu_0 R^2}{4} \int_0^L \int_0^{2\pi} \left[\sum_{h=1}^{\infty} \bar{H}_{rh}(\vartheta_m, z)e^{-jh\vartheta_s} + \bar{H}_{rh}^*(\vartheta_m, z)e^{jh\vartheta_s} \right] \left[\sum_{h=1}^{\infty} \bar{H}_{th}(\vartheta_m, z)e^{-jh\vartheta_s} + \bar{H}_{th}^*(\vartheta_m, z)e^{jh\vartheta_s} \right] d\vartheta_s dz = \\ &= \pi\mu_0 R^2 \int_0^L \sum_{h=1}^{\infty} \Re\{\bar{H}_{r,h}(\vartheta_m, z)\bar{H}_{t,h}^*(\vartheta_m, z)\} dz. \end{aligned} \quad (2.262)$$

However, the proposed analytical model neglects the tangential component of the magnetic field in the airgap. Therefore, the evaluated radial force is approximated, and the torque is evaluated by means of the coenergy of the system or by the analysis of the components of the electrical power in input to the system.

2.8 Summary and Advantages of a Multi-Harmonic Model for Multiphase Machines

Moving towards multiphase machines makes the machine model inevitably more complex. Indeed, in order to describe the machine behaviour, all the degrees of freedom of the control must be taken into account. From an electromagnetic point of view, the degrees of freedom of a machine are the controllable sources of magnetomotive force: the currents (in the armature winding). Indeed, the harmonics of the armature magnetic field are directly related to the winding currents, or better to the current space vectors.

However, in order to control the currents, the most common method is by means of a voltage source (an electrical grid or a voltage source converter). This makes essential the modelling of the relationships between the currents and the voltages. Therefore, this chapter presented a deep analysis of the voltage space vector equations of a generic multiphase machine.

Advantages of a multi-harmonic SVD model

Because of the direct relationship between the current space vectors and the related field harmonics, it seems promising to write also the voltage equations in terms of space vectors.

The voltage space vector equation for a general symmetrical multiphase machine with an isotropic magnetic circuit and with negligible mutual leakage inductances between the different phases (2.120) is reported here below:

$$\bar{v}_h = R_s \bar{i}_h + (Ll + L_h) \frac{d\bar{i}_h}{dt} + \frac{d\bar{\phi}_{mutual,h}}{dt}. \quad (2.263)$$

In a standard three-phase machine control the final goal is to properly define the best value of the main field harmonic ($h=p$) in order to generate the required reference torque (or speed, or position as well). Therefore, the space vector equation for a three-phase machine is simply:

$$\bar{v}_p = R_s \bar{i}_p + (Ll + L_p) \frac{d\bar{i}_p}{dt} + \frac{d\bar{\phi}_{mutual,p}}{dt}. \quad (2.264)$$

Indeed, in a standard three-phase machine there are two independent currents (owing to the star connection). The same number of degrees of freedom must be kept in the choice of the numbers of controllable current space vectors. Because a space vector is made by two variables (being a complex number it has a real and an imaginary component), the control of a three-phase machine can be defined by the control of a single space vector.

The only independent current space vector of a three-phase machine is indirectly the source of all the higher order field harmonics caused by the armature. Improved controls can be adopted in order to take into account for this effect to provide better performance. However, each trial of controlling a higher order harmonic affects also the fundamental one and all the others. This means that the ideal control of the machine should consider in the same time all the field harmonics effects as function of the fundamental current space vector, and this can result in a quite complex and customized control for the analysed machine.

Instead, a multiphase machine with m phases and N_{star} stars has in general $m - N_{star}$ independent currents, which results in having almost $\frac{m - N_{star}}{2}$ independent current space vectors (this value depends on the number of phases and how the space vector are defined). Each of these current vectors allows independently controlling a related field harmonic; in particular, the current space vector \bar{i}_h is related to the field harmonic \bar{H}_h (still under the hypothesis of isotropic magnetic circuit and ideal conditions) by (2.47), reported here below:

$$\bar{H}_p = \frac{Nmpq}{\pi\delta} \frac{K_{ap}}{\rho} \bar{i}_p.$$

Therefore, it is possible to control independently $\frac{m - N_{star}}{2}$ field harmonics as if each harmonic were generated in a different machine connected to the same shaft of the others and magnetically coupled with them by its mutual flux equations. The voltage space vector equation of each space represents the electrical equation of the equivalent machine. As expected, the performance can significantly increase in a multiphase multi harmonic control.

The easier example is related to the torque contributions of an electrical machine. In a multiphase machine, the ripples related to the higher order field harmonics can be easily

CHAPTER 2

eliminated by imposing as zero the relative reference current space vector. This can be done for all the independent spaces (or field harmonics).

It is possible to think about many other possibilities for exploiting the multiphase degrees of freedom. Some example are presented in the following chapters of this thesis.

Multi-harmonic models (summary of the equations – simplified model)

The equations that describe a multiphase machine (model) have been presented in this chapter and are summarized here below in their simplified shapes.

The stator phase equations, independently from the rotor topology are as in the next paragraph.

Stator (armature)

Space vector transformation (2.53):

$$\bar{y}_h = \frac{2}{m} \sum_{k \in \mathcal{R}} x_{k\mathcal{R}} \bar{\alpha}^{h(k-1)} \quad \text{with} \quad \bar{\alpha} = e^{j \frac{2\pi}{N_s}}$$

Magnetic field (2.47):

$$\bar{H}_\rho = \frac{Nmpq}{\pi\delta} \frac{K_{a\rho}}{\rho} \bar{i}_\rho$$

Voltage equation (2.120):

$$\bar{v}_h = R_s \bar{i}_h + (Ll + L_h) \frac{d\bar{i}_h}{dt} + \frac{d\bar{\phi}_{mutual,h}}{dt},$$

where the mutual coupling between the different spaces is not considered, knowing that, if there are anisotropies or the winding is not a standard full pitch one (as for the sectorized topology), also the mutual coupling between the armature spaces must be considered.

The rotor equations are presented in the two following paragraph for an SPM and a squirrel cage IM respectively.

SPM multiphase machine (rotor effects)

The magnetic field harmonics of ad SPM rotor (2.134) are evaluated as:

$$\bar{H}_\rho(z) = \bar{H}_{ph_{odd}}(z) = \frac{4B_r \tau_M}{\mu_M h_{odd} \pi \delta} \sin\left(h_{odd} \frac{\pi}{2}\right) e^{jph_{odd}\vartheta_m} e^{jph_{odd}\psi_{skew,w}}, \quad z \in \left[z_w - \frac{\Delta L_w}{2}; z_w + \frac{\Delta L_w}{2} \right].$$

The mutual linked flux space vector produced by the magnets and linked with the armature winding $\bar{\phi}_{mutual,h}$ (named $\bar{\phi}_{PM,h}$) can be written as (2.142):

$$\bar{\phi}_{PM,h} = \frac{2}{m} \mu_0 L R p q N N_s \frac{4 B_r \tau_M p}{\mu_M \pi \delta} \left[\sum_{\substack{y=0 \\ \left(\frac{yN_s+h}{p}\right)_{odd,int}}}^{\infty} \frac{K_{a(yN_s+h)} K_{skew(yN_s+h)}}{(yN_s+h)^2} \sin\left((yN_s+h) \frac{\pi}{2p}\right) e^{j(yN_s+h)\vartheta_m} \right] + \frac{2}{m} \mu_0 L R p q N N_s \frac{4 B_r \tau_M p}{\mu_M \pi \delta} \left[\sum_{\substack{y=\left(\frac{h}{N_s}\right)_{int} \\ \left(\frac{yN_s-h}{p}\right)_{odd,int}}}^{\infty} \frac{K_{a(yN_s-h)} K_{skew(yN_s-h)}}{(yN_s-h)^2} \sin\left((yN_s-h) \frac{\pi}{2p}\right) e^{-j(yN_s-h)\vartheta_m} \right].$$

The resulting torque components (2.218) are given by (2.217):

$$T_{PM,h} = \Re \left\{ \sum_{\substack{y=0 \\ \left(\frac{yN_s+h}{p}\right)_{odd,int}}}^{\infty} j K_{T,PM,y,h}^+ e^{j(yN_s+h)\vartheta_m} \bar{i}_h^* \right\} + \Re \left\{ \sum_{\substack{y=\left(\frac{h}{N_s}\right)_{int} \\ \left(\frac{yN_s-h}{p}\right)_{odd,int}}}^{\infty} -j K_{T,PM,y,h}^- e^{-j(yN_s-h)\vartheta_m} \bar{i}_h^* \right\},$$

With:

$$K_{T,PM,y,h}^+ = m \mu_0 L R p^2 q N \frac{4 B_r \tau_M}{\mu_M \pi \delta} \frac{K_{a(yN_s+h)} K_{skew(yN_s+h)}}{(yN_s+h)} \sin\left((yN_s+h) \frac{\pi}{2p}\right),$$

$$K_{T,PM,y,h}^- = m \mu_0 L R p^2 q N \frac{4 B_r \tau_M}{\mu_M \pi \delta} \frac{K_{a(yN_s-h)} K_{skew(yN_s-h)}}{(yN_s-h)} \sin\left((yN_s-h) \frac{\pi}{2p}\right).$$

The main torque contributions are evaluated as:

$$T_{PM,h,main} = \Re \left\{ j K_{T,PM,0,h}^+ e^{jh\vartheta_m} \bar{i}_h^* \right\}.$$

Squirrel cage multiphase induction machine (rotor effects)

The space vector transformation (2.53) for a squirrel cage analysed as a N_b -phase N_b -slot multiphase winding is:

$$\bar{y}_h = \frac{2}{N_b} \sum_{k=1}^{N_b} x_k \bar{\alpha}^{h(k-1)}, \text{ with } \bar{\alpha} = e^{j\frac{2\pi}{N_b}}.$$

CHAPTER 2

The equation of the magnetic field harmonics for a squirrel cage rotor (2.165) is:

$$\bar{H}_h(z) = \frac{N_b}{\pi\delta} \frac{\sin\left(h \frac{\pi}{N_b}\right)}{h} \bar{i}_h e^{jh\left(z-\frac{L}{2}\right)\frac{\Delta\psi_{skew}}{L}} e^{jh\vartheta_m}.$$

The voltage equation is (2.169):

$$0 = R_{rh}\bar{i}_h + (Ll_{rh} + L_{cage,h})\frac{d\bar{i}_h}{dt} + \frac{d\bar{\phi}_{mutual,h}}{dt}.$$

The mutual linked flux space vector produced by the cage and linked with the armature winding $\bar{\phi}_{mutual,h}$ (named $\bar{\phi}_{cage,h}$) can be written as (2.187):

$$\bar{\phi}_{cage,h} = \frac{2\mu_0 RLpqNN_s N_b}{\pi\delta m} \sum_{\rho=0}^{N_b-1} \left[\sum_{\substack{y=0 \\ \left(\frac{yn+h-\rho}{N_b}\right)_{int \geq 0}}}^{\infty} (X_{ca,(yN_s+h)} e^{j(yN_s+h)\vartheta_m}) \bar{i}_\rho + \sum_{\substack{y=0 \\ y \geq \left(\frac{h}{N_s}\right)_{int} \\ \left(\frac{yn-h-\rho}{N_b}\right)_{int \geq 0}}}^{\infty} (X_{ca,(yN_s-h)} e^{-j(yN_s-h)\vartheta_m}) \bar{i}_\rho^* \right].$$

The mutual linked flux space vector produced by the armature winding and linked with the squirrel cage equivalent winding $\bar{\phi}_{mutual,h}$ (named $\bar{\phi}_{winding,h}$) can be written as (2.177):

$$\bar{\phi}_{winding,h} = \frac{2Nmpq\mu_0 RL}{\pi\delta} \sum_{\rho=0}^{N_s-1} \left[\sum_{\substack{y=0 \\ \left(\frac{yN_b+h-\rho}{N_s}\right)_{int \geq 0}}}^{\infty} (X_{ca,(yN_b+h)} e^{-j(yN_b+h)\vartheta_m}) \bar{i}_\rho + \sum_{\substack{y=0 \\ y \geq \left(\frac{h}{N_b}\right)_{int} \\ \left(\frac{yN_b-h-\rho}{N_s}\right)_{int \geq 0}}}^{\infty} (X_{ca,(yN_b-h)} e^{j(yN_b-h)\vartheta_m}) \bar{i}_\rho^* \right].$$

The resulting torque components (2.223) are given by (2.222) as:

$$T_{cage,h} = \Re \left\{ \sum_{\rho=0}^{N_b-1} \sum_{\substack{y=0 \\ \left(\frac{yn+h-\rho}{N_b}\right)_{int \geq 0}}}^{\infty} jK_{T,cage,y,h}^+ e^{j(yN_s+h)\vartheta_m} \bar{i}_{cage,\rho} \bar{i}_h^* \right\} + \Re \left\{ \sum_{\rho=0}^{N_b-1} \sum_{\substack{y=0 \\ y \geq \left(\frac{h}{N_s}\right)_{int} \\ \left(\frac{yn-h-\rho}{N_b}\right)_{int \geq 0}}}^{\infty} -jK_{T,cage,y,h}^- e^{-j(yN_s-h)\vartheta_m} \bar{i}_{cage,\rho} \bar{i}_h^* \right\},$$

with:

$$K_{T,cage,y,h}^+ = \frac{\mu_0 RLmpqNN_b}{\pi\delta} (yN_s + h) X_{ca,(yN_s+h)},$$

$$K_{T,cage,y,h}^- = \frac{\mu_0 RLmpqNN_b}{\pi\delta} (yN_s - h) X_{ca,(yN_s-h)}.$$

The main torque contributions are evaluated as:

$$T_{cage,h} = jK_{T,cage,0,h}^+ e^{jh\theta_m} \bar{i}_{cage,h} \bar{i}_h^* .$$

Force Equation

The eventual force effects can be evaluated by the proposed model, for all the rotor topologies, by (2.257):

$$\bar{F} = \frac{\pi\mu_0 R}{4} \int_0^L \sum_{h=1}^{\infty} [\bar{H}_h \bar{H}_{h-1}^* + \bar{H}_h^* \bar{H}_{h+1}] dz .$$

All the equations of the models presented in the next chapters refer to the model proposed in this one.

References:

- [1] A. Galassini, A. Costabeber, and C. Gerada, "Speed control for multi-three phase synchronous electrical motors in fault condition," in *IEEE EUROCON 2017 -17th International Conference on Smart Technologies*, 2017, pp. 698-703.
- [2] A. R. Munoz and T. A. Lipo, "Complex vector model of the squirrel-cage induction machine including instantaneous rotor bar currents," *IEEE Transactions on Industry Applications*, vol. 35, pp. 1332-1340, 1999.
- [3] H. A. Toliyat, S. P. Waikar, and T. A. Lipo, "Analysis and simulation of five-phase synchronous reluctance machines including third harmonic of airgap MMF," *IEEE Transactions on Industry Applications*, vol. 34, pp. 332-339, 1998.
- [4] G. Sala, "Controllo sensorless attuatori tubolari pentafase," Master's Degree Thesis in Electrical Energy Engineering [LM-DM270], Department of Electrical, Electronic and Information Engineering 'Guglielmo Marconi', University of Bologna, amslaurea, 2014.
- [5] G. Sala, D. Gerada, C. Gerada, and A. Tani, "Radial force control for triple three-phase sectorized SPM machines. Part II: Open winding fault tolerant control," in *2017 IEEE Workshop on Electrical Machines Design, Control and Diagnosis (WEMDCD)*, 2017, pp. 275-280.
- [6] S. Serri, A. Tani, and G. Serra, "Analytical model of radial forces considering mutual effects between torque and levitation current space vectors in 5-phase PM bearingless motors," in *IECON 2013 - 39th Annual Conference of the IEEE Industrial Electronics Society*, 2013, pp. 5142-5147.
- [7] C. L. Fortescue, "Method of Symmetrical Co-Ordinates Applied to the Solution of Polyphase Networks," *Transactions of the American Institute of Electrical Engineers*, vol. XXXVII, pp. 1027-1140, 1918.
- [8] G. Grandi, G. Serra, and A. Tani, "General Analysis of Multi-Phase Systems Based on Space Vector Approach," in *2006 12th International Power Electronics and Motion Control Conference*, 2006, pp. 834-840.
- [9] (October 2017). *Arnold Magnetic Technologies - RECOMA 35E*. Available: http://www.arnoldmagnetics.com/Portals/0/Files/Catalogs%20and%20Lit/Recoma/Arnold_DS_RECOMA35E_FINAL6.pdf?ver=2016-09-28-121046-147×tamp=1475079000706
- [10] A. Toba and T. A. Lipo, "Generic torque-maximizing design methodology of surface permanent-magnet vernier machine," *IEEE Transactions on Industry Applications*, vol. 36, pp. 1539-1546, 2000.
- [11] R. J. Strahan, "Energy conversion by nonlinear permanent magnet machines," *IEE Proceedings - Electric Power Applications*, vol. 145, pp. 193-198, 1998.

CHAPTER 3

Open Phase Faults and Fault Tolerant Controls in Multiphase Drives

The open phase fault is the most probable electric fault in electrical drives. More phases can open in the same time and the effect of the fault on the machine behaviour depends on the machine design and winding. An in-deep analysis of compensation algorithms for multiple open phase faults is carried out in this chapter considering Voltage Source Inverters (VSIs) feeding multiphase electrical machines.

In this chapter, the fault compensation is realised by means of a Fault Tolerant Control (FTC), generalized to whatever standard distributed winding multiphase machine under the following hypotheses:

- *The winding is not an open end-winding*
- *The phase number is odd, or it is a multiple of three*
- *The machine is symmetrical under each pole pair*

Simulations and experimental results are presented for the multi three-phase winding topology.

Open Phase faults in Electrical Drives

An open phase fault can appear on the converter side or on the machine side, as shown in Fig. 3.1 for a standard three-phase drive.

The breakdown of the switching devices or the activation of the drive active and passive protections can cause converter open phase faults. In particular, in case of missing of the control signals (Digital Signal Processor, DSP, failure) all the devices are generally open. A typical example is the desaturation protection that opens part of the switches in order to avoid dangerous short circuit currents.

The machine open phase faults are more likely related to the disconnection of the phases from the terminal box or from the switching devices (converter connections). This might happen

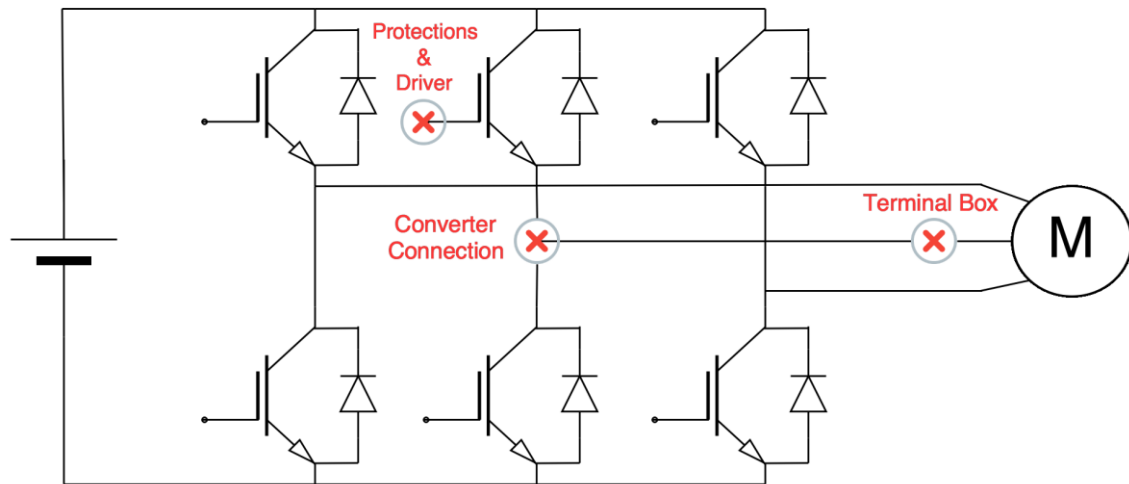


Fig. 3.1 – Open phase faults in a standard three-phase drive (most typical faults).

because of assembly mistakes or connections deterioration. Among the terminal box open phase faults, it is considered also the star connection failure. If the star connection is realised inside the housing and not in the terminal box (in this case it is usually in the end windings), this fault is often included in the winding fault category. However, this nomenclature might be misleading because the reader can easily think about a physical cut of the wires, which is quite improbable (this is the reason why here this fault is still considered under the category of terminal box faults).

The possibility to manage a phase opening is essential to prevent the failure of the drive control system and allows minimizing the performance derating. Furthermore, the proposed FTC allows controlling to zero the current in one or more phases by means of the same technique used to compensate the open phase fault. Zeroing the current in some phases gives the possibility to avoid the related copper losses and eventually disconnect these phases on purpose with a reduced effort.

As example, if a localized temperature increase is detected in one slot, the current flowing in that slot can be controlled to zero in order to avoid the accelerated ageing of the insulation in the slot and in general in the full system.

Furthermore, in case of a redundant layout of the winding and the converter (as in a multi three-phase configuration) it is possible to control to zero the currents of the phases connected to one converter in order to open them with a limited effort (the electric arc is theoretically avoided being the current in the phases equal to zero). Once the phases are open, the converter can be replaced or its maintenance can be easily carried out without an unscheduled stop of the system.

3.1 Open Phase Faults in Inverter Fed Multiphase Machines

This section presents the open phase faults in inverter fed multiphase machines. Before, considering for a fault in the connections of the phases and, then, in the switches of the inverter legs.

Terminal Box and Converter Connection Faults

The electric arc is not analysed in this work. Therefore, in case of a physical opening of an electrical connection, the transient needed for the current to become zero is neglected. Under this hypothesis, (2.89) gives the phase voltage equation for the analysed x -th phase, named as xf -th in order to highlight that the phase is the faulty one. Neglecting the mutual leakage inductances between different phases and considering all the phases having the same resistance and self-leakage inductance parameters, the voltage equation for the faulty phase can be written as:

$$v_{xf} = Ri_{xf} + Ll \frac{di_{xf}}{dt} + \frac{d\phi_{fx}}{dt}. \quad (3.1)$$

A physical open fault results in having a zero current in the faulty phase ($i_{xf} = 0$), therefore (3.1) can be rewritten as:

$$v_{xf} = \frac{d\phi_{fx}}{dt}. \quad (3.2)$$

This relationship allows modelling a machine with an opened phase. Because the electric arc is not modelled, the transient behaviour of the machine during the fault transient is simulated by an R-L response. A better analysis and simulation of the fault is not carried out in this work because the focus is posed on the control of the machine after the fault transient.

Protections and Drives

If the fault happens on a single switching device of a VSI in such a way that the current can flow only through its anti-parallel diode (this might happen because of the driver protections, as the the DeSat, or for a missing signal from the DSP), the resulting current is unipolar (it can flow only in one direction). In the next two paragraph, it is analysed what happens in case of open fault of one of the two switching devices (the top or the bottom one). Hereafter, with S_{top} and S_{bottom} are defined the states of the switches (“0” means that the considered switch is off, open circuit state, and “1” means that it is on, short circuit state).

Top switch open fault

The scheme in Fig. 3.2 allows easily explaining this fault behaviour for the fault of the top switch. If the fault happens when the current in the considered phase is positive (left in the figure), the current can only pass through the bottom diode as soon as the top switch is controlled as open (open fault). The equation that describes the phase behaviour is:

$$\begin{aligned} & \text{Fault} \\ & \text{with } \Rightarrow (S_{top} = 0) \Rightarrow 0 - v_{star} = Ri_{xf} + Ll \frac{di_{xf}}{dt} + \frac{d\phi_{fx}}{dt}, \\ & i_{xf} > 0 \end{aligned} \quad (3.3)$$

where v_{star} is the instantaneous potential of the neutral point (star connection) and “0” is the potential of the negative point of the dc bus (reference potential).

Once the current i_{xf} becomes zero and changes its sign (or if the fault happens when the current is already negative), it flows in the bottom switch, when it is on, or in the top diode, when the bottom switch is off (left in the figure). The phase equation is as the one of a standard VSI control:

$$\begin{aligned} & \text{Fault} \\ & \text{with } \Rightarrow \begin{cases} v_{dc} - v_{star} = Ri_{xf} + Ll \frac{di_{xf}}{dt} + \frac{d\phi_{fx}}{dt} \Leftrightarrow S_{bottom} = 0 \\ 0 - v_{star} = Ri_{xf} + Ll \frac{di_{xf}}{dt} + \frac{d\phi_{fx}}{dt} \Leftrightarrow S_{bottom} = 1 \end{cases} \\ & i_{xf} < 0 \end{aligned} \quad (3.4)$$

There is a particular machine behaviour when the current becomes again equal to zero and it wants to change its sign. Indeed, in order to make the current change its sign (from negative to positive), the needed phase voltage is:

$$v_{xf} \Big|_{i_{xf} < 0 \rightarrow i_{xf} > 0} > Ll \frac{di_{xf}}{dt} + \frac{d\phi_{fx}}{dt}. \quad (3.5)$$

However, if the current becomes positive it must flow on the bottom diode (because the top switch can only be open being in fault). Therefore, (3.5) results as in (3.3):

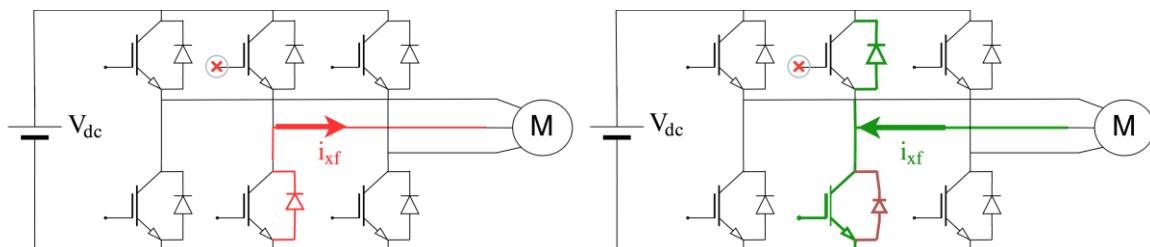


Fig. 3.2 – Single switching open fault scheme in case of a top driver protections or missing signal from the DSP fault. Transient behaviour of the fault with a positive current (left) and steady state behaviour (right).

$$(0 - v_{star}) \Big|_{i_{xf} < 0 \rightarrow i_{xf} > 0} > Ll \frac{di_{xf}}{dt} + \frac{d\phi_{fx}}{dt}. \quad (3.6)$$

This means that it must be verified the following relationship:

$$\left(v_{star} + Ll \frac{di_{xf}}{dt} + \frac{d\phi_{fx}}{dt} \right) \Big|_{i_{xf} < 0 \rightarrow i_{xf} > 0} < 0. \quad (3.7)$$

However, (3.7) is not verified if the uncontrolled generator behaviour is avoided and if the zero state of the three-phase inverter (in particular the zero state “0, 0, 0” that can lead to a three-phase short circuit configuration of the machine) is not commanded.

The analysis of the behaviour of the current when it becomes positive because (3.7) is true is not investigated.

Bottom switch open fault

The same analysis is done here for the failure of the bottom switch. The scheme in Fig. 3.3 allows easily explaining this fault behaviour. If the fault happens when the current in the considered phase is negative (left in the figure), the current can only pass through the top diode as soon as the bottom switch is controlled as open (open fault). The equation that describes the phase behaviour is:

$$\begin{aligned} & \text{Fault} \\ & \text{with } \Rightarrow (S_{bottom} = 0) \Rightarrow v_{dc} - v_{star} = Ri_{xf} + Ll \frac{di_{xf}}{dt} + \frac{d\phi_{fx}}{dt}, \\ & i_{xf} < 0 \end{aligned} \quad (3.8)$$

where v_{dc} is the potential of the positive point of the dc bus.

Once the current i_{xf} becomes zero and changes its sign (or if the fault happens when the current is already positive), it flows in the top switch, when it is on, or in the bottom, when the top switch is off (left in the figure). The phase equation is as the one of a standard VSI control:

$$\begin{aligned} & \text{Fault} \\ & \text{with } \Rightarrow \begin{cases} 0 - v_{star} = Ri_{xf} + Ll \frac{di_{xf}}{dt} + \frac{d\phi_{fx}}{dt} \Leftrightarrow S_{top} = 0 \\ v_{dc} - v_{star} = Ri_{xf} + Ll \frac{di_{xf}}{dt} + \frac{d\phi_{fx}}{dt} \Leftrightarrow S_{top} = 1 \end{cases} \\ & i_{xf} > 0 \end{aligned} \quad (3.9)$$

In order to make the current change its sign (from positive to negative) once the current becomes equal to zero, the needed phase voltage is:

$$v_{xf} \Big|_{i_{xf} > 0 \rightarrow i_{xf} < 0} < Ll \frac{di_{xf}}{dt} + \frac{d\phi_{fx}}{dt}. \quad (3.10)$$

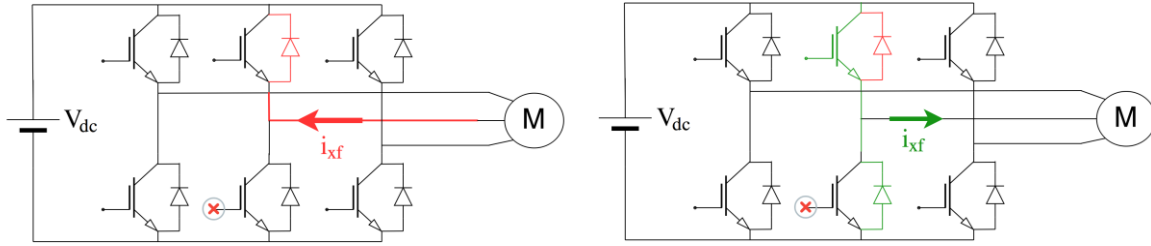


Fig. 3.3 – Single switching open fault scheme in case of a bottom driver protections or missing signal from the DSP fault. Transient behaviour of the fault with a positive current (left) and steady state behaviour (right).

If the current becomes negative it must flow on the top diode, and (3.10) results as in (3.8):

$$(v_{dc} - v_{star}) \Big|_{i_{xf} > 0 \rightarrow i_{xf} < 0} < Ll \frac{di_{xf}}{dt} + \frac{d\phi_{fx}}{dt}. \quad (3.11)$$

This means that it must be verified the following relationship:

$$\left(v_{star} + Ll \frac{di_{xf}}{dt} + \frac{d\phi_{fx}}{dt} \right) \Big|_{i_{xf} > 0 \rightarrow i_{xf} < 0} > v_{dc}. \quad (3.12)$$

However, (3.12) is not verified if the uncontrolled generator behaviour is avoided and if the zero state of the three-phase inverter (in particular the zero state “1, 1, 1” that can lead to a three-phase short circuit configuration of the machine) is not commanded.

The analysis presented for describing the open phase fault is approximated, but it well represents most of the machine working conditions.

Zero Current Control and Uncontrolled Generator Behaviour

Equation (3.2) describes the instantaneous phase voltage that is needed to keep the current in one phase equal to zero. The proposed control technique allows zeroing the current by the closed loop control and keeping it to zero. However, if the emf on the windings exceeds a threshold value (in particular if the phase to phase terminal voltage is higher than the dc link voltage) the inverter behaves like a three-phase rectifier, and neither a control nor the opening of the switches allows avoiding the generating current. This operating condition is named as Uncontrolled Generator (UCG). Mechanical circuit breakers might be used to ensure that this dangerous generating current is zero, or the converter protections must be designed in order to manage the power flow related to this uncontrolled current (back-to-back configuration, brake resistance, etc.).

3.2 Modelling and Fault Tolerant Control for Open Phase Faults

In this thesis, the proposed machine controls are based on the SVD approach. This means that the space vector theory presented in Chapter 1 is used to define the control algorithm. The theory behind the modelling of the fault is simplified in the development of the control algorithm, with the hypothesis that the current in the considered faulty phases suddenly reaches the zero value when the fault happens. This also means that as soon as the FTC turns on, it sets the reference current for the faulty phases equal to zero. Doing this, even in case of a false detection the FTC forces the phase current to zero in the analysed phases.

This section introduces the equations used to take into account for an open phase fault in the general model of a multiphase machine presented in Chapter 1. The idea of fault tolerant control is explained and a brief introduction to the open phase fault in three-phase machine is given. Then, the proposed fault tolerant control for multiphase machines is presented in its general shape.

Model of and Open Phase Fault

The constraint in the machine model and control of an open phase fault is simply as:

$$i_{xf} = 0, \quad (3.13)$$

for each of the open phases.

The inverse transformation for a general multiphase winding (2.54) allows writing (3.13) as:

$$i_{xf} = \frac{m}{2N_s} \sum_{h=0}^{N_s-1} \bar{i}_h \bar{\alpha}^{-h(xf-1)} = 0, \quad (3.14)$$

with \bar{i}_h the current space vector of the h-th space defined by (2.53) as:

$$\bar{i}_h = \frac{2}{m} \sum_{x=1}^{N_s} i_x e^{jh \frac{2\pi}{N_s}(x-1)}.$$

Indeed, as discussed in Chapter 2, the generalized model of an m -phase machine is developed by means of a redundant transformation in order to develop a unique theory and adapt it to different multiphase windings and layouts.

Open Phase Fault Tolerant Control (FTC) Concept

In a standard current control, the torque production is related to the interaction between the stator and rotor main harmonics of the magnetic field in the airgap. The general torque equation for an isotropic machine is the one given by (2.249) and reported here below:

$$T(\mathcal{G}_m) = \pi\mu_0 R \delta \int_0^L \sum_{h=1}^{\infty} \Re \left\{ jh \bar{H}_{stator,h}^* \bar{H}_{rotor,h,0} e^{jh\mathcal{G}_m} \right\} dz.$$

In a machine with p pole pairs, the fundamental harmonic is the p -th one (\bar{H}_p) and the main torque contribution is related to this field harmonic. Indeed, the models are often developed in electrical degrees considering only for this spatial harmonic. In case of fault, in order to generate the desired average torque, the fundamental harmonic must be maintained to the same values. Because this harmonic is related to the main current space vector \bar{i}_p by (2.47), the proposed FTC aims to take into account of the fault in order to keep the same p -th current space vector. To do this, the other current space vectors must be controlled according to (3.14). This result in the introduction of additional losses and torque components caused by the field harmonics related to the FTC of the other current space vectors. The FTC proposed here neglects these additional effects assuming that they are secondary when compared to the effect of the main field harmonic control.

Open Phase Fault in Three-Phase Electrical Drives

Most of the electrical drives are three-phase star connected ones. In this particular case of multiphase machines, the open phase fault theory is quite different from the one proposed for a general multiphase machine, because the main current space vector will never be maintained as in the healthy operation. Indeed, in order to generate a desired current space vector, at least two independent currents are needed. In case of only one degree of freedom in the currents, the current space vectors can move only on segments, making impossible to generate a FTC with reasonable performance. In literature there are FTC techniques for three-phase machines based on the control of the three-phases as independent windings, or on the control of the zero sequence current by means of an extended converter that has an additional leg for the control of the neutral point of the star connection [1, 2].

Because the aim of the work is to propose an in-deep analysis of the open phase faults in multiphase machines, the control is developed on the assumption that there are always enough degrees of freedom to completely generate the main current space vector (\bar{i}_p). In other words, the FTC is based on the hypothesis that there are at least three healthy phases connected to the same star or two pairs of phases connected to two different stars.

Open Phase Fault Tolerant Control in Multiphase Electrical Drives

In a multiphase machine, the main current space vector (\bar{i}_p) can be generally generated in an infinite ways both in the healthy and faulty behaviour. One particular and quite common solution is the one that aims to minimize the total copper losses in the stator windings [3-5].

The losses in the stator windings are defined by the relative term in (2.209), reported here below:

$$P_J = \frac{m^2}{4N_s} \left(R_s i_0^2 + R_s i_{\frac{N_s}{2}}^2 \right) + \frac{m^2}{4N_s} \sum_{\substack{h=1 \\ h \neq \frac{N_s}{2}}}^{N_s-1} R_s |\bar{i}_h|^2. \quad (3.15)$$

Introducing the vector of the current space vector components (\mathbf{i}_{vec}) it is possible to rewrite (3.15) in a suitable way for the solution of the problem as:

$$P_J = \frac{m^2}{4N_s} R_s \mathbf{i}_{vec} \mathbf{i}_{vec}^T, \quad (3.16)$$

with \mathbf{i}_{vec} equal to:

$$\mathbf{i}_{vec} = \left[i_0 \quad i_{\alpha 1} \quad i_{\beta 1} \quad i_{\alpha 2} \quad i_{\beta 2} \quad \dots \quad i_{\alpha p} \quad i_{\beta p} \quad \dots \quad \frac{i_{N_s}}{2} \quad \dots \quad i_{\alpha, N_s-1} \quad i_{\beta, N_s-1} \right]^T,$$

where “ T ” is the transposition operator.

The vector representing the current space vectors can be divided in two terms, the component related to the main current vector \mathbf{i}_p and the component that takes in to account of all the other auxiliary current space vectors \mathbf{i}_{aux} . They are defined as

$$\mathbf{i}_p = \left[i_{\alpha p} \quad i_{\beta p} \right]^T, \quad (3.17)$$

$$\mathbf{i}_{aux} = \left[i_{\alpha 1} \quad i_{\beta 1} \quad i_{\alpha 2} \quad i_{\beta 2} \quad \dots \quad i_{\alpha, p-1} \quad i_{\beta, p-1} \quad i_{\alpha, p+1} \quad i_{\beta, p+1} \quad \dots \quad i_{\alpha, N_s-1} \quad i_{\beta, N_s-1} \quad \frac{i_{N_s}}{2} \quad i_0 \right]^T,$$

where the two scalar space vectors are placed at the end of the vector because of their particular meanings.

The FTC equation (3.14) can be rewritten by the inverse transformation for a general multiphase winding, with $\bar{\alpha} = e^{j\frac{2\pi}{N_s}}$, as:

$$\frac{m}{2N_s} \sum_{h=0}^{N_s-1} \bar{i}_h e^{-j\frac{2\pi}{N_s}h(xf-1)} = 0. \quad (3.18)$$

In order to simplify the problem, hereafter only the current space vectors multiple of the pole pairs number (p) are considered, under the assumption that the machine can be analysed in electrical degrees ($p=1$). Therefore, the main current space vector becomes the first one. A further approximation is that for the analysed windings, it is possible to use only the odd electrical current space vectors in the definition of the inverse transformation (this is true in most of the multiphase symmetrical and asymmetrical machines as discussed in Chapter 1). Therefore, if the machine has a symmetrical winding with an odd number of phases N_s is equal to the number of phases (m) and if the machine has a standard asymmetrical winding with an even number of phases N_s is twice the number of phases ($2m$). Note that this approach is correct only if the machine transformation with the equivalent N_s variables is symmetrical and completely describes the machine behaviour. Under this hypothesis, even in case of an asymmetrical winding, the number of considered independent space vectors can be still identified with the odd vectors up to the m -th. With the new simplification, the FTC relationship between the current space vectors is defined rewriting (3.18), leaving only the main current vector components in the first member as:

$$\bar{i}_1 e^{-j\frac{2\pi}{N_s}(xf-1)} = \sum_{h \text{ odd}=3}^{m-1} \Re \left\{ \bar{i}_h e^{-j\frac{2\pi}{N_s}h(xf-1)} \right\}. \quad (3.19)$$

Note that the m -th space vector component in a machine with an odd number of phases represents the homopolar sequence. However, this component is always zero if the open end winding layout is not considered and all the phases are star connected (as in the analysed case).

Equation (3.19) can be defined for all the N_f faulty phases in matrix form as:

$$\mathbf{B}\mathbf{i}_1 + \mathbf{A}\mathbf{i}_{ham} = 0, \quad (3.20)$$

where the \mathbf{A} and \mathbf{B} matrixes are defined as:

$$\mathbf{B} = \begin{bmatrix} c_{1,1} & s_{1,1} \\ \dots & \dots \\ c_{1,xN_f} & s_{1,xN_f} \end{bmatrix}, \quad (3.21)$$

$$\mathbf{A} = \begin{bmatrix} c_{3,x1} & s_{3,x1} & c_{5,x1} & s_{5,x1} & \dots & c_{N_s-1,x1} & s_{N_s-1,x1} \\ \dots & \dots & \dots & \dots & \dots & \dots & \dots \\ c_{3,xN_f} & s_{3,xN_f} & c_{5,xN_f} & s_{5,xN_f} & \dots & c_{N_s-1,xN_f} & s_{N_s-1,xN_f} \end{bmatrix},$$

with $c_{h,xf}$ equal to $\cos(h\gamma xf)$, $s_{h,xf}$ equal to $\sin(h\gamma xf)$, and $\gamma = 2\pi/N_s$.

The copper Joule losses equation (3.16) can be written for the considered current space vector as:

$$P_f = \frac{m}{2} R_s \mathbf{i}_1^T \mathbf{i}_1 + \frac{m}{2} R_s \mathbf{i}_{aux}^T \mathbf{i}_{aux}, \quad (3.22)$$

with

$$\mathbf{i}_1 = [i_{\alpha 1} \quad i_{\beta 1}]^T,$$

$$\mathbf{i}_{aux} = [i_{\alpha 3} \quad i_{\beta 3} \quad i_{\alpha 5} \quad i_{\beta 5} \quad \dots \quad i_{\alpha, m-2} \quad i_{\beta, m-2}]^T \text{ if } m \text{ is odd,} \quad (3.23)$$

$$\mathbf{i}_{aux} = [i_{\alpha 3} \quad i_{\beta 3} \quad i_{\alpha 5} \quad i_{\beta 5} \quad \dots \quad i_{\alpha, m-1} \quad i_{\beta, m-1}]^T \text{ if } m \text{ is even.}$$

It is quite intuitive that in order to minimize the stator copper losses, the square values of the current space vectors must be minimized, but the problem must consider also the constraints related to the open phases (3.20) and the star connections.

In order to take into account for the constraints of the winding design (in terms of star connections), a new set of current space vectors (\mathbf{i}'_{aux}) is introduced.

$$\mathbf{i}_{aux} = \mathbf{C}_{aux} \mathbf{i}'_{aux}. \quad (3.24)$$

Note that (as mentioned above), hereafter the zero sequence is considered as zero because the open end-winding configuration is not analysed in this work.

Optimized FTC algorithm by means of the Lagrange multipliers method

The optimization problem can be solved by means of the Lagrange multipliers method. In particular, the aim of the problem is the minimization of the total stator copper losses.

By means of (3.22) and (3.20), the objective function of the Lagrange problem is:

$$L = \frac{m}{2} R_s \mathbf{i}_1^T \mathbf{i}_1 + \frac{m}{2} R_s \mathbf{i}'_{aux}{}^T \mathbf{i}_{aux} + \boldsymbol{\lambda}^T (\mathbf{B} \mathbf{i}_1 + \mathbf{A} \mathbf{i}_{aux}), \quad (3.25)$$

with $\boldsymbol{\lambda}$ the vector of the Lagrange multipliers ($\boldsymbol{\lambda} = [\lambda_\alpha \quad \lambda_\beta]^T$).

By means of (3.20), (3.24) and (3.25), the Lagrange multipliers method applied to the presented problem is based on the solution of the following system of equations:

$$\left\{ \begin{array}{l} \frac{\partial L}{\partial \mathbf{i}'_{aux}} = \frac{\partial \left(\frac{m}{2} R_s \mathbf{i}_1^T \mathbf{i}_1 + \frac{m}{2} R_s \mathbf{i}'_{aux}{}^T \mathbf{i}_{aux} + \boldsymbol{\lambda}^T (\mathbf{B} \mathbf{i}_1 + \mathbf{A} \mathbf{i}_{aux}) \right)}{\partial \mathbf{i}'_{aux}} = 0 \\ \mathbf{B} \mathbf{i}_1 + \mathbf{A} \mathbf{i}_{aux} = 0 \\ \mathbf{i}_{aux} = \mathbf{C} \mathbf{i}'_{aux} \end{array} \right. \quad (3.26)$$

where $\frac{\partial}{\partial \mathbf{i}'_{aux}}$ are the partial derivatives of the Lagrange function with respect to the α and β components of the auxiliary current space vectors.

Equation (3.26) can be reformulate as:

$$\begin{cases} \frac{m}{2} R_s \frac{\partial \left((\mathbf{C}\mathbf{i}'_{aux})^T \mathbf{C}\mathbf{i}'_{aux} \right)}{\partial \mathbf{i}'_{aux}} + \frac{\partial (\boldsymbol{\lambda}^T (\mathbf{A}\mathbf{C}\mathbf{i}'_{aux}))}{\partial \mathbf{i}'_{aux}} = 0 \\ \mathbf{B}\mathbf{i}_1 + \mathbf{A}\mathbf{i}'_{aux} = 0 \\ \mathbf{i}'_{aux} = \mathbf{C}\mathbf{i}'_{aux} \end{cases} \quad (3.27)$$

The first term of the equation system can be simplified as:

$$\begin{aligned} 0 &= \frac{m}{2} R_s \left[\mathbf{C}^T \mathbf{C}\mathbf{i}'_{aux} + \left((\mathbf{C}\mathbf{i}'_{aux})^T \mathbf{C} \right)^T \right] + (\boldsymbol{\lambda}^T \mathbf{A}\mathbf{C})^T = \\ &= \frac{m}{2} R_s \left[\mathbf{C}^T \mathbf{C}\mathbf{i}'_{aux} + \mathbf{C}^T \mathbf{C}\mathbf{i}'_{aux} \right] + (\mathbf{A}\mathbf{C})^T \boldsymbol{\lambda} = \\ &= mR_s \mathbf{C}^T \mathbf{C}\mathbf{i}'_{aux} + (\mathbf{A}\mathbf{C})^T \boldsymbol{\lambda}. \end{aligned} \quad (3.28)$$

It results that the auxiliary current space vectors are related to the Lagrange multipliers by:

$$\mathbf{i}'_{aux} = -\frac{1}{mR_s} (\mathbf{C}^T \mathbf{C})^+ (\mathbf{A}\mathbf{C})^T \boldsymbol{\lambda}, \quad (3.29)$$

where $^+$ is the pseudo inverse operator.

By the second equation of (3.27), the Lagrange multipliers can be evaluated by the following relationship:

$$\mathbf{B}\mathbf{i}_1 - \mathbf{A}\mathbf{C} \frac{1}{mR_s} (\mathbf{C}^T \mathbf{C})^+ (\mathbf{A}\mathbf{C})^T \boldsymbol{\lambda} = 0, \quad (3.30)$$

reformulated as:

$$\boldsymbol{\lambda} = mR_s \left(\mathbf{A}\mathbf{C}(\mathbf{C}^T \mathbf{C})^+ (\mathbf{A}\mathbf{C})^T \right)^+ \mathbf{B}\mathbf{i}_1. \quad (3.31)$$

Therefore, the system can be rewritten as:

$$\begin{cases} \boldsymbol{\lambda} = mR_s \left(\mathbf{A}\mathbf{C}(\mathbf{C}^T \mathbf{C})^+ (\mathbf{A}\mathbf{C})^T \right)^+ \mathbf{B}\mathbf{i}_1 \\ \mathbf{B}\mathbf{i}_1 + \mathbf{A}\mathbf{C}\mathbf{i}'_{aux} = 0 \\ \mathbf{i}'_{aux} = \mathbf{C}\mathbf{i}'_{aux} \end{cases} \quad (3.32)$$

Therefore, (3.29) results as:

$$\mathbf{i}'_{aux} = -(\mathbf{C}^T \mathbf{C})^+ (\mathbf{A} \mathbf{C})^T (\mathbf{A} \mathbf{C} (\mathbf{C}^T \mathbf{C})^+ (\mathbf{A} \mathbf{C})^T)^+ \mathbf{B} \mathbf{i}_1. \quad (3.33)$$

Equation (3.33) and the last of (3.32) allows evaluating the auxiliary current space vectors as:

$$\mathbf{i}_{aux} = \mathbf{C} \mathbf{i}'_{aux} = -\mathbf{C} (\mathbf{C}^T \mathbf{C})^+ (\mathbf{A} \mathbf{C})^T (\mathbf{A} \mathbf{C} (\mathbf{C}^T \mathbf{C})^+ (\mathbf{A} \mathbf{C})^T)^+ \mathbf{B} \mathbf{i}_1. \quad (3.34)$$

It is worth to notice that (3.34) can be adopted only if there are at least three healthy phases in the system (the number of open phases is lower than $m - 3$).

Healthy machine

For a healthy machine, the auxiliary current space vectors are independent from the main current space vector, and the solution that minimizes the stator copper losses is simply:

$$\mathbf{i}_{aux} = \mathbf{0}. \quad (3.35)$$

This means that in order to control the machine main current space vector (as in a standard FOC) with the lowest stator copper losses, the auxiliary current space vectors must be controlled to zero.

Open phase faults for symmetrical odd-phase machines with a single star

For a machine with an odd number of phases and a single star ($\mathbf{i}_{aux} = \mathbf{i}'_{aux}$ and \mathbf{C} is the identity matrix) and (3.34) can be simplified as:

$$\mathbf{i}_{aux} = -\mathbf{A}^T (\mathbf{A} \mathbf{A}^T)^{-1} \mathbf{B} \mathbf{i}_1. \quad (3.36)$$

In the easier case for which only the first phase (A1) is open, \mathbf{A} and \mathbf{B} are:

$$\mathbf{B} = [1 \ 0], \quad \mathbf{A} = [c_{3,1} \ s_{3,1} \ c_{5,1} \ s_{5,1} \ \dots \ c_{N_s-2,1} \ s_{N_s-2,1}]. \quad (3.37)$$

It is possible to verify that in this particular case, the FTC relationship becomes:

$$\mathbf{i}_{aux} = -\frac{2}{m-3} [1 \ 0 \ 1 \ 0 \ \dots \ 1 \ 0]^T i_{\alpha 1}. \quad (3.38)$$

The resulting auxiliary current space vectors are:

$$(i_{\alpha h} + j i_{\beta h}) = -\frac{2}{m-3} i_{\alpha 1}. \quad (3.39)$$

This case is a particular result, but it is interesting because all the other cases of single phase FTC for a multiphase machine with an odd number of phases and a single star can be identified by (3.39), with just a shift in the reference frame of the model in the position of the analysed faulty phase. Indeed, if the fault is in the xf -th phase, the relationship becomes [5]:

$$\bar{i}_h = i_{oh} + ji_{\beta h} = -\frac{2e^{-j\frac{2\pi}{m}h(xf-1)}}{m-3} \Re\left\{\bar{i}_1 e^{j\frac{2\pi}{m}h(xf-1)}\right\}. \quad (3.40)$$

However, in case of different star connections and in case of asymmetrical windings, also the case of a single-phase opening is not as easy as in a symmetrical odd-phase winding.

3.3 Current Sharing and Fault Tolerant Control for Independently Star Connected Multi Three-Phase Machines under Open Phase Faults

A typical solution of multiphase layout is the multi three-phase one, where there is a number of three-phase symmetrical windings shifted between each other in the stator slots. The multi three-phase configuration has the advantage that in terms of machine modelling, it can be analysed as the sum of the effects of multi three-phase subsystems.

The currents of each T -th three-phase subsystem can be completely described by their standard representation:

$$\bar{i}_{T1} = \frac{2}{3} \left(i_{T1} + i_{T2} e^{j\frac{2\pi}{3}} + i_{T3} e^{j\frac{4\pi}{3}} \right), \quad T = 1, 2, \dots, N_T, \quad (3.41)$$

and

$$i_{T0} = \frac{2}{3} (i_{T1} + i_{T2} + i_{T3}), \quad T = 1, 2, \dots, N_T, \quad (3.42)$$

or, alternatively, by the general transformation:

$$\bar{i}_{Th} = \frac{2}{3} \left(i_{T1} + i_{T2} e^{jh\frac{2\pi}{3}} + i_{T3} e^{jh\frac{4\pi}{3}} \right), \quad T = 1, 2, \dots, N_T, \quad (3.43)$$

with the relative inverse transformation:

$$i_{Tk} = \frac{i_{T0}}{2} + \Re\left\{\bar{i}_{T1} e^{-j\frac{2\pi}{3}(k-1)}\right\}, \quad k = 1, 2, 3, \quad T = 1, 2, \dots, N_T, \quad (3.44)$$

The space vector transformation allows easily defining the main and auxiliary current space vectors of the analysed machine as:

$$\bar{i}_h = \frac{2}{m} \sum_{T=1}^{N_T} \left(i_{T1} + i_{T2} e^{j\frac{2\pi}{3}} + i_{T3} e^{j\frac{4\pi}{3}} \right) e^{j\frac{2\pi}{N_s} h(x_T-1)} = \frac{1}{N_T} \sum_{T=1}^{N_T} \bar{i}_{Th} e^{j\frac{2\pi}{N_s} h(x_T-1)}, \quad (3.45)$$

where x_T represents the position of the first phase of each three-phase subsystem. If all the three-phase subsystems are independently star connected, all the current space vectors with an order multiple of three are zero. However, in some cases, it can be interesting to analyse also the machine behaviour when two or more three-phase subsystems (up to the single star configuration) are connected together. In this cases all the current space vectors must be taken into account. An in-deep analysis of the constraints caused by the star connections is done in the next section in order to show how it is possible to define a machine control that takes into account for them. Instead, this section focuses on the multi three-phase configuration (three-phase independent star connected subsystems).

Current sharing: concept

An interesting control for multi three-phase machines is the current sharing one. The idea is that, if it is possible to independently control the currents of the different three-phase subsystems, the total power requested from the load can be shared between the three-phase subsystems in a not equal distribution. For example, it is also possible to make some inverter work in generating mode while the others are supplying the machine with the power required by the load plus the one generated by the inverter which is generating (without considering the effect of this control on the overall losses). With this approach, the fault tolerant control in case of an open fault of one three-phase subsystem can be developed just setting to zero the reference currents (power) in input to the analysed subsystem. The next subsection presents the current sharing concept already existing in literature. The following subsection proposes a new improvement to this control algorithm. Finally, the method is applied for the compensation of one subsystem open phase fault.

Current Sharing for Independently Star Connected Three-Phase Subsystems

In a standard FOC of a multiphase machine, the main goal is the production of the requested main current space vector (\bar{i}_1). For a multi three-phase machine, the main current vector can be written by (3.45) as:

$$\bar{i}_1 = \frac{1}{N_T} \sum_{T=1}^{N_T} \bar{i}_{T1} e^{j\frac{2\pi}{N_s}(x_T-1)}. \quad (3.46)$$

The stator copper losses of each three-phase subsystem are given by (3.22) with only the main current space vector components. It is logical that the contribution of each three-phase current space vector must be in phase with the others (in particular in phase with the reference of the main current vector \bar{i}_1) in order to minimize the total stator copper losses. This concept is well

represented in Fig. 3.4, where the current space vectors of the three-phase subsystems are named with letters (A,B,C,D) to better distinguish them from the current space vectors that represents the full machine currents.

Considering only the fundamental current space vector in (3.22) allows writing the stator copper losses for the t -th three-phase subsystem as:

$$P_{J,T} = \frac{m}{2} R_s \bar{i}_{T1}^T \bar{i}_{T1} . \quad (3.47)$$

The total stator copper losses equation by (3.22) for typical odd symmetrical and even asymmetrical is:

$$P_J = \sum_{hodd=1}^{N_s} \frac{m}{2} R_s \bar{i}_h^T \bar{i}_h .$$

Alternatively, directly by the sum of the subsystem losses, (3.22) can be defined as:

$$P_J = \sum_{T=1}^{N_T} P_{J,T} = \sum_{T=1}^{N_T} \frac{3}{2} R_s \bar{i}_{T1}^T \bar{i}_{T1} . \quad (3.48)$$

According to the principle of losses minimization, it is possible to introduce a constant K for each three-phase subsystem that identifies how much the considered subsystem is involved in the production of the main current space vector (and therefore the machine power). By means of these new coefficients (K_T), named current sharing coefficients, (3.46) can be rewritten as:

$$\bar{i}_1 = \bar{i}_1 \sum_{T=1}^{N_T} K_T , \quad (3.49)$$

where the control assumption is that each three-phase current vector is controlled as:

$$\bar{i}_{T1} = N_T K_T \bar{i}_1 e^{-j \frac{2\pi}{N_s} (x_T - 1)} . \quad (3.50)$$

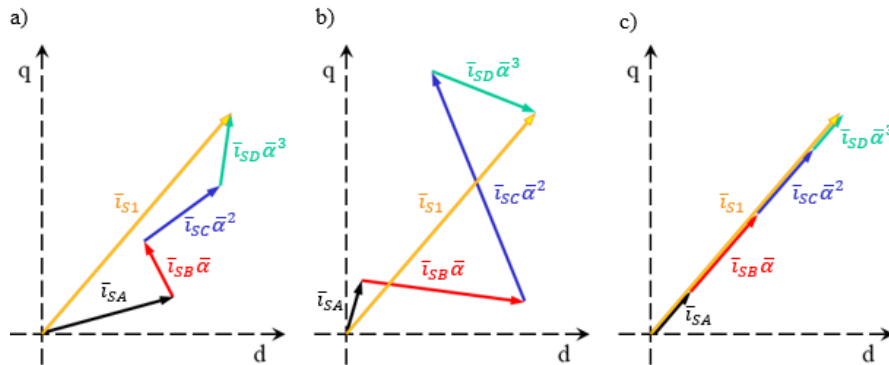


Fig. 3.4 – Schematic draw of the three-phase subsystem FTC. a) and b) show example of not optimized current controls, while c) shows the solution with the phase of the inverter current contributions that minimizes the stator Joule losses to maintain the same \bar{i}_{S1} value for a quadruple three-phase systems ($N_T=4$).

It is clear from (3.49) that the current sharing coefficients, as they are defined, must respect the following constraint:

$$\sum_{T=1}^{N_T} K_T = 1 . \quad (3.51)$$

Under this assumption, (3.45) evaluates all the auxiliary current space vectors. However, because of the properties of the three-phase transformation, (3.45) results in the following system of three equations:

$$\begin{cases} \bar{i}_h = \bar{i}_1 \left[\sum_{T=1}^{N_T} K_T e^{j \frac{2\pi}{N_s} (h-1)(x_T-1)} \right] \Leftrightarrow h = 3k + 1 \\ \bar{i}_h = \bar{i}_1^* \left[\sum_{T=1}^{N_T} K_T e^{j \frac{2\pi}{N_s} (h+1)(x_T-1)} \right] \Leftrightarrow h = 3k - 1 \\ \bar{i}_h = \left[\sum_{T=1}^{N_T} i_{T0} e^{j \frac{2\pi}{N_s} h(x_T-1)} \right] = 0 \Leftrightarrow h = 3k \end{cases} \quad (3.52)$$

The homopolar current space vector of each three-phase subsystem (i_{T0}) is not affected by the control of the main current space vector, therefore, even if there was not a constraint given by the star connections, the minimization of the losses would make it be controlled equal to zero when the machine is healthy. Furthermore, (3.48) and (3.49) allow writing the stator Joule losses as:

$$P_J = \frac{3}{2} \bar{i}_1^T \bar{i}_1 R_s \sum_{T=1}^{N_T} (N_T K_T)^2 . \quad (3.53)$$

The minimum value of the losses is given with all the same current sharing coefficient, equal to $K_T = K = \frac{1}{N_T}$. The resulting copper losses are equal to $P_J = \frac{3}{2} \bar{i}_1^T \bar{i}_1 R_s N_T$.

In different operating scenarios, the current sharing coefficients (K_T) can be controlled in order to make some of the three-phase subsystem work in positive torque operation ($K_T > 0$, motoring mode) and others in negative torque operation ($K_T < 0$, generating mode). In other words, the power of some three-phase subsystems can be positive while in other it is negative. This makes some of the power circulate between the three-phase subsystems without affecting the total power of the load, realising a power transfer between the different inverters. However, this result is quite valid in case of permanent magnet machines, while in case of induction machines a better current sharing control must be considered in order to minimize the losses. Indeed, part of the main current vector, the d-axis component in the reference frame of the rotor flux, is magnetizing current. Even if the magnetizing current is only related to the reactive power, the d-axis component of the main current vector generates losses and must be considered separately in a proper power sharing control of the machine.

Current Sharing for Independently Star Connected Three-Phase Subsystems (d-q axis control enhancement)

In order to take into account for the d-q FOC of the machine, the current sharing theory can be improved defining all the equations in the rotor field reference frame rewriting (3.46) as:

$$\bar{i}_1 = (i_d + j i_q) = \left(i_d \sum_{T=1}^{N_T} K_{Td} + j i_q \sum_{T=1}^{N_T} K_{Tq} \right), \quad (3.54)$$

where now the control assumption is that each three-phase current vector is controlled as:

$$\bar{i}_{T1} = N_T K_{Td} i_d e^{-j \frac{2\pi}{N_s} (x_T-1)} + j N_T K_{Tq} i_q e^{-j \frac{2\pi}{N_s} (x_T-1)}. \quad (3.55)$$

The current sharing coefficients must now respect the following constraints:

$$\sum_{T=1}^{N_T} K_{Td} = 1 \text{ and } \sum_{T=1}^{N_T} K_{Tq} = 1. \quad (3.56)$$

The auxiliary current space vectors can be now evaluated by the following equation system:

$$\left\{ \begin{array}{l} \bar{i}_h = i_d \sum_{T=1}^{N_T} K_{Td} e^{j \frac{2\pi}{N_s} (h-1)(x_T-1)} + j i_q \sum_{T=1}^{N_T} K_{Tq} e^{j \frac{2\pi}{N_s} (h-1)(x_T-1)} \Leftrightarrow h = 3k + 1 \\ \bar{i}_h = i_d \sum_{T=1}^{N_T} K_{Td} e^{j \frac{2\pi}{N_s} (h+1)(x_T-1)} - j i_q \sum_{T=1}^{N_T} K_{Tq} e^{j \frac{2\pi}{N_s} (h+1)(x_T-1)} \Leftrightarrow h = 3k - 1 \\ \bar{i}_h = \left[\sum_{T=1}^{N_T} i_{T0} e^{j \frac{2\pi}{N_s} h(x_T-1)} \right] = 0 \Leftrightarrow h = 3k \end{array} \right. \quad (3.57)$$

By (3.55) and (3.56) it is possible to implement a current sharing technique for the rotor flux control by the choice of the K_{Td} coefficients (for the rotor flux generation in IM or for flux weakening in PM machines), and for the torque and power production by the choice of the K_{Tq} coefficients. This allows minimizing the reactive power (and the related losses) by keeping for example all the K_{Td} coefficients equal to $K_{Td} = K_d = \frac{1}{N_T}$ and managing the input and output active power by the K_{Tq} coefficients.

In particular, having a negative K_{Td} coefficient only results in an increase of the reactive power asked from the T -th converter and by the others in order to compensate this negative effect. Therefore, the proposed current sharing control mainly aims to avoid negative d-axis current sharing values.

Open Phase FTC Algorithm for Independently Star Connected Three-Phase Subsystems

The easier approach in the definition of a FTC algorithm for a multi three-phase machine is based on the current sharing approach presented in the previous subsection.

The idea is that in case of an open phase fault in one of the three-phase subsystems, all its three phases are controlled to zero.

Although this thesis is focused on the development of FTC techniques for multiphase drives, it is worth to notice that it is a typical practice to develop converter devices based on a hardware fault communication. This means that if a fault is detected in the switching devices, it is possible that the logic circuits (or the controller) intervene to open the faulty leg of the inverter as in Fig. 3.5. Another possibility is that the protections open all the phases of the three-phase inverter as in Fig. 3.6. This second protection solution is the suitable one for a FTC control based on the multi three-phase current sharing theory.

Having a missing three-phase subsystem, or controlling its current to zero in order to protect the machine from a failure, results in the simple relationship:

$$K_f = 0, \quad (3.58)$$

where K_f is the current sharing coefficient that describes the faulty three-phase subsystem.

If all the other three-phase subsystems are controlled with the same amplitude (solution that minimizes the stator copper losses), in order to respect the constraint (3.51) the current sharing coefficients of the healthy phases must be:

$$K_T = \frac{1}{N_T - 1}. \quad (3.59)$$

If there are N_f faulty subsystem, the general relationship for the healthy subsystem is:

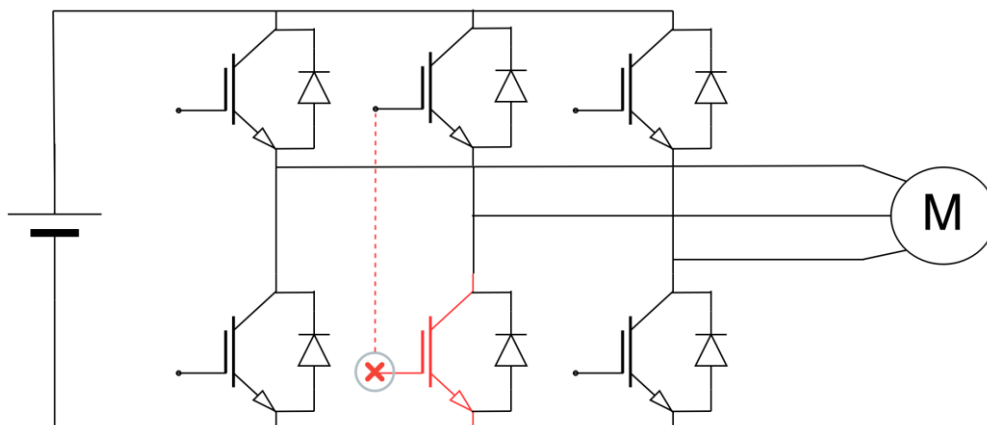


Fig. 3.5 – Logic for the fault protection on a single leg.

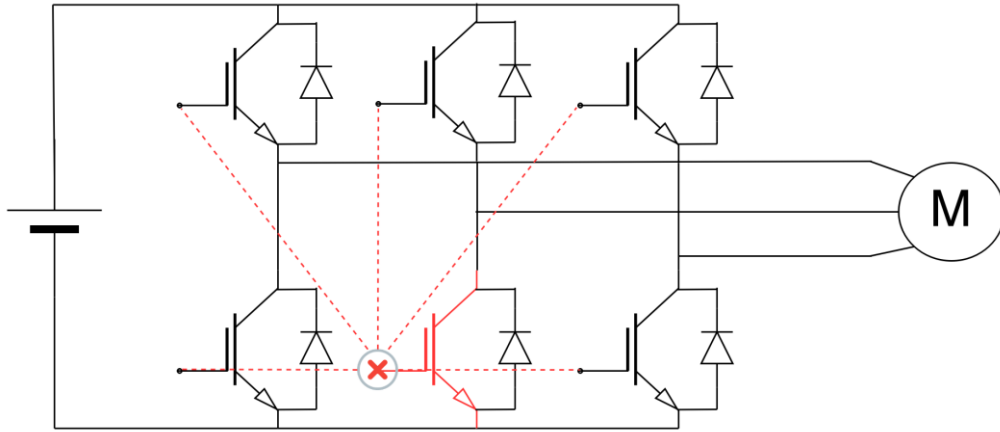


Fig. 3.6 – Full three-phase fault protection logic.

$$K_T = \frac{1}{N_T - N_f}. \quad (3.60)$$

In this optimized FTC, the references for the auxiliary current space vector, in a multi three-phase machine with independently star connected three-phase windings, can be evaluated as:

$$\left\{ \begin{array}{l} \bar{i}_h = \frac{\bar{i}_1}{N_T - N_f} \left[\sum_{T=1}^{N_T} e^{j \frac{2\pi}{N_s} (h-1)(x_T-1)} \right] \Leftrightarrow h = 3k + 1 \\ \bar{i}_h = \frac{\bar{i}_1^*}{N_T - N_f} \left[\sum_{T=1}^{N_T} K_T e^{j \frac{2\pi}{N_s} (h+1)(x_T-1)} \right] \Leftrightarrow h = 3k - 1 \\ \bar{i}_h = 0 \Leftrightarrow h = 3k \end{array} \right. \quad (3.61)$$

Equation (3.61) completely defines the optimized FTC control of a multi three-phase machine with independently star connected subsystems with an algorithm based on the disconnection of a full subsystem. This solution is the optimised one also for subsystems with more than three-phases (until they are done by symmetrical windings) and if the stars are connected to each other in whatever configuration. However, if only one phase is in fault, this algorithm open (or control to zero the currents) also the remaining healthy phases of the faulty subsystem. It is clear that some advantages can be expected by a FTC based on the exploitation of all the available degrees of freedom (healthy phase currents) of the faulty machine.

3.4 Improved Fault Tolerant Control for Multiphase Machines under Open Phase Faults

In section 3.2 the proposed FTC, optimized for the stator copper losses, has been extended to a general multiphase machine with an odd number of phases and a single star connection. In section 3.3, a simplified method, based on the current sharing approach, has been proposed to manage a fault in a multi three-phase machine by disconnecting the faulty three-phase subsystems.

In this section, the generalized method based on the Lagrange multipliers is analysed for multi three-phase windings with whatever star connection configuration.

The results are generalised to the most common star configurations and for whatever number of faulty phases (up to $m-3$).

Optimized FTC Algorithm by means of the Lagrange Multipliers method for Multi Independently Star Connected n -Phase Subsystems (n odd)

The theory developed in the previous section 3.3 can be extended to the improved optimized FTC proposed in section 3.2 by taking into account of the connection constraints represented by the \mathbf{C} matrix.

The general FTC equation (3.34) is reported here below:

$$\mathbf{i}_{aux} = \mathbf{C}\mathbf{i}'_{aux} = -\mathbf{C}(\mathbf{C}^T\mathbf{C})^+(\mathbf{AC})^T(\mathbf{AC}(\mathbf{C}^T\mathbf{C})^+(\mathbf{AC})^T)^+\mathbf{B}\mathbf{i}_l.$$

The definition of the \mathbf{A} and \mathbf{B} matrixes is clear, but how to define the constraints of the current space vectors in relation with the star connections is in general quite challenging.

The star connection constraints in multi n -phase systems are well represented by relationships between the homopolar current space vectors of the various n -phase subsystems. In case of independently star connected symmetrical n -phase subsystems (therefore with n an odd number), (3.45) can be generalized to define the space vector constraints as:

$$\bar{i}_h = \frac{1}{N_T} \left[\sum_{T=1}^{N_T} i_{T0} e^{j\frac{2\pi}{N_s} h(x_T-1)} \right] = 0 \Leftrightarrow h = nk, \quad (3.62)$$

where in case of multi three-phase windings n is equal to three.

In terms of \mathbf{C} matrix, (3.62) is equal to impose:

$$\mathbf{C}_{(n-2)+2n(x-1),(n-2)+2n(x-1)} = 0, \quad \mathbf{C}_{(n-1)+2n(x-1),(n-1)+2n(x-1)} = 0, \quad (3.63)$$

with x up to half the number of subsystems (n -phase windings).

If the subsystems are star connected between each other, the evaluation of the **C** matrix becomes challenging. Because having more than three phases for each subsystem is not common, hereafter the analysis focuses on the multi three-phase windings. The possible star configuration in a multi three-phase winding are limited. As example, Fig. 3.7 shows the most common star configurations for a quadruple three-phase winding.

Optimized FTC Algorithm by means of the Lagrange Multipliers method for Multi Three-Phase Subsystems Connected to a Single Star

In case of a single star connection, there are two typical winding configurations: the symmetrical one (with an odd number of phases) and the asymmetrical one (with an even number of phases). The first solution has already be presented in section 3.2, being the direct result of the FTC algorithm once the possibility of having an open end-winding configuration is neglected. This case is easy because the star constraint can be easily defined by considering the zero current space vector (homopolar component of the full machine) equal to zero.

Instead, in case of an even number of three-phase subsystems the single star constraint is more complex to be defined.

Single-star even-phase asymmetrical multi three-phase windings

The single star constraint for a multi three-phase winding with an even number of phases can be defined as:

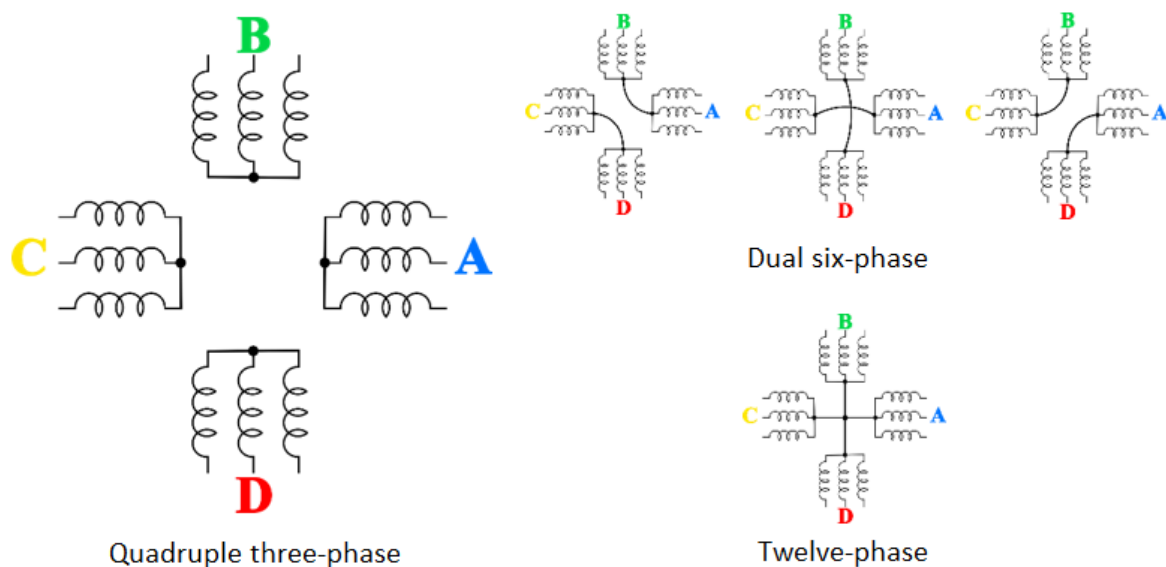


Fig. 3.7 – Typical star configurations for a quadruple three-phase winding.

$$\sum_{T=1}^{N_T} i_{T0} = 0. \quad (3.64)$$

Because the FOC aims to control the main current space vector (\bar{i}_1 for a model developed in electrical degrees), the suitable inverse transformation for an asymmetrical even-phase machine is the one that takes into account for only the odd space vectors, as in (2.20) with the transformation constant (C) equal to 4. The current inverse transformation for a typical even phase asymmetrical machine is reported here below:

$$i_k = \sum_{h_{\text{odd}}=1,3,\dots}^{m-1} \Re\{\bar{i}_h \bar{\alpha}^{-h(k-1)}\}, \quad (3.65)$$

with $\bar{\alpha} = e^{j\frac{2\pi}{N_s}}$ and $N_s = 2m$.

Because the model, the control and the losses are easily defined for the inverse transformation with the odd current space vectors, the single star constraint cannot be written as for a symmetrical odd-phase winding ($i_0 = 0$). Indeed this component is related to an even space vector. The constraint is more complex to be considered. In particular, the odd current space vectors related to the zero sequences of the three-phase subsystems are defined by (3.62) with n equal to 3 and k an odd number as:

$$\bar{i}_h = \frac{1}{N_T} \left[\sum_{T=1}^{N_T} i_{T0} e^{j\frac{2\pi}{N_s} h(x_T-1)} \right] \Leftrightarrow h = 3k_{\text{odd}}. \quad (3.66)$$

Because the inverse transformation (2.20) takes into account for a number of variables (in terms of current space vectors) equal to the degrees of freedom of the system (the currents), the star connection constraints are completely defined by the odd current space vector multiple of 3 in (2.20). The homopolar current space vector of each three-phase subsystem can be derived by a suitable inverse transformation related to these current space vectors.

It is possible to write (2.20) in matrix form as:

$$\mathbf{i}_{\text{star,even}} = \mathbf{G} \mathbf{i}_{T0}, \quad (3.67)$$

with:

$$\mathbf{i}_{\text{star,even}} = \begin{bmatrix} i_{S3,\alpha} & i_{S3,\beta} & i_{S9,\alpha} & i_{S9,\beta} & \cdots & i_{S \max(3k_{\text{odd}}),\alpha} & i_{S \max(3k_{\text{odd}}),\beta} \end{bmatrix}^T, \\ \mathbf{i}_{T0} = \begin{bmatrix} i_{10} & \cdots & i_{N_T0} \end{bmatrix}^T,$$

and:

$$\mathbf{G}_{r_{\text{odd}},c} = \frac{1}{N_T} \cos\left(\frac{2\pi}{N_s} 3r_{\text{odd}}(c-1)\right), \quad (3.68)$$

$$\mathbf{G}_{r_{odd}+1,c} = \frac{1}{N_T} \sin\left(\frac{2\pi}{N_S} 3r_{odd}(c-1)\right),$$

with r the row number and c the column number. Is it worth to notice that the vector of the current space components and the one of the three-phase homopolar currents have always the same dimension. Therefore, the inverse of the \mathbf{G} matrix allows evaluating the three-phase homopolar currents as function of the related current space vectors as:

$$\mathbf{i}_{T0} = \mathbf{G}^{-1} \mathbf{i}_{star,even}, \quad (3.69)$$

The star connection constraint (3.64) can be written for a single star winding as:

$$\sum_{T=1}^{N_T} i_{T0} = [\mathbf{ones}(N_T)]^T \mathbf{i}_{T0} = [\mathbf{ones}(N_T)]^T \mathbf{G}^{-1} \mathbf{i}_{star,even} = 0, \quad (3.70)$$

with $[\mathbf{ones}(N_T)]^T$ the transpose of a vector of N_T ones.

Equation (3.70) allows writing the single-star constraint by setting one component, the x -th, of the current space vectors (the related to the three-phase homopolar currents ones) in function of the others as:

$$\sum_{T=1}^{N_T} [\mathbf{G}^{-1}]_{r,x} \mathbf{i}_{star,even,x} = - \sum_{\substack{y=1 \\ y \neq x}}^{N_T} \sum_{T=1}^{N_T} [\mathbf{G}^{-1}]_{r,y} \mathbf{i}_{star,even,y}, \quad (3.71)$$

resulting in the space vector constraint:

$$\mathbf{i}_{star,even,x} = - \sum_{\substack{y=1 \\ y \neq x}}^{N_T} \frac{\sum_{T=1}^{N_T} [\mathbf{G}^{-1}]_{r,y}}{\sum_{T=1}^{N_T} [\mathbf{G}^{-1}]_{r,x}} \mathbf{i}_{star,even,y}. \quad (3.72)$$

This constraint for the star connection matrix (\mathbf{C}) used to evaluate (3.34) results as:

$$\mathbf{C}_{1+6(x-1),1+6(y-1)} = - \frac{\sum_{T=1}^{N_T} [\mathbf{G}^{-1}]_{r,y}}{\sum_{T=1}^{N_T} [\mathbf{G}^{-1}]_{r,x}}, \quad \mathbf{C}_{1+6(x-1),2+6(y-1)} = - \frac{\sum_{T=1}^{N_T} [\mathbf{G}^{-1}]_{r,y+1}}{\sum_{T=1}^{N_T} [\mathbf{G}^{-1}]_{r,x}}, \quad (3.73)$$

$$\mathbf{C}_{1+6(x-1),1+6(x-1)} = 0,$$

setting a constraint on the α component of the x -th current space vector related to the three-phase homopolar currents, or:

$$\mathbf{C}_{2+6(x-1),1+6(y-1)} = -\frac{\sum_{T=1}^{N_T} [\mathbf{G}^{-1}]_{T,y}}{\sum_{T=1}^{N_T} [\mathbf{G}^{-1}]_{T,x}}, \quad \mathbf{C}_{2+6(x-1),2+6(y-1)} = -\frac{\sum_{T=1}^{N_T} [\mathbf{G}^{-1}]_{T,y+1}}{\sum_{T=1}^{N_T} [\mathbf{G}^{-1}]_{T,x}}, \quad (3.74)$$

$$\mathbf{C}_{2+6(x-1),2+6(x-1)} = 0,$$

setting a constraint on the β component of the x -th current space vector related to the three-phase homopolar currents .

The choice of the x -th current space vector that is used to set the constraint for the single-star connection is arbitrary, but only one component of this current space vector must be chosen, because the constraint must be unique. Indeed, the single star result in the loss of only one degree of freedom in the current control. Therefore, only one equation must be added as constraint to the solution of the problem.

If there are more stars, there must be an independent equation (constraint) for each of them.

Optimized FTC Algorithm by means of the Lagrange Multipliers method for Multi-Star Connected Three-Phase Subsystems

The approach used to take into account for the single-star connection can be generalized to consider different star connections in multi three-phase machines. A general constraint equation system has not been found, but the methodology for defining it according to the analysed winding is presented hereafter.

Multi-star multi three-phase windings

The star connection constraint for a machine with an odd number of phases can be defined as done for the single star analysis in case of an even number of phases, just considering also the homopolar current i_0 . The star connection constraints can still be identified by means of (3.67), reported here below:

$$\mathbf{i}_{star} = \mathbf{G}\mathbf{i}_{T0}. \quad (3.75)$$

In case of an odd number of three-phase subsystems, there is just the additional constraint related to the homopolar current component of the full system (i_0). Therefore, the vector of the space vectors related to the homopolar currents of the three-phase subsystems is:

$$\mathbf{i}_{star,odd} = \begin{bmatrix} i_0 & i_{3,\alpha} & i_{3,\beta} & i_{9,\alpha} & i_{9,\beta} & \cdots & i_{\max(3k_{odd} \neq m),\alpha} & i_{\max(3k_{odd} \neq m),\beta} \end{bmatrix}^T.$$

The constraint for each Sx -th star connected system is:

$$i_{Sx0} = \sum_{T=1}^{N_{TSx}} i_{TSx0} = 0, \quad (3.76)$$

that can be written making explicit the equation for the k -th three-phase subsystem of the Sx -th star connected system as:

$$i'_{kSx,0} = - \sum_{\substack{T=1 \\ T \neq k}}^{N_{TSx}} i_{TSx0}. \quad (3.77)$$

This means that considering (3.75), it is possible to evaluate the star connection relationships for each z -th component as:

$$\mathbf{i}_{star,k} = \mathbf{G}_{z,(1:N_T)} \mathbf{i}_{T0}. \quad (3.78)$$

If (3.77) is taken into account, the previous equation results as:

$$\mathbf{i}_{star,k} = \mathbf{G}_{z,(1:N_T)} \mathbf{i}'_{T0}, \quad (3.79)$$

where \mathbf{i}'_{T0} is considered as the modified vector of three-phase homopolar currents described as:

$$\mathbf{i}'_{T0} = \begin{bmatrix} i_{10} & i_{20} & \dots & i_{n-1,0} & i'_{n,0} & i_{n+1,0} & \dots & i_{N_T,0} \end{bmatrix}^T,$$

where (3.77) describes a modified vector for each star connection. In matrix form, this relationship can be written as:

$$\mathbf{i}'_{T0} = \mathbf{Z} \mathbf{i}_{T0}, \quad (3.80)$$

with \mathbf{Z} a matrix defined as an identity matrix with a zero on the main diagonal for each star (on the row related to one of the star connected three-phase subsystem, n -th), for which the elements on the other columns are -1 for all the three-phase subsystems connected to the same star (n -th).

It result that

$$\mathbf{i}_{star} = \mathbf{G} \mathbf{i}'_{T0} = \mathbf{G} \mathbf{Z} \mathbf{i}_{T0} = \mathbf{H} \mathbf{i}''_{T0}, \quad (3.81)$$

where \mathbf{H} is the $\mathbf{G} \mathbf{Z}$ matrix without the n -th columns of the homopolar components that have been written as function of the others, and \mathbf{i}''_{T0} is the vector of the homopolar components neglecting the ones written as function of the others by (3.77). Therefore, \mathbf{H} is a $(N_T; N_T - N_S)$ matrix and \mathbf{i}''_{T0} is a $(N_S; 1)$ column vector.

For each star (but the ones with a single three-phase subsystem connected to the star), it is possible to find one redundant set of equations in the relationships between the three-phase homopolar currents and the related current space vectors. By properly choosing the redundant equations set, it is possible to identify in (3.81) two systems of relationships like:

$$\begin{cases} \mathbf{i}_{star,1} = \mathbf{H}_1 \mathbf{i}''_{T0} \\ \mathbf{i}_{star,2} = \mathbf{H}_2 \mathbf{i}''_{T0} \end{cases} \quad (3.82)$$

One of the two matrixes (\mathbf{H}_2) must be a $(N_T - N_S ; N_T - N_S)$ invertible one, and its relative vector of the current components ($\mathbf{i}_{star,2}$) is a $(N_T - N_S ; 1)$ one.

The final constraint equation can be found as:

$$\mathbf{i}_{star,1} = \mathbf{H}_1 (\mathbf{H}_2)^{-1} \mathbf{i}_{star,2}. \quad (3.83)$$

Indeed, the number of constraints (dimension of the $\mathbf{i}_{star,1}$ vector) is N_S and the related matrix (\mathbf{H}_1) is a $(N_T - N_S ; N_S)$ one.

Here below the method is applied for multi three-phase machines up to 12 phases (quadruple three-phase configuration).

Optimized Open Phase FTC Algorithm for a dual three-phase winding (star connection constraints)

A six-phase machine has usually a double three-phase winding that can be connected in a single star or in a double star configuration. The winding is composed of two three-phase subsystems shifted by 30 electrical degrees. The model is based on a 12 phase symmetrical winding where half of the phases do not exist, and therefore the space vectors are defined by a 12-phase symmetrical transformation.

A schematic example of a standard dual three-phase drive is shown in Fig. 3.8, where also the magnetic axes of the machine are highlighted.

The currents of the two three-phase subsystems (A and B) can be described by the relative space vector representation by (3.41) and (3.42) as:

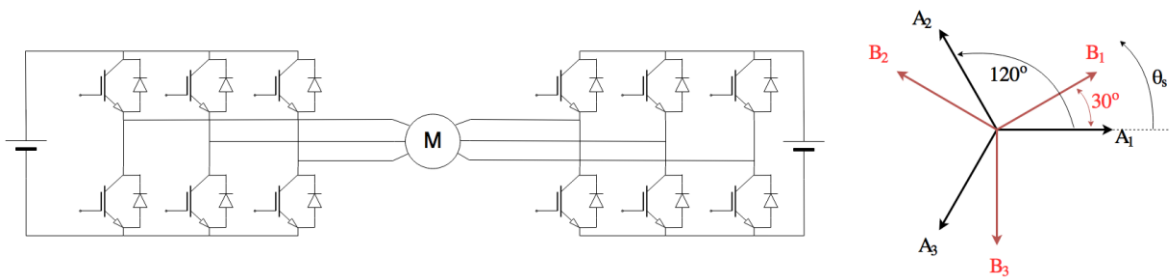


Fig. 3.8 – Double three-phase standard drive and relative magnetic axis directions.

$$\bar{i}_{T1} = \frac{2}{3} \left(i_{T1} + i_{T2} e^{j\frac{2\pi}{3}} + i_{T3} e^{j\frac{4\pi}{3}} \right), \quad T = A, B,$$

and

$$i_{T0} = \frac{2}{3} (i_{T1} + i_{T2} + i_{T3}), \quad T = A, B,$$

The current space vectors related to the three-phase homopolar current components are defined by the relationship (3.75):

$$\mathbf{i}_{star} = \mathbf{G} \mathbf{i}_{T0},$$

with $\mathbf{i}_{star} = [i_{3,\alpha} \ i_{3,\beta}]^T$, $\mathbf{i}_{T0} = [i_{A0} \ i_{B0}]^T$ and the G matrix given by (3.68) is:

$$\mathbf{G} = \begin{bmatrix} \frac{1}{2} & \frac{1}{2} \cos\left(\frac{2\pi}{12} 3\right) \\ 0 & \frac{1}{2} \sin\left(\frac{2\pi}{12} 3\right) \end{bmatrix}.$$

Independent Stars

In case of independent stars, the \mathbf{Z} matrix defined in (3.80) is:

$$\mathbf{Z} = \begin{bmatrix} 0 & 0 \\ 0 & 0 \end{bmatrix}.$$

Therefore (3.81) results as:

$$\mathbf{i}_{star} = \mathbf{G} \mathbf{Z} \mathbf{i}_{T0} = \begin{bmatrix} 0 & 0 \\ 0 & 0 \end{bmatrix} \mathbf{i}_{T0} = \begin{bmatrix} 0 \\ 0 \end{bmatrix}.$$

The solution of the system (3.82) is:

$$\begin{cases} i_{3,\alpha} = 0 \\ i_{3,\beta} = 0 \end{cases}$$

The constraints on the \mathbf{C} matrix (originally an identity one) are given as:

$$\mathbf{C}_{1+6(x-1), 1+6(x-1)} = 0, \quad x = 1, \dots, N_S,$$

$$\mathbf{C}_{2+6(x-1), 2+6(x-1)} = 0, \quad x = 1, \dots, N_S,$$

that means:

$$\mathbf{C}_{1,1} = 0 \quad \mathbf{C}_{2,2} = 0. \quad (3.84)$$

Single Star

In case of a single star, the \mathbf{Z} matrix defined in (3.80) is:

$$\mathbf{Z} = \begin{bmatrix} 1 & 0 \\ -1 & 0 \end{bmatrix}.$$

Therefore (3.81) results as:

$$\mathbf{i}_{star} = \mathbf{GZ} \mathbf{i}_{T0} = \begin{bmatrix} \frac{1}{2} & 0 \\ 0 & \frac{1}{2} \end{bmatrix} \begin{bmatrix} 1 & 0 \\ -1 & 0 \end{bmatrix} \mathbf{i}_{T0} = \begin{bmatrix} \frac{1}{2} & 0 \\ -\frac{1}{2} & 0 \end{bmatrix} \mathbf{i}_{T0}.$$

The solution of the system (3.82) is:

$$\begin{cases} i_{3,\alpha} = \mathbf{H}_1 i_{A0} = \frac{i_{A0}}{2} \\ i_{3,\beta} = \mathbf{H}_2 i_{A0} = -\frac{i_{A0}}{2} \end{cases}$$

Note that the constraint can be defined in two ways, but in order to define the same result given by (3.73), \mathbf{H}_1 and \mathbf{H}_2 are chosen in a suitable way. If the other solution is chosen, the constraint is defined as in (3.74).

The final constraint equation (3.83) is:

$$i_{3,\alpha} = \mathbf{H}_1 (\mathbf{H}_2)^{-1} i_{3,\beta} = \frac{1}{2} \left(-\frac{1}{2} \right)^{-1} i_{3,\beta} = -i_{3,\beta}.$$

The constraint on the \mathbf{C} matrix (originally an identity one) is given as:

$$\mathbf{C}_{1,1} = 0 \quad \mathbf{C}_{2,2} = 0 \quad \mathbf{C}_{1,2} = -1. \quad (3.85)$$

Optimized Open Phase FTC Algorithm for a triple three-phase winding (star connection constraints)

A nine-phase machine has usually a triple three-phase winding, which can be connected in a single star or in a double star configuration, however here only a particular solution with two stars is presented. The symmetrical winding layout is composed of three three-phase

CHAPTER 3

subsystems shifted by 40 electrical degrees (the resulting model is based on a 9-phase symmetrical winding, and therefore a 9-phase symmetrical transformation).

A schematic example of a symmetrical triple three-phase drive is shown in Fig. 3.9, where also the magnetic axes of the machine are highlighted.

The currents of the three three-phase subsystems (A, B and C) can be described by the relative space vector representation by (3.41) and (3.42) as:

$$\bar{i}_{T1} = \frac{2}{3} \left(i_{T1} + i_{T2} e^{j\frac{2\pi}{3}} + i_{T3} e^{j\frac{4\pi}{3}} \right), \quad T = A, B, C,$$

and

$$i_{T0} = \frac{2}{3} (i_{T1} + i_{T2} + i_{T3}), \quad T = A, B, C,$$

The current space vectors related to the three-phase homopolar current components are defined by the relationship (3.75)

$$\mathbf{i}_{star} = \mathbf{G} \mathbf{i}_{T0},$$

with:

$$\mathbf{i}_{star} = [i_{3,\alpha} \quad i_{3,\beta} \quad i_0]^T,$$

$$\mathbf{i}_{T0} = [i_{A0} \quad i_{B0} \quad i_{C0}]^T,$$

and the G matrix given by (3.68) as:

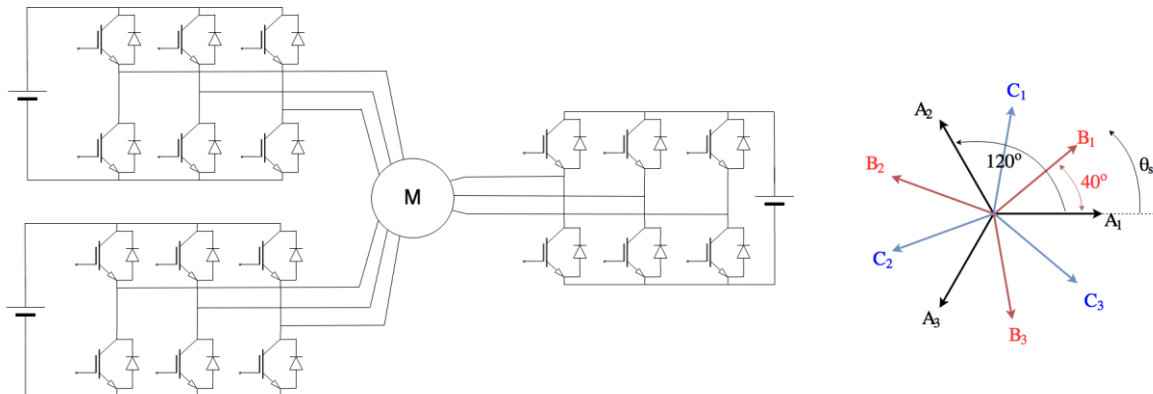


Fig. 3.9 – Triple three-phase standard drive and relative magnetic axis directions.

$$\mathbf{G} = \begin{bmatrix} \frac{1}{3} & \frac{1}{3} \cos\left(\frac{2\pi}{9}3\right) & \frac{1}{3} \cos\left(\frac{2\pi}{9}6\right) \\ 0 & \frac{1}{3} \sin\left(\frac{2\pi}{9}3\right) & \frac{1}{3} \sin\left(\frac{2\pi}{9}6\right) \\ \frac{1}{3} & \frac{1}{3} \cos\left(\frac{2\pi}{9}9\right) & \frac{1}{3} \cos\left(\frac{2\pi}{9}18\right) \end{bmatrix} = \begin{bmatrix} \frac{1}{3} & \frac{1}{3} \cos\left(\frac{2\pi}{9}3\right) & \frac{1}{3} \cos\left(\frac{2\pi}{9}6\right) \\ 0 & \frac{1}{3} \sin\left(\frac{2\pi}{9}3\right) & \frac{1}{3} \sin\left(\frac{2\pi}{9}6\right) \\ \frac{1}{3} & \frac{1}{3} & \frac{1}{3} \end{bmatrix}.$$

Independent Stars

In case of independent stars, the \mathbf{Z} matrix defined in (3.80) is:

$$\mathbf{Z} = \begin{bmatrix} 0 & 0 & 0 \\ 0 & 0 & 0 \\ 0 & 0 & 0 \end{bmatrix}.$$

Therefore (3.81) results as:

$$\mathbf{i}_{star} = \mathbf{GZ} \mathbf{i}_{T0} = \begin{bmatrix} 0 & 0 & 0 \\ 0 & 0 & 0 \\ 0 & 0 & 0 \end{bmatrix} \mathbf{i}_{T0} = \begin{bmatrix} 0 \\ 0 \\ 0 \end{bmatrix}.$$

The solution of the system (3.82) is:

$$\begin{cases} i_{3,\alpha} = 0 \\ i_{3,\beta} = 0 \\ i_0 = 0 \end{cases}$$

The constraint on the \mathbf{C} matrix (originally an identity one) are:

$$\begin{aligned} \mathbf{C}_{1+6(x-1),1+6(x-1)} &= 0, & x &= 1, \dots, N_s, \\ \mathbf{C}_{2+6(x-1),2+6(x-1)} &= 0, & x &= 1, \dots, N_s - 1, \end{aligned}$$

where the second relationship is evaluated up to the $N_s - 1$ -th element because the homopolar space vector does not have an imaginary part, that means:

$$\mathbf{C}_{1,1} = 0, \quad \mathbf{C}_{2,2} = 0, \quad \mathbf{C}_{7,7} = 0. \quad (3.86)$$

Single Star

CHAPTER 3

In case of a single star, the \mathbf{Z} matrix defined in (3.80) is:

$$\mathbf{Z} = \begin{bmatrix} 1 & 0 & 0 \\ 0 & 1 & 0 \\ -1 & -1 & 0 \end{bmatrix}.$$

Therefore (3.81) results as:

$$\mathbf{i}_{star} = \mathbf{GZ} \mathbf{i}_{T0} = \begin{bmatrix} \frac{1}{3} & \frac{1}{3} \cos\left(\frac{2\pi}{9} 3\right) & \frac{1}{3} \cos\left(\frac{2\pi}{9} 6\right) \\ 0 & \frac{1}{3} \sin\left(\frac{2\pi}{9} 3\right) & \frac{1}{3} \sin\left(\frac{2\pi}{9} 6\right) \\ \frac{1}{3} & \frac{1}{3} & \frac{1}{3} \end{bmatrix} \begin{bmatrix} 1 & 0 & 0 \\ 0 & 1 & 0 \\ -1 & -1 & 0 \end{bmatrix} \mathbf{i}_{T0} = \begin{bmatrix} \frac{1}{2} & 0 \\ 0.2887 & 0.5774 \\ 0 & 0 \end{bmatrix} \mathbf{i}_{T0}.$$

The solution of the system (3.82) is:

$$\begin{cases} \begin{bmatrix} i_{3,\alpha} \\ i_{3,\beta} \end{bmatrix} = \mathbf{H}_1 \begin{bmatrix} i_{A0} \\ i_{B0} \end{bmatrix} = \begin{bmatrix} \frac{1}{2} & 0 \\ 0.2887 & 0.5774 \end{bmatrix} \begin{bmatrix} i_{A0} \\ i_{B0} \end{bmatrix} \\ i_0 = \mathbf{H}_2 \begin{bmatrix} i_{A0} \\ i_{B0} \end{bmatrix} = \begin{bmatrix} 0 & 0 \end{bmatrix} \begin{bmatrix} i_{A0} \\ i_{B0} \end{bmatrix} = 0 \end{cases}$$

The final constraint equation (3.83) is:

$$\begin{bmatrix} i_{3,\alpha} \\ i_{3,\beta} \end{bmatrix} = \mathbf{H}_1 (\mathbf{H}_2)^{-1} i_0 = NaN.$$

Indeed, there are infinite solutions on the $\begin{bmatrix} i_{3,\alpha} \\ i_{3,\beta} \end{bmatrix}$ values. Therefore, the only constraint is that the homopolar sequence is zero.

The constraint on the \mathbf{C} matrix (originally an identity one) is given as:

$$\mathbf{C}_{7,7} = 0. \quad (3.87)$$

Double Star (AB-C)

Because this example does not have a practical application, the problem is solved only for the case of the first two stars connected together and the third one independently star connected.

In this case, the \mathbf{Z} matrix defined in (3.80) is:

$$\mathbf{Z} = \begin{bmatrix} 1 & 0 & 0 \\ -1 & 0 & 0 \\ 0 & 0 & 0 \end{bmatrix}.$$

Therefore (3.81) results as:

$$\mathbf{i}_{star} = \mathbf{GZ} \mathbf{i}_{T0} = \begin{bmatrix} \frac{1}{3} & \frac{1}{3} \cos\left(\frac{2\pi}{9}3\right) & \frac{1}{3} \cos\left(\frac{2\pi}{9}6\right) \\ 0 & \frac{1}{3} \sin\left(\frac{2\pi}{9}3\right) & \frac{1}{3} \sin\left(\frac{2\pi}{9}6\right) \\ \frac{1}{3} & \frac{1}{3} & \frac{1}{3} \end{bmatrix} \begin{bmatrix} 1 & 0 & 0 \\ -1 & 0 & 0 \\ 0 & 0 & 0 \end{bmatrix} \mathbf{i}_{T0} = \begin{bmatrix} \frac{1}{2} & 0 \\ -0.2887 & 0 \\ 0 & 0 \end{bmatrix} \mathbf{i}_{T0}.$$

The solution of the system (3.82) is:

$$\begin{cases} i_{3,\alpha} = \mathbf{H}_1 i_{A0} = \frac{1}{2} i_{A0} \\ i_{3,\beta} = \mathbf{H}_2 i_{A0} = -0.2887 i_{A0} = 0 \end{cases}$$

Indeed, if the homopolar component is considered, the equation system will result in an infinite number of solutions for the values of the third current vector components. However, by this simplification, the additional constraint can be found neglecting the homopolar components.

The final constraint equation (3.83) is:

$$i_{3,\alpha} = \mathbf{H}_1 (\mathbf{H}_2)^{-1} i_{3,\beta} = -1.7319 i_{3,\beta} = \operatorname{tg}\left(\frac{2\pi}{3}\right) i_{3,\beta}.$$

Indeed, there are infinite solutions on the $\begin{bmatrix} i_{3,\alpha} \\ i_{3,\beta} \end{bmatrix}$ values. Therefore, the only constraint is that the homopolar sequence is zero.

The constraint on the \mathbf{C} matrix (originally an identity one) is given as:

$$\mathbf{C}_{1,1} = 0, \quad \mathbf{C}_{1,2} = \operatorname{tg}\left(\frac{2\pi}{3}\right), \quad \mathbf{C}_{7,7} = 0. \quad (3.88)$$

Optimized Open Phase FTC Algorithm for a quadruple three-phase winding (star connection constraints)

A twelve-phase machine has usually a quadruple three-phase winding that can be connected in a single star, in a quadruple star or in a dual six-phase star configuration, (other more unusual solutions are not analysed). The winding is composed of four three-phase subsystems shifted

by 15 electrical degrees. The model is based on a 24 phase symmetrical winding where half of the phases do not exist, and therefore a 24 phase symmetrical transformation is used.

A schematic example of a standard quadruple three-phase drive is shown in Fig. 3.10, where also the magnetic axes of the machine phases are highlighted.

The currents of the four three-phase subsystems (A, B, C and D) can be described by the relative space vector representation by (3.41) and (3.42) as:

$$\bar{i}_{T1} = \frac{2}{3} \left(i_{T1} + i_{T2} e^{j\frac{2\pi}{3}} + i_{T3} e^{j\frac{4\pi}{3}} \right), \quad T = A, B, C, D,$$

and

$$i_{T0} = \frac{2}{3} (i_{T1} + i_{T2} + i_{T3}), \quad T = A, B, C, D.$$

The current space vectors related to the three-phase homopolar current components are defined by the relationship (3.75)

$$\mathbf{i}_{star} = \mathbf{G} \mathbf{i}_{T0},$$

with:

$$\mathbf{i}_{star} = [i_{3,\alpha} \quad i_{3,\beta} \quad i_{9,\alpha} \quad i_{9,\beta}]^T,$$

$$\mathbf{i}_{T0} = [i_{A0} \quad i_{B0} \quad i_{C0} \quad i_{D0}]^T.$$

and the G matrix given by (3.68) as:

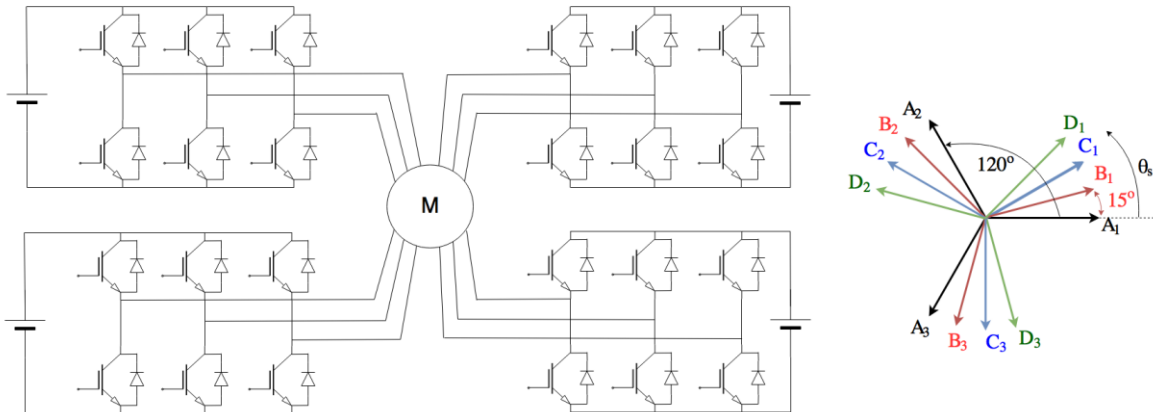


Fig. 3.10 – Quadruple three-phase standard drive and relative magnetic axis directions.

$$\mathbf{G} = \begin{bmatrix} \frac{1}{4} & \frac{1}{4} \cos\left(\frac{2\pi}{24} 3\right) & \frac{1}{4} \cos\left(\frac{2\pi}{24} 6\right) & \frac{1}{4} \cos\left(\frac{2\pi}{24} 9\right) \\ 0 & \frac{1}{4} \sin\left(\frac{2\pi}{24} 3\right) & \frac{1}{4} \sin\left(\frac{2\pi}{24} 6\right) & \frac{1}{4} \sin\left(\frac{2\pi}{24} 9\right) \\ \frac{1}{4} & \frac{1}{4} \cos\left(\frac{2\pi}{24} 9\right) & \frac{1}{4} \cos\left(\frac{2\pi}{24} 18\right) & \frac{1}{4} \cos\left(\frac{2\pi}{24} 27\right) \\ 0 & \frac{1}{4} \sin\left(\frac{2\pi}{24} 9\right) & \frac{1}{4} \sin\left(\frac{2\pi}{24} 18\right) & \frac{1}{4} \sin\left(\frac{2\pi}{24} 27\right) \end{bmatrix} = \begin{bmatrix} 0.25 & 0.1768 & 0 & -0.1768 \\ 0 & 0.1768 & 0.25 & 0.1768 \\ 0.25 & -0.1768 & 0 & 0.1768 \\ 0 & 0.1768 & -0.25 & 0.1768 \end{bmatrix}.$$

Independent Stars

In case of independent stars, the \mathbf{Z} matrix defined in (3.80) is:

$$\mathbf{Z} = \begin{bmatrix} 0 & 0 & 0 & 0 \\ 0 & 0 & 0 & 0 \\ 0 & 0 & 0 & 0 \\ 0 & 0 & 0 & 0 \end{bmatrix}.$$

Therefore (3.81) results as:

$$\mathbf{i}_{star} = \mathbf{GZ} \mathbf{i}_{T0} = \begin{bmatrix} 0 & 0 & 0 & 0 \\ 0 & 0 & 0 & 0 \\ 0 & 0 & 0 & 0 \\ 0 & 0 & 0 & 0 \end{bmatrix} \mathbf{i}_{T0} = \begin{bmatrix} 0 \\ 0 \\ 0 \\ 0 \end{bmatrix}.$$

The solution of the system (3.82) is:

$$\begin{cases} i_{3,\alpha} = 0 \\ i_{3,\beta} = 0 \\ i_{9,\alpha} = 0 \\ i_{9,\beta} = 0 \end{cases}$$

The constraint on the \mathbf{C} matrix (originally an identity one) are given as:

$$\mathbf{C}_{1+6(x-1),1+6(x-1)} = 0, \quad x = 1, \dots, N_S,$$

$$\mathbf{C}_{2+6(x-1),2+6(x-1)} = 0, \quad x = 1, \dots, N_S,$$

that means:

$$\mathbf{C}_{1,1} = 0, \quad \mathbf{C}_{2,2} = 0, \quad \mathbf{C}_{7,7} = 0, \quad \mathbf{C}_{8,8} = 0. \quad (3.89)$$

Single Star

In case of a single star, the \mathbf{Z} matrix defined in (3.80) is:

$$\mathbf{Z} = \begin{bmatrix} 1 & 0 & 0 & 0 \\ 0 & 1 & 0 & 0 \\ 0 & 0 & 1 & 0 \\ -1 & -1 & -1 & 0 \end{bmatrix}.$$

Therefore (3.81) results as:

$$\begin{aligned} \mathbf{i}_{star} = \mathbf{GZ} \mathbf{i}_{T0} &= \begin{bmatrix} 0.25 & 0.1768 & 0 & -0.1768 \\ 0 & 0.1768 & 0.25 & 0.1768 \\ 0.25 & -0.1768 & 0 & 0.1768 \\ 0 & 0.1768 & -0.25 & 0.1768 \end{bmatrix} \begin{bmatrix} 1 & 0 & 0 & 0 \\ 0 & 1 & 0 & 0 \\ 0 & 0 & 1 & 0 \\ -1 & -1 & -1 & 0 \end{bmatrix} \mathbf{i}_{T0} = \\ &= \begin{bmatrix} 0.4268 & 0.3536 & 0.1768 & 0 \\ -0.1768 & 0 & 0.0732 & 0 \\ 0.0732 & -0.3536 & -0.1768 & 0 \\ -0.1768 & 0 & -0.4268 & 0 \end{bmatrix} \mathbf{i}_{T0}. \end{aligned}$$

The solution of the system (3.82) is:

$$\left\{ \begin{array}{l} \mathbf{i}_{3,\alpha} = \mathbf{H}_1 \begin{bmatrix} i_{A0} \\ i_{B0} \\ i_{C0} \end{bmatrix} \\ \begin{bmatrix} i_{3,\beta} \\ i_{9,\alpha} \\ i_{9,\beta} \end{bmatrix} = \mathbf{H}_2 \begin{bmatrix} i_{A0} \\ i_{B0} \\ i_{C0} \end{bmatrix} \end{array} \right.$$

The final constraint equation (3.83) is:

$$i_{3,\alpha} = \mathbf{H}_1 (\mathbf{H}_2)^{-1} \begin{bmatrix} i_{3,\beta} \\ i_{9,\alpha} \\ i_{9,\beta} \end{bmatrix} = \begin{bmatrix} -2.4142 & -1 & -0.4142 \end{bmatrix} \begin{bmatrix} i_{3,\beta} \\ i_{9,\alpha} \\ i_{9,\beta} \end{bmatrix}.$$

In terms of analytical result, this can be written as:

$$i_{3,\alpha} = - \frac{\begin{bmatrix} 0 + \frac{1}{4} \sin\left(\frac{2\pi}{24} 3\right) + \frac{1}{4} \sin\left(\frac{2\pi}{24} 6\right) + \frac{1}{4} \sin\left(\frac{2\pi}{24} 9\right) \\ \frac{1}{4} + \frac{1}{4} \cos\left(\frac{2\pi}{24} 9\right) + \frac{1}{4} \cos\left(\frac{2\pi}{24} 18\right) + \frac{1}{4} \cos\left(\frac{2\pi}{24} 27\right) \\ 0 + \frac{1}{4} \sin\left(\frac{2\pi}{24} 9\right) + \frac{1}{4} \sin\left(\frac{2\pi}{24} 18\right) + \frac{1}{4} \sin\left(\frac{2\pi}{24} 27\right) \end{bmatrix}^T}{\frac{1}{4} + \frac{1}{4} \cos\left(\frac{2\pi}{24} 3\right) + \frac{1}{4} \cos\left(\frac{2\pi}{24} 6\right) + \frac{1}{4} \cos\left(\frac{2\pi}{24} 9\right)} \begin{bmatrix} i_{3,\beta} \\ i_{9,\alpha} \\ i_{9,\beta} \end{bmatrix}.$$

The constraint on the \mathbf{C} matrix (originally an identity one) is given as:

$$\mathbf{C}_{1,1} = 0, \quad \mathbf{C}_{1,2} = -2.4142, \quad \mathbf{C}_{1,7} = -1, \quad \mathbf{C}_{1,8} = -0.4142. \quad (3.90)$$

Double Star (AB-CD)

One possibility is to connect the two consecutive three-phase subsystems in two independent six-phase stars. This configuration is named here as ‘‘AB-CD’’ stars configuration.

In this case, the \mathbf{Z} matrix defined in (3.80) is:

$$\mathbf{Z} = \begin{bmatrix} 1 & 0 & 0 & 0 \\ -1 & 0 & 0 & 0 \\ 0 & 0 & 1 & 0 \\ 0 & 0 & -1 & 0 \end{bmatrix}.$$

Therefore (3.81) results as:

$$\begin{aligned} \mathbf{i}_{star} = \mathbf{GZ} \mathbf{i}_{T0} &= \begin{bmatrix} 0.25 & 0.1768 & 0 & -0.1768 \\ 0 & 0.1768 & 0.25 & 0.1768 \\ 0.25 & -0.1768 & 0 & 0.1768 \\ 0 & 0.1768 & -0.25 & 0.1768 \end{bmatrix} \begin{bmatrix} 1 & 0 & 0 & 0 \\ -1 & 0 & 0 & 0 \\ 0 & 0 & 1 & 0 \\ 0 & 0 & -1 & 0 \end{bmatrix} \mathbf{i}_{T0} = \\ &= \begin{bmatrix} 0.0732 & 0 & 0.1768 & 0 \\ -0.1768 & 0 & 0.0732 & 0 \\ 0.4268 & 0 & -0.1768 & 0 \\ -0.1768 & 0 & -0.4268 & 0 \end{bmatrix} \mathbf{i}_{T0}. \end{aligned}$$

The solution of the system (3.82) is:

$$\left\{ \begin{array}{l} \begin{bmatrix} i_{3,\alpha} \\ i_{9,\alpha} \end{bmatrix} = \mathbf{H}_1 \begin{bmatrix} i_{A0} \\ i_{B0} \end{bmatrix} \\ \begin{bmatrix} i_{3,\beta} \\ i_{9,\beta} \end{bmatrix} = \mathbf{H}_2 \begin{bmatrix} i_{A0} \\ i_{B0} \end{bmatrix} \end{array} \right.$$

Note that this choice of the H matrixes allows having always a finite solution (in other cases the system cannot be solved).

The final constraint equation (3.83) is:

$$\begin{bmatrix} i_{3,\alpha} \\ i_{9,\alpha} \end{bmatrix} = \mathbf{H}_1 (\mathbf{H}_2)^{-1} \begin{bmatrix} i_{3,\beta} \\ i_{9,\beta} \end{bmatrix} = \begin{bmatrix} 0 & -0.4142 \\ -2.4142 & 0 \end{bmatrix} \begin{bmatrix} i_{3,\beta} \\ i_{9,\beta} \end{bmatrix}.$$

The constraint on the C matrix (originally an identity one) is given as:

$$\mathbf{C}_{1,1} = 0, \quad \mathbf{C}_{1,8} = -0.4142, \quad \mathbf{C}_{7,7} = 0, \quad \mathbf{C}_{7,2} = -2.4142. \quad (3.91)$$

Double Star (AC-BD)

For a double six-phase configuration “AC-BD”, the steps are the same presented for the “AB-CD” solution. The Z matrix defined in (3.80) is:

$$\mathbf{Z} = \begin{bmatrix} 1 & 0 & 0 & 0 \\ 0 & 1 & 0 & 0 \\ -1 & 0 & 0 & 0 \\ 0 & -1 & 0 & 0 \end{bmatrix}.$$

Therefore (3.81) results as:

$$\mathbf{i}_{star} = \mathbf{GZ} \mathbf{i}_{T0} = \begin{bmatrix} 0.25 & 0.3536 & 0 & 0 \\ -0.25 & 0 & 0 & 0 \\ 0.25 & -0.3536 & 0 & 0 \\ -0.25 & 0 & 0 & 0 \end{bmatrix} \mathbf{i}_{T0}.$$

The solution of the system (3.82) is:

$$\left\{ \begin{array}{l} \begin{bmatrix} i_{3,\alpha} \\ i_{3,\beta} \end{bmatrix} = \mathbf{H}_1 \begin{bmatrix} i_{A0} \\ i_{B0} \end{bmatrix} \\ \begin{bmatrix} i_{9,\alpha} \\ i_{9,\beta} \end{bmatrix} = \mathbf{H}_2 \begin{bmatrix} i_{A0} \\ i_{B0} \end{bmatrix} \end{array} \right.$$

Note that this choice of the H matrixes allows having always a defined solution (in other cases, as the solution used for the “AB-CD” layout, the system is unsolvable).

The final constraints equation (3.83) is:

$$\begin{bmatrix} i_{3,\alpha} \\ i_{3,\beta} \end{bmatrix} = \mathbf{H}_1(\mathbf{H}_2)^{-1} \begin{bmatrix} i_{9,\alpha} \\ i_{9,\beta} \end{bmatrix} = \begin{bmatrix} -1 & 2 \\ 0 & -1 \end{bmatrix} \begin{bmatrix} i_{9,\alpha} \\ i_{9,\beta} \end{bmatrix}.$$

The constraints on the C matrix (originally an identity one) are given as:

$$\mathbf{C}_{1,1} = 0, \quad \mathbf{C}_{1,7} = -1, \quad \mathbf{C}_{1,8} = 2, \quad \mathbf{C}_{2,2} = 0, \quad \mathbf{C}_{2,8} = -1. \quad (3.92)$$

Double Star (AD-BC)

For a double six-phase configuration “AD-BC”, the steps are the same presented for previous solutions.

The Z matrix defined in (3.80) is:

$$\mathbf{Z} = \begin{bmatrix} 1 & 0 & 0 & 0 \\ 0 & 1 & 0 & 0 \\ 0 & -1 & 0 & 0 \\ -1 & 0 & 0 & 0 \end{bmatrix}.$$

Therefore (3.81) results as:

$$\mathbf{i}_{star} = \mathbf{GZ} \mathbf{i}_{T0} = \begin{bmatrix} 0.25 & 0.3536 & 0 & 0 \\ -0.25 & 0 & 0 & 0 \\ 0.25 & -0.3536 & 0 & 0 \\ -0.25 & 0 & 0 & 0 \end{bmatrix} \mathbf{i}_{T0}.$$

The solvable solution of the system (3.82) in this case (as for the “AB-CD” case) is:

$$\begin{cases} \begin{bmatrix} i_{3,\alpha} \\ i_{9,\alpha} \end{bmatrix} = \mathbf{H}_1 \begin{bmatrix} i_{A0} \\ i_{B0} \end{bmatrix} \\ \begin{bmatrix} i_{3,\beta} \\ i_{9,\beta} \end{bmatrix} = \mathbf{H}_2 \begin{bmatrix} i_{A0} \\ i_{B0} \end{bmatrix} \end{cases}$$

Note that this choice of the H matrixes allows having always a finite solution (in other cases the system cannot be solved).

The final constraint equation (3.83) is:

$$\begin{bmatrix} i_{3,\alpha} \\ i_{9,\alpha} \end{bmatrix} = \mathbf{H}_1 (\mathbf{H}_2)^{-1} \begin{bmatrix} i_{3,\beta} \\ i_{9,\beta} \end{bmatrix} = \begin{bmatrix} -2.4142 & 0 \\ 0 & -0.4142 \end{bmatrix} \begin{bmatrix} i_{3,\beta} \\ i_{9,\beta} \end{bmatrix}.$$

The constraints on the \mathbf{C} matrix (originally an identity one) are given as:

$$\mathbf{C}_{1,1} = 0, \quad \mathbf{C}_{1,2} = -2.4142, \quad \mathbf{C}_{7,7} = 0, \quad \mathbf{C}_{7,8} = -0.4142. \quad (3.93)$$

The next section summarizes the fault tolerant control technique presented in this chapter. The following sections show the simulation and experimental results.

3.5 Summary of the proposed Fault Tolerant Control for Open Phase Faults

The method proposed in the previous sections has been generalized to whatever standard distributed winding multiphase machine under the following hypothesis:

- The winding is not an open end-winding (each phase is connected with others to a star);
- The phase number is odd, or it is a multiple of three, in a typical symmetrical or asymmetrical winding layout;
- The machine is symmetrical under each pole pair.

The considered FTC is based on the minimization of the total stator copper losses in the production of the main current space vectors ($\mathbf{i}_1 = [i_{1,\alpha} \quad i_{1,\beta}]^T$), and is based on the solution of (3.34) for the evaluation of the auxiliary current space vectors:

$$\mathbf{i}_{aux} = -\mathbf{C}(\mathbf{C}^T \mathbf{C})^+ (\mathbf{A}\mathbf{C})^T (\mathbf{A}\mathbf{C}(\mathbf{C}^T \mathbf{C})^+ (\mathbf{A}\mathbf{C})^T)^+ \mathbf{B}\mathbf{i}_1.$$

While the matrixes \mathbf{A} and \mathbf{B} depend on the fault (they represent one equation for each faulty phase), the \mathbf{C} matrix is related to the constraints introduced by the star connection of the winding. According to the hypotheses of the analysed windings, odd and even phase machines can be analysed in the same way. In particular, the solutions have been presented for:

- Single star (with the number of phases, m , odd or multiple of three)
- Independent n -phase stars (with n an odd number of symmetrical distributed phases)
- Double stars for multi three-phase windings

Single Star (with the number of phases, m , odd or multiple of three)

In case of an odd number of phases, the simplified method that neglects the zero order current space vector already takes into account for the single star connection constraint. In case of an

even number of three-phase subsystems, the constraint results in having the \mathbf{C} matrix with (3.73):

$$\mathbf{C}_{1+6(x-1),1+6(y-1)} = -\frac{\sum_{T=1}^{N_T} [\mathbf{G}^{-1}]_{T,y}}{\sum_{T=1}^{N_T} [\mathbf{G}^{-1}]_{T,x}}, \quad \mathbf{C}_{1+6(x-1),2+6(y-1)} = -\frac{\sum_{T=1}^{N_T} [\mathbf{G}^{-1}]_{T,y+1}}{\sum_{T=1}^{N_T} [\mathbf{G}^{-1}]_{T,x}},$$

$$\mathbf{C}_{1+6(x-1),1+6(x-1)} = 0,$$

setting a constraint on the α component, or (3.74):

$$\mathbf{C}_{2+6(x-1),1+6(y-1)} = -\frac{\sum_{T=1}^{N_T} [\mathbf{G}^{-1}]_{T,y}}{\sum_{T=1}^{N_T} [\mathbf{G}^{-1}]_{T,x}}, \quad \mathbf{C}_{2+6(x-1),2+6(y-1)} = -\frac{\sum_{T=1}^{N_T} [\mathbf{G}^{-1}]_{T,y+1}}{\sum_{T=1}^{N_T} [\mathbf{G}^{-1}]_{T,x}},$$

$$\mathbf{C}_{2+6(x-1),2+6(x-1)} = 0$$

setting a constraint on the β component, with \mathbf{G} the matrix that relates the current space vectors to the three-phase homopolar currents ($\mathbf{i}_{star} = \mathbf{G}\mathbf{i}_{T0}$) defined by (3.68) with N_s equal to m (total phase number) for an odd-phase machine and N_s equal to $2m$ for an even-phase machine:

$$\mathbf{G}_{r_{odd},c} = \frac{1}{N_T} \cos\left(\frac{2\pi}{N_s} 3r_{odd}(c-1)\right), \quad \mathbf{G}_{r_{odd}+1,c} = \frac{1}{N_T} \sin\left(\frac{2\pi}{N_s} 3r_{odd}(c-1)\right).$$

Independent n-phase stars (with n an odd number of phases)

Equation (3.63) defines the constraints related to a multi n-phase machine with nN_T phases independently connected:

$$\mathbf{C}_{(n-2)+2n(x-1),(n-2)+2n(x-1)} = 0, \quad \mathbf{C}_{(n-1)+2n(x-1),(n-1)+2n(x-1)} = 0.$$

Double stars for multi three-phase windings

A unique general solution for the double star configurations has not been found. However, the result for a triple three-phase winding has been shown and the one for a twelve-phase machine in double six-phase layout are reported here below. Equations (3.91)-(3.93) define the double six-phase constraints, depending on the winding layout as:

$$\mathbf{C}_{1,1} = 0, \quad \mathbf{C}_{1,8} = -0.4142, \quad \mathbf{C}_{7,7} = 0, \quad \mathbf{C}_{7,2} = -2.4142, \quad \text{for "AB|CD" layout}$$

$$\mathbf{C}_{1,1} = 0, \mathbf{C}_{1,7} = -1, \mathbf{C}_{1,8} = 2, \mathbf{C}_{2,2} = 0, \mathbf{C}_{2,8} = -1, \quad \text{for "AC|BD" layout}$$

$$\mathbf{C}_{1,1} = 0, \mathbf{C}_{1,2} = -2.4142, \mathbf{C}_{7,7} = 0, \mathbf{C}_{7,8} = -0.4142, \quad \text{for "AD|BC" layout}$$

The proposed method can be used to compensate whatever open phase fault condition or to set to zero the current in the desired phases. The approach is general, and allows developing a suitable FTC for also other winding configurations. A general equation has not been found because the current space vector constraints, that must be defined in order to solve the problem, can be defined in more ways, and the solution is not unique.

Anyway, the solution for the definition of the optimized FTC can be found only if the model is described by a number of space vector components that is equal to the number of degrees of freedom available for the current control, making the star connection constraints essential.

Simplified FTC and Current Sharing Approach

In order to simplify the solution for a multi three-phase machine with independently star connected subsystems, the current sharing approach can be adopted. In this case, a fault is compensated by the loss of all the three-phase faulty subsystem.

The current sharing technique can be also used for a power sharing control of the machine. In particular, it is possible to make some three-phase subsystems working in motoring mode and others in generating mode, realizing a power transfer between them. The general current sharing equations (3.57) are defined by the proper choice of the current sharing coefficients, and are:

$$\left\{ \begin{array}{l} \bar{i}_h = i_d \sum_{T=1}^{N_T} K_{Td} e^{j\frac{2\pi}{N_s}(h-1)(x_T-1)} + j i_q \sum_{T=1}^{N_T} K_{Tq} e^{j\frac{2\pi}{N_s}(h-1)(x_T-1)} \Leftrightarrow h = 3k + 1 \\ \bar{i}_h = i_d \sum_{T=1}^{N_T} K_{Td} e^{j\frac{2\pi}{N_s}(h+1)(x_T-1)} - j i_q \sum_{T=1}^{N_T} K_{Tq} e^{j\frac{2\pi}{N_s}(h+1)(x_T-1)} \Leftrightarrow h = 3k - 1 \\ \bar{i}_h = \left[\sum_{T=1}^{N_T} i_{T0} e^{j\frac{2\pi}{N_s}h(x_T-1)} \right] = 0 \Leftrightarrow h = 3k \end{array} \right. \quad (3.94)$$

with the following constraints (3.56):

$$\sum_{T=1}^{N_T} K_{Td} = 1 \quad \text{and} \quad \sum_{T=1}^{N_T} K_{Tq} = 1.$$

The FTC simplified technique is based on setting K_{Td} and K_{Tq} equal to zero for the faulty T -th three-phase subsystem.

3.6 Case study: 12-Phase Asymmetrical Machine

As case study, the methods are verified for a 12-phase induction machine. The analysed squirrel-cage induction machine has four independent three-phase windings, fed by four VSIs. The three-phase windings are spatially shifted by 15 electrical degrees and independently star connected. The distribution of the magnetic axes of the phases is shown in Fig. 3.11. The converters can be connected to one or more shared dc links and the three-phase subsystems can be star connected between them in whatever configuration.

The machine has 48 stator slots and 40 rotor slots, and the main control parameters are summarized in Table 3.1 under the hypothesis that the higher order field harmonics can be neglected (this is the hypothesis behind the proposed FTC).

Analytical results

By the equations summarised in the section 3.5, it is possible to evaluate the current values for each working condition of the machine and whatever fault tolerant operation in the hypothesis that the current control is properly working (zero error condition). Indeed, the proposed FTC defines a machine FOC that is based on the generation of the desired main current space vector ($\mathbf{i}_1 = [i_{1,\alpha} \quad i_{1,\beta}]^T$). Therefore, the auxiliary current space vectors are all set to zero in the standard behaviour, while they assume different values only if a current sharing technique or a FTC are applied. The reference values for the auxiliary current space vectors are defined in order to follow the reference of the main current vector minimizing the total stator copper Joule losses.

The stator copper Joule losses and the maximum value of the phase current are analysed for a given control technique (fault condition). The losses are used to compare the different control techniques in order to give an approximated evaluation of the machine power derating, while the maximum phase current is analysed in order to understand the derating required by the converter constraint (instantaneous maximum current).

A first comparison is done for a single phase fault with independent three-phase stars, showing the losses with a current sharing based FTC (named also “three-phase FTC”) and comparing them with the obtained by the improved FTC (named also “single-phase FTC”). Fig. 3.12 shows

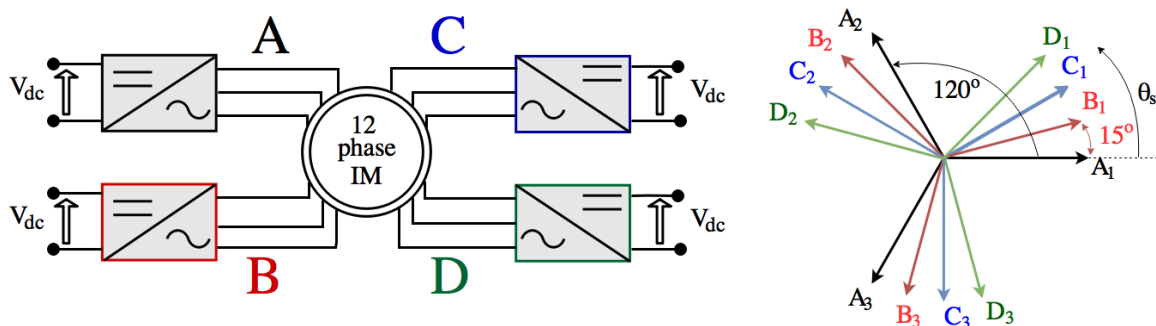


Fig. 3.11 – Schematic of a standard quadruple three-phase drive and magnetic axis directions of the 12-phase machine.

Table 3.1 – Main machine SVD control parameters.

INDUCTION MACHINE PARAMETERS (50 Hz)								
P_{rated}	=	10 kW	R_S	=	0.188 Ω	L_{S15}	=	1.20 mH
I_{max}	=	23 A _{pk}	R_R	=	0.156 Ω	L_{S17}	=	1.00 mH
$I_{S1d,rated}$	=	10 A _{pk}	L_{S1}	=	12.8 mH	L_{S111}	=	0.85 mH
$v_{S1,rated}$	=	186 V	L_{R1}	=	12.8 mH	p	=	2 (pairs)
$I_{S1,rated}$	=	16 A _{pk}	M_1	=	12.0 mH			

the difference between the two FTCs ideas. Then the performance is compared also with the other possible star configurations and faults.

Independent Stars: comparison between three-phase FTC and single-phase FTC

The three-phase simplified FTC results in controlling the auxiliary current space vectors by (3.94) setting $K_A = K_{Ad} = K_{Aq} = 0$ and $K_T = K_{Td} = K_{Tq} = \frac{1}{3}$ for the healthy T -th three-phase subsystems B, C and D. The auxiliary current space vectors result as:

$$\left\{ \begin{array}{l} \bar{i}_5 = (K_A + jK_B - K_C - jK_D)\bar{i}_1^* = -\frac{1}{3}\bar{i}_1^* \\ \bar{i}_7 = (K_A + jK_B - K_C - jK_D)\bar{i}_1 = -\frac{1}{3}\bar{i}_1 \\ \bar{i}_{11} = (K_A - K_B + K_C - K_D)\bar{i}_1^* = -\frac{1}{3}\bar{i}_1^* \\ \bar{i}_3 = \bar{i}_9 = 0 \end{array} \right. \quad (3.95)$$

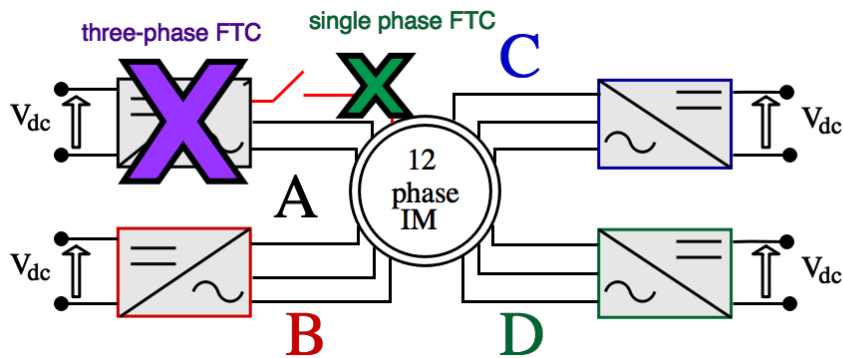


Fig. 3.12 – Schematic of the basic idea of the three-phase FTC (purple) and the single-phase FTC (green) in case of single phase open fault for an independent star configuration of a multi three-phase machine.

The single-phase enhanced FTC results in controlling the auxiliary current space vectors by (3.34), setting the star connection constraint by the proper \mathbf{C} matrix. The auxiliary current space vectors result as:

$$\left\{ \begin{array}{l} i_{5d} = -\frac{1}{3}i_{1d}; \quad i_{5q} = 0 \\ i_{7d} = -\frac{1}{3}i_{1d}; \quad i_{7q} = 0 \\ i_{11d} = -\frac{1}{3}i_{1d}; \quad i_{11q} = 0 \\ \bar{i}_3 = \bar{i}_9 = 0 \end{array} \right. \quad (3.96)$$

Fig. 3.13 shows the analytical value of the stator copper Joule losses when the main current space vector (\bar{i}_1) is increased up to its rated value (16 A). The figure compares the losses in case of healthy and faulty machine (phase A1 open fault) for both the FTCs. It is clear that a single-phase FTC allows reducing the total stator copper Joule losses. This means that a lower de-rating is expected. Indeed, to avoid the thermal overload of the stator windings, the magnitude of the main current vector (\bar{i}_1) has to be lower than the rated value ($I_{S1, rated}$) by about 6% for the single-phase FTC, and by about 12% for the three-phase FTC.

Fig. 3.14 compares the maximum peak value of the phase currents for both the FTCs as a function of the magnitude of the main current space vector (\bar{i}_1). Although the Joule losses are significantly reduced in the single-phase FTC, they are not equally distributed among the phases and it can be verified that the maximum peak value of the phase currents is almost the same for the two methods for a given main current vector. The result in Fig. 3.14 shows also that the reduction of the overload performance (related to the inverter maximum phase current) is almost the same in the two FTC. The red dotted line (that describes the maximum phase current value allowed by the converter) crosses the two I_{max} curves almost in the same points in the

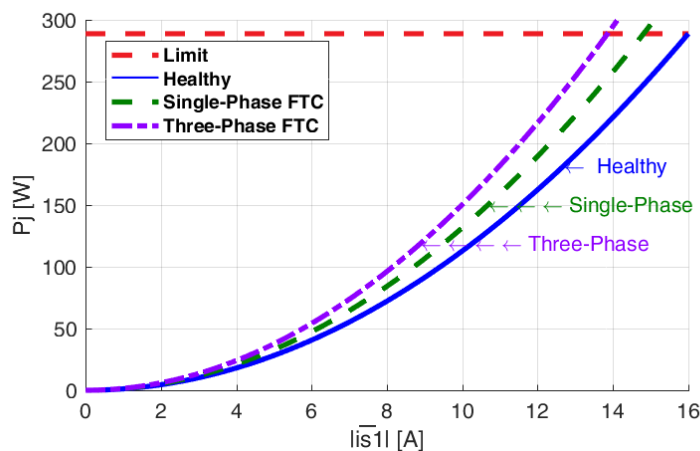


Fig. 3.13 – Analytical Joule losses comparison of the healthy machine (blue) and the faulty machine (phase A1 open), with three-phase FTC (purple) and single-phase FTC (green).

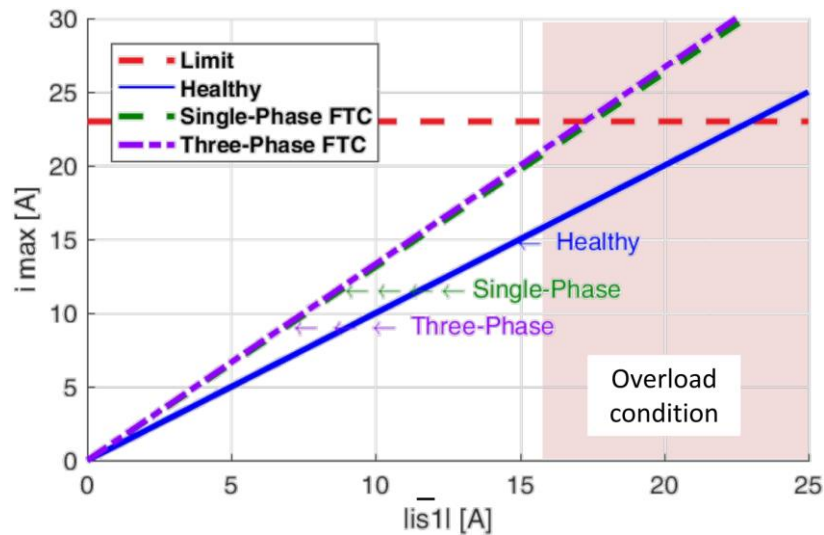


Fig. 3.14 – Analytical maximum phase current comparison of the healthy machine (blue) and the faulty machine (phase A1 open), with three-phase FTC (purple) and single-phase FTC (green).

overload area. The derating of the maximum allowed magnitude of the main current space vector is of 17.25 A with the three-phase FTC and 17.51 A with the single-phase FTC, compared to 23 A in case of healthy machine. With a single-phase FTC the maximum current increase is of 0.26 A, about 1.13% of the maximum magnitude in case of healthy machine. Therefore, the overload performance have almost the same de-rating in the two FTCs.

Star configuration comparison for a single phase open fault

It is possible to connect the stars of a quadruple three-phase machine between each other in order to mainly reduce the machine stator copper losses. In particular, the more attractive star configurations are:

- Multi three-phase (A|B|C|D), as the one analysed in the previous subsection;
- Double six-phase configuration with star connection of neighbouring three-phase subsystems (AB|CD);
- Double six-phase configuration with star connection of alternated three-phase subsystems (AC|BD);
- Double six-phase configuration with star connection of concentric three-phase subsystems (AD|BC);
- Twelve-phase single-star configuration (ABCD).

Fig. 3.15 shows the analytical value of the stator copper Joule losses when the main current space vector (\bar{i}_1) is increased up to its rated value (16 A). The figure compares the losses in case of healthy and faulty machine (phase A1 open fault) for the FTCs in all the star connection configurations. It is clear that the losses can be reduced by connecting together the stars of the three-phase windings. In particular, as expected the multi-phase single-star configuration allows having the better performance. The multi six-phase layouts result in the same losses, making them equal from this first analysis.

Open Phase Faults and Fault Tolerant Controls in Multiphase Drives

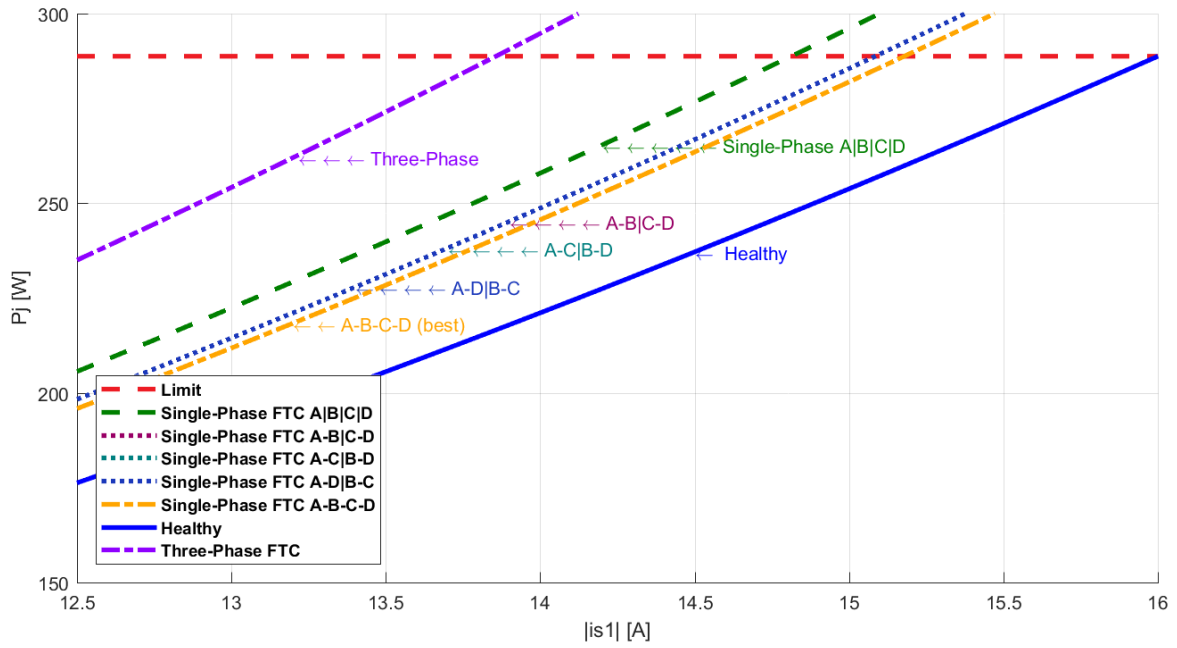


Fig. 3.15 – Analytical Joule losses comparison with healthy machine (blue) and the faulty machine (phase A1 open). Three-phase FTC (purple) and single-phase FTC: quadruple three-phase layout (green), double six-phase layouts (spotted) and twelve-phase layout (orange). The rated copper Joule losses are highlighted in red.

Fig. 3.16 compares the maximum peak value of the phase currents for the FTCs as a function of the magnitude of the main current space vector (\bar{i}_1) in all the star connection configurations.

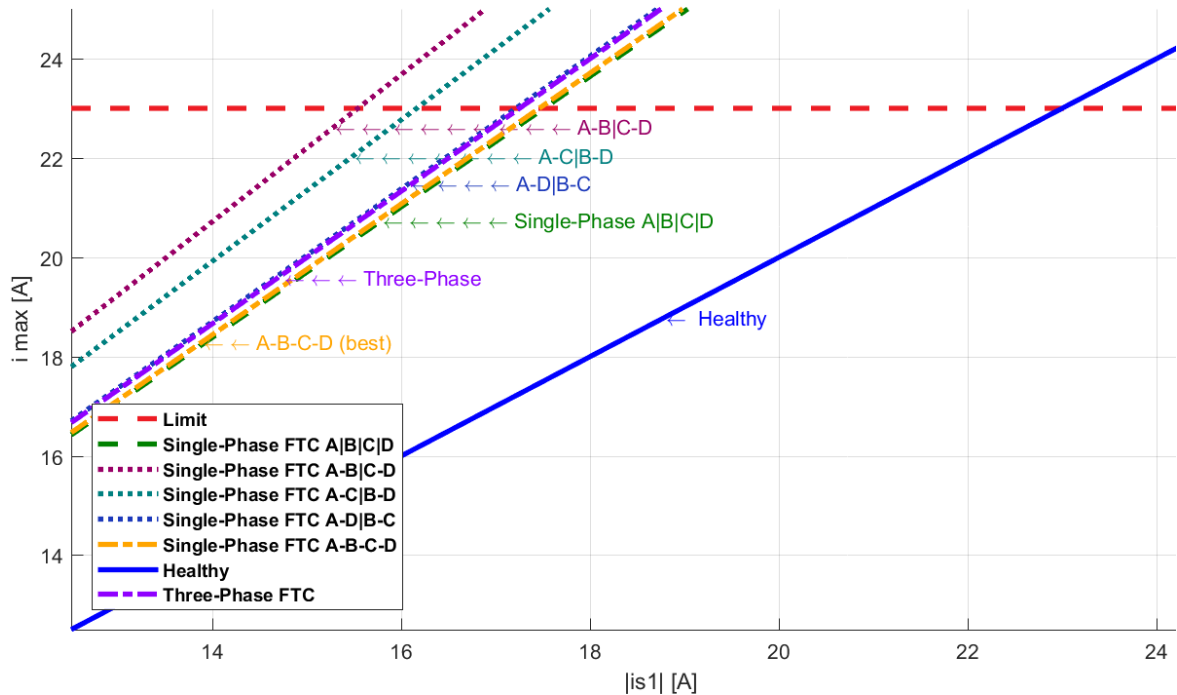


Fig. 3.16 – Analytical maximum phase current comparison with healthy machine (blue) and the faulty machine (phase A1 open). Three-phase FTC (purple) and single-phase FTC: quadruple three-phase layout (green), double six-phase layouts (spotted) and twelve-phase layout (orange). The maximum phase current is highlighted in red.

It is interesting to note that the maximum current in some winding configurations is higher than the one resulting from the three-phase FTC. In particular, all the dual six-phase configurations give a higher peak current with the single phase FTC when compared with the three-phase FTC.

Furthermore, also the multi-phase single-star layout results in a higher peak current than the multi three-phase independent stars one with the single phase FTC.

These results can be used in order to identify a proper FTC according to the machine limits. During a machine overload operation, the best control is the single-phase FTC with a multi three-phase configuration. Instead, at steady state operation, the minimization of the losses can be achieved with better performance exploiting the increased degrees of freedom of a double six-phase or better a full twelve-phase winding.

It is worth noticing that the twelve-phase configuration makes possible the implementation of all the proposed FTC algorithms, and the star constraints can be implemented by the control. Therefore, also a multi six-phase layout can be controlled as a multi three-phase one.

It results that in terms of current control, the multi-phase winding is the more flexible, allowing for the implementation of all the proposed FTCs according to the performance requirements. Between the double six-phase configurations, the peak current is significantly higher in the AB|CD configuration, while the two other configurations seem to have reduced maximum currents. However, the AD|BC layout behaves like the AB|CD one when the faulty phase is in the three-phase system B or C, while the peak current in case of the AC|BD stars remains as in Fig. 3.16. It results that the better configuration is the AC|BD one. The maximum current in the phases affects also the machine behaviour in terms of saturations as is shown in one of the following subsections. The results are the same if the faulty phase is the first, second or third of a three-phase subsystem. Therefore, this analysis is general for whatever single-phase fault.

The phase currents for the healthy and faulty machine with FTC are shown in Fig. 3.17-Fig. 3.23 in order to give a better understanding of the phenomena.

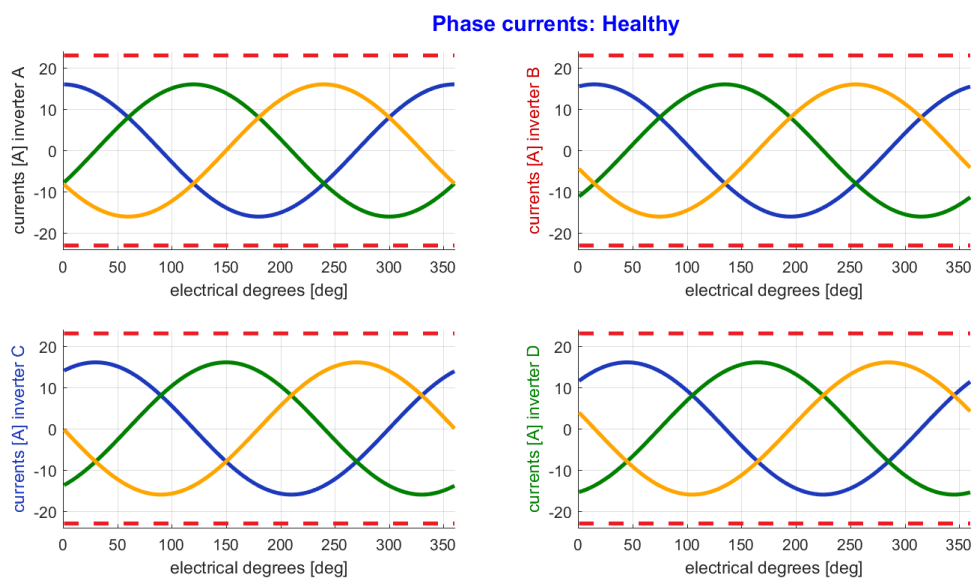


Fig. 3.17 – Analytical phase currents at rated value of the main current space vector. Healthy machine.

Open Phase Faults and Fault Tolerant Controls in Multiphase Drives

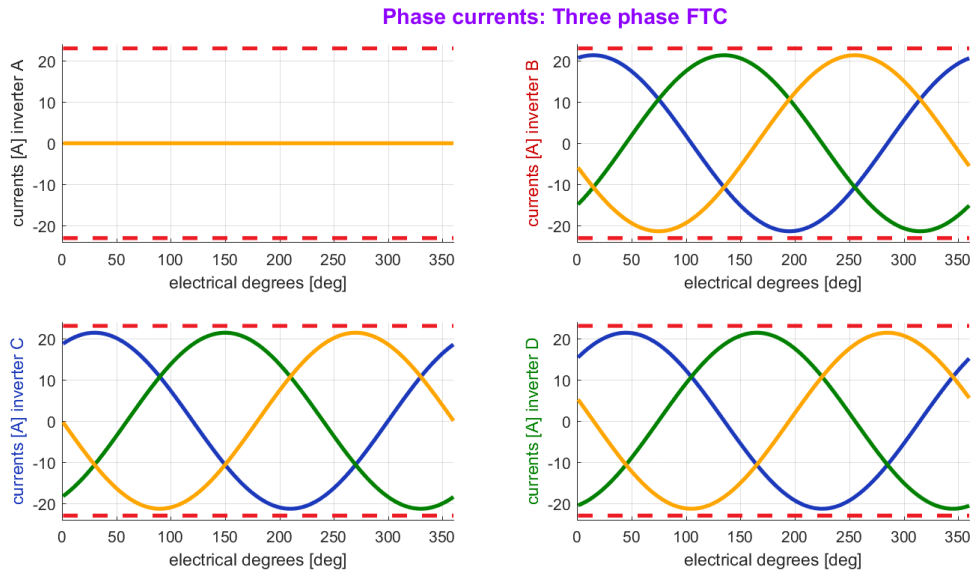


Fig. 3.18 – Analytical phase currents at rated value of the main current space vector. Three-phase FTC (phase A1 open).

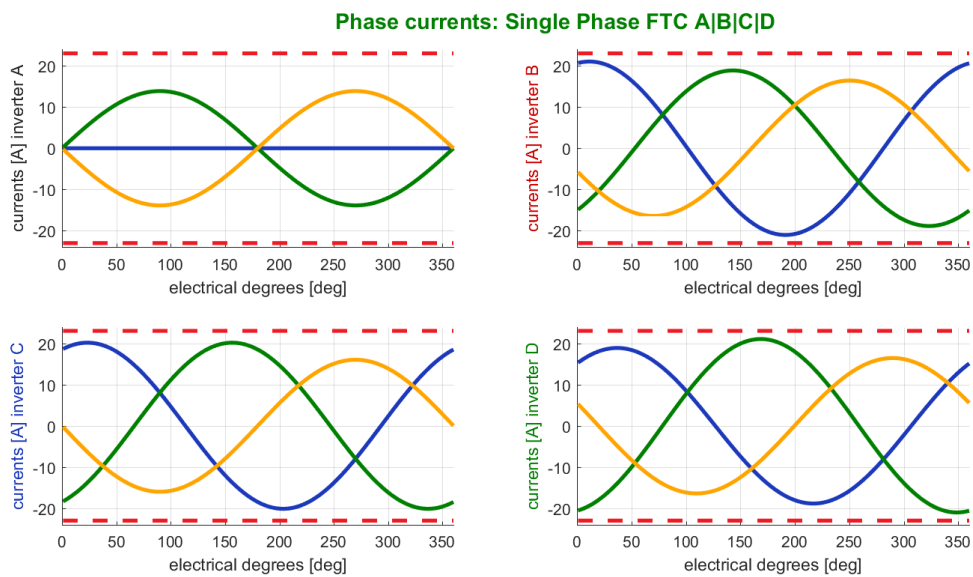


Fig. 3.19 – Analytical phase currents at rated value of the main current space vector. Single-phase FTC (phase A1 open)

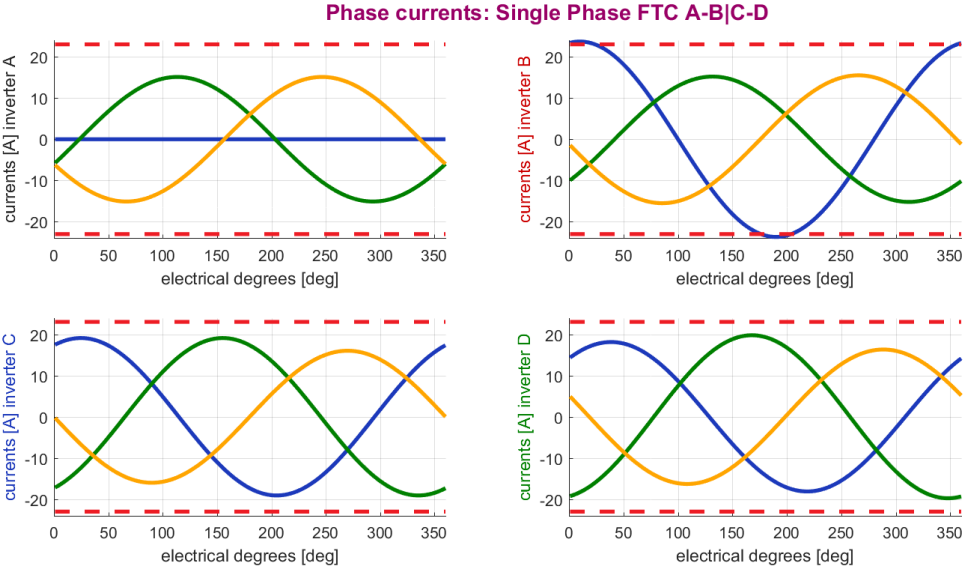


Fig. 3.20 – Analytical phase currents at rated value of the main current space vector. Double six-phase layout AB|CD (phase A1 open).

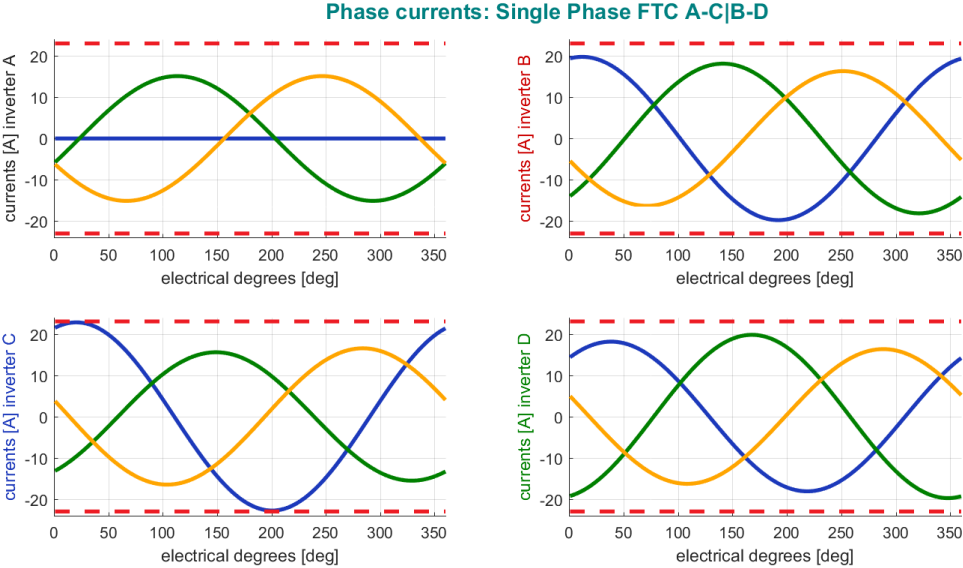


Fig. 3.21 – Analytical phase currents at rated value of the main current space vector. Double six-phase layout AC|BD (phase A1 open).

Open Phase Faults and Fault Tolerant Controls in Multiphase Drives

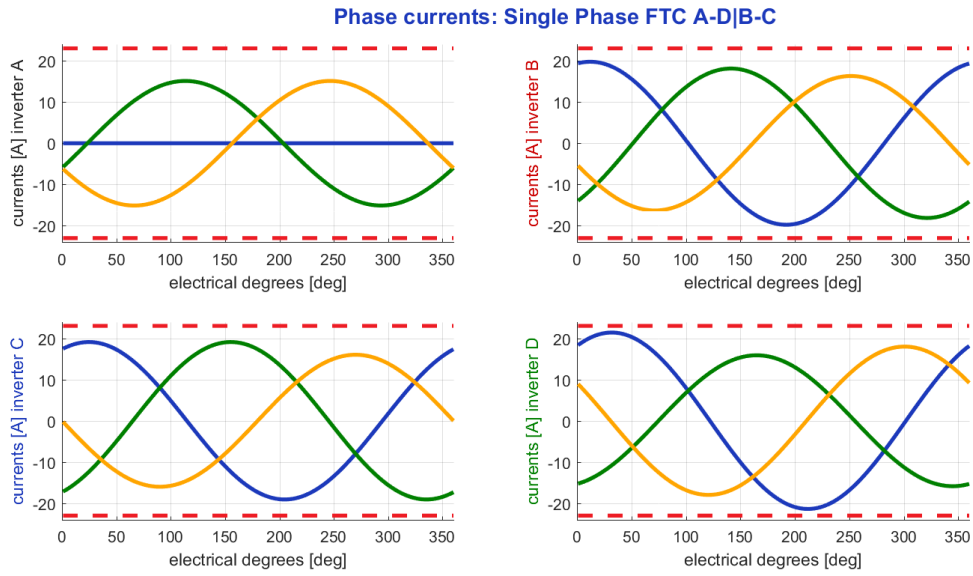


Fig. 3.22 – Analytical phase currents at rated value of the main current space vector. Double six-phase layout AD|BC (phase A1 open).

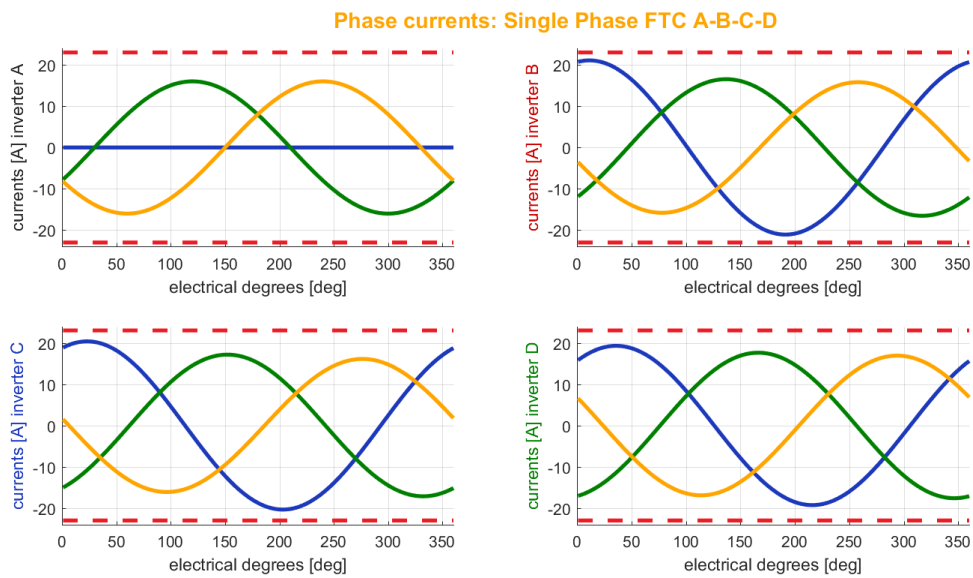


Fig. 3.23 – Analytical phase currents at rated value of the main current space vector. Twelve-phase layout ABCD (phase A1 open).

Star configuration comparison for a multi-phase open fault

The number of open phase faults and their distribution among the phases results in a huge amount of possible fault scenarios. Therefore, here it is presented a particularly critical fault with almost half of the phases open. The result is interesting only to validate the advantage of the star connections also in case of a catastrophic fault.

The working scenario is represented by the following fault configuration:

$$i_{A1} = i_{B1} = i_{B2} = i_{D1} = i_{D2} = 0.$$

Therefore, only one three-phase subsystem is completely working. Such a fault might represent the case of a mechanical or thermal fault in some areas of the machine, for example caused by a partial failure of the cooling system. However, the aim of this analysis is not to justify the fault phenomenology but just showing the differences in terms of FTC algorithms and star connections.

Fig. 3.24 shows the analytical value of the stator copper Joule losses when the main current space vector (\bar{i}_1) is increased up to its rated value (16 A). The figure compares the losses in case of healthy and faulty machine for the FTCs in all the star connection configurations. As expected, the multi-phase single-star configuration allows having the better performance. The multi six-phase layouts result in different losses, but the best solution depends from the fault configuration.

Fig. 3.25 compares the maximum peak value of the phase currents for the FTCs as a function of the magnitude of the main current space vector (\bar{i}_1) in all the star connection configurations, showing that aslo in this case the best solution is one of the double six-phase according to the

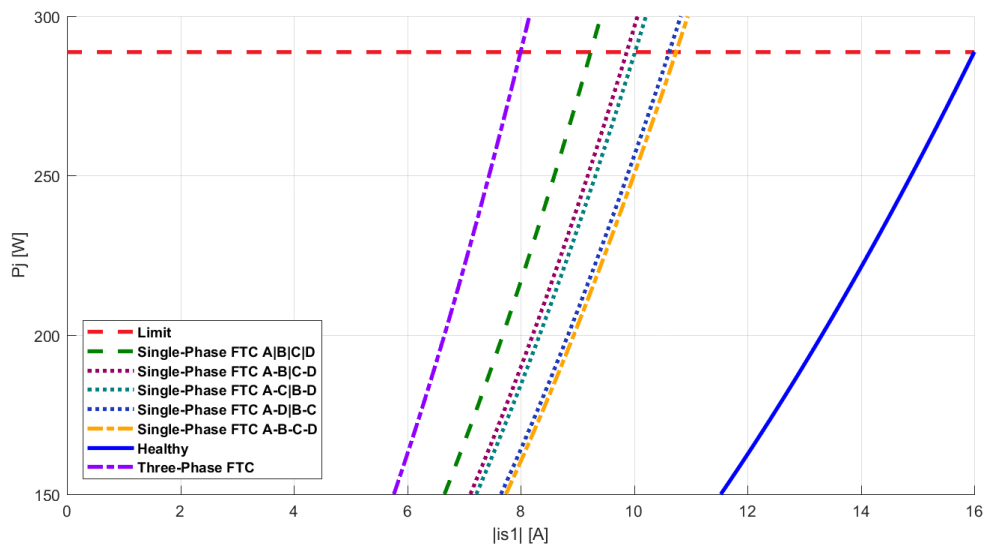


Fig. 3.24 – Analytical Joule losses comparison with healthy machine (blue) and the faulty machine (phases A1, B1, B2, D1, D2 open). Three-phase FTC (purple) and single-phase FTC: quadruple three-phase layout (green), double six-phase layouts (spotted) and twelve-phase layout (orange). The rated copper Joule losses are highlighted in red.

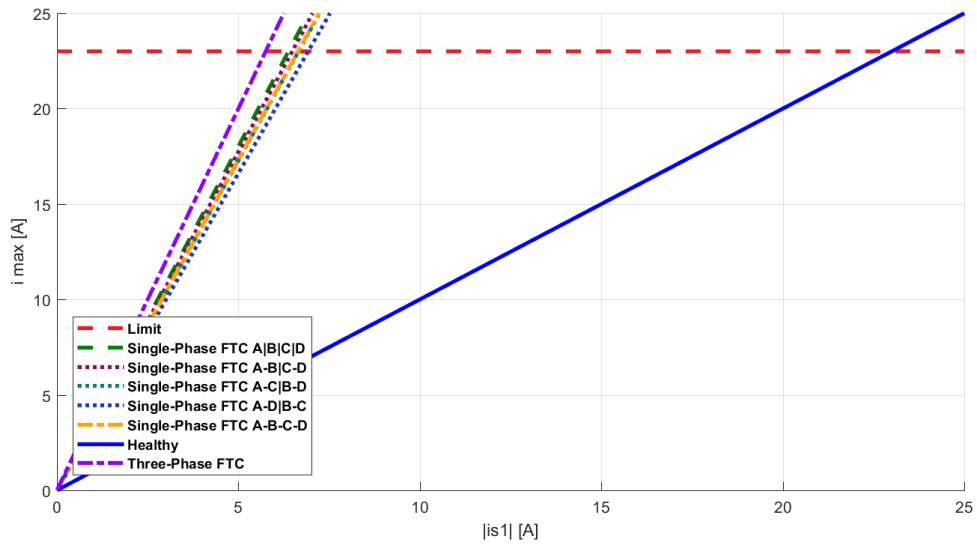


Fig. 3.25 – Analytical maximum phase current comparison with healthy machine (blue) and the faulty machine (phases A1, B1, B2, D1, D2 open). Three-phase FTC (purple) and single-phase FTC: quadruple three-phase layout (green), double six-phase layouts (spotted) and twelve-phase layout (orange). The maximum phase current is highlighted in red.

analysed fault. In general, the single star still results the best solution also in terms of maximum expected peak current.

Figures Fig. 3.26-Fig. 3.32 show the phase currents in the different FTCs and star connection layouts.

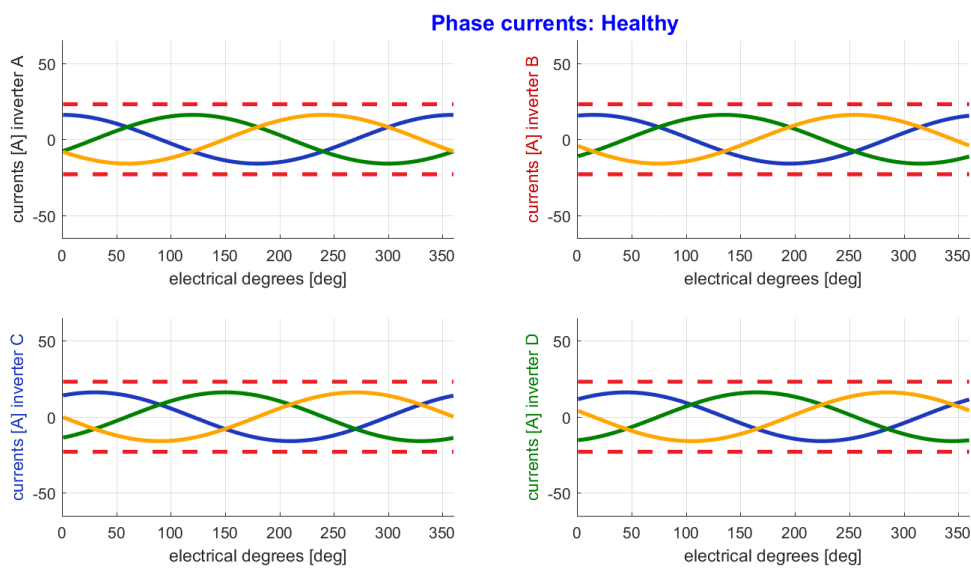


Fig. 3.26 – Analytical phase currents at rated value of the main current space vector. Healthy machine.

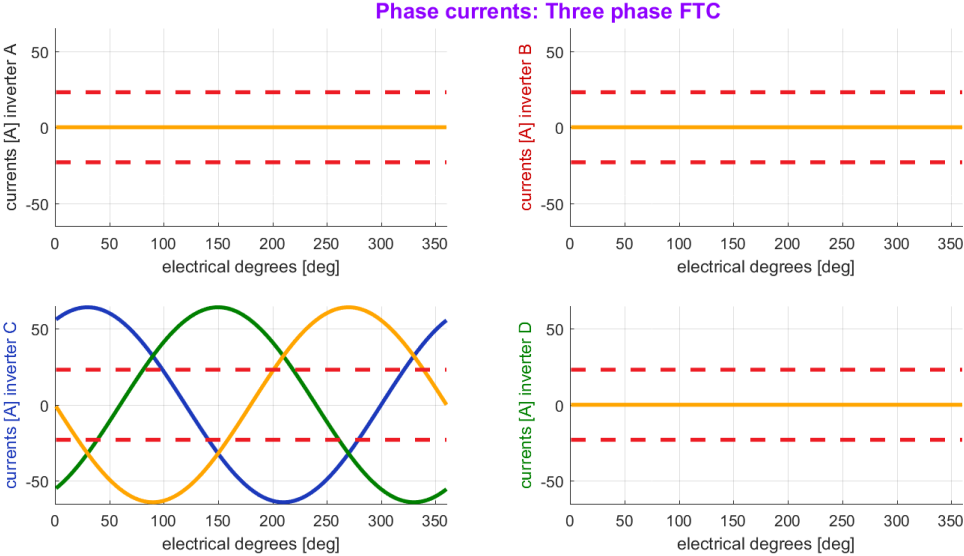


Fig. 3.27 – Analytical phase currents at rated value of the main current space vector.
 Three-phase FTC (phases A1, B1, B2, D1, D2 open).

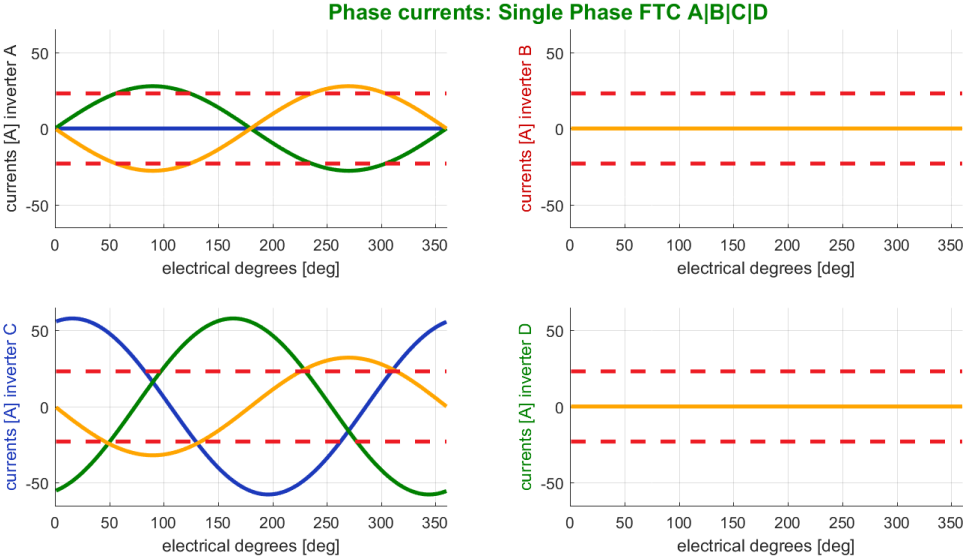


Fig. 3.28 – Analytical phase currents at rated value of the main current space vector.
 Single-phase FTC (phases A1, B1, B2, D1, D2 open).

Open Phase Faults and Fault Tolerant Controls in Multiphase Drives

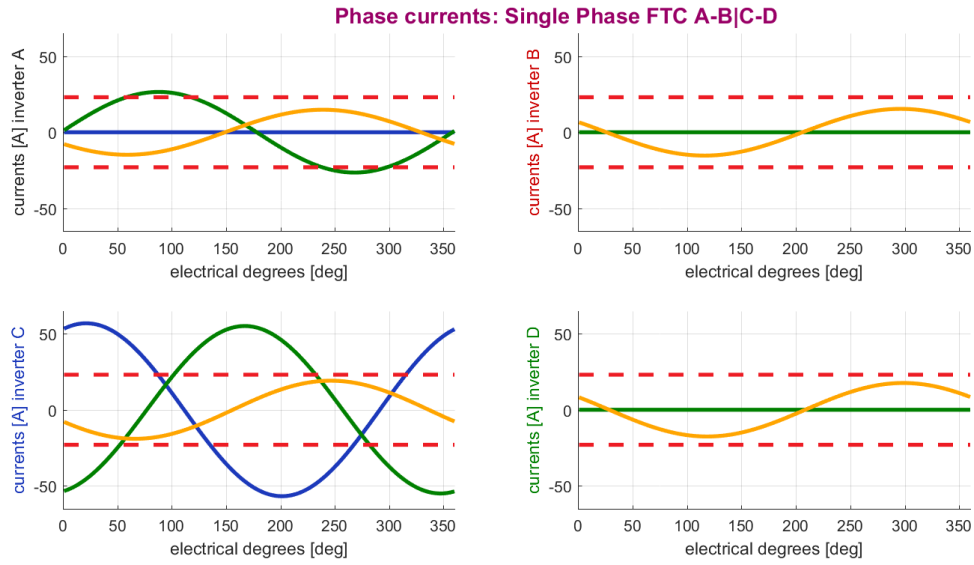


Fig. 3.29 – Analytical phase currents at rated value of the main current space vector.
 Double six-phase layout AB/CD (phases A1, B1, B2, D1, D2 open).

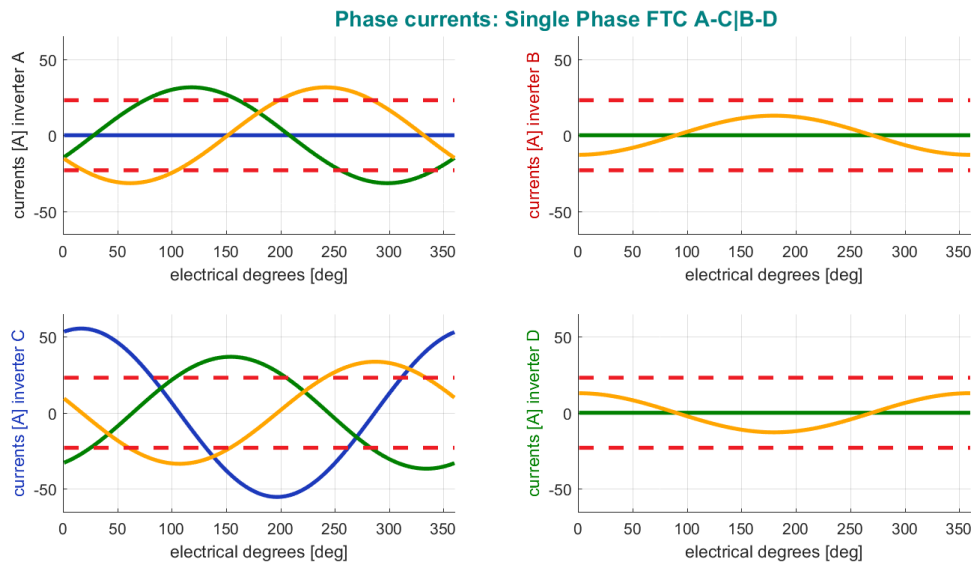


Fig. 3.30 – Analytical phase currents at rated value of the main current space vector.
 Double six-phase layout AC/BD (phases A1, B1, B2, D1, D2 open).

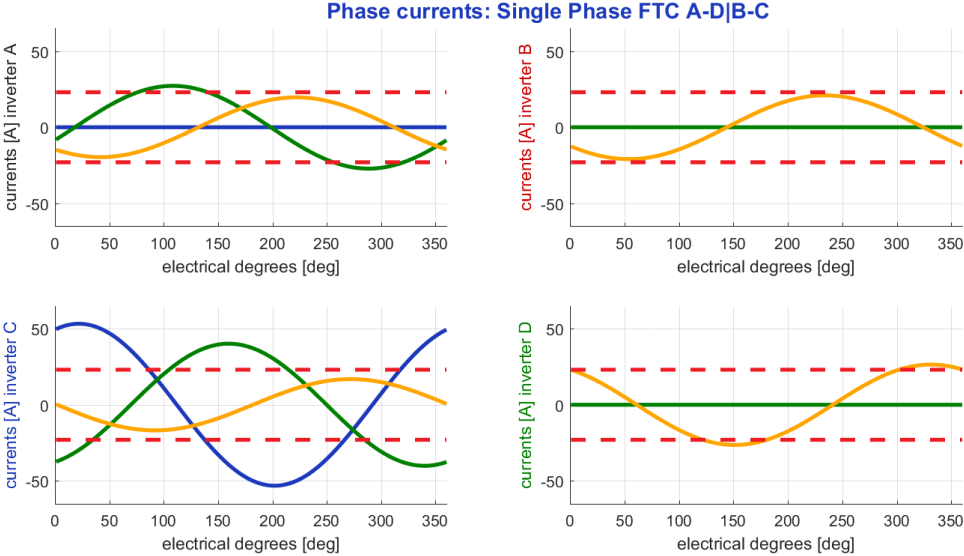


Fig. 3.31 – Analytical phase currents at rated value of the main current space vector.
 Double six-phase layout AD|BC (phases A1, B1, B2, D1, D2 open).

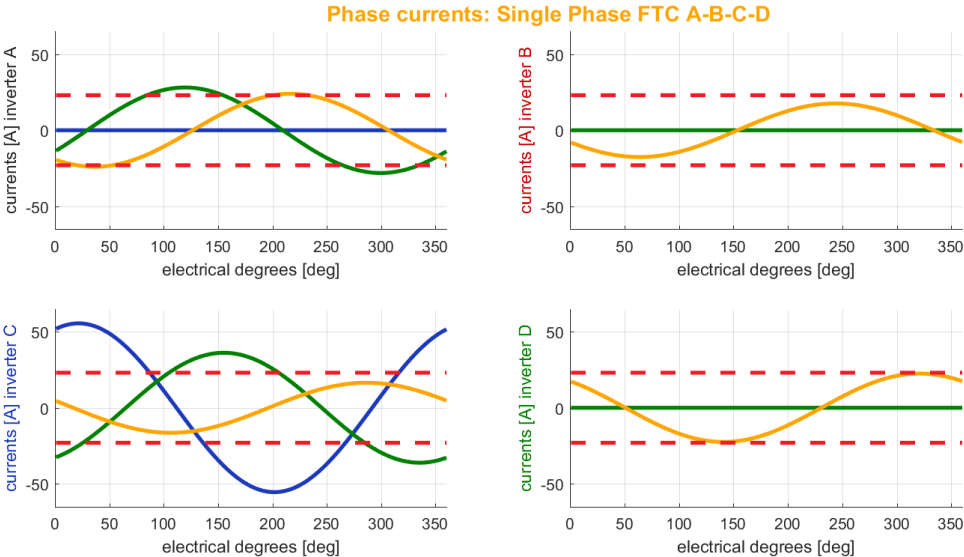


Fig. 3.32 – Analytical phase currents at rated value of the main current space vector.
 Twelve-phase layout ABCD (phases A1, B1, B2, D1, D2 open).

Control Schemes - Comparison

The current control of a multiphase machine differs from a standard three-phase one because of the increased number of degrees of freedom. A suitable way to develop the current control of an electrical machine is by means of a space vector approach. This means that the control is developed analysing the SVD machine model. Each space can be controlled on the idea that it represents an equivalent three-phase system (controlled in its d-q components) that interacts with the other ones as described by the machine model. In this subsection, the control schemes for a quadruple three-phase machine are presented, comparing the different possible solutions according to the star connection and desired FTC requirements.

Current Control– Independent stars: Current sharing (three-phase FTC)

The simplified current sharing equation for a quadruple three-phase machine (3.95) is:

$$\begin{cases} \bar{i}_5 = (K_A + jK_B - K_C - jK_D)\bar{i}_1^* \\ \bar{i}_7 = (K_A + jK_B - K_C - jK_D)\bar{i}_1 \\ \bar{i}_{11} = (K_A - K_B + K_C - K_D)\bar{i}_1^* \end{cases} \quad (3.97)$$

In this control scenario, owing to the star connections or to the current control algorithm, the current space vectors related to the homopolar sequences of the three-phase subsystems are zero ($\bar{i}_3 = \bar{i}_9 = 0$). In case of one or more open phase faults in one or more three-phase subsystems, the FTC algorithm works setting the current sharing coefficients (K_T) related to the faulty subsystems equal to zero.

According to (3.97), the auxiliary current space vectors are directly related to the main current space vector or to its conjugate.

Fig. 3.33 shows the current sharing control scheme of the machine.

As in a standard FOC for an induction machine, the d-axis current control of the main space vector is synchronous and directed in the direction of the rotor flux (\mathcal{G}), and it is used for generating the rotor flux itself. For a given rotor flux magnitude, the q-axis current control of the main space vector (synchronous with the rotor flux, but shifted by 90 electrical degrees from the d-axis in the positive direction) is used to control the machine torque (or in other words it allows the position, speed or power control).

At steady state operation, the main current space vector is a vector rotating at constant speed around a circular trajectory. Therefore, it is represented by a direct sequence of the currents, highlighted with a “+” in the control scheme. In the d-axis reference frame, the main current space vector \bar{i}_1 results as: $\bar{i}_1 = \bar{i}_{S1+,ref} = i_{S1d,ref} + j i_{S1q,ref}$. The PI regulator used for controlling

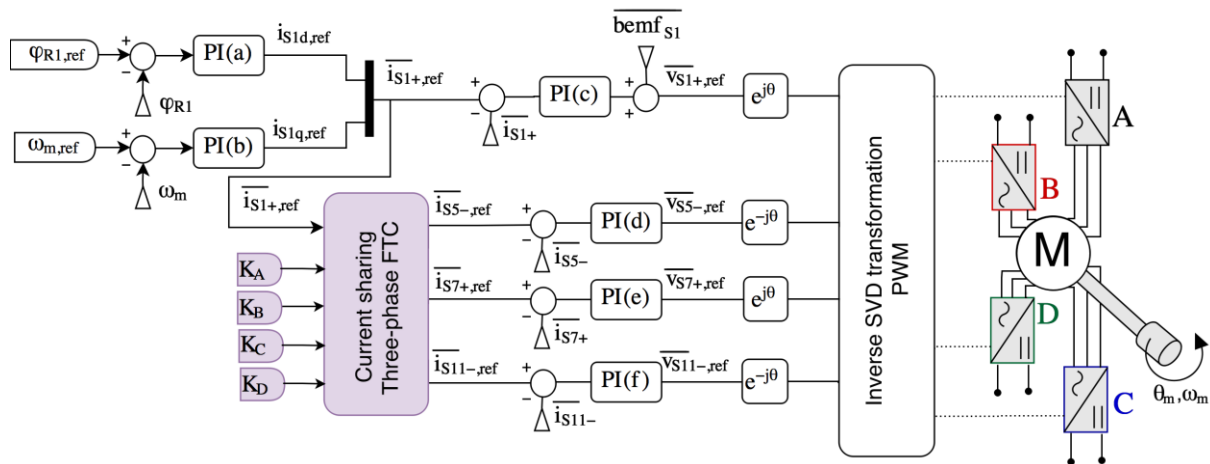


Fig. 3.33 – Block diagram of the current sharing and three-phase FTC control scheme.

the main current space vector d-q components is named as PI(c) in Fig. 3.33. Note that this PI is the sum of two regulators, one for the real part of the vector control and one for the imaginary one. The figure shows only one regulator for sake of scheme clarity, and the same is done for the other current space PI regulators.

The auxiliary current space vectors are represented by direct sequences (7th) or inverse ones (5th and 11th) as in (3.97). For this reason, the machine healthy and FT controls can be defined by means of a pair of synchronous PI regulators for each space (PI c, d, e and f in Fig. 3.33). The inverse sequences are highlighted with a “-“.

Owing to the hypothesis of the FTC algorithm, (it neglects the presence of the higher order field harmonics in the airgap), the compensation of the bemfs in the auxiliary spaces is not implemented. The PI outputs are the voltage space vectors. By means of standard Park transformations, the voltage space vectors are transferred to the stator reference frame. The inverse SVD transformation is used to evaluate the reference phase voltages and finally a standard PWM technique is used to define the inverter control. In case of more than three-phases connected to the same star, the multiphase PWM technique is used, as in [6].

Six additional PI regulators (the pairs related to PI(d), PI(e) and PI(f) in Fig. 3.33) are needed to implement a standard current sharing control (with the same d-axis and q-axis sharing coefficients) or a three-phase FTC. Then, there are also the remaining four standard FOC PIs (PI(a), PI(b) and PI(c)). However, these additional PI regulators are needed in the control of the multiphase machine also in a healthy operation. Indeed, in a standard multiphase FOC, the auxiliary current space vectors must be controlled to zero. In many cases, this already allows obtaining the best machine performance (there are also techniques that aim to improve the performance by exploiting also the auxiliary spaces, but usually the efficiency of the drive is reduced in these operations [7]).

Current Control– Independent Stars: single-phase FTC

When a single-phase FTC is implemented, the auxiliary current space vectors are controlled with both direct and inverse sequences. Therefore, the current control requires twice the PI regulators, as shown in Fig. 3.34. Fig. 3.34 highlights the logic of the three-phase FTC (in purple) and the single-phase FTC (in green). In particular, the additional PI regulators and transformations requested by the single-phase FTC are highlighted in green. The total number of additional regulators compared with a standard FOC is 12 (six pair of PI, two pairs for each auxiliary current space vector).

Current Control– General Solution (double six-phase or single star control): optimised single-phase FTC

If a double six-phase or a single-phase winding layouts are chosen, the homopolar currents flowing from one three-phase subsystem to another must be controlled. The control of these currents is related to the control of the auxiliary current space vectors \vec{i}_3 and \vec{i}_9 , as shown in Fig. 3.35. It result that the control of a double six-phase or a twelve-phase machine requires at least 10 auxiliary PI regulators (a pair for each of the five auxiliary space vectors: 3rd, 5th, 7th, 9th and 11th).

The FTC control of the machine requires just the 10 additional PIs if a three-phase FTC (or a basic current sharing technique) is implemented or if the machine is healthy. Instead, as soon as the method is enhanced to the single-phase FTC, the additional PIs must be twice. In total, the auxiliary PIs for an improved FTC are 20 (ten pairs, two pairs for each of the additional

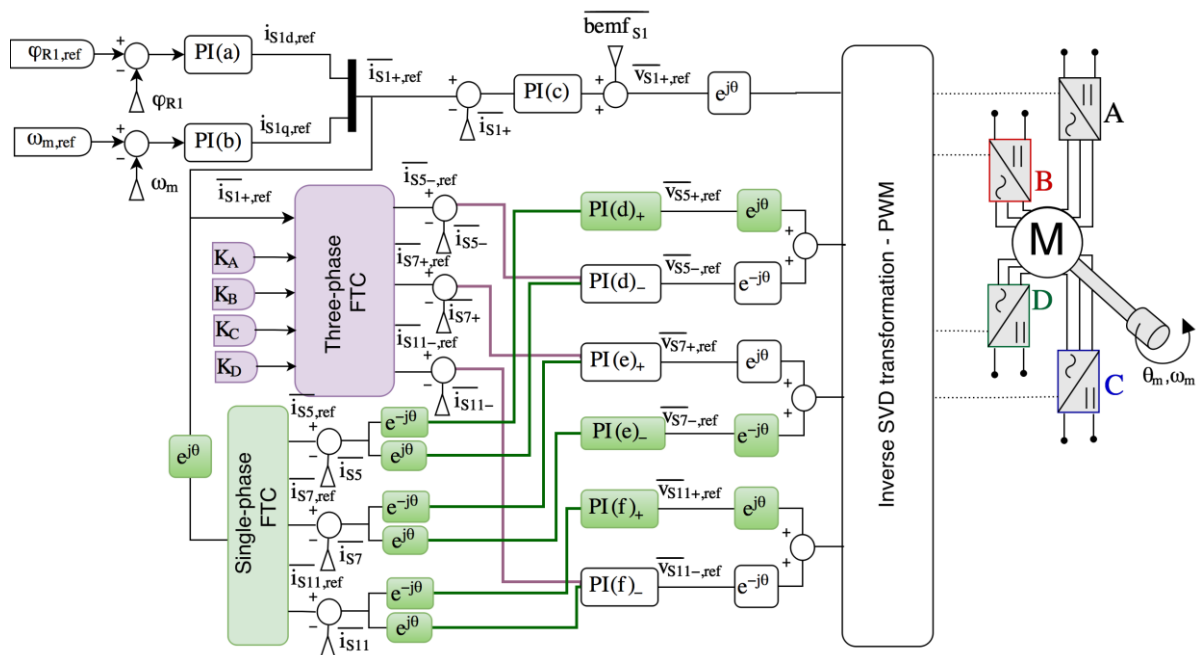


Fig. 3.34 – Block diagram of the single-phase and three-phase FTC control schemes.

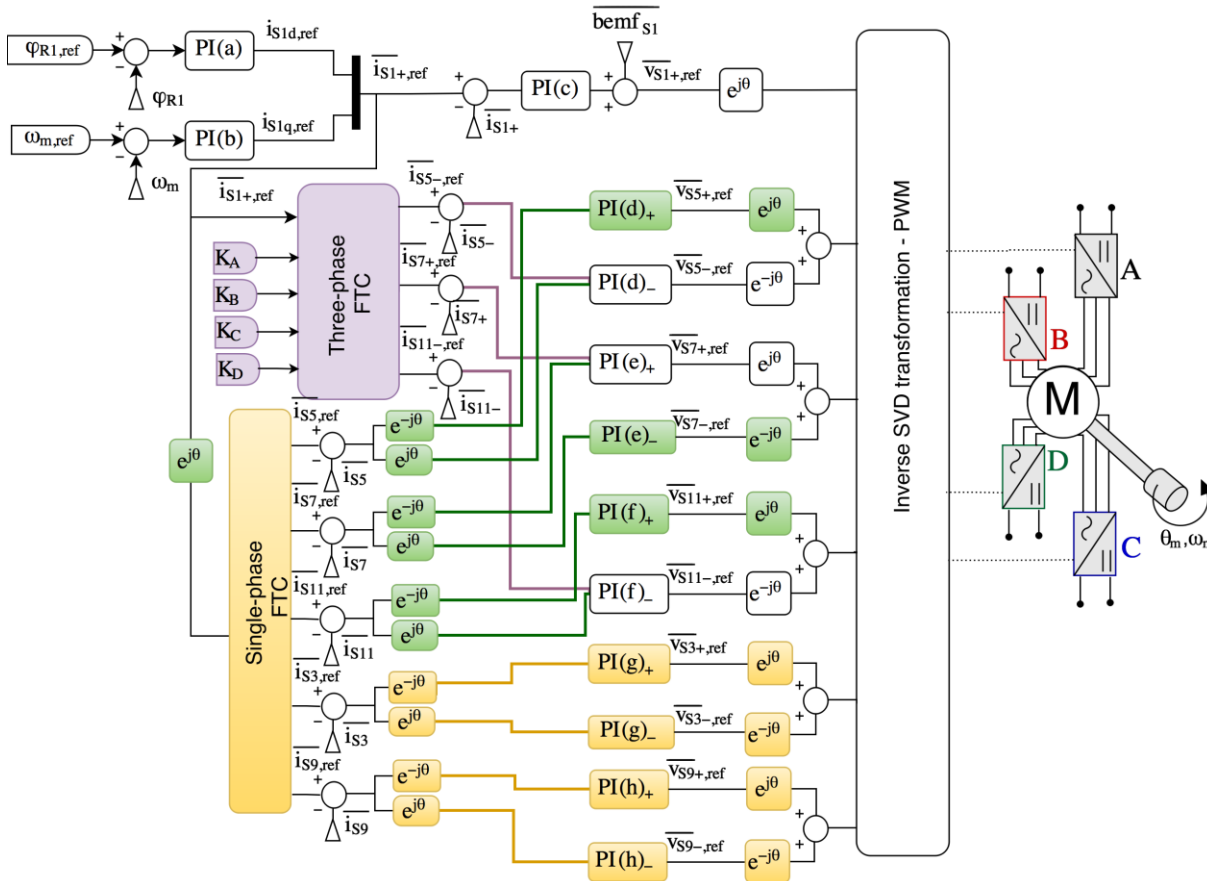


Fig. 3.35 – Block diagram of the single-phase and three-phase FTC control schemes.

space vectors). The additional PIs required by the optimized FTC are highlighted in orange in Fig. 3.35.

It is clear that the implementation of the machine control is more complex if the number of stars is reduced. Indeed, each star connection adds a constraint in the current control, reducing the number of controllable degrees of freedom. The reduced number of degrees of freedom can be found also in the current space vectors, and this must be taken into account in the development of the current control. If the star constraints are not properly considered, the PI regulators diverge (saturate) resulting in a deterioration or unfeasibility of the control.

Numerical simulation results (Matlab-Simulink)

Numerical simulation results are presented in this subsection to compare the different FTCs in terms of control complexity. The machine model is simplified in order to take into account for a reduced number of field harmonics (up to the 11th one). The space parameters are simplified and the cage is analysed as a 12-phase machine with a single star connection. In other words, the degrees of freedom of the cage is constrained to the same number of the stator ones. The simulations are based on a Matlab-Simulink code, where most of the blocks are developed by Matlab scripts.

The simulation results are presented for reduced speed and currents, in order to compare them with the obtained experimental results (done at no load, reduced speed and with a limited power supply in order to avoid risks in case of fault behaviour and FTC).

Simulation results– Independent Stars: three-phase and single-phase FTC

Fig. 3.36 shows the Matlab-Simulink simulation results for the quadruple three-phase configuration (four independently star connected three-phase windings). Firstly, the machine is magnetized and it is accelerated up to 300 rpm (with a smooth slope starting at 0.25 s). At $t=1$ s a sudden fault happens (in the first analysis the single-phase fault is investigated, with the phase A1 opening) and the FTC acts instantaneously. The FTC compensates the open phase fault by increasing the current in the remaining healthy phases according to the desired FTC method (three-phase FTC from 1 to 1.25 s, and single phase FTC from 1.25 to 1.5 s).

It can be noticed that the maximum phase current remains almost the same in the two FTCs. Fig. 3.37 shows the comparison of the phase currents in the different steady state working conditions (healthy, with three-phase FTC and with single-phase FTC). The results are the same

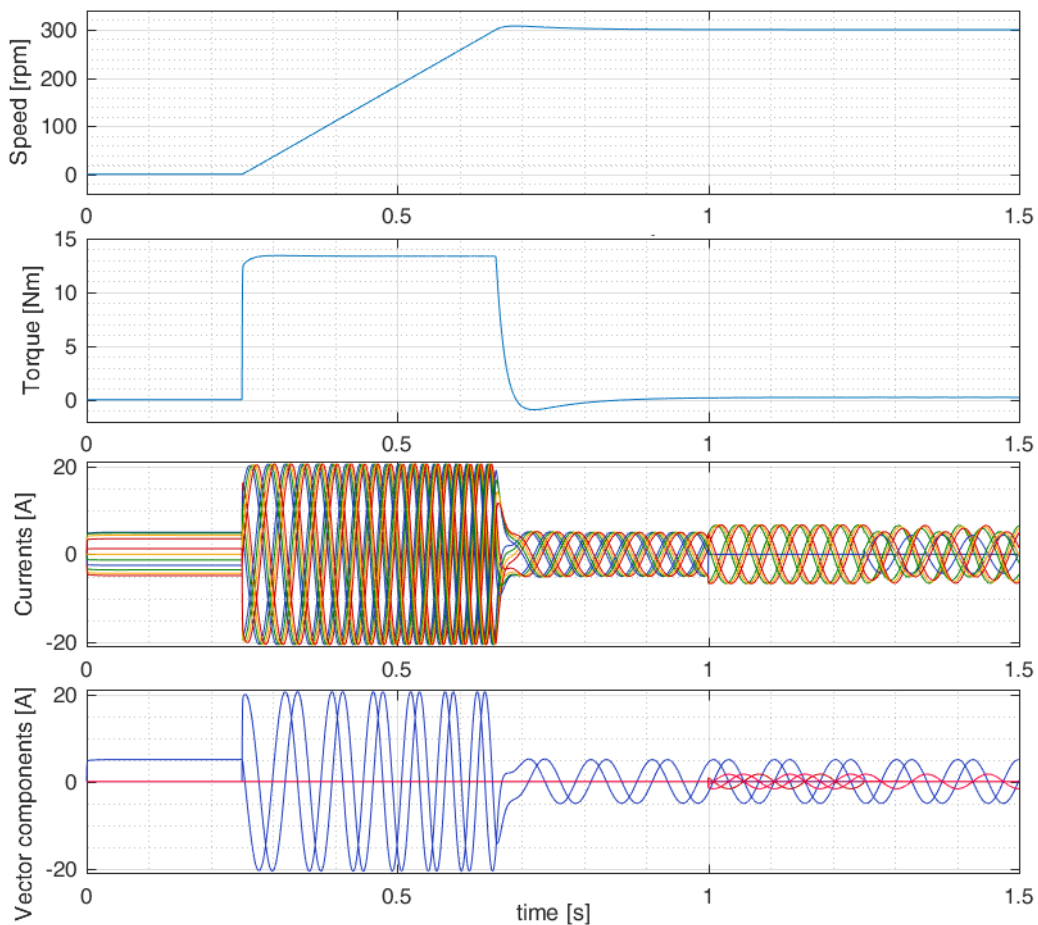


Fig. 3.36 – Simulation of a speed transient from 0 to 300 rpm, followed by the fault of phase A1 open ($t=1$ s). From 1 to 1.25 s three-phase subsystem FTC, from 1.25 to 1.5 s single-phase FTC. The last subplot shows the α - β components of the main current space vector i_{S1} (blue) and of the auxiliary ones (red).

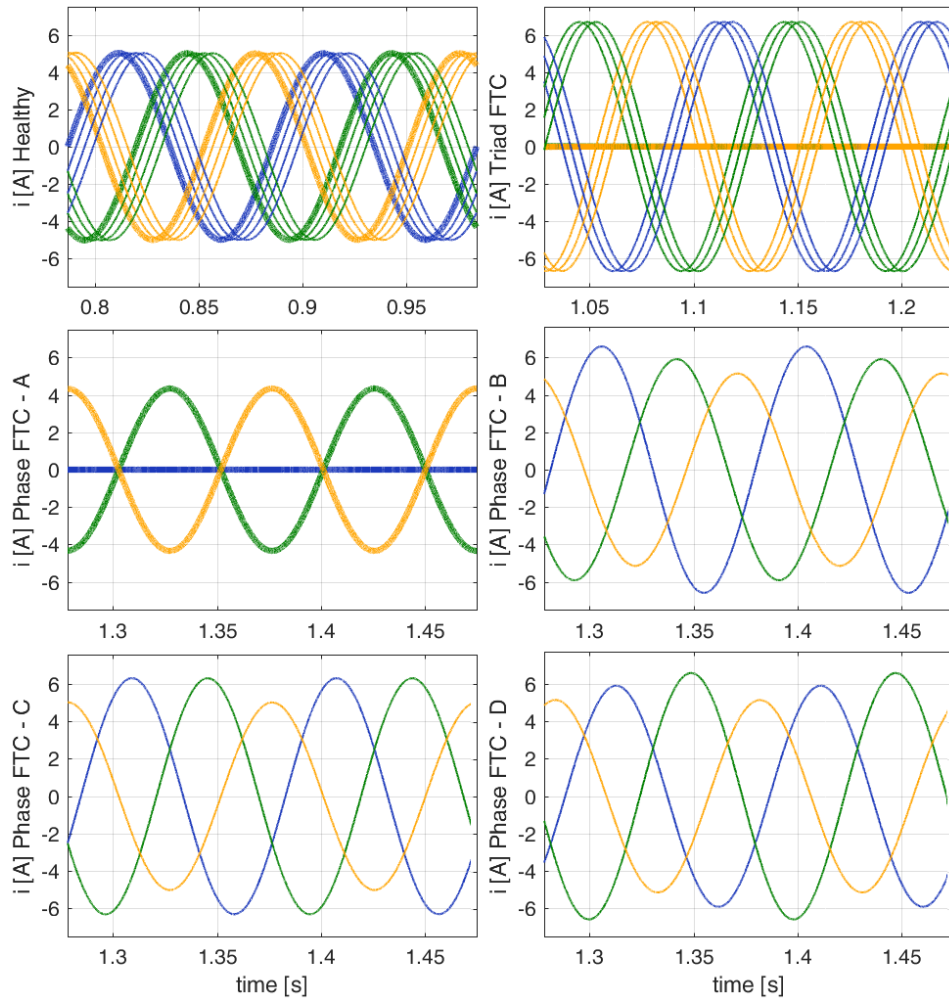


Fig. 3.37 – Simulated phase currents. The machine is healthy (top left) and then has phase A1 opened, with the three-phase FTC (top right) and the single-phase FTC (centre and bottom). With colours are differentiated the 1st phase (blue), the 2nd (green) and the 3rd (orange) of each inverter. The thickest lines refer to the phase currents of inverter A.

expected from the analytical comparison. Indeed, with the single-phase FTC the currents are better distributed in the remaining healthy phases, but the maximum peak current is almost the same as in the three-phase FTC.

What is more interesting in terms of current control implementation is that the trajectories of the current space vectors are significantly different in the two methods.

Fig. 3.38 shows the trajectories of the current space vectors resulting from the Matlab-Simulink simulations. As expected, the main current space vector trajectory is always the same independently from the working scenario (the main FTC goal is to do this). When the machine is healthy (blue trajectories in Fig. 3.38), the auxiliary current space vectors are controlled to zero (being a result of an ideal simulation, the references are followed really well by the PI controllers). When the three-phase FTC is working, the auxiliary current space vectors are controlled according to (3.97). Being the trajectories circumferences, a direct sequence regulator (7th space) or an inverse one (5th and 11th spaces) for each component of the current vectors is enough.

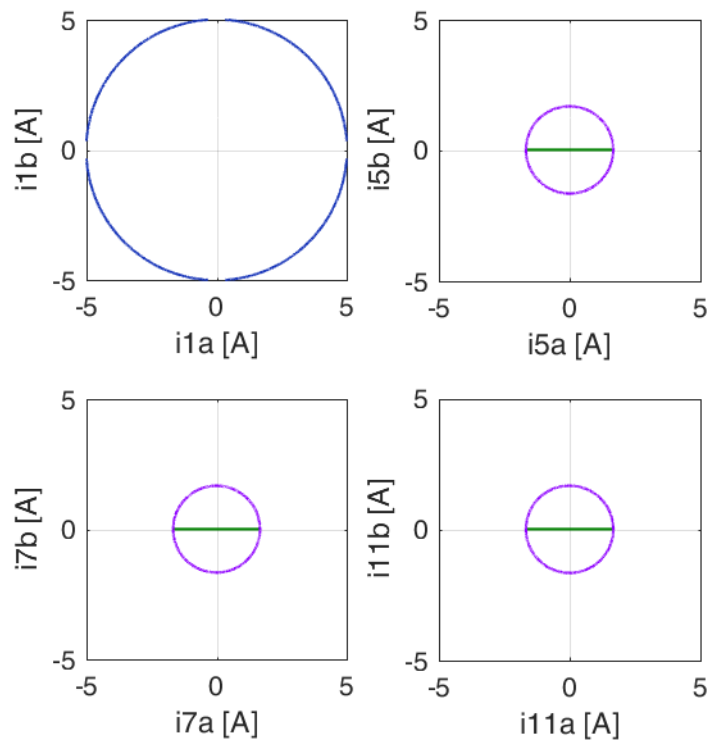


Fig. 3.38 – Simulated current space vectors trajectories. Trajectory of \hat{i}_{Ω} (blue) and of the auxiliary vectors in case of single-phase FTC (green) and three-phase subsystem FTC (purple).

When the single-phase FTC is activated, the trajectories of the current space vectors are segments. A segment trajectory can be analysed, in terms of space vector control, as the sum of a direct and an inverse sequence of the rotating space vector with same amplitude and speed, with the only difference that the inverse sequence is rotating in the opposite direction. In this particular case (phase A1 open fault), the segments are moving on the real-axis (α), but in general the segments are shifted according to the fault condition. Instead, the effect of the FTC on the trajectory and the distribution of the currents between the phases is not affected by the working operation (on-load and no-load operation result in the same FTC behaviour).

The current distribution between the remaining healthy phases is presented in Table 3.2.

As can be noticed, in this particular case the peak current in the B1 and D2 phases is almost the same in the two FTCs, while in the other phases the currents are significantly reduced with the single-phase FTC.

Table 3.2 – Maximum phase current in case of A1 open phase fault (in p.u. to the value of the healthy machine)

	Healthy	Three-phase FTC	Single-phase FTC
A1	1	0	0
A2	1	0	0.87
A3	1	0	0.87
B1	1	1.33	1.31
B2	1	1.33	1.18
B3	1	1.33	1.03
C1	1	1.33	1.26
C2	1	1.33	1.26
C3	1	1.33	1
D1	1	1.33	1.18
D2	1	1.33	1.31
D3	1	1.33	1.03

Simulation results– Double Six-Phase winding: Single-phase FTC

The simulations have been carried out also for the other winding layouts (double six-phase and twelve-phase). When the three-phase homopolar currents can flow from one three-phase subsystem to another, the 3rd and 9th current space vectors are no more zero.

Fig. 3.39 shows the three-phase homopolar currents with the different double six-phase configurations in case of single phase FTC with phase A1 open fault. The three-phase homopolar currents are related to the 3rd and 9th space vectors. Therefore, the auxiliary current space vectors are all different from zero in the FT operation.

Open Phase Faults and Fault Tolerant Controls in Multiphase Drives

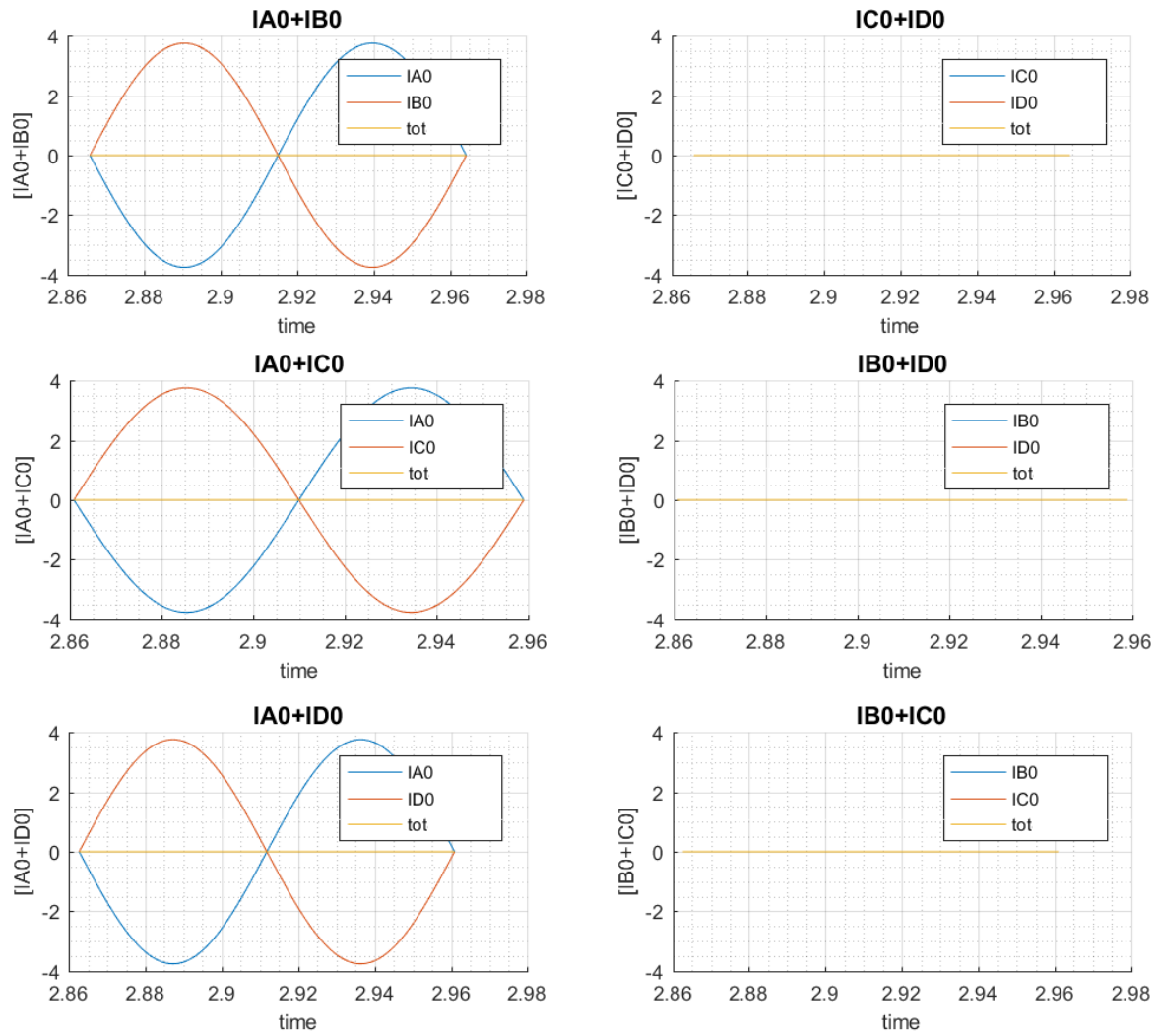
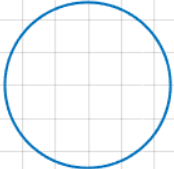
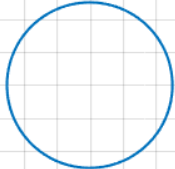
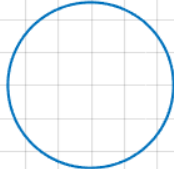
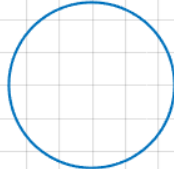

















Fig. 3.39 – Three-phase homopolar currents in case of phase A1 open fault and single phase FTC. AB/CD star connection (top), AC/BD star connection (centre) and AD/BC star connection (bottom).

CHAPTER 3

Table 3.3 shows the current space vector trajectories when the machine is healthy and when the single-phase FTC is on.

Table 3.3 – Comparison of the current space vector trajectories in respect to the healthy behaviour in case of A1 open phase fault. The scale is of 2A/div in all the figures.

Space	Healthy	AB CD	AC BD	AD BC
1				
3				
5				
7				
9				
11				

It is interesting to note that the trajectory are similar in the 5th, 7th and 11th auxiliary spaces, with just different magnitudes of the vectors. Instead, the 3rd and 9th current space vectors are different also in terms of phase angle.

Table 3.4 shows the current distribution between the remaining healthy phases according to the different double six-phase layouts. The AB|CD layout seems the best in terms or current distribution among the healthy phases, but this happens only for the particular analysed fault.

Indeed, if the fault happens in the three-phase subsystem B or C, the AD|BC configuration behaves with a maximum current as the one given by the AB|CD winding configuration (that remains always as in the analysed case). Therefore, the winding that results in the best current distribution (minimum peak current) in all the faulty conditions is the AC|BD one. The AD|BC behaves better than the others only when the fault is in the A or D three-phase subsystems, but being the fault location unpredictable, the AC|BD is still the best solution.

Simulation results–Single-Star winding: Single-phase FTC

The single-star configuration is the one that allows exploiting the highest number of degrees of freedom (the open end-winding configuration is not analysed).

Fig. 3.40 shows the three-phase homopolar currents with the single-star (twelve-phase) configuration in case of single phase FTC with phase A1 open fault. As in the double six-phase layout, the auxiliary current space vectors are all different from zero in the FT operation.

Table 3.5 shows the current space vector trajectories when the machine is healthy and when the single-phase FTC is on, comparing all the proposed FTC techniques.

Table 3.6 presents the current distribution between the remaining healthy phases according to the different star connection layouts.

Table 3.4 – Maximum phase current in case of A1 open phase fault (in p.u of the value of the healthy machine).

	Healthy	AB CD	AC BD	AD BC
A1	1	0	0	0
A2	1	0.94	0.94	0.94
A3	1	0.94	0.94	0.94
B1	1	1.48	1.24	1.24
B2	1	0.95	1.13	1.13
B3	1	0.97	1.02	1.02
C1	1	1.19	1.42	1.19
C2	1	1.19	0.97	1.19
C3	1	1	1.03	1
D1	1	1.13	1.13	1.33
D2	1	1.23	1.24	0.99
D3	1	1.02	1.02	1.12

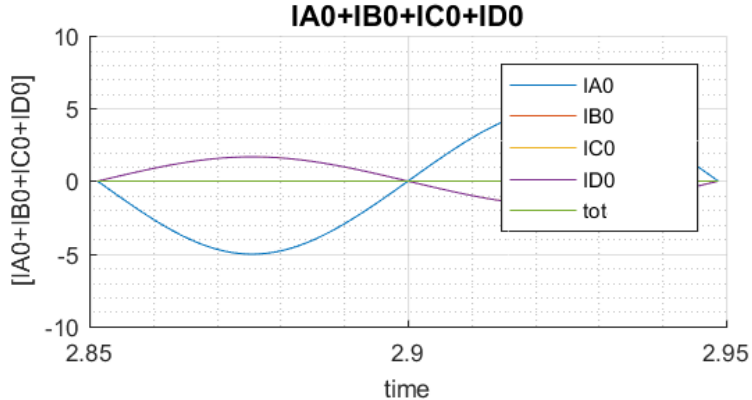


Fig. 3.40 – Three-phase homopolar currents in case of phase A1 open fault and single phase FTC. Single-star layout.

Table 3.5 – Comparison of the current space vector trajectories in respect to the healthy behaviour in case of A1 open phase fault. The scale is of 2A/div in all the figures.

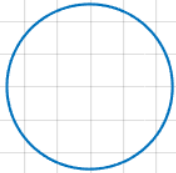
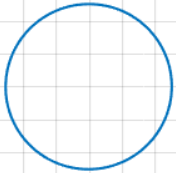





Space	Healthy	Single Star	Space	Single Star
1			7	
3			9	
5			11	

Table 3.6 – Maximum phase current in case of A1 open phase fault (in p.u of the value of the healthy machine).

	Healthy	3-ph FTC	1-ph FTC	AB CD	AC BD	AD BC	Single-Star
A1	1	0	0	0	0	0	0
A2	1	0	0.87	0.94	0.94	0.94	1
A3	1	0	0.87	0.94	0.94	0.94	1
B1	1	1.33	1.31	1.48	1.24	1.24	1.32
B2	1	1.33	1.18	0.95	1.13	1.13	1.03
B3	1	1.33	1.03	0.97	1.02	1.02	0.99
C1	1	1.33	1.26	1.19	1.42	1.19	1.28
C2	1	1.33	1.26	1.19	0.97	1.19	1.07
C3	1	1.33	1	1	1.03	1	1.01
D1	1	1.33	1.18	1.13	1.13	1.34	1.21
D2	1	1.33	1.31	1.23	1.24	0.99	1.1
D3	1	1.33	1.03	1.02	1.02	1.12	1.06

Simulation results–Comparison: multi-phase critical fault FTC

The same fault configuration used as example for the analytical study, has been simulated to show the control and performance behaviour when a catastrophic fault happens. The fault is described by the following relationship:

$$i_{A1} = i_{B1} = i_{B2} = i_{D1} = i_{D2} = 0.$$

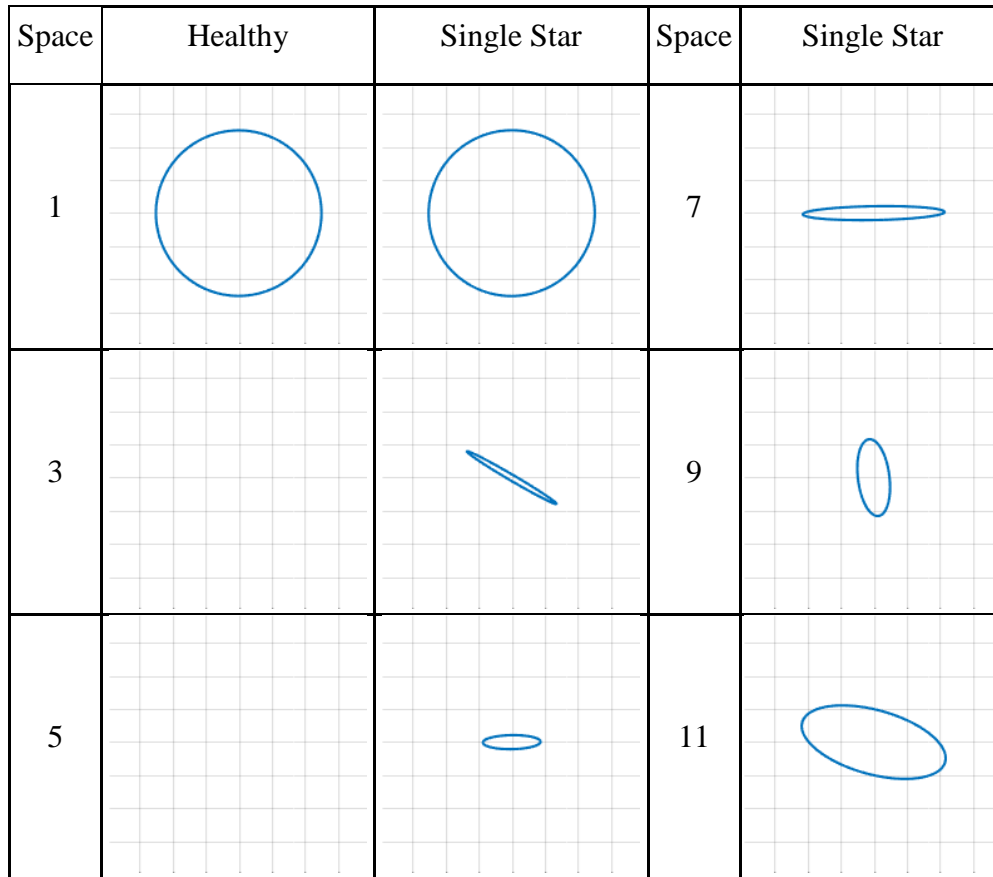
Therefore, only one three-phase subsystem is completely working. As mentioned in the previous analysis, the aim is not to justify the fault phenomenology but just showing the differences in terms of FTC algorithms and star connections. Without showing all the simulation results, it is interesting to note that in this fault scenario (as happens in general) the auxiliary current space vector trajectories are ellipsoids, as shown in Table 3.7 for the single-star configuration. It is also interesting to note that the amplitude of the auxiliary current space vectors is quite big when a fault as the one analysed here happens. Therefore, the hypothesis of the model to neglect the effects of the higher order space vectors in the magnetic field in the airgap might not be admissible, and some additional effects might be considered.

Table 3.8 reports the maximum phase currents reached in the different FTCs. It is clear that the proposed algorithm does not aim to distribute the current contributions to the main current space vector in order to minimize the peak current. Indeed, the algorithm is developed for the stator copper Joule losses minimization.

The significant increase of current and related copper losses in the remaining healthy phases result in an excessive overrating. As previously shown in Fig. 3.24 and Fig. 3.25, the main current space vector (machine output power) must be reduced at least of about two times in terms of total stator copper losses (steady state derating), and of about three times (in transient overload conditions) to not exceed the maximum current in the switching devices. Therefore, for the analysed drive the maximum current constraint affects the FTC steady state performance

CHAPTER 3

Table 3.7 – Comparison of the current space vector trajectories in respect to the healthy behaviour in case of A1, B1, B2, D1 and D2 open phases fault. The scale is 2A/div in all the figures.



more than the Joule losses constraint in case of a catastrophic fault. Instead, for a single phase fault, the Joule losses and maximum current constraints can still be taken into account separately for the steady state and overload working operations (as in the healthy condition).

Table 3.8 – Maximum phase current in case of A1, B1, B2, D1 and D2 open phase faults (in p.u of the value of the maximum peak current for the healthy machine).

	Healthy	3-ph FTC	1-ph FTC	AB CD	AC BD	AD BC	Single-Star
A1	1	0	0	0	0	0	0
A2	1	0	1.73	1.65	1.97	1.7	1.75
A3	1	0	1.73	0.93	1.97	1.23	1.51
B1	1	0	0	0	0	0	0
B2	1	0	0	0	0	0	0
B3	1	0	0	0.96	0.8	1.31	1.1
C1	1	4	3.61	3.55	3.47	3.33	3.49
C2	1	4	3.61	3.43	2.3	2.51	2.26
C3	1	4	1	1.19	2.1	1.05	1.03
D1	1	0	0	0	0	0	0
D2	1	0	0	0	0	0	0
D3	1	0	0	1.1	0.81	1.65	1.41

Finite Element Results (Flux): Comparison of iron saturation and related torque reduction in case of two three-phase subsystem open phase fault (best double six-phase configuration for simplified six-phase FTC performance enhancement)

FE simulations have been carried out to understand the machine behaviour in case of open phase fault, and understand if the hypothesis behind the developed FTC are sufficient. In particular, the three-phase FTC with one and two faulty subsystems is analysed here.

The simulations are carried out at rated speed (5941 rpm, with electrical frequency of about 200 Hz) and at rated current (16 Apk, 11.5 Arms).

Between the differences in terms of winding configuration, it is clear that the increased complexity of the control for a twelve-phase machine compared with a quadruple three-phase one can be justified by the improved FTC performance. Indeed, the stator copper losses are significantly reduced in the single-star FTC. Instead, the double six-phase configurations analysis shows advantages on the AC|BD star connection for keeping the maximum phase current lower in the worst fault scenario.

As it has been done for the quadruple three-phase FTC, also for the double six-phase layout it is possible to define a FTC that controls to zero all the currents in the faulty subsystem (the one where the open phase fault happens). This FTC is named here as six-phase FTC. The method is based on the current sharing technique, with the difference that the current sharing constants in (3.97) are equal for the two three-phase subsystems connected to the same star. Because this control technique is much easier to implement in a double six-phase machine than a single-phase FTC one, some FE analysis are done to define which is the best double six-phase configuration also for the double six-phase FTC.

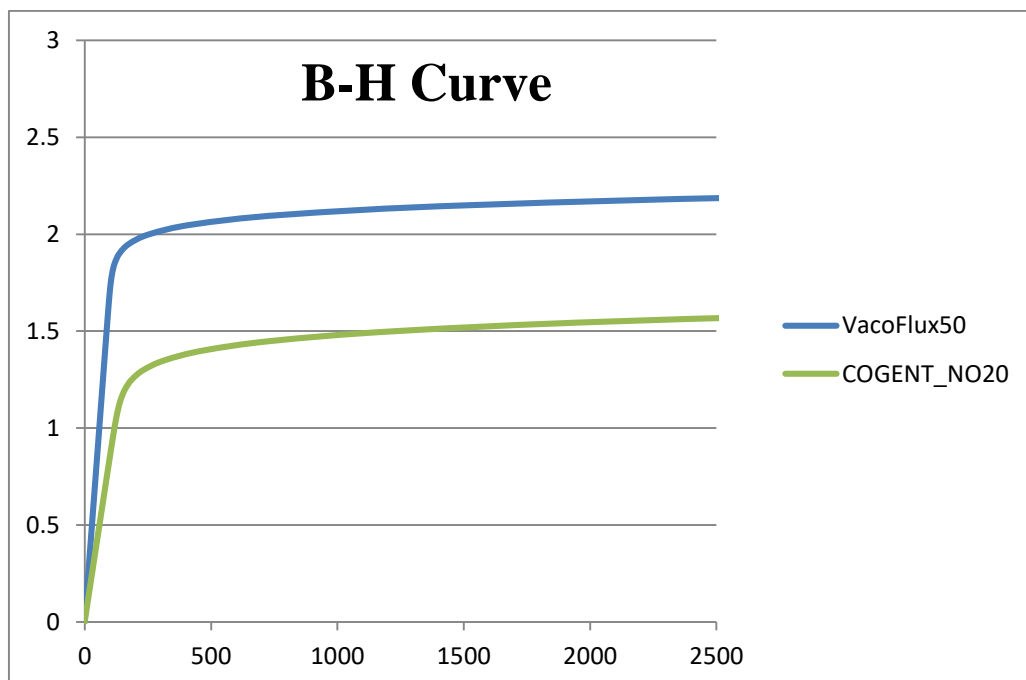


Fig. 3.41 – B-H curve of the stator (NO 20) and rotor (VacoFlux 50) laminations.

Note that the analysed machine has FeCo laminations in the rotor. In particular, a VACOFLUX 50 supplied by VACUUMSCHMELZE GmbH & Co. Therefore, the iron saturation is at much higher value (at about 2 T) than the one of a standard lamination (as the one of the stator, NO 20 supplied by Cogent Power Ltd). Fig. 3.41 shows the B-H curve of the two materials.

Quadruple Three-Phase Configuration (Three-phase FTC)

Fig. 3.42 shows the machine behaviour at rated conditions when the machine is healthy (left), when the currents of one three-phase subsystem are set to zero while the currents in the others are maintained as before the fault (centre), and when the three-phase FTC is implemented in order to compensate the fault by the remaining healthy phases.

Because the remaining healthy phases work in an overload condition, the iron saturation reduces the actual torque of about 1.5 %.

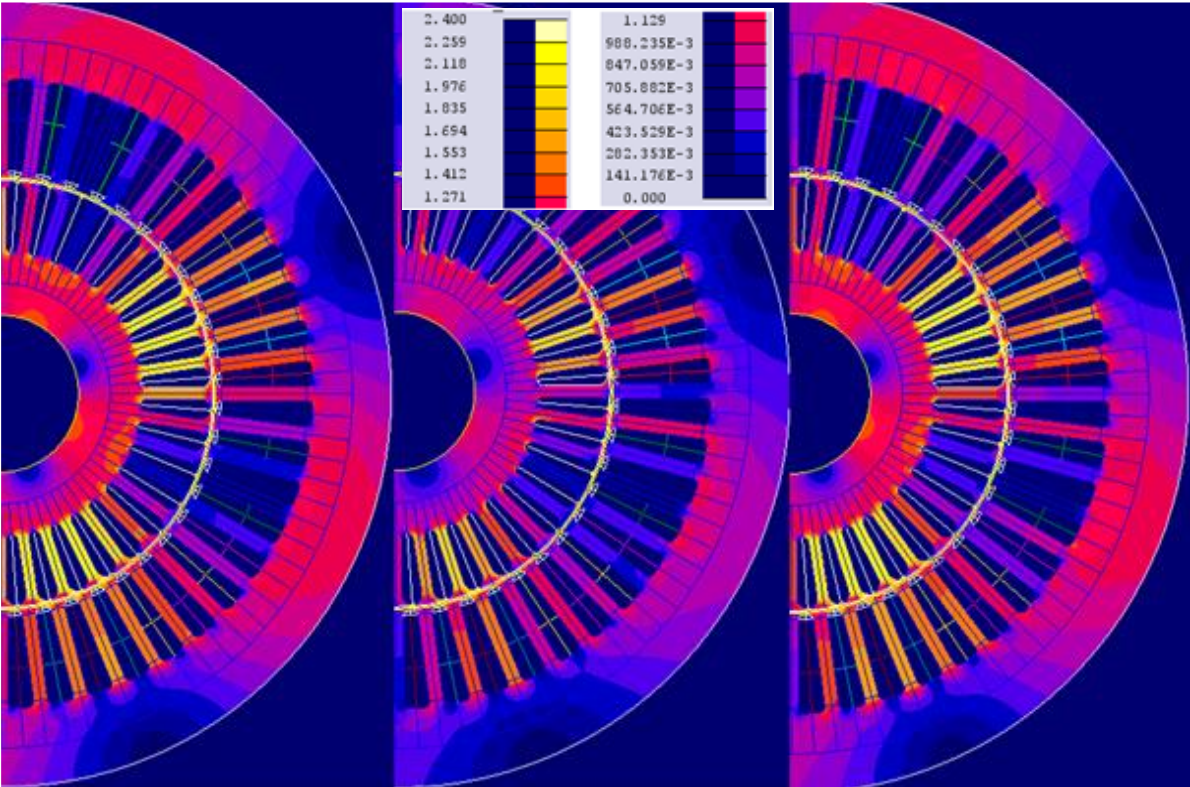


Fig. 3.42 – Flux view for the healthy machine (left), the machine working with a three-phase open fault without FTC (centre) and with three-phase FTC (right). Inverter D three-phase open fault.

Dual Six-Phase Configuration (Neighbouring three-phase subsystems - AB|CD and AD|BC)

The dual six phase configurations AB|CD and AD|BC behave in the same way in the worst scenario of six-phase FTC (six-phase open fault), because in both cases the fault happens in two series connected neighbouring three-phase subsystems. Therefore, the analysis is presented only for the AB|CD configuration with the six-phase subsystem CD FTC.

Fig. 3.43 shows the machine behaviour at rated conditions when the machine is healthy (left), when a six-phase subsystem current are set to zero and the others maintain the same amplitudes (centre), and when the six-phase FTC is implemented. The same main current space vector is generated by the AB subsystem to compensate the fault.

Because the remaining healthy phases work in an overload condition, the iron saturation reduces the actual torque of about 5.5 %. This torque reduction is quite important, and it is intensified by the concentration of the magneto motive force produced by the stator currents (because the two remaining three-phase subsystems are neighbouring).

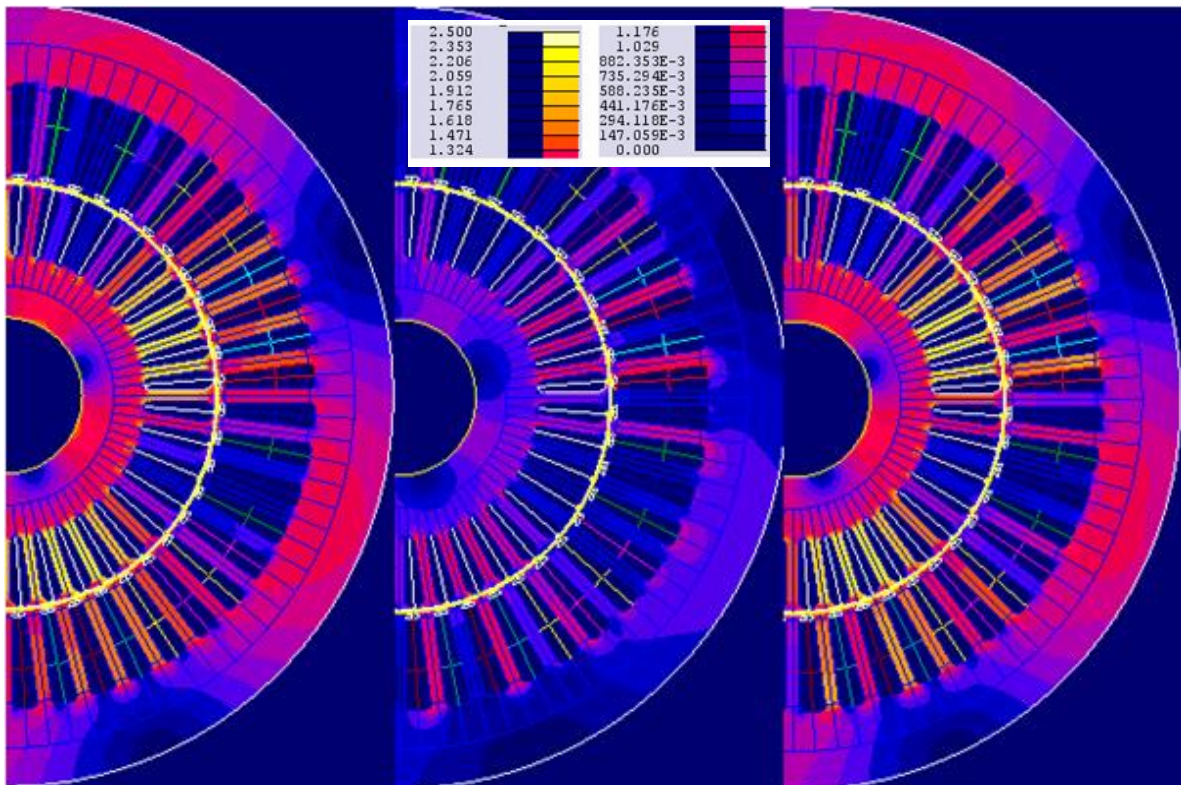


Fig. 3.43 – Flux view for the healthy machine (left), the machine working with a six-phase open fault without FTC (centre) and with six-phase FTC (right). Inverters C and D six-phase open fault.

Dual Six-Phase Configuration (Not neighbouring three-phase subsystems – AC|BD)

Fig. 3.44 shows the machine behaviour at rated conditions when the machine is healthy (left), when the currents of one six-phase subsystem (BD) are zero and the others are maintained as before the fault (centre), and when the six-phase FTC is implemented in order subsystem (AC) to compensate the fault by its remaining healthy phases.

Because the remaining healthy phases work in an overload condition, the iron saturation reduces the actual torque of about 3.6 %. This torque reduction is less than the one found for the case of neighbouring three-phase subsystems fault. It results that also in terms of iron saturation in case of six-phase open FTC the best FTC performance is reached with an AC|BD double six-phase layout.

It is important to notice that if the machine is not a 12-phase machine, but just a six-phase one, this result does not mean that the six-phase machine winding must be defined following this idea. Indeed, if the phases are distributed in more slots per pole, the best solution for increasing the machine torque/Ampere ratio is the one with the phases distributed in neighbouring slots. The result reported here is only for a 12-phase current control.

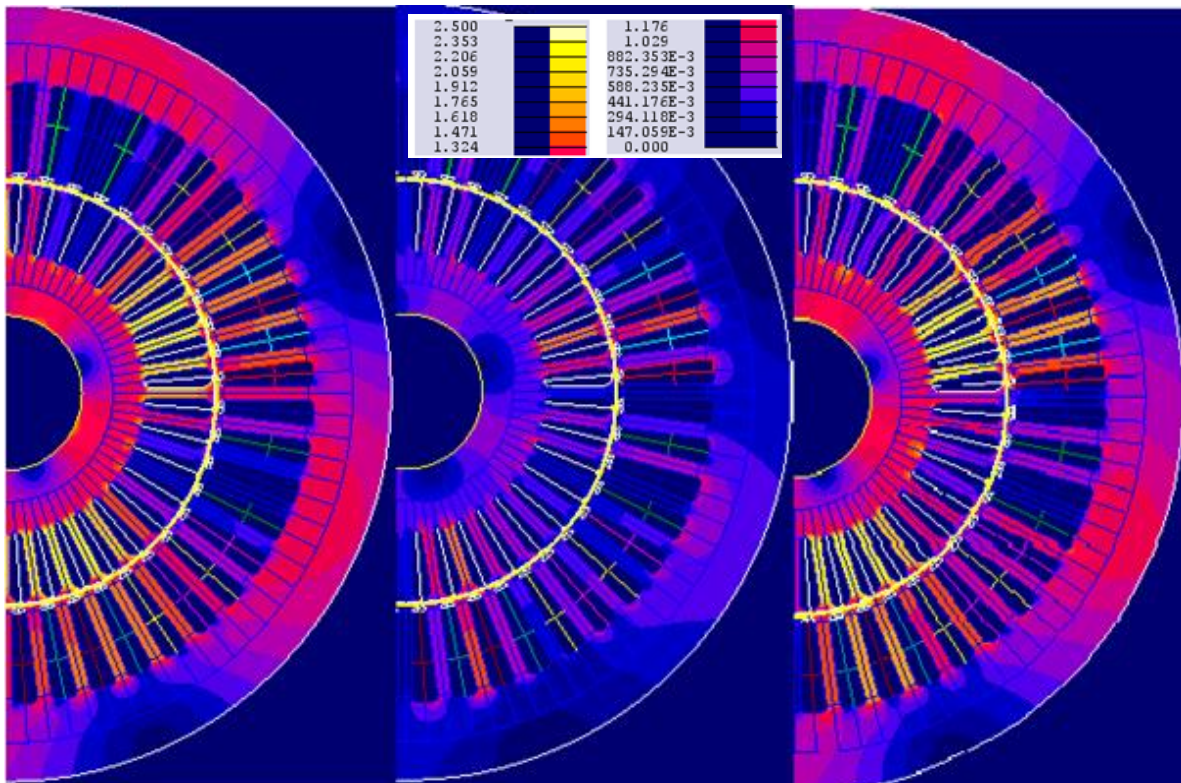


Fig. 3.44 – Flux view for the healthy machine (left), the machine working with a six-phase open fault without FTC (centre) and with six-phase FTC (right). Inverters B and D six-phase open fault.

Experimental results

Some experimental results are presented in this subsection in order to validate the possibility to implement the FTC and verify the theory presented in this chapter. Where not specified, the presented tests are at no load, 5 A of magnetizing current (d-axis component) and 300 rpm speed.

Test bench

Fig. 3.45 shows the test bench, where a gearbox (9:1) connects an electrical machine to the analysed drive. The torque is measured by a Kistler 4503A50H00B1000.

The tests have been carried out on a scaled prototype of starter-generator for MEE applications (right side of Fig. 3.45). The machine has twelve phases that can be star connected in the terminal box in whatever configuration. The main machine control parameters are the ones already presented in Table 3.1. Fig. 3.46 shows the exploded inverter components.

Fig. 3.47 shows the full quadruple three-phase inverter and control platform (left) and the induction machine prototype (right).

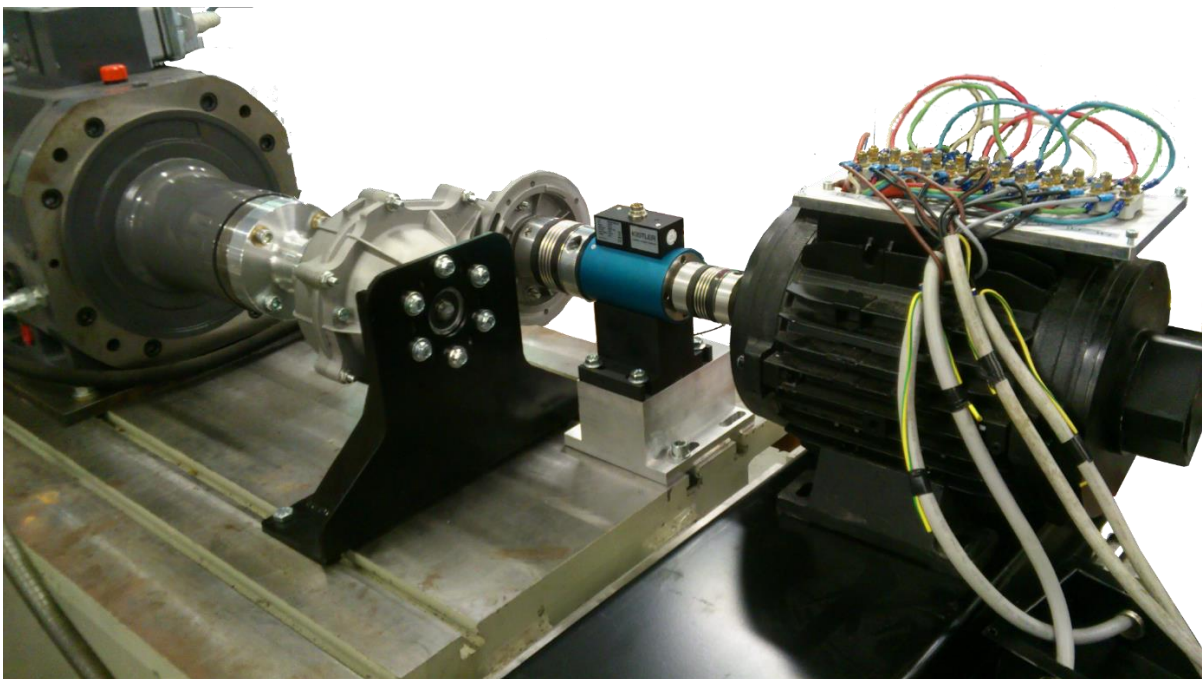


Fig. 3.45 – Test bench. From left to right: load (bidirectional drive) gearbox 9:1, torque meter, scaled prototype.

Independent Stars: Simplified current sharing control (matryoshka and circulating power)

Two examples of the simplified current sharing theory have been verified by experimental tests at 1000 rpm and 9 Nm torque.

The first one, named here as “matryoshka current sharing”, is presented in order to verify that it is possible to control the four three-phase subsystems of the quadruple three-phase machine with different current sharing constants.

The “matryoshka current sharing” control is defined by the relationship:

$$K_A = 2K_B = 4K_C = 8K_D.$$

Fig. 3.48 shows the first currents of each of the four three-phase subsystems.

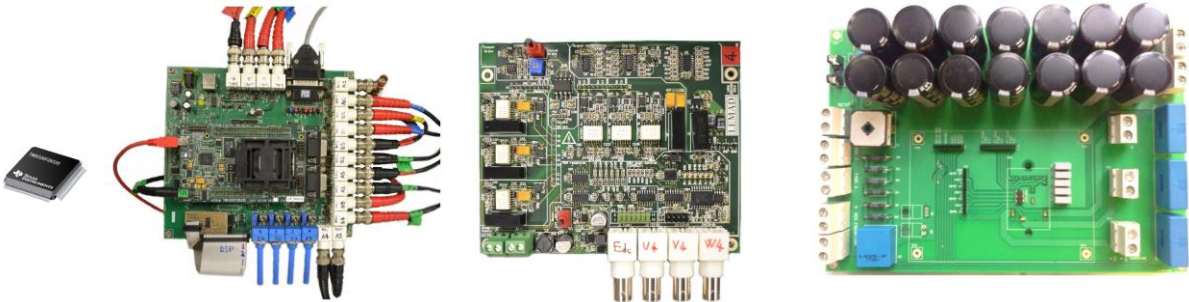


Fig. 3.46 – Test bench. From the left to the right: DSP TMS320F28335, control board (with DSP), driver’s board for one three-phase winding, power board for one three-phase winding.

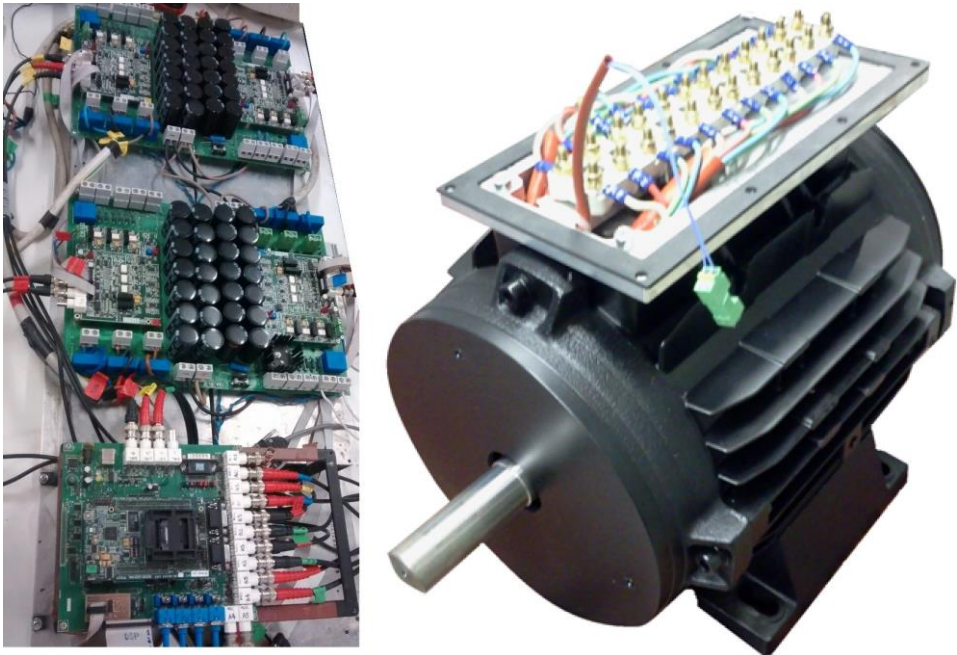


Fig. 3.47 – Quadruple three-phase inverter (left) and twelve phase starter/generator scaled prototype (right).

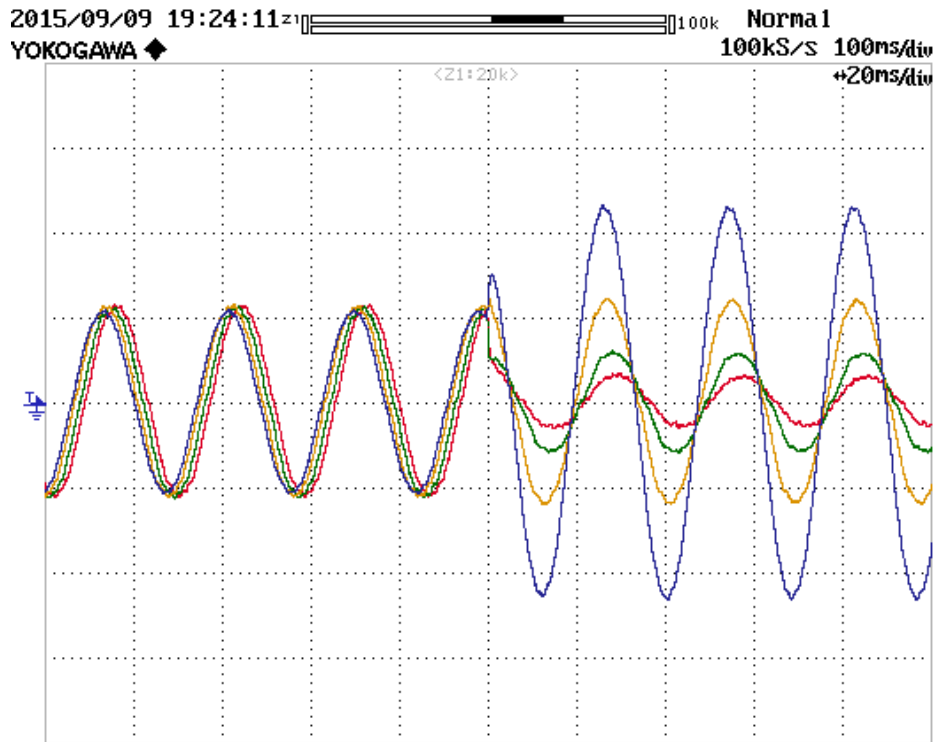


Fig. 3.48 – Matryoshka current sharing control with $K_A = 2K_B = 4K_C = 8K_D$, [10 A/div].

The second example, shown in Fig. 3.49, validates the possibility to control one three-phase

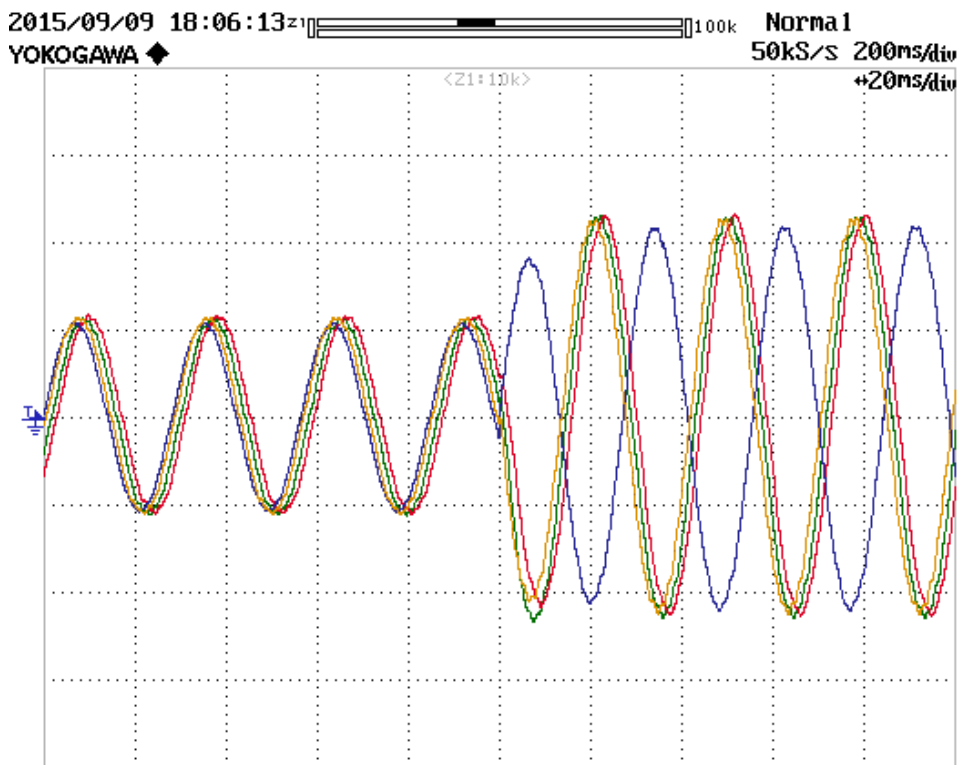


Fig. 3.49 – Simplified current sharing control with $K_A = -0.5$ and $K_B = K_C = K_D = 0.5$, [10 A/div].

subsystem with a negative current sharing coefficient. This means that the considered three-phase subsystem is working in generating mode while the three others are working in motoring mode. Note that the current sharing technique in Fig. 3.49 is not the optimized one for the generation of the rotor flux (while three subsystems are working to produce it, the subsystem A is working in flux weakening control). If this technique is likely to be used in a real application, it must be improved with different current sharing coefficients on the d and q axes as explained in 3.3.

Independent Stars: comparison between three-phase and single-phase FTC

The experimental results for the FTC are presented for the machine working at 300 rpm and no load condition. Fig. 3.50 shows the experimental comparison of the phase currents in the different steady state working conditions (healthy, with three-phase FTC and with single-phase FTC).

The results are the same expected from the analytical and simulation comparison. Indeed, with the single-phase FTC the currents are better distributed in the remaining healthy phases, but the maximum peak current is almost the same as in the three-phase FTC.

Fig. 3.51 shows the trajectories of the current space vectors resulting from the experimental measurements. As expected, the main current space vector trajectories are always the same independently from the working scenario (the main FTC goal is to do this). When the machine is healthy, the auxiliary current space vectors are controlled to zero. Therefore, the auxiliary current space vectors are almost equal to zero (except for measurement errors and limited bandwidth of the PI regulators) and are not shown in Fig. 3.51. When the three-phase FTC is working, the auxiliary current space vectors are controlled according to (3.97). Being the trajectories circumferences (except for some secondary effects, mainly related to the dead times and voltage drops on the switching devices), a direct sequence regulator (7th space) or an inverse one (5th and 11th spaces) for each component of the current vector is enough.

When the single-phase FTC is activated, the trajectories of the current space vectors are segments (except for the secondary effects). In general, the segments are shifted according to the fault condition.

The FTC current distribution between the remaining healthy phases is the same presented in Table 3.2, with a maximum experimental mismatch for the peak current of about 5%.

Fig. 3.52 compares the stator copper Joule losses for the two FTCs, evaluated from the measured currents and phase resistances. As can be noticed, the total stator copper losses are constant in the three-phase FTC and present a ripple in the single-phase FTC. A ripple in the losses might result in a ripple in the total power requested by the dc link that can be a further drawback of the single phase FTC.

Open Phase Faults and Fault Tolerant Controls in Multiphase Drives

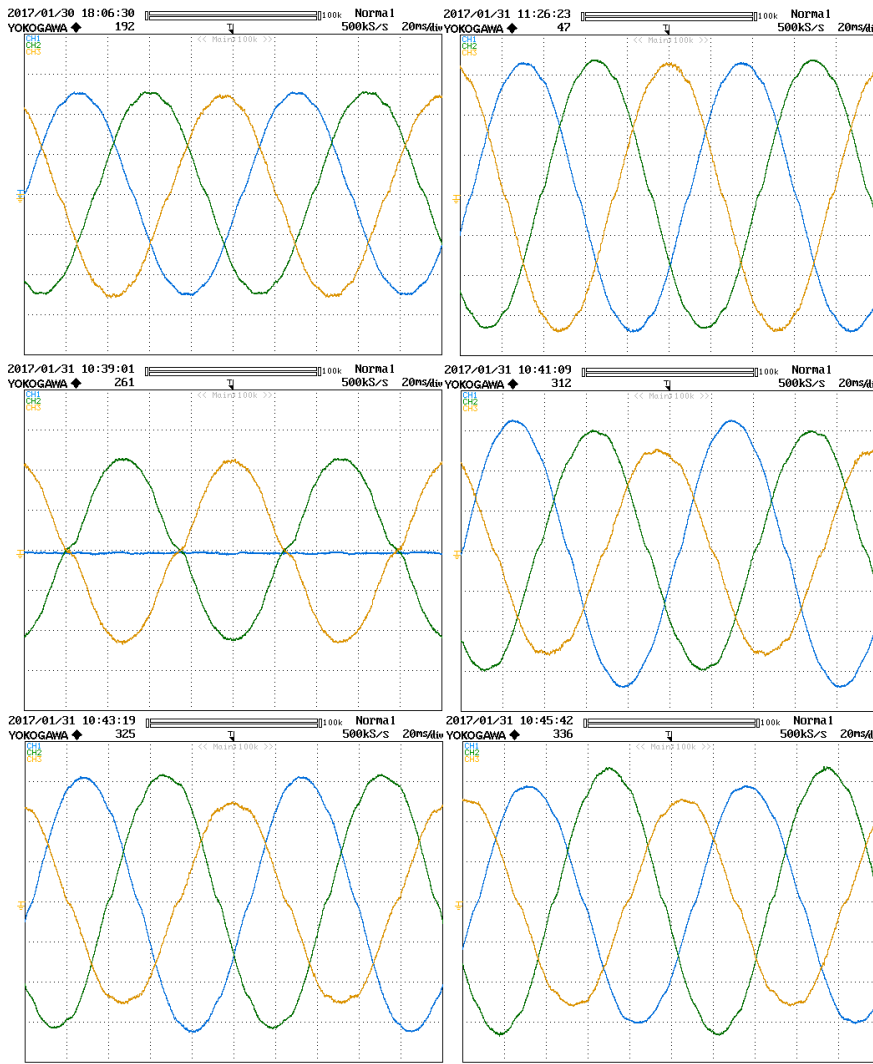


Fig. 3.50 – Measured currents of the inverter-B, when the machine is healthy (top left) and then has phase A1 opened, with the three-phase subsystem FTC (top right). Then all the inverter currents with the single-phase FTC are shown: inverter-A (centre left), inverter-B (centre right), inverter-C (bottom left), inverter-D (bottom right). With colours are differentiated the 1st phase (blue), the 2nd (green) and the 3rd (orange) of each inverter, [2A/div].

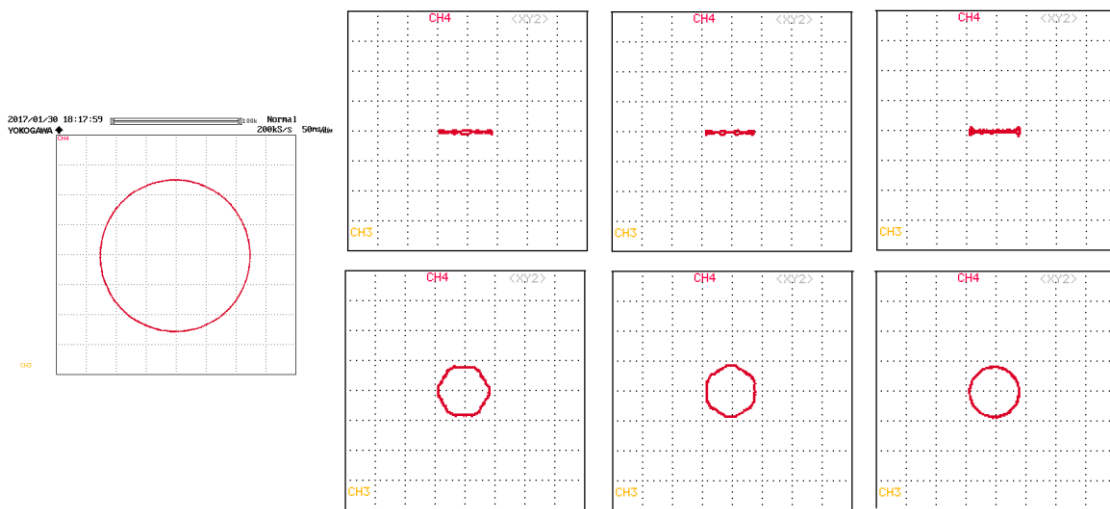


Fig. 3.51 – Measured current space vectors trajectories. Trajectory of \vec{i}_{S1} (left) and of the auxiliary vectors (5th, 7th and 11th from the left to the right) in case of single-phase FTC (top) and three-phase subsystem FTC (bottom), [2A/div].

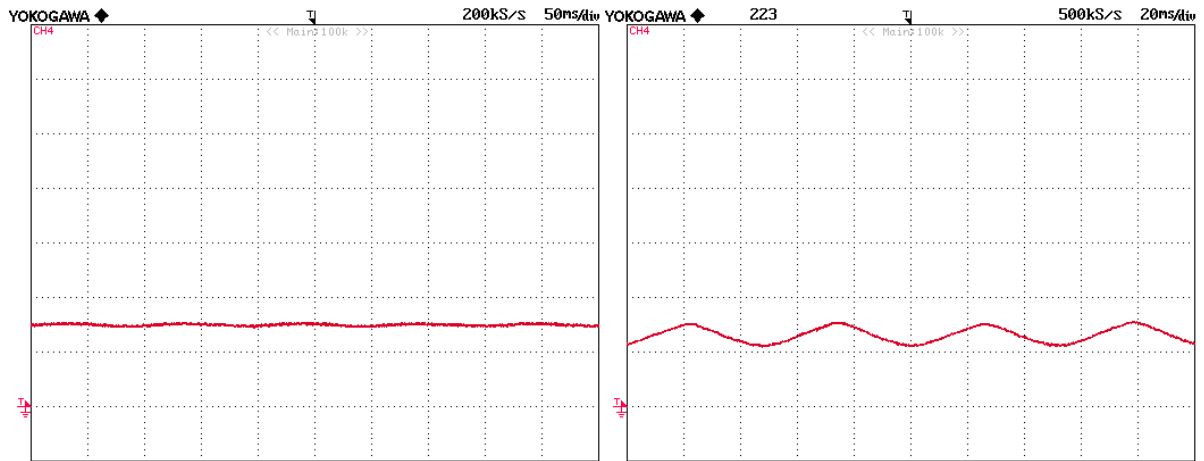


Fig. 3.52 – Total stator copper Joule losses in case of phase A1 open fault with three-phase FTC (left) and single-phase FTC (right), [20W/div].

Experimental results– Double Six-Phase winding: Single-phase FTC

Fig. 3.53, Fig. 3.54 and Fig. 3.55 show the three-phase homopolar currents with the different double six-phase configurations in case of single phase FTC with phase A1 open fault.

The three-phase homopolar currents are related to the 3rd and 9th space vectors. Therefore, the auxiliary current space vectors are all different from zero in the FT operation.

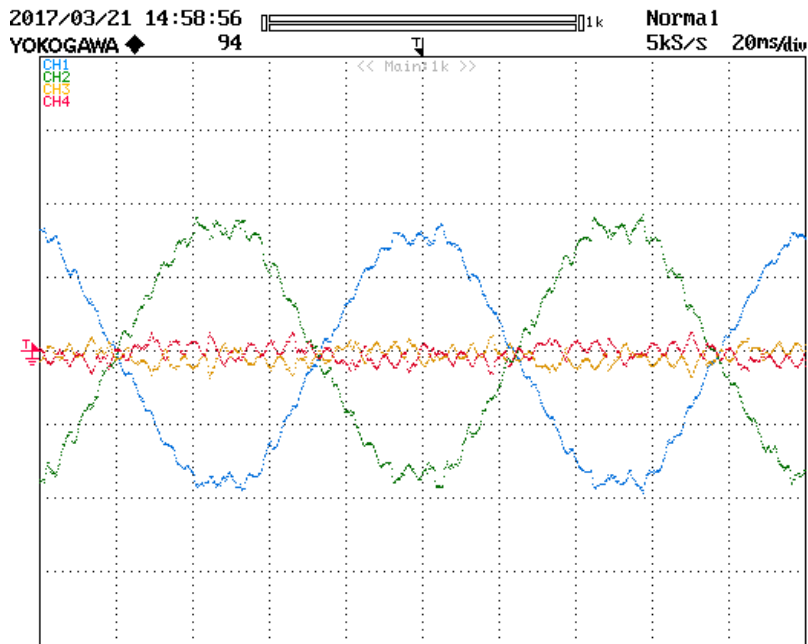


Fig. 3.53 – Three-phase homopolar currents in case of phase A1 open fault and single-phase FTC. AB/CD star layout, [2A/div].

Open Phase Faults and Fault Tolerant Controls in Multiphase Drives

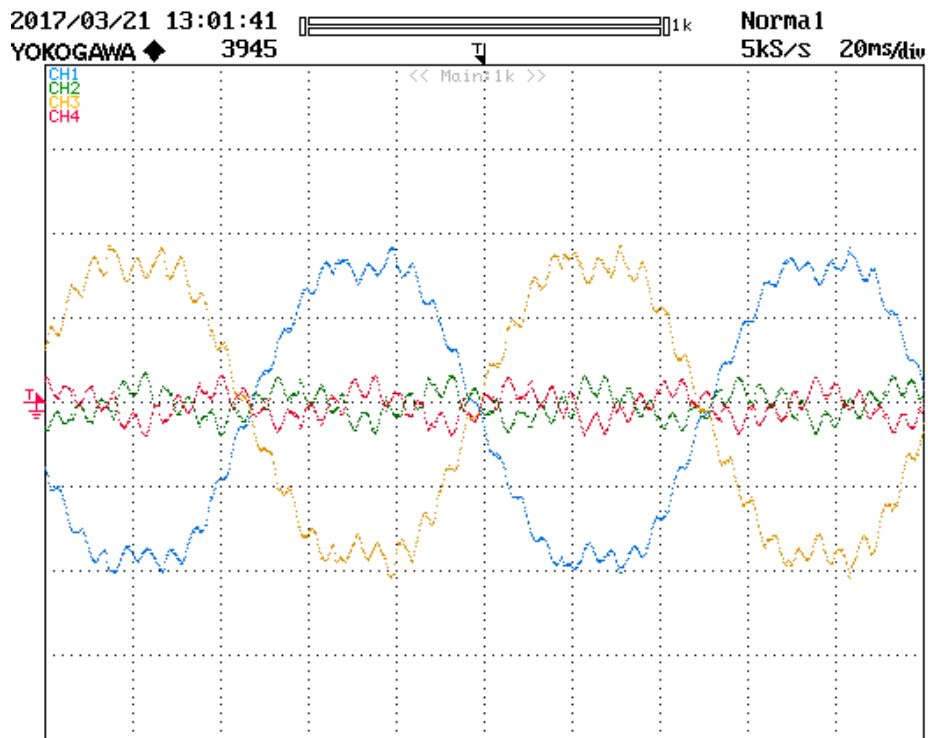


Fig. 3.54 – Three-phase homopolar currents in case of phase A1 open fault and single-phase FTC. AC|BD star layout, [2A/div].

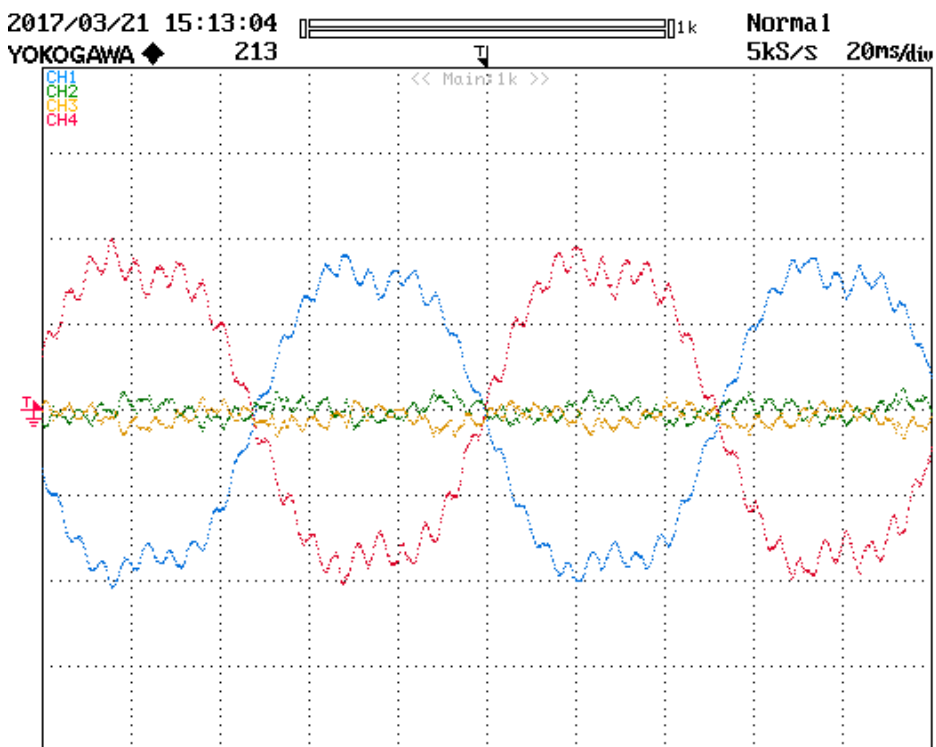
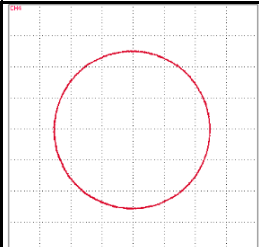
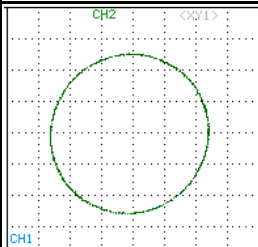
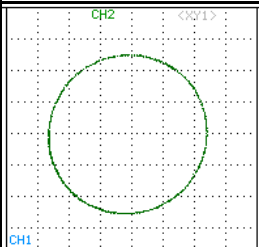
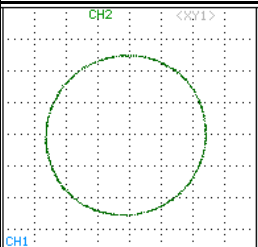
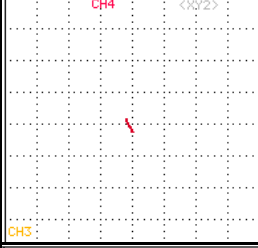
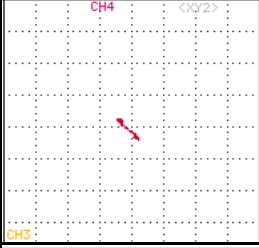
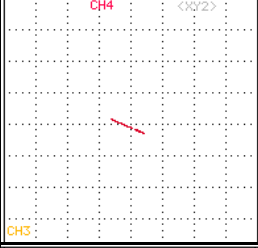
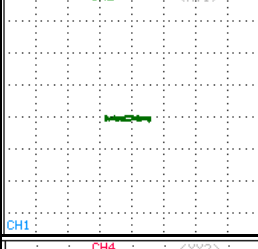
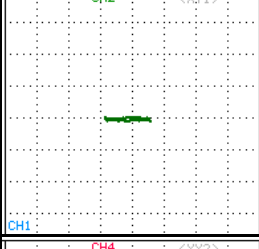
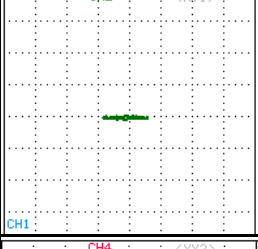
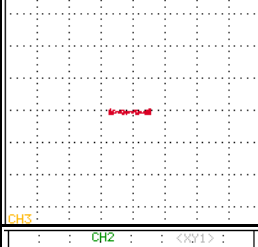
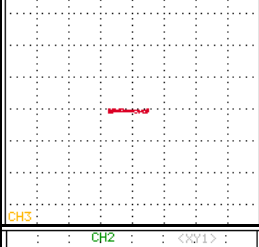
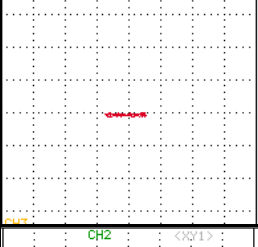
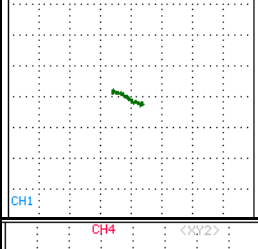
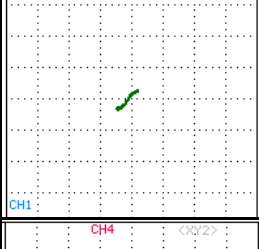
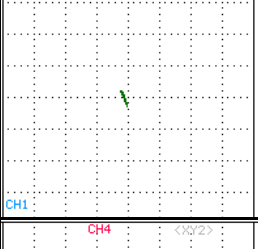
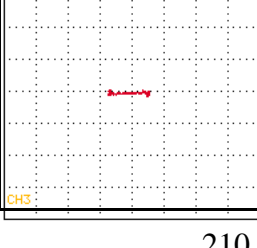
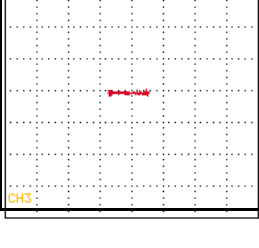
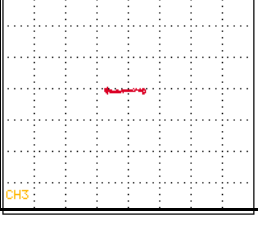


Fig. 3.55 – Three-phase homopolar currents in case of phase A1 open fault and single-phase FTC. AD|BC star layout, [2A/div].

CHAPTER 3

Table 3.9 shows the current space vector trajectories for the healthy machine and for the FTC in case of phase A1 open fault.

Table 3.9 – Comparison of the current space vector trajectories in respect to the healthy behaviour in case of A1 open phase fault. The scale is of 2A/div in all the figures.

Space	Healthy	AB CD	AC BD	AD BC
1				
3				
5				
7				
9				
11				

Experimental results–Single-Star winding: Single-phase FTC

Fig. 3.56 shows the three-phase homopolar currents with the single-star (twelve-phase) configuration in case of single-phase FTC with phase A1 open fault.

Table 3.10 shows the current space vector trajectories when the machine is healthy and when the single-phase FTC is on.

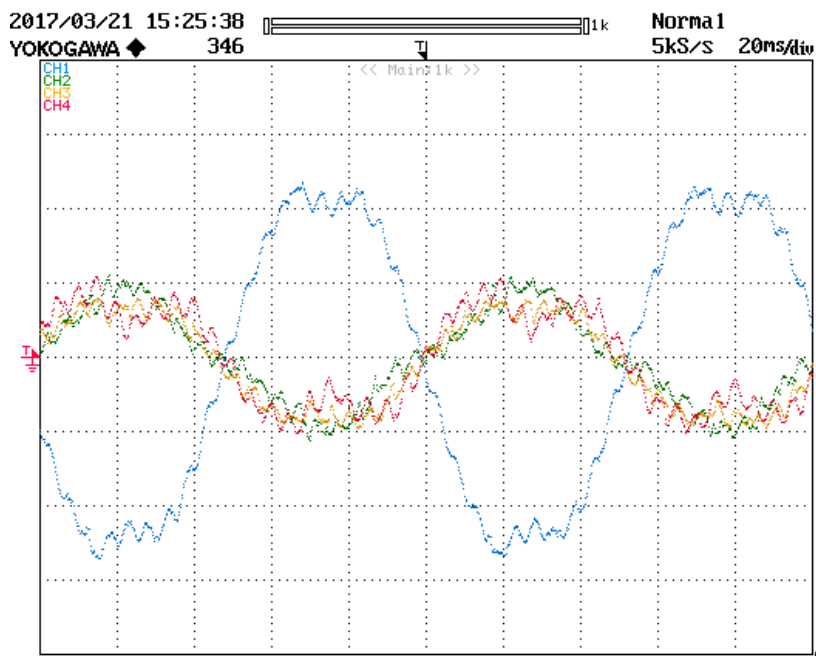
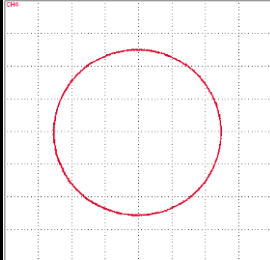
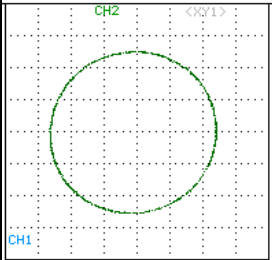
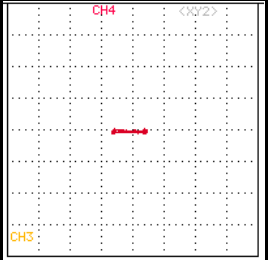
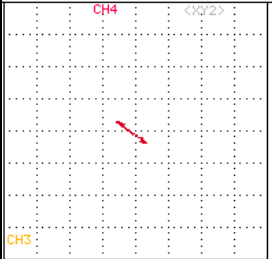
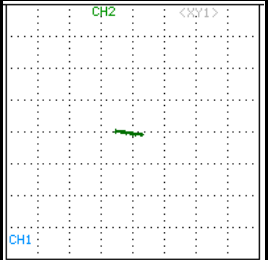
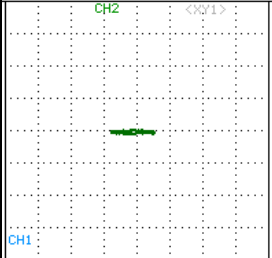
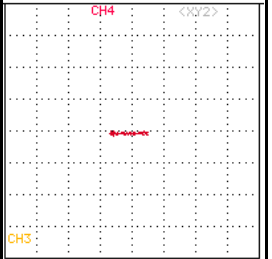


Fig. 3.56 – Three-phase homopolar currents in case of phase A1 open fault and single phase FTC. Single-star layout, [2A/div].

CHAPTER 3

Table 3.10 – Comparison of the current space vector trajectories in respect to the healthy behaviour in case of A1 open phase fault. The scale is of 2A/div in all the figures.

Space	Healthy	Single Star	Space	Single Star
1			7	
3			9	
5			11	

3.7 Conclusions

In this chapter, an in-deep analysis of the open phase faults has been carried out, focusing on the development of optimised FTCs for multiphase machines.

The attention is posed on the quadruple three-phase winding topology.

Two main control techniques are proposed and compared: the first one (three-phase FTC) is based on the opening of all the phases of the faulty subsystem (ex. disabling the faulty inverter); in contrast, the second one (single-phase FTC) tries to exploit all the remaining healthy phases of the inverters. The three-phase FTC is a particular case of current sharing control. To be thorough, also the current sharing theory has been explained and validated.

Both the proposed FTCs aim to minimize the stator copper Joule losses without changing the reference value of the fundamental current space vector (\bar{i}_1), leading to different results.

Owing to the higher number of available phases, the single-phase FTC shows reduced stator Joule losses but needs twice the number of PI regulators to control the auxiliary current vectors.

In order to enhance the FTC performance, it is also possible to connect the three-phase subsystems in various star configurations (mainly double six-phase or twelve-phase). Reducing the number of stars results in increasing the degrees of freedom in the current control. These degrees of freedom allow reducing the stator Joule losses in case of fault, but the control of more auxiliary current vectors result in having four additional PI regulators for the control of the homopolar currents between the three-phase subsystems. Also FEA (in Flux) has been done to consider the effects of the iron saturation, in order to define which is the best double six-phase winding layout in terms of fault tolerant behaviour.

The analytical results and the FTC techniques have been verified by Matlab-Simulink simulations and by experimental tests on a scaled prototype of quadruple three-phase starter-generator. The tests confirmed the feasibility of the proposed FTCs in all the analysed star configurations.

To conclude, if only the stator copper Joule losses are taken into account, the single-phase FTC with a single star layout is the best one. Conversely, if the controller cannot afford the introduction of additional regulators in terms of memory usage and calculation time, the three-phase FTC with independent three-phase subsystems has lower control requirements. As an intermediate solution, the double six-phase layout with the star connection of not neighbouring three-phase subsystems seems another possible solution for FTC improvement.

References:

- [1] B. A. Welchko, T. A. Lipo, T. M. Jahns, and S. E. Schulz, "Fault tolerant three-phase AC motor drive topologies: a comparison of features, cost, and limitations " *IEEE Transactions on Power Electronics*, vol. 19, pp. 1108-1116, July 2004 2004.
- [2] S. Bolognani, M. Zordan, and M. Zigliotto, "Experimental fault-tolerant control of a PMSM drive," *IEEE Transactions on Industrial Electronics*, vol. 47, pp. 1134-1141, Oct 2000 2000.
- [3] G. Sala, P. Girardini, M. Mengoni, L. Zarri, A. Tani, and G. Serra, "Comparison of fault tolerant control techniques for quadruple three-phase induction machines under open-circuit fault," in *2017 IEEE 11th International Symposium on Diagnostics for Electrical Machines, Power Electronics and Drives (SDEMPED)*, 2017, pp. 213-219.
- [4] M. Mengoni, G. Sala, L. Zarri, A. Tani, G. Serra, Y. Gritli, *et al.*, "Control of a fault-tolerant quadruple three-phase induction machine for More Electric Aircrafts," in *IECON 2016 - 42nd Annual Conference of the IEEE Industrial Electronics Society*, 2016, pp. 5747-5753.
- [5] A. Tani, M. Mengoni, L. Zarri, G. Serra, and D. Casadei, "Control of Multiphase Induction Motors With an Odd Number of Phases Under Open-Circuit Phase Faults," *IEEE Transactions on Power Electronics*, vol. 27, pp. 565-577, 2012.
- [6] L. Zarri, M. Mengoni, A. Tani, G. Serra, and D. Casadei, "Minimization of the Power Losses in IGBT Multiphase Inverters with Carrier-Based Pulsewidth Modulation," *IEEE Transactions on Industrial Electronics*, vol. 57, pp. 3695-3706, 2010.
- [7] R. O. C. Lyra and T. A. Lipo, "Torque density improvement in a six-phase induction motor with third harmonic current injection," *IEEE Transactions on Industry Applications*, vol. 38, pp. 1351-1360, 2002.

CHAPTER 4

High Resistance and Interturn Short Circuit Faults

High resistance (HR) connections and interturn short circuits (ISC) are among the most probable faults related to the deterioration and ageing of electrical machines. Winding faults are cause of about the 30% of failures in electrical machines [1]. The insulation can be damaged by unexpected heat sources, mechanical and chemical alterations or because of electrical stress and partial discharges (in particular, for machine fed by converters based on switching devices). As example, the localised temperature increase could happen in a healthy machine, working in its standard conditions, in case of unexpected missing cooling of a machine volume (obstructing material, cooling system failure). This might affect the material properties and bring to a HR fault in one winding before the system failure. It is clear that the early detection of these faults is significantly important for applications with high reliability requirements, or if the maintenance costs are critical.

The aim of this chapter is to model the HR and ISC faults and show how it is possible to implement an online detection algorithm based on a standard controller (without requiring additional expensive and bulky measurement devices).

Many techniques have been proposed to detect winding faults, such as Motor Current Signature Analysis (MCSA), sequence impedances and Artificial Intelligence (AI) [2]. The presented approach is based on the sequence impedances evaluation, where the detected values are compared with the ones expected from an analytical model. The model of the faulty machine is based on a winding function approach [3, 4], as the ones developed in Chapter 2.

The HR fault is analysed with an accurate modelling of the phenomena. The presented HR detection algorithm is based on the idea already tested for other machines [5, 6]. The same approach is extended for the ISC detection. The considered ISC is supposed to happen between turns of the same phase (the phase-to-phase and the phase to ground faults are not analysed) and the phenomena is simplified in order to simulate the fault and describe its behaviour. While Chapters 3 focuses on the optimised control of the armature field harmonics for increasing the control performance and fault tolerance, this chapter aims for the development of a fault detection algorithm. Therefore, Fault Tolerant Controls (FTC) are not considered.

Simulations and experimental results are presented in Section 4.8-4.10. Firstly, considering an open loop voltage control with the aim of validating the proposed model for the detection of

HR and ISC faults [7-9]. Then, the analysis of a current controlled machine is performed highlighting the sensitivity of the detection algorithm to the fault and machine behaviour. Finally, the HR detection algorithm is verified by experimental tests for a prototype of nine-phase IM.

Introduction to High Resistance (HR) and Interturn Short Circuit (ISC) Faults

Among the causes of HR connections and ISC faults, the following ones can be highlighted:

- assembly or manufacturing of the phase connections;
- winding process;
- temperature increase (hotspots);
- chemical reactions;
- electric stress (partial discharges);
- mechanical stress (vibrations, Ampère's force, reluctance forces).

The first step needed for the definition of a diagnostic algorithm for an electrical machine is the development of a reliable model. The proposed model is based on the winding function approach, and the resistances and leakage inductances are considered as the lumped parameters of the equivalent electrical circuit.

Fig. 4.1 shows the simplified electrical circuit that describes the HR and ISC faults.

An HR condition can affect all the phases in the same way (as happens in case of extended overloads), or only some parts of the winding (asymmetrical HR). In case of an ideal machine current control, the resulting machine behaviour might be the same of the healthy case with just an increase of the voltage needed to feed the faulty phases. However, a hotspot might change the material behaviour (iron lamination B-H curve) and in PM machines might bring to a PM demagnetisation.

Instead, in case of ISC faults, the magnetic behaviour is not directly related to the machine current control. Indeed, as deeply explained in the next section, the short circuit loop generates an uncontrolled circulating current. The materials might change their behaviour as in an HR

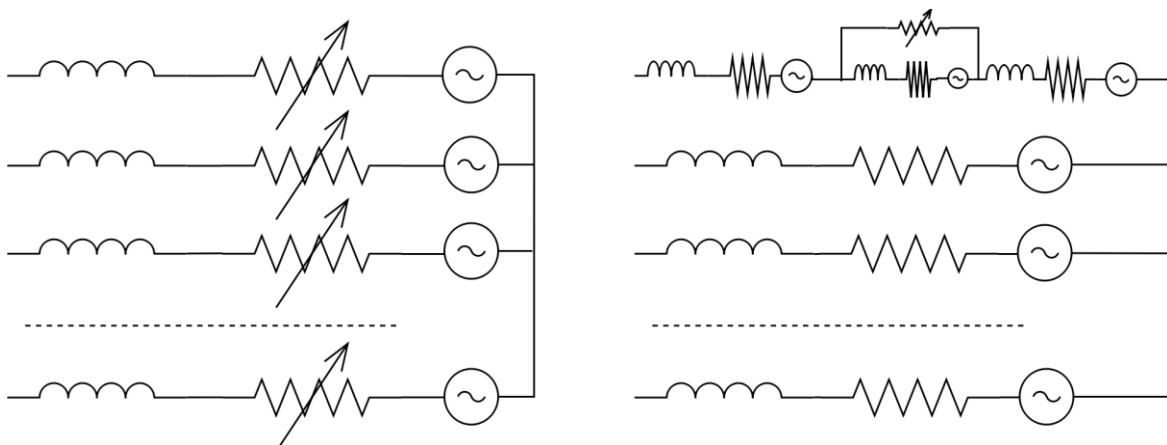


Fig. 4.1 – High resistance (left) and Interturn short circuit (right) faults. Concept.

fault, with the difference that the iron saturation and PM demagnetisation must also take into account for the presence of the uncontrolled ISC current. Indeed, the ISC current introduces additional losses, but also an uncontrolled distortion of the flux density in the airgap. This generates torque and forces, as verified also in Chapter 6 for a three-phase short circuit fault in a triple three-phase machine.

Only to briefly introduce this effect, an ISC might be simplified as an additional and independent short-circuited winding as in Fig. 4.2. This winding reacts to the flux in the airgap in a similar way of a squirrel cage in blocked rotor conditions, but in an asymmetrical way. The ideal ISC results in the effect of an asymmetrical winding for the faulty phase (with a reduced number of turns) plus the effect of the ISC loop that interacts with the stator and the rotor but does not directly depend from the phase voltages (or by the current control), as happens for a blocked squirrel cage rotor. However, considering for a not ideal ISC the model is even more complicated. In this chapter, the HR and ISC faults are modelled and analysed in deep. The next section introduces the equivalent circuit used to take into account for the electrical passive components of the winding, while the following ones present the complete electromagnetic model of the machine. Finally, a simplified model and the detection algorithms are explained and verified by simulations and experimental tests.

4.1 Equivalent circuit for High Resistance and Interturn Short Circuit Faults

This section aims to introduce the model of the passive components (resistances and leakage inductances) related to HR and ISC faults, considered as lumped parameters in the winding equivalent circuits.

In order to simplify the fault analysis, the materials behaviour is considered linear and independent from the machine operating conditions and faults (that is, independent from the currents, magnetic field and temperature). As in Chapter 3, the transient of the fault is not analysed. As additional simplifications: the considered winding is a single layer one; the mutual leakage inductances between turns in different slots are neglected; and the different coils are supposed to be identical in terms of electromagnetic behaviour (same leakage inductances and turns number). Furthermore, the ISC fault is supposed to happen between two turns of the same phase.

The next subsection shows the equivalent circuit used to describe the HR and ISC faults, while the following one defines how the passive components are considered in the phase voltage equations. In case of an HR fault the phase voltage equations are enough to represent the fault

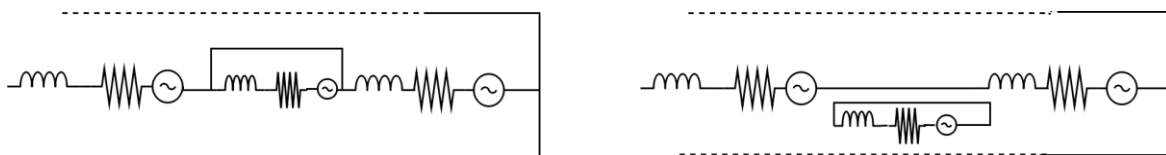


Fig. 4.2 – Ideal Interturn short circuit fault (left) and equivalent circuit (right). Concept.

condition. Instead, the analysis of the distortion of the field is needed to complete the ISC modelling. Therefore, Section 4.2 aims to analyse the electromagnetic effect of the ISC current. The model, as in Chapter 3, refers to the equations developed in Chapter 2 (taken for granted their effectiveness for the model hypotheses).

Circuitual representation of HR and ISC faults

This paragraph introduces the equivalent circuit of a winding in case of HR and ISC faults.

Fig. 4.3 shows the circuit of a healthy phase (x, in the bottom), a phase with an HR condition (y, in the centre), and a phase with an ISC fault (z, in the top). The HR condition is represented by the variation of the relative phase resistance (R_y , highlighted in blue in Fig. 4.3). Instead, an ISC fault is represented by the short circuit resistance (r_{sc}), the number of short circuited turns (N_f , to highlight that are affected by the fault) and the short circuit current (i_{sc}). The parameters that describe an ISC fault are highlighted in red in Fig. 4.3.

The main passive components of the circuitual representation are the phase self leakage inductance Ll and the phase resistance R for the healthy phases and R_y for the general y-th phase with unbalanced resistance.

The phase equation (2.90) for a healthy phase or a phase with an HR condition (x-th phase), neglecting the mutual leakage inductances between coils in different slots, is:

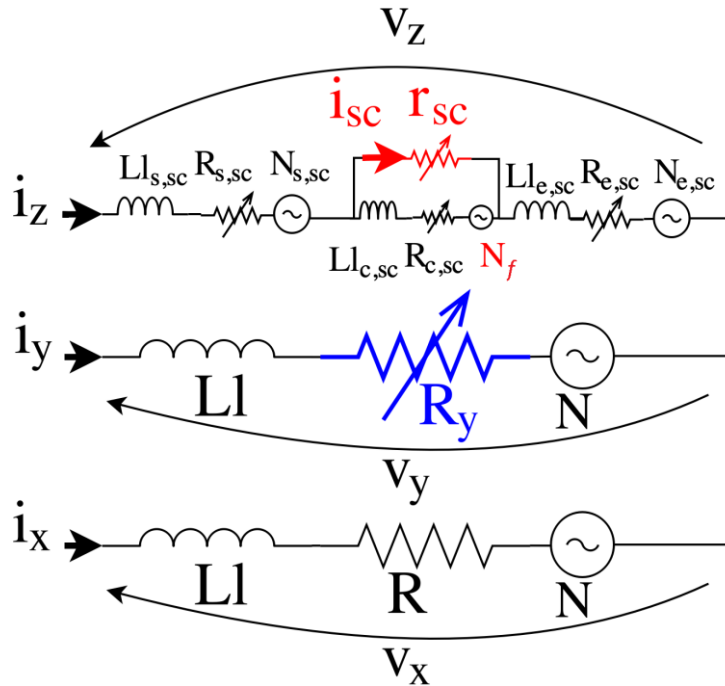


Fig. 4.3 – High Resistance and Interturn Short Circuit concept and proposed nomenclature. Phase x (bottom) is healthy; phase y (centre) is affected by a HR condition; phase z (top) is affected by an ISC fault (with a resulting possible resistance variation).

$$v_x = R_x i_x + Ll_x \frac{di_x}{dt} + \frac{d\phi_x}{dt}, \quad (4.1)$$

The x -th phase series resistance is:

$$R_x = \sum_{kx=1}^{N_{tx}} r_{kx},$$

where kx is the lowercase used for indicating the k -th series turn of the x -th phase, and the self leakage inductance of the x -th phase is defined as:

$$Ll_x = \sum_{kx=1}^{N_{tx}} ll_{kx} + \sum_{kx=1}^{N_{tx}} \sum_{\substack{tx=1 \\ tx \neq k}}^{N_{tx}} ml_{tx,kx}.$$

with ll_{kx} the self leakage inductance of each kx -th turn and $ml_{tx,kx}$ the mutual leakage inductance between the tx -th and kx -th turns. The linked flux ϕ_x is the sum of the flux that pass through the airgap and links all the series turns:

$$\phi_x = \sum_{kx=1}^N \phi_{kx}.$$

Under the hypothesis of having only one coil geometry for all the winding, the self leakage inductance can be assumed the same for all the phases that are healthy or affected by a HR condition. Therefore, it is possible to write (2.88) as:

$$v_x = R_x i_x + Ll \frac{di_x}{dt} + \frac{d\phi_x}{dt}. \quad (4.2)$$

Equation (4.2) is sufficient for the analysis of HR faults in electrical machines. Instead, the description of an ISC fault requires more explanation. Indeed, Fig. 4.3 shows a circuitual approach for describing the ISC defined by a series of three electrical subcircuits:

- the starting phase subcircuit (named with the subscript “s”);
- the ending phase subcircuit (named with the subscript “e”);
- the ISC loop (named with the subscript “c”, being this subcircuit in general located between the s -th and the e -th ones).

Each subcircuit might in general have different series resistances ($R_{s,sc}$, $R_{c,sc}$ and $R_{e,sc}$) and a self leakage inductances ($Ll_{s,sc}$, $Ll_{c,sc}$ and $Ll_{e,sc}$). However, with a high probability some turns of the three subcircuits (starting, central and ending), or all of them (in case of two slot per phase single layer winding), are located in the same slots. Therefore, the mutual leakage effect between the subcircuits must be taken into account also in the simplified hypotheses of neglecting the mutual leakage inductances between coils in different slots.

The next two subsections aims to define the evaluation of the passive components in the different subcircuits. The proposed simplified model of the equivalent circuit takes into account for also the slot mutual leakage inductances of the subcircuits in the short-circuited phase.

ISC faults – leakage inductances analysis

In order to consider for all the slot leakage effects in case of ISC faults Fig. 4.3 can be represented as in Fig. 4.4. The main difference is that in the new representation the mutual leakage couplings are highlighted by the respective constants ($Ml_{s,c}$, $Ml_{c,e}$ and $Ml_{s,e}$, where it is implicit that they refer to the couplings related to the coils affected by the ISC fault).

Indeed, the leakage flux linked with the k -th turn of the x -th phase, sum of N series turns in each of the N_c series coils (for a total of $N_t = NN_c$ series turns, that for a traditional distributed winding is $N_t = Npq$), is:

$$\phi_{Ll,kx} + \phi_{Ml,kx} = ll_{kx} i_{kx} + \sum_{\substack{kx=1 \\ tx \neq k}}^N \sum_{tx=1}^N ml_{tx,kx} i_{tx}. \quad (4.3)$$

For a healthy phase, described by (4.2), the total phase leakage inductance is:

$$\phi_{L,x} = \sum_{c=1}^{N_c} \left(\sum_{kx=1}^N ll_{kx} + \sum_{\substack{kx=1 \\ tx \neq k}}^N \sum_{tx=1}^N ml_{tx,kx} \right) i_x = N_c Ll_c i_x = Ll i_x. \quad (4.4)$$

However, in case of an ISC fault, the leakage linked flux depends on the position of the ISC. Fig. 4.5 shows the two considered ISC configurations: turn-to-turn between two different coils and between turns of the same coil. The total number of coils is the same in all the phases, N_c , and each coil still has the same turns number, N .

The z phase in Fig. 4.5 is affected by an ISC in the end winding between two different coils. In particular, there are n_s and n_e healthy coils before and after the fault. The fault affects in

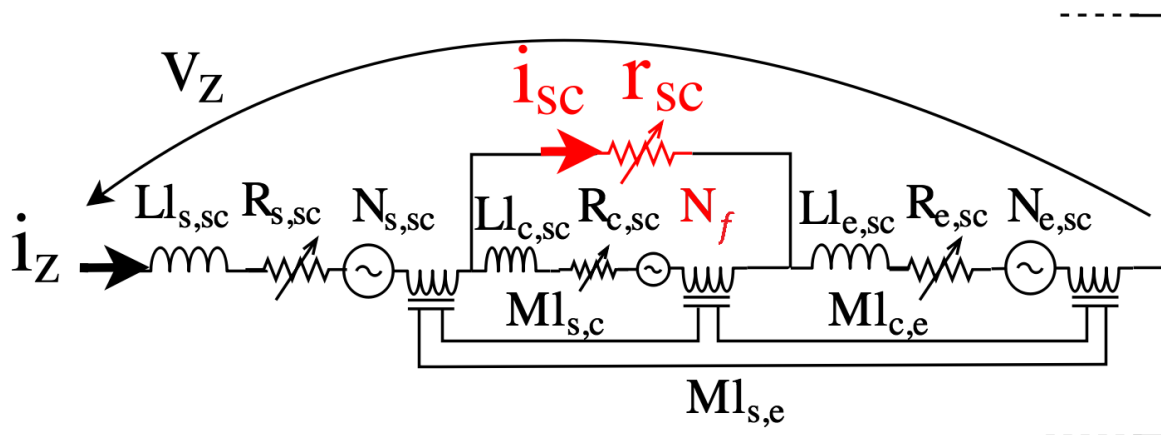


Fig. 4.4 – Interturn Short Circuit concept and proposed nomenclature. Phase z is affected by an ISC fault (with a resulting possible resistance variation), and all the slot leakage effects are represented by their respective constants in case of a single slot pair per phase winding.

with the coil self leakage inductance $Ll_c = N^2l$. Therefore, the equivalent turn self and mutual leakage constant (4.5) is evaluated by the phase total leakage inductance (the conventional one) as:

$$l = \frac{Ll}{N_c N^2}. \quad (4.7)$$

In the next two paragraphs, the mutual couplings related to the leakage flux between the different subcircuits in Fig. 4.5 are evaluated (in case of ISC between two coils, first, and in the same coil, later).

Mutual leakage inductances in case of coil-to-coil ISC

In case of an interturn short circuit in the end winding of one phase (as for the $z1$ phase in Fig. 4.5), or better between two different coils, the simplified leakage effect can be described by the following relationships.

For the starting coils (n_s plus the not short-circuited turns of the first short-circuited coil):

$$\begin{aligned} \phi_{L_s,z1} &= n_s Ll_c i_{z1} + Ll_{s,sc} i_{z1} + Ml_{s,c} (i_{z1} - i_{sc}) = \\ &= n_s Ll_c i_{z1} + ((N - N_{fs})l + (N - N_{fs})(N - N_{fs} - 1)l) i_{z1} + (N - N_{fs})N_{fs}l(i_{z1} - i_{sc}) = \\ &= [n_s Ll_c + (N - N_{fs})^2 l + (N - N_{fs})N_{fs}l] i_{z1} - (N - N_{fs})N_{fs}l i_{sc}, \end{aligned} \quad (4.8)$$

where N_{fs} is the number of short-circuited turns in the coil where the shot circuit fault starts.

For the short-circuited coils (n_c):

$$\begin{aligned} \phi_{L_c,z1} &= Ml_{s,c} i_{z1} + Ll_{cs,sc} (i_{z1} - i_{sc}) + (n_c - 2)Ll_c (i_{z1} - i_{sc}) + Ll_{ce,sc} (i_{z1} - i_{sc}) + Ml_{c,e} i_{z1} = \\ &= N_{fs} (N - N_{fs})l i_{z1} + (N_{fs}l + N_{fs}(N_{fs} - 1)l)(i_{z1} - i_{sc}) + (n_c - 2)Ll_c (i_{z1} - i_{sc}) + \\ &+ (N_{fe}l + N_{fe}(N_{fe} - 1)l)(i_{z1} - i_{sc}) + N_{fe}(N - N_{fe})l i_{z1} = \\ &= -[N_{fs}^2 l + (n_c - 2)Ll_c + N_{fe}^2 l] i_{sc} + \\ &+ [N_{fs}(N - N_{fs})l + N_{fs}^2 l + (n_c - 2)Ll_c + N_{fe}^2 l + N_{fe}(N - N_{fe})l] i_{z1}, \end{aligned} \quad (4.9)$$

For the ending coils (n_e plus the not short-circuited turns of the last short-circuited coil):

$$\begin{aligned} \phi_{L_e,z1} &= Ll_{e,sc} i_{z1} + Ml_{c,e} (i_{z1} - i_{sc}) + n_e Ll_c i_{z1} = \\ &= ((N - N_{fe})l + (N - N_{fe})(N - N_{fe} - 1)l) i_{z1} + (N - N_{fe})N_{fe}l(i_{z1} - i_{sc}) + n_e Ll_c i_{z1} = \\ &= [(N - N_{fe})^2 l + (N - N_{fe})N_{fe}l + n_e Ll_c] i_{z1} - (N - N_{fe})N_{fe}l i_{sc}, \end{aligned} \quad (4.10)$$

where N_{fe} is the number of short-circuited turns in the coil where the short circuit fault starts.

The total number of short-circuited turns is:

$$N_f = N_{fs} + (n_c - 2)N + N_{fe}.$$

Mutual leakage inductances in case of single coil ISC

In case of an interturn short circuit in a slot of one phase (as for the z_2 phase in Fig. 4.5), or more in general between two turns of the same coil, the simplified leakage effect can be described by the following relationships.

For the starting coils (n_s plus the first part of not short-circuited turns in the short-circuited coil):

$$\begin{aligned} \phi_{L,s,z_2} &= n_s Ll_c i_{z_2} + Ll_{s,sc} i_{z_2} + Ml_{s,c} (i_{z_2} - i_{sc}) + Ml_{s,e} i_{z_2} = \\ &= n_s Ll_c i_{z_2} + (N_{s,sc} l + N_{s,sc} (N_{s,sc} - 1) l) i_{z_2} + N_{s,sc} N_f l (i_{z_2} - i_{sc}) + N_{s,sc} (N - N_f - N_{s,sc}) i_{z_2} = \quad (4.11) \\ &= [n_s Ll_c + N_{s,sc} Nl] i_{z_2} - N_{s,sc} N_f l i_{sc}, \end{aligned}$$

where N_f is the number of short-circuited turns in the coil and $N_{s,sc}$ is the number of healthy turns in the faulty coil after which the short circuit fault starts.

For the short circuit loop in the short-circuited coil ($n_c = 1$):

$$\begin{aligned} \phi_{L,c,z_2} &= Ml_{s,c} i_{z_2} + Ll_{c,sc} (i_{z_2} - i_{sc}) + Ml_{c,e} i_{z_2} = \\ &= N_f N_{s,sc} l i_{z_2} + (N_f l + N_f (N_f - 1) l) (i_{z_2} - i_{sc}) + N_f (N - N_{s,sc} - N_f) i_{z_2} = \quad (4.12) \\ &= -[N_f^2 l] i_{sc} + [N_f Nl] i_{z_2}. \end{aligned}$$

For the ending coils (n_e plus the ending part of not short-circuited turns in the short-circuited coil):

$$\begin{aligned} \phi_{L,e,z_2} &= Ll_{e,sc} i_{z_2} + Ml_{c,e} (i_{z_2} - i_{sc}) + Ml_{s,e} i_{z_2} + n_e Ll_c i_{z_2} = \\ &= ((N - N_f - N_{s,sc}) l + (N - N_f - N_{s,sc}) (N - N_f - N_{s,sc} - 1) l) i_{z_2} + \\ &+ (N - N_f - N_{s,sc}) N_f l (i_{z_2} - i_{sc}) + (N - N_f - N_{s,sc}) N_{s,sc} l i_{z_2} + n_e Ll_c i_{z_2} = \quad (4.13) \\ &= [(N - N_f - N_{s,sc}) Nl + n_e Ll_c] i_{z_2} - (N - N_f - N_{s,sc}) N_f l i_{sc}. \end{aligned}$$

This subsection presented the evaluation of the leakage effects related to an ISC fault. The next one aims to repeat the analysis for the resistance effects.

HR and ISC faults – resistances analysis

In this paragraph, the ISC equivalent circuit is analysed in terms of subcircuit resistances. The proposed model of ISC fault consider also for a possible resistance increase in the short circuited turns. Therefore, if the short circuit current is zero (infinite short circuit resistance)

the resistance increase in the short circuit loop results as an HR fault in the analysed phase. Indeed, in the next sections, the model is developed for the ISC fault, and then it is simplified for the analysis of the HR condition.

The phase voltage equation for a phase with an ISC fault differs from (4.2) in terms of presence of subcircuits, but also because the new subcircuits have different parameters than the healthy phase ones. In particular, the same approach used for the analysis of the leakage inductances in the previous paragraph can be used for highlighting the probable temperature increase in the slots where the short circuit happens. Fig. 4.6 shows the proposed modelling of the series resistances in the subcircuits for a healthy phase, and for the two analysed cases of short circuit faults. The resistances in Fig. 4.6 are drawn as constants (only the short circuit fault resistance r_c is maintained as variable) for clarity. However, they are in general all depending from the temperature (that is, they are function of the time and the losses distribution). The proposed model defines only two resistance values: one for the short-circuited turns (r_c) and one for the not short-circuited turns (r), neglecting the heat transfer between the healthy turns and the faulty ones. In reality, this is not true. However, the approximation is useful in order to take into account for a different resistance in the short circuit loop (expected from the high copper losses caused by the short circuit current) and a possible HR condition in the faulty phase outside the ISC loop is also added from Section 4.3.

By means of the hypothesis above, the voltage drops on the resistances are modelled according to the following equations.

In a healthy machine:

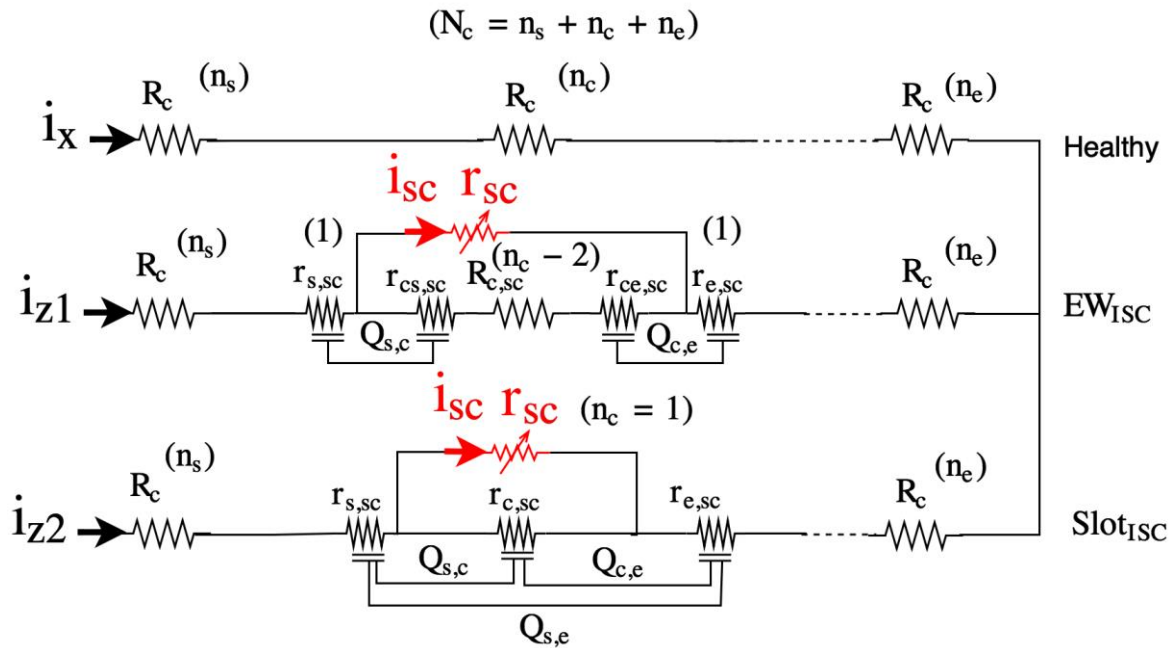


Fig. 4.6 – Interturn Short Circuit concept and proposed nomenclature for the resistances analysis. Phase x is healthy; phase $z1$ is affected by an ISC in the end winding; phase $z2$ is affected by a slot ISC fault. With “ Q ” are highlighted the main radial thermal paths related to the short circuit current copper Joule losses (the axial path is implicit).

$$\sum_{c=1}^{N_c} R_c i_x = N_c R_c i_x = N_c N r i_x = R_s i_x, \quad (4.14)$$

with the coil resistance $R_c = Nr$ and r the resistance of each series turn. Therefore, the turn resistance for the healthy phases is evaluated by the total phase resistance (the conventional one) as:

$$r = \frac{R_s}{N_c N}. \quad (4.15)$$

The resistances of the faulty phase subcircuit are analysed in the two following paragraphs for the two ISC conditions (coil-to-coil and single coil).

Subcircuit resistances in case of coil-to-coil ISC

In case of an interturn short circuit between two coils of one phase (as for the $z1$ phase in Fig. 4.6), the resistance voltage drops can be described by the following relationships.

For the starting coils (n_s plus the not short-circuited turns of the first short-circuited coil):

$$n_s R_c i_{z1} + r_{s,sc} i_{z1} = n_s N_c N r i_{z1} + (N - N_{fs}) r i_{z1} = (n_s N + N - N_{fs}) r i_{z1}, \quad (4.16)$$

where N_{fs} is the number of short-circuited turns in the coil where the short circuit fault starts.

For the short-circuited coils (n_c):

$$\begin{aligned} r_{cs,sc} (i_{z1} - i_{sc}) + (n_c - 2) R_{c,sc} (i_{z1} - i_{sc}) + r_{ce,sc} (i_{z1} - i_{sc}) &= \\ &= (N_{fs} r_c + (n_c - 2) N r_c + N_{fe} r_c) (i_{z1} - i_{sc}) = \\ &= -N_f r_c i_{sc} + N_f r_c i_{z1}, \end{aligned} \quad (4.17)$$

where the total number of short-circuited turns is:

$$N_f = N_{fs} + (n_c - 2) N + N_{fe}.$$

For the ending coils (n_e plus the not short-circuited turns of the last short-circuited coil):

$$r_{e,sc} i_{z1} + n_e R_c i_{z1} = (N - N_{fe}) r i_{z1} + n_e N_c N r i_{z1} = (n_e N + N - N_{fe}) r i_{z1}, \quad (4.18)$$

where N_{fe} is the number of short-circuited turns in the coil where the shot circuit fault starts.

Resistances in case of single coil ISC

In case of an ISC between two turns of the same coil (as for the z_2 phase in Fig. 4.6), the resistance voltage drops can be described by the following relationships.

For the starting coils (n_s plus the first part of not short-circuited turns in the short-circuited coil):

$$n_s R_c i_{z_2} + r_{s,sc} i_{z_2} = n_s N_c N r i_{z_2} + N_{s,sc} r i_{z_2} = (n_s N + N_{s,sc}) r i_{z_2}, \quad (4.19)$$

where $N_{s,sc}$ is the number of healthy turns in the faulty coil after which the short circuit fault starts.

For the short circuit loop in the short-circuited coil ($n_c = 1$):

$$r_{c,sc} (i_{z_2} - i_{sc}) = N_f r_c i_{z_2} - N_f r_c i_{sc}. \quad (4.20)$$

For the ending coils (n_e plus the ending part of not short-circuited turns in the short-circuited coil):

$$r_{e,sc} i_{z_2} + n_e R_c i_{z_2} = (N - N_{s,sc} - N_f) r i_{z_2} + n_e N r i_{z_2} = (N - N_{s,sc} - N_f + n_e N) r i_{z_2}. \quad (4.21)$$

At this point, the passive parameters of the equivalent electrical circuit are completely defined. Therefore, it is possible to write the phase voltage equations for the healthy and faulty phases, as described in the next subsection.

Circuit phase voltage equations for HR and ISC faults

The phase voltage equation (2.88) resulting by the model presented in the previous subsection for the x -th healthy phase is simply:

$$v_x = R_s i_x + Ll \frac{di_x}{dt} + \frac{d\phi_x}{dt}, \quad (4.22)$$

with $R_s = N_c N r$ and $Ll = N_c N^2 l$; where the turn leakage inductance l and the turn resistance r represent the average leakage and resistance contribution associated to each of the series turns in one coil.

Instead, in case of fault the voltage phase and the ISC loop equations are as described in the paragraphs here below.

Circuitual phase voltage equation for HR fault

In case of a high phase resistance condition, (2.88) results for the y -th phase as:

$$v_y = R_y i_y + Ll \frac{di_y}{dt} + \frac{d\phi_y}{dt}, \quad (4.23)$$

with $R_y = N_c N r_y$ in case of a uniform resistance increase in all the turns (from r to r_y).

In order to highlight the turn resistance increase, it is useful to introduce the new parameter r_{HR} (the turn resistance increase). The phase resistance increase in the y -phase can be associated to some of the series turns as:

$$R_y = (N_c N - N_f) r + N_f (r + r_{HR}) = N_c N r + N_f r_{HR} = R_s + N_f r_{HR},$$

with a localised resistance increase of r_{HR} in N_f of the series turns.

Circuitual voltage equation for coil-to-coil ISC

In case of an ISC between two coils of a phase (the $z1$ -th in Fig. 4.5 and Fig. 4.6), the phase voltage equation (2.88) results as:

$$\begin{aligned} v_{z1} &= v_{z1,s} + v_{z1,c} + v_{z1,e} = \\ &= n_s R_c i_{z1} + r_{s,sc} i_{z1} + n_s Ll_c \frac{di_{z1}}{dt} + Ll_{s,sc} \frac{di_{z1}}{dt} + Ml_{s,c} \left(\frac{di_{z1}}{dt} - \frac{di_{sc}}{dt} \right) + \frac{d\phi_{z1,s}}{dt} + \\ &+ r_{cs,sc} (i_{z1} - i_{sc}) + (n_c - 2) R_{c,sc} (i_{z1} - i_{sc}) + r_{ce,sc} (i_{z1} - i_{sc}) + \\ &Ml_{s,c} \frac{di_{z1}}{dt} + Ll_{cs,sc} \left(\frac{di_{z1}}{dt} - \frac{di_{sc}}{dt} \right) + (n_c - 2) Ll_c \left(\frac{di_{z1}}{dt} - \frac{di_{sc}}{dt} \right) + \\ &+ Ll_{ce,sc} \left(\frac{di_{z1}}{dt} - \frac{di_{sc}}{dt} \right) + Ml_{c,e} \frac{di_{z1}}{dt} + \frac{d\phi_{z1,c}}{dt} + \\ &+ r_{e,sc} i_{z1} + n_e R_c i_{z1} + Ll_{e,sc} \frac{di_{z1}}{dt} + Ml_{c,e} \left(\frac{di_{z1}}{dt} - \frac{di_{sc}}{dt} \right) + n_e Ll_c \frac{di_{z1}}{dt} + \frac{d\phi_{z1,e}}{dt}. \end{aligned} \quad (4.24)$$

Substituting (4.8)-(4.10) and (4.16)-(4.18), and considering the turn resistance increase in the turns crossed by the ISC current r_{HR} as described for the HR fault ($r_c = r + r_{HR}$), (4.24) results as:

$$\begin{aligned} v_{z1} &= (N_c N - N_f) r i_{z1} + N_f (r_{HR} + r) i_{z1} - N_f (r_{HR} + r) i_{sc} + \\ &+ [n_s + (n_c - 2) + n_e] N^2 l \frac{di_{z1}}{dt} + 2l \frac{di_{z1}}{dt} + \\ &- [(N - N_{fs}) N_{fs} + (N - N_{fe}) N_{fe} + N_{fs}^2 + (n_c - 2) Ll_c + N_{fe}^2] l \frac{di_{sc}}{dt} + \frac{d\phi_{z1}}{dt}, \end{aligned} \quad (4.25)$$

with ϕ_{z1} the total flux that pass through the airgap and links the turns of the faulty phases. Indeed, the ISC fault do not change the relationship between the flux in the airgap and the linked flux with the considered phase because the geometry of the turns is unchanged.

Finally, because the total number of coils is $N_c = n_s + (n_c - 2) + n_e$, the phase voltage equation results as:

$$\begin{aligned} v_{z1} &= \\ &= R_s i_{z1} + N_f r_{HR} i_{z1} - N_f (r_{HR} + r) i_{sc} + Ll \frac{di_{z1}}{dt} - [N(N_{fs} + N_{fe}) + (n_c - 2)Ll_c] \frac{di_{sc}}{dt} + \frac{d\phi_{z1}}{dt} = (4.26) \\ &= R_s i_{z1} + N_f r_{HR} i_{z1} - N_f (r_{HR} + r) i_{sc} + Ll \frac{di_{z1}}{dt} - NN_f l \frac{di_{sc}}{dt} + \frac{d\phi_{z1}}{dt}. \end{aligned}$$

Voltage equation for single coil ISC

The same analysis can be carried out for an ISC between two turns of the same coil. The phase voltage equation of phase affected by the fault (as the z2-th in Fig. 4.5 and Fig. 4.6) is:

$$\begin{aligned} v_{z2} &= v_{z2,s} + v_{z2,c} + v_{z2,e} = \\ &= n_s R_c i_{z2} + r_{s,sc} i_{z2} + n_s Ll_c \frac{di_{z2}}{dt} + Ll_{s,sc} \frac{di_{z2}}{dt} + Ml_{s,c} \left(\frac{di_{z2}}{dt} - \frac{di_{sc}}{dt} \right) + Ml_{s,e} \frac{di_{z2}}{dt} + \frac{d\phi_{z2,s}}{dt} + \\ &+ r_{c,sc} (i_{z2} - i_{sc}) + Ml_{s,c} \frac{di_{z2}}{dt} + Ll_{c,sc} \left(\frac{di_{z2}}{dt} - \frac{di_{sc}}{dt} \right) + Ml_{c,e} \frac{di_{z2}}{dt} + \frac{d\phi_{z2,c}}{dt} + \\ &+ r_{e,sc} i_{z2} + n_e R_c i_{z2} + Ll_{e,sc} \frac{di_{z2}}{dt} + Ml_{c,e} \left(\frac{di_{z2}}{dt} - \frac{di_{sc}}{dt} \right) + Ml_{s,e} \frac{di_{z2}}{dt} + n_e Ll_c \frac{di_{z2}}{dt} + \frac{d\phi_{z2,e}}{dt}. \end{aligned} \quad (4.27)$$

Substituting (4.11)-(4.13) and (4.19)-(4.21) and considering that in this case the total number of coils are $N_c = n_s + 1 + n_e$, the final equation becomes:

$$v_{z2} = R_s i_{z2} + N_f r_{HR} i_{z2} - N_f (r_{HR} + r) i_{sc} + Ll \frac{di_{z2}}{dt} - NN_f l \frac{di_{sc}}{dt} + \frac{d\phi_{z2}}{dt}. \quad (4.28)$$

As already mentioned, in case of zero short circuit current (4.26) and (4.28) result in a particular HR condition:

$$v_z = R_s i_z + N_f r_{HR} i_z + Ll \frac{di_z}{dt} + \frac{d\phi_z}{dt}. \quad (4.29)$$

Therefore, hereafter the HR condition is modelled as a particular case of ISC fault with zero short circuit current.

Voltage equation for the ISC loop

To complete the circuital analysis, the voltage drop on the short circuit resistance (r_{sc}) defines the short circuit loop equation:

$$v_{z,c} = r_{sc} i_{sc}, \quad (4.30)$$

with $v_{z,c}$ the voltage drop defined for a coil-to-coil short circuit fault ($v_{z,c} = v_{z1,c}$) as:

$$\begin{aligned} v_{z1,c} &= r_{cs,sc} (i_{z1} - i_{sc}) + (n_c - 2) R_{c,sc} (i_{z1} - i_{sc}) + r_{ce,sc} (i_{z1} - i_{sc}) + \\ &Ml_{s,c} \frac{di_{z1}}{dt} + Ll_{cs,sc} \left(\frac{di_{z1}}{dt} - \frac{di_{sc}}{dt} \right) + (n_c - 2) Ll_c \left(\frac{di_{z1}}{dt} - \frac{di_{sc}}{dt} \right) + \\ &+ Ll_{ce,sc} \left(\frac{di_{z1}}{dt} - \frac{di_{sc}}{dt} \right) + Ml_{c,e} \frac{di_{z1}}{dt} + \frac{d\phi_{z1,c}}{dt} = \\ &= -N_f (r_{HR} + r) i_{sc} + N_f (r_{HR} + r) i_{z1} + NN_f l \frac{di_{z1}}{dt} + \\ &- \left[N_{fs}^2 + (n_c - 2) N^2 + N_{fe}^2 \right] \frac{di_{sc}}{dt} + \frac{d\phi_{z1,c}}{dt}, \end{aligned} \quad (4.31)$$

whereas, in case of short circuit between two turns of the same coil ($v_{z,c} = v_{z2,c}$) it results as:

$$\begin{aligned} v_{z2,c} &= r_{c,sc} (i_{z2} - i_{sc}) + Ml_{s,c} \frac{di_{z2}}{dt} + Ll_{c,sc} \left(\frac{di_{z2}}{dt} - \frac{di_{sc}}{dt} \right) + Ml_{c,e} \frac{di_{z2}}{dt} + \frac{d\phi_{z2,c}}{dt} = \\ &= -N_f (r_{HR} + r) i_{sc} + N_f (r_{HR} + r) i_{z2} - N_f^2 l \frac{di_{sc}}{dt} + N_f N l \frac{di_{z2}}{dt} + \frac{d\phi_{z2,c}}{dt}, \end{aligned} \quad (4.32)$$

resulting respectively in the short circuit loop equation:

$$\begin{aligned} r_{sc} i_{sc} + N_f (r_{HR} + r) i_{sc} + \left[N_{fs}^2 + (n_c - 2) N^2 + N_{fe}^2 \right] \frac{di_{sc}}{dt} = \\ = N_f (r_{HR} + r) i_{z1} + N_f N l \frac{di_{z1}}{dt} + \frac{d\phi_{z1,c}}{dt}, \end{aligned} \quad (4.33)$$

for a coil-to-coil ISC, and:

$$\begin{aligned} r_{sc} i_{sc} + N_f (r_{HR} + r) i_{sc} + N_f^2 l \frac{di_{sc}}{dt} = \\ = N_f (r_{HR} + r) i_{z2} + N_f N l \frac{di_{z2}}{dt} + \frac{d\phi_{z2,c}}{dt}, \end{aligned} \quad (4.34)$$

in case of single coil ISC.

As expected, in case of infinite short circuit resistance (healthy machine or HR condition) the short circuit current is zero.

To complete the analysis of the phase voltage equations the next subsection aims to evaluate the linked flux with a generic phase (healthy or faulty) and with the ISC loop.

Linked fluxes equations for HR and ISC faults

The linked flux evaluation (without considering for the leakage components) in a phase with a HR fault is the same of a healthy one. Instead, the linked flux evaluation for the ISC loop is different, as described here below.

Linked flux for a healthy phase

The airgap flux linked with a single turn has been already defined in Chapter 2, (2.104), as:

$$\phi_k = \sum_{h=1}^{\infty} \frac{\mu_0 R}{h} \sin\left(h \frac{\Delta\psi_k}{2}\right) \left(\int_{z=0}^L \bar{H}_h(z) dz e^{-jh\psi_k} + \int_{z=0}^L \bar{H}_h^*(z) dz e^{jh\psi_k} \right), \quad (4.35)$$

with ψ_k the angular position of the magnetic axis of the k -th turn compared to the magnetic axis of the first phase of the winding (considered as the angular position of the α - β stator reference frame), and $\Delta\psi_k$ the pitch of the k -th turn.

From the linked flux with one turn the total flux linked with the general x -th healthy phase is:

$$\phi_x = \sum_{cx=1}^{N_c} \sum_{h=1}^{\infty} \frac{2\mu_0 NR}{h} \sin\left(h \frac{\Delta\psi}{2}\right) \Re \left\{ \int_{z=0}^L \bar{H}_h(z) dz e^{-jh\psi_{cx}} \right\} = \sum_{h=1}^{\infty} \frac{2\mu_0 R p q N K_{ah}}{h} \Re \left\{ \int_{z=0}^L \bar{H}_h(z) dz e^{-jh\psi_x} \right\}, \quad (4.36)$$

with $\bar{H}_h(z)$ h -th harmonic of the total field in the airgap and K_{ah} the winding factor of the x -th phase defined by (2.45) (equal to all the phases in the hypotheses of the model, as explained in Chapter 2).

Linked flux for the ISC loop

For the ISC loop, the evaluation of the linked flux is more complicated. Indeed, it is important to highlight that for a machine with coils distributed in order to generate an overall magnetic axis centred with the position that defines the phase to which they belong to, it is possible to define a winding factor, which is a real number, and it is the same for all the phases. Instead, in case of ISC the asymmetrical distribution of the short circuited turns in the different coils makes impossible to defined in advance the phase of the equivalent magnetic axis. Therefore, the short circuit loop linked flux $\phi_{z,c}$ cannot be simplified considering just a real winding factor and maintaining the same magnetic axis of the faulty phase.

The airgap linked flux with the ISC loop ($\phi_{z,c}$) can be defined as:

$$\begin{aligned}\phi_{z,c} &= \sum_{kf=1}^{N_f} \sum_{h=1}^{\infty} \frac{2\mu_0 R}{h} \sin\left(h \frac{\Delta\psi}{2}\right) \Re \left\{ \int_{z=0}^L \bar{H}_h(z) dz e^{-jh\psi_{kf}} \right\} = \\ &= \sum_{h=1}^{\infty} \frac{2\mu_0 R}{h} \sin\left(h \frac{\Delta\psi}{2}\right) \Re \left\{ \int_{z=0}^L \bar{H}_h(z) dz \sum_{kf=1}^{N_f} e^{-jh\psi_{kf}} \right\}.\end{aligned}\quad (4.37)$$

In order to define a suitable relationship, the complex winding factor (\bar{K}_{fh}) is introduced as:

$$\bar{K}_{fh} = \frac{\sum_{kf=1}^{N_f} \sin\left(h \frac{\Delta\psi}{2}\right) e^{-jh\psi_{kf}}}{N_f} = K_{fh} e^{-jh\psi_f}.\quad (4.38)$$

The overall phase of this new complex variable ($e^{-jh\psi_f}$) identifies the magnetic axis of the short circuit fault in respect to the considered spatial harmonic order (or space, h), with ψ_f the magnetic axis of the ISC loop. The magnitude of the complex winding factor, K_{fh} , can be seen as the standard winding factor associated to the subcircuit of the ISC loop.

By the previous result, the ISC linked flux equation can be written as:

$$\phi_{z,c} = \sum_{h=1}^{\infty} \frac{2\mu_0 R N_f K_{fh}}{h} \Re \left\{ \int_{z=0}^L \bar{H}_h(z) e^{-jh\psi_f} dz \right\}.\quad (4.39)$$

If the fault affects only one series coil, ψ_{kf} is the same for all the short-circuited turns, equal to ψ_f , and if the fault happens in the central coil of one phase (if the coils number is odd) the ISC loop and the faulty phase have the same magnetic axis ($\psi_{kf} = \psi_f = \psi_x$). However, in general the angle can be whatever in the span between the magnetic axis of the first and the last of the series turns of the short-circuited phase.

This last paragraph concludes the definition of the phase and ISC loop circuital voltage equations. However, to complete the model of the machine the harmonics of the magnetic field in the airgap must be evaluated according to the analysis of their sources. Indeed, they appear in the phase voltage equations, or better in the linked flux evaluation. The general theory presented in Chapter 2 is considered in the next section in order to analyse the effect of the ISC current on the magnetic field in the airgap and define the effect of the rotor in terms of field distribution and torque.

4.2 Interturn Short Circuit Faults: Electromagnetic Analysis of the Short Circuit Loop

The voltage equations described in the previous section completely describe the electrical behaviour of the machine under the hypothesis of the model once the linked magnetic flux through the airgap is known. This section aims to evaluate the linked flux through the airgap in order to define a general electromagnetic model of a faulty machine in case of ISC fault. Indeed, the short circuit current affects the magnetomotive force (MMF) distribution producing an uncontrolled asymmetrical distortion of the flux in the airgap, with consequent torque ripples and forces on the rotor. As the machine is assumed isotropic and working in linearity, the analysis is based on the equations presented in Chapter 2. Firstly, the magnetic field related to the ISC current is evaluated. Then, the equations of the model are summarised, and finally the torque and force equations are presented.

Magnetic field generated by the ISC loop current

The magnetic field generated by the short-circuited phase can be described (still under the hypothesis of linear material behaviours) as the sum of the effects of the phase current flowing in all the turns plus the short circuit current flowing only in the ISC loop. Because the short circuit current is considered as positive when it flows as in Fig. 4.3, the current in the short-circuited turns is the difference between the faulty phase current and the ISC one, $i_z - i_{sc}$. However, it is found convenient to consider separately the effects of the two currents. According to the theory developed in Chapter 2, the magnetic field harmonic generated by the k -th turn (2.39) for an isotropic machine is:

$$\bar{H}_{kh} = \frac{\bar{F}_{kh}}{\delta} = \frac{2i_k}{h\pi\delta} \sin\left(h \frac{\Delta\psi}{2}\right) e^{jh\psi_k}. \quad (4.40)$$

The magnetic field generated by the x -phase current is described in the same way by (2.42) for both a healthy and a faulty phase as:

$$\bar{H}_{xh} = \frac{2NpqK_{ah}}{h\pi\delta} i_x e^{jh\psi_x}. \quad (4.41)$$

Instead, in case of ISC fault, the overall magnetic field is evaluated adding the effect of the magnetic field generated by the short circuit current as:

$$\bar{H}_{sc,h} = \sum_{kf=1}^{N_f} \bar{H}_{kf,h} = - \sum_{kf=1}^{N_f} \frac{2i_{kf}}{h\pi\delta} \sin\left(h \frac{\Delta\psi}{2}\right) e^{jh\psi_{kf}} = - \frac{2N_f K_{fh}}{h\pi\delta} e^{jh\psi_f} i_{sc}, \quad (4.42)$$

with $K_{fh}e^{jh\psi_f}$ the complex winding factor defined by (4.38). The “-” sign is used to highlight that the short circuit current is considered as positive when it flows in the opposite direction of the phase current in the short-circuited loop as in Fig. 4.4.

(4.41) and (4.42) evaluate the armature magnetic field in the airgap generated by the overall multiphase winding in presence of an ISC fault. The resulting field space harmonics are evaluated as:

$$\bar{H}_h = \sum_{x=1}^m \bar{H}_{xh} + \bar{H}_{sc,h} = \frac{mN_p q K_{ah}}{h\pi\delta} \bar{i}_h - \frac{2N_f K_{fh}}{h\pi\delta} e^{jh\psi_f} i_{sc}, \quad (4.43)$$

with \bar{i}_h the space vector of the stator phase currents defined by the general space vector transformation (2.53):

$$\bar{i}_h = \frac{2}{m} \sum_{x=1}^{N_s} i_x e^{jh\frac{2\pi}{N_s}(x-1)} = \frac{2}{m} \sum_{x=1}^m i_x e^{jh\psi_x}. \quad (4.44)$$

The current space vectors represent completely the machine phase currents that are measured and controlled by the closed loop voltage control, while the short circuit current i_{sc} is uncontrolled and function of the fault parameters.

Before analysing the force and torque equations for an ISC fault, the next subsection summarizes the electromagnetic model of the faulty machine presented up to this point and adding the effect of the rotor on the magnetic field distribution.

HR and ISC fault armature equations - Summary

In this subsection are summarised the electromagnetic equations of the model of an electrical machine in case of HR or ISC faults adding the effect of an SPM or squirrel cage IM rotor.

The voltage equation for the x-th healthy phase is:

$$v_x = R_s i_x + Ll \frac{di_x}{dt} + \frac{d\phi_x}{dt}. \quad (4.45)$$

The voltage equation for a phase with an ISC fault (or a HR condition if $i_{sc} = 0$) is:

$$v_z = R_s i_z + N_f r_{HR} i_z - N_f (r_{HR} + r) i_{sc} + Ll \frac{di_z}{dt} - Ml_{sc} \frac{di_{sc}}{dt} + \frac{d\phi_z}{dt}, \quad (4.46)$$

with:

$$Ml_{sc} = NN_f l.$$

The voltage equation for the ISC loop is:

$$r_{sc}i_{sc} + N_f(r_{HR} + r)i_{sc} + Ll_{sc} \frac{di_{sc}}{dt} = N_f(r_{HR} + r)i_z + Ml_{sc} \frac{di_z}{dt} + \frac{d\phi_{z,c}}{dt}, \quad (4.47)$$

with:

$$Ll_{sc} = [N_{fs}^2 + (n_c - 2)N^2 + N_{fe}^2] l,$$

in case of coil-to-coil ISC, and:

$$Ll_{sc} = N_f^2 l,$$

in case of ISC between turns of the same coil.

The airgap flux linked with a phase ϕ_x (or ϕ_z as well) is:

$$\phi_x = \sum_{h=1}^{\infty} \frac{2\mu_0 R p q N K_{ah}}{h} \Re \left\{ \left(L\bar{H}_h + \int_{z=0}^L \bar{H}_{r,h}(z) dz \right) e^{-jh\psi_x} \right\}, \quad (4.48)$$

where the rotor field harmonics are considered in the $\bar{H}_{r,h}(z)$ term, and the armature ones in the \bar{H}_h one. The airgap flux linked with the short circuit loop $\phi_{z,c}$ is:

$$\phi_{z,c} = \sum_{h=1}^{\infty} \frac{2\mu_0 R N_f K_{fh}}{h} \Re \left\{ \left(L\bar{H}_h + \int_{z=0}^L \bar{H}_{r,h}(z) dz \right) e^{-jh\psi_f} \right\}. \quad (4.49)$$

Given the phase voltages, the linked flux through the phases and the short circuit loop, the voltage equations evaluate the phase and short circuit currents.

The flux linked with the armature windings (phases and ISC loop) depends from the armature but also from the rotor field distribution.

The armature field harmonics as function of the phase and short circuit current are as:

$$\bar{H}_h = \frac{m N p q K_{ah}}{h \pi \delta} \bar{i}_h - \frac{2 N_f K_{fh}}{h \pi \delta} e^{jh\psi_f} i_{sc}. \quad (4.50)$$

Instead, the rotor field harmonics already defined in (2.134) and (2.165) for an SPM and an IM squirrel cage rotors are as follows. For an SPM rotor:

$$\bar{H}_{r,h}(z) = \bar{H}_{r,ph_{odd}}(z) = \frac{4B_r \tau_M}{\mu_M h_{odd} \pi \delta} \sin \left(h_{odd} \frac{\pi}{2} (1 - Sh_{PM}) \right) e^{jph_{odd}\vartheta_m} e^{jph_{odd}\psi_{skew,w}} \quad (4.51)$$

with Sh_{PM} the magnet pitch shortening parameter (reduction of the magnets pitch in per unit) in each segmentation length of a SPM rotor:

$$z \in \left[z_w - \frac{\Delta L_w}{2}; z_w + \frac{\Delta L_w}{2} \right].$$

For a squirrel cage rotor, it results as:

$$\bar{H}_{r,h}(z) = \frac{N_b}{\pi\delta} \frac{\sin\left(h \frac{\pi}{N_b}\right)}{h} \bar{i}_{r,h} e^{jh\left(\frac{L}{2} - \frac{\Delta W_{skew}}{L}\right)} \quad (4.52)$$

By (4.45)-(2.165) the machine electromagnetic behaviour is completely defined once the rotor speed and phase voltages are known in function of the time (plus the rotor currents in case of an IM). The next subsection aims to define the torque and radial force from the magnetomotive force distribution (function of current and magnets) given by the solution of the electromagnetic model.

Torque and radial force evaluation for ISC faults

The torque and radial force have been evaluated in Chapter 2 with a general approach. Here below, the equations are represented highlighting the effect of an ISC current.

Being the phase and short circuit currents analysed in two separate contributions of the armature field, also the related torque and radial force can be evaluated separately.

Phase currents torque contribution

The general torque equation presented in Chapter 2 in case of a healthy machine is considered as sum of a number of contributions as:

$$T = \frac{T_0}{2} + \frac{T_{N_s}}{2} + \sum_{h=1}^{N_s/2-1} T_h \quad (4.53)$$

For a SPM machine (2.217) defines the torque contributions as:

$$T_{PM,h} = \Re \left\{ \sum_{\substack{y=0 \\ \left(\frac{yN_s+h}{P}\right)_{\text{odd,int}}}}^{\infty} jK_{T,PM,y,h}^+ e^{j(yN_s+h)g_m} \bar{i}_h^* \right\} + \Re \left\{ \sum_{\substack{y=\left(\frac{h}{N_s}\right)_{\text{int}} \\ \left(\frac{yN_s-h}{P}\right)_{\text{odd,int}}}}^{\infty} -jK_{T,PM,y,h}^- e^{-j(yN_s-h)g_m} \bar{i}_h^* \right\}, \quad (4.54)$$

with:

$$K_{T,PM,y,h}^+ = m\mu_0 L R p^2 q N \frac{4B_r \tau_M}{\mu_M \pi \delta} \frac{K_{a(yN_s+h)} K_{skew(yN_s+h)}}{(yN_s+h)} \sin\left((yN_s+h) \frac{\pi}{2p} (1 - Sh_{PM})\right),$$

$$K_{T,PM,y,h}^- = m\mu_0 LR p^2 q N \frac{4B_r \tau_M}{\mu_M \pi \delta} \frac{K_{a(yN_s-h)} K_{skew(yN_s-h)}}{(yN_s-h)} \sin\left((yN_s-h) \frac{\pi}{2p} (1-Sh_{PM})\right).$$

Instead, for a squirrel cage rotor IM the torque contributions are expressed by (2.222) as:

$$T_{cage,h} = \Re \left\{ \sum_{\rho=0}^{N_b-1} \sum_{\substack{y=0 \\ \left(\frac{yn+h-\rho}{N_b}\right)_{int \geq 0}}}^{\infty} jK_{T,r,y,h}^+ e^{j(yN_s+h)\vartheta_m} \bar{i}_{r,\rho} \bar{i}_h^* \right\} + \Re \left\{ \sum_{\rho=0}^{N_b-1} \sum_{\substack{y=0 \\ y \geq \left(\frac{h}{N_s}\right)_{int} \\ \left(\frac{yn-h-\rho}{N_b}\right)_{int \geq 0}}}^{\infty} -jK_{T,r,y,h}^- e^{-j(yN_s-h)\vartheta_m} \bar{i}_{r,\rho}^* \bar{i}_h \right\}, \quad (4.55)$$

with:

$$K_{T,r,y,h}^+ = \frac{\mu_0 RLmpqNN_b}{\pi\delta} (yN_s+h) \frac{\sin\left((yN_s+h) \frac{\pi}{N_b}\right) K_{a,(yN_s+h)} K_{skew,(yN_s+h)}}{(yN_s+h)^2},$$

$$K_{T,r,y,h}^- = \frac{\mu_0 RLmpqNN_b}{\pi\delta} (yN_s-h) \frac{\sin\left((yN_s-h) \frac{\pi}{N_b}\right) K_{a,(yN_s-h)} K_{skew,(yN_s-h)}}{(yN_s-h)^2}.$$

ISC current torque contribution

In case of ISC, there is an additional torque component caused by the interaction between the rotor magnetic field and the generated by the short circuit current one. The relationships for the short circuit torque are the same resulting by the phase currents, with the only difference that rather than be function of the phase current space vector \bar{i}_h , they are function of the current vector related to the short circuit loop $i_{sc} e^{jh\psi_f}$. The short circuit loop could also be seen as an equivalent multiphase winding (with one phase), but this would make the analysis much more complicated. In Chapter 2, the torque effect of a single turn of the armature winding has been presented. The obtained result is used here to define the effect of the N_f short-circuited turns.

The total short circuit torque equation for a SPM machine (2.195) results as:

$$\begin{aligned} T_{PM,sc} &= -8\mu_0 LR \frac{B_r \tau_M}{\mu_M \pi \delta} \sum_{h=1}^{\infty} \Re \left\{ j i_{sc} e^{-jh\psi_f} \frac{N_f K_{fh}}{ph} \sin\left(h \frac{\pi}{2}\right) e^{jph\vartheta_m} K_{skew,ph} \right\} = \\ &= -\sum_{h=1}^{\infty} \Re \left\{ j i_{sc} K_{T,PM,sc,h} e^{-jh\psi_f} e^{jph\vartheta_m} \right\} = \sum_{h_{odd}=1}^{\infty} K_{T,PM,sc,ph} \sin(ph(\vartheta_m - \psi_f)) \Big|_{sc}, \end{aligned} \quad (4.56)$$

with:

$$K_{T,PM,sc,ph} = 8\mu_0 LR \frac{B_r \tau_M}{\mu_M \pi \delta} \frac{N_f K_{fph}}{ph} \sin\left(h \frac{\pi}{2}\right) K_{skew,ph}.$$

The total short circuit torque equation for a squirrel cage rotor IM (2.200) results as:

$$T_{cage,sc} = \left[\sum_{h=1}^{\infty} K_{T,cage,sc,h} \Re\left\{ \bar{j}i_{r,h} e^{-jh(\psi_f - \vartheta_m)} \right\} \right] i_{sc}, \quad (4.57)$$

with:

$$K_{T,cage,sc,h} = \frac{2\mu_0 RL N_b}{\pi \delta} \frac{\sin\left(\frac{h\pi}{N_b}\right) N_f K_{fh}}{h} K_{skew,h},$$

$$K_{fh} e^{jh\psi_f} = \frac{\sum_{kf=1}^{N_f} \sin\left(h \frac{\Delta\psi}{2}\right) e^{jh\psi_{kf}}}{N_f}.$$

The “-” sign is still caused by the opposite convention for the positive short circuit current in the turns where it flows.

It is interesting to note that the considered short circuit affects one set of series turns and not a full three-phase winding. Therefore, the resulting armature field is a pulsating one and the resulting torque for an SPM machine presents a significant ripple and reduction of its average value. In case of a cage machine, the analysis is more complicated depending on the reaction of the cage, but a reduction of the average torque and a higher torque ripple are expected.

The simplified radial force evaluation (2.257) is:

$$\bar{F}(\vartheta_m) = \frac{\pi\mu_0 R}{4} \int_0^L \sum_{h=1}^{\infty} \left[\bar{H}_h(\vartheta_m, z) \bar{H}_{h-1}^*(\vartheta_m, z) + \bar{H}_h^*(\vartheta_m, z) \bar{H}_{h+1}(\vartheta_m, z) \right] dz. \quad (4.58)$$

The analysis of the force coefficients has not been carried out, but some considerations can be done. In particular, the force equation is the same independently from the sources of the magnetic field harmonics. Therefore, if the machine is with full pitch turns and a single pole pair (each turn has a 180 degrees mechanical pitch) an ISC fault do not generate radial forces, because only odd harmonics are generated in the airgap ($p=1$). Instead, if the turn pitch is different from 180 mechanical degrees (as in a machine with a short pitch winding or in general with a number of pole pairs higher than one, $p>1$) the ISC current generates both odd and even field harmonics. These harmonics interact with themselves and with the rotor ones producing a radial force qualitatively described by (2.257).

The equations presented in this section are completed in the next one, where the complete model is presented in terms of space vector representation.

4.3 Space Vector Model of a Multiphase Machine with a High Resistance or Interturn Short Circuit Fault

The electromagnetic equations presented in the previous section are based on the relationships between the current space vectors and the field harmonics in the airgap. Indeed, a suitable current control of a multiphase machine (or three-phase as well) is usually based on the machine voltage space vector equations defined for the stator phases in the general form as:

$$\bar{v}_h = \frac{2}{m} \sum_{x=1}^{N_s} v_x \bar{\alpha}^{h(x-1)}, \quad (4.59)$$

with $\bar{\alpha} = e^{j \frac{2\pi}{N_s}}$. In case of a squirrel cage IM, the rotor is modelled as a N_b -phase symmetrical machine as described in Chapter 2.

In this section, all the electromagnetic equations are rewritten in terms of space vector representation for the three sources of MMF:

- stator phase winding;
- ISC loop;
- rotor magnets (SPM) or squirrel cage (IM).

Stator Phase Voltage Space Vector Equation

The stator voltage equation results by the space vector transformation of (4.46) as:

$$\begin{aligned} \bar{v}_h = & \frac{2}{m} \sum_{x=1}^{N_s} \left(R_s i_x + Ll \frac{di_x}{dt} + \frac{d\phi_x}{dt} \right) \bar{\alpha}^{h(x-1)} + \\ & + \frac{2}{m} \left(N_f r_{HR} i_z - N_f (r_{HR} + r) i_{sc} - Ml_{sc} \frac{di_{sc}}{dt} \right) \bar{\alpha}^{h(z-1)}. \end{aligned} \quad (4.60)$$

Considering the airgap linked flux in three components related to the various sources of MMF (stator, rotor and short circuit loop), (4.60) becomes:

$$\begin{aligned} \bar{v}_h = & R_s \bar{i}_h + (Ll + L_h) \frac{d\bar{i}_h}{dt} + \frac{d\bar{\phi}_{r,h}}{dt} + \\ & + \frac{2}{m} N_f r_{HR} i_z \bar{\alpha}^{h(z-1)} + \\ & + \frac{2}{m} \left(-N_f (r_{HR} + r) i_{sc} - Ml_{sc} \frac{di_{sc}}{dt} \right) \bar{\alpha}^{h(z-1)} + \frac{d\bar{\phi}_{sc,h}}{dt}. \end{aligned} \quad (4.61)$$

where the first row of (4.61) is the voltage space vector equation of an healthy multiphase winding, the second row represents the contribution related the HR in the faulty turns, and finally the third row represents the effect of the ISC current.

The self inductance of the h -space defined in (2.117) and (2.118) is written here below:

$$L_h = \frac{2}{m} \mu_0 L R p q N N_s \left[\sum_{y=0}^{\infty} \frac{K_{a(yN_s+h)}^2}{(yN_s+h)^2} \frac{N m p q}{\pi \delta} + \sum_{y=\left(\frac{h}{N_s}\right)_{\text{int}}}^{\infty} \frac{K_{a(yN_s-h)}^2}{(yN_s-h)^2} \frac{N m p q}{\pi \delta} \right].$$

The second term:

$$\frac{2}{m} N_f r_{HR} i_z \bar{\alpha}^{h(z-1)},$$

can be analysed as a HR fault in the faulty phase (now only in the z -th phase), by an additional voltage drop space vector $\bar{v}_{HR,h}$ defined as:

$$\bar{v}_{HR,h} = \frac{2}{m} N_f r_{HR} i_z \bar{\alpha}^{h(z-1)} = \sum_{\rho=0}^{N_s-1} \frac{\bar{i}_\rho}{N_s} N_f r_{HR} \bar{\alpha}^{(h-\rho)(z-1)} = \frac{m}{2N_s} \sum_{\rho=0}^{N_s-1} \bar{i}_\rho \bar{R}_{HR,(h-\rho)}, \quad (4.62)$$

with $\bar{R}_{HR,h}$ the HR space vector (representing only the resistance increase from the expected value) localised in the faulty phase as:

$$\bar{R}_{HR,h} = \frac{2}{m} N_f r_{HR} e^{jh\psi_z}, \quad (4.63)$$

with the relative general inverse transformation that evaluate the overall phase resistance increase:

$$R_{HR,x} = \frac{m}{2N_s} \sum_{h=0}^{N_s-1} \bar{R}_{HR,h} \bar{\alpha}^{-h(x-1)}. \quad (4.64)$$

$\bar{\phi}_{sc,h}$ is the linked flux space vector related to the field produced by the ISC current, which can be evaluated by (4.48) and (4.50) as:

$$\begin{aligned} \bar{\phi}_{sc,h} &= \frac{2}{m} \mu_0 L R p q N N_s \left[\sum_{y=0}^{\infty} \frac{K_{a(yN_s+h)}}{(yN_s+h)} \bar{H}_{sc,(yN_s+h)} + \sum_{y=\left(\frac{h}{N_s}\right)_{\text{int}}}^{\infty} \frac{K_{a(yN_s-h)}}{(yN_s-h)} \bar{H}_{sc,(yN_s-h)}^* \right] = \\ &= -\frac{4\mu_0 L R p q N N_s N_f}{m \pi \delta} \left[\sum_{y=0}^{\infty} \frac{K_{a(yN_s+h)} K_{f(yN_s+h)}}{(yN_s+h)^2} e^{j(yN_s+h)\psi_f} + \sum_{y=\left(\frac{h}{N_s}\right)_{\text{int}}}^{\infty} \frac{K_{a(yN_s-h)} K_{f(yN_s-h)}}{(yN_s-h)^2} e^{-j(yN_s-h)\psi_f} \right] \bar{i}_{sc}. \end{aligned}$$

(4.65)

The linked flux space vector related to the rotor MMF ($\bar{\phi}_{r,h}$, for an SPM or a squirrel cage rotor) are the same defined for a healthy machine. Their equations, presented in Chapter 2, are summarised here below.

The linked rotor flux space vector for a SPM rotor is (2.142):

$$\begin{aligned} \bar{\phi}_{PM,h} = & \frac{2}{m} \mu_0 LRpqNN_s \frac{4B_r \tau_M P}{\mu_M \pi \delta} \left[\sum_{\substack{y=0 \\ \left(\frac{yN_s+h}{P}\right)_{\text{odd,int}}}}^{\infty} \frac{K_{a(yN_s+h)} K_{skew(yN_s+h)}}{(yN_s+h)^2} \sin\left((yN_s+h) \frac{\pi}{2p}\right) e^{j(yN_s+h)\vartheta_m} \right] + \\ & + \frac{2}{m} \mu_0 LRpqNN_s \frac{4B_r \tau_M P}{\mu_M \pi \delta} \left[\sum_{\substack{y=\left(\frac{h}{N_s}\right)_{\text{int}} \\ \left(\frac{yN_s-h}{P}\right)_{\text{odd,int}}}}^{\infty} \frac{K_{a(yN_s-h)} K_{skew(yN_s-h)}}{(yN_s-h)^2} \sin\left((yN_s-h) \frac{\pi}{2p}\right) e^{-j(yN_s-h)\vartheta_m} \right]. \end{aligned} \quad (4.66)$$

The linked rotor flux space vector for a squirrel cage IM is (2.185):

$$\begin{aligned} \bar{\phi}_{cage,h} = & \frac{2}{m} \mu_0 RLpqNN_s \frac{N_b}{\pi \delta} \left[\sum_{y=0}^{\infty} \frac{K_{a(yN_s+h)} K_{skew,(yN_s+h)}}{(yN_s+h)^2} \sin\left((yN_s+h) \frac{\pi}{N_b}\right) \bar{i}_{r,(yN_s+h)} e^{j(yN_s+h)\vartheta_m} \right] + \\ & + \frac{2}{m} \mu_0 RLpqNN_s \frac{N_b}{\pi \delta} \left[\sum_{y=\left(\frac{h}{N_s}\right)_{\text{int}}}^{\infty} \frac{K_{a(yN_s-h)} K_{skew,(yN_s-h)}}{(yN_s-h)^2} \sin\left((yN_s-h) \frac{\pi}{N_b}\right) \bar{i}_{r,(yN_s-h)}^* e^{-j(yN_s-h)\vartheta_m} \right]. \end{aligned} \quad (4.67)$$

The last equations completely describe the stator phase electromagnetic behaviour once the ISC and rotor MMFs are known. In the next paragraphs, the equations for the ISC loop and the squirrel cage (in case of IM) that allows solving the full equations of the system and therefore evaluating the MMFs of the three components (stator, ISC loop and rotor) are presented.

ISC loop Equation

The voltage equation for the ISC loop (4.47) can be rewritten in terms of phase current space vectors, and considering for the airgap linked flux $\phi_{z,c}$ in three components related to the various sources of MMF (stator $\phi_{s,z,c}$, rotor $\phi_{r,z,c}$ and short circuit loop $\phi_{sc,z,c}$). The ISC loop equation results as:

$$\begin{aligned}
 & r_{sc} i_{sc} + N_f (r_{HR} + r) i_{sc} + L l_{sc} \frac{di_{sc}}{dt} = \\
 & = N_f (r_{HR} + r) \frac{m}{2N_s} \sum_{h=0}^{N_s-1} \bar{i}_h e^{-jh\psi_z} + M l_{sc} \frac{m}{2N_s} \sum_{h=0}^{N_s-1} \frac{d\bar{i}_h}{dt} e^{-jh\psi_z} + \\
 & + \frac{d\phi_{s,z,c}}{dt} + \frac{d\phi_{r,z,c}}{dt} + \frac{d\phi_{sc,z,c}}{dt}.
 \end{aligned} \tag{4.68}$$

The airgap flux generated by the stator phase currents and linked with the ISC loop ($\phi_{s,z,c}$) can be evaluated by (4.49) as:

$$\begin{aligned}
 \phi_{s,z,c} &= \frac{2\mu_0 R L N_f m N p q}{\pi \delta} \sum_{h=1}^{\infty} \Re \left\{ \frac{K_{fh} K_{ah}}{h^2} \bar{i}_h e^{-jh\psi_f} \right\} = \\
 &= \frac{2\mu_0 R L N_f m N p q}{\pi \delta} \sum_{h=0}^{N_s-1} \sum_{y=0}^{\infty} \Re \left\{ \frac{K_{f(yN_s+h)} K_{a(yN_s+h)}}{(yN_s+h)^2} \bar{i}_h e^{-j(yN_s+h)\psi_f} \right\}.
 \end{aligned} \tag{4.69}$$

The airgap flux generated by the rotor and linked with the ISC loop ($\phi_{r,z,c}$) can be evaluated doing the same steps presented in Chapter 2 for the flux linked with a single turn, and simplifying as follows.

For a SPM rotor, it results by (2.139) as:

$$\phi_{r,z,c} = \frac{8\mu_0 R L N_f B_r \tau_M}{\pi \delta p \mu_M} \sum_{h_{odd}=1}^{\infty} \Re \left\{ \frac{K_{f,ph} K_{skew,ph}}{h^2} \sin\left(h \frac{\pi}{2}\right) e^{jph_{odd}\vartheta_m} e^{-jph\psi_f} \right\}. \tag{4.70}$$

For a squirrel cage rotor, it results by (2.172) as:

$$\phi_{r,z,c} = \frac{2\mu_0 R L N_f N_b}{\pi \delta} \sum_{h=1}^{\infty} \Re \left\{ \frac{K_{fh} K_{skew,h} \sin\left(h \frac{\pi}{N_b}\right)}{h^2} \bar{i}_{r,h} e^{jh\vartheta_m} e^{-jh\psi_f} \right\}. \tag{4.71}$$

Finally, the airgap flux generated by the ISC loop and linked with the ISC loop itself ($\phi_{sc,z,c}$) can be evaluated considering the self inductance of the ISC loop by (4.49) and (4.50) as:

$$\phi_{sc,z,c} = \sum_{h=1}^{\infty} \frac{2\mu_0 R N_f K_{fh}}{h} \Re \left\{ L \bar{H}_{sc,h} e^{-jh\psi_f} \right\} = -\frac{4\mu_0 R L N_f^2}{\pi \delta} \sum_{h=1}^{\infty} \left(\frac{K_{fh}}{h} \right)^2 i_{sc} = -L_{sc} i_{sc}, \tag{4.72}$$

with:

$$L_{sc} = \frac{4\mu_0 R L N_f^2}{\pi \delta} \sum_{h=1}^{\infty} \left(\frac{K_{fh}}{h} \right)^2,$$

the self inductance of the ISC loop.

Given the phase voltages and the linked flux through the phases and the short circuit loop, the voltage equations allows evaluating the phase and short circuit currents.

The only missing equation is the squirrel cage voltage equation that considers also for the effect of the ISC current, topic of the next paragraph.

Rotor Cage Space Vector Equation

The squirrel cage voltage space vector equation (2.169) in case of ISC can be defined as:

$$0 = R_{rh} \bar{i}_h + (Ll_{rh} + L_{cage,h}) \frac{d\bar{i}_h}{dt} + \frac{d\bar{\phi}_{mutual,h}}{dt} + \frac{d\bar{\phi}_{mutual,sc,h}}{dt}, \quad (4.73)$$

with $\bar{\phi}_{mutual,h}$ the cage linked flux space vector resulting by the machine phase currents.

The linked flux space vector generated by the stator phase currents (2.176) is:

$$\begin{aligned} \bar{\phi}_{mutual,h} = & \frac{2Nmpq\mu_0 RL}{\pi\delta} \left[\sum_{y=0}^{\infty} \frac{\sin\left((yN_b + h)\frac{\pi}{N_b}\right) K_{a(yN_b+h)}}{(yN_b + h)^2} \bar{i}_{(yN_b+h)} K_{skew(yN_b+h)} e^{-j(yN_b+h)\vartheta_m} \right] + \\ & + \frac{2Nmpq\mu_0 RL}{\pi\delta} \left[\sum_{y=\left(\frac{h}{N_b}\right)_{int}}^{\infty} \frac{\sin\left((yN_b - h)\frac{\pi}{N_b}\right) K_{a(yN_b-h)}}{(yN_b - h)^2} \bar{i}_{(yN_b-h)}^* K_{skew(yN_b-h)} e^{j(yN_b-h)\vartheta_m} \right]. \end{aligned} \quad (4.74)$$

Instead, $\bar{\phi}_{mutual,sc,h}$ represents the cage linked flux space vector resulting by the ISC fault current.

The ISC effect can be evaluated by (2.172) and (4.42) as:

$$\begin{aligned} \bar{\phi}_{mutual,sc,h} = & -\frac{4\mu_0 RL N_f}{\pi\delta} \left[\sum_{y=0}^{\infty} \frac{\sin\left((yN_b + h)\frac{\pi}{N_b}\right) K_{f(yN_b+h)}}{(yN_b + h)^2} e^{j(yN_b+h)\vartheta_f} e^{-j(yN_b+h)\vartheta_m} K_{skew,(yN_b+h)} \right] \bar{i}_{sc} + \\ & -\frac{4\mu_0 RL N_f}{\pi\delta} \left[\sum_{y=\left(\frac{h}{N_b}\right)_{int}}^{\infty} \frac{\sin\left((yN_b - h)\frac{\pi}{N_b}\right) K_{f(yN_b-h)}}{(yN_b - h)^2} e^{-j(yN_b-h)\vartheta_f} e^{j(yN_b-h)\vartheta_m} K_{skew,(yN_b-h)} \right] \bar{i}_{sc}. \end{aligned} \quad (4.75)$$

The other cage parameters (self inductance, resistance and leakage inductance related to the considered rotor space equation) in the space vector equations are the same presented in Chapter 2, summarised here below.

$$L_{cage,h} = 2 \frac{\mu_0 R L N_b}{\pi \delta} \left[\sum_{y=0}^{\infty} \frac{\sin\left((yN_b + h)\frac{\pi}{N_b}\right)^2}{(yN_b + h)^2} + \sum_{y=\left(\frac{h}{N_b}\right)_{int}}^{\infty} \frac{\sin\left((yN_b - h)\frac{\pi}{N_b}\right)^2}{(yN_b - h)^2} \bar{i}_{(yN_b-h)}^* \right],$$

$$R_{rh} = 2R_b \left(1 - \cos\left(\frac{2\pi h}{N_b}\right) \right) + R_{rR} + R_{rF},$$

$$Ll_{rh} = 2ll_b \left(1 - \cos\left(\frac{2\pi h}{N_b}\right) \right) + ll_{rR} + ll_{rF}.$$

The presented equations are used to analyse the ISC and HR faults. Before simplifying the equations for simulating and presenting the results obtained for the fault analysis, the ISC fault is generalised in the following subsection considering the presence of an additional HR condition in more phases outside the ISC loop.

General Interturn Short Circuit with High Resistance Fault in Multiphase Electrical Machines

In case of a general fault condition (with both an ISC and an HR fault), the phase resistance might change also in other phases. Instead the ISC fault is considered to happen only in one phase. As mentioned in the previous section, it is useful to represent the resistance variation from the normal value rather than the overall resistance. Therefore, the voltage drop space vector $\bar{v}_{HR,h}$ can be still defined as in (4.62), but the resistance increase space vector of the phases is now defined as:

$$\begin{aligned} \bar{R}_{HR,h} &= \frac{2}{m} \sum_{x=1}^{N_s} N_{HR,x} r_{HR,x} e^{jh \frac{2\pi}{N_s}(x-1)} + \\ &+ \frac{2}{m} N_f r_{HR} e^{jh\psi_z} = \frac{2}{m} \sum_{x=1}^m R_{HR,x} e^{jh\psi_x} + \frac{2}{m} N_f r_{HR} e^{jh\psi_z} \end{aligned} \quad (4.76)$$

with the relative general inverse transformation (4.64) that consider for the total phase resistance increase.

$$R_{HR,x} = \frac{m}{2N_s} \sum_{h=0}^{N_s-1} \bar{R}_{HR,h} \bar{\alpha}^{-h(x-1)}. \quad (4.77)$$

To conclude the model, the complete equations are summarised in the next subsection.

Summary of the complete Space Vector model for HR and ISC faults in multiphase machines

The space vector equations for the stator, ISC loop and rotor with also the possibility of having an HR fault are summarised here below.

Stator Phase Voltage Space Vector Equation

The stator voltage space vector equation is:

$$\begin{aligned} \bar{v}_h = R_s \bar{i}_h + (Ll + L_h) \frac{d\bar{i}_h}{dt} + \frac{m}{2N_s} \sum_{\rho=0}^{N_s-1} \bar{i}_\rho \bar{R}_{HR,(h-\rho)} + \frac{d\bar{\phi}_{r,h}}{dt} + \\ + \frac{2}{m} \left(-N_f (r_{HR} + r) \bar{i}_{sc} - Ml_{sc} \frac{d\bar{i}_{sc}}{dt} \right) \bar{\alpha}^{h(z-1)} + \frac{d\bar{\phi}_{sc,h}}{dt}, \end{aligned} \quad (4.78)$$

with the HR phase resistance increase space vector as:

$$\bar{R}_{HR,h} = \frac{2}{m} \sum_{x=1}^m R_{HR,x} e^{jh\psi_x} + \frac{2}{m} N_f r_{HR} e^{jh\psi_z}, \quad (4.79)$$

the stator linked flux space vector generated from the ISC current:

$$\begin{aligned} \bar{\phi}_{sc,h} = -\frac{4\mu_0 L R p q N N_s N_f}{m \pi \delta} \sum_{y=0}^{\infty} \frac{K_{a(yN_s+h)} K_{f(yN_s+h)}}{(yN_s+h)^2} e^{j(yN_s+h)\psi_f} \bar{i}_{sc} + \\ + -\frac{4\mu_0 L R p q N N_s N_f}{m \pi \delta} \sum_{y=\left(\frac{h}{N_s}\right)_{\text{int}}}^{\infty} \frac{K_{a(yN_s-h)} K_{f(yN_s-h)}}{(yN_s-h)^2} e^{-j(yN_s-h)\psi_f} \bar{i}_{sc}, \end{aligned} \quad (4.80)$$

the stator linked flux space vector generated from an SPM rotor:

$$\begin{aligned} \bar{\phi}_{PM,h} = \frac{2}{m} \mu_0 L R p q N N_s \frac{4B_r \tau_M p}{\mu_M \pi \delta} \left[\sum_{\substack{y=0 \\ \left(\frac{yN_s+h}{p}\right)_{\text{odd,int}}}}^{\infty} \frac{K_{a(yN_s+h)} K_{skew(yN_s+h)}}{(yN_s+h)^2} \sin\left((yN_s+h)\frac{\pi}{2p}\right) e^{j(yN_s+h)\vartheta_m} \right] + \\ + \frac{2}{m} \mu_0 L R p q N N_s \frac{4B_r \tau_M p}{\mu_M \pi \delta} \left[\sum_{\substack{y=\left(\frac{h}{N_s}\right)_{\text{int}} \\ \left(\frac{yN_s-h}{p}\right)_{\text{odd,int}}}}^{\infty} \frac{K_{a(yN_s-h)} K_{skew(yN_s-h)}}{(yN_s-h)^2} \sin\left((yN_s-h)\frac{\pi}{2p}\right) e^{-j(yN_s-h)\vartheta_m} \right], \end{aligned} \quad (4.81)$$

or for a squirrel cage rotor:

$$\begin{aligned} \bar{\phi}_{cage,h} = & \frac{2}{m} \mu_0 R L p q N N_s \frac{N_b}{\pi \delta} \left[\sum_{y=0}^{\infty} \frac{K_{a(yN_s+h)} K_{skew,(yN_s+h)}}{(yN_s+h)} \frac{\sin\left((yN_s+h)\frac{\pi}{N_b}\right)}{(yN_s+h)} \bar{i}_{r,(yN_s+h)} e^{j(yN_s+h)\theta_m} \right] + \\ & + \frac{2}{m} \mu_0 R L p q N N_s \frac{N_b}{\pi \delta} \left[\sum_{y=\left(\frac{h}{N_s}\right)_{int}}^{\infty} \frac{K_{a(yN_s-h)} K_{skew,(yN_s-h)}}{(yN_s-h)} \frac{\sin\left((yN_s-h)\frac{\pi}{N_b}\right)}{(yN_s-h)} \bar{i}_{r,(yN_s-h)}^* e^{-j(yN_s-h)\theta_m} \right]. \end{aligned} \quad (4.82)$$

ISC loop Equation

The ISC loop voltage equation is:

$$\begin{aligned} r_{sc} i_{sc} + N_f (r_{HR} + r) i_{sc} + (L l_{sc} + L_{sc}) \frac{d i_{sc}}{dt} = N_f (r_{HR} + r) \frac{m}{2N_s} \sum_{h=0}^{N_s-1} \bar{i}_h e^{-jh\psi_z} + \\ + M l_{sc} \frac{m}{2N_s} \sum_{h=0}^{N_s-1} \frac{d \bar{i}_h}{dt} e^{-jh\psi_z} + \frac{d \phi_{s,z,c}}{dt} + \frac{d \phi_{r,z,c}}{dt}, \end{aligned} \quad (4.83)$$

with the stator related linked flux:

$$\phi_{s,z,c} = \frac{2\mu_0 R L N_f m N p q}{\pi \delta} \sum_{h=0}^{N_s-1} \sum_{y=0}^{\infty} \Re \left\{ \frac{K_{f(yN_s+h)} K_{a(yN_s+h)}}{(yN_s+h)^2} \bar{i}_h e^{-j(yN_s+h)\psi_f} \right\}, \quad (4.84)$$

the rotor related linked flux for an SPM rotor:

$$\phi_{r,z,c} = \frac{8\mu_0 R L N_f B_r \tau_M}{\pi \delta p \mu_M} \sum_{h_{odd}=1}^{\infty} \Re \left\{ \frac{K_{f,ph} K_{skew,ph}}{h^2} \sin\left(h_{odd} \frac{\pi}{2}\right) e^{jph_{odd}\theta_m} e^{-jph\psi_f} \right\}, \quad (4.85)$$

or for a squirrel cage rotor:

$$\phi_{r,z,c} = \frac{2\mu_0 R L N_f N_b}{\pi \delta} \sum_{h=1}^{\infty} \Re \left\{ \frac{K_{fh} K_{skew,h} \sin\left(h \frac{\pi}{N_b}\right)}{h^2} \bar{i}_{r,h} e^{jh\theta_m} e^{-jh\psi_f} \right\}, \quad (4.86)$$

Rotor Cage Space Vector Equation

The squirrel cage voltage space vector equation is:

$$0 = R_{rh} \bar{i}_h + (L l_{rh} + L_{cage,h}) \frac{d \bar{i}_h}{dt} + \frac{d \bar{\phi}_{mutual,h}}{dt} + \frac{d \bar{\phi}_{mutual,sc,h}}{dt}, \quad (4.87)$$

with the cage linked flux space vector resulting by the machine phase currents:

$$\begin{aligned} \bar{\phi}_{mutual,h} = & \frac{2Nmpq\mu_0RL}{\pi\delta} \left[\sum_{y=0}^{\infty} \frac{\sin\left((yN_b+h)\frac{\pi}{N_b}\right) K_{a(yN_b+h)}}{(yN_b+h)^2} \bar{i}_{(yN_b+h)} K_{skew(yN_b+h)} e^{-j(yN_b+h)g_m} \right] + \\ & + \frac{2Nmpq\mu_0RL}{\pi\delta} \left[\sum_{y=\left(\frac{h}{N_b}\right)_{int}}^{\infty} \frac{\sin\left((yN_b-h)\frac{\pi}{N_b}\right) K_{a(yN_b-h)}}{(yN_b-h)^2} \bar{i}_{(yN_b-h)}^* K_{skew(yN_b-h)} e^{j(yN_b-h)g_m} \right], \end{aligned} \quad (4.88)$$

and the cage linked flux space vector resulting by the ISC fault current:

$$\begin{aligned} \bar{\phi}_{mutual,sc,h} = & -\frac{4\mu_0RLN_f}{\pi\delta} \left[\sum_{y=0}^{\infty} \frac{\sin\left((yN_b+h)\frac{\pi}{N_b}\right) K_{f(yN_b+h)}}{(yN_b+h)^2} e^{-j(yN_b+h)g_m} e^{j(yN_b+h)\psi_f} K_{skew,(yN_b+h)} \right] i_{sc} + \\ & -\frac{4\mu_0RLN_f}{\pi\delta} \left[\sum_{y=\left(\frac{h}{N_b}\right)_{int}}^{\infty} \frac{\sin\left((yN_b-h)\frac{\pi}{N_b}\right) K_{f(yN_b-h)}}{(yN_b-h)^2} e^{j(yN_b-h)g_m} e^{-j(yN_b-h)\psi_f} K_{skew,(yN_b-h)} \right] i_{sc}, \end{aligned} \quad (4.89)$$

This paragraph concludes the machine model for HR and ISC faults in SPM and squirrel cage IMs. The following section considers a simplification of the model. In particular, only the most main field harmonics in the airgap are taken into account, and the machine is supposed to be a distributed multi three-phase winding (not sectored) squirrel cage IM. Then the proposed HR and ISC detection algorithms are presented, before showing the simulation and experimental results.

4.4 Principle for High Resistance and Interturn Short Circuit Faults Detection with Ideal Current Control (FOC) in distributed winding Induction Machines

A typical machine control aims to generate the desired torque with the highest efficiency and the lowest torque ripple. Therefore, the machine design and control are often optimised for producing the most sinusoidal field in the airgap minimising the reduction of torque density (the final design is usually a compromise for the two requirements). In order to simplify the model equations, the field in the airgap is considered to have only the lowest space harmonics that can be independently controlled by a multiphase machine control. For distributed windings (not sectored), this means to consider the odd harmonics multiple of the pole pairs number (p). In case of three-phase machines, this is equal to consider a sinusoidal field in the airgap with polarity equal to p . Then, the current control is still considered the one that aims to maintain all

the current space vectors equal to zero but the main one (p -th). As a further simplification, the considered winding are multi three-phase and not sectored, as the ones presented in Chapter 3 (this allows considering a reduced number of independent space vectors also if they are asymmetrical windings, defined with a redundant transformation). The model is presented for a squirrel cage rotor, aware that the same conclusion can be done for a SPM one.

These assumptions allow writing all the equations of the previous section as follows.

Simplified model for distributed multiphase windings

Under the simplified hypothesis above, the new set of equations for the stator, ISC loop and rotor is presented here below.

Stator Phase Voltage Space Vector Equation

The stator voltage space vector equation for the p -th space is:

$$\begin{aligned} \bar{v}_p = & R_s \bar{i}_p + (Ll + L_p) \frac{d\bar{i}_p}{dt} + \frac{1}{2} (\bar{i}_p R_{HR,0} + \bar{i}_p^* \bar{R}_{HR,2p}) + M_{rs,p} \frac{d(\bar{i}_{r,p} e^{jp\vartheta_m})}{dt} + \\ & - \frac{2}{m} N_f (r_{HR} + r) \bar{i}_{sc} \bar{\alpha}^{p(z-1)} - \left(\frac{2}{m} M l_{sc} \bar{\alpha}^{p(z-1)} + M_{fs,p} e^{jp\psi_f} \right) \frac{di_{sc}}{dt}, \end{aligned} \quad (4.90)$$

with:

$$\begin{aligned} L_p = & \frac{2N_s}{m} \frac{\mu_0 LR}{\pi\delta} \left(Npq \frac{K_{a,p}}{p} \right)^2, \\ M_{rs,h} = & 2\mu_0 R L p q N \frac{N_b}{\pi\delta} \frac{K_{ah} K_{skew,h} \sin\left(h \frac{\pi}{N_b}\right)}{h^2}, \\ M_{fs,h} = & 4\mu_0 R L p q N \frac{N_f}{\pi\delta} \frac{K_{ah} K_{fh}}{h^2}. \end{aligned}$$

For the higher order independent spaces (up to the pm -th):

$$\begin{aligned} \bar{v}_h = & \frac{1}{2} (\bar{i}_p \bar{R}_{HR,(h-p)} + \bar{i}_p^* \bar{R}_{HR,(h+p)}) + M_{rs,h} \frac{d(\bar{i}_{r,h} e^{jh\vartheta_m})}{dt} + \\ & - \frac{2}{m} N_f (r_{HR} + r) \bar{i}_{sc} \bar{\alpha}^{h(z-1)} - \left(\frac{2}{m} M l_{sc} \bar{\alpha}^{h(z-1)} + M_{fs,h} e^{jh\psi_f} \right) \frac{di_{sc}}{dt}, \end{aligned} \quad (4.91)$$

and for the zero sequence:

$$v_0 = \frac{1}{2} \Re\{\bar{i}_p \bar{R}_{HR,p}^*\} - \frac{2}{m} \left(N_f (r_{HR} + r) \bar{i}_{sc} + M l_{sc} \frac{d\bar{i}_{sc}}{dt} \right). \quad (4.92)$$

ISC loop Equation

The ISC loop voltage equation is:

$$\begin{aligned} r_{sc} \bar{i}_{sc} + N_f (r_{HR} + r) \bar{i}_{sc} + (L l_{sc} + L_{sc}) \frac{d\bar{i}_{sc}}{dt} &= \frac{N_b}{2} \sum_{z_{odd}=1}^{m-1} M_{fr,zp} \Re\left\{ \frac{d(\bar{i}_{r,zp} e^{-jzp(\psi_f - \vartheta_m)})}{dt} \right\} + \\ &+ N_f (r_{HR} + r) \Re\{\bar{i}_p e^{-jp\psi_z}\} + M l_{sc} \Re\left\{ \frac{d\bar{i}_p}{dt} e^{-jp\psi_z} \right\} + \frac{m}{2} M_{fs,p} \Re\left\{ \frac{d\bar{i}_p}{dt} e^{-jp\psi_f} \right\}, \end{aligned} \quad (4.93)$$

with:

$$M_{fr,h} = 4 \frac{\mu_0 R L N_f}{\pi \delta} \frac{\sin\left(h \frac{\pi}{N_b}\right) K_{f,h} K_{skew,h}}{h^2}.$$

Rotor Cage Space Vector Equation

The squirrel cage voltage space vector equation for the p -th space (being the only analysed space vectors in case of three-phase winding):

$$0 = R_{rp} \bar{i}_{r,p} + (L l_{rp} + L_{cage,p}) \frac{d\bar{i}_{r,p}}{dt} + \frac{m}{N_b} M_{rs,p} \frac{d(\bar{i}_p e^{-jp\vartheta_m})}{dt} + M_{fr,p} \frac{d(\bar{i}_{sc} e^{jp(\psi_f - \vartheta_m)})}{dt}, \quad (4.94)$$

with:

$$L_{cage,h} = 2 \frac{\mu_0 R L N_b}{\pi \delta} \frac{\sin\left(h \frac{\pi}{N_b}\right)^2}{h^2}.$$

For the higher order independent spaces of the stator winding (up to the pm -th):

$$0 = R_{rh} \bar{i}_{r,h} + (L l_{rh} + L_{cage,h}) \frac{d\bar{i}_{r,h}}{dt} + M_{fr,h} \frac{d(\bar{i}_{sc} e^{jh(\psi_f - \vartheta_m)})}{dt}. \quad (4.95)$$

The detection algorithm can be now introduced from the simplified equations presented in this last subsection.

Detection algorithm: concept

The proposed detection algorithm is based on the analysis of the direct and inverse sequences of the different stator voltage space vectors (sequence impedances).

Voltage space vector analysis for detection algorithm

The voltage space vector equations (4.90)-(4.92) can be rewritten considering the voltage drops related to the ISC fault (with or without additional HR conditions) as:

$$\bar{v}_p = R_s \bar{i}_p + (Ll + L_p) \frac{d\bar{i}_p}{dt} + M_{rs,p} \frac{d(\bar{i}_{r,p} e^{jp\theta_m})}{dt} + \bar{v}_{HR,p} + \bar{v}_{ISC,p}, \quad (4.96)$$

with:

$$\bar{v}_{HR,p} = \frac{1}{2} (\bar{i}_p R_{HR,0} + \bar{i}_p^* \bar{R}_{HR,2p}), \quad (4.97)$$

and the ISC current direct contribution:

$$\bar{v}_{ISC,p} = -\frac{2}{m} N_f (r_{HR} + r) \bar{i}_{sc} \bar{\alpha}^{p(z-1)} - \left(\frac{2}{m} M_{sc} \bar{\alpha}^{p(z-1)} + M_{fs,p} e^{jp\psi_f} \right) \frac{d\bar{i}_{sc}}{dt}, \quad (4.98)$$

where in reality also the rotor reaction, related to the term:

$$M_{rs,p} \frac{d(\bar{i}_{r,p} e^{jp\theta_m})}{dt},$$

is affected by the short circuit fault, as described later.

For the higher order independent spaces (up to the pm -th):

$$\bar{v}_h = \bar{v}_{HR,h} + \bar{v}_{ISC,h}, \quad (4.99)$$

with:

$$\bar{v}_{HR,h} = \frac{1}{2} (\bar{i}_p \bar{R}_{HR,(h-p)} + \bar{i}_p^* \bar{R}_{HR,(h+p)}), \quad (4.100)$$

and the ISC direct contribution:

$$\begin{aligned} \bar{v}_{ISC,h} = & -\frac{2}{m} N_f (r_{HR} + r) \bar{i}_{sc} \bar{\alpha}^{h(z-1)} + \\ & + M_{rs,h} \frac{d(\bar{i}_{r,h} e^{jh\vartheta_m})}{dt} - \left(\frac{2}{m} Ml_{sc} \bar{\alpha}^{h(z-1)} + M_{fs,h} e^{jh\psi_f} \right) \frac{di_{sc}}{dt}, \end{aligned} \quad (4.101)$$

where in this case all the rotor cage effects are considered related to the ISC fault because the stator phase currents do not generate these field harmonics in the considered current control and model simplification.

Finally, for the zero sequence:

$$v_0 = v_{HR,0} + v_{ISC,0}, \quad (4.102)$$

with:

$$v_{HR,0} = \frac{1}{2} \Re \{ \bar{i}_p \bar{R}_{HR,p}^* \}, \quad (4.103)$$

and the ISC current contribution:

$$v_{ISC,0} = -\frac{2}{m} \left(N_f (r_{HR} + r) \bar{i}_{sc} + Ml_{sc} \frac{di_{sc}}{dt} \right). \quad (4.104)$$

The proposed detection method is based on the solution of the equations presented here above for the evaluation of the sequence impedances.

Detection algorithm

When the stator is supplied with a main space vector trajectory which is a circumference covered at constant speed $\bar{i}_p = I_p e^{j\omega t}$, the voltage space vectors are expected to have a direct and an inverse sequences (compensating or neglecting the higher order harmonics of the back electromotive force) as:

$$\bar{v}_h = \bar{v}_{h,dir} + \bar{v}_{h,inv} = V_{h,dir} e^{j(\omega t + \vartheta_{V,h,dir})} + V_{h,inv} e^{j(-\omega t + \vartheta_{V,h,inv})}. \quad (4.105)$$

Therefore, the detection algorithm is based on the analysis of the following space vector indexes:

$$\bar{x}_{h,dir} = \frac{\bar{v}_{h,dir}}{\bar{i}_p}, \quad \bar{x}_{h,inv} = \frac{\bar{v}_{h,inv}}{\bar{i}_p^*}. \quad (4.106)$$

The simplified model is quite a good approximation for describing the HR faults as described in the next section (Section 4.5). However, for the analysis of the ISC faults there are more approximations and the effect of the cage must be better highlighted. This analysis is done in Section 4.6.

The following section presents the HR detection algorithm based on the equations of this last paragraph.

4.5 High Resistance Fault Detection Algorithm with Ideal Current Control (FOC)

In the considered Field Oriented Control (FOC), the current space vectors are controlled to zero but the fundamental one (p -th), which is controlled to the reference value needed for controlling the torque and in general also the rotor flux (as happens in IM, but also for PM machines in flux weakening operation): $\bar{i}_p = \bar{i}_{p,ref}$ and $\bar{i}_{h \neq p} = 0$ (if $\bar{i}_{h \neq p}$ does not depend from \bar{i}_p).

In particular, for the hypothesis of the model and the control technique, for a given rotor speed also the rotor linked flux space vector $\bar{\phi}_{r,h}$ in a squirrel cage IMs are zero for all the spaces but the p -th one. Instead, in an SPM machine they are vectors with constant magnitude that can be predicted and compensated. Therefore, the p -th space voltage equation is:

$$\bar{v}_p = R_s \bar{i}_p + (Ll + L_p) \frac{d\bar{i}_p}{dt} + \frac{d\bar{\phi}_{r,p}}{dt} + \frac{1}{2} (\bar{i}_p \bar{R}_{HR,(h-p)} + \bar{i}_p^* \bar{R}_{HR,(h+p)}). \quad (4.107)$$

Instead, for the higher order spaces ($\bar{i}_{h \neq p} = 0$):

$$\bar{v}_h = \frac{1}{2} (\bar{i}_p \bar{R}_{HR,(h-p)} + \bar{i}_p^* \bar{R}_{HR,(h+p)}) + \frac{d\bar{\phi}_{r,h}}{dt}, \quad (4.108)$$

where $\frac{d\bar{\phi}_{r,h}}{dt}$ represents the possible back-emf in case of SPM rotor. Instead, in case of IM $\frac{d\bar{\phi}_{r,h}}{dt}$ is zero according to the considered control technique for all the spaces but the main one.

For the main space, the rotor flux space vector $\bar{\phi}_{r,p}$ in an IM depends from the stator current control, and in an SPM machine it is usually known. Therefore, the $\frac{d\bar{\phi}_{r,h}}{dt}$ terms can be evaluated in the control algorithm (as the voltage drop on the expected resistance and total inductance of the main space, $R_s \bar{i}_p + (Ll + L_p) \frac{d\bar{i}_p}{dt}$) and the effect of the HR fault $\bar{v}_{HR,h}$ can be discriminated from them as below.

Considering a steady state working condition ($\bar{i}_p = I_p e^{j\omega t}$), the detection algorithm defined by (4.105) and (4.106) can be used for the HR detection as follows.

The HR detection equations result as:

$$\begin{cases} \bar{R}_{HR,p(h-1)} = 2 \frac{\bar{v}_{HR,ph,dir}}{\bar{i}_p} \\ \bar{R}_{HR,p(h+1)} = 2 \frac{\bar{v}_{HR,ph,inv}}{\bar{i}_p^*} \end{cases} \quad (4.109)$$

and eventually:

$$\Re\{\bar{i}_p \bar{R}_{HR,p}^*\} = v_0. \quad (4.110)$$

Equations (4.109) are the main HR detection equations. It is interesting to note that for each h -th space it is possible to evaluate two resistance space vector equations. Therefore, for each independent space available in the current control there is an increased number of degrees of freedom that can be exploited for detecting the HR fault. The next subsection highlights the advantage of the redundant system of equations for the improved accuracy of the HR detection algorithm.

Hereafter, for the HR detection analysis the equations are written in electrical degrees. Indeed, in distributed winding multiphase machines (not sectored) the HR fault does not affect the field in the airgap, which remains symmetrical under the different pole pairs.

Advantages of redundant equations in the HR detection algorithm for improved accuracy

The possibility to have a redundant system of HR detection equations is exploited for improving the accuracy of the proposed algorithm. In particular, here below it is explained how the method allows also to eliminate from the analysis possible unbalances in the leakage inductances of the different phases.

An asymmetry in the phase leakage inductances can be analysed in the same way of a phase resistance unbalance. The main difference is that the voltage drop is related to the derivative of the current space vectors (and not just the current vector).

The resulting voltage space vector equation at steady state ($\bar{i}_1 = I_1 e^{j\omega t}$, considering the model in electrical degrees) for the main space is:

$$\bar{v}_1 = \bar{v}_{1,dir} + \bar{v}_{1,inv} + \frac{d\bar{\phi}_{r,1}}{dt}, \quad (4.111)$$

with:

$$\begin{aligned} \bar{v}_{1,dir} &= \left(R_s + \frac{1}{2} R_{HR,0} \right) \bar{i}_1 + j\omega \left(Ll + \frac{1}{2} Ll_{HL,0} \right) \bar{i}_1 + j\omega L_1 \bar{i}_1, \\ \bar{v}_{1,inv} &= \bar{i}_1^* \frac{1}{2} \bar{R}_{HR,2} - j\omega \frac{1}{2} \bar{L}l_{HL,2} \bar{i}_1^*. \end{aligned}$$

The voltage space vector equations for the higher order spaces are:

$$\bar{v}_h = \bar{v}_{h,dir} + \bar{v}_{h,inv} + \frac{d\bar{\phi}_{r,h}}{dt}, \quad (4.112)$$

with:

$$\begin{aligned} \bar{v}_{h,dir} &= \frac{1}{2} \bar{R}_{HR,(h-1)} \bar{i}_1 + \frac{1}{2} j\omega \bar{L}l_{HL,(h-1)} \bar{i}_1, \\ \bar{v}_{h,inv} &= \frac{1}{2} \bar{R}_{HR,(h+1)} \bar{i}_1^* - \frac{1}{2} j\omega \bar{L}l_{HL,(h+1)} \bar{i}_1^*. \end{aligned}$$

Finally, the homopolar voltage equation is:

$$v_0 = \Re\{\bar{i}_1 \bar{R}_{HR,1}^*\} + \Re\{j\omega \bar{i}_1 \bar{L}l_{HR,1}^*\} + \frac{d\phi_{r,0}}{dt}, \quad (4.113)$$

with the space resistances and leakage inductances defined as:

$$\begin{aligned} \bar{R}_{HR,h} &= \frac{2}{m} \sum_{x=1}^{N_s} R_{HR,x} e^{jh \frac{2\pi}{N_s}(x-1)}, \\ \bar{L}l_{HL,h} &= \frac{2}{m} \sum_{x=1}^{N_s} Ll_{HL,x} e^{jh \frac{2\pi}{N_s}(x-1)}. \end{aligned}$$

The same detection algorithm used for the HR detection can be used for the High Leakage inductance (HL) detection, or better to define a method that allows discriminating the HR detection from an unbalance in the phase leakage inductances (HL).

In the following equations, the rotor effects are neglected to simplify the analysis, knowing that they can be evaluated according the machine topology and control technique.

The resulting detection algorithm would result in the following steady state equations:

$$\begin{cases} R_{HR,0} + j\omega Ll_{HL,0} = 2 \frac{\bar{v}_{1,dir}}{\bar{i}_1} - j\omega (Ll + L_1) - 2R_s \\ \bar{R}_{HR,2} - j\omega \bar{L}l_{HL,2} = 2 \frac{\bar{v}_{1,inv}}{\bar{i}_1^*} \end{cases} \quad (4.114)$$

and for the higher order spaces ($h=3, 5, \dots, m-2$):

$$\begin{cases} \bar{R}_{HR,(h-1)} + j\omega \bar{L}l_{HL,(h-1)} = 2 \frac{\bar{v}_{h,dir}}{\bar{i}_1} \\ \bar{R}_{HR,(h+1)} - j\omega \bar{L}l_{HL,(h+1)} = 2 \frac{\bar{v}_{h,inv}}{\bar{i}_1^*} \end{cases} \quad (4.115)$$

It results that a full detection of the passive impedances unbalance (resistances and leakage inductances) can be achieved only if one of the two contributions can be neglected. The h-space passive impedance unbalance is defined as:

$$\bar{Z}_{H,h} = \bar{R}_{HR,h} + j\omega \bar{L}l_{HL,h}. \quad (4.116)$$

One possibility to overcome this problem and discriminate between the resistances and leakage inductances is to carry out a sensitivity analysis varying the control frequency (ω). The constant part of the space vector passive impedance with the frequency is the HR resistance space vector, while the part that changes linearly with the frequency is the HL leakage inductance space vector.

Another approach is to couple the detection equations in order to avoid a change in the control algorithm (frequency and eventually speed). Equation (4.115) can be rewritten as:

$$\begin{cases} \bar{R}_{HR,h} + j\omega \bar{L}l_{HL,h} = 2 \frac{\bar{v}_{(h+1),dir}}{\bar{i}_1} \\ \bar{R}_{HR,h} - j\omega \bar{L}l_{HL,h} = 2 \frac{\bar{v}_{(h-1),inv}}{\bar{i}_1^*} \end{cases} \quad (4.117)$$

Resulting in the final detection algorithm equations:

$$\begin{cases} \bar{R}_{HR,h} = \frac{\bar{v}_{(h+1),dir}}{\bar{i}_1} + \frac{\bar{v}_{(h-1),inv}}{\bar{i}_1^*} \\ j\omega \bar{L}l_{HL,h} = \frac{\bar{v}_{(h+1),dir}}{\bar{i}_1} - \frac{\bar{v}_{(h-1),inv}}{\bar{i}_1^*} \end{cases} \quad (4.118)$$

which is valid for $h=2, 4, 6, \dots, m-3$ ($m-2$ if m is an even number).

For the zero component (average resistance increase), the equation remains as:

$$R_{HR,0} + j\omega Ll_{HL,0} = 2 \frac{\bar{v}_{1,dir}}{\bar{i}_1} - j\omega(Ll + L_1) - 2R_s. \quad (4.119)$$

Therefore, the detection algorithm for the zero sequence of the space impedance results as:

$$\begin{cases} R_{HR,0} = \Re \left\{ 2 \frac{\bar{v}_{1,dir}}{\bar{i}_1} - 2R_s \right\} \\ \omega Ll_{HL,0} = \Im \left\{ 2 \frac{\bar{v}_{1,dir}}{\bar{i}_1} - j\omega(Ll + L_1) \right\} \end{cases} \quad (4.120)$$

It is immediate to note that the zero sequence HR and HL (average resistance and leakage increase) detection is significantly affected by the machine parameters (self inductance and normal leakage and resistance parameters) plus the effect of the main contribution of the rotor (implicit in all the voltage space vector equations). Instead, the HR and HL space vectors are only affected by the rotor flux control (in case of IM) or evaluation (in case of SPM machine).

Finally, in case of a symmetrical winding with an odd number of phases, the missing space vector equations are:

$$\begin{cases} \Re\{\bar{i}_1 \bar{R}_{HR,(m-1)}\} + \Re\{j\omega \bar{i}_1 \bar{L}l_{HR,(m-1)}\} = v_0 \\ \bar{R}_{HR,(m-1)} - j\omega \bar{L}l_{HL,(m-1)} = 2 \frac{\bar{v}_{(m-2),inv}}{\bar{i}_1^*} \end{cases} \quad (4.121)$$

Therefore, in a machine with an odd number of phases there are three scalar equations related to the $m-1$ components and four degrees of freedom (two for the resistance and two for the leakage). Therefore, the system cannot be completely solved if there are both an HR and an HL unbalances. The proposed solution is based on the use of only the not zero sequence equations (being the star connection voltage measurement usually not available) considering one of the two asymmetries as:

$$\bar{R}_{HR,(m-1)} = 2 \frac{\bar{v}_{(m-2),inv}}{\bar{i}_1^*} \quad \text{or} \quad -j\omega \bar{L}l_{HL,(m-1)} = 2 \frac{\bar{v}_{(m-2),inv}}{\bar{i}_1^*}. \quad (4.122)$$

Instead, in case of an asymmetrical multi three-phase distributed winding with an even number of phases, the missing equations are:

$$\begin{cases} \Re\{\bar{i}_1 \bar{R}_{HR,1}^*\} + \Re\{j\omega \bar{i}_1 \bar{L}l_{HR,1}^*\} = v_0 \\ R_{HR,m} - j\omega Ll_{HL,m} = 2 \frac{\bar{v}_{(m-1),inv}}{\bar{i}_1^*} \end{cases} \quad (4.123)$$

Therefore, the analysis of the star connection voltage is more complicated (the information on an odd impedance space vector is not easy to consider when an inverse transformation based on the even space vectors is used) and only the $m-1$ sequence component is used to evaluate the m -space impedance as:

$$\begin{cases} R_{HR,m} = \Re\left\{2 \frac{\bar{v}_{(m-1),inv}}{\bar{i}_1^*}\right\} \\ \omega Ll_{HL,m} = \Im\left\{j \frac{\bar{v}_{(m-1),inv}}{\bar{i}_1^*}\right\} \end{cases} \quad (4.124)$$

Star connection constraints

For optimising the dc link voltage or for fault tolerance, multi three-phase machines are often fed by independent three-phase converters, and each resulting three-phase winding subsystem is connected to an independent star.

The difference between the multi three-phase configuration and the single star is that the multi three-phase has a reduced number of degrees of freedom. In particular, the control of the homopolar currents of the three-phase subsystems must not be implemented. Indeed, if there

were an offset in the current measurements of one three-phase subsystem, the presence of a PI controller that aims to maintain the homopolar current to zero would diverge in order to try to change the current value. In other words, the reference voltages would be forced to be theoretically equal to the plus or the minus of the DC link voltage with a consequent loss of the current control and just an effect on the voltage of the star connection. In reality, the zero sequence control interacts with the other PI regulators when the voltage limit is reached and if the other spaces are prioritised in the voltage limits management algorithm it would still be possible to control the machine. It is clear that it is better to avoid the zero sequence current control in a three-phase star connected winding. Indeed, the HR detection algorithm would detect a wrong resistance (theoretically infinite) between the various three-phase star connections.

Therefore, the star connection reduces the degrees of freedom in the current control and in the detection algorithm, because the information on the zero sequence three-phase resistances is no more evaluated by a redundant number of resistance current space vectors and a reduced accuracy is expected. Indeed, from the previous analysis if there is more than one star connection, a reduction of the degrees of freedom makes the decoupling between resistance and leakage variations more complicated.

The proposed HR detection algorithm is completely defined for some case studies of symmetrical and asymmetrical distributed windings in the next two subsections respectively.

High Resistance Faults in Symmetrical Multiphase Machines (odd phases)

In a symmetrical multiphase winding with an odd number of phases, the machine model can be defined in electrical degrees and with a symmetrical transformation with an odd number of variables (one for each phase), as:

$$\bar{y}_h = \frac{2}{m} \sum_{k=1}^m x_k e^{jh \frac{2\pi}{m}(k-1)}.$$

The odd current space vectors in a standard FOC are controlled to zero but \bar{i}_1 and the detection algorithm is based on analysis of the odd voltage space vectors defined in the equations (4.118), (4.122) and (4.120), reported here below:

$$\begin{cases} \bar{R}_{HR,h} = \frac{\bar{v}_{(h+1),dir}}{\bar{i}_1} + \frac{\bar{v}_{(h-1),inv}}{\bar{i}_1^*} \\ j\omega \bar{L}l_{HL,h} = \frac{\bar{v}_{(h+1),dir}}{\bar{i}_1} - \frac{\bar{v}_{(h-1),inv}}{\bar{i}_1^*} \end{cases} \quad (4.125)$$

for $h=2, 4, 6, \dots, m-3$, plus

$$\bar{R}_{HR,(m-1)} = 2 \frac{\bar{v}_{(m-2),inv}}{\bar{i}_1^*} \quad \text{or} \quad -j\omega \bar{L}l_{HL,(m-1)} = 2 \frac{\bar{v}_{(m-2),inv}}{\bar{i}_1^*}, \quad (4.126)$$

and

$$\begin{cases} R_{HR,0} = \Re \left\{ 2 \frac{\bar{v}_{1,dir}}{\bar{i}_1} - 2R_s \right\} \\ \omega L L_{HL,0} = \Im \left\{ 2 \frac{\bar{v}_{1,dir}}{\bar{i}_1} - j\omega(Ll + L_1) \right\} \end{cases}. \quad (4.127)$$

Once the resistance space vectors are defined, the evaluated phase resistances are calculated by the general inverse transformation for odd symmetrical windings based on the even space vectors:

$$R_x = R_s + \frac{1}{2} R_{HR,0} + \sum_{h_{even}=2}^{m-1} \Re \left\{ \bar{R}_{HR,h} \bar{\alpha}^{-h(x-1)} \right\}, \quad (4.128)$$

with $\bar{\alpha} = e^{j\frac{2\pi}{m}}$.

Here below the equations are presented for a three-phase and a nine phase symmetrical winding.

Three-Phase Symmetrical Winding

For a symmetrical three-phase winding (standard), it is possible to evaluate the resistance space vectors by the direct and inverse components of the current and voltage space vectors as:

$$\begin{cases} R_{HR,0} = 2 \frac{\bar{v}_{1,dir} - (Ll + L_1) \frac{d\bar{i}_1}{dt}}{\bar{i}_1} - 2R_s \\ \bar{R}_{HR,2} = 2 \frac{\bar{v}_{1,inv}}{\bar{i}_1^*} \end{cases} \quad (4.129)$$

and in case of having also the star connection voltage measurement, an improved accuracy can be obtained considering the zero information given by the zero sequence as:

$$\Re \left\{ \bar{R}_{HR,2} \right\} \Re \left\{ \bar{i}_1 \right\} - \Im \left\{ \bar{R}_{HR,2} \right\} \Im \left\{ \bar{i}_1 \right\} = v_0 - \frac{d\phi_{r,0}}{dt}. \quad (4.130)$$

Finally, the phase resistances are evaluated as:

$$R_x = R_s + \frac{1}{2} R_{HR,0} + \Re \left\{ \bar{R}_{HR,2} e^{-j2\frac{2\pi}{3}(x-1)} \right\} = R_s + \frac{1}{2} R_{HR,0} + \Re \left\{ \bar{R}_{HR,1} e^{-j\frac{2\pi}{3}(x-1)} \right\}. \quad (4.131)$$

It is worth noticing that in a three-phase winding there are not redundant resistance space vectors that can be used to improve the accuracy of the model or discriminate between an HR and an HL asymmetry.

Nine-Phase Symmetrical Winding (Nine-Phase, single star connections)

The HR detection algorithm for a symmetrical nine-phase winding (with a single star connection) results from the following equations.

$$\left\{ \begin{array}{l} \bar{R}_{HR,2} = 2 \frac{\bar{v}_{1,inv}}{\bar{i}_1^*} \\ \bar{R}_{HR,2} = 2 \frac{\bar{v}_{3,dir}}{\bar{i}_1} \\ \bar{R}_{HR,4} = 2 \frac{\bar{v}_{3,inv}}{\bar{i}_1^*} \\ \bar{R}_{HR,4} = 2 \frac{\bar{v}_{5,dir}}{\bar{i}_1} \\ \bar{R}_{HR,6} = 2 \frac{\bar{v}_{5,inv}}{\bar{i}_1^*} \\ \bar{R}_{HR,6} = 2 \frac{\bar{v}_{7,dir}}{\bar{i}_1} \end{array} \right. \text{ and } \left\{ \begin{array}{l} R_{HR,0} = 2 \frac{\bar{v}_{1,dir} - (Ll + L_1) \frac{d\bar{i}_1}{dt}}{\bar{i}_1} - 2R_s \\ \bar{R}_{HR,8} = 2 \frac{\bar{v}_{7,inv}}{\bar{i}_1^*} \end{array} \right. \quad (4.132)$$

where the redundant space vectors are in the first equation system and the not redundant are in the second one. In case of having also the star connection voltage measurement, an improved accuracy for the 8th resistance space vector can be obtained considering also for the information given by the zero sequence:

$$\Re\{\bar{R}_{HR,8}\} \Re\{\bar{i}_1\} - \Im\{\bar{R}_{HR,8}\} \Im\{\bar{i}_1\} = v_0. \quad (4.133)$$

The phase resistances are evaluated as:

$$R_x = R_s + \frac{1}{2} R_{HR,0} + \sum_{h_{even}=2}^8 \Re\left\{ \bar{R}_{HR,h} e^{-jh \frac{2\pi}{9}(x-1)} \right\}. \quad (4.134)$$

The detection algorithm for a nine phase symmetrical IM has been verified analytically and by experimental tests. The obtained results are presented in Section 4.10.

Nine-Phase Symmetrical Winding (Triple Three-Phase star connection)

As mentioned before, in case of a phase number multiple of three, it is also common to opt for a multi three-phase winding layout (realising a system of symmetrical three-phase subsystems shifted in the space).

The difference between the triple three-phase configuration and the nine-phase (single star) one, is that the triple three-phase has a reduced number of degrees of freedom. In particular, the control of the homopolar currents of the three-phase subsystems must not be implemented.

The HR detection algorithm could be implemented for each three-phase subsystem (T -th, with $T = A, B$ or C) independently, as mentioned for the standard three-phase winding as:

$$\begin{cases} R_{HR,T,0} = 2 \frac{\bar{v}_{T,1,dir} - (Ll + L_{T,1}) \frac{d\bar{i}_{T,1}}{dt}}{\bar{i}_{T,1}} - 2R_s \\ \bar{R}_{HR,T,2} = 2 \frac{\bar{v}_{T,1,inv}}{\bar{i}_{T,1}^*} \end{cases} \quad (4.135)$$

plus the possible information obtained from the star connections measurements, and:

$$R_{T,x} = R_s + \frac{1}{2} R_{HR,T,0} + \Re \left\{ \bar{R}_{HR,T,2} e^{-j2\frac{2\pi}{3}(x-1)} \right\}. \quad (4.136)$$

However, the multi-harmonic control of the machine is more likely based on the space harmonic control. Therefore, the detection algorithm is based on a reduced number of equations. In particular, the 3rd voltage space vector equation is not considered in the algorithm, resulting in the following set of equations:

$$\begin{cases} \bar{R}_{HR,2} = 2 \frac{\bar{v}_{1,inv}}{\bar{i}_1^*} \\ \bar{R}_{HR,4} = 2 \frac{\bar{v}_{5,dir}}{\bar{i}_1} \\ \bar{R}_{HR,6} = 2 \frac{\bar{v}_{5,inv}}{\bar{i}_1^*} \\ \bar{R}_{HR,6} = 2 \frac{\bar{v}_{7,dir}}{\bar{i}_1} \end{cases} \text{ and } \begin{cases} R_{HR,0} = 2 \frac{\bar{v}_{1,dir} - (Ll + L_1) \frac{d\bar{i}_1}{dt}}{\bar{i}_1} - 2R_s \\ \bar{R}_{HR,8} = 2 \frac{\bar{v}_{7,inv}}{\bar{i}_1^*} \end{cases} \quad (4.137)$$

The phase resistances are still evaluated by (4.134). The difference is that $\bar{R}_{HR,2}$ and $\bar{R}_{HR,4}$ are evaluated by a redundant set of equations anymore (a reduced accuracy is expected if the voltages of the star connections are not measured).

In the next subsection, the HR detection algorithm is analysed for asymmetrical six-phase and twelve-phase machines.

High Resistance Fault in Asymmetrical Multi Three-Phase Machines (even phases)

In an asymmetrical distributed multi three-phase winding with an even number of phases, the machine model can be still defined in electrical degrees and with a symmetrical redundant transformation, as:

$$\bar{y}_h = \frac{2}{m} \sum_{k=1}^m x_k e^{jh \frac{2\pi}{2m}(k-1)}.$$

The odd current space vectors in a standard FOC are controlled to zero but \bar{i}_1 and the detection algorithm is based on the analysis of the odd voltage space vectors defined in the equations (4.118), (4.124) and (4.120), reported here below:

$$\begin{cases} \bar{R}_{HR,h} = \frac{\bar{v}_{(h+1),dir}}{\bar{i}_1} + \frac{\bar{v}_{(h-1),inv}}{\bar{i}_1^*} \\ j\omega \bar{L}L_{HL,h} = \frac{\bar{v}_{(h+1),dir}}{\bar{i}_1} - \frac{\bar{v}_{(h-1),inv}}{\bar{i}_1^*} \end{cases} \quad (4.138)$$

for $h=2, 4, 6, \dots, m-2$,

$$\begin{cases} R_{HR,m} = \Re \left\{ 2 \frac{\bar{v}_{(m-1),inv}}{\bar{i}_1^*} \right\} \\ \omega L L_{HL,m} = \Im \left\{ j \frac{\bar{v}_{(m-1),inv}}{\bar{i}_1^*} \right\} \end{cases} \quad (4.139)$$

and

$$\begin{cases} R_{HR,0} = \Re \left\{ 2 \frac{\bar{v}_{1,dir}}{\bar{i}_1} - 2R_s \right\} \\ \omega L L_{HL,0} = \Im \left\{ 2 \frac{\bar{v}_{1,dir}}{\bar{i}_1} - j\omega(L + L_1) \right\} \end{cases}. \quad (4.140)$$

Once the resistance space vectors are defined, the evaluated phase resistances could be defined by the inverse transformation for asymmetrical windings based on the even space vectors as:

$$R_x = R_s + \frac{1}{2} R_{HR,0} + \frac{1}{2} R_{HR,m} \bar{\alpha}^{-m(x-1)} + \sum_{h_{even}=2}^{m-2} \Re \left\{ \bar{R}_{HR,h} \bar{\alpha}^{-h(x-1)} \right\}, \quad (4.141)$$

with $\bar{\alpha} = e^{j \frac{2\pi}{2m}}$. As mentioned in Chapter 2, it is essential to verify that the analysed system can be solved by the simplified inverse transformation (4.141).

The next paragraphs present the HR detection equations for a six-phase and twelve-phase asymmetrical windings.

Six -Phase Asymmetrical Winding (Six-Phase, single star connection)

In case of a six-phase asymmetrical winding, the phase resistances can be evaluated by the multiphase resistance space vectors) as:

$$R_x = R_s + \frac{1}{2}R_{HR,0} + \frac{1}{2}R_{HR,6}\bar{\alpha}^{-6(x-1)} + \Re\{\bar{R}_{HR,2}\bar{\alpha}^{-2(x-1)}\} + \Re\{\bar{R}_{HR,4}\bar{\alpha}^{-4(x-1)}\}, \quad (4.142)$$

where x indicates the position of the phase in the redundant representation. The HR detection algorithm evaluates the resistance space vectors as:

$$\left\{ \begin{array}{l} \bar{R}_{HR,2} = 2 \frac{\bar{v}_{1,inv}}{\bar{i}_1^*} \\ \bar{R}_{HR,2} = 2 \frac{\bar{v}_{3,dir}}{\bar{i}_1} \\ \bar{R}_{HR,4} = 2 \frac{\bar{v}_{3,inv}}{\bar{i}_1^*} \\ \bar{R}_{HR,4} = 2 \frac{\bar{v}_{5,dir}}{\bar{i}_1} \end{array} \right. \text{ and } \left\{ \begin{array}{l} R_{HR,0} = 2 \frac{\bar{v}_{1,dir} - (Ll + L_1) \frac{d\bar{i}_1}{dt}}{\bar{i}_1} - 2R_s \\ R_{HR,6} = 2 \frac{\bar{v}_{5,inv}}{\bar{i}_1^*} \end{array} \right. \quad (4.143)$$

As for the machine with an odd number of phases, the zero sequence equation could be used as an additional fault index. It is interesting to note that in this case, the sixth resistance space vector is a real number ($R_{HR,6}$). Therefore, the decoupling between the resistances and leakages asymmetries is easier to be implemented just considering the real part of the detected value. The complete impedance detection equation is:

$$R_{HR,6} - j\omega Ll_{HL,6} = 2 \frac{\bar{v}_{5,inv}}{\bar{i}_1^*}.$$

Six-Phase Asymmetrical Winding (Double Three-Phase star connection)

In case of a double three-phase winding, the star constraint makes the control of the 3rd current space vector impossible. Therefore, the HR detection equations result as:

$$\left\{ \begin{array}{l} \bar{R}_{HR,2} = 2 \frac{\bar{v}_{1,inv}}{\bar{i}_1^*} \\ \bar{R}_{HR,4} = 2 \frac{\bar{v}_{5,dir}}{\bar{i}_1} \end{array} \right. \text{ and } \left\{ \begin{array}{l} R_{HR,0} = 2 \frac{\bar{v}_{1,dir} - (Ll + L_1) \frac{d\bar{i}_1}{dt}}{\bar{i}_1} - 2R_s \\ R_{HR,6} = 2 \frac{\bar{v}_{5,inv}}{\bar{i}_1^*} \end{array} \right. \quad (4.144)$$

As mentioned in the previous paragraph, a possible solution to easily discriminate between a HR and HL asymmetrical behaviour could be obtained from the analysis of the $2 \frac{\bar{v}_{5,inv}}{\bar{i}_1^*}$ term.

If it is a real number the fault is an HR, otherwise it is an HL condition. However, the sixth space resistance is:

$$R_{HR,6} = \frac{1}{2} (R_{HR,A,0} - R_{HR,B,0}).$$

This means that its value is a good index of unbalance between the two three-phase subsystems, but if there is an unbalance in only one of them, $R_{HR,6}$ gives an averaged result of the phenomena.

Twelve -Phase Asymmetrical Winding (Twelve -Phase, single star connection)

The same approach used to model the phenomena in a six-phase machine can be used for a twelve-phase machine. The resulting detection equations are:

$$\left\{ \begin{array}{l} \bar{R}_{HR,2} = 2 \frac{\bar{v}_{1,inv}}{\bar{i}_1^*} \\ \bar{R}_{HR,2} = 2 \frac{\bar{v}_{3,dir}}{\bar{i}_1} \\ \bar{R}_{HR,4} = 2 \frac{\bar{v}_{3,inv}}{\bar{i}_1^*} \\ \bar{R}_{HR,4} = 2 \frac{\bar{v}_{5,dir}}{\bar{i}_1} \\ \bar{R}_{HR,6} = 2 \frac{\bar{v}_{5,inv}}{\bar{i}_1^*} \\ \bar{R}_{HR,6} = 2 \frac{\bar{v}_{7,dir}}{\bar{i}_1} \end{array} \right. \text{ and } \left\{ \begin{array}{l} R_{HR,0} = 2 \frac{\bar{v}_{1,dir} - (Ll + L_1) \frac{d\bar{i}_1}{dt}}{\bar{i}_1} - 2R_s \\ \bar{R}_{HR,8} = 2 \frac{\bar{v}_{7,inv}}{\bar{i}_1^*} \\ \bar{R}_{HR,8} = 2 \frac{\bar{v}_{9,dir}}{\bar{i}_1} \\ \bar{R}_{HR,10} = 2 \frac{\bar{v}_{9,inv}}{\bar{i}_1^*} \\ \bar{R}_{HR,10} = 2 \frac{\bar{v}_{11,dir}}{\bar{i}_1} \\ R_{HR,12} = 2 \frac{\bar{v}_{11,inv}}{\bar{i}_1^*} \end{array} \right. \quad (4.145)$$

Also in this case the zero sequence equation could be used as an additional fault index.

Finally, the phase resistances are evaluated as:

$$R_x = R_s + \frac{1}{2} R_{HR,0} + \frac{1}{2} R_{HR,12} + \Re \{ \bar{R}_{HR,2} e^{-j2\psi_x} \} + \Re \{ \bar{R}_{HR,4} e^{-j4\psi_x} \} + \Re \{ \bar{R}_{HR,6} e^{-j6\psi_x} \} + \Re \{ \bar{R}_{HR,8} e^{-j8\psi_x} \} + \Re \{ \bar{R}_{HR,10} e^{-j10\psi_x} \}. \quad (4.146)$$

In this case, the twelfth resistance space vector is a real number ($R_{HR,12}$). Therefore, as in a six-phase machine the decoupling between the resistances and leakages asymmetries might be implemented by analysing the asymmetry in this space as:

$$R_{HR,12} - j\omega Ll_{HL,12} = 2 \frac{\bar{v}_{11,inv}}{\bar{i}_1^*}.$$

Twelve-Phase Asymmetrical Winding (Quadruple Three-Phase star connection)

In case of a quadruple three-phase winding, the star constraint makes the control of the 3rd and 9th current space vectors impossible. Therefore, the HR detection equations result as:

$$\left\{ \begin{array}{l} \bar{R}_{HR,2} = 2 \frac{\bar{v}_{1,inv}}{\bar{i}_1^*} \\ \bar{R}_{HR,4} = 2 \frac{\bar{v}_{5,dir}}{\bar{i}_1} \\ \bar{R}_{HR,6} = 2 \frac{\bar{v}_{5,inv}}{\bar{i}_1^*} \\ \bar{R}_{HR,6} = 2 \frac{\bar{v}_{7,dir}}{\bar{i}_1} \end{array} \right. \text{ and } \left\{ \begin{array}{l} R_{HR,0} = 2 \frac{\bar{v}_{1,dir} - (Ll + L_1) \frac{d\bar{i}_1}{dt}}{\bar{i}_1} - 2R_s \\ \bar{R}_{HR,8} = 2 \frac{\bar{v}_{7,inv}}{\bar{i}_1^*} \\ \bar{R}_{HR,10} = 2 \frac{\bar{v}_{11,dir}}{\bar{i}_1} \\ R_{HR,6} = 2 \frac{\bar{v}_{11,inv}}{\bar{i}_1^*} \end{array} \right. \quad (4.147)$$

As for the double three-phase machine, a possible solution to easily discriminate between a HR and HL asymmetrical behaviour could be done from the analysis of the $2 \frac{\bar{v}_{11,inv}}{\bar{i}_1^*}$ term. If it is a real number the fault is an HR, otherwise it is an HL condition. However, in this case:

$$R_{HR,12} = \frac{1}{2} (R_{HR,A,0} - R_{HR,B,0} + R_{HR,C,0} - R_{HR,D,0}).$$

This means that its value is a good index of unbalance between the two pairs of not neighbouring three-phase subsystems, but if there is an unbalance in only one of them, $R_{HR,12}$ gives an averaged result of the phenomena.

The advantages in the HR detection for single star multiphase windings can be considered an additional parameter of the system reliability when the winding is compared to its multi three-phase layout.

This paragraph concludes the proposed HR detection algorithm. The next two sections show the ISC fault detection algorithm. The following sections present the obtained simulation and experimental results.

4.6 Interturn Short Circuit Fault Detection with Ideal Current Control in Multiphase Machines

In this section, the equations presented in Section 4.4 are analysed to show how the ISC loop makes the space equations interact between each other in case of multiphase machines. Then the model is simplified to the case of a three-phase machine to develop an analytical model that can represent the fault in steady state conditions.

Simplified model for distributed multiphase windings – space couplings caused by ISC fault in squirrel cage Induction Machines

The stator voltage space vector equations for an IM (4.90)-(4.92) are rewritten here below.

Stator phase voltage equations

For the main space the voltage vector equation is:

$$\begin{aligned} \bar{v}_p = R_s \bar{i}_p + (Ll + L_p) \frac{d\bar{i}_p}{dt} + \frac{1}{2} (\bar{i}_p R_{HR,0} + \bar{i}_p^* \bar{R}_{HR,2p}) + M_{rs,p} \frac{d(\bar{i}_{r,p} e^{jp\vartheta_m})}{dt} + \\ - \frac{2}{m} N_f (r_{HR} + r) \bar{i}_{sc} \bar{\alpha}^{p(z-1)} - \left(\frac{2}{m} Ml_{sc} \bar{\alpha}^{p(z-1)} + M_{fs,p} e^{jp\psi_f} \right) \frac{di_{sc}}{dt}. \end{aligned} \quad (4.148)$$

For the higher order independent spaces (up to the $p(m-2)$ -th for odd phase symmetrical windings, or $(m-1)$ -th for even phase asymmetrical windings):

$$\begin{aligned} \bar{v}_h = \frac{1}{2} (\bar{i}_p \bar{R}_{HR,(h-p)} + \bar{i}_p^* \bar{R}_{HR,(h+p)}) + M_{rs,h} \frac{d(\bar{i}_{r,h} e^{jh\vartheta_m})}{dt} + \\ - \frac{2}{m} N_f (r_{HR} + r) \bar{i}_{sc} \bar{\alpha}^{h(z-1)} - \left(\frac{2}{m} Ml_{sc} \bar{\alpha}^{h(z-1)} + M_{fs,h} e^{jh\psi_f} \right) \frac{di_{sc}}{dt}. \end{aligned} \quad (4.149)$$

For the zero sequence:

$$v_0 = \frac{1}{2} \Re\{\bar{i}_p \bar{R}_{HR,p}^*\} - \frac{2}{m} \left(N_f (r_{HR} + r) \bar{i}_{sc} + Ml_{sc} \frac{di_{sc}}{dt} \right). \quad (4.150)$$

ISC loop equation

The ISC loop voltage equation (4.93) is:

$$\begin{aligned} r_{sc} i_{sc} + N_f (r_{HR} + r) \bar{i}_{sc} + (Ll_{sc} + L_{sc}) \frac{di_{sc}}{dt} = \frac{N_b}{2} \sum_{z_{odd}=1}^{m-1} M_{fr,zp} \Re\left\{ \frac{d(\bar{i}_{r,zp} e^{-jzp(\psi_f - \vartheta_m)})}{dt} \right\} + \\ + N_f (r_{HR} + r) \Re\{\bar{i}_p e^{-jp\psi_z}\} + Ml_{sc} \Re\left\{ \frac{d\bar{i}_p}{dt} e^{-jp\psi_z} \right\} + \frac{m}{2} M_{fs,p} \Re\left\{ \frac{d\bar{i}_p}{dt} e^{-jp\psi_f} \right\}. \end{aligned} \quad (4.151)$$

Rotor cage Space Vector equation

The squirrel cage voltage space vector equations (4.94)-(4.95) are, for the p -th space (being the only analysed space vectors in case of three-phase winding):

$$0 = R_{rp} \bar{i}_{r,p} + (Ll_{rp} + L_{cage,p}) \frac{d\bar{i}_{r,p}}{dt} + \frac{m}{N_b} M_{rs,p} \frac{d(\bar{i}_p e^{-jp\vartheta_m})}{dt} + M_{fr,p} \frac{d(i_{sc} e^{jp(\psi_f - \vartheta_m)})}{dt}. \quad (4.152)$$

For the higher order independent spaces of the stator winding:

$$0 = R_{rh} \bar{i}_{r,h} + (Ll_{rh} + L_{cage,h}) \frac{d\bar{i}_{r,h}}{dt} + M_{fr,h} \frac{d(i_{sc} e^{jh(\psi_f - \vartheta_m)})}{dt}. \quad (4.153)$$

Space coupling caused by the ISC current in squirrel cage IMs

The field in the airgap produced by the stator phase currents is considered as an ideal field (sinusoidal with p pole pairs). Therefore, the higher order harmonics in the airgap field are caused by the short circuit current which interact with all the considered rotor spaces by the following term in (4.153):

$$M_{fr,h} \frac{d(i_{sc} e^{jh(\psi_f - \vartheta_m)})}{dt}.$$

This term is the only source of electromotive force in the higher order spaces representing the rotor. Furthermore, the short circuit current interacts with all these rotor current space vectors because of the following term in (4.151):

$$\frac{N_b}{2} \sum_{z_{odd}=1}^{m-1} M_{fr,zp} \Re \left\{ \frac{d(\bar{i}_{r,zp} e^{-jzp(\psi_f - \vartheta_m)})}{dt} \right\}.$$

It results that the evaluation of the ISC current is affected by the solution of all the considered rotor space vector equations (4.152)-(4.153). In case of SPM machine there would be the relative space back-emf independent from the short circuit current.

Because in general the ISC current generates a contribution of voltage drop in all the stator space vector equations, all the direct and inverse sequences of the voltages are function of the simultaneous solution of all the rotor space vector equations with the ISC loop and the main stator voltage space vector equations. However, this analysis has not been done yet for a multiphase winding with more than three phases.

The next subsection describes the same analysis, but for an SPM rotor.

Simplified model for distributed multiphase windings – space couplings caused by ISC fault in SPM machines with sinusoidal MMF of the rotor magnets

In a multiphase SPM machine, the short circuit current does not affect the rotor field (at least until the machine is working in linear conditions and there are not demagnetisation phenomena). However, each PM field harmonics interact with the ISC loop and generate a contribution to

the ISC current as happens for the current space vectors of a squirrel cage rotor. Therefore, in general each of these components generates a ripple in the ISC current and an additional effect in all the stator voltage space vectors. If the PM field can be simplified as a sinusoidal one, the analysis is significantly simplified as follows.

Stator phase voltage equations

For the main space, the voltage space vector equation is:

$$\begin{aligned} \bar{v}_p = & R_s \bar{i}_p + (Ll + L_p) \frac{d\bar{i}_p}{dt} + \frac{1}{2} (\bar{i}_p R_{HR,0} + \bar{i}_p^* \bar{R}_{HR,2p}) + \frac{d(\phi_{PM,p} e^{jp\theta_m})}{dt} + \\ & - \frac{2}{m} N_f (r_{HR} + r) \bar{i}_{sc} \bar{\alpha}^{p(z-1)} - \left(\frac{2}{m} Ml_{sc} \bar{\alpha}^{p(z-1)} + M_{fs,p} e^{jp\psi_f} \right) \frac{di_{sc}}{dt}. \end{aligned} \quad (4.154)$$

For the higher order independent spaces (up to the pm -th):

$$\begin{aligned} \bar{v}_h = & \frac{1}{2} (\bar{i}_p \bar{R}_{HR,(h-p)} + \bar{i}_p^* \bar{R}_{HR,(h+p)}) + \\ & - \frac{2}{m} N_f (r_{HR} + r) \bar{i}_{sc} \bar{\alpha}^{h(z-1)} - \left(\frac{2}{m} Ml_{sc} \bar{\alpha}^{h(z-1)} + M_{fs,h} e^{jh\psi_f} \right) \frac{di_{sc}}{dt}. \end{aligned} \quad (4.155)$$

For the zero sequence:

$$v_0 = \frac{1}{2} \Re \{ \bar{i}_p \bar{R}_{HR,p}^* \} - \frac{2}{m} \left(N_f (r_{HR} + r) \bar{i}_{sc} + Ml_{sc} \frac{di_{sc}}{dt} \right). \quad (4.156)$$

ISC loop Equation

The ISC loop voltage equation (4.93) is:

$$\begin{aligned} r_{sc} \bar{i}_{sc} + N_f (r_{HR} + r) \bar{i}_{sc} + (Ll_{sc} + L_{sc}) \frac{d\bar{i}_{sc}}{dt} = & \Re \left\{ \frac{d(\phi_{PM,sc,p} e^{-jp(\psi_f - \theta_m)})}{dt} \right\} + \\ & + N_f (r_{HR} + r) \Re \{ \bar{i}_p e^{-jp\psi_z} \} + Ml_{sc} \Re \left\{ \frac{d\bar{i}_p}{dt} e^{-jp\psi_z} \right\} + \frac{m}{2} M_{fs,p} \Re \left\{ \frac{d\bar{i}_p}{dt} e^{-jp\psi_f} \right\}. \end{aligned} \quad (4.157)$$

In a FOC of the machine, the stator currents are at the electrical frequency of the rotor. Therefore, all the equations can be solved considering only this frequency.

In particular, the ISC loop equation (4.157) can be completely solved as function of only the fault parameters (r_{sc} , N_f and eventually also r_{HR}). Then, the stator voltage space vectors in steady state condition are expected to have a direct and inverse sequence at the frequency of

the stator current and their values can be defined by substituting the short circuit current equation. This analysis is left for future works.

In the next section, the equations for a squirrel cage IM with an ISC fault are simplified for a three-phase winding in order to have a complete analytical steady state equation for the ISC current and the voltage space vector sequences. The following sections present the analytical and experimental results.

4.7 Interturn Short Circuit Fault Detection Algorithm with Ideal Current Control in Three-Phase Squirrel Cage Induction Machines

In this section, the model is analysed in steady state condition, aware that this assumption results in neglecting the transient behaviour of the fault. The transient model of the machine has been simulated and the results are presented in the following section, but it is clear that an analytical model of the steady state phenomena is important to describe the behaviour of a fault such as an ISC one, which is defined by many variables.

Simplified model for ISC fault detection in Three-Phase IMs

In the simplified model of three-phase machine with and ISC fault, only the fundamental harmonic in the airgap is analysed. Therefore, the resulting equations of the simplified space vector model for a three-phase IM affected by an ISC fault are as follows.

Stator phase voltage equations

For stator voltage space vector equation is:

$$\begin{aligned} \bar{v}_p = R_s \bar{i}_p + (Ll + L_p) \frac{d\bar{i}_p}{dt} + \frac{1}{2} (\bar{i}_p R_{HR,0} + \bar{i}_p^* \bar{R}_{HR,2p}) + M_{rs,p} \frac{d(\bar{i}_{r,p} e^{jp\theta_m})}{dt} + \\ - \frac{2}{m} N_f (r_{HR} + r) \bar{i}_{sc} \bar{\alpha}^{p(z-1)} - \left(\frac{2}{m} Ml_{sc} \bar{\alpha}^{p(z-1)} + M_{fs,p} e^{jp\psi_f} \right) \frac{di_{sc}}{dt}. \end{aligned} \quad (4.158)$$

The zero sequence voltage equation is:

$$v_0 = \frac{1}{2} \Re \{ \bar{i}_p \bar{R}_{HR,p}^* \} - \frac{2}{m} \left(N_f (r_{HR} + r) \bar{i}_{sc} + Ml_{sc} \frac{di_{sc}}{dt} \right). \quad (4.159)$$

ISC loop Equation

The ISC loop voltage equation (4.93) is:

$$\begin{aligned}
 r_{sc} \dot{i}_{sc} + N_f (r_{HR} + r) \dot{i}_{sc} + (Ll_{sc} + L_{sc}) \frac{di_{sc}}{dt} &= \frac{N_b}{2} M_{fr,p} \Re \left\{ \frac{d(\bar{i}_{r,p} e^{-jp(\psi_f - \vartheta_m)})}{dt} \right\} + \\
 + N_f (r_{HR} + r) \Re \left\{ \bar{i}_p e^{-jp\psi_z} \right\} + Ml_{sc} \Re \left\{ \frac{d\bar{i}_p}{dt} e^{-jp\psi_z} \right\} &+ \frac{m}{2} M_{fs,p} \Re \left\{ \frac{d\bar{i}_p}{dt} e^{-jp\psi_f} \right\}.
 \end{aligned} \tag{4.160}$$

Rotor Cage Space Vector Equation

The squirrel cage voltage space vector equation (4.94) for the p -th space is:

$$0 = R_{rp} \bar{i}_{r,p} + (Ll_{rp} + L_{cage,p}) \frac{d\bar{i}_{r,p}}{dt} + \frac{m}{N_b} M_{rs,p} \frac{d(\bar{i}_p e^{-jp\vartheta_m})}{dt} + M_{fr,p} \frac{d(i_{sc} e^{jp(\psi_f - \vartheta_m)})}{dt}. \tag{4.161}$$

The equations above have been used to simulate the machine transient behaviour in case of ISC fault. In the next subsection, the equations are solved considering a steady state scenario.

Simplified model for ISC fault detection in Three-Phase IMs at steady state conditions

This paragraph defines the steady state equations for the short circuit current and the phase voltages once the current space vector \bar{i}_p is defined by a standard FOC.

If the main current vector is controlled as a vector moving at constant speed on a circular trajectory, it can be defined as:

$$\bar{i}_p = I_p e^{j\omega t}. \tag{4.162}$$

In this condition, the stator voltage space vector is expected to have a direct and inverse sequence as:

$$\bar{v}_p = V_{p,dir} e^{j(\omega t + \vartheta_{v,dir})} + V_{p,inv} e^{j(-\omega t + \vartheta_{v,inv})}. \tag{4.163}$$

Instead, the rotor current space vector (under the hypothesis of sinusoidal field in the airgap) is expected to have a direct and inverse sequence but at a frequency which is function of the slip (or load torque as well). In particular, the main squirrel cage current space vector is expected to be as:

$$\bar{i}_{r,p} = I_{r,p,dir} e^{j\left(\left(\omega - p \frac{d\vartheta_m}{dt}\right)t + \vartheta_{r,dir}\right)} + I_{r,p,inv} e^{j\left(-\left(\omega + p \frac{d\vartheta_m}{dt}\right)t + \vartheta_{r,inv}\right)}, \quad (4.164)$$

and the short circuit current as:

$$i_{sc} = I_{sc} \cos(\omega t + \vartheta_{sc}) = I_{sc} \frac{e^{j(\omega t + \vartheta_{sc})} + e^{-j(\omega t + \vartheta_{sc})}}{2}. \quad (4.165)$$

In this condition, the machine equations in case of steady state ISC and sinusoidal field in the airgap can be simplified as follows.

The stator voltage space vector equation becomes as:

$$\begin{aligned} & V_{p,dir} e^{j(\omega t + \vartheta_{v,dir})} + V_{p,inv} e^{j(-\omega t + \vartheta_{v,inv})} = \\ & = R_s I_p e^{j\omega t} + j\omega(Ll + L_p) I_p e^{j\omega t} + \frac{1}{2} (I_p e^{j\omega t} R_{HR,0} + I_p e^{-j\omega t} \bar{R}_{HR,2p}) + \\ & - \frac{2}{3} \left(\frac{N_f (r_{HR} + r)}{2} I_{sc} (e^{j(\omega t + \vartheta_{sc})} + e^{-j(\omega t + \vartheta_{sc})}) + j\omega \frac{M_{sc}}{2} I_{sc} (e^{j(\omega t + \vartheta_{sc})} - e^{-j(\omega t + \vartheta_{sc})}) \right) e^{jp\psi_z} + \\ & - j\omega \frac{M_{fs,p}}{2} e^{jp\psi_f} I_{sc} (e^{j(\omega t + \vartheta_{sc})} - e^{-j(\omega t + \vartheta_{sc})}) + j\omega M_{rs,p} (I_{r,p,dir} e^{j(\omega t + \vartheta_{r,dir})} - I_{r,p,inv} e^{j(-\omega t + \vartheta_{r,inv})}). \end{aligned} \quad (4.166)$$

The ISC loop equation in steady state conditions results as:

$$\begin{aligned} & (r_{sc} + N_f (r_{HR} + r)) I_{sc} \frac{e^{j(\omega t + \vartheta_{sc})} + e^{-j(\omega t + \vartheta_{sc})}}{2} + j\omega \frac{Ll_{sc} + L_{sc}}{2} I_{sc} (e^{j(\omega t + \vartheta_{sc})} - e^{-j(\omega t + \vartheta_{sc})}) = \\ & = N_f (r_{HR} + r) \Re \{ I_p e^{j\omega t} e^{-jp\psi_z} \} + M_{sc} \Re \{ j\omega I_p e^{j\omega t} e^{-jp\psi_z} \} + \\ & + \frac{3}{2} M_{fs,p} \Re \{ j\omega I_p e^{j\omega t} e^{-jp\psi_f} \} + \frac{N_b}{2} M_{fr,p} \Re \{ j\omega (I_{r,p,dir} e^{j(\omega t + \vartheta_{r,dir})} - I_{r,p,inv} e^{j(-\omega t + \vartheta_{r,inv})}) e^{-jp\psi_f} \}. \end{aligned} \quad (4.167)$$

The rotor cage space vector equation is:

$$\begin{aligned} 0 & = R_{rp} (I_{r,p,dir} e^{j(\omega t + \vartheta_{r,dir} - p\vartheta_m)} + I_{r,p,inv} e^{j(-\omega t + \vartheta_{r,inv} - p\vartheta_m)}) + \\ & + j \left(\omega - p \frac{d\vartheta_m}{dt} \right) (Ll_{rp} + L_{cage,p}) I_{r,p,dir} e^{j(\omega t + \vartheta_{r,dir} - p\vartheta_m)} + \\ & - j \left(\omega + p \frac{d\vartheta_m}{dt} \right) I_{r,p,inv} (Ll_{rp} + L_{cage,p}) e^{j(-\omega t + \vartheta_{r,inv} - p\vartheta_m)} + \\ & + j \left(\omega - p \frac{d\vartheta_m}{dt} \right) \frac{3}{N_b} M_{rs,p} I_p e^{j(\omega t - p\vartheta_m)} + \\ & - j \left(\omega - p \frac{d\vartheta_m}{dt} \right) \frac{M_{fr,p}}{2} I_{sc} e^{j(\omega t + \vartheta_{sc} + p\psi_f - p\vartheta_m)} + \\ & + j \left(\omega + p \frac{d\vartheta_m}{dt} \right) \frac{M_{fr,p}}{2} I_{sc} e^{-j(\omega t + \vartheta_{sc} - p\psi_f + p\vartheta_m)}. \end{aligned} \quad (4.168)$$

In order to solve the equation system it is possible to consider separately the direct and inverse sequences resulting in the various equations.

The rotor voltage equation (4.168) results for the direct sequence as:

$$I_{r,p,dir} e^{j\vartheta_{r,dir}} = -j \frac{\left(\omega - p \frac{d\vartheta_m}{dt}\right) \frac{3}{N_b} M_{rs,p} I_p - \left(\omega - p \frac{d\vartheta_m}{dt}\right) \frac{M_{fr,p}}{2} I_{sc} e^{j(\vartheta_{sc} + p\psi_f)}}{R_{rp} + j\left(\omega - p \frac{d\vartheta_m}{dt}\right)(Ll_{rp} + L_{cage,p})}, \quad (4.169)$$

and for the inverse sequence as:

$$I_{r,p,inv} e^{j\vartheta_{r,inv}} = -j \frac{\left(\omega + p \frac{d\vartheta_m}{dt}\right) \frac{M_{fr,p}}{2}}{R_{rp} - j\left(\omega + p \frac{d\vartheta_m}{dt}\right)(Ll_{rp} + L_{cage,p})} I_{sc} e^{-j(\vartheta_{sc} - p\psi_f)}. \quad (4.170)$$

At this point, the rotor direct and inverse sequence equations can be substituted in the ISC loop equation (4.167) and the stator voltage equation (4.166).

The stator voltage space equation becomes:

$$\begin{aligned} V_{p,dir} e^{j(\omega t + \vartheta_{V,dir})} + V_{p,inv} e^{j(-\omega t + \vartheta_{V,inv})} &= R_s I_p e^{j\omega t} + \\ &+ j\omega (Ll + L_p) I_p e^{j\omega t} + \frac{1}{2} (I_p e^{j\omega t} R_{HR,0} + I_p e^{-j\omega t} \bar{R}_{HR,2p}) + \\ &- \frac{2}{3} \left(\frac{N_f (r_{HR} + r)}{2} I_{sc} (e^{j(\omega t + \vartheta_{sc})} + e^{-j(\omega t + \vartheta_{sc})}) \right) e^{jp\psi_z} + \\ &- \frac{2}{3} \left(j\omega \frac{Ml_{sc}}{2} I_{sc} (e^{j(\omega t + \vartheta_{sc})} - e^{-j(\omega t + \vartheta_{sc})}) \right) e^{jp\psi_z} + \\ &- j\omega \frac{M_{fs,p}}{2} e^{jp\psi_f} I_{sc} (e^{j(\omega t + \vartheta_{sc})} - e^{-j(\omega t + \vartheta_{sc})}) + \\ &+ \omega M_{rs,p} \frac{\left(\omega - p \frac{d\vartheta_m}{dt}\right) \frac{3}{N_b} M_{rs,p} I_p - \left(\omega - p \frac{d\vartheta_m}{dt}\right) \frac{M_{fr,p}}{2} I_{sc} e^{j(\vartheta_{sc} + p\psi_f)}}{R_{rp} + j\left(\omega - p \frac{d\vartheta_m}{dt}\right)(Ll_{rp} + L_{cage,p})} e^{j\omega t} + \\ &- \omega M_{rs,p} \frac{\left(\omega + p \frac{d\vartheta_m}{dt}\right) \frac{M_{fr,p}}{2}}{R_{rp} - j\left(\omega + p \frac{d\vartheta_m}{dt}\right)(Ll_{rp} + L_{cage,p})} I_{sc} e^{-j(\vartheta_{sc} - p\psi_f)} e^{-j\omega t}, \end{aligned} \quad (4.171)$$

while the ISC loop equation, making explicit the real components, results as:

$$\begin{aligned}
 & (r_{sc} + N_f(r_{HR} + r))I_{sc} \frac{e^{j(\omega t + \vartheta_{sc})} + e^{-j(\omega t + \vartheta_{sc})}}{2} + j\omega \frac{Ll_{sc} + L_{sc}}{2} I_{sc} (e^{j(\omega t + \vartheta_{sc})} - e^{-j(\omega t + \vartheta_{sc})}) = \\
 & = N_f(r_{HR} + r)I_p \frac{e^{j\omega t} e^{-jp\psi_z} + e^{-j\omega t} e^{+jp\psi_z}}{2} + j\omega Ml_{sc} I_p \frac{e^{j\omega t} e^{-jp\psi_z} - e^{-j\omega t} e^{+jp\psi_z}}{2} + \\
 & + j\omega \frac{3}{2} M_{fs,p} I_p \frac{e^{j\omega t} e^{-jp\psi_f} - e^{-j\omega t} e^{+jp\psi_f}}{2} + \\
 & + \frac{\frac{1}{2}\omega \left(\omega - p \frac{d\vartheta_m}{dt} \right) \frac{3}{N_b} \frac{N_b}{2} M_{fr,p} M_{rs,p} I_p e^{j\omega t} e^{-jp\psi_f}}{R_{rp} + j \left(\omega - p \frac{d\vartheta_m}{dt} \right) (Ll_{rp} + L_{cage,p})} + \frac{\frac{1}{2}\omega \left(\omega - p \frac{d\vartheta_m}{dt} \right) \frac{3}{N_b} \frac{N_b}{2} M_{fr,p} M_{rs,p} I_p e^{-j\omega t} e^{jp\psi_f}}{R_{rp} - j \left(\omega - p \frac{d\vartheta_m}{dt} \right) (Ll_{rp} + L_{cage,p})} + \\
 & + \frac{-\frac{1}{2}\omega \left(\omega - p \frac{d\vartheta_m}{dt} \right) \frac{N_b}{2} M_{fr,p} \frac{M_{fr,p}}{2}}{R_{rp} + j \left(\omega - p \frac{d\vartheta_m}{dt} \right) (Ll_{rp} + L_{cage,p})} I_{sc} e^{j\vartheta_{sc}} e^{j\omega t} + \frac{-\frac{1}{2}\omega \left(\omega - p \frac{d\vartheta_m}{dt} \right) \frac{N_b}{2} M_{fr,p} \frac{M_{fr,p}}{2}}{R_{rp} - j \left(\omega - p \frac{d\vartheta_m}{dt} \right) (Ll_{rp} + L_{cage,p})} I_{sc} e^{-j\vartheta_{sc}} e^{-j\omega t} + \\
 & + \frac{-\frac{1}{2}\omega \left(\omega + p \frac{d\vartheta_m}{dt} \right) \frac{N_b}{2} M_{fr,p} \frac{M_{fr,p}}{2}}{R_{rp} + j \left(\omega + p \frac{d\vartheta_m}{dt} \right) (Ll_{rp} + L_{cage,p})} I_{sc} e^{j\vartheta_{sc}} e^{j\omega t} + \frac{-\frac{1}{2}\omega \left(\omega + p \frac{d\vartheta_m}{dt} \right) \frac{N_b}{2} M_{fr,p} \frac{M_{fr,p}}{2}}{R_{rp} - j \left(\omega + p \frac{d\vartheta_m}{dt} \right) (Ll_{rp} + L_{cage,p})} I_{sc} e^{-j\vartheta_{sc}} e^{-j\omega t}.
 \end{aligned} \tag{4.172}$$

As expected, the ISC loop equation can be analysed in the same way considering the direct or the inverse sequence component of the short circuit current, being one the conjugate of the other.

Interturn short circuit current and voltage space vector sequences

Considering only for the direct sequence component, the ISC equation results as:

$$\begin{aligned}
 & \frac{I_{sc}}{I_p} e^{j\vartheta_{sc}} = \\
 & \frac{(N_f(r_{HR} + r) + j\omega Ml_{sc}) e^{-jp\psi_z} + \left(j\omega \frac{3}{2} M_{fs,p} + \frac{\frac{1}{2}\omega \left(\omega - p \frac{d\vartheta_m}{dt} \right) \frac{3}{N_b} \frac{N_b}{2} M_{fr,p} M_{rs,p}}{R_{rp} + j \left(\omega - p \frac{d\vartheta_m}{dt} \right) (Ll_{rp} + L_{cage,p})} \right) e^{-jp\psi_f}}{\left(r_{sc} + N_f(r_{HR} + r) \right) + j\omega (Ll_{sc} + L_{sc}) + \frac{\omega \left(\omega - p \frac{d\vartheta_m}{dt} \right) \frac{N_b M_{fr,p}^2}{4}}{R_{rp} + j \left(\omega - p \frac{d\vartheta_m}{dt} \right) (Ll_{rp} + L_{cage,p})} + \frac{\omega \left(\omega + p \frac{d\vartheta_m}{dt} \right) \frac{N_b M_{fr,p}^2}{4}}{R_{rp} + j \left(\omega + p \frac{d\vartheta_m}{dt} \right) (Ll_{rp} + L_{cage,p})}}.
 \end{aligned} \tag{4.173}$$

Finally, from the ISC current it is possible to evaluate the direct and inverse voltage space vector in the current reference frame. Theoretically, the PI regulators will give as output this voltage space vector sequences from the converter in order to have the desired current control. The direct sequence voltage space vector in the reference frame synchronous with the current space vector is:

$$V_{p,dir} e^{j\vartheta_{v,dir}} = \left(R_s + \frac{1}{2} R_{HR,0} + j\omega(Ll + L_p) + \frac{\omega \left(\omega - p \frac{d\vartheta_m}{dt} \right) \frac{3M_{rs,p}^2}{N_b}}{R_{rp} + j \left(\omega - p \frac{d\vartheta_m}{dt} \right) (Ll_{rp} + L_{cage,p})} \right) I_p + \left[\frac{2}{3} \left(\frac{N_f (r_{HR} + r)}{2} + j\omega \frac{Ml_{sc}}{2} \right) e^{jp\psi_z} + \left(j\omega \frac{M_{fs,p}}{2} + \frac{\omega \left(\omega - p \frac{d\vartheta_m}{dt} \right) \frac{M_{rs,p} M_{fr,p}}{2}}{R_{rp} + j \left(\omega - p \frac{d\vartheta_m}{dt} \right) (Ll_{rp} + L_{cage,p})} \right) e^{jp\psi_f} \right] I_{sc} e^{j\vartheta_{sc}} . \quad (4.174)$$

The inverse sequence voltage space vector in a reference frame synchronous with the conjugate of the current space vector is:

$$V_{p,inv} e^{j\vartheta_{v,inv}} = \frac{1}{2} I_p \bar{R}_{HR,2p} + \left[\frac{2}{3} \left(\frac{N_f (r_{HR} + r)}{2} - j\omega \frac{Ml_{sc}}{2} \right) e^{jp\psi_z} + \left(-j\omega \frac{M_{fs,p}}{2} + \frac{\omega \left(\omega + p \frac{d\vartheta_m}{dt} \right) \frac{M_{rs,p} M_{fr,p}}{2}}{R_{rp} - j \left(\omega + p \frac{d\vartheta_m}{dt} \right) (Ll_{rp} + L_{cage,p})} \right) e^{jp\psi_f} \right] I_{sc} e^{-j\vartheta_{sc}} . \quad (4.175)$$

At this point, because of the complexity of the problem, only the inverse voltage space vector is analysed. However, it is clear that the same analysis can be carried out considering also for the direct sequence of the voltage space vector separating the components related to the fault from the ones related to the healthy machine behaviour.

Fault index

Equation (4.175) is analysed to evaluate the expected fault index in case of ISC fault, where the fault index is defined as:

$$\bar{x} = \frac{\bar{v}_{p,inv}}{\bar{i}_p^*} = \frac{V_{p,inv}}{I_p} e^{j\vartheta_{v,inv}} = X e^{j\vartheta_x}. \quad (4.176)$$

The fault index represents the impedance of the direct-inverse sequence (related to the effect of a direct current sequence on the inverse voltage sequence).

It is worth noticing that usually the current control for the direct and inverse sequences is defined in the rotor flux reference frame (standard FOC algorithm). This means that the direct sequence reference frame is synchronous with $p\vartheta_{\phi,r}$ and the inverse sequence reference frame is synchronous with $-p\vartheta_{\phi,r}$. In this case, the output voltage space vector from the inverse sequence PI regulators can still be divided by the conjugate of the reference d-q axis current of the direct sequence, and to get the fault index it must be rotate of the angle of the current space vector in the rotor flux reference frame:

$$\bar{x} = \frac{\bar{v}_{p,inv}}{\bar{i}_p^*} = \frac{\bar{v}_{p,dq,inv} e^{-jp\vartheta_{\phi,r}}}{\bar{i}_{p,dq}^* e^{-jp\vartheta_{\phi,r}}} = \frac{\bar{v}_{p,dq,inv}}{I_p e^{-j\vartheta_{FOC}}} = \frac{\bar{v}_{p,dq,inv} e^{j\vartheta_{FOC}}}{I_p} = \frac{V_{p,inv} e^{j(\angle\bar{v}_{p,dq,inv} + \vartheta_{FOC})}}{I_p}. \quad (4.177)$$

Therefore, $\vartheta_x = \angle\bar{v}_{p,dq,inv} + \vartheta_{FOC}$, where ϑ_{FOC} is the angle of the current space vector in the rotor flux reference frame (FOC control) and $\angle\bar{v}_{p,dq,inv}$ is the phase of the inverse sequence voltage space vector in the reference frame synchronous with the conjugate of the rotor flux. The same result is obtained evaluating the direct-inverse sequence impedance as:

$$\bar{x} = \frac{\bar{v}_{p,dq,inv} \bar{i}_{p,dq}}{|\bar{i}_{p,dq}|^2}. \quad (4.178)$$

The equation of the diagnostic index (\bar{x}) is quite complicated, as it is the expression of the short circuit current (i_{sc}). Indeed, they are both function of the following variables:

- The short circuit fault resistance (r_{sc});
- The number of short circuited turns (N_f);
- The magnetic axis of the short circuit loop (ψ_f);
- The magnetic axis of the faulty phase (ψ_z);
- The resistance increase in the faulty phase in the ISC loop (r_{HR}) and eventually also in the other phases;
- The rotor speed ($\frac{d\vartheta_m}{dt}$);

- The machine current control (\bar{i}_p).

The last two variables ($\frac{d\mathcal{G}_m}{dt}$ and \bar{i}_p) are known. Instead, the fault position (ψ_f and ψ_z) and the fault size (N_f) and advancement (r_{sc}) are four degrees of freedom. In particular, the last two (N_f and r_{sc}) define the magnitude of the short circuit current. Eventually, also the increase of resistance in the short circuited turns (r_{HR}) and in the different phases outside the short circuit loop ($R_{HR,x}$) could be considered as additional degrees of freedom as defined by (4.76).

In this section, the model of an ISC fault has been simplified to allow easily implementing a transient simulation. Then, a further simplification has been done considering the steady state equations on the assumption of an ideal current control. The evaluation of the ISC current and the impedance of the direct-inverse sequence have been defined from the steady state model.

Their analytical expressions are used in Section 4.9 to understand how an ISC behaves in a three-phase squirrel cage IM and which information can be derived by the measurement of the direct-inverse sequence impedance. Therefore, the direct-inverse sequence impedance is chosen as diagnostic index for the analysis of the ISC fault.

The next section compares the transient model with some experimental results obtained with a voltage control of a three-phase IM. The aim is to validate the model and the hypotheses behind it.

4.8 Analytical and Experimental Results: High Resistance and Interturn Short Circuits in Three-phase Induction Machines with V/f Control

This initial analysis shows the validation of the proposed model for a three-phase IM in case of HR and ISC faults. In particular, a series of V/f machine control tests at half the rated speed (about 750 rpm) and no load, 10 Nm and 20 Nm have been carried out in order to understand if the proposed model allows discriminating between an HR and an ISC fault (the rated torque is at about 27 Nm). Furthermore, the analysis is done to highlight how much the load affects the fault behaviour. The V/f control is set at 145 V (peak phase voltage) and 25 Hz electrical frequency in order to have almost the rated rotor flux. In the first subsection the prototype that is used for the experimental tests is presented, summarising how it has been manufactured. Then the transient simulations in Matlab/Simulink are compared with the experimental results for the healthy machine and in case of HR and ISC faults.

Test rig and prototype

This subsection shows how a prototype of nine-phase squirrel cage IM for HR and ISC tests has been prototyped. The prototype is an industrial three-phase machine (M.G.M Motori Elettrici S.p.A – BA 112 MB4) with a rewound stator.

Fig. 4.7 shows the initial prototype and the winding scheme [10]. The copper has been removed, and a new winding has been manufactured (as shown in Fig. 4.8). The new winding significantly differs from the previous one also if the same turns per coil and fill factor are maintained. In particular, the new prototype has a nine-phase open end winding layout with the possibility of testing many interturn short circuit fault configurations. The open end winding layout allows configuring the machine as a standard three-phase or a symmetrical nine-phase one (the asymmetrical nine-phase winding is not analysed). The rewinding of the prototype has been possible thanks to Lucchi R. Elettromeccanica s.r.l.

Fig. 4.9 shows the test rig with the final prototype (left) and the winding scheme (right). It is interesting to note that the new winding allows for many layout and fault configurations, with clear advantages for a medium and long-term research activity.

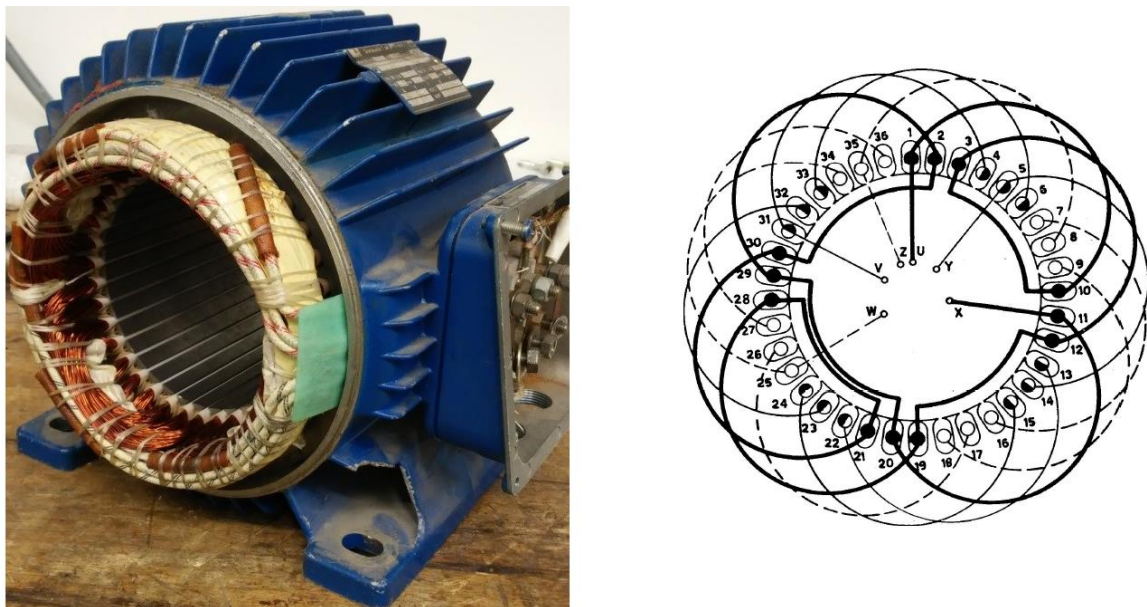


Fig. 4.7 – Three-phase IM BA 112 MB4 from M.G.M. Motori Elettrici S.p.A (left) and winding scheme (right).



Fig. 4.8 – Rewinding process from the original three-phase machine to the new customized winding.

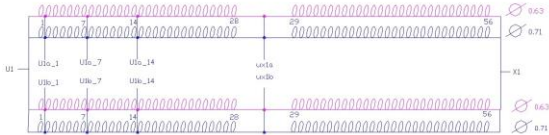
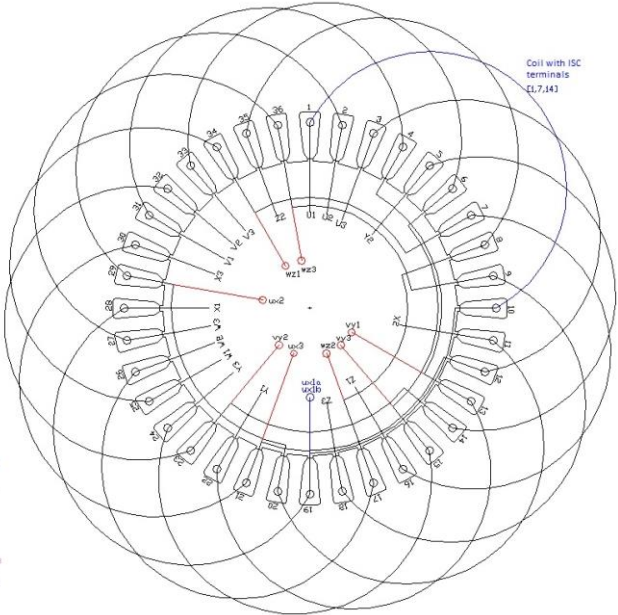
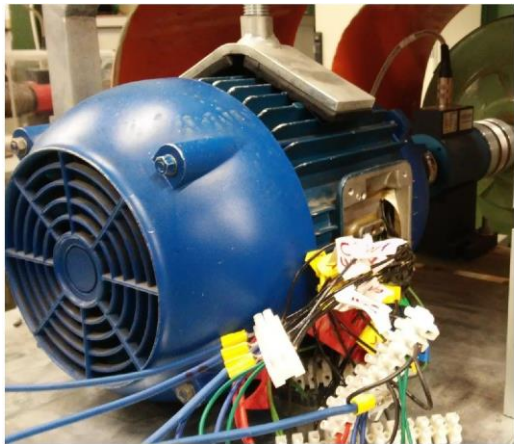


Fig. 4.9 - New prototype of nine phase IM and test rig (left top), new winding scheme (right) and electrical winding scheme of the phase U1, where there are many additional terminals for interturn short circuit tests (left bottom).

Table 4.1 lists the main machine parameters of the machine in its three-phase winding configuration.

The next subsections show the comparison between the transient simulations (in Matlab/Simulink) and the experimental results obtained on the machine in healthy conditions and with HR and ISC faults.

Healthy Machine

The healthy machine behaviour is simulated and verified by experimental tests to compare the healthy machine with the faulty one. The simulations are carried out with a Matlab-Simulink model based on the equations (4.158)-(4.161). Hereafter, only the steady state results are reported. In all the graphs, the d-q reference frame is synchronised with the starting phase of the direct sequence of the current space vector in the acquisition period. The small black circle represents the starting phase of the direct sequence (always zero, being the plot rotated in its reference frame), while the red rhombus represents the starting phase of the inverse sequence current space vector in the same d-q reference frame.

Table 4.1 - Main machine parameters in its three-phase winding configuration.

IEC Duty Cycle	S1	Inner Diameter [mm]	110
Poles	4	Active Length [mm]	140
Power (kW)	4.0	Slots Number (N_c)	36
International Protection code	IP 55	Bars Number (N_b)	28
P-P Voltage (Vrms) Δ/Y	220/380	Phase Pole Slots (q)	3
Insulation Class	F	Stator Resistance (R_s) [Ohm]	1.303
Speed (rpm)	1440	Stator Leakage Inductance (Ll) [H]	0.0111
Phase current (Arms) Δ/Y	16.6/9.6	Rotor Resistance (R_r') [Ohm]	1.383
Power Factor Cos φ	0.83	Rotor Leakage Inductance (Ll_r') [H]	0.0114
Fundamental Frequency (Hz)	50	Mutual Inductance (M') [H]	0.172
Efficiency (%)	83.7	Stator Inductance (L_s) [H]	0.183
Airgap (mm)	0.7	Rotor Inductance (L_r') [H]	0.183

The upper character “ ’ ” is used for the parameters of the equivalent circuit.

Simulation results

Fig. 4.10 shows the currents and current space vector trajectory of the simulated healthy machine at no load conditions. As expected the current space vector has a circular trajectory and the inverse sequence of the current is zero.

Experimental results

The experimental tests have been performed by using the drive presented in Fig. 4.11. Fig. 4.12 shows the scheme of the test setup and the connections of the coils for realising the three-phase winding configuration. Fig. 4.12 also shows how the HR and ISC faults have been realised.

Fig. 4.13 shows the phase currents and the current space vector trajectory for the healthy machine.

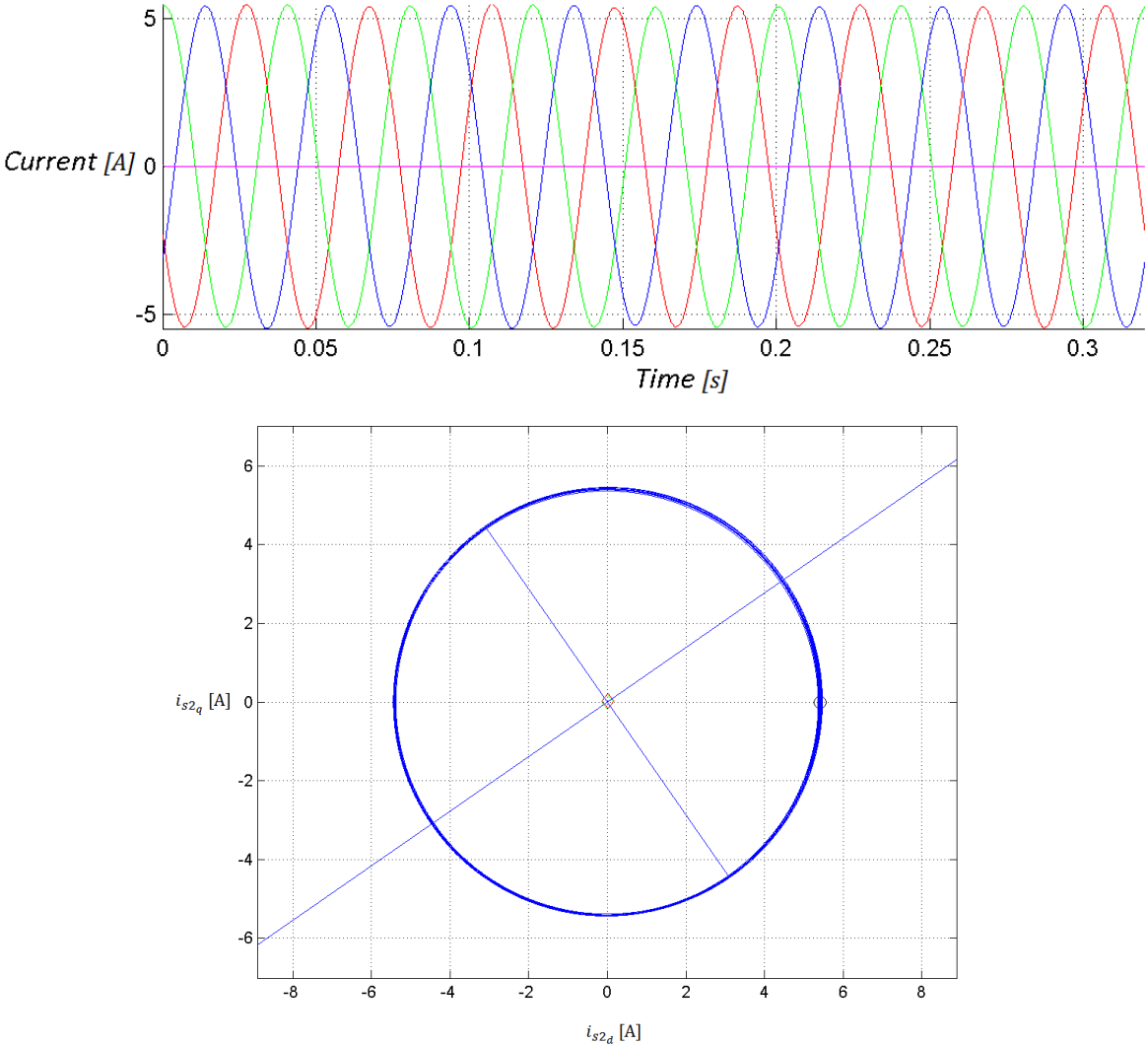


Fig. 4.10 - Matlab-Simulink simulation V/f control with healthy machine. Phase currents (red, blue and green) and short circuit current (purple) at the top; current space vector trajectory at the bottom.

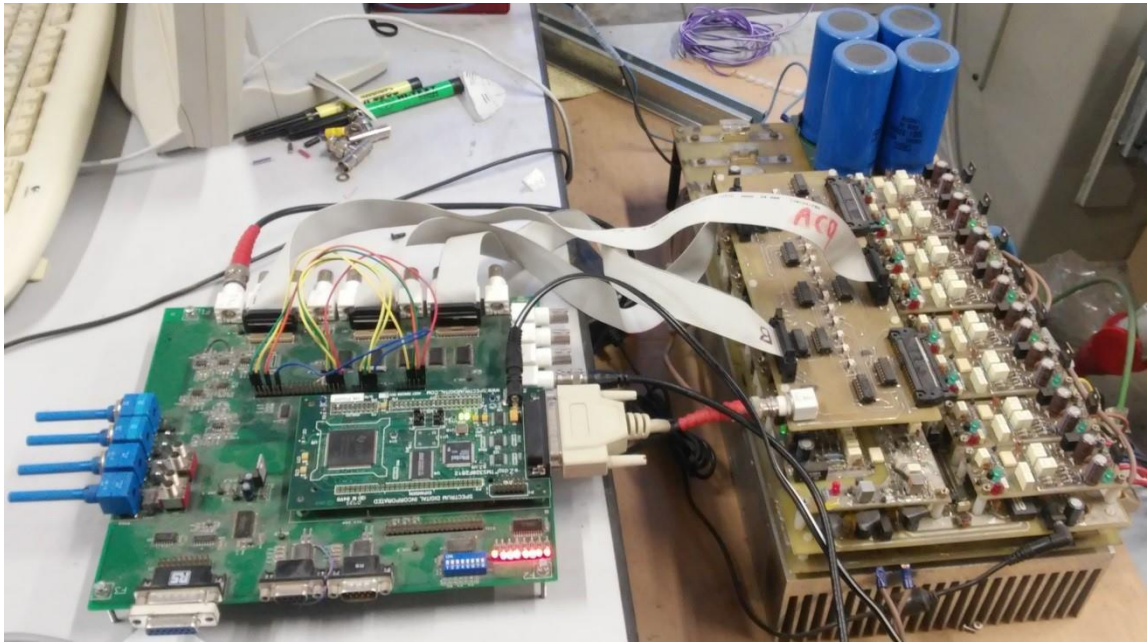


Fig. 4.11 - Drive used for the V/f experimental tests on the prototype in its three-phase winding configuration. Control board (left) and inverter (right). The DSP of the control board is a TMS320F2812.

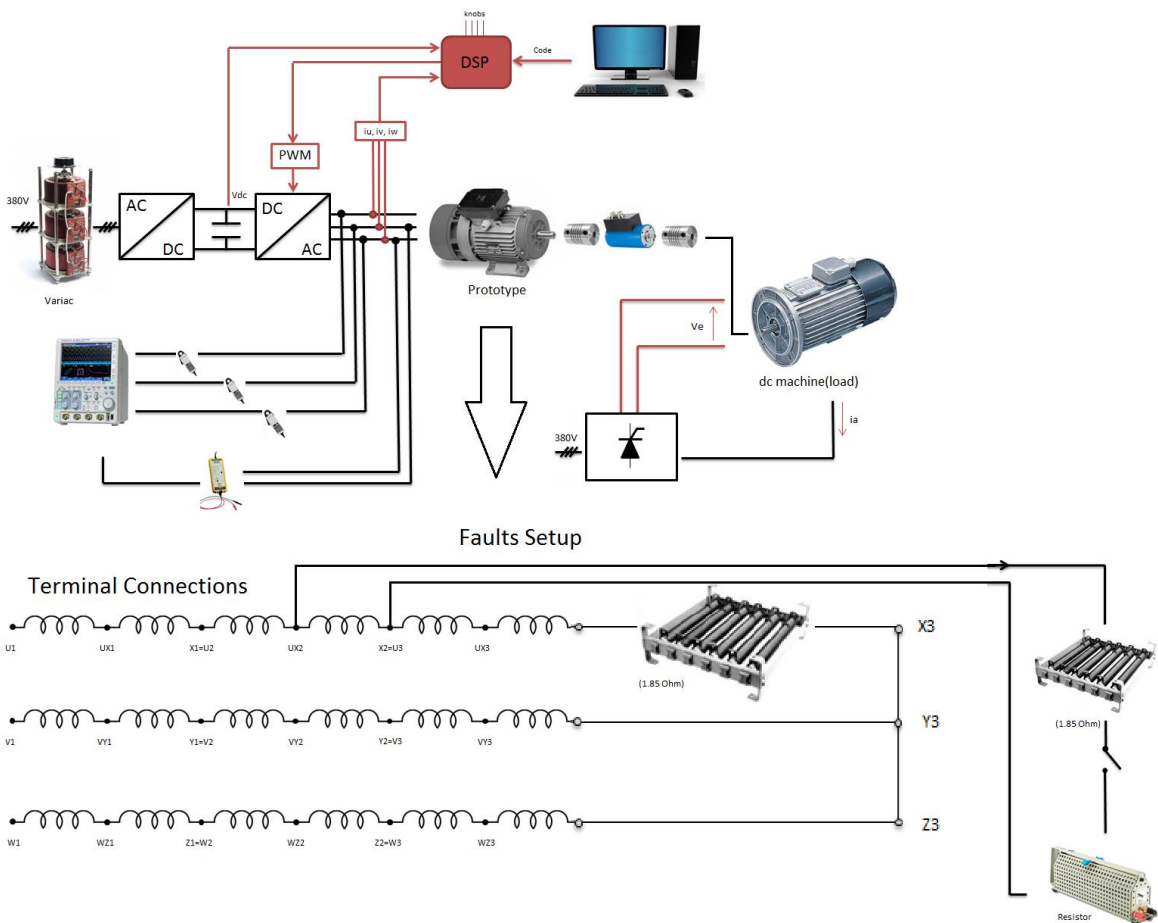


Fig. 4.12 - Test setup scheme (top), terminal box connections for three-phase winding configuration and setup for the ISC and HR tests (bottom).

As it is better explained in the next section, there is a series of small asymmetries in the machine (probably because of the manufacturing related to the not standard winding design) that makes the current space vector trajectory slightly elliptical. Indeed, the current on the U phase (blue in Fig. 4.13) is slightly smaller, and from the trajectory of the current space vector, the asymmetrical behaviour seems related to a higher resistance value in the U phase.

Instead, for the same voltage and frequency all the phase currents are smaller compared to the simulation results because of the parameter uncertainties. Indeed, some experimental tests and FEA have been carried out in order to match the simulated model with the prototype, but because of missing data on the lamination there are uncertainties mainly related to the cage geometry and mechanical parameters. However, for this analysis, the following results have been considered sufficient and further tests for the matching of the parameters have not been carried out.

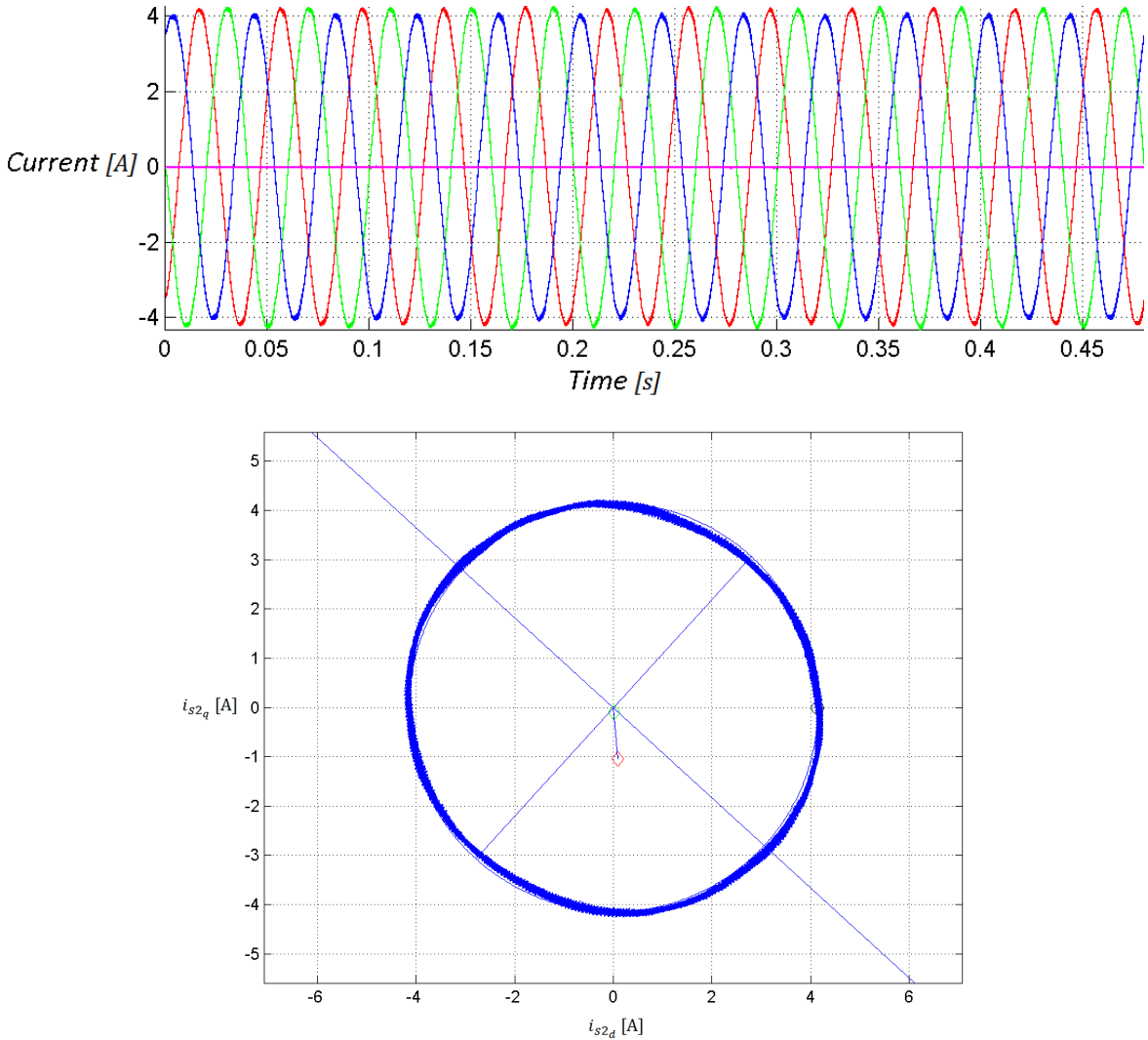


Fig. 4.13 - Experimental tests V/f control with healthy machine. Phase currents (red, blue and green) and short circuit current (purple) at the top; Current space vector trajectory at the bottom.

High Resistance faults

The machine behaviour in case of HR condition has been validated introducing a resistance in the series of each phase turns. In this subsection, only the results with an increase of 1.85 Ohm are presented. This value is the same used for the ISC analysis in order to simplify the understanding of the tests and have a significant asymmetrical behaviour of the machine in case of fault. However, it is clear that the two fault conditions are significantly different and not comparable in terms of fault resistance.

Simulations

Fig. 4.14 shows the current space vector trajectories at no load when a HR of 1.85 Ohm is connected in series to one of the three phases in each plot. As expected by (4.107), in case of a V/f control, the introduction of a HR generates an inverse current sequence.

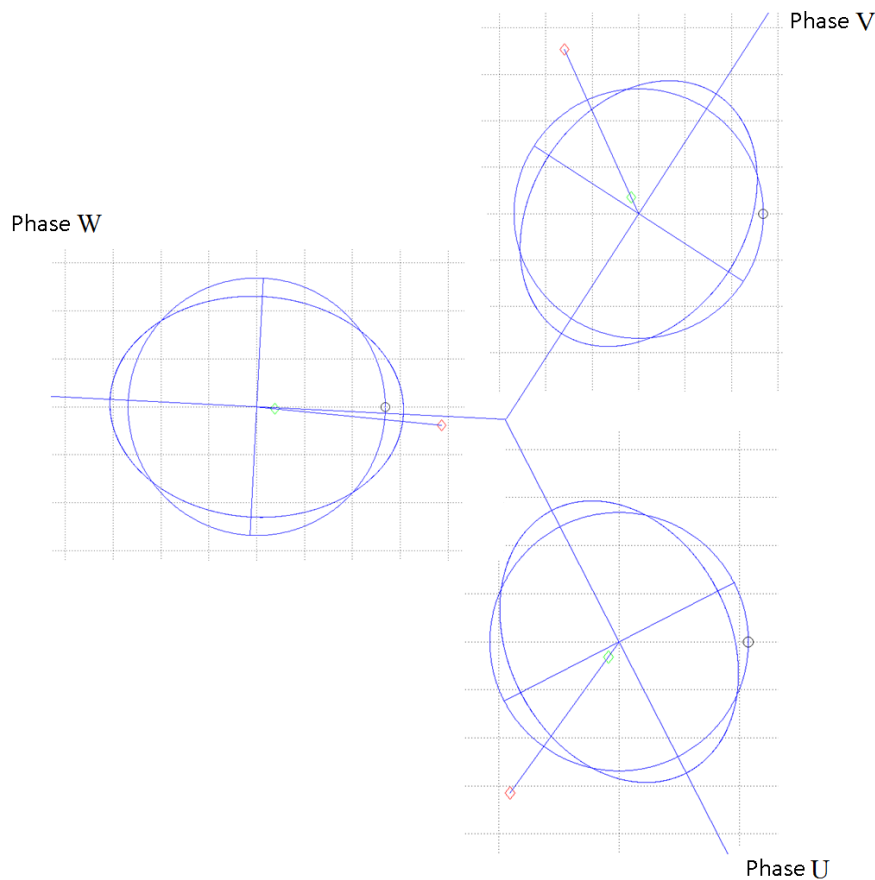


Fig. 4.14 - Matlab-Simulink simulation V/f control with High Resistance fault (1.85 Ohm additional) in the mentioned phases. Current space vector trajectories [2A/div].

Experimental results

Fig. 4.15 shows the same analysis of Fig. 4.14 carried out by experimental tests (the test setup is described in Fig. 4.12). The qualitative behaviour is almost as expected by the simulations in Fig. 4.14. The main difference is that the trajectories are all shifted of an offset (because of the not perfect match of the model parameters, as already mentioned).

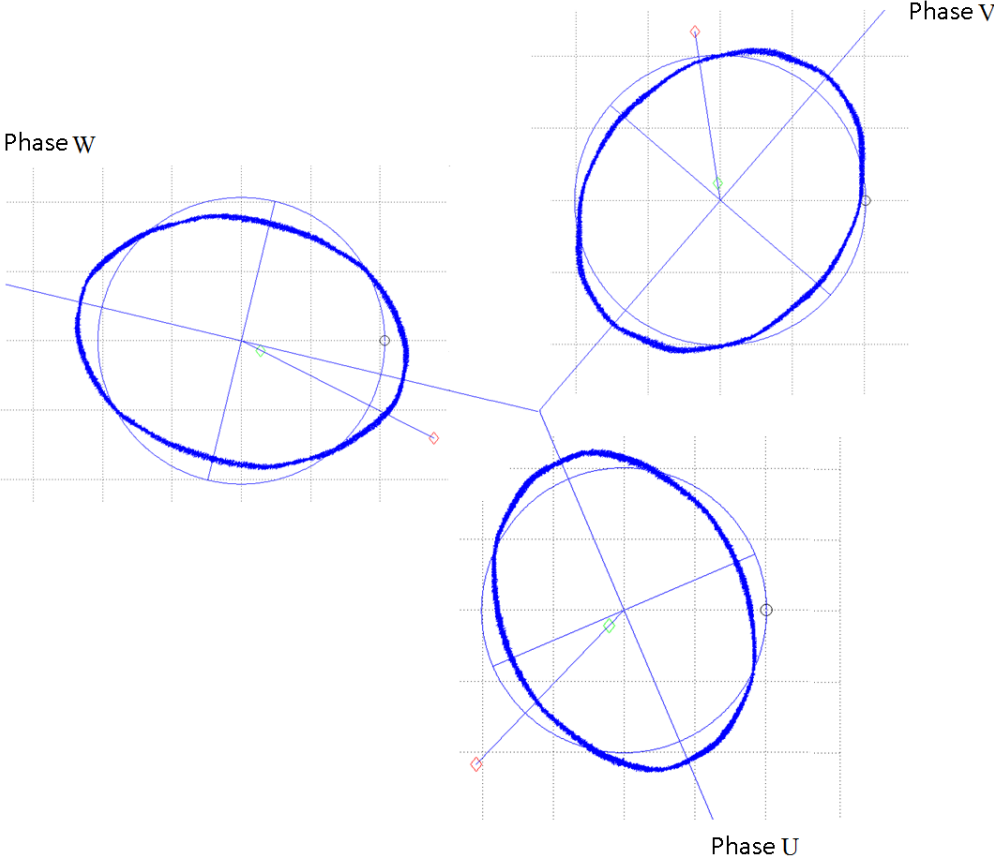


Fig. 4.15 - Experimental results V/f control with High Resistance fault (1.85 Ohm additional) in the mentioned phases. Current space vector trajectories [2A/div].

Interturn Short Circuit faults

The ISC faults have been performed considering the same fault resistance used for the HR ones (1.85 Ohm). The main goal is to show that the proposed model can properly simulate this fault in such a way that it result in different space vector trajectories according to the fault topology and location in the different coils. The short circuits are simulated and tested for a full coil short circuit (1/6 of the phase, 28 turns), as shown in Fig. 4.12.

Simulations

Fig. 4.16 shows the current space vector trajectories in case of an ISC fault, comparing the same fault in the three phases and, only for the phase V, also in the three different coils under one pole pair. It is worth noticing that if the fault happens in a different pole pair the behaviour is exactly the same, and from the measurements the difference cannot be detected if there are not additional sensors (as thermocouples or searching coils).

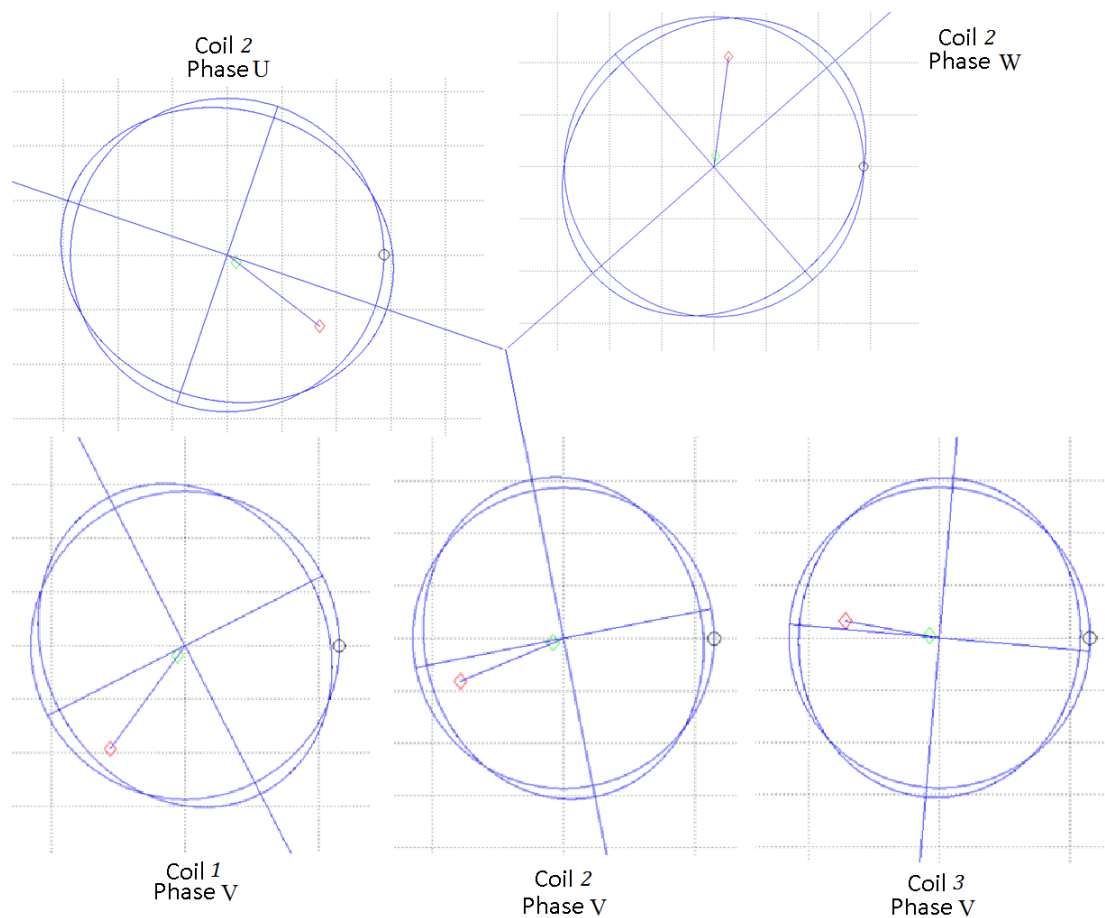


Fig. 4.16 - Matlab-Simulink simulation V/f control with Interturn Short Circuit fault at no load (1.85 Ohm short circuit resistance) in the mentioned phases and coils. Current space vector trajectories [2A/div].

Fig. 4.17 shows the phase currents and the short circuit current in case of short circuit of the central coil (coil 2) of the U phase at no load and with 10 and 20 Nm load torque.

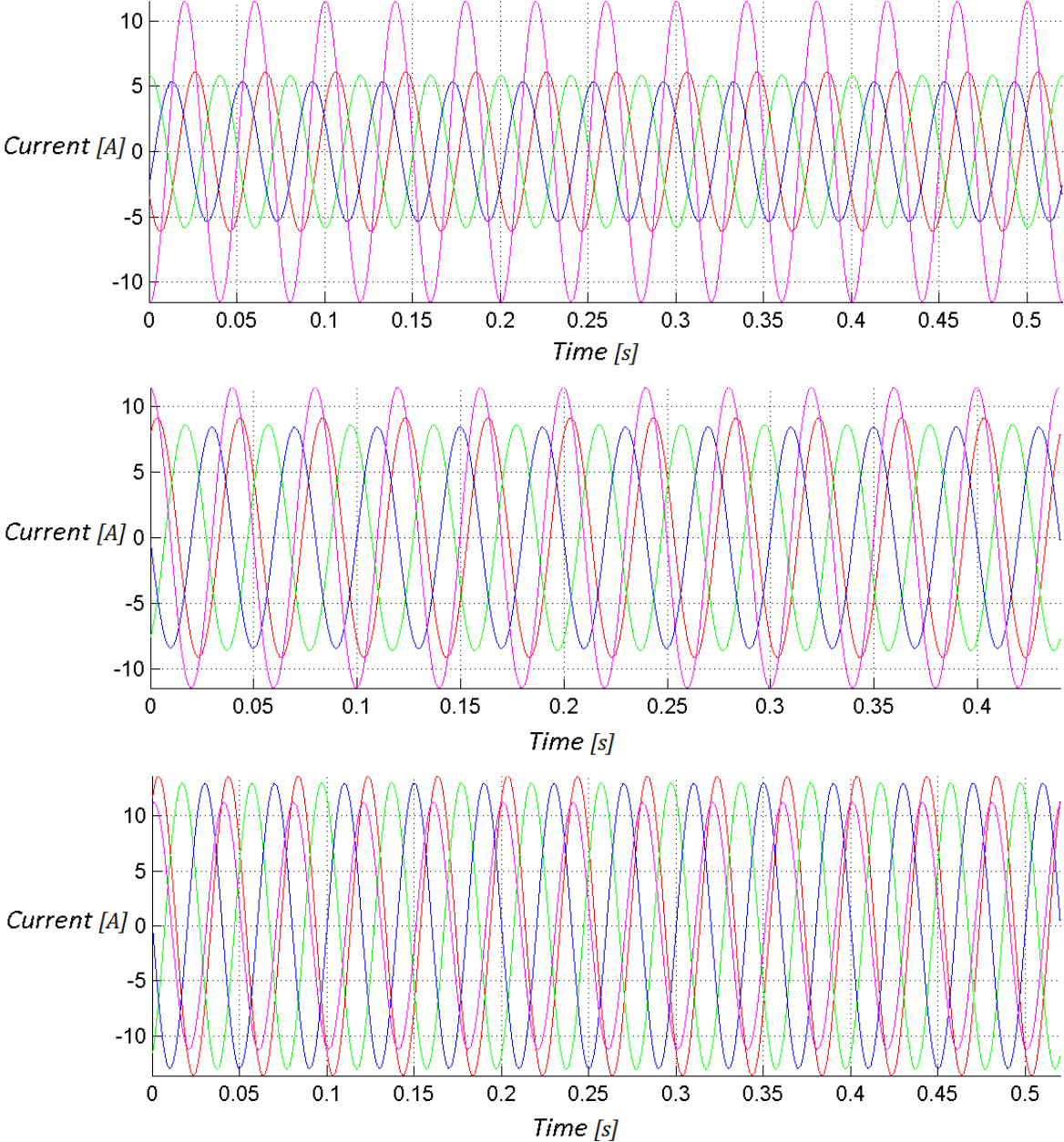


Fig. 4.17 - Matlab-Simulink simulation V/f control with Interturn Short Circuit fault on the U phase at no load (top), 10 Nm (centre) and 20 Nm (bottom) (1.85 Ohm short circuit resistance) in the mentioned phases and coils. Phase currents (red, blue and green) and short circuit current (purple).

Experimental results

Fig. 4.18 and Fig. 4.19 show the experimental results of the same tests. The no load currents are zoomed to better see the phase and short circuit currents behaviour. It is interesting to note that the magnitude of the short circuit current is almost independent from the load (torque), while its phase significantly changes (this is because of the high fault resistance). The other important result is that the short circuit current has almost a sinusoidal waveform at the stator electrical frequency independently from the load condition (allowing to simplify the model considering only the fundamental frequency).

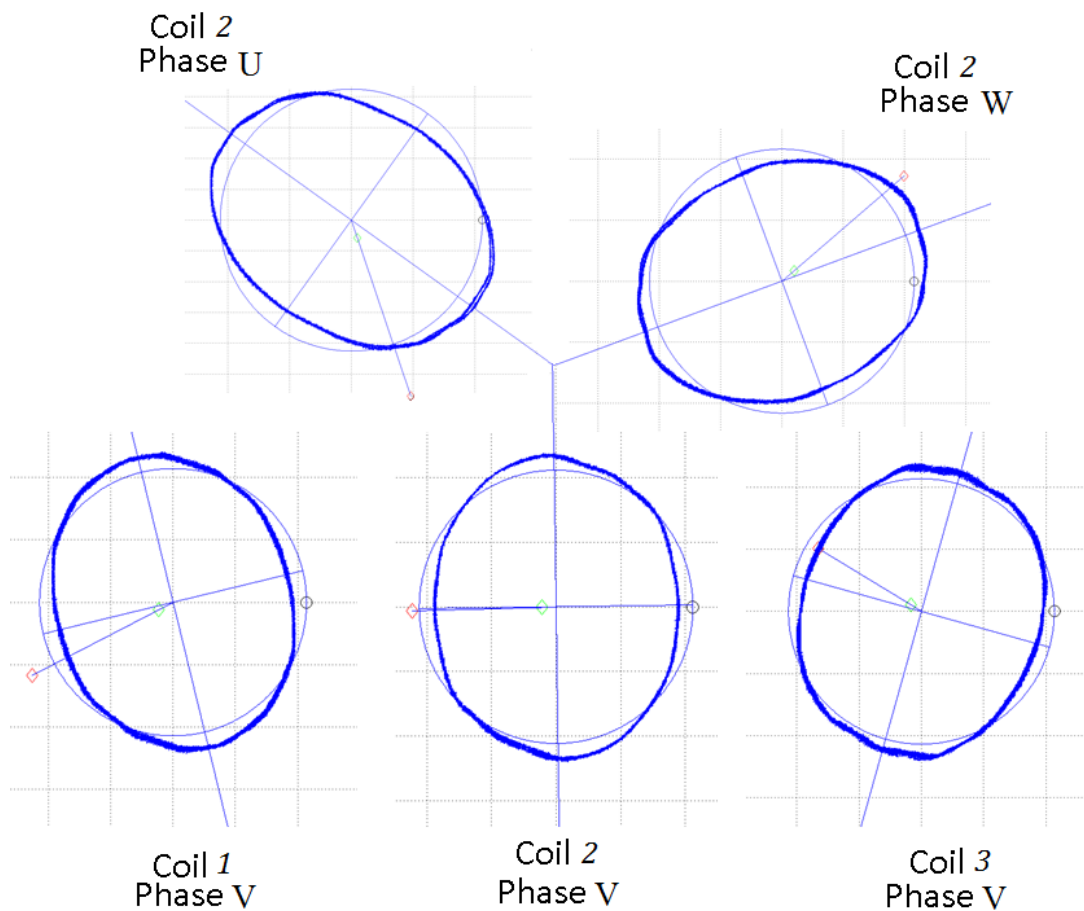


Fig. 4.18 - Experimental results V/f control with Interturn Short Circuit fault at no load (1.85 Ohm short circuit resistance) in the mentioned phases and coils. Current space vector trajectories [2A/div].

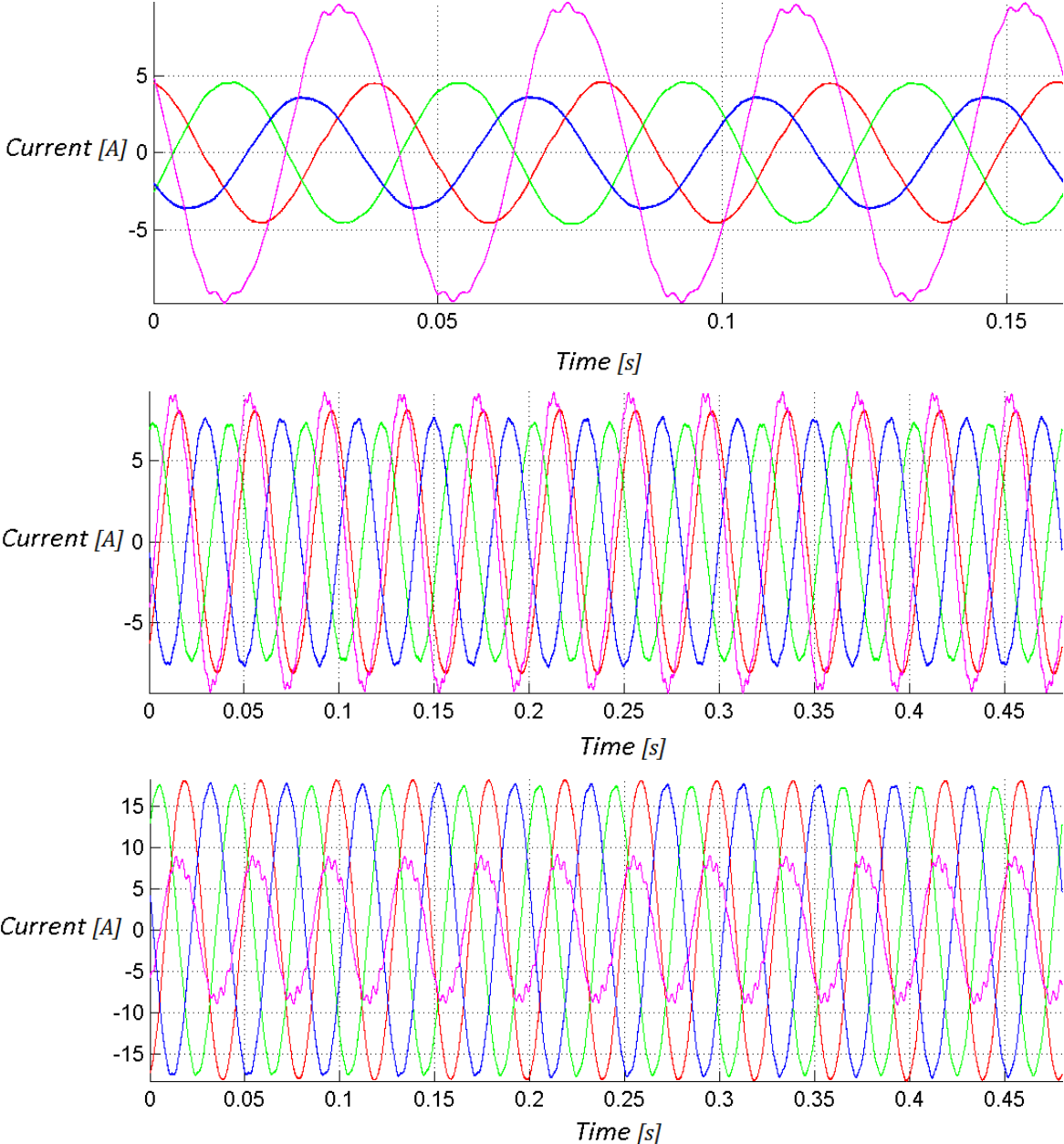


Fig. 4.19 - Experimental results V/f control with Interturn Short Circuit fault on the U phase at no load (top), 10 Nm (centre) and 20 Nm (bottom) (1.85 Ohm short circuit resistance) in the mentioned phases and coils. Phase currents (red, blue and green) and short circuit current (purple).

High Resistance and Interturn Short Circuit faults: Comparison with V/f control

Table 4.2 summarizes the Matlab-Simulink and experimental results. In the table it is highlighted the fact that the short circuit resistance when the short circuit do not happen is 300 Ohm and not infinite. Indeed, this approximation was needed for the numerical solution of the Matlab-Simulink model (having a current in the model that is too small increases the simulation efforts, while with 300 Ohm resistance the short circuit effect is still negligible for the analysis but allows a much faster solution). The phases of the current sequences are different between the simulations and the experimental tests (for the already mentioned reasons). However, the relative phases with the various tested faults are almost as expected.

Table 4.2 – Simulation of a faulty three-phase IM. Results comparison.

	Faulty phase	Faulty coil	R_{sc} [Ohm]	$N_f T_{HR}$ [Nm]	T [Nm]	I_{inv} mag [A]	I_{inv} phase [deg]	I_{inv} mag [A]	I_{inv} phase [deg]	
No Load						Matlab-Simulink		Experimental		
	Short circuit fault (phase discrimination)									
	U	2	1.85	0	0	0.426	322	0.6034	289	
	V	2	1.85	0	0	0.426	202	0.4463	182	
	W	2	1.85	0	0	0.426	82	0.5260	41	
	Short circuit fault (coil discrimination)									
	V	1	1.85	0	0	0.475	234	0.5095	207	
	V	2	1.85	0	0	0.426	202	0.4463	182	
	V	3	1.85	0	0	0.364	170	0.3892	149	
	High resistance fault (phase discrimination)									
	U	-	(300)	1.85	0	0.776	234	0.6029	226	
	V	-	(300)	1.85	0	0.776	114	0.4731	98	
	W	-	(300)	1.85	0	0.776	354	0.6225	333	
	Load	Short circuit fault (load sensitivity)								
U		2	14.3	0	10	0.061	342	0.1499	331	
U		2	1.85	0	10	0.424	346	0.4885	22	
U		2	14.3	0	20	0.059	353	0.1933	326	
U		2	1.85	0	20	0.419	356	0.4658	14	

Fig. 4.20 shows the phase and short circuit currents at no load when the short circuit resistance is decreased from 14.3 to 1.85 Ohm. The current space vector trajectory is presented in the same figure, to highlight that at no load conditions the phase of the current space vector for quite high short circuit resistance values does not significantly change. The obtained results are similar to the one proposed in [9], with the difference that the ISC faults are also compared with the HR ones as in [3]. The simulation and experimental analysis was useful to validate the model for the analysis presented in the next section, where the detection algorithm is analysed in case of an ideal vector current control of the machine, showing the dependence of the detection algorithm to the fault and machine behaviour.

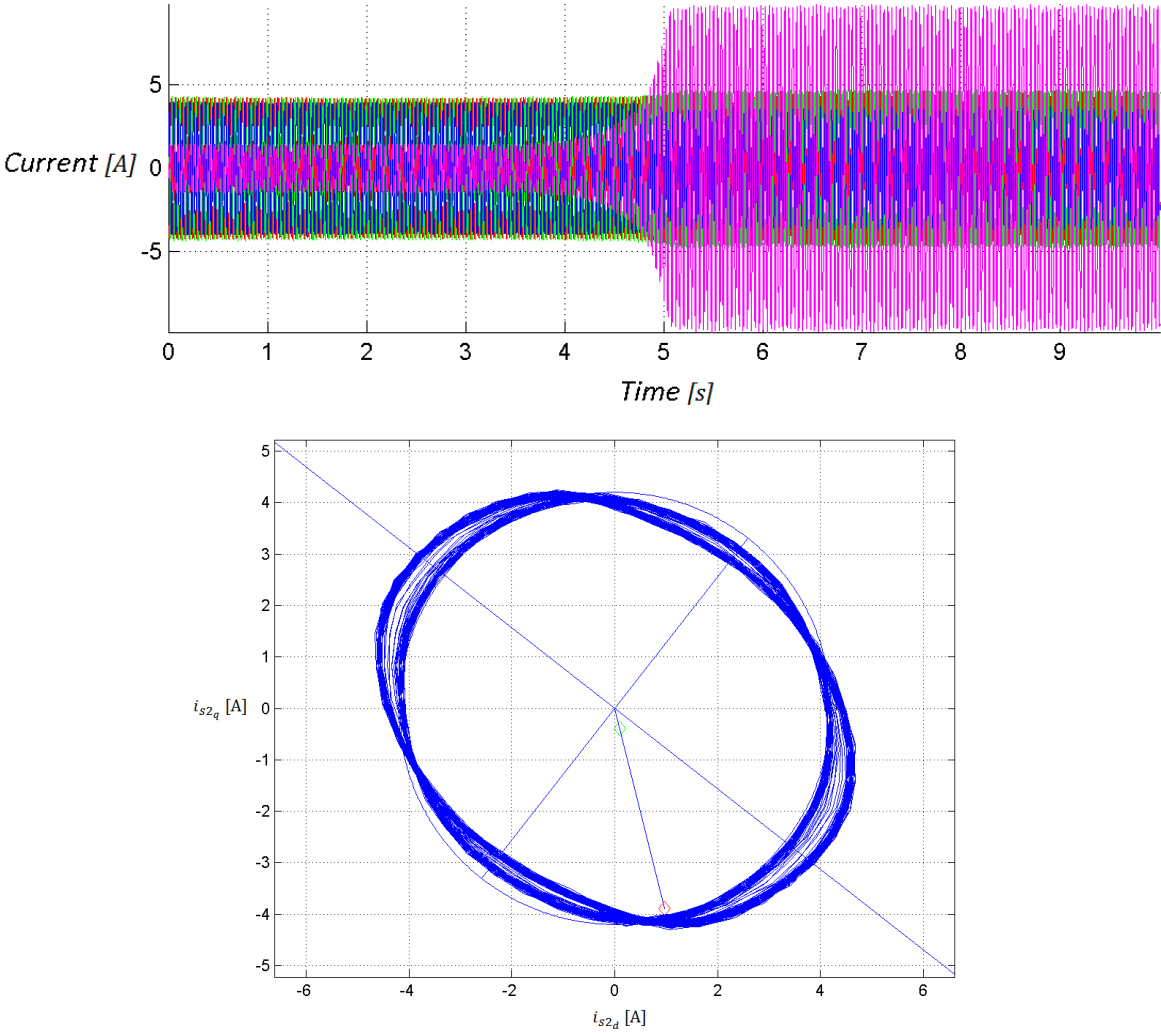


Fig. 4.20 - Experimental results V/f control with Interturn Short Circuit fault on the U phase at no load varying the short circuit resistance from 14.3 to 1.85 Ohm. Phase currents (red, blue and green) and short circuit current (purple) on the top; current space vector trajectory on the bottom.

4.9 Analytical Results of ISC fault detection for Three-phase IMs

In order to have a better understanding of the ISC phenomena, the steady state analysis of the fault is evaluated analytically under the hypothesis of ideal current FOC control as described in Section 4.7. Therefore, the ISC analysis is carried out considering the direct-inverse sequence impedance as fault index:

$$\bar{x} = \frac{\bar{v}_{p,inv}}{\bar{i}_p^*}. \quad (4.179)$$

In case of a HR fault the index represents the asymmetrical phase resistance configuration as:

$$\bar{x} = \frac{1}{2} \bar{R}_{HR,p}^* = \frac{1}{2} \bar{R}_{HR,2p}. \quad (4.180)$$

In case of an ISC fault, the fault index (\bar{x}) has a much more complicated expression. The fault index equation is derived by (4.175) as:

$$\begin{aligned} \bar{x} = & \frac{\bar{v}_{p,inv}}{\bar{i}_p^*} = \frac{V_{p,inv}}{I_p} e^{j\vartheta_{v,inv}} = \frac{1}{2} \bar{R}_{HR,2p} + \\ & - \frac{2}{3} \left(\frac{N_f (r_{HR} + r)}{2} - j\omega \frac{Ml_{sc}}{2} \right) e^{jp\psi_z} \frac{I_{sc}}{I_p} e^{-j\vartheta_{sc}} + \\ & - \left(-j\omega \frac{M_{fs,p}}{2} + \frac{\omega \left(\omega + p \frac{d\vartheta_m}{dt} \right) \frac{M_{rs,p} M_{fr,p}}{2}}{R_{rp} - j \left(\omega + p \frac{d\vartheta_m}{dt} \right) (Ll_{rp} + L_{cage,p})} \right) e^{jp\psi_f} \frac{I_{sc}}{I_p} e^{-j\vartheta_{sc}}. \end{aligned} \quad (4.181)$$

Introducing the conjugate of the short circuit current space vector (4.173), the final fault index in steady state condition and with the hypothesis of sinusoidal field in the airgap is:

$$\begin{aligned}
 \bar{x} = & \frac{1}{2} \bar{R}_{HR,2p} + \\
 & - \left[\frac{2}{3} \left(\frac{N_f (r_{HR} + r)}{2} - j\omega \frac{M l_{sc}}{2} \right) e^{jp\psi_z} + \left(-j\omega \frac{M_{fs,p}}{2} + \frac{\omega \left(\omega + p \frac{d\mathcal{G}_m}{dt} \right) \frac{M_{rs,p} M_{fr,p}}{2}}{R_{rp} - j \left(\omega + p \frac{d\mathcal{G}_m}{dt} \right) (Ll_{rp} + L_{cage,p})} \right) e^{jp\psi_f} \right] \\
 & \frac{(N_f (r_{HR} + r) - j\omega M l_{sc}) e^{jp\psi_z} + \left(-j\omega \frac{3}{2} M_{fs,p} + \frac{\frac{1}{2} \omega \left(\omega - p \frac{d\mathcal{G}_m}{dt} \right) \frac{3}{N_b} \frac{N_b}{2} M_{fr,p} M_{rs,p}}{R_{rp} - j \left(\omega - p \frac{d\mathcal{G}_m}{dt} \right) (Ll_{rp} + L_{cage,p})} \right) e^{jp\psi_f}}{r_{sc} + N_f (r_{HR} + r) - j\omega (Ll_{sc} + L_{sc}) + \frac{\omega \left(\omega - p \frac{d\mathcal{G}_m}{dt} \right) \frac{N_b M_{fr,p}^2}{4}}{R_{rp} - j \left(\omega - p \frac{d\mathcal{G}_m}{dt} \right) (Ll_{rp} + L_{cage,p})} + \frac{\omega \left(\omega + p \frac{d\mathcal{G}_m}{dt} \right) \frac{N_b M_{fr,p}^2}{4}}{R_{rp} - j \left(\omega + p \frac{d\mathcal{G}_m}{dt} \right) (Ll_{rp} + L_{cage,p})}}
 \end{aligned} \tag{4.182}$$

Hereafter, the analytical evaluation of the amplitude of the short circuit current and the magnitude and phase of the fault index given by (4.182) are presented, showing how they are affected by the following variables:

- The short circuit fault resistance (r_{sc})
- The number of short circuited turns (N_f)
- The magnetic axis of the short circuit loop (ψ_f)
- The magnetic axis of the faulty phase (ψ_z)
- The resistance increase in the faulty phase in the ISC loop ($R_{HR,z}$)
- The rotor speed ($\frac{d\mathcal{G}_m}{dt}$)
- The electrical frequency (ω), or in other words the slip:

$$s = \frac{\omega - p \frac{d\mathcal{G}_m}{dt}}{\omega}.$$

It is interesting to note that the fault index is independent from the magnitude of the stator current space vector (\bar{i}_p). Indeed, it represents the direct-inverse sequence impedance. Compared to a three-phase SPM machine, the main additional parameter is the slip of the rotor flux compared to the rotor. The slip can be evaluated directly from the FOC and the measurement of the rotor speed, or can be evaluated (in case of sensorless control of the IM). However, the different behaviour of the machine with the various working conditions (slip) makes the diagnosis of the ISC fault much more complicated than the HR one.

Some figures are presented here below in order to understand how the diagnostic index depends from the fault parameters and the working condition. All the analysis is carried out at rated current (9.6 Arms) and frequency (50 Hz).

Fig. 4.21 shows the detection parameters \bar{x} defined by (4.182) in case of HR fault, with fault resistance up to about 1 Ohm, and in case of ISC of the central coils of the three phases (highlighted with different colours). The short circuit resistance varies from 20 Ohm to zero (full short circuit). The machine is operating at no load conditions. As expected, the trajectories of the diagnostic index in Fig. 4.21 are straight lines in case of HR fault in one phase, and the phase of the diagnostic index depends only from the faulty phase. Instead, in case of ISC, the trajectories have the shape of a spiral with a different phase of the detection parameter for different short circuit resistance values. In both the cases, the magnitude of the fault index increases with the fault severity.

Fig. 4.22 presents the same machine behaviour, but considering for all the possible fault locations (1st, 2nd and 3rd coil of each phase). While the HR fault position do not affect the machine behaviour, the position of the ISC fault in one phase changes the phase of the inverse sequence of the voltage and therefore also the phase of the diagnostic index. In Fig. 4.22 the fault position is highlighted for the U phase (red), where with a square and a rhombus are distinguished the ISC faults in the first and the last coils of the U phase.

In the following figures, the ISC faults are presented only for the fault in the central coil (2nd) of the U phase.

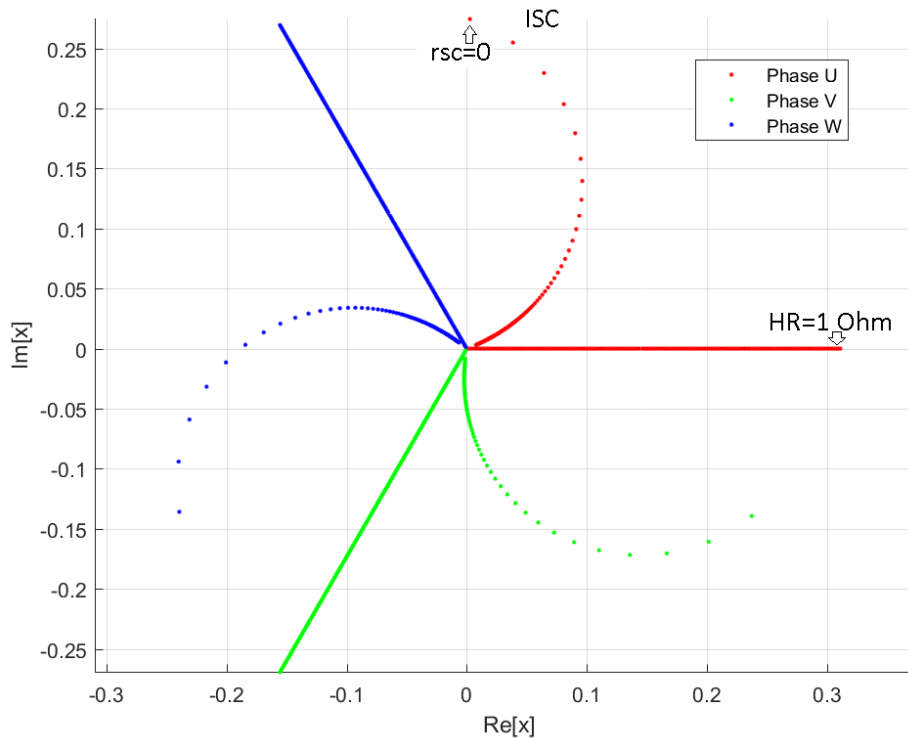


Fig. 4.21 - Detection parameter \bar{x} at no load and rated frequency (50 Hz). HR connection up to about 1 Ohm and ISC detection with full short circuit of the central coil (28 turns) for each phase and short circuit resistance from 20 Ohm to 0 resistance (complete short circuit).

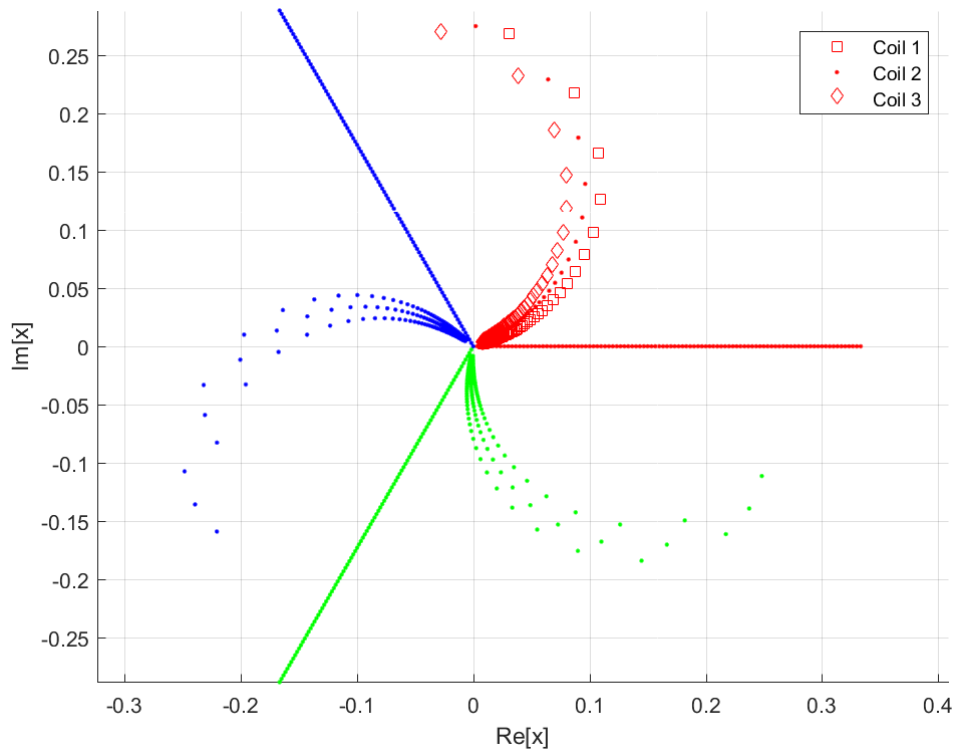


Fig. 4.22 - Detection parameter \bar{x} at no load and rated frequency (50 Hz). HR connection up to about 1 Ohm and ISC detection with full short circuit of the different coils (28 turns) for each phase and short circuit resistance from 20 Ohm to 0 resistance (complete short circuit). The coils are identified with a different symbol only for the phase U.

Fig. 4.23 shows the detection index when the slip is changed from 0 (no load) to 0.1. The rated load condition (0.04 slip) is highlighted with a blue rhombus. As can be noticed, also the slip affects the detection index both in terms of magnitude and in terms of phase.

Fig. 4.24 shows what is found to be the most critical ISC fault parameter: the number of short-circuited turns. The results presented in Fig. 4.24 are at rated speed and load (0.04 slip). With black circles are highlighted the values of the detection index in case of full coil short circuit (28 turns) for different short circuit resistance values (from zero to 1 Ohm, as shown in Fig. 4.25). For the same short circuit resistance all the possible number of short-circuited turns are presented (up to the single turn ISC fault). Fig. 4.25 shows the peak value of the evaluated short circuit current for the same working conditions of Fig. 4.24. It is important to notice that, also if the detection index does not change significantly its magnitude when the fault affects a reduced number of turns, the short circuit current is significantly higher (up to 15 times the rated current in case of complete ISC of one turn).

The short circuit current decreases with the increase of short-circuited turns for small values of short circuit resistance. For higher values, the short circuit current becomes higher with a higher number of short-circuited turns. This obtained results are in agreement with the ones obtained by FEA in [11]. Indeed, for small short circuit resistances the fault impedance is mainly inductive and therefore it decreases with the number of short-circuited turns. For high fault resistance values, the impedance becomes mainly resistive and related to the fault resistance itself, resulting in a higher short circuit current in case of more turns (higher ISC loop emf). The critical resistance value is about 0.1 Ohm in the simulated machine (0.05 Ohm in [11]).

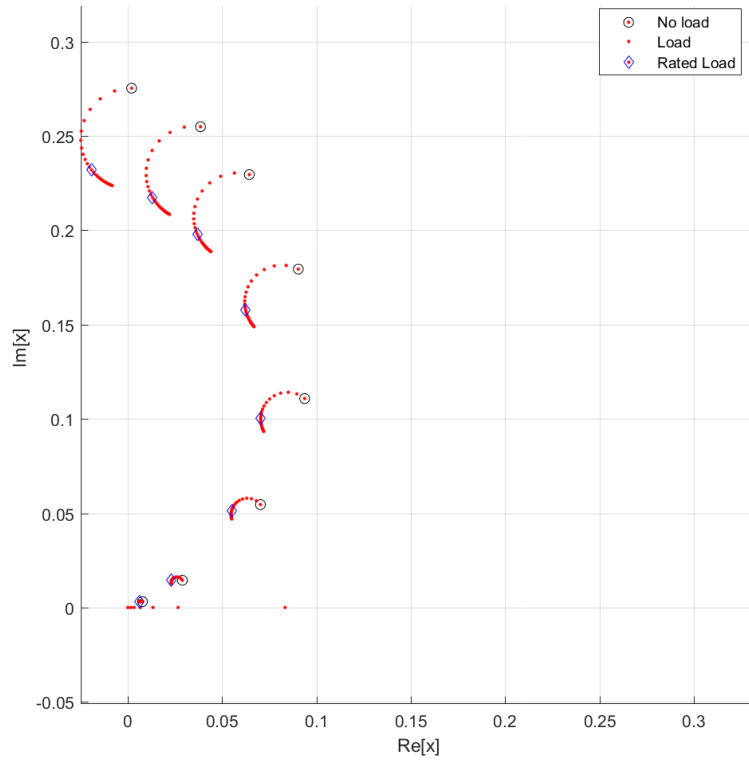
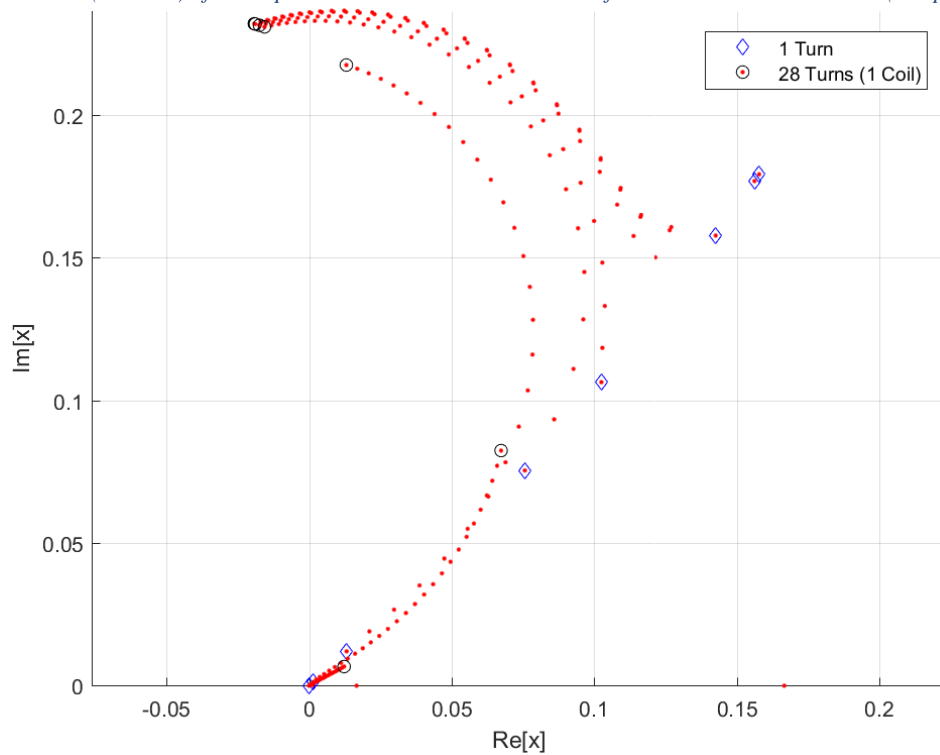


Fig. 4.23 - Detection parameter \bar{X} at different slip values and rated frequency (50 Hz). ISC detection with full short circuit of the central coil (28 turns) of the U phase and short circuit resistance from 20 Ohm to 0 resistance (complete



short circuit).

Fig. 4.24 - Detection parameter \bar{X} at rated slip and rated frequency (50 Hz). ISC detection with a variable number of short circuited turns from 1 to 28 (one coil) of the U phase and short circuit resistance from 1 Ohm to 0 resistance (complete short circuit).

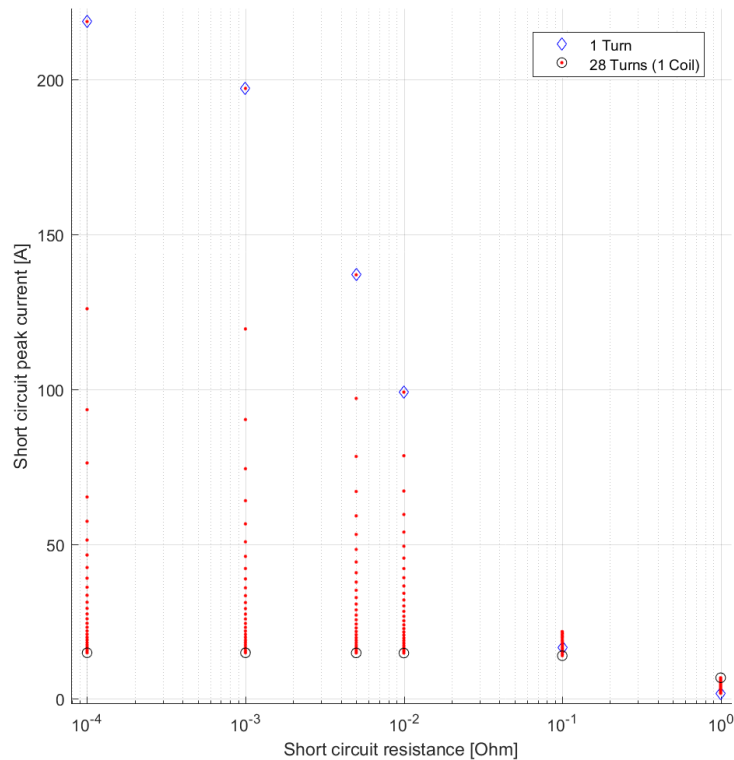


Fig. 4.25 – Short circuit current at rated slip and rated frequency (50 Hz). The number of short circuited turns varies from 1 to 28 (one coil) of the U phase and short circuit resistance from 1 to 0 Ohm.

The last analysis is related to the effect of the resistance increase in the short-circuited turns. This phenomenon can be expected in case of a high short circuit current (heat source). Fig. 4.26 and Fig. 4.27 show the detection index and the short circuit current at rated working conditions and a variable number of short-circuited turns when their resistance is increased up to twice the nominal value. In case of a small number of short-circuited turns, the short circuit current and the magnitude of the detection index significantly decrease with an increase of the turns resistance. Instead, in case of a higher number of short-circuited turns, the resistance increase in the ISC loop do not affect significantly the machine behaviour. The effect is similar to the one explained in the analysis of the short circuit resistance.

The ISC detection in case of machine FOC has not been proved by experimental results yet. However, the analysis of the detection index shows that it is possible to discriminate between a HR fault and an ISC looking at the phase of the detection index. However, the discrimination of the fault criticality (number of short-circuited turns and short circuit resistance) are not predictable. Indeed, the fact that the diagnostic index changes its phase with the faulty coil results in some values that can be related to an important ISC fault (reduced number of short circuited turns with high short circuit current) or a less significant one (high number of short circuited turns with a small short circuit current).

In the next section, the HR detection algorithm is verified by analytical and experimental results in case of a nine-phase machine with a single star. Instead, the theory of the ISC detection has not been analysed for the multiphase machine, but the equations presented in this chapter are already general for the ISC detection in multiphase machines.

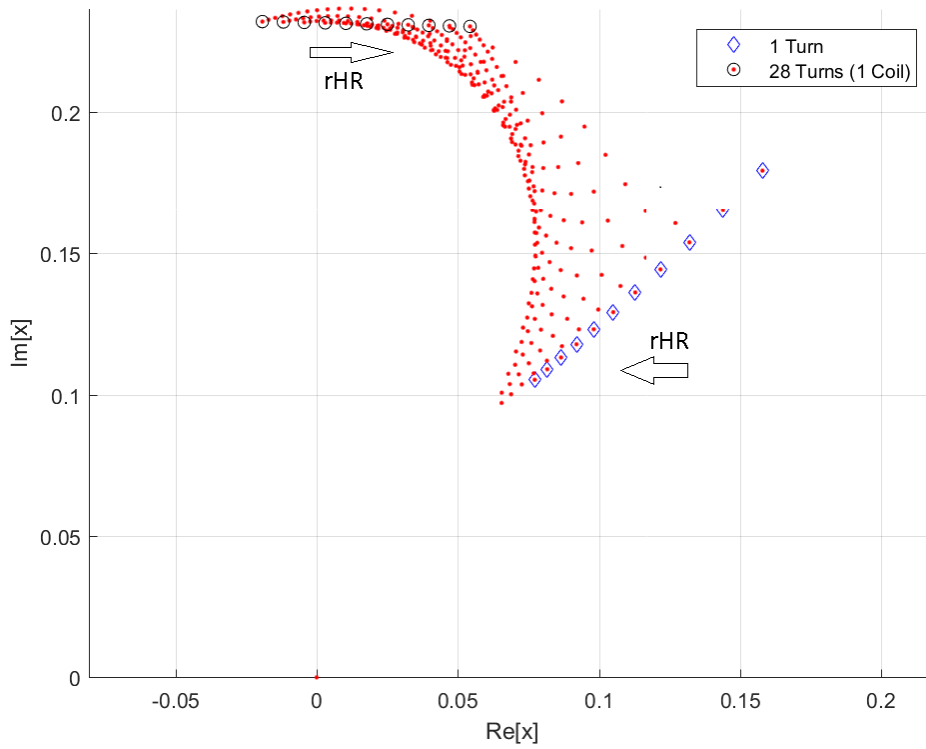


Fig. 4.26 – Detection parameter \bar{x} at rated slip and rated frequency (50 Hz). The number of short circuited turns varies from 1 to 28 (one coil) of the U phase, the short circuit resistance is zero (full short circuit) and the short circuited turns have a resistance that increases from 1 to 2 times the normal value.

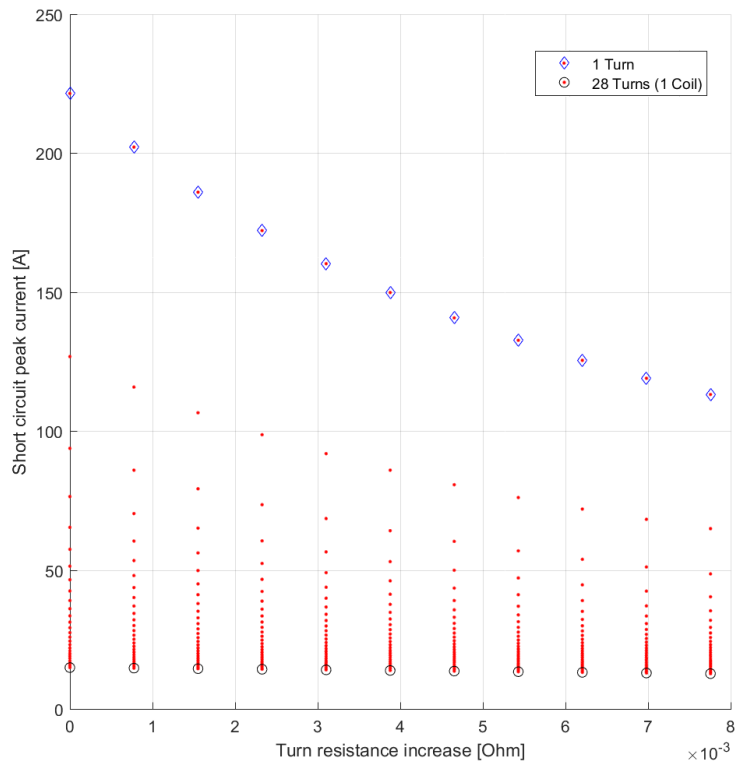


Fig. 4.27 – Short circuit current at rated slip and rated frequency (50 Hz). The number of short circuited turns varies from 1 to 28 (one coil) of the U phase, the short circuit resistance is zero (full short circuit) and the short circuited turns have a resistance that increases from 1 to 2 times the normal value.

4.10 Analytical and Experimental Results of High Resistance Detection in Nine-Phase Induction Machines

This section shows the results of the HR detection algorithm for the same prototype presented in Section 4.8 (squirrel cage IM) configured in a symmetrical nine-phase winding layout (the asymmetrical and symmetrical winding configurations have been explained in Chapter 2).

The detection algorithm is based on equations (4.132)-(4.134), with the nine-phase machine connected in a single star configuration. In particular, the winding is a triple three-phase one in a nine-phase configuration (single star connection) as the one in Fig. 4.28. The phases of the inverters are named as U, V and W and the inverter numbered as 1, 2 and 3. The experimental tests are performed at no load and 300 rpm with 4 A of d-axis current, aware that the working condition should not affect the results.

The detection algorithm is described by the equations here below:

$$R_0 = 2 \frac{\bar{v}_{1,dir} - (Ll + L_1) \frac{d\bar{i}_1}{dt} - \frac{d\bar{\phi}_{r,1}}{dt}}{\bar{i}_1}, \quad \left\{ \begin{array}{l} \bar{R}_2 = \frac{\bar{v}_{1,inv}}{\bar{i}_1^*} + \frac{\bar{v}_{3,dir}}{\bar{i}_1} \\ \bar{R}_4 = \frac{\bar{v}_{3,inv}}{\bar{i}_1^*} + \frac{\bar{v}_{5,dir}}{\bar{i}_1} \\ \bar{R}_6 = \frac{\bar{v}_{5,inv}}{\bar{i}_1^*} + \frac{\bar{v}_{7,dir}}{\bar{i}_1} \\ \bar{R}_8 = 2 \frac{\bar{v}_{7,inv}}{\bar{i}_1^*} \end{array} \right. \quad (4.183)$$

Finally, the phase resistances are evaluated as:

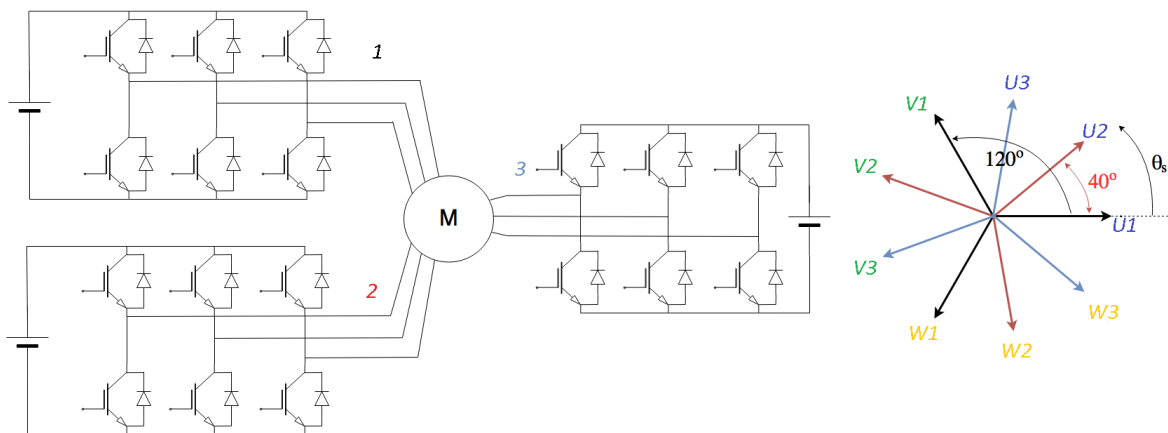


Fig. 4.28 – Symmetrical triple three-phase machine concept (left) and magnetic axes (right). In blue, green and orange are highlighted the U, V and W phases of the three inverters (1, 2 and 3).

$$R_x = \frac{1}{2}R_0 + \sum_{h_{\text{even}}=2}^8 \Re \left\{ \bar{R}_h e^{-jh \frac{2\pi}{9}(x-1)} \right\}. \quad (4.184)$$

The following subsection presents and compare the analytical and experimental results.

High Resistance Fault Detection

The analytical results are adapted to the experimental tests. Indeed, the phase resistances are not exactly equal in the healthy machine (probably because of the customized winding process). Therefore, an offset is introduced in the analytical model in order to match the analytical and experimental results. The offset is based on the evaluation of the healthy machine behaviour as in the next paragraph.

Healthy Machine

Fig. 4.29 and Fig. 4.30 show the resistance space vectors (or in other words the behaviour of the detection index \bar{x} in case of HR fault) and the evaluated phase resistances when the machine is healthy. While the analytical results are just matched with the experimental ones in order to take into account for the offset of the machine when there is not a fault condition, the experimental results are defined from the measured currents and the reference voltages. In order to obtain an improved performance of the machine and the detection algorithm, the dead times and the voltage drops on the switching devices have been compensated in the control algorithm. Therefore, the real phase voltages are expected to be almost equal to their reference values.

Fig. 4.29 shows the analytical resistance space vectors (and the zero sequence) related to the defined values of phase resistances. Fig. 4.30 shows the resistance evaluation from the experimental tests in the same resistance condition.

This test was only needed for setting the initial phase resistances in the analytical model.

CHAPTER 4

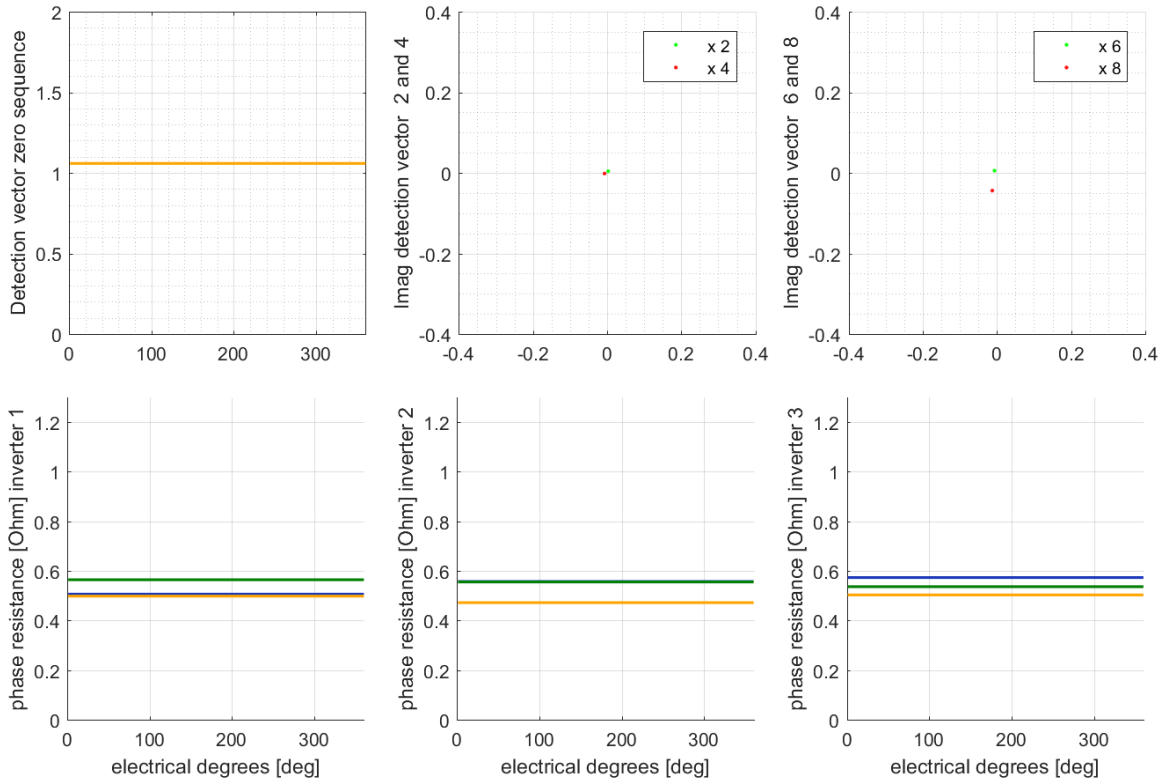


Fig. 4.29 – Analytical results for the HR detection in the healthy machine matched with the prototype. Zero sequence (top left) 2nd and 4th space (top centre) and 6th and 8th spaces (top right) of the detection vectors. Evaluated Phase resistances for the U, V and W phases of each inverter (bottom). In blue, green and orange are highlighted the U, V and W phase resistances.

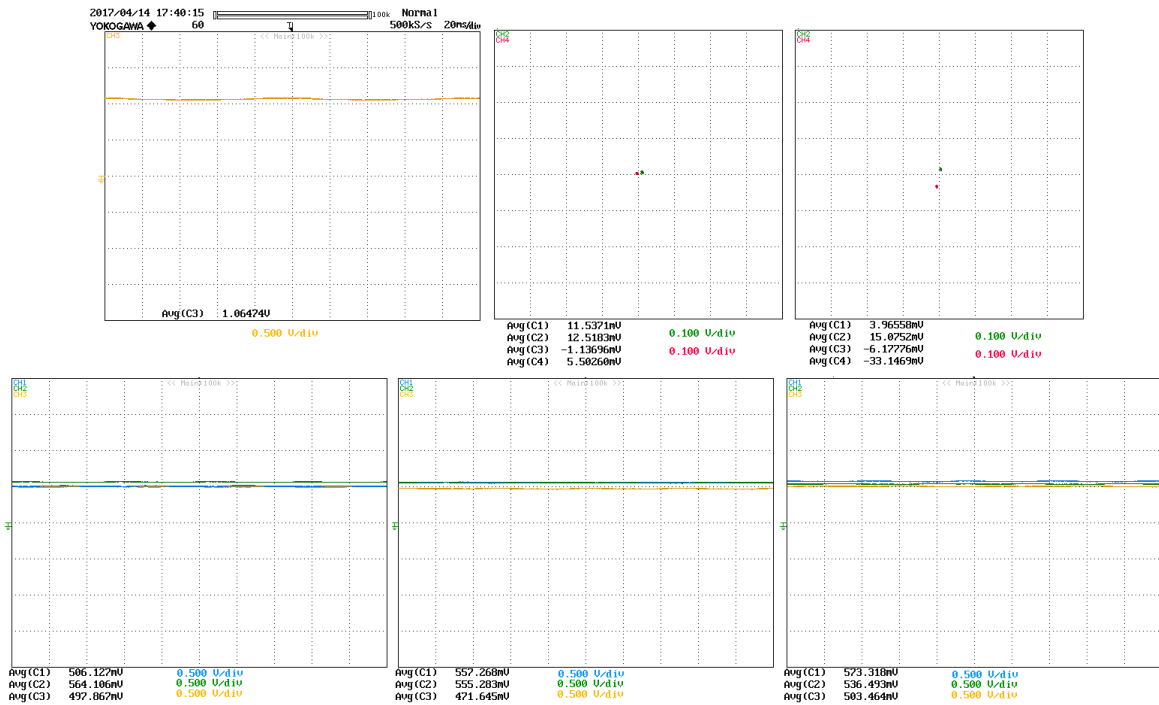


Fig. 4.30 – Experimental results at no load, 4A of magnetizing current and 300 rpm speed. HR detection in the healthy machine. Zero sequence (top left) 2nd and 4th space (top centre) and 6th and 8th spaces (top right) detection vectors. Evaluated phase resistances for the U, V and W phases of each inverter (bottom). In blue, green and orange are highlighted the U, V and W phase resistances. [1V=10hm].

HR fault in phase U, V and W of inverter 1 (0.345 Ohm of additional resistance)

Fig. 4.31 shows the expected phase resistances and resistance space vectors when the phase U of the inverter 1 has an additional resistance of 0.345 Ohm in series. Fig. 4.32 shows the resistance and related space vectors evaluated by the experimental tests, when the phase resistance is placed between the end of the U phase on the inverter 1 and the star connection as in Fig. 4.12 for the three-phase winding configuration.

Thanks to the matching of the initial resistance values and the improved detection algorithm, that exploits all the direct and inverse voltage space vectors according to (4.183), there is a good match between the experimental and analytical results.

Fig. 4.33 and Fig. 4.34 show the analytical and experimental results obtained for the same HR condition, but in the V phase of the inverter 1. Finally, Fig. 4.35 and Fig. 4.36 show the results for the phase W of the same inverter.

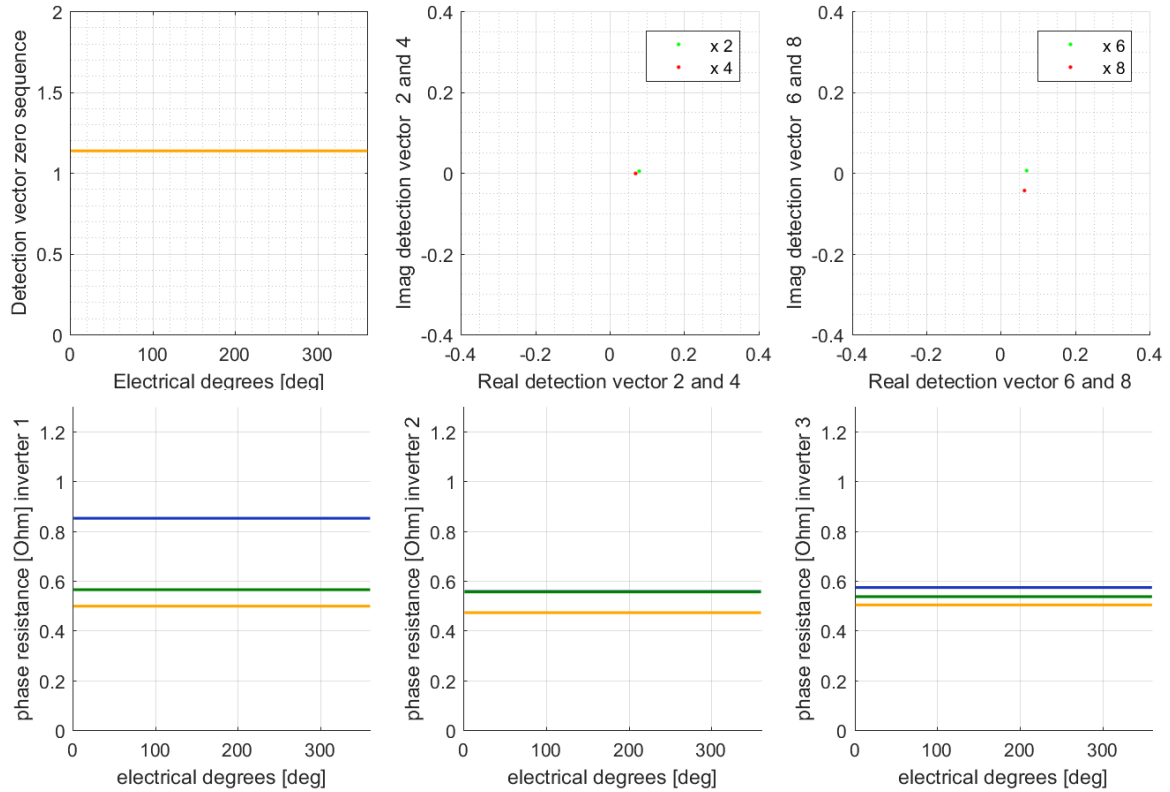


Fig. 4.31 – Analytical results for the HR detection of an HR fault of 0.345 Ohm in the phase U of the Inverter 1. Zero sequence (top left) 2nd and 4th space (top centre) and 6th and 8th spaces (top right) of the detection vectors. Evaluated Phase resistances for the U, V and W phases of each inverter (bottom). In blue, green and orange are highlighted the U, V and W phase resistances.

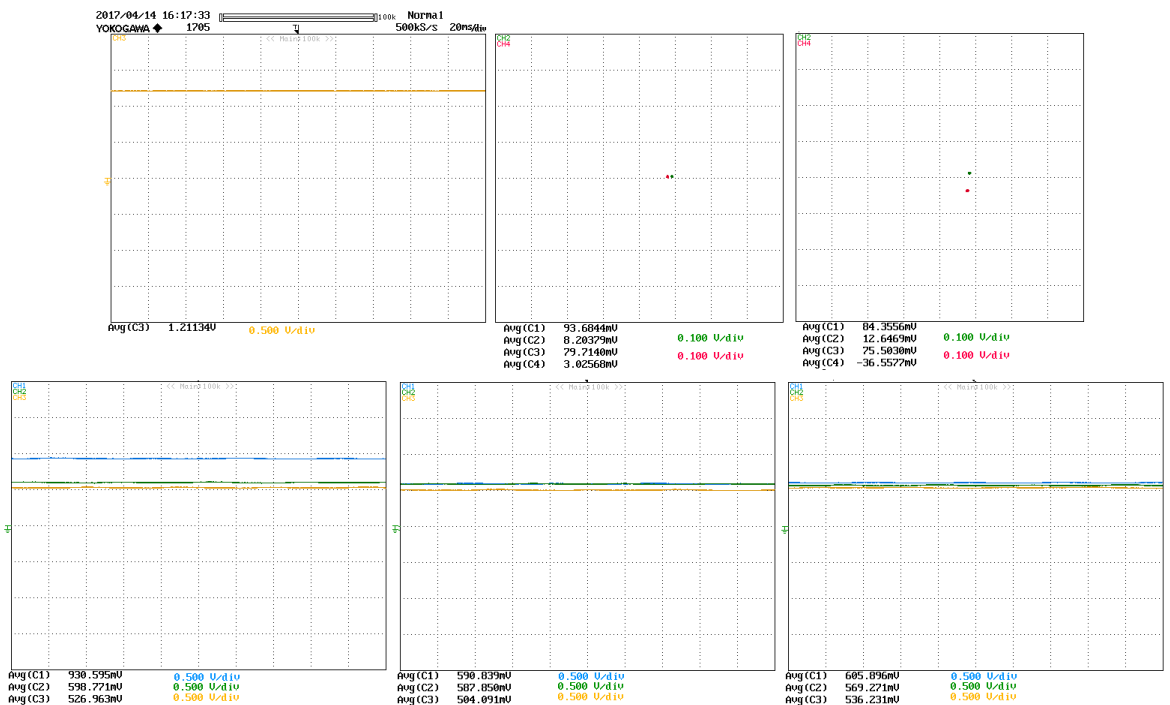


Fig. 4.32 – Experimental results at no load, 4A of magnetizing current and 300 rpm speed. HR detection with 0.345 Ohm of additional resistance in series of phase U of inverter 1. Zero sequence (top left) 2nd and 4th space (top centre) and 6th and 8th spaces (top right) detection vectors. Evaluated phase resistances for the U, V and W phases of each inverter (bottom). In blue, green and orange are highlighted the U, V and W phase resistances. [1V=10hm].

High Resistance and Interturn Short Circuit Faults

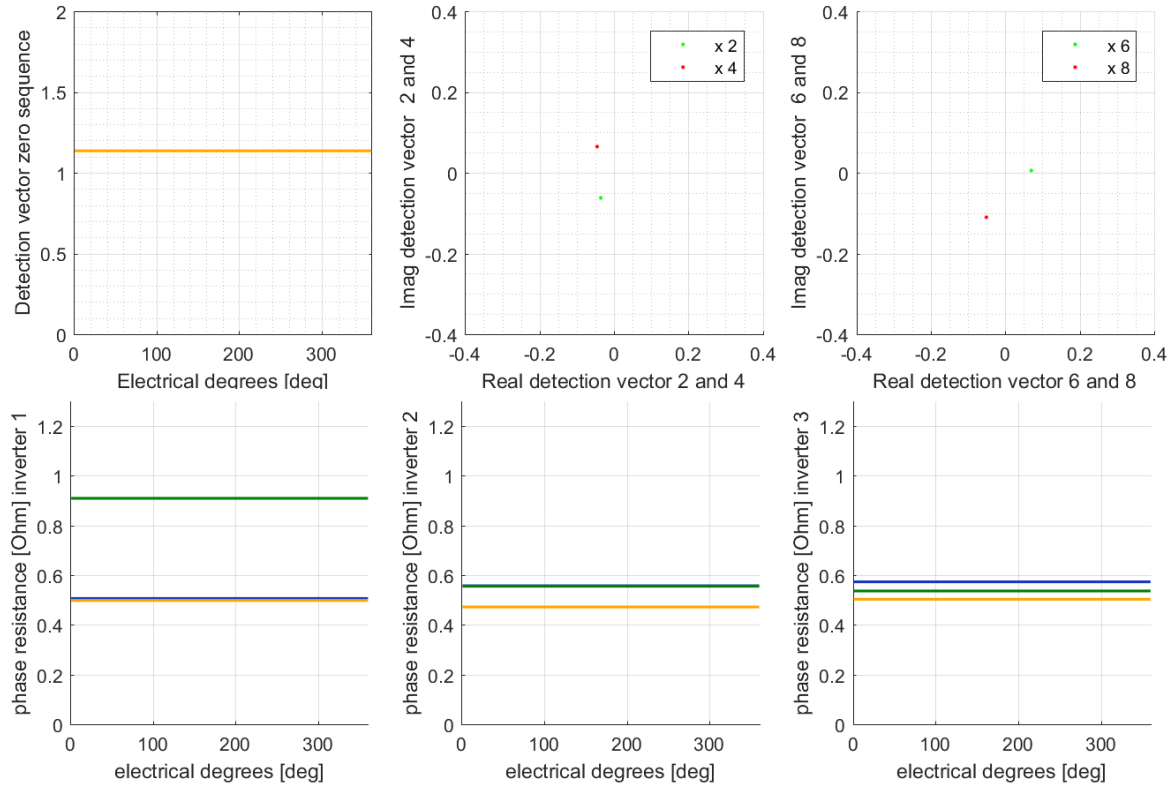


Fig. 4.33 – Analytical results for the HR detection of an HR fault of 0.345 Ohm in the phase V of the Inverter 1. Zero sequence (top left) 2nd and 4th space (top centre) and 6th and 8th spaces (top right) of the detection vectors. Evaluated Phase resistances for the U, V and W phases of each inverter (bottom). In blue, green and orange are highlighted the U, V and W phase resistances.

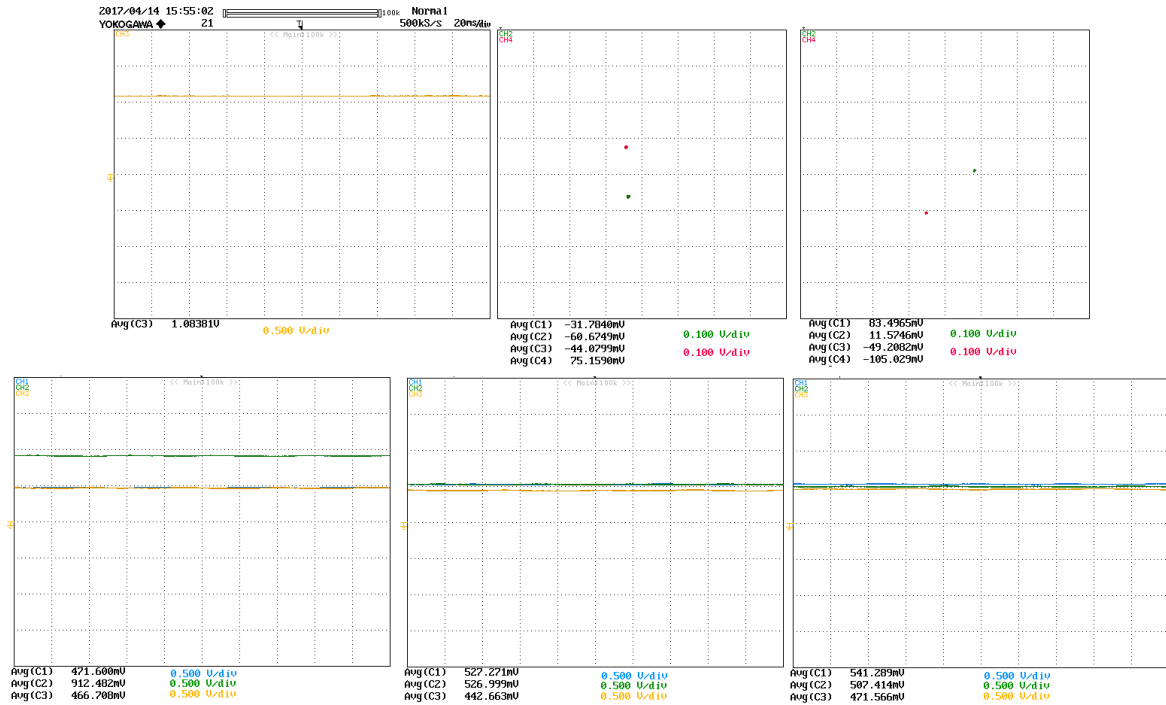


Fig. 4.34 – Experimental results at no load, 4A of magnetizing current and 300 rpm speed. HR detection with 0.345 Ohm of additional resistance in series of phase V of inverter 1. Zero sequence (top left) 2nd and 4th space (top centre) and 6th and 8th spaces (top right) detection vectors. Evaluated phase resistances for the U, V and W phases of each inverter (bottom). In blue, green and orange are highlighted the U, V and W phase resistances. [1V=1Ohm].

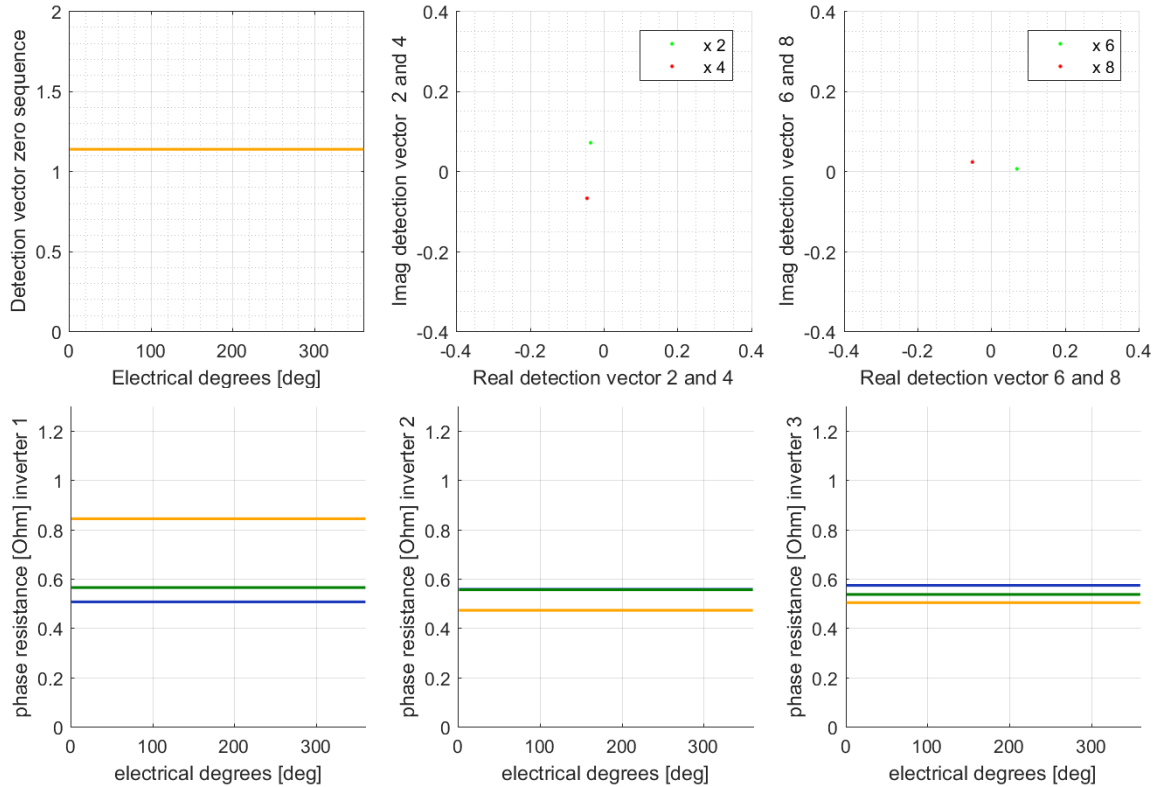


Fig. 4.35 – Analytical results for the HR detection of an HR fault of 0.345 Ohm in the phase W of the Inverter 1. Zero sequence (top left) 2nd and 4th space (top centre) and 6th and 8th spaces (top right) of the detection vectors. Evaluated Phase resistances for the U, V and W phases of each inverter (bottom). In blue, green and orange are highlighted the U, V and W phase resistances.

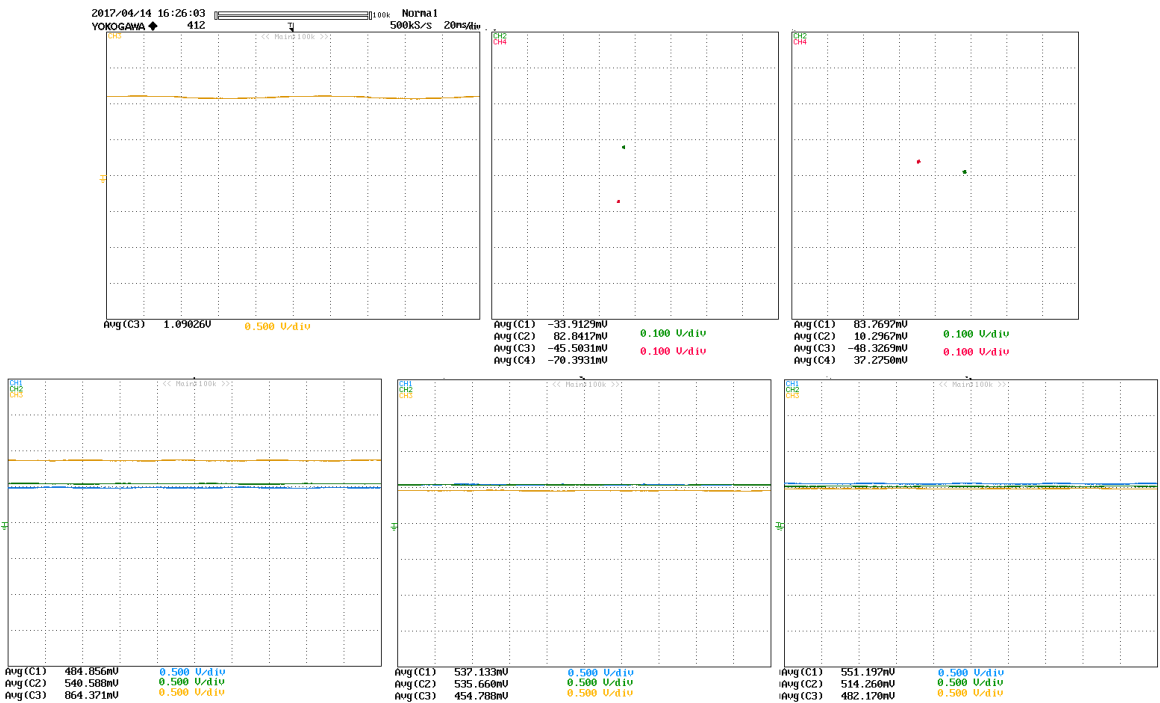


Fig. 4.36 – Experimental results at no load, 4A of magnetizing current and 300 rpm speed. HR detection with 0.345 Ohm of additional resistance in series of phase W of inverter 1. Zero sequence (top left) 2nd and 4th space (top centre) and 6th and 8th spaces (top right) detection vectors. Evaluated phase resistances for the U, V and W phases of each inverter (bottom). In blue, green and orange are highlighted the U, V and W phase resistances. [1V=10hm].

4.11 Conclusion

High resistance connections and interturn short circuits are among the most probable faults related to the deterioration and ageing of electrical machines. The online early detection of these faults is essential to meet high levels of reliability in critical systems as the ones required in MEA applications.

The presented model of these faults in multiphase SPM and squirrel cage IMs is based on the winding function approach.

Initially, a general multiphase machine is considered and, theoretically, all the field harmonics in the airgap are taken into account. Then, the model is simplified considering only for the lowest field harmonics that is possible to independently control by the stator currents. The voltage equations are rewritten in terms of space vector representation. A transient Matlab/Simulink model of a three-phase squirrel cage IM is developed from the resulting space vector equations.

Based on the assumption of an ideal control of the stator currents, the transient model is simplified considering a steady state working condition. The equations of the direct and inverse sequences of the voltage space vectors are evaluated.

A diagnostic index (correspondent to the sequence impedance) is defined for each space vector equation by the elaboration of the voltage and current space vector sequences. The same detection method is proposed for both HR and ISC faults.

The detection algorithm for HR faults is presented in its general shape, adding some improvements in terms of detection accuracy and showing the advantage of having a reduced number of star connections in multiphase machines. Analytical and experimental results validated the algorithm.

The ISC detection algorithm is analysed in deep for a three-phase IM. The ISC transient model is simulated and compared with experimental tests with an open loop V/f control of the machine. Then, the analytical model of the steady state behaviour with an ideal current control is presented. Instead, the closed loop control and the proposed detection algorithm has not been verified by experimental tests yet. However, the analytical results are in agreement with the FE and experimental analyses published by other research groups.

The basis for the development of an ISC detection algorithm in multiphase machines have been presented and will be implemented in future works, and better results than the one for the three-phase topology are expected.

The fault detection algorithm is based on a redundant system of PI regulators (direct and inverse PIs for each independent current space vector, as the ones needed in the case of the optimised open phase fault tolerant control described in Chapter 3). These PI regulators allow compensating the HR fault by adapting the voltage waveforms to the new machine impedances obtaining the desired output currents. Instead, how to better control the machine when an ISC fault is detected (without considering the shutdown solution) is still an open question.

References:

- [1] B. Mirafzal and N. A. O. Demerdash, "On innovative methods of induction motor interturn and broken-bar fault diagnostics," *IEEE Transactions on Industry Applications*, vol. 42, pp. 405-414, 2006.
- [2] A. Gandhi, T. Corrigan, and L. Parsa, "Recent Advances in Modeling and Online Detection of Stator Interturn Faults in Electrical Motors," *IEEE Transactions on Industrial Electronics*, vol. 58, pp. 1564-1575, 2011.
- [3] L. Sang Bin, R. M. Tallam, and T. G. Habetler, "A robust, on-line turn-fault detection technique for induction machines based on monitoring the sequence component impedance matrix," *IEEE Transactions on Power Electronics*, vol. 18, pp. 865-872, 2003.
- [4] A. Bellini, F. Filippetti, C. Tassoni, and G. A. Capolino, "Advances in Diagnostic Techniques for Induction Machines," *IEEE Transactions on Industrial Electronics*, vol. 55, pp. 4109-4126, 2008.
- [5] M. Mengoni, L. Zarri, A. Tani, Y. Gritli, G. Serra, F. Filippetti, *et al.*, "Online Detection of High-Resistance Connections in Multiphase Induction Machines," *IEEE Transactions on Power Electronics*, vol. 30, pp. 4505-4513, 2015.
- [6] A. Tani, L. Zarri, M. Mengoni, G. Serra, and D. Casadei, "Detection and localization of high resistance connections in quadruple three-phase induction motor drives," in *2014 International Conference on Electrical Machines (ICEM)*, 2014, pp. 2094-2100.
- [7] J. Yun, K. Lee, K. W. Lee, S. B. Lee, and J. Y. Yoo, "Detection and Classification of Stator Turn Faults and High-Resistance Electrical Connections for Induction Machines," *IEEE Transactions on Industry Applications*, vol. 45, pp. 666-675, 2009.
- [8] R. M. Tallam, T. G. Habetler, and R. G. Harley, "Transient model for induction machines with stator winding turn faults," *IEEE Transactions on Industry Applications*, vol. 38, pp. 632-637, 2002.
- [9] D. C. Patel and M. C. Chandorkar, "Modeling and Analysis of Stator Interturn Fault Location Effects on Induction Machines," *IEEE Transactions on Industrial Electronics*, vol. 61, pp. 4552-4564, 2014.
- [10] G. Crisci, *Costruzione schemi e calcolo degli avvolgimenti delle macchine elettriche rotanti*. Modena: S.T.E.M.- MUCCHI, 1978.
- [11] B. Vaseghi, N. Takorabet, and F. Meibody-Tabar, "Fault Analysis and Parameter Identification of Permanent-Magnet Motors by the Finite-Element Method," *IEEE Transactions on Magnetics*, vol. 45, pp. 3290-3295, 2009.

CHAPTER 5

Modelling of Multi Three-Phase Sectored Machines for Radial Force Control

The bearing element is one of the most critical component when dealing with high rotational speed and reliability of electrical machines [1]. The magnetic levitation would allow to overcome the aforementioned issues as well as to eliminate the bearing friction, maintenance and monitoring [2].

Nowadays, Active Magnetic Bearings (AMB) are the most exploited technology for the levitation. They are employed in several industrial and commercial applications such as compressors, spindles, flywheels and generators where high rotation speed is a requirement [3-5]. However, magnetic bearings generally lead to an increased overall length of the machine, added weight and higher cost of the drive. To this regard, Bearingless Motors (BMs) offer the advantage to generate both torque and suspension force in a single machine structure, consequently maximizing the power to weight and power to volume ratio.

The most exploited method to produce a controllable suspension force consists of providing the BMs with two separate windings, one responsible for motoring (torque generation) and the other for levitation (force generation). Several papers can be found in the literature adopting the two-winding configuration for bearingless operation [6-8]. However, the additional winding is still not a completely embedded solution. Therefore, different solutions have been proposed more recently, among which the multiphase BM is one of the most promising since it presents simpler construction, higher power density and better fault tolerance capabilities [9-11].

Multi Sector Permanent Magnet machines (MSPM) as a possible multiphase machine solution for radial force control

In this thesis, the MSPM multiphase winding configuration is analysed in terms of radial force control performance. The sectorization concept refers to a design in which a set of multiphase windings are supplied by different VSIs, and each of these resulting systems is located in a different stator area (sector), as in Fig. 5.1 for a triple three-phase sectored machine.

A multi-sector machine can be controlled as a system of redundant three-phase machines with coupled shafts, as in [12], but this approach to control a MSPM can be adopted only if the inverters under each sector are working exactly in the same way and the manufacturing and assembly asymmetries can be neglected. As soon as the currents in the sectors are differently controlled, the machine must be analysed by using a multiphase model, as the one presented in Chapter 1. The complexity of the control of such a system emerges when a detailed analysis is carried out to allow a radial force control, or if asymmetries and faults are taken into account in order to avoid performance deterioration [13-16].

In this thesis, radial force controls are proposed. The control algorithms exploit the SVD technique to generate appropriate magnetic field harmonics in the airgap responsible for both torque and suspension force generation [13, 14].

The SVD approach is an alternative solution to the methods based on the pseudo inverse matrix [17, 18] that have already been proposed for the analysis of MSPM machines.

The method is verified for the two degrees of freedom bearingless operation, controlling the radial position of the rotor while removing one bearing. Simulations and FEA results are provided to determine the force control performance and efficiency.

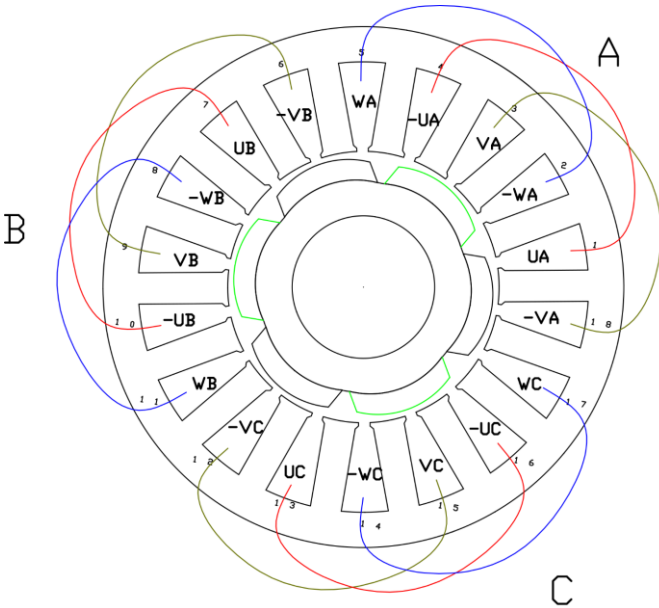


Fig. 5.1 – Triple three-phase sectored winding for a SPM machine. Machine drawing and winding layout.

Finally, experimental tests are performed to validate the proposed technique for the machine prototype, consisting in a conventional 18 slots - 6 poles PMSM with a re-arranged winding in a triple three-phase sectored configuration.

5.1 Modelling of Multi Three-Phase Sectored Stator Windings

A brief introduction to the multi three-phase sectored windings have been presented in the Chapter 2 (Section 2.2). Here below the analysis is extended and examined in depth.

In general, a multiphase sectored machine has an identical multiphase winding under each pole pair. The only difference with a standard multiphase machine with p pole pairs is that in a sectored one the phases located in each pole pair are not series (or parallel) connected with the phases under the others pole pairs. If the phases are controlled equally under the pole pairs, the model can be simplified to a standard multiphase one (in electrical degrees). Instead, if the phases in each pole pair are independently controlled, the model must be defined in the most general way as described in Chapter 1. Therefore, the model is developed describing the spatial quantities in mechanical angles and all the field harmonics in the airgap are taken into account.

The proposed model is initially generalized to whatever multi three-phase sectored winding, and then it is simplified to the triple three-phase layout in order to focus the analysis on the prototype under study. The hypothesis of the model are the same presented in Chapter 1. In particular, the method is based on the hypothesis of neglecting the tangential component of the magnetic field in the airgap. To make the analysis easier, only full pitch windings are taken into account (where full pitch means a 180 electrical degrees pitch).

General SVD model – additional transformation

Each three-phase subsystem of a multi three-phase machine can be completely described by the standard three-phase transformation.

As discussed in Chapter 3, the currents of each T -th three-phase subsystem are well represented by the following three-phase transformation:

$$\bar{i}_{TP1} = \frac{2}{3} \left(i_{TP,U} + i_{TP,V} e^{j\frac{2\pi}{3}} + i_{TP,W} e^{j\frac{4\pi}{3}} \right), \quad T = 1, 2, \dots, N_T, \quad P = 1, 2, \dots, p, \quad (5.1)$$

and

$$i_{TP0} = \frac{2}{3}(i_{TP,U} + i_{TP,V} + i_{TP,W}), \quad T = 1, 2, \dots, N_T, \quad P = 1, 2, \dots, p, \quad (5.2)$$

where the subscripts T and P are used to represent the T -th three-phase subsystem located in the P -th pole pair. The subscripts U, V and W are used to define the phases of each three-phase subsystem as shown in Fig. 5.1. The general transformation is:

$$\bar{i}_{TP,h} = \frac{2}{3} \left(i_{TP,U} + i_{TP,V} e^{j\frac{2\pi}{3}} + i_{TP,W} e^{j\frac{4\pi}{3}} \right), \quad T = 1, 2, \dots, N_T, \quad P = 1, 2, \dots, p, \quad (5.3)$$

with the relative inverse transformation:

$$i_{TP,k} = \frac{i_{TP,0}}{2} + \Re \left\{ \bar{i}_{TP,1} e^{-j\frac{2\pi}{3}(Z_k-1)} \right\}, \quad k = U, V, W, \quad T = 1, 2, \dots, N_T, \quad P = 1, 2, \dots, p, \quad (5.4)$$

where $Z_U = 1$, $Z_V = 2$ and $Z_W = 3$ are the indexes that represent the phases of each three-phase subsystem.

The space vector transformation (2.53) allows defining the overall machine current space vectors as:

$$\bar{i}_h = \frac{2}{m} \sum_{x=1}^{N_s} i_x e^{j\frac{2\pi}{N_s}h(x-1)}. \quad (5.5)$$

However, because of the hypotheses of the used transformation, all the phases must have the same coils geometry (in terms of winding in the slots). The phases are only placed in different stator areas, the pitch of the coils of each phase is the same (π/p in mechanical radians) and so are their relative positions (ψ_y), number (N_C) and turns number in each one (N). It results that for a three-phase subsystem in one pole pair, the angle that defines the position of each phase is in the position of the mechanical magnetic axis of the considered phase, in the radial outgoing direction and never in the opposite direction. This allows defining a symmetry in the axis of the full winding. This means that the general transformation is always a symmetrical one and it is not defined according to the common convention for the positive currents as in (5.3). The general transformation (3.45) results as:

$$\begin{aligned} \bar{i}_h &= \frac{2}{3N_T P} \sum_{T=1}^{N_T} \sum_{P=1}^P \left(i_{TP,U} e^{j\frac{2\pi}{N_s}h(x_{TP,U}-1)} - i_{TP,V} e^{j\frac{2\pi}{N_s}h(x_{TP,U}-1-N_T)} - i_{TP,W} e^{j\frac{2\pi}{N_s}h(x_{TP,U}-1+N_T)} \right) = \\ &= \frac{2}{3N_T P} \sum_{T=1}^{N_T} \sum_{P=1}^P \left(i_{TP,U} - i_{TP,V} e^{-j\frac{2\pi}{N_s}hN_T} - i_{TP,W} e^{j\frac{2\pi}{N_s}hN_T} \right) e^{j\frac{2\pi}{N_s}h(x_{TP,U}-1)}, \end{aligned} \quad (5.6)$$

where $x_{TP,U}$ is the number that identifies the slots where the central phases of each three-phase subsystem start, considering that the first phase of the first three-phase subsystem under the first pole pair is in the first slot: $x_{1,1,U} = 1$ ($x_{A,U} = 1$ in Fig. 5.1). Note that if there are more slot

per pole and per phase (q), it is enough to consider an equivalent number of machine slots equal to $N_s' = \frac{N_s}{q}$ in (5.6) as described in Chapter 2.

Introducing (5.4) in (5.6) and considering all the three-phase subsystems independently star connected ($i_{TP,0} = 0$, according to the rules that are commonly used to design a winding for the machine torque control), it is possible to write (3.45) with the following simplifications:

$$\begin{aligned}
 \bar{i}_h &= \frac{2}{3N_T P} \sum_{T=1}^{N_T} \sum_{P=1}^p \left(i_{TP,U} e^{j\frac{2\pi}{N_s} h(x_{TP,U}-1)} - i_{TP,V} e^{j\frac{2\pi}{N_s} h(x_{TP,U}-1-N_T)} - i_{TP,W} e^{j\frac{2\pi}{N_s} h(x_{TP,U}-1+N_T)} \right) = \\
 &= \frac{2}{3N_T P} \sum_{T=1}^{N_T} \sum_{P=1}^p \left(\Re \left\{ \bar{i}_{TP,1} e^{-j\frac{2\pi}{3}(Z_U-1)} \right\} - \Re \left\{ \bar{i}_{TP,1} e^{-j\frac{2\pi}{3}(Z_V-1)} \right\} e^{-j\frac{2\pi}{N_s} h N_T} - \Re \left\{ \bar{i}_{TP,1} e^{-j\frac{2\pi}{3}(Z_W-1)} \right\} e^{j\frac{2\pi}{N_s} h N_T} \right) e^{j\frac{2\pi}{N_s} h(x_{TP,U}-1)} = \\
 &= \frac{2}{3N_T P} \sum_{T=1}^{N_T} \sum_{P=1}^p \left(\Re \left\{ \bar{i}_{TP,1} \right\} - \Re \left\{ \bar{i}_{TP,1} e^{-j\frac{2\pi}{3}} \right\} e^{-j\frac{2\pi}{N_s} h N_T} - \Re \left\{ \bar{i}_{TP,1} e^{j\frac{2\pi}{3}} \right\} e^{j\frac{2\pi}{N_s} h N_T} \right) e^{j\frac{2\pi}{N_s} h(x_{TP,U}-1)} = \\
 &= \frac{1}{3N_T P} \sum_{T=1}^{N_T} \sum_{P=1}^p \left(\bar{i}_{TP,1} \left[1 - e^{-j\left(\frac{2\pi}{3} + \frac{2\pi}{N_s} h N_T\right)} - e^{j\left(\frac{2\pi}{3} + \frac{2\pi}{N_s} h N_T\right)} \right] + \bar{i}_{TP,1}^* \left[1 - e^{j\left(\frac{2\pi}{3} - \frac{2\pi}{N_s} h N_T\right)} - e^{-j\left(\frac{2\pi}{3} - \frac{2\pi}{N_s} h N_T\right)} \right] \right) e^{j\frac{2\pi}{N_s} h(x_{TP,U}-1)}.
 \end{aligned}$$

It is possible to introduce the two following new constants, depending on the winding layout and the harmonic order:

$$\begin{cases} c_{mh} = 1 - e^{-j\left(\frac{2\pi}{3} + \frac{2\pi}{N_s} h N_T\right)} - e^{j\left(\frac{2\pi}{3} + \frac{2\pi}{N_s} h N_T\right)} \\ c_{nh} = 1 - e^{j\left(\frac{2\pi}{3} - \frac{2\pi}{N_s} h N_T\right)} - e^{-j\left(\frac{2\pi}{3} - \frac{2\pi}{N_s} h N_T\right)} \end{cases} \quad (5.7)$$

By (5.7), (5.6) becomes:

$$\bar{i}_h = \frac{1}{3N_T P} \sum_{T=1}^{N_T} \sum_{P=1}^p \left(\bar{i}_{TP,1} c_{mh} + \bar{i}_{TP,1}^* c_{nh} \right) e^{j\frac{2\pi}{N_s} h(x_{TP,U}-1)}. \quad (5.8)$$

Because there are six slots (or equivalent slots if q is different from 1) for each three-phase subsystem, $x_{TP,U}$ is equal to $x_{TP,U} = 6N_T(P-1) + T$. The equation that describes the machine current space vectors as function of the standard three-phase ones is:

$$\bar{i}_h = \frac{1}{3N_T P} \sum_{T=1}^{N_T} \sum_{P=1}^p \left(\bar{i}_{TP,1} c_{mh} + \bar{i}_{TP,1}^* c_{nh} \right) e^{j\frac{2\pi}{P} h(P-1)} e^{j\frac{2\pi}{N_s} h(T-1)}. \quad (5.9)$$

The following set of current space vectors, named hereafter as ‘‘additional current space vectors’’, is introduced in order to simplify the space vector equations:

$$\begin{cases} \bar{i}_{mT,h} = \frac{1}{P} \sum_{P=1}^P \bar{i}_{TP,1} e^{j \frac{2\pi}{P} h(P-1)} \\ \bar{i}_{nT,h} = \frac{1}{P} \sum_{P=1}^P \bar{i}_{TP,1} e^{-j \frac{2\pi}{P} h(P-1)} \end{cases} \quad (5.10)$$

Where $\bar{i}_{mT,h}$ and $\bar{i}_{nT,h}$ represent the contributions of the current of all the three-phase subsystems under the different pole pairs that have the same electrical position ($\frac{2\pi p}{N_s} (T-1)$ electrical radians) to the full current space vector of h -th space (\bar{i}_h). Note that this approach is similar to the one described in Chapter 3 for defining the current sharing technique of not sectored multi three-phase machines.

The final current space vector equation for a multi three-phase sectored machine is:

$$\bar{i}_h = \frac{1}{3N_T} \sum_{T=1}^{N_T} (\bar{i}_{mT,h} c_{mh} + \bar{i}_{nT,h}^* c_{nh}) e^{j \frac{2\pi}{N_s} h(T-1)}. \quad (5.11)$$

The general inverse transformation of (5.11) is (2.54):

$$i_x = \frac{m}{2N_s} \sum_{x=0}^{N_s-1} \bar{i}_h e^{-j \frac{2\pi}{N_s} h(x-1)}, \quad (5.12)$$

evaluated in terms of current in the phase starting in the x -th slot (if there is not a phase starting in the x -th slot, (5.12) results in a zero value).

For the properties of the symmetrical transformation (2.5), and considering that the machine slots are in general an even number, (5.12) results also as (2.17).

$$i_x = \frac{i_0}{4} + \frac{i_{N_s/2}}{4} (-1)^{(x-1)} + \frac{1}{2} \sum_{h=1}^{N_s/2-1} \Re \left\{ \bar{i}_h e^{-j \frac{2\pi}{N_s} h(x-1)} \right\}. \quad (5.13)$$

Equation (5.12) takes into account for two real current space vectors (i_0 and $i_{N_s/2}$) and $N_s/2 - 2$ complex current space vectors. Therefore, the total number of current space vector components is N_s , that is twice the number of the phase currents (degrees of freedom of the system). Furthermore, the effective degrees of freedom are significantly reduced because of the star connection of the three-phase subsystems. This means that the model is defined for a redundant system of variables. However, the machine current space vectors can be evaluated by (5.11) with the additional set of current space vector defined by (5.10). The additional variables in (5.10) are reducible to the degrees of freedom of the machine, noticing that it is possible to define the following relationships:

$$\left\{ \begin{array}{l}
 \bar{i}_{mT,h} = \bar{i}_{ST} = \sum_{P=1}^p \bar{i}_{TP,1} \Leftrightarrow h = kp \\
 \bar{i}_{mT,h} = \bar{i}_{MT,1} = \frac{1}{P} \sum_{P=1}^p \bar{i}_{TP,1} e^{j\frac{2\pi}{P}(P-1)} \Leftrightarrow h = kp + 1 \\
 \bar{i}_{mT,h} = \bar{i}_{MT,2} = \frac{1}{P} \sum_{P=1}^p \bar{i}_{TP,1} e^{j\frac{2\pi}{P}2(P-1)} \Leftrightarrow h = kp + 2 \\
 \dots \\
 \bar{i}_{mT,h} = \bar{i}_{\frac{p}{2}T} = \frac{1}{P} \sum_{P=1}^p \bar{i}_{TP,1} e^{j\pi(P-1)} \Leftrightarrow h = kp \pm \frac{P}{2} \\
 \dots \\
 \bar{i}_{mT,h} = \bar{i}_{MT,2}^* \Leftrightarrow h = kp - 2 \\
 \bar{i}_{mT,h} = \bar{i}_{MT,1}^* \Leftrightarrow h = kp - 1
 \end{array} \right. \quad (5.14)$$

and

$$\left\{ \begin{array}{l}
 \bar{i}_{nT,h} = \bar{i}_{ST} = \sum_{P=1}^p \bar{i}_{TP,1} \Leftrightarrow h = kp \\
 \bar{i}_{nT,h} = \bar{i}_{NT,1} = \frac{1}{P} \sum_{P=1}^p \bar{i}_{TP,1} e^{-j\frac{2\pi}{P}(P-1)} \Leftrightarrow h = kp + 1 \\
 \bar{i}_{nT,h} = \bar{i}_{NT,2} = \frac{1}{P} \sum_{P=1}^p \bar{i}_{TP,1} e^{-j\frac{2\pi}{P}2(P-1)} \Leftrightarrow h = kp + 2 \\
 \dots \\
 \bar{i}_{nT,h} = \bar{i}_{\frac{p}{2}T} = \frac{1}{P} \sum_{P=1}^p \bar{i}_{TP,1} e^{-j\pi(P-1)} \Leftrightarrow h = kp \pm \frac{P}{2} \Leftrightarrow p = \text{even} \\
 \dots \\
 \bar{i}_{nT,h} = \bar{i}_{NT,2}^* \Leftrightarrow h = kp - 2 \\
 \bar{i}_{nT,h} = \bar{i}_{NT,1}^* \Leftrightarrow h = kp - 1
 \end{array} \right. \quad (5.15)$$

It results that there are $N_T \frac{p-2}{2}$ ($N_T \frac{p-1}{2}$ if p is an odd number) independent additional current space vectors $\bar{i}_{mT,h}$ and $\bar{i}_{nT,h}$ plus N_T independent current space vector \bar{i}_{ST} (plus N_T independent current space vector $\bar{i}_{\frac{p}{2}T}$ if p is an even number). There are in total

$$\left(N_T \frac{p-2}{2} + N_T \frac{p-2}{2} + 2N_T \right) = N_T p \quad (\text{or} \quad \left(N_T \frac{p-1}{2} + N_T \frac{p-1}{2} + N_T \right) = N_T p, \text{ if } p \text{ is odd})$$

additional current space vectors that completely describe the machine behaviour. Each additional current space vector is represented by its real and imaginary parts, resulting in $2N_T p$ independent variables for describing the system. Because the total number of independent three-phase subsystems is equal to $N_T p$ and each three-phase subsystem has two degrees of freedom for its current control (three currents and a star connection constraint), the effective degrees of freedom in the current control of the machine is $2N_T p$. This result is important,

because allows completely describing the machine behaviour and defining its control algorithm considering only the independent additional vectors ($\bar{i}_{MT,h}$, $\bar{i}_{NT,h}$ and \bar{i}_{ST}).

Transformation and inverse transformation: summary

In order to take into account for the degrees of freedom of the current control of a multi three-phase sectored machine, the proposed general transformation (5.11) is:

$$\bar{i}_h = \frac{1}{3N_T} \sum_{T=1}^{N_T} \left(\bar{i}_{mT,h} c_{mh} + \bar{i}_{nT,h}^* c_{nh} \right) e^{j \frac{2\pi}{N_s} h(T-1)},$$

where the current space vectors $\bar{i}_{mT,h}$ and $\bar{i}_{nT,h}$ are fully defined by (5.14) and (5.15) for $N_T p$

($N_T p$ is the total number of three-phase subsystems) additional independent vectors

($\bar{i}_{MT,h}$, $\bar{i}_{NT,h}$, \bar{i}_{ST} , plus $\frac{\bar{i}_{pT}}{2}$ if p is even).

Once the independent additional vectors ($\bar{i}_{MT,h}$, $\bar{i}_{NT,h}$ and \bar{i}_{ST}) are defined, it is possible to use (5.11) and finally (5.13) for evaluating the phase quantities from the space vector ones as:

$$i_x = \frac{i_0}{4} + \frac{i_{N_s/2}}{4} (-1)^{(x-1)} + \frac{1}{2} \sum_{x=1}^{N_s/2-1} \Re \left\{ \bar{i}_h e^{-j \frac{2\pi}{N_s} h(x-1)} \right\}.$$

General SVD model – Voltage equations for MSPM machines

The general voltage equation for a MSPM multiphase machine (2.94) is:

$$\bar{v}_h = R_s \bar{i}_h + Ll \frac{d\bar{i}_h}{dt} + \sum_{\rho=0}^{N_s-1} \overline{Ml}_{h\rho} \frac{d\bar{i}_\rho}{dt} + \frac{d\bar{\phi}_h}{dt}, \quad (5.16)$$

As done in Chapter 2, the mutual leakage inductances between the different phases are neglected (in other words $\overline{Ml}_{h\rho}$ is zero), leading to:

$$\bar{v}_h = R_s \bar{i}_h + Ll \frac{d\bar{i}_h}{dt} + \frac{d\bar{\phi}_h}{dt}, \quad (5.17)$$

where the linked flux space vector $\bar{\phi}_h$ takes into account for the self inductance of the h -th space and the PM linked flux.

If the magnets are symmetrical and equal in each pole pairs, their effects in terms of space vector equations is defined as in an electrical model of the machine by (2.145). Adding the

magnet pitch shortening parameter Sh_{PM} (reduction of the magnets pitch in per unit), the magnet related linked flux space vector is:

$$\begin{aligned} \bar{\phi}_{PM,h} \left(\frac{h}{p} \right)_{\text{odd.int}} &= \frac{2}{m} \mu_0 L R p q N N_s \frac{4 B_r \tau_M p}{\mu_M \pi \delta} \left[\sum_{\substack{y=0 \\ \left(\frac{yN_s+h}{p} \right)_{\text{odd.int}}}}^{\infty} \frac{K_{a(yN_s+h)} K_{skew(yN_s+h)}}{(yN_s+h)^2} \sin \left((yN_s+h) \frac{\pi(1-Sh_{PM})}{2p} \right) e^{j(yN_s+h)g_m} \right] + \\ &+ \frac{2}{m} \mu_0 L R p q N N_s \frac{4 B_r \tau_M p}{\mu_M \pi \delta} \left[\sum_{\substack{y=\left(\frac{h}{N_s} \right)_{\text{int}} \\ \left(\frac{yN_s-h}{p} \right)_{\text{odd.int}}}}^{\infty} \frac{K_{a(yN_s-h)} K_{skew(yN_s-h)}}{(yN_s-h)^2} \sin \left((yN_s-h) \frac{\pi(1-Sh_{PM})}{2p} \right) e^{-j(yN_s-h)g_m} \right]. \end{aligned} \quad (5.18)$$

The self linked flux component is still defined by (2.117) as:

$$\bar{\phi}_{self,h} = L_h \bar{i}_h, \quad (5.19)$$

with the h -space self inductance defined as:

$$L_h = \frac{2 \mu_0 L R N_s}{\pi \delta} \left[\sum_{y=0}^{\infty} \left(\frac{p q N K_{a(yN_s+h)}}{(yN_s+h)} \right)^2 + \sum_{y=\left(\frac{h}{N_s} \right)_{\text{int}}}^{\infty} \left(\frac{p q N K_{a(yN_s-h)}}{(yN_s-h)} \right)^2 \right].$$

The final voltage space vector equation for a MSPM machine results as:

$$\bar{v}_h = R_s \bar{i}_h + (L_l + L_h) \frac{d\bar{i}_h}{dt} + \frac{d\bar{\phi}_{PM,h}}{dt}. \quad (5.20)$$

To define (5.20) it is also possible to take into account for the reduced degrees of freedom of the system considering only the existing phases in the generation of the linked fluxes produced by the armature itself. This analysis is presented in the following subsection.

MSPM particular SVD model – Voltage equations for MSPM machines

In order to verify the general method, it is also possible to reduce the number of variables in the definition of the linked flux space vector $\bar{\phi}_h$. This can be done reanalysing the linked flux space vector equation considering only the linked fluxes with the existing x -th phases:

$$\bar{\phi}_h = \frac{2}{m} \sum_{\rho=1}^{\infty} \frac{\mu_0 R p q N K_{a\rho}}{\rho} \left(\int_{z=0}^L \bar{H}_\rho(z) dz \sum_{x=1}^{N_s} \bar{\alpha}^{-(\rho-h)(x-1)} + \int_{z=0}^L \bar{H}_\rho^*(z) dz \sum_{x=1}^{N_s} \bar{\alpha}^{(\rho+h)(x-1)} \right), \quad (5.21)$$

with the reduced number of considered variables, if the anisotropy of the magnetic circuit is neglected, it is possible to separately consider the magnets effect $\bar{\phi}_{PM,h}$ from the mutual effect with all the other spaces generated by the armature field $\bar{\phi}_{mutual,h\rho}$ as:

$$\bar{\phi}_h = \bar{\phi}_{PM,h} + \sum_{\rho=1}^{\infty} \bar{\phi}_{mutual,h\rho} . \quad (5.22)$$

The magnet effect is still described by (5.18), while the mutual effects with the other spaces are taken into account in the analysis of the term $\bar{\phi}_{mutual,h\rho}$ defined as:

$$\bar{\phi}_{mutual,h\rho} = \frac{2\mu_0 RLpqN}{m} \frac{K_{a\rho}}{\rho} \left(\bar{H}_\rho \sum_{x=1}^{N_s} \bar{\alpha}^{-(\rho-h)(x-1)} + \bar{H}_\rho^* \sum_{x=1}^{N_s} \bar{\alpha}^{(\rho+h)(x-1)} \right), \quad (5.23)$$

that can be written as well as:

$$\bar{\phi}_{mutual,h\rho} = \frac{2\mu_0 RL}{\pi\delta} \left(\frac{pqNK_{a\rho}}{\rho} \right)^2 \left(\bar{i}_\rho \sum_{x=1}^{N_s} \bar{\alpha}^{-(\rho-h)(x-1)} + \bar{i}_\rho^* \sum_{x=1}^{N_s} \bar{\alpha}^{(\rho+h)(x-1)} \right), \quad (5.24)$$

alternatively, introducing the partial mutual space vector inductances, $\bar{m}_{h\rho}^+$ and $\bar{m}_{h\rho}^-$, as:

$$\bar{\phi}_{mutual,h\rho} = \bar{i}_\rho \bar{m}_{h\rho}^+ + \bar{i}_\rho^* \bar{m}_{h\rho}^-, \quad (5.25)$$

with:

$$\bar{m}_{h\rho}^+ = \frac{2\mu_0 RL}{\pi\delta} \left(\frac{pqNK_{a\rho}}{\rho} \right)^2 \sum_{x=1}^{N_s} \bar{\alpha}^{-(\rho-h)(x-1)},$$

$$\bar{m}_{h\rho}^- = \frac{2\mu_0 RL}{\pi\delta} \left(\frac{pqNK_{a\rho}}{\rho} \right)^2 \sum_{x=1}^{N_s} \bar{\alpha}^{(\rho+h)(x-1)}.$$

It is worth to note that in the general model the $\bar{m}_{h\rho}^+$ and $\bar{m}_{h\rho}^-$ parameters are always zero or equal to N_s , while considering only the m existing phases, they can be equal to m or others complex numbers.

The equation of the armature related linked flux could be simplified as:

$$\begin{aligned} \sum_{\rho=1}^{\infty} \bar{\phi}_{mutual,h\rho} &= \sum_{\rho=1}^{\infty} \bar{i}_\rho \bar{m}_{h\rho}^+ + \bar{i}_\rho^* \bar{m}_{h\rho}^- = \sum_{\rho=1}^{N_s} \sum_{y=0}^{\infty} \left(\bar{m}_{h(yN_s+\rho)}^+ \bar{i}_\rho + \bar{m}_{h(yN_s+\rho)}^- \bar{i}_\rho^* \right) = \\ &= \sum_{\rho=1}^{N_s/2-1} \sum_{y=0}^{\infty} \left(\bar{m}_{h(yN_s+\rho)}^+ + \bar{m}_{h(yN_s+N_s-\rho)}^- \right) \bar{i}_\rho + \sum_{\rho=1}^{N_s/2-1} \sum_{y=0}^{\infty} \left(\bar{m}_{h(yN_s+\rho)}^- + \bar{m}_{h(yN_s+N_s-\rho)}^+ \right) \bar{i}_\rho^* + \\ &+ \sum_{y=0}^{\infty} \left(\bar{m}_{h(yN_s+N_s/2)}^+ + \bar{m}_{h(yN_s+N_s/2)}^- \right) \bar{i}_{N_s/2} + \sum_{y=0}^{\infty} \left(\bar{m}_{h(yN_s+N_s)}^+ + \bar{m}_{h(yN_s+N_s)}^- \right) \bar{i}_{N_s}. \end{aligned} \quad (5.26)$$

Considering the space vector relationships, (5.22) results as:

$$\bar{\phi}_h = \bar{\phi}_{PM,h} + \sum_{\rho=1}^{N_s/2-1} (\bar{M}_{h\rho}^+ \bar{i}_\rho + \bar{M}_{h\rho}^- \bar{i}_\rho^*) + \bar{M}_{hN_s/2} \bar{i}_{N_s/2} + \bar{M}_{hN_s} \bar{i}_{N_s}, \quad h=1,2,\dots,N_s, \quad (5.27)$$

with the new complex parameters, named as “mutual space vector inductances”, defined as:

$$\bar{M}_{h\rho}^+ = \sum_{y=0}^{\infty} (\bar{m}_{h(yN_s+\rho)}^+ + \bar{m}_{h(yN_s+N_s-\rho)}^-), \quad \bar{M}_{h\rho}^- = \sum_{y=0}^{\infty} (\bar{m}_{h(yN_s+\rho)}^- + \bar{m}_{h(yN_s+N_s-\rho)}^+),$$

$$\bar{M}_{hN_s/2} = \sum_{y=0}^{\infty} (\bar{m}_{h(yN_s+N_s/2)}^+ + \bar{m}_{h(yN_s+N_s/2)}^-), \quad \bar{M}_{hN_s} = \sum_{y=0}^{\infty} (\bar{m}_{h(yN_s+N_s)}^+ + \bar{m}_{h(yN_s+N_s)}^-).$$

It results that the mutual space vector inductances for the analysed machine are evaluated as:

$$\bar{M}_{h\rho}^+ = \frac{2\mu_0 RL(pqN)^2}{\pi\delta} \sum_{y=0}^{\infty} \left[\left(\frac{K_{a(yN_s+\rho)}}{(yN_s+\rho)} \right)^2 \sum_{x=1}^{N_s} \bar{\alpha}^{-(yN_s+\rho-h)(x-1)} + \left(\frac{K_{a(yN_s+N_s-\rho)}}{(yN_s+N_s-\rho)} \right)^2 \sum_{x=1}^{N_s} \bar{\alpha}^{(yN_s+N_s-\rho+h)(x-1)} \right],$$

$$\bar{M}_{h\rho}^- = \frac{2\mu_0 RL(pqN)^2}{\pi\delta} \sum_{y=0}^{\infty} \left[\left(\frac{K_{a(yN_s+\rho)}}{(yN_s+\rho)} \right)^2 \sum_{x=1}^{N_s} \bar{\alpha}^{(yN_s+\rho+h)(x-1)} + \left(\frac{K_{a(yN_s+N_s-\rho)}}{(yN_s+N_s-\rho)} \right)^2 \sum_{x=1}^{N_s} \bar{\alpha}^{-(yN_s+N_s-\rho-h)(x-1)} \right],$$

$$\bar{M}_{hN_s/2} = \frac{2\mu_0 RL(pqN)^2}{\pi\delta} \sum_{y=0}^{\infty} \left[\left(\frac{K_{a(yN_s+N_s/2)}}{(yN_s+N_s/2)} \right)^2 \sum_{x=1}^{N_s} \bar{\alpha}^{-(yN_s+N_s/2-h)(x-1)} + \left(\frac{K_{a(yN_s+N_s/2)}}{(yN_s+N_s/2)} \right)^2 \sum_{x=1}^{N_s} \bar{\alpha}^{(yN_s+N_s/2+h)(x-1)} \right],$$

$$\bar{M}_{hN_s} = \frac{2\mu_0 RL(pqN)^2}{\pi\delta} \sum_{y=0}^{\infty} \left[\left(\frac{K_{a(yN_s+N_s)}}{(yN_s+N_s)} \right)^2 \sum_{x=1}^{N_s} \bar{\alpha}^{-(yN_s+N_s-h)(x-1)} + \left(\frac{K_{a(yN_s+N_s)}}{(yN_s+N_s)} \right)^2 \sum_{x=1}^{N_s} \bar{\alpha}^{(yN_s+N_s+h)(x-1)} \right] = 0.$$

The final voltage space vector equation for a MSPM machine results as:

$$\bar{v}_h = R_s \bar{i}_h + Ll \frac{d\bar{i}_h}{dt} + \sum_{\rho=1}^{N_s/2-1} \left(\bar{M}_{h\rho}^+ \frac{d\bar{i}_\rho}{dt} + \bar{M}_{h\rho}^- \frac{d\bar{i}_\rho^*}{dt} \right) + \bar{M}_{hN_s/2} \frac{d\bar{i}_{N_s/2}}{dt} + \frac{d\bar{\phi}_{PM,h}}{dt}. \quad (5.28)$$

The equivalence of (5.20) and (5.28) has been numerically verified for a case study of triple three-phase MSPM machine.

General SVD model – Torque and Force for MSPM machines

Torque equation

The general torque equation for a SPM machine can be evaluated as described in Chapter 1, adding the effect of the PM pitch shortening and considering only the components related to the odd harmonics multiple of the pole pairs number p , as:

$$T = \frac{T \binom{N_s}{2} \frac{N_s}{2} = k_{odd} p}{2} + \sum_{h=k_{odd} p}^{N_s/2-1} T_h, \quad (5.29)$$

where:

$$T_{PM,h} = \Re \left\{ \sum_{\substack{y=0 \\ \left(\frac{yN_s+h}{p}\right)_{odd,int}}}^{\infty} jK_{T,PM,y,h}^+ e^{j(yN_s+h)g_m} \bar{i}_h^* \right\} + \Re \left\{ \sum_{\substack{y=\left(\frac{h}{N_s}\right)_{int} \\ \left(\frac{yN_s-h}{p}\right)_{odd,int}}}^{\infty} -jK_{T,PM,y,h}^- e^{-j(yN_s-h)g_m} \bar{i}_h^* \right\}, \quad (5.30)$$

with the direct (+) and inverse (-) sequence torque constants related to the h -th armature current space vector as:

$$K_{T,PM,y,h}^{\pm} = m\mu_0 L R p^2 q N \frac{4B_r \tau_M}{\mu_M \pi \delta} \frac{K_{a(yN_s \pm h)} K_{skew(yN_s \pm h)}}{(yN_s \pm h)} \sin \left((yN_s \pm h) \frac{\pi(1 - Sh_{PM})}{2p} \right),$$

where Sh_{PM} is the PM pitch shortening in p.u.. It is worth noticing that only the field harmonics odd multiple of p are considered in the torque equation. Therefore, the torque is only related to the additional current vectors \bar{i}_{ST} ($T = 1, 2, \dots, N_T$) defined in (5.14).

Force equation

The general force equation for an electrical machine can be evaluated as described in Chapter 2 by (2.257) as:

$$\bar{F} = \frac{\pi\mu_0 R}{4} \int_0^L \sum_{h=1}^{\infty} [\bar{H}_h \bar{H}_{h-1}^* + \bar{H}_h^* \bar{H}_{h+1}] dz. \quad (5.31)$$

It is interesting to note that the radial force (the resultant of the magnetic pressure acting on the rotor) is generated by the interaction of the odd and even field harmonics, no matter how they are generated. It results that it is also possible to apply a force on a laminated ferromagnetic rotor without windings or magnets by just a proper control of the stator currents. Fig. 5.2 shows this physical principle, considering two field harmonics with different polarities generated by two windings. Multiphase machines, with suitable winding designs as the sectored one, can generate field harmonics with different polarities too.

In this thesis, the focus is on the radial force control of isotropic MSPM machines with multi three-phase windings. The hypothesis of isotropic machine results in neglecting the eccentricities in the model.

Considering a MSPM machine, the magnetic field in the airgap H is the sum of the armature field (produced by the stator currents) and the magnets one.

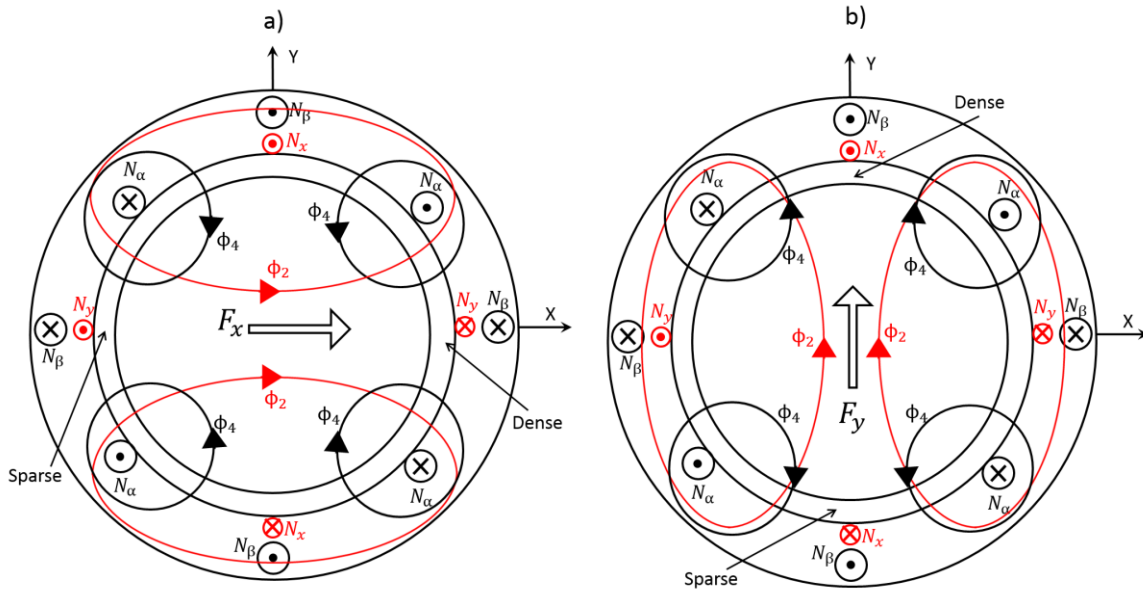


Fig. 5.2 – Force generation principle for a solid rotor machine in a dual-winding configuration. In black it is represented the magnetomotive force distribution of a 4-poles winding; in red it is represented the magnetomotive force distribution of a 2-poles winding. The two distributions represent the magnetomotive forces of typical three-phase star connected machines, defined by their α - β components.

Equation (2.47) defines the harmonics of the magnetic field for a multiphase winding as:

$$\bar{H}_{cu,h} = \frac{Nmpq}{\pi\delta} \frac{K_{ah}}{h} \bar{i}_h, \quad (5.32)$$

with K_{ah} the winding factor related to the h -th field harmonic (2.45). For a multi three-phase sectored machine with full pitch windings, the winding factor is defined as:

$$K_{ah} = \frac{\sum_{y=1}^{N_c} \sin\left(h \frac{\pi}{2p}\right) e^{j h \frac{2\pi}{N_s} \left(y - \frac{N_c+1}{2}\right)}}{pq}. \quad (5.33)$$

Equation (2.134) defines the harmonics of the magnetic field for a SPM symmetrical rotor as:

$$\bar{H}_{PM,ph_{odd}}(z) = \frac{4B_r \tau_M}{\mu_M h_{odd} \pi \delta} \sin\left(h_{odd} \frac{\pi(1 - Sh_{PM})}{2}\right) e^{jph_{odd}\vartheta_m} e^{jph_{odd}\psi_{skew,w}} \quad z \in \left[z_w - \frac{\Delta L_w}{2}; z_w + \frac{\Delta L_w}{2} \right], \quad (5.34)$$

where Sh_{PM} is the PM pitch shortening in p.u..

It results that the force components can be separated in four terms as:

$$\bar{F} = \bar{F}_{cu,cu} + \bar{F}_{cu,PM} + \bar{F}_{PM,cu} + \bar{F}_{PM,PM}, \quad (5.35)$$

where:

$$\bar{F}_{cu,cu} = \frac{\pi\mu_0 RL}{4} \sum_{h=1}^{\infty} [\bar{H}_{cu,h} \bar{H}_{cu,h-1}^* + \bar{H}_{cu,h}^* \bar{H}_{cu,h+1}], \quad (5.36)$$

$$\bar{F}_{cu,PM} = \frac{\pi\mu_0 R}{4} \int_0^L \sum_{h=1}^{\infty} [\bar{H}_{PM,h} \bar{H}_{cu,h-1}^* + \bar{H}_{PM,h}^* \bar{H}_{cu,h+1}] dz, \quad (5.37)$$

$$\bar{F}_{PM,cu} = \frac{\pi\mu_0 R}{4} \int_0^L \sum_{h=1}^{\infty} [\bar{H}_{cu,h} \bar{H}_{PM,h-1}^* + \bar{H}_{cu,h}^* \bar{H}_{PM,h+1}] dz, \quad (5.38)$$

$$\bar{F}_{PM,PM} = \frac{\pi\mu_0 RL}{4} \sum_{h=1}^{\infty} [\bar{H}_{PM,h} \bar{H}_{PM,h-1}^* + \bar{H}_{PM,h}^* \bar{H}_{PM,h+1}]. \quad (5.39)$$

In a standard SPM machine, the PM field harmonics are only odd multiples of the pole pairs number, as in (5.34). Therefore, for a given (ph_{odd})-th order PM field harmonic ($\bar{H}_{PM,ph_{odd}}$), the ($ph_{odd} \pm 1$)-th PM field harmonics are even ones, and therefore they are always equal to zero in a standard magnets geometry. It results that all the components in (5.39) are always zero ($\bar{F}_{PM,PM} = 0$). This is no more true if the magnets are asymmetrical or partially demagnetised.

Equations (5.37) and (5.38) are exactly equal. Therefore, (5.35) is written in terms of the two following components:

$$\bar{F}_{cu} = \bar{F}_{cu,cu} = \frac{\pi\mu_0 RL}{4} \sum_{h=1}^{\infty} [\bar{H}_{cu,h} \bar{H}_{cu,h-1}^* + \bar{H}_{cu,h}^* \bar{H}_{cu,h+1}], \quad (5.40)$$

and

$$\bar{F}_{PM} = \bar{F}_{PM,cu} + \bar{F}_{cu,PM} = 2\bar{F}_{cu,PM} = \frac{\pi\mu_0 RL}{2} \sum_{h=1}^{\infty} K_{skew,h} [\bar{H}_{PM,h} \bar{H}_{cu,h-1}^* + \bar{H}_{PM,h}^* \bar{H}_{cu,h+1}], \quad (5.41)$$

with $K_{skew,h}$ defined by (2.137) as:

$$K_{skew,h} = \frac{1}{N_{skew}} \sum_{w=1}^{N_{skew}} e^{jh \frac{\Delta\theta_{skew}}{N_{skew}} (w - \frac{N_{skew}+1}{2})},$$

and considering the PM field harmonics with the amplitude obtained in one skew slice and with the phase as the magnetic axis of the overall skewed machine.

The resulting force equation is:

$$\bar{F} = \bar{F}_{cu} + \bar{F}_{PM}, \quad (5.42)$$

being aware of the meaning of the two components: the first one represents the radial force produced by the interaction between the currents related field harmonics (as shown in Fig. 5.2); the second one represents the radial force produced by the interaction between the currents and the magnets related field harmonics.

Force equation: current components

The first component of the radial force can be evaluated by (5.32) and (5.33) as:

$$\begin{aligned}
 \bar{F}_{cu} &= \frac{\pi\mu_0 RL}{4} \sum_{h=1}^{\infty} \left[\bar{H}_{cu,h} \bar{H}_{cu,h-1}^* + \bar{H}_{cu,h}^* \bar{H}_{cu,h+1} \right] = \\
 &= \frac{\pi\mu_0 RL}{4} \left(\frac{Nmpq}{\pi\delta} \right)^2 \sum_{h=1}^{\infty} \left[\left(\frac{K_{ah}}{h} \frac{K_{a,h-1}}{h-1} \right) \bar{i}_h \bar{i}_{h-1}^* + \left(\frac{K_{ah}}{h} \frac{K_{a,h+1}}{h+1} \right) \bar{i}_h^* \bar{i}_{h+1} \right] = \\
 &= \sum_{h=1}^{\infty} \left[K_{cu(h,h-1)} \bar{i}_h \bar{i}_{h-1}^* + K_{cu(h,h+1)} \bar{i}_h^* \bar{i}_{h+1} \right] = \sum_{h=1}^{\infty} \left[2K_{cu(h,h+1)} \bar{i}_h^* \bar{i}_{h+1} \right] = \\
 &= \sum_{h=1}^{\infty} \left[K_{cu,h} \bar{i}_h^* \bar{i}_{h+1} \right],
 \end{aligned} \tag{5.43}$$

with the new parameters, named current force constants, defined as:

$$K_{cu,h} = \frac{\pi}{2} \mu_0 RL \left(\frac{Nmpq}{\pi\delta} \right)^2 \left(\frac{K_{ah}}{h} \frac{K_{a,h+1}}{h+1} \right). \tag{5.44}$$

Force equation: magnet and current components

The second component of the radial force can be evaluated by (5.32), (5.33) and (5.34) as:

$$\begin{aligned}
 \bar{F}_{PM} &= \frac{\pi\mu_0 RL}{2} \sum_{h=1}^{\infty} K_{skew,h} \left[\bar{H}_{PM,h} \bar{H}_{cu,h-1}^* + \bar{H}_{PM,h}^* \bar{H}_{cu,h+1} \right] = \\
 &= \frac{\pi\mu_0 RL}{2} \frac{4B_r \tau_M}{\mu_M \pi\delta} \sum_{\substack{h=1 \\ h_{odd}}}^{\infty} \frac{K_{skew,ph}}{h} \sin\left(h \frac{\pi}{2}\right) \left[\bar{H}_{cu,ph-1}^* e^{jph\vartheta_m} + \bar{H}_{cu,ph+1} e^{-jph\vartheta_m} \right] = \\
 &= \frac{\mu_0 RL}{2} \frac{4B_r \tau_M}{\mu_M \delta} \frac{Nmpq}{\pi\delta} \sum_{\substack{h=1 \\ h_{odd}}}^{\infty} \frac{K_{skew,ph}}{h} \sin\left(\frac{h\pi(1-Sh_{PM})}{2}\right) \left[\frac{K_{a,ph-1}}{ph-1} \bar{i}_{ph-1}^* e^{jph\vartheta_m} + \frac{K_{a,ph+1}}{ph+1} \bar{i}_{ph+1} e^{-jph\vartheta_m} \right] = \\
 &= \sum_{\substack{h=1 \\ h_{odd}}}^{\infty} \left[K_{PM(ph,ph-1)} \bar{i}_{ph-1}^* e^{jph\vartheta_m} + K_{PM(ph,ph+1)} \bar{i}_{ph+1} e^{-jph\vartheta_m} \right],
 \end{aligned} \tag{5.45}$$

with the new parameter, named magnet force constant, defined as:

$$K_{PM(ph,ph\pm 1)} = \frac{\mu_0 RL}{2} \frac{4B_r \tau_M}{\mu_M \delta} \frac{Nmpq}{\pi\delta} \frac{K_{skew,ph}}{h} \sin\left(\frac{h\pi(1-Sh_{PM})}{2}\right) \frac{K_{a,ph\pm 1}}{ph\pm 1}, \tag{5.46}$$

The force constants (current and magnet ones) are used to evaluate the force resulting from the current control of MSPM machines.

5.2 Modelling of a Triple Three-Phase Sectored Machine (three pole pairs)

The general model for MSPM machines is simplified and in deep analysed in this section for the machine shown in Fig. 5.1. The machine has a single three-phase winding in each pole pair ($N_T = 1$) and three pole pairs ($p = 3$). The machine parameters used for defining the analytical model are shown in Table 5.1.

SVD transformation – Current space vectors

Considering a triple three-phase MSPM as the one in Fig. 5.1, (or Fig. 2.10 as well) the space vector transformation (3.45) is:

$$\bar{i}_h = \frac{2}{9} \sum_{x=18,1,2,6,7,8,12,13,14} i_x e^{j \frac{2\pi}{N_s} h(x-1)}. \quad (5.47)$$

It can be written by (5.11) with $N_T = 1$ as:

$$\bar{i}_h = \frac{1}{3} (\bar{i}_{m1,h} c_{mh} + \bar{i}_{n1,h}^* c_{nh}). \quad (5.48)$$

According to (5.14), (5.15) and (5.7), the transformations for all the independent current space vectors are, neglecting the T subscript ($T = 1$), as:

$$\left\{ \begin{array}{l} \bar{i}_1 = \frac{1}{3} (\bar{i}_M c_{m1} + \bar{i}_N^* c_{n1}) \\ \bar{i}_2 = \frac{1}{3} (\bar{i}_N c_{m2} + \bar{i}_M^* c_{n2}) \\ \bar{i}_4 = \frac{1}{3} (\bar{i}_M c_{m2} + \bar{i}_N^* c_{n4}) \\ \bar{i}_5 = \frac{1}{3} (\bar{i}_N c_{m1} + \bar{i}_M^* c_{n5}) \\ \bar{i}_7 = \frac{1}{3} (\bar{i}_N c_{n1} + \bar{i}_M^* c_{n5}) \\ \bar{i}_8 = \frac{1}{3} (\bar{i}_N c_{n2} + \bar{i}_M^* c_{n4}) \end{array} \right. \quad \text{and} \quad \left\{ \begin{array}{l} \bar{i}_0 = \frac{2}{3} (\bar{i}_S + \bar{i}_S^*) \\ \bar{i}_3 = \bar{i}_S \\ \bar{i}_6 = \frac{1}{3} (2\bar{i}_S - \bar{i}_S^*) \\ \bar{i}_9 = 0 \end{array} \right. \quad (5.49)$$

Table 5.1 – Machine main parameters used in the model.

Parameter	Value	Unit	Parameter	Value	Unit
Slots Number	18		Magnet thickness	4	mm
Phase Pitch	180	el deg	Magnet skew	0.5	slot
Active Length	91	mm	Skew slices	3	slices
Turns Number	22	series	Remanence	1.235	T
Average airgap radius	24.3	mm	PM Pitch reduction	17 (=100/6)	%
Tot. airgap	5	mm	Relative permeability	1.05	

with:

$$\left\{ \begin{array}{l} \bar{i}_M = \bar{i}_{m1,1} = \frac{1}{3} \left(\bar{i}_{A,1} + \bar{i}_{B,1} e^{j\frac{2\pi}{3}} + \bar{i}_{C,1} e^{-j\frac{2\pi}{3}} \right) \\ \bar{i}_N = \bar{i}_{n1,1} = \frac{1}{3} \left(\bar{i}_{A,1} + \bar{i}_{B,1} e^{-j\frac{2\pi}{3}} + \bar{i}_{C,1} e^{j\frac{2\pi}{3}} \right) \\ \bar{i}_S = \frac{1}{3} (\bar{i}_{A,1} + \bar{i}_{B,1} + \bar{i}_{C,1}) \end{array} \right. \quad (5.50)$$

The current space vectors are considered in two categories because of their physical meaning.

The main current space vector (\bar{i}_3) and the auxiliary ones (\bar{i}_h with $h = 0,1,\dots,9$) are directly related to the field harmonics with the same order. The additional current space vectors (\bar{i}_M ,

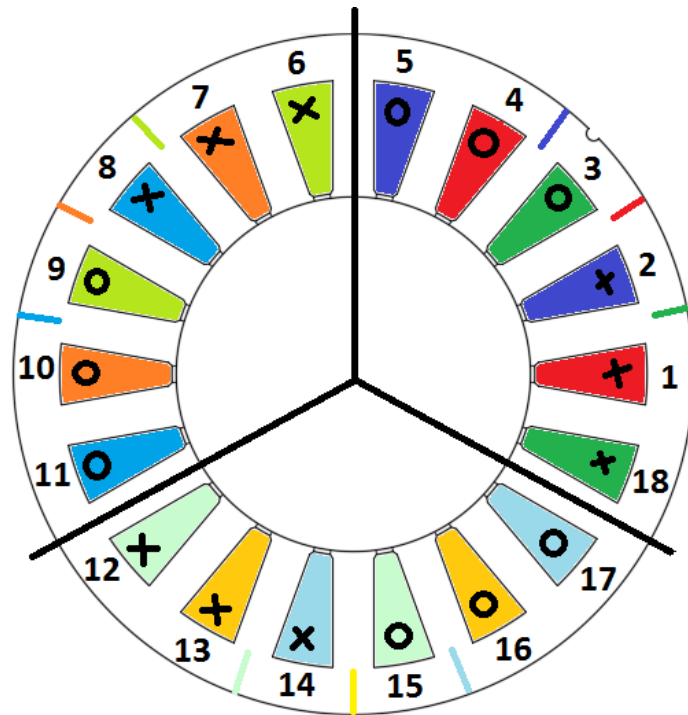


Fig. 5.3 – 18 slots and 3 pole pairs sectored winding 9-phase machine. The starting slots of the phases and their magnetic axes are highlighted with crosses in the slots and lines in the back iron respectively.

\bar{i}_N and \bar{i}_S) are used for taking into account of the machine current constraints according to the winding design, being directly related to the conventional current space vectors describing each three-phase subsystem.

The current space vectors related to the \bar{i}_M and \bar{i}_N additional vectors (first system of (5.49)) are always zero if the machine is controlled in the same way in all the pole pairs. Therefore, \bar{i}_M and \bar{i}_N represent what is different in the currents under the various pole pairs. On the other hand, the space vectors related to \bar{i}_S (second system of (5.49)) represent what is equally in the currents under the various pole pairs.

It is easy to conclude that in a standard machine control, the only additional space vector needed to control the machine is \bar{i}_S . Indeed, \bar{i}_S is equal to the 3rd current space vector ($p=3$), which is the main current vector of the equivalent model of the machine developed in electrical degrees.

As already mentioned, in case of a multi three-phase winding in each pole pair, there are in general N_T vectors that can be used for the machine control in electrical degrees (\bar{i}_{ST}).

The inverse transformation (5.13) for the triple three-phase sector winding is:

$$i_x = \frac{i_0}{4} + \frac{i_9}{4}(-1)^{(x-1)} + \frac{1}{2} \sum_{h=1}^8 \Re \left\{ \bar{i}_h e^{-j\frac{2\pi}{18}h(x-1)} \right\}, \quad x = 1, 2, \dots, 18. \quad (5.51)$$

Triple Three-Phase MSPM machine – Voltage Equations by General Method (redundant)

The voltage equation for a three pole pairs triple three-phase MSPM, neglecting the mutual leakage inductances between the different phases, (5.20) is:

$$\bar{v}_h = R_s \bar{i}_h + (Ll + L_h) \frac{d\bar{i}_h}{dt} + \frac{d\bar{\phi}_{PM,h}}{dt}, \quad (5.52)$$

where the h -space magnets back emf is:

$$\begin{aligned} \bar{\phi}_{PM,h} \left| \left(\frac{h}{3} \right)_{\text{odd,int}} \right. &= 16\mu_0 L R N 3 \frac{B_r \tau_M}{\mu_M \pi \delta} \left[\sum_{\substack{y=0 \\ \left(\frac{y18+h}{3} \right)_{\text{odd,int}}}}^{\infty} \frac{\sin\left((y18+h) \frac{\pi}{6} \right) K_{skew(y18+h)}}{(y18+h)^2} \sin\left((y18+h) \frac{\pi(1-Sh_{PM})}{6} \right) e^{j(y18+h)g_m} \right] + \\ &+ 16\mu_0 L R N 3 \frac{B_r \tau_M}{\mu_M \pi \delta} \left[\sum_{\substack{y=\left(\frac{h}{18} \right)_{\text{int}} \\ \left(\frac{y18-h}{3} \right)_{\text{odd,int}}}}^{\infty} \frac{\sin\left((y18-h) \frac{\pi}{6} \right) K_{skew(y18-h)}}{(y18-h)^2} \sin\left((y18-h) \frac{\pi(1-Sh_{PM})}{6} \right) e^{-j(y18-h)g_m} \right], \end{aligned} \quad (5.53)$$

and the h -space self inductance is defined as:

$$L_h = \frac{2\mu_0 LR18N^2}{\pi\delta} \left[\sum_{y=0}^{\infty} \left(\frac{\sin\left((y18+h)\frac{\pi}{6}\right)}{(y18+h)} \right)^2 + \sum_{y=\left(\frac{h}{18}\right)_{\text{int}}}^{\infty} \left(\frac{\sin\left((y18-h)\frac{\pi}{6}\right)}{(y18-h)} \right)^2 \right].$$

Table 5.2 shows the space self inductances. The advantage of the general model is that the space vector equations are completely independent. This allows controlling the machine as a sum of three-phase machines electromagnetically independent between each other (one every two degrees of freedom of the machine control).

Triple Three-Phase MSPM machine – Voltage Equations by Particular Method

The voltage equation for a three pole pairs triple three-phase MSPM, neglecting the mutual leakage inductances between the different phases, (5.28) is:

$$\bar{v}_h = R_s \bar{i}_h + Ll \frac{d\bar{i}_h}{dt} + \sum_{\rho=1}^8 \left(\bar{M}_{h\rho}^+ \frac{d\bar{i}_{\rho}}{dt} + \bar{M}_{h\rho}^- \frac{d\bar{i}_{\rho}^*}{dt} \right) + \bar{M}_{h9} \frac{di_9}{dt} + \frac{d\bar{\phi}_{PM,h}}{dt}, \quad (5.54)$$

where the stator winding factor is:

$$K_{ah} = \frac{\sin\left(h\frac{\pi}{6}\right)}{3}.$$

Therefore, the space vectors of the magnet linked fluxes is:

$$\begin{aligned} \bar{\phi}_{PM,h} \left| \left(\frac{h}{3} \right)_{\text{odd,int}} \right. &= 16\mu_0 LRN3 \frac{B_r \tau_M}{\mu_M \pi \delta} \left[\sum_{y=0}^{\infty} \frac{\sin\left((y18+h)\frac{\pi}{6}\right) K_{skew(y18+h)}}{(y18+h)^2} \sin\left((y18+h)\frac{\pi(1-Sh_{PM})}{6}\right) e^{j(y18+h)g_m} \right] + \\ &+ 16\mu_0 LRN3 \frac{B_r \tau_M}{\mu_M \pi \delta} \left[\sum_{y=\left(\frac{h}{18}\right)_{\text{int}}}^{\infty} \frac{\sin\left((y18-h)\frac{\pi}{6}\right) K_{skew(y18-h)}}{(y18-h)^2} \sin\left((y18-h)\frac{\pi(1-Sh_{PM})}{6}\right) e^{-j(y18-h)g_m} \right]. \end{aligned} \quad (5.55)$$

The mutual space vector inductances for the analysed machine are evaluated as:

Table 5.2 – Self inductance space parameters in μH .

h	0	1	2	3	4	5	6	7	8	9
1	0	778.46	601.9	375.54	170.41	39.99	0	26.57	72.58	93.86

$$\bar{M}_{h\rho}^+ = \frac{2\mu_0 R L N^2}{\pi\delta} \sum_{y=0}^{\infty} \left[\left(\frac{\sin\left((y18+\rho)\frac{\pi}{6}\right)}{(y18+\rho)} \right)^2 \sum_{x=1}^{18} \bar{\alpha}^{-(y18+\rho-h)(x-1)} + \left(\frac{\sin\left((y18+18-\rho)\frac{\pi}{6}\right)}{(y18+18-\rho)} \right)^2 \sum_{x=1}^{18} \bar{\alpha}^{(y18+18-\rho+h)(x-1)} \right],$$

$$\bar{M}_{h\rho}^- = \frac{2\mu_0 R L N^2}{\pi\delta} \sum_{y=0}^{\infty} \left[\left(\frac{\sin\left((y18+\rho)\frac{\pi}{6}\right)}{(y18+\rho)} \right)^2 \sum_{x=1}^{18} \bar{\alpha}^{(y18+\rho+h)(x-1)} + \left(\frac{\sin\left((y18+18-\rho)\frac{\pi}{6}\right)}{(y18+18-\rho)} \right)^2 \sum_{x=1}^{18} \bar{\alpha}^{-(y18+18-\rho-h)(x-1)} \right],$$

$$\bar{M}_{h9} = \frac{2\mu_0 R L N^2}{\pi\delta} \sum_{y=0}^{\infty} \left[\left(\frac{\sin\left((y18+18/2)\frac{\pi}{6}\right)}{(y18+18/2)} \right)^2 \sum_{x=1}^{18} \bar{\alpha}^{-(y18+18/2-h)(x-1)} + \left(\frac{\sin\left((y18+18/2)\frac{\pi}{6}\right)}{(y18+18/2)} \right)^2 \sum_{x=1}^{18} \bar{\alpha}^{(y18+18/2+h)(x-1)} \right].$$

Defining a machine model for the spaces from 0 to 9, as discussed in the previous subsection (for the current space vector analysis in (5.49)), it is possible to analyse which spaces may interact and how do they interact by Table 5.3 and Table 5.4. These tables show that all the mutual space vector constants are real numbers.

Table 5.3 and Table 5.4 allow completely solving the voltage space vector equations given the current space vector values.

The obtained results have been numerically compared with the one derived by the general model, leading to the same solution.

The drawback of the particular model is that the space vector equations are coupled between the various spaces even this coupling is just analytical, as verified by the numerical validation of the general model. It results that by using the general model it is possible to consider separately the control of the different spaces as if they would represent different equivalent three-phase machines acting on the same rotor, while the particular approach leads to additional calculation for the correct emf compensation.

Table 5.3 – Matrix of the machine space vector inductances in μm (direct sequence interactions $\bar{M}_{h\rho}^+$ and $\bar{M}_{hN_s/2}$)

$h \setminus \rho$	1	2	3	4	5	6	7	8	9
1	389.2	0.0	0.0	56.8	0.0	0.0	0.0	0.0	0.0
2	0.0	300.9	0.0	0.0	13.3	0.0	0.0	0.0	0.0
3	0.0	0.0	187.7	0.0	0.0	0.0	0.0	0.0	0.0
4	259.5	0.0	0.0	85.1	0.0	0.0	8.8	0.0	0.0
5	0.0	200.6	0.0	0.0	20.0	0.0	0.0	24.2	0.0
6	0.0	0.0	125.1	0.0	0.0	0.0	0.0	0.0	31.2
7	0.0	0.0	0.0	56.8	0.0	0.0	13.3	0.0	0.0
8	0.0	0.0	0.0	0.0	13.3	0.0	0.0	36.2	0.0
9	0.0	0.0	0.0	0.0	0.0	0.0	0.0	0.0	46.9
0	0.0	0.0	125.1	0.0	0.0	0.0	0.0	0.0	-15.6

Table 5.4 – Matrix of the machine space vector inductances in μH (inverse sequence interactions $\overline{M}_{h\rho}^-$)

$h \setminus \rho$	1	2	3	4	5	6	7	8
1	0.0	200.6	0.0	0.0	0.0	0.0	0.0	-12.1
2	259.5	0.0	0.0	0.0	0.0	0.0	-4.4	0.0
3	0.0	0.0	0.0	0.0	0.0	0.0	0.0	0.0
4	0.0	0.0	0.0	0.0	-6.7	0.0	0.0	0.0
5	0.0	0.0	0.0	-28.4	0.0	0.0	0.0	0.0
6	0.0	0.0	-62.6	0.0	0.0	0.0	0.0	0.0
7	0.0	-100.3	0.0	0.0	0.0	0.0	0.0	24.2
8	-129.7	0.0	0.0	0.0	0.0	0.0	8.8	0.0

Triple Three-Phase MSPM machine – Torque and Force

The torque and force equations (2.217) and (5.42) are simplified to the specific winding and analysed aiming to define a suitable machine control.

Torque equation

The torque equations (5.29)-(2.217) result from only the odd multiple of p current space vectors, associated to the additional current vector \vec{i}_s ($\vec{i}_s = \vec{i}_3$) as $T = \frac{T_9}{2} + T_3 = T_3 = T_{PM}$.

Therefore, the torque can be defined as:

$$T_{PM} = \Re \left\{ \sum_{y=0}^{\infty} jK_{T,PM,y,3}^+ e^{j(y18+3)g_m} \vec{i}_s^* \right\} + \Re \left\{ \sum_{y=1}^{\infty} -jK_{T,PM,y,3}^- e^{-j(y18-3)g_m} \vec{i}_s^* \right\}, \quad (5.56)$$

with:

$$K_{T,PM,y,3}^{\pm} = 27 \mu_0 L R N \frac{4B_r \tau_M}{\mu_M \pi \delta} \frac{K_{skew(y18 \pm 3)}}{(y18 \pm 3)} \sin \left((y18 \pm 3) \frac{\pi(1 - Sh_{PM})}{6} \right) \sin \left((y18 \pm 3) \frac{\pi}{6} \right).$$

Force equation

The force equation (5.42) results as:

$$\vec{F} = \vec{F}_{cu} + \vec{F}_{PM}, \quad (5.57)$$

where:

$$\bar{F}_{cu} = \sum_{h=1}^{\infty} [K_{cu,h} \bar{i}_h^* \bar{i}_{h+1}], \quad (5.58)$$

with the current force constant $K_{cu,h}$:

$$K_{cu,h} = \frac{\mu_0 RL}{2\pi\delta^2} N^2 9^2 \frac{\sin\left(h\frac{\pi}{6}\right) \sin\left((h+1)\frac{\pi}{6}\right)}{h(h+1)}, \quad (5.59)$$

and:

$$\bar{F}_{PM} = \sum_{\substack{h=1 \\ h_{odd}}}^{\infty} [K_{PM(3h,3h-1)} \bar{i}_{3h-1}^* e^{j3h\theta_m} + K_{PM(3h,3h+1)} \bar{i}_{3h+1} e^{-j3h\theta_m}], \quad (5.60)$$

with the magnet force constant $K_{PM(h,h\pm 1)}$:

$$K_{PM(h,h\pm 1)} = 6\mu_0 RL \frac{B_r \tau_M}{\mu_M \pi \delta^2} 9NK_{skew,h} \frac{\sin\left(h\frac{\pi(1-Sh_{PM})}{6}\right) \sin\left((h\pm 1)\frac{\pi}{6}\right)}{h(h\pm 1)} \Leftrightarrow h = 3k_{odd}. \quad (5.61)$$

Torque constants

Table 5.5 Table 3.2 shows the machine torque constants for the direct sequences of the armature field harmonics, comparing also them in per unit (p.u.) to the fundamental torque constant. In the same table, there are also the electrical frequencies of the torque ripples in per unit to the fundamental electrical frequency. This means that the real mechanical frequencies of these ripples are 3 times higher than the electrical ones. The lowest frequency torque ripple is at 18 times the mechanical frequency of the rotor. The amplitude of the torque ripples in p.u. of the fundamental torque are named $T_{PM,\rho}^{\pm}$ in Table 5.5. Indeed, the analysed machine has a single three-phase subsystem in each pole pair ($T=1$). Therefore, the torque ripples are directly related to the control of the fundamental torque component (as in the control of a conventional three-phase machine).

The simplified torque constants are compared with the evaluated for the real design ones, that is with a skew of half slot, obtained dividing the magnets in three segments along the axial direction. Furthermore, the model takes also into account for the magnet pitch shortening of 1/6 the magnet full pitch (0.17 in per unit to the theoretical pitch of a SPM rotor: $\pi/3$ radians for the analysed machine). As known, the rotor design allows significantly reducing the torque ripples losing in machine torque density.

Table 5.7 shows the machine torque constants for the inverse sequences of the armature field harmonics.

Table 5.5 – Table of the machine torque constants for the direct sequences of the armature field harmonics

y	$T_{PM} = \Re \left\{ \sum_{y=0}^{\infty} jK_{T,PM,y,3}^+ e^{j(y18+3)\vartheta_m} \bar{i}_S^* \right\} + \Re \left\{ \sum_{y=1}^{\infty} -jK_{T,PM,y,3}^- e^{-j(y18-3)\vartheta_m} \bar{i}_S^* \right\}$					frequency
	Ideal SPM (no skew)			With skew and magnet short		p.u.
0	$K_{T,PM,0,3}^+ = 0.5246$			$K_{T,PM,0,3}^+ = 0.5008$		0
		$K_{T,PM,y,3}^+$	$\frac{K_{T,PM,y,3}^+}{K_{T,PM,0,3}^+}$	$K_{T,PM,y,3}^+$	$\frac{K_{T,PM,y,3}^+}{K_{T,PM,0,3}^+}$	
1	$T_{PM,7}^+$	0.075	0.143	-0.012	-0.025	6
2	$T_{PM,13}^+$	0.040	0.077	0.004	0.007	12
3	$T_{PM,19}^+$	0.028	0.053	-0.003	-0.006	18
4	$T_{PM,25}^+$	0.021	0.040	0.002	0.004	24
5	$T_{PM,31}^+$	0.017	0.032	-0.005	-0.011	30
6	$T_{PM,37}^+$	0.014	0.027	-0.013	-0.025	36
7	$T_{PM,43}^+$	0.012	0.023	0.003	0.006	42
8	$T_{PM,49}^+$	0.011	0.020	-0.001	-0.002	48
9	$T_{PM,55}^+$	0.010	0.018	0.002	0.003	54
10	$T_{PM,61}^+$	0.009	0.016	-0.001	-0.002	60

The analysis of the torque components leads to the definition of a torque control based on only the fundamental field harmonic (the p -th, with p equal to 3 in this case). The simplified torque equation results as:

$$T_{PM} = \Re \left\{ jK_T e^{j3\vartheta_m} \bar{i}_S^* \right\}, \quad (5.62)$$

with:

$$K_T = K_{T,PM,0,3}^+ = 9\mu_0 L R N \frac{4B_r \tau_M}{\mu_M \pi \delta} K_{skew,3} \sin \left(\frac{\pi(1-1/6)}{2} \right) = 0.5008.$$

This approach to the torque control is typical for three-phase machines, where the torque ripple are just a result of the main component control. The idea is proposed again in the next paragraph for the force control definition.

Force Constants

Table 5.6 shows the current force coefficients, while Table 5.8 and Table 5.9 show the magnet force constants for the $h-1$ and $h+1$ harmonic interactions respectively.

Table 5.7 – Table of the machine torque constants for the inverse sequences of the armature field harmonics

y	$T_{PM} = \Re \left\{ \sum_{y=0}^{\infty} jK_{T,PM,y,3}^+ e^{j(y18+3)\theta_m} \bar{i}_S^* \right\} + \Re \left\{ \sum_{y=1}^{\infty} -jK_{T,PM,y,3}^- e^{-j(y18-3)\theta_m} \bar{i}_S^* \right\}$					frequency
	Ideal SPM (no skew)		With skew and magnet short			p.u.
0	$K_{T,PM,0,3}^+ = 0.5246$		$K_{T,PM,0,3}^+ = 0.5008$			0
		$K_{T,PM,y,3}^-$	$\frac{K_{T,PM,y,3}^-}{K_{T,PM,0,3}^+}$	$K_{T,PM,y,3}^-$	$\frac{K_{T,PM,y,3}^-}{K_{T,PM,0,3}^+}$	
1	$T_{PM,5}^-$	0.105	0.200	0.019	0.037	6
2	$T_{PM,11}^-$	0.048	0.091	-0.005	-0.010	12
3	$T_{PM,17}^-$	0.031	0.059	0.002	0.003	18
4	$T_{PM,23}^-$	0.023	0.043	-0.002	-0.004	24
5	$T_{PM,29}^-$	0.018	0.034	0.001	0.002	30
6	$T_{PM,35}^-$	0.015	0.029	-0.015	-0.030	36
7	$T_{PM,41}^-$	0.013	0.024	0.000	-0.001	42
8	$T_{PM,47}^-$	0.011	0.021	0.001	0.002	48
9	$T_{PM,53}^-$	0.010	0.019	0.000	0.000	54
10	$T_{PM,59}^-$	0.009	0.017	0.001	0.002	60

As for the torque analysis, the force contributions have significantly different magnitudes for the same amount of current. It results that the force produced by the interaction between the only armature field harmonics generate force components with a lower efficiency (the related force constants are limited) than the related to the interaction between the magnets and armature field harmonics ones. Indeed, the magnet force constants are significantly higher, and the force equation can be simplified as:

$$\bar{F} = \bar{F}_{PM} = K_{PM(3,2)} \bar{i}_2^* e^{j3\theta_m} + K_{PM(3,4)} \bar{i}_4 e^{-j3\theta_m}, \quad (5.63)$$

Table 5.6 – Table of the current force constants

h	$K_{cu,h}$	$\bar{F}_{cu} = \sum_{h=1}^{\infty} [K_{cu,h} \bar{i}_h^* \bar{i}_{h+1}]$	$\frac{K_{cu,h}}{K_{cu,1}}$	h	$K_{cu,h}$	$\bar{F}_{cu} = \sum_{h=1}^{\infty} [K_{cu,h} \bar{i}_h^* \bar{i}_{h+1}]$	$\frac{K_{cu,h}}{K_{cu,1}}$
1	$K_{cu,1}$	0.150	1.000	11	$K_{cu,11}$	0.000	0.000
2	$K_{cu,2}$	0.100	0.667	12	$K_{cu,12}$	0.000	0.000
3	$K_{cu,3}$	0.050	0.333	13	$K_{cu,13}$	0.002	0.011
4	$K_{cu,4}$	0.015	0.100	14	$K_{cu,14}$	0.003	0.019
5	$K_{cu,5}$	0.000	0.000	15	$K_{cu,15}$	0.003	0.017
6	$K_{cu,6}$	0.000	0.000	16	$K_{cu,16}$	0.001	0.007
7	$K_{cu,7}$	0.005	0.036	17	$K_{cu,17}$	0.000	0.000
8	$K_{cu,8}$	0.008	0.056	18	$K_{cu,18}$	0.000	0.000
9	$K_{cu,9}$	0.007	0.044	19	$K_{cu,19}$	0.001	0.005
10	$K_{cu,10}$	0.003	0.018	20	$K_{cu,20}$	0.001	0.010

Table 5.8 – Table of the magnet force constants for the $h-1$ components of the armature field harmonics

h	$\bar{F}_{PM} = \sum_{\substack{h=1 \\ h_{\text{odd}}}}^{\infty} \left[K_{PM(3h,3h-1)} \bar{i}_{3h-1}^* e^{j3h\theta_m} + K_{PM(3h,3h+1)} \bar{i}_{3h+1} e^{-j3h\theta_m} \right]$				
	Ideal SPM (no skew)			With skew and magnet short	
		$K_{PM3,2} = 22.714$		$K_{PM3,2} = 21.6869$	
		$K_{PM(h,h-1)}$	$\frac{K_{PM(h,h-1)}}{K_{PM3,2}}$	$K_{PM(h,h-1)}$	$\frac{K_{PM(h,h-1)}}{K_{PM3,2}}$
3	$K_{PM,3,2}$	22.714	1.000	21.687	1.000
9	$K_{PM,9,8}$	1.893	0.083	1.200	0.055
15	$K_{PM,15,14}$	0.649	0.029	0.115	0.005
21	$K_{PM,21,20}$	0.324	0.014	-0.054	-0.002
27	$K_{PM,27,26}$	0.194	0.009	-0.048	-0.002
33	$K_{PM,33,32}$	0.129	0.006	-0.013	-0.001
39	$K_{PM,39,38}$	0.092	0.004	0.008	0.000
45	$K_{PM,45,44}$	0.069	0.003	0.011	0.001
51	$K_{PM,51,50}$	0.053	0.002	0.003	0.000
57	$K_{PM,57,56}$	0.043	0.002	-0.005	0.000

Table 5.9 – Table of the magnet force constants for the $h+1$ components of the armature field harmonics

h	$\bar{F}_{PM} = \sum_{\substack{h=1 \\ h_{\text{odd}}}}^{\infty} \left[K_{PM(3h,3h-1)} \bar{i}_{3h-1}^* e^{j3h\theta_m} + K_{PM(3h,3h+1)} \bar{i}_{3h+1} e^{-j3h\theta_m} \right]$				
	Ideal SPM (no skew)			With skew and magnet short	
		$K_{PM3,2} = 22.714$		$K_{PM3,2} = 21.6869$	
		$K_{PM(h,h+1)}$	$\frac{K_{PM(h,h+1)}}{K_{PM3,2}}$	$K_{PM(h,h+1)}$	$\frac{K_{PM(h,h+1)}}{K_{PM3,2}}$
3	$K_{PM,3,4}$	11.357	0.500	10.843	0.500
9	$K_{PM,9,10}$	1.514	0.067	0.960	0.044
15	$K_{PM,15,15}$	0.568	0.025	0.101	0.005
21	$K_{PM,21,22}$	0.295	0.013	-0.049	-0.002
27	$K_{PM,27,28}$	0.180	0.008	-0.044	-0.002
33	$K_{PM,33,34}$	0.121	0.005	-0.013	-0.001
39	$K_{PM,39,40}$	0.087	0.004	0.008	0.000
45	$K_{PM,45,46}$	0.066	0.003	0.010	0.000
51	$K_{PM,51,52}$	0.051	0.002	0.003	0.000
57	$K_{PM,57,58}$	0.041	0.002	-0.005	0.000

with the magnet force constant:

$$K_{PM(3,2)} = 9\mu_0 RL \frac{B_r \tau_M}{\mu_M \pi \delta^2} NK_{skew,3} \sin\left(\frac{\pi(1-1/6)}{2}\right) \sin\left(\frac{\pi}{3}\right) \cong 21.7,$$

$$K_{PM(3,4)} = \mu_0 RL \frac{B_r \tau_M}{\mu_M \pi \delta^2} \frac{9}{2} NK_{skew,3} \sin\left(\frac{\pi(1-1/6)}{2}\right) \sin\left(2\frac{\pi}{3}\right) \cong 10.9.$$

Torque and Force Main Constants and simplified Control Equations (summary)

From the torque and force equations, it is possible to define the reference current space vectors for the machine control algorithm.

The main torque and force equations (5.62) and (5.63) are:

$$T_{PM} = \Re\{jK_T e^{j3\theta_m} \bar{i}_s^*\},$$

and

$$\bar{F} = \bar{F}_{PM} = K_{PM(3,2)} \bar{i}_2^* e^{j3\theta_m} + K_{PM(3,4)} \bar{i}_4 e^{-j3\theta_m}.$$

The voltage space vector equations (5.54) are:

$$\bar{v}_3 = R_s \bar{i}_3 + (Ll + M_{33}^+) \frac{d\bar{i}_3}{dt} + \frac{d\bar{\phi}_{PM,3}}{dt},$$

$$\bar{v}_2 = R_s \bar{i}_2 + (Ll + M_{22}^+) \frac{d\bar{i}_2}{dt} + M_{25}^+ \frac{d\bar{i}_5}{dt} + M_{21}^- \frac{d\bar{i}_1^*}{dt} + M_{27}^- \frac{d\bar{i}_7^*}{dt},$$

$$\bar{v}_4 = R_s \bar{i}_4 + (Ll + M_{44}^+) \frac{d\bar{i}_4}{dt} + M_{41}^+ \frac{d\bar{i}_1}{dt} + M_{47}^+ \frac{d\bar{i}_7}{dt} + M_{45}^- \frac{d\bar{i}_5^*}{dt}.$$

or, with the proposed general model (5.52):

$$\bar{v}_3 = R_s \bar{i}_3 + (Ll + L_3) \frac{d\bar{i}_3}{dt} + \frac{d\bar{\phi}_{PM,3}}{dt}, \quad (5.64)$$

$$\bar{v}_2 = R_s \bar{i}_2 + (Ll + L_2) \frac{d\bar{i}_2}{dt}, \quad (5.65)$$

$$\bar{v}_4 = R_s \bar{i}_4 + (Ll + L_4) \frac{d\bar{i}_4}{dt}. \quad (5.66)$$

The advantage of the general approach is that the independence between the space vector equations is highlighted, while in the particular study of the machine (without a redundant analysis) the independence is hidden under the constraints of the system that are defined by (5.49). Hereafter, the general approach is considered.

5.3 Force and Torque Control of a Triple Three-Phase Sectored Machine

The degrees of freedom of the current control (6 DoF in total) allow controlling the machine by means of up to three independent current space vectors (6 vector components in total).

In particular, as it is usually done in the torque control of three-phase machines, the control is defined for the field harmonics related to the higher torque constant (the p -th one in mechanical degrees). The same approach is used to define which field harmonics to take into account for the radial force control. Therefore, the torque and force equations are easily simplified as (5.62) and (5.63) in order to consider the control of only three space vectors.

Therefore, the control of the analysed machine must properly select the value of the current space vectors of order 2, 3 and 4 for controlling the torque and the force.

Control equations (multi synchronous reference frames)

The third current space vector is controlled as the main space vector of a standard PM machine with a FOC. Indeed, it is possible to write the simplified torque equation, considering the current space vector \bar{i}_s in the reference frame synchronous with the d axis of the rotor (the d axis is chosen as centred with one magnet north pole):

$$\bar{i}_s^+ = \bar{i}_s e^{-j3\theta_m} = \bar{i}_3 e^{-j3\theta_m} = i_{3d}^+ + j i_{3q}^+.$$

The torque control equation results from (5.62) as:

$$T_{PM} = \Re\{jK_T e^{j3\theta_m} \bar{i}_s^*\} = \Re\{jK_T (i_{3d}^+ - j i_{3q}^+)\} = K_T i_{3q}^+.$$

The same approach is used for the force control, defining what is here named as Force Field Oriented Control (FFOC). The force equation (5.63) can be analysed in its two main components:

$$\bar{F} = F e^{j\theta_F} = \bar{F}_2 + \bar{F}_4 = K_{PM(3,2)} \bar{i}_2^* e^{j3\theta_m} + K_{PM(3,4)} \bar{i}_4 e^{-j3\theta_m}. \quad (5.67)$$

The first force component \bar{F}_2 can be controlled by considering the second current space vector in a reference frame synchronous with the force vector in the rotor reference frame

($\bar{i}_2^{+F} = \bar{i}_2 e^{-j(3\theta_m - \theta_F)} = i_{2d}^{+F} + j i_{2q}^{+F}$) as:

$$\bar{F}_2 = F_2 e^{j\theta_F} = K_{PM(3,2)} [(i_{2d}^{+F} - j i_{2q}^{+F}) e^{-j3\theta_m} e^{j\theta_F}] e^{j3\theta_m} = K_{PM(3,2)} (i_{2d}^{+F} - j i_{2q}^{+F}) e^{j\theta_F}. \quad (5.68)$$

The same is done for the second force component \bar{F}_4 , but synchronizing it with the conjugate of the force vector in the rotor reference frame ($\bar{i}_4^{-F} = \bar{i}_4 e^{-j3\theta_m} e^{-j\theta_F} = i_{4d}^{-F} + j i_{4q}^{-F}$). The resulting force equation for the fourth space contribution is:

$$\bar{F}_4 = F_4 e^{j\theta_F} = K_{PM(3,4)} \left[(i_{4d}^{-F} + j i_{4q}^{-F}) e^{j3\theta_m} e^{j\theta_F} \right] e^{-j3\theta_m} = K_{PM(3,4)} (i_{4d}^{-F} + j i_{4q}^{-F}) e^{j\theta_F}. \quad (5.69)$$

In the respective reference frames, all the three current space vectors (complex numbers) have one component that is useful for the control of the desired quantity (magnitude of the torque or force component) and one that does not gives any contribution.

In particular, the d-axis component of the 3rd current space vector in the rotor flux reference frame does not affect the torque production (it can be just used in order to reduce the magnet back-emf in order to work in flux weakening operation). Regarding the force control equations, the components of the 2nd and 4th current space vectors on the q-axis of the relative reference frames contribute to the force in the wrong direction and therefore they are likely to be controlled to zero.

Therefore, the current control of the 3rd space vector is defined as:

$$i_{3q}^+ = \frac{T_{ref}}{K_T}, \quad i_{3d}^+ = 0, \quad (5.70)$$

while the current control of the 2nd space vector is defined as:

$$i_{2d}^{+F} = \frac{F_2}{K_{PM(3,2)}}, \quad i_{2q}^{+F} = 0, \quad (5.71)$$

and the current control of the 4th space vector is defined as:

$$i_{4d}^{-F} = \frac{F_4}{K_{PM(3,4)}}, \quad i_{4q}^{-F} = 0. \quad (5.72)$$

The voltage space vector equations are (5.64), (5.65) and (5.66). In addition, the tuning of the PI regulators can be defined by the standard control procedures that are used for the d-q control of three-phase machines. The only difference is that the 2nd and 4th spaces do not need a compensation of the PM back-emf (feedforward control). In general, the tuning of the three current space vector regulators is different for each, but the method is the conventional one.

Radial Force Control: F2/F ratio (F2pu)

An important difference between the force and the torque equations is that two independent current space vectors can generate the radial force. As mentioned above, both the force contributions must be controlled in such a way that they generate a positive effect to make the radial force follow its reference value. This allows considering in (5.67) the two force components in phase with the reference force:

$$\bar{F} = Fe^{j\theta_F} = (F_2 + F_4)e^{j\theta_F} = F(F_{2,pu} + F_{4,pu})e^{j\theta_F}, \quad (5.73)$$

with the relationship $F_{2,pu} + F_{4,pu} = 1$ that must be verified in order to follow the reference force. Therefore, the force control equations can be written as:

$$i_{2d}^{+F} = F \frac{F_{2,pu}}{K_{PM(3,2)}}, \quad (5.74)$$

and:

$$i_{4d}^{-F} = F \frac{(1 - F_{2,pu})}{K_{PM(3,4)}}. \quad (5.75)$$

The control variable $F_{2,pu}$ is a degree of freedom of the machine control. Indeed, there are six degrees of freedom in the current control of a triple three-phase machine. Three degrees of freedom are used to keep the useless component of each current space vector equal to zero (minimising the machine losses), one degree of freedom is used for the torque control and another for the force control. It results that there is an additional degree of freedom that is available in the control: the ratio F_2 / F_4 or $i_{2d}^{+F} / i_{4d}^{-F}$ as well. Fig. 5.4 shows the control scheme of the drive under study. The force is controlled in its x and y components. In the scheme, the force control is done in an open loop configuration, but it can also be done in closed loop depending on the availability of force sensors, or position sensors as in Fig. 5.4. The control of the torque is developed as in a standard three-phase machine acting on the q –axis component of the 3rd current space vector in the rotor field reference frame, with the compensation of the back emf produced by the magnets. The control of the 2nd and 4th spaces is defined in different reference frames as described above. The voltage space vectors are used to define the desired phase voltages by means of (5.50), (5.49) and (5.51) referred to the voltages. To avoid using three inverse transformations, the following subsection defines a direct inverse transformation for the voltages. The same approach can be used for the currents if it is needed for the control algorithm, as happens in case of machine fault (discussed later).

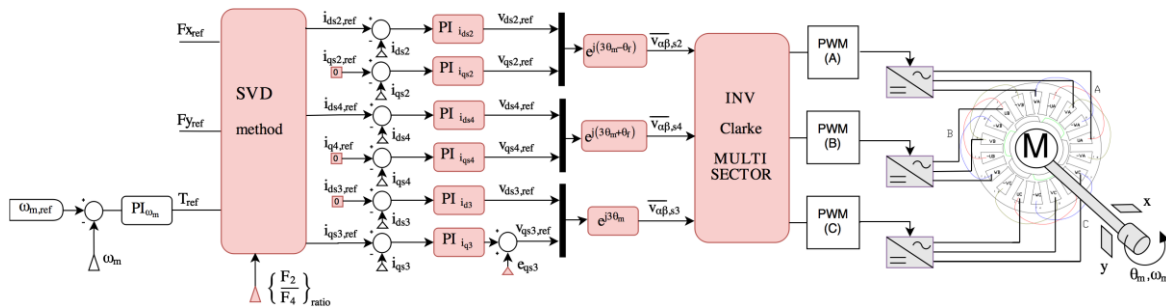


Fig. 5.4 – Triple three-phase MSPM machine control scheme for torque and radial force.

Triple Three-Phase Inverse Transformation: From the multiphase space vectors to the three-phase ones

The current voltage space vectors related to the machine torque and force control are related to the 2nd, 3rd and 4th spaces:

$$\begin{cases} \bar{y}_2 = \frac{1}{3}(\bar{y}_N c_{m2} + \bar{y}_M^* c_{n2}) \\ \bar{y}_3 = \bar{y}_s \\ \bar{y}_4 = \frac{1}{3}(\bar{y}_M c_{m2} + \bar{y}_N^* c_{n4}) \end{cases} \quad (5.76)$$

with:

$$\begin{cases} c_{m2} = 1 - e^{-j\left(\frac{2\pi}{3} + \frac{2\pi}{9}\right)} - e^{j\left(\frac{2\pi}{3} + \frac{2\pi}{9}\right)} = 1 - 2\cos\left(\frac{8\pi}{9}\right) = 2.8794 \\ c_{n2} = 1 - e^{j\left(\frac{2\pi}{3} - \frac{2\pi}{9}\right)} - e^{-j\left(\frac{2\pi}{3} - \frac{2\pi}{9}\right)} = 1 - 2\cos\left(\frac{4\pi}{9}\right) = 0.6527 \\ c_{n4} = 1 - e^{j\left(\frac{2\pi}{3} - \frac{4\pi}{9}\right)} - e^{-j\left(\frac{2\pi}{3} - \frac{4\pi}{9}\right)} = 1 - 2\cos\left(\frac{2\pi}{9}\right) = -0.5321 \end{cases} \quad (5.77)$$

and:

$$\begin{cases} \bar{y}_M = \frac{1}{3}\left(\bar{y}_{A,1} + \bar{y}_{B,1}e^{j\frac{2\pi}{3}} + \bar{y}_{C,1}e^{j\frac{4\pi}{3}}\right) \\ \bar{y}_N = \frac{1}{3}\left(\bar{y}_{A,1} + \bar{y}_{B,1}e^{-j\frac{2\pi}{3}} + \bar{y}_{C,1}e^{-j\frac{4\pi}{3}}\right) \\ \bar{y}_s = \frac{1}{3}(\bar{y}_{A,1} + \bar{y}_{B,1} + \bar{y}_{C,1}) \end{cases} \quad (5.78)$$

From (5.76) it is possible to define the additional space vectors $(\bar{y}_M, \bar{y}_N, \bar{y}_s)$ as function of the multiphase ones used for the machine control $(\bar{y}_2, \bar{y}_3, \bar{y}_4)$ as:

$$\begin{cases} \bar{y}_N = \frac{\bar{y}_2 3c_{m2} - 3\bar{y}_4^* c_{n2}}{c_{m2}^2 - c_{n2}c_{n4}} \\ \bar{y}_s = \bar{y}_3 \\ \bar{y}_M = \frac{3\bar{y}_4 c_{m2} - 3\bar{y}_2^* c_{n4}}{c_{m2}^2 - c_{n2}c_{n4}} \end{cases} \quad (5.79)$$

From (5.78) it is possible to define the standard three-phase space vectors $(\bar{y}_{A,1}, \bar{y}_{B,1}, \bar{y}_{C,1})$ as function of the additional ones $(\bar{y}_M, \bar{y}_N, \bar{y}_s)$ as:

$$\begin{cases} \bar{y}_{A,1} = \bar{y}_M + \bar{y}_N + \bar{y}_S \\ \bar{y}_{B,1} = \bar{y}_M e^{-j\frac{2\pi}{3}} + \bar{y}_N e^{j\frac{2\pi}{3}} + \bar{y}_S \\ \bar{y}_{C,1} = \bar{y}_M e^{j\frac{2\pi}{3}} + \bar{y}_N e^{-j\frac{2\pi}{3}} + \bar{y}_S \end{cases} \quad (5.80)$$

Substituting (5.79) in (5.80), it is possible to write:

$$\begin{aligned} \bar{y}_{A,1} &= \frac{3c_{m2}}{c_{m2}^2 - c_{n2}c_{n4}} \bar{y}_2 + \frac{-3c_{n4}}{c_{m2}^2 - c_{n2}c_{n4}} \bar{y}_2^* + \frac{3c_{m2}}{c_{m2}^2 - c_{n2}c_{n4}} \bar{y}_4 + \frac{-3c_{n2}}{c_{m2}^2 - c_{n2}c_{n4}} \bar{y}_4^* + \bar{y}_3, \\ \bar{y}_{B,1} &= \frac{3c_{m2}}{c_{m2}^2 - c_{n2}c_{n4}} e^{j\frac{2\pi}{3}} \bar{y}_2 + \frac{-3c_{n4}}{c_{m2}^2 - c_{n2}c_{n4}} e^{-j\frac{2\pi}{3}} \bar{y}_2^* + \frac{3c_{m2}}{c_{m2}^2 - c_{n2}c_{n4}} e^{-j\frac{2\pi}{3}} \bar{y}_4 + \frac{-3c_{n2}}{c_{m2}^2 - c_{n2}c_{n4}} e^{j\frac{2\pi}{3}} \bar{y}_4^* + \bar{y}_3, \\ \bar{y}_{C,1} &= \frac{3c_{m2}}{c_{m2}^2 - c_{n2}c_{n4}} e^{-j\frac{2\pi}{3}} \bar{y}_2 + \frac{-3c_{n4}}{c_{m2}^2 - c_{n2}c_{n4}} e^{j\frac{2\pi}{3}} \bar{y}_2^* + \frac{3c_{m2}}{c_{m2}^2 - c_{n2}c_{n4}} e^{j\frac{2\pi}{3}} \bar{y}_4 + \frac{-3c_{n2}}{c_{m2}^2 - c_{n2}c_{n4}} e^{-j\frac{2\pi}{3}} \bar{y}_4^* + \bar{y}_3. \end{aligned} \quad (5.81)$$

Considering the α - β components, (5.81) becomes:

$$\begin{aligned} y_{A,\alpha} &= C_{m2n4}^- y_{2,\alpha} + C_{m2n2}^- y_{4,\alpha} + y_{3,\alpha}, \\ y_{A,\beta} &= C_{m2n4}^+ y_{2,\beta} + C_{m2n2}^+ y_{4,\beta} + y_{3,\beta}, \\ y_{B,\alpha} &= C_{m2n4}^- \cos\left(\frac{2\pi}{3}\right) y_{2,\alpha} - C_{m2n4}^- \sin\left(\frac{2\pi}{3}\right) y_{2,\beta} + C_{m2n2}^- \cos\left(-\frac{2\pi}{3}\right) y_{4,\alpha} - C_{m2n2}^- \sin\left(-\frac{2\pi}{3}\right) y_{4,\beta} + y_{3,\alpha}, \\ y_{B,\beta} &= C_{m2n4}^+ \sin\left(\frac{2\pi}{3}\right) y_{2,\alpha} + C_{m2n4}^+ \cos\left(\frac{2\pi}{3}\right) y_{2,\beta} + C_{m2n2}^+ \sin\left(-\frac{2\pi}{3}\right) y_{4,\alpha} + C_{m2n2}^+ \cos\left(-\frac{2\pi}{3}\right) y_{4,\beta} + y_{3,\beta}, \\ y_{C,\alpha} &= C_{m2n4}^- \cos\left(-\frac{2\pi}{3}\right) y_{2,\alpha} - C_{m2n4}^- \sin\left(-\frac{2\pi}{3}\right) y_{2,\beta} + C_{m2n2}^- \cos\left(\frac{2\pi}{3}\right) y_{4,\alpha} - C_{m2n2}^- \sin\left(\frac{2\pi}{3}\right) y_{4,\beta} + y_{3,\alpha}, \\ y_{C,\beta} &= C_{m2n4}^+ \sin\left(-\frac{2\pi}{3}\right) y_{2,\alpha} + C_{m2n4}^+ \cos\left(-\frac{2\pi}{3}\right) y_{2,\beta} + C_{m2n2}^+ \sin\left(\frac{2\pi}{3}\right) y_{4,\alpha} + C_{m2n2}^+ \cos\left(\frac{2\pi}{3}\right) y_{4,\beta} + y_{3,\beta}, \end{aligned} \quad (5.82)$$

with:

$$C_{m2n4}^- = 3 \frac{c_{m2} - c_{n4}}{c_{m2}^2 - c_{n2}c_{n4}}, C_{m2n2}^- = 3 \frac{c_{m2} - c_{n2}}{c_{m2}^2 - c_{n2}c_{n4}}, C_{m2n4}^+ = 3 \frac{c_{m2} + c_{n4}}{c_{m2}^2 - c_{n2}c_{n4}}, C_{m2n2}^+ = 3 \frac{c_{m2} + c_{n2}}{c_{m2}^2 - c_{n2}c_{n4}}.$$

This relationship allows finding the standard α - β components for each three-phase subsystem once the α - β components of the general space vectors are defined. In terms of voltage control, the α - β components for each three-phase subsystem are used to define the desired modulation technique (usually SVM or PWM) as in a standard three-phase machine.

The resulting transformation in matrix form is:

$$\begin{bmatrix} y_{A,\alpha} \\ y_{A,\beta} \\ y_{B,\alpha} \\ y_{B,\beta} \\ y_{C,\alpha} \\ y_{C,\beta} \end{bmatrix} = \begin{bmatrix} C_{m2n4}^- & 0 & 1 & 0 & C_{m2n2}^- & 0 \\ 0 & C_{m2n4}^+ & 0 & 1 & 0 & C_{m2n2}^+ \\ C_{m2n4}^- \cos\left(\frac{2\pi}{3}\right) & -C_{m2n4}^- \sin\left(\frac{2\pi}{3}\right) & 1 & 0 & C_{m2n2}^- \cos\left(-\frac{2\pi}{3}\right) & -C_{m2n2}^- \sin\left(-\frac{2\pi}{3}\right) \\ C_{m2n4}^+ \sin\left(\frac{2\pi}{3}\right) & C_{m2n4}^+ \cos\left(\frac{2\pi}{3}\right) & 0 & 1 & C_{m2n2}^+ \sin\left(-\frac{2\pi}{3}\right) & C_{m2n2}^+ \cos\left(-\frac{2\pi}{3}\right) \\ C_{m2n4}^- \cos\left(-\frac{2\pi}{3}\right) & -C_{m2n4}^- \sin\left(-\frac{2\pi}{3}\right) & 1 & 0 & C_{m2n2}^- \cos\left(\frac{2\pi}{3}\right) & -C_{m2n2}^- \sin\left(\frac{2\pi}{3}\right) \\ C_{m2n4}^+ \sin\left(-\frac{2\pi}{3}\right) & C_{m2n4}^+ \cos\left(-\frac{2\pi}{3}\right) & 0 & 1 & C_{m2n2}^+ \sin\left(\frac{2\pi}{3}\right) & C_{m2n2}^+ \cos\left(\frac{2\pi}{3}\right) \end{bmatrix} \begin{bmatrix} y_{2,\alpha} \\ y_{2,\beta} \\ y_{3,\alpha} \\ y_{3,\beta} \\ y_{4,\alpha} \\ y_{4,\beta} \end{bmatrix}. \quad (5.83)$$

The inverse of the transformation matrix allows also defining the general space vectors once the three-phase space vectors are known.

5.4 Force Control of a Triple Three-Phase Sectored Machine: optimised control for minimum stator copper Joule losses

As discussed in the previous section, the force control is based on the exploitation of two current space vectors. How much one or the other space vector is involved in the force control depends on the choice of the $F_{2,pu}$ variable.

It is possible to choose the control variable $F_{2,pu}$ in order to minimize the stator copper Joule losses in the radial force production. Here below the analytical solution of the minimization problem is explained and the optimised $F_{2,pu}$ value is defined as function of the machine parameters.

Equations (5.70), (5.74) and (5.75), written in the rotor d - q reference frame are:

$$\begin{aligned} \bar{i}_3 &= j i_{3q}^+ = j \frac{T_{ref}}{K_T}, \\ \bar{i}_2 &= i_{2d}^{+F} e^{-j\theta_F} = F \frac{F_{2,pu}}{K_{PM(3,2)}} e^{-j\theta_F}, \\ \bar{i}_4 &= i_{4d}^{-F} e^{j\theta_F} = F \frac{(1-F_{2,pu})}{K_{PM(3,4)}} e^{j\theta_F}. \end{aligned} \quad (5.84)$$

The related three-phase space vector components result from (5.82) and (5.81) as:

$$\begin{aligned}
 i_{A,d} &= F \left[C_{m2n4}^- \frac{F_{2,pu}}{K_{PM(3,2)}} + C_{m2n2}^- \frac{(1-F_{2,pu})}{K_{PM(3,4)}} \right] \cos(\vartheta_F), \\
 i_{A,q} &= F \left[-C_{m2n4}^+ \frac{F_{2,pu}}{K_{PM(3,2)}} + C_{m2n2}^+ \frac{(1-F_{2,pu})}{K_{PM(3,4)}} \right] \sin(\vartheta_F) + \frac{T_{ref}}{K_T},
 \end{aligned} \tag{5.85}$$

$$\begin{aligned}
 i_{B,d} &= F \left[C_{m2n4}^- \frac{F_{2,pu}}{K_{PM(3,2)}} + C_{m2n2}^- \frac{(1-F_{2,pu})}{K_{PM(3,4)}} \right] \left(\cos(\vartheta_F) \cos\left(\frac{2\pi}{3}\right) + \sin\left(\frac{2\pi}{3}\right) \sin(\vartheta_F) \right), \\
 i_{B,q} &= F \left[C_{m2n4}^+ \frac{F_{2,pu}}{K_{PM(3,2)}} - C_{m2n2}^+ \frac{(1-F_{2,pu})}{K_{PM(3,4)}} \right] \left(\cos(\vartheta_F) \sin\left(\frac{2\pi}{3}\right) - \cos\left(\frac{2\pi}{3}\right) \sin(\vartheta_F) \right) + \frac{T_{ref}}{K_T},
 \end{aligned} \tag{5.86}$$

$$\begin{aligned}
 i_{C,d} &= F \left[C_{m2n4}^- \frac{F_{2,pu}}{K_{PM(3,2)}} + C_{m2n2}^- \frac{(1-F_{2,pu})}{K_{PM(3,4)}} \right] \left(\cos(\vartheta_F) \cos\left(\frac{2\pi}{3}\right) - \sin\left(\frac{2\pi}{3}\right) \sin(\vartheta_F) \right), \\
 i_{C,q} &= F \left[-C_{m2n4}^+ \frac{F_{2,pu}}{K_{PM(3,2)}} + C_{m2n2}^+ \frac{(1-F_{2,pu})}{K_{PM(3,4)}} \right] \left(\cos(\vartheta_F) \sin\left(\frac{2\pi}{3}\right) + \cos\left(\frac{2\pi}{3}\right) \sin(\vartheta_F) \right) + \frac{T_{ref}}{K_T}.
 \end{aligned} \tag{5.87}$$

They can be rewritten as:

$$\begin{aligned}
 i_{A,d} &= K_{Fd} \cos(\vartheta_F), \\
 i_{A,q} &= K_{Fq} \sin(\vartheta_F) + \frac{T_{ref}}{K_T},
 \end{aligned} \tag{5.88}$$

$$\begin{aligned}
 i_{B,d} &= K_{Fd} \cos\left(\vartheta_F - \frac{2\pi}{3}\right), \\
 i_{B,q} &= K_{Fq} \sin\left(\vartheta_F - \frac{2\pi}{3}\right) + \frac{T_{ref}}{K_T},
 \end{aligned} \tag{5.89}$$

$$\begin{aligned}
 i_{C,d} &= K_{Fd} \cos\left(\vartheta_F + \frac{2\pi}{3}\right), \\
 i_{C,q} &= K_{Fq} \sin\left(\vartheta_F + \frac{2\pi}{3}\right) + \frac{T_{ref}}{K_T},
 \end{aligned} \tag{5.90}$$

with:

$$K_{Fd} = F \left[C_{m2n4}^- \frac{F_{2,pu}}{K_{PM(3,2)}} + C_{m2n2}^- \frac{(1-F_{2,pu})}{K_{PM(3,4)}} \right], \quad K_{Fq} = F \left[-C_{m2n4}^+ \frac{F_{2,pu}}{K_{PM(3,2)}} + C_{m2n2}^+ \frac{(1-F_{2,pu})}{K_{PM(3,4)}} \right].$$

The stator copper Joule losses related to the three-phase subsystems (3.48), written in the d - q reference frame are:

$$P_J = \sum_{T=A,B,C} P_{J,T} = \frac{3}{2} R_s (i_{A,d}^2 + i_{A,q}^2 + i_{B,d}^2 + i_{B,q}^2 + i_{C,d}^2 + i_{C,q}^2), \tag{5.91}$$

resulting as:

$$\begin{aligned}
 P_J \frac{2}{3R_s} &= K_{Fd}^2 \left[\cos^2(\vartheta_F) + \cos^2\left(\vartheta_F - \frac{2\pi}{3}\right) + \cos^2\left(\vartheta_F + \frac{2\pi}{3}\right) \right] + \\
 &+ K_{Fq}^2 \left[\sin^2(\vartheta_F) + \sin^2\left(\vartheta_F - \frac{2\pi}{3}\right) + \sin^2\left(\vartheta_F + \frac{2\pi}{3}\right) \right] + \\
 &+ 2K_{Fq} \frac{T_{ref}}{K_T} \left[\sin(\vartheta_F) + \sin\left(\vartheta_F - \frac{2\pi}{3}\right) + \sin\left(\vartheta_F + \frac{2\pi}{3}\right) \right] + 3\left(\frac{T_{ref}}{K_T}\right)^2 = \quad (5.92) \\
 &= K_{Fd}^2 \left[\cos^2(\vartheta_F) + \cos^2\left(\vartheta_F - \frac{2\pi}{3}\right) + \cos^2\left(\vartheta_F + \frac{2\pi}{3}\right) \right] + \\
 &+ K_{Fq}^2 \left[\sin^2(\vartheta_F) + \sin^2\left(\vartheta_F - \frac{2\pi}{3}\right) + \sin^2\left(\vartheta_F + \frac{2\pi}{3}\right) \right] + 3\left(\frac{T_{ref}}{K_T}\right)^2.
 \end{aligned}$$

Simplifying, it results that:

$$P_J \frac{2}{3R_s} = \frac{3}{2} (K_{Fd}^2 + K_{Fq}^2) + 3\left(\frac{T_{ref}}{K_T}\right)^2. \quad (5.93)$$

It is possible to separate the term of the torque generation from the force ones as:

$$P_{J.Torque} = R_s \frac{9}{2} \left(\frac{T_{ref}}{K_T}\right)^2, \quad (5.94)$$

and

$$P_{J.Force} = R_s \frac{9}{4} (K_{Fd}^2 + K_{Fq}^2). \quad (5.95)$$

Introducing the parameters related to the force control K_{Fd} and K_{Fq} the force related Joule losses expressed in function of the control variable $F_{2,pu}$ are:

$$\begin{aligned}
 P_{J.Force} &= R_s \frac{9}{4} F^2 \left[\left(\frac{C_{m2n4}^-}{K_{PM(3,2)}} - \frac{C_{m2n2}^-}{K_{PM(3,4)}} \right)^2 + \left(-\frac{C_{m2n4}^+}{K_{PM(3,2)}} - \frac{C_{m2n2}^+}{K_{PM(3,4)}} \right)^2 \right] F_{2,pu}^2 + \\
 &+ R_s \frac{9}{4} F^2 \left[2 \frac{C_{m2n2}^-}{K_{PM(3,4)}} \left(\frac{C_{m2n4}^-}{K_{PM(3,2)}} - \frac{C_{m2n2}^-}{K_{PM(3,4)}} \right) + 2 \frac{C_{m2n2}^+}{K_{PM(3,4)}} \left(-\frac{C_{m2n4}^+}{K_{PM(3,2)}} - \frac{C_{m2n2}^+}{K_{PM(3,4)}} \right) \right] F_{2,pu} + (5.96) \\
 &+ R_s \frac{9}{4} F^2 \left[\left(\frac{C_{m2n2}^-}{K_{PM(3,4)}} \right)^2 + \left(\frac{C_{m2n2}^+}{K_{PM(3,4)}} \right)^2 \right].
 \end{aligned}$$

Therefore, the minimum of the force related copper Joule losses is defined by:

$$\begin{aligned} \frac{dP_{J,Force}}{dF_{2,pu}} &= 2R_s \frac{9}{4} F^2 \left[\left(\frac{C_{m2n4}^-}{K_{PM(3,2)}} - \frac{C_{m2n2}^-}{K_{PM(3,4)}} \right)^2 + \left(-\frac{C_{m2n4}^+}{K_{PM(3,2)}} - \frac{C_{m2n2}^+}{K_{PM(3,4)}} \right)^2 \right] F_{2,pu} + \\ &+ R_s \frac{9}{4} F^2 \left[2 \frac{C_{m2n2}^-}{K_{PM(3,4)}} \left(\frac{C_{m2n4}^-}{K_{PM(3,2)}} - \frac{C_{m2n2}^-}{K_{PM(3,4)}} \right) + 2 \frac{C_{m2n2}^+}{K_{PM(3,4)}} \left(-\frac{C_{m2n4}^+}{K_{PM(3,2)}} - \frac{C_{m2n2}^+}{K_{PM(3,4)}} \right) \right] = 0, \end{aligned} \quad (5.97)$$

resulting in:

$$F_{2,pu} = -K_{PM(3,2)} \frac{\left[C_{m2n2}^- (C_{m2n4}^- K_{PM(3,4)} - C_{m2n2}^- K_{PM(3,2)}) + C_{m2n2}^+ (-C_{m2n4}^+ K_{PM(3,4)} - C_{m2n2}^+ K_{PM(3,2)}) \right]}{\left[(C_{m2n4}^- K_{PM(3,4)} - C_{m2n2}^- K_{PM(3,2)})^2 + (-C_{m2n4}^+ K_{PM(3,4)} - C_{m2n2}^+ K_{PM(3,2)})^2 \right]}. \quad (5.98)$$

This $F_{2,pu}$ value is the one that allows generating the reference radial force with the minimum stator copper Joule losses. An in-deep analysis of this control variable is presented in the sections of the simulation and finite element results.

5.5 Current Sharing Technique for Triple Three-Phase Machines (Radial Force Control and Compensation)

In the previous section, it has been proposed a torque and radial force control based on the exploitation of all the machine degrees of freedom. In particular, the control algorithm is based on maintaining the torque control (and if needed the flux weakening) as in a standard three-phase machine, while the force control is based on the choice of the control variable $F_{2,pu}$. The $F_{2,pu}$ optimisation for the stator copper Joule losses minimisation was proposed as a possible solution.

In this section and in the following one, the method is enhanced for the torque and force control of the machine in case of current sharing technique and three-phase open fault.

The evaluation of the undesired radial force is carried out, developing fault tolerant controls that aim to compensate them. Force control equations in case of current sharing and open phase faults are also presented.

Radial Force Evaluation in case of Current Sharing Control (standard method)

The current sharing control of a sectored triple three-phase machine is defined as:

$$\begin{cases} \bar{i}_{A,1} = 3K_A \bar{i}_3 \\ \bar{i}_{B,1} = 3K_B \bar{i}_3 \\ \bar{i}_{C,1} = 3K_C \bar{i}_3 \end{cases} \quad (5.99)$$

The three-phase open fault can be analysed as a particular case of current sharing control, and it is well described by (5.78), according to the faulty three-phase subsystem, as:

$$\begin{cases} \bar{i}_M = \left(K_A + K_B e^{j\frac{2\pi}{3}} + K_C e^{-j\frac{\pi}{3}} \right) \bar{i}_3 \\ \bar{i}_N = \left(K_A + K_B e^{-j\frac{2\pi}{3}} + K_C e^{j\frac{2\pi}{3}} \right) \bar{i}_3 \\ \bar{i}_S = (K_A + K_B + K_C) \bar{i}_3 \end{cases} \quad (5.100)$$

depending on if the faulty inverter is A, B or C respectively, or if a current sharing control is commanded, with $(K_A + K_B + K_C = 1)$.

In terms of current space vectors, the fault constraint results from (5.76) as:

$$\begin{cases} \bar{i}_2 = \frac{1}{3} \left(\left(K_A + K_B e^{-j\frac{2\pi}{3}} + K_C e^{-j\frac{4\pi}{3}} \right) \bar{i}_3 c_{m2} + \left(K_A + K_B e^{-j\frac{2\pi}{3}} + K_C e^{-j\frac{4\pi}{3}} \right) \bar{i}_3^* c_{n2} \right) \\ \bar{i}_3 = (K_A + K_B + K_C) \bar{i}_3 = \bar{i}_3 \\ \bar{i}_4 = \frac{1}{3} \left(\left(K_A + K_B e^{j\frac{2\pi}{3}} + K_C e^{j\frac{4\pi}{3}} \right) \bar{i}_3 c_{m2} + \left(K_A + K_B e^{j\frac{2\pi}{3}} + K_C e^{j\frac{4\pi}{3}} \right) \bar{i}_3^* c_{n4} \right) \end{cases} \quad (5.101)$$

It results that if the current sharing coefficient are different, the 2nd and 4th current space vectors are no more equal to zero. The resulting radial force can be described by (5.67), considering the fault constraints for the 2nd and 4th current space vectors and introducing the current sharing control variable:

$$\bar{K}_{ABC} = K_A + K_B e^{j\frac{2\pi}{3}} + K_C e^{j\frac{4\pi}{3}},$$

as:

$$\begin{aligned} \bar{F} &= K_{PM(3,2)} \bar{i}_2^* e^{j3\vartheta_m} + K_{PM(3,4)} \bar{i}_4 e^{-j3\vartheta_m} = \\ &= K_{PM(3,2)} \frac{1}{3} \left(\bar{K}_{ABC} \bar{i}_3^* c_{m2} + \bar{K}_{ABC} \bar{i}_3 c_{n2} \right) e^{j3\vartheta_m} + \\ &+ K_{PM(3,4)} \frac{1}{3} \left(\bar{K}_{ABC} \bar{i}_3 c_{m2} + \bar{K}_{ABC} \bar{i}_3^* c_{n4} \right) e^{-j3\vartheta_m} = \\ &= \frac{1}{3} \bar{K}_{ABC} \left[K_{PM(3,2)} \left(\bar{i}_3^* c_{m2} + \bar{i}_3 c_{n2} \right) e^{j3\vartheta_m} + K_{PM(3,4)} \left(\bar{i}_3 c_{m2} + \bar{i}_3^* c_{n4} \right) e^{-j3\vartheta_m} \right]. \end{aligned} \quad (5.102)$$

Considering a standard torque FOC (without showing the flux-weakening behaviour for sake of simplicity), the 3rd current space vector is controlled as $\bar{i}_3 = j\bar{i}_{3q}^+ e^{j3\vartheta_m}$, and the force equation becomes:

$$\begin{aligned} \bar{F} = & j\frac{1}{3}\bar{K}_{ABC}(K_{PM(3,4)} - K_{PM(3,2)})c_{m2}\bar{i}_{3q}^+ + \\ & + \frac{1}{3}\bar{K}_{ABC}\left[K_{PM(3,2)}c_{n2}(je^{j6\vartheta_m}) + K_{PM(3,4)}c_{n4}(-je^{-j6\vartheta_m})\right]\bar{i}_{3q}^+. \end{aligned} \quad (5.103)$$

Because $A\bar{X} + B\bar{X}^*$ can be also written as $A\bar{X} - B\bar{X} + B\bar{X} + B\bar{X}^* = (A - B)\bar{X} + 2B\Re\{\bar{X}\}$, the force can be evaluated as:

$$\begin{aligned} \bar{F} = & j\frac{1}{3}\bar{K}_{ABC}(K_{PM(3,4)} - K_{PM(3,2)})c_{m2}\bar{i}_{3q}^+ + \\ & + \frac{1}{3}\bar{K}_{ABC}\left[(K_{PM(3,2)}c_{n2} - K_{PM(3,4)}c_{n4})je^{j6\vartheta_m} + 2K_{PM(3,4)}c_{n4}\Re\{je^{j6\vartheta_m}\}\right]\bar{i}_{3q}^+ = \\ = & j\frac{1}{3}\bar{K}_{ABC}(K_{PM(3,4)} - K_{PM(3,2)})c_{m2}\bar{i}_{3q}^+ + \\ & + \frac{1}{3}\bar{K}_{ABC}\left[(K_{PM(3,2)}c_{n2} - K_{PM(3,4)}c_{n4})je^{j6\vartheta_m} - 2K_{PM(3,4)}c_{n4}\sin(6\vartheta_m)\right]\bar{i}_{3q}^+. \end{aligned} \quad (5.104)$$

The force in case of current sharing results as the sum of three components, a constant force \bar{F}_{dc} plus a rotating $\bar{F}_{rotating}$ and a pulsating component $\bar{F}_{pulsating}$ at twice the rotor electrical frequency (six times the rotor mechanical frequency):

$$\bar{F} = \bar{F}_{dc} + \bar{F}_{rotating}e^{j6\vartheta_m} + \bar{F}_{pulsating}\sin(6\vartheta_m), \quad (5.105)$$

with magnitudes and phases defined as:

$$\left\{ \begin{aligned} \bar{F}_{dc} &= j\frac{1}{3}\bar{K}_{ABC}(K_{PM(3,4)} - K_{PM(3,2)})c_{m2}\bar{i}_{3q}^+ \\ \bar{F}_{rotating} &= j\frac{1}{3}\bar{K}_{ABC}(K_{PM(3,2)}c_{n2} - K_{PM(3,4)}c_{n4})\bar{i}_{3q}^+ \\ \bar{F}_{pulsating} &= -\frac{1}{3}\bar{K}_{ABC}2K_{PM(3,4)}c_{n4}\bar{i}_{3q}^+ \end{aligned} \right. \quad (5.106)$$

For a given current sharing configuration, the force vector is expected to rotate on an elliptical trajectory shifted by an offset in the x-y plane. The ellipsoid is defined by a sum of a direct and an inverse vector rotating at the same speed but in opposite directions and with different phases and amplitudes. Therefore, the force can be also analysed as:

$$\bar{F} = j\bar{K}_{ABC}\bar{i}_{3q}^+ F_{3ABCDq,dc}^+ + j\bar{K}_{ABC}\bar{i}_{3q}^+ F_{3ABCDq,direct}^+ e^{j6\vartheta_m} - j\bar{K}_{ABC}\bar{i}_{3q}^+ F_{3ABCDq,inverse}^+ e^{-j6\vartheta_m}, \quad (5.107)$$

with:

$$F_{3ABCDq,dc}^+ = \frac{1}{3} (K_{PM(3,4)} - K_{PM(3,2)}) c_{m2},$$

$$F_{3ABCDq,direct}^+ = \frac{1}{3} K_{PM(3,2)} c_{n2},$$

$$F_{3ABCDq,inverse}^+ = \frac{1}{3} K_{PM(3,4)} c_{n4}.$$

If there is a current sharing control for each inverter, the open fault behaviour is just a particular case of current sharing behaviour (as explained in Chapter 3). Therefore, the analysis is the same with just one current sharing coefficient equal to zero and the other equal to 1/2.

It results that the current sharing control of a sectored MSPM machine must be considered with caution, as already shown in previous research works [15, 16, 19].

In the next subsection, the radial force control principle with an advanced current sharing technique is proposed. This method can be also used for defining a FTC in case of one three-phase subsystem open phase fault when the two others are working with the advanced current sharing algorithm. The new current sharing control is introduced, as it has been done in Chapter 3, because the force control and FTC are not possible in case of basic current sharing algorithm. Indeed, the basic current sharing control already sets all the degrees of freedom of the machine control.

Current Sharing advanced control of MSPM machines and Radial Force control

As described in Chapter 3, it is possible to define a different current sharing algorithm for the control of the d -axis and q -axis components of the main current space vector (related to the torque generation). The idea is to define a current sharing only for the q -axis components of the three-phase subsystems and compensate (or control) the generated force by means of the d -axis component.

This can be done reconsidering (5.102) for the d -axis components, knowing that the current sharing technique on the q -axis is defined by the current sharing complex number:

$$\bar{K}_{ABC,q} = K_{A,q} + K_{B,q} e^{j\frac{2\pi}{3}} + K_{C,q} e^{j\frac{4\pi}{3}}.$$

The additional current space vectors can be written considering the constraints on the q -axis control of the 3rd space. In the d - q rotor reference frame the resulting equation is:

$$\left\{ \begin{array}{l} \bar{i}_{Mdq} = \frac{1}{3} \left(i_{3Ad}^+ + i_{3Bd}^+ e^{j\frac{2\pi}{3}} + i_{3Cd}^+ e^{j\frac{4\pi}{3}} \right) + j \left(K_{Aq} + K_{Bq} e^{j\frac{2\pi}{3}} + K_{Cq} e^{j\frac{4\pi}{3}} \right) i_{3q}^+ \\ \bar{i}_{Ndq} = \frac{1}{3} \left(i_{3Ad}^+ + i_{3Bd}^+ e^{-j\frac{2\pi}{3}} + i_{3Cd}^+ e^{-j\frac{4\pi}{3}} \right) + j \left(K_{Aq} + K_{Bq} e^{-j\frac{2\pi}{3}} + K_{Cq} e^{-j\frac{4\pi}{3}} \right) i_{3q}^+ \\ \bar{i}_{sdq} = \frac{1}{3} \left(i_{3Ad}^+ + i_{3Bd}^+ + i_{3Cd}^+ \right) + j \left(K_{Aq} + K_{Bq} + K_{Cq} \right) i_{3q}^+ \end{array} \right. \quad (5.108)$$

The effect on the force caused by the q-axis components is described by (5.103), while for the d-axis components, the 2nd and 4th current space vectors are evaluated as:

$$\left\{ \begin{array}{l} \bar{i}_2 = \frac{1}{9} \left(\left(i_{3Ad}^+ + i_{3Bd}^+ e^{-j\frac{2\pi}{3}} + i_{3Cd}^+ e^{-j\frac{4\pi}{3}} \right) c_{m2} e^{j3\vartheta_m} + \left(i_{3Ad}^+ + i_{3Bd}^+ e^{-j\frac{2\pi}{3}} + i_{3Cd}^+ e^{-j\frac{4\pi}{3}} \right) c_{n2} e^{-j3\vartheta_m} \right) \\ \bar{i}_4 = \frac{1}{9} \left(\left(i_{3Ad}^+ + i_{3Bd}^+ e^{j\frac{2\pi}{3}} + i_{3Cd}^+ e^{j\frac{4\pi}{3}} \right) c_{m2} e^{j3\vartheta_m} + \left(i_{3Ad}^+ + i_{3Bd}^+ e^{j\frac{2\pi}{3}} + i_{3Cd}^+ e^{j\frac{4\pi}{3}} \right) c_{n4} e^{-j3\vartheta_m} \right) \\ i_{3d}^+ = \frac{1}{3} \left(i_{3Ad}^+ + i_{3Bd}^+ + i_{3Cd}^+ \right) \end{array} \right. \quad (5.109)$$

Introducing the d-axis space vector considering the three-phase components:

$$\bar{i}_{3ABCd}^+ = \frac{1}{3} \left(i_{3Ad}^+ + i_{3Bd}^+ e^{j\frac{2\pi}{3}} + i_{3Cd}^+ e^{j\frac{4\pi}{3}} \right),$$

the space vectors can be rewritten as:

$$\left\{ \begin{array}{l} \bar{i}_2 = \frac{1}{3} \left(\bar{i}_{3ABCd}^{+*} c_{m2} e^{j3\vartheta_m} + \bar{i}_{3ABCd}^{+*} c_{n2} e^{-j3\vartheta_m} \right) \\ \bar{i}_4 = \frac{1}{3} \left(\bar{i}_{3ABCd}^+ c_{m2} e^{j3\vartheta_m} + \bar{i}_{3ABCd}^+ c_{n4} e^{-j3\vartheta_m} \right) \\ i_{3d}^+ = \frac{1}{3} \left(i_{3Ad}^+ + i_{3Bd}^+ + i_{3Cd}^+ \right) \end{array} \right. \quad (5.110)$$

The force equation for the d-axis components (5.67), results as:

$$\begin{aligned} \bar{F}_{3ABCd}^+ &= K_{PM(3,2)} \frac{1}{3} \left(\bar{i}_{3ABCd}^+ c_{m2} e^{-j3\vartheta_m} + \bar{i}_{3ABCd}^+ c_{n2} e^{j3\vartheta_m} \right) e^{j3\vartheta_m} + \\ &+ K_{PM(3,4)} \frac{1}{3} \left(\bar{i}_{3ABCd}^+ c_{m2} e^{j3\vartheta_m} + \bar{i}_{3ABCd}^+ c_{n4} e^{-j3\vartheta_m} \right) e^{-j3\vartheta_m} = \\ &= \frac{1}{3} \bar{i}_{3ABCd}^+ \left[K_{PM(3,2)} \left(c_{m2} + c_{n2} e^{j6\vartheta_m} \right) + K_{PM(3,4)} \left(c_{m2} + c_{n4} e^{-j6\vartheta_m} \right) \right]. \end{aligned} \quad (5.111)$$

Therefore, the space vector \bar{i}_{3ABCd}^+ generates three force components as:

$$\bar{F}_{3ABCd}^+ = \bar{i}_{3ABCd}^+ F_{3ABCd,dc}^+ + \bar{i}_{3ABCd}^+ F_{3ABCd,direct}^+ e^{j6\vartheta_m} + \bar{i}_{3ABCd}^+ F_{3ABCd,inverse}^+ e^{-j6\vartheta_m}, \quad (5.112)$$

with:

$$F_{3ABCd,dc}^+ = \frac{1}{3}(K_{PM(3,4)} + K_{PM(3,2)})c_{m2},$$

$$F_{3ABCd,direct}^+ = \frac{1}{3}K_{PM(3,2)}c_{n2} = F_{3ABCdq,direct}^+,$$

$$F_{3ABCd,inverse}^+ = \frac{1}{3}K_{PM(3,4)}c_{n4} = F_{3ABCdq,inverse}^+.$$

To eliminate the force ripples caused by the current sharing control or to control the force to a desired value, the resultant force must be controlled according to the following relationship:

$$\bar{F} = \bar{F}_{3ABCq}^+ + \bar{F}_{3ABCd}^+. \quad (5.113)$$

That means it is possible to write:

$$\begin{aligned} \bar{F} &= \bar{F}_{3ABCq}^+ + \bar{F}_{3ABCd}^+ = \\ &= j\bar{K}_{ABC}i_{3q}^+ F_{3ABCdq,dc}^+ + j\bar{K}_{ABC}i_{3q}^+ F_{3ABCdq,direct}^+ e^{j6\theta_m} - j\bar{K}_{ABC}i_{3q}^+ F_{3ABCdq,inverse}^+ e^{-j6\theta_m} + \\ &+ \bar{i}_{3ABCd}^+ F_{3ABCd,dc}^+ + \bar{i}_{3ABCd}^+ F_{3ABCd,direct}^+ e^{j6\theta_m} + \bar{i}_{3ABCd}^+ F_{3ABCd,inverse}^+ e^{-j6\theta_m}. \end{aligned} \quad (5.114)$$

Therefore, the force control (or elimination, if \bar{F} is set equal to zero) can be obtained by:

$$\bar{i}_{3ABCd}^+ = \frac{\bar{F} + \left(-j\bar{K}_{ABC,q} F_{3ABCdq,dc}^+ - j\bar{K}_{ABC,q} F_{3ABCdq,direct}^+ e^{j6\theta_m} + j\bar{K}_{ABC,q} F_{3ABCdq,inverse}^+ e^{-j6\theta_m} \right) i_{3q}^+}{F_{3ABCd,dc}^+ + F_{3ABCd,direct}^+ e^{j6\theta_m} + F_{3ABCd,inverse}^+ e^{-j6\theta_m}}. \quad (5.115)$$

The solution becomes unique if there is one sector open phase fault ($i_{3Td}^+ = 0$ with T equal to A , B or C) or if the overall d -axis component of the 3rd space vector is maintained equal to zero:

$$i_{3d}^+ = \frac{1}{3}(i_{3Ad}^+ + i_{3Bd}^+ + i_{3Cd}^+) = 0.$$

On the other hand, it is also possible to have a unique solution optimising the d -axis component of each three-phase subsystem for minimising the total stator copper Joule losses needed to generate the desired \bar{i}_{3ABCd}^+ space vector:

$$\bar{i}_{3ABCd}^+ = \frac{1}{3} \left(i_{3Ad}^+ + i_{3Bd}^+ e^{j\frac{2\pi}{3}} + i_{3Cd}^+ e^{j\frac{4\pi}{3}} \right).$$

The optimised solution can be found considering the d -axis related copper losses as:

$$P_J = \frac{3}{2} R_s (i_{3Ad}^+{}^2 + i_{3Bd}^+{}^2 + i_{3Cd}^+{}^2). \quad (5.116)$$

Substituting the \bar{i}_{3ABCd}^+ constraint, the following relationship can be written:

$$\begin{aligned} \frac{2P_J}{3R_s} = & \left(9\bar{i}_{3ABCd}^+ \bar{i}_{3ABCd}^{+*} - 3i_{3Bd}^+ e^{j\frac{2\pi}{3}} \bar{i}_{3ABCd}^{+*} - 3i_{3Bd}^+ e^{-j\frac{2\pi}{3}} \bar{i}_{3ABCd}^+ + 2i_{3Bd}^+{}^2 \right) + \\ & + \left(-3e^{j\frac{4\pi}{3}} \bar{i}_{3ABCd}^{+*} + i_{3Bd}^+ e^{-j\frac{2\pi}{3}} e^{j\frac{4\pi}{3}} - 3e^{-j\frac{4\pi}{3}} \bar{i}_{3ABCd}^+ + e^{-j\frac{4\pi}{3}} i_{3Bd}^+ e^{j\frac{2\pi}{3}} \right) i_{3Cd}^+ + 2i_{3Cd}^+{}^2, \end{aligned} \quad (5.117)$$

deriving by i_{3Cd}^+ , the i_{3Cd}^+ value that allows minimising the stator copper Joule losses in the generation of the \bar{i}_{3ABCd}^+ control vector is found as:

$$i_{3Cd}^+ = -\frac{-3e^{j\frac{4\pi}{3}} \bar{i}_{3ABCd}^{+*} - 3e^{-j\frac{4\pi}{3}} \bar{i}_{3ABCd}^+ + i_{3Bd}^+ \left(e^{j\frac{2\pi}{3}} + e^{-j\frac{2\pi}{3}} \right)}{4}. \quad (5.118)$$

Substituting this result in the \bar{i}_{3ABCd}^+ equation, it results:

$$9\bar{i}_{3ABCd}^+ - 3e^{j\frac{2\pi}{3}} \bar{i}_{3ABCd}^{+*} = 4i_{3Ad}^+ + \left(3e^{j\frac{2\pi}{3}} - 1 \right) i_{3Bd}^+. \quad (5.119)$$

Considering the real and imaginary part of the last equation, the B and A sectors d -axis components are evaluated as:

$$i_{3Bd}^+ = \frac{\Im \left\{ 9\bar{i}_{3ABCd}^+ - 3e^{j\frac{2\pi}{3}} \bar{i}_{3ABCd}^{+*} \right\}}{3 \sin \left(\frac{2\pi}{3} \right) - 1}, \quad (5.120)$$

and:

$$i_{3Ad}^+ = \frac{\Re \left\{ 9\bar{i}_{3ABCd}^+ - 3e^{j\frac{2\pi}{3}} \bar{i}_{3ABCd}^{+*} \right\} - \left(3 \cos \left(\frac{2\pi}{3} \right) - 1 \right) i_{3Bd}^+}{4}. \quad (5.121)$$

Finally, the C sector component is evaluated by (5.118).

Equations (5.120), (5.121) and (5.118) together with (5.115) allow controlling (or avoiding) the radial force minimising the stator copper Joule losses while q -axis control of each three-phase subsystem (inverter) is independently controlled in order to define the desired power sharing among the subsystems.

Radial force control for equally distributed q -axis currents (advanced current sharing)

If the active power is likely to be equally distributed, (5.115) can be used to maintain the q -axis current sharing constant equal to $1/3$ (equal distribution of the mechanical power and zero

related force generation, $\bar{K}_{ABC,q} = 0$), and the d -axis components can be used to control the force by (5.120), (5.121) and (5.118) without affecting the equal power sharing operation with:

$$\bar{i}_{3ABCd}^+ = \frac{\bar{F}}{F_{3ABCd,dc}^+ + F_{3ABCd,direct}^+ e^{j6\theta_m} + F_{3ABCd,inverse}^+ e^{-j6\theta_m}}. \quad (5.122)$$

In case of one sector open phase fault ($i_{3Td}^+ = 0$ with T equal to A , B or C) or if the overall d -axis component of the 3rd space vector is maintained equal to zero ($i_{3d}^+ = i_{3Ad}^+ + i_{3Bd}^+ + i_{3Cd}^+ = 0$) the minimisation of the stator copper losses cannot be defined because to generate \bar{i}_{3ABCd}^+ with only two components there are not control DoFs.

Hereafter, the machine is considered as a unique triple three-phase system, without considering the current sharing control. This means that the constraint of the active power distribution among the three-phase subsystems is not more taken into account.

5.6 Radial Force FTC in case of Three-Phase Open Phase Fault

In this section, the force control for a triple three-phase sectored machine in case of three-phase open fault is presented.

It is worth noticing that in case of two inverters open fault the degrees of freedom of the system are reduced to two. Therefore, there are no more enough degrees of freedom for controlling both the torque and the force. It is possible to produce only the force (by using all the two degrees of freedom of one three-phase subsystem) or only the torque (as in a standard three-phase machine). As previously explained, if an open phase fault (or current sharing) happens when the machine is torque controlled and there is not a force control, there are undesired forces acting on the rotor.

The FTC proposed in the next subsection is based on the exploitation of the 2nd and 4th current space vector in the force production without affecting the space related to the torque control (the 3rd one). In other words, the FTC aims to maintain the overall q -axis component of the 3rd space vector at the value required from the torque control and the overall d -axis component equal to zero (or to a different value in case of general flux weakening). The sharing of these current vector components among the three inverters has been considered in the previous section.

In the following subsection, the FTC algorithm exploits also the overall d -axis component of the 3rd space vector with an optimised technique that aims to minimise the stator copper Joule losses, still considering the machine as an overall multiphase system rather than controlling it by current sharing techniques for the different inverters.

Radial Force Equation in case of Three-Phase Open Fault (independent 3rd space control)

If a current sharing technique is abandoned, the compensation of a three-phase open fault can be investigated maintaining the same control of the 3rd current space vector.

The three-phase open fault is described in terms of additional current space vector constraints by (5.78) as:

$$\begin{cases} \bar{i}_M = \frac{1}{3} \left(\bar{i}_{A,1} + \bar{i}_{B,1} e^{j\frac{2\pi}{3}} + \bar{i}_{C,1} e^{j\frac{4\pi}{3}} \right) \\ \bar{i}_N = \frac{1}{3} \left(\bar{i}_{A,1} + \bar{i}_{B,1} e^{-j\frac{2\pi}{3}} + \bar{i}_{C,1} e^{-j\frac{4\pi}{3}} \right) \\ \bar{i}_S = \frac{1}{3} (\bar{i}_{A,1} + \bar{i}_{B,1} + \bar{i}_{C,1}) \end{cases} \quad (5.123)$$

with the current space vector of the faulty subsystem equal to zero $\bar{i}_{Pf,1} = 0$ with Pf the faulty three-phase subsystem under the pole pair P ($P=A, B$ or C). Therefore, there are three possible equation systems for the open phase constraint:

$$\begin{cases} \bar{i}_M = \frac{1}{3} \left(\bar{i}_{B,1} e^{j\frac{2\pi}{3}} + \bar{i}_{C,1} e^{j\frac{4\pi}{3}} \right) \\ \bar{i}_N = \frac{1}{3} \left(\bar{i}_{B,1} e^{-j\frac{2\pi}{3}} + \bar{i}_{C,1} e^{-j\frac{4\pi}{3}} \right) \\ \bar{i}_S = \frac{1}{3} (\bar{i}_{B,1} + \bar{i}_{C,1}) \end{cases}, \begin{cases} \bar{i}_M = \frac{1}{3} \left(\bar{i}_{A,1} + \bar{i}_{C,1} e^{j\frac{4\pi}{3}} \right) \\ \bar{i}_N = \frac{1}{3} \left(\bar{i}_{A,1} + \bar{i}_{C,1} e^{-j\frac{4\pi}{3}} \right) \\ \bar{i}_S = \frac{1}{3} (\bar{i}_{A,1} + \bar{i}_{C,1}) \end{cases} \text{ or } \begin{cases} \bar{i}_M = \frac{1}{3} \left(\bar{i}_{A,1} + \bar{i}_{B,1} e^{j\frac{2\pi}{3}} \right) \\ \bar{i}_N = \frac{1}{3} \left(\bar{i}_{A,1} + \bar{i}_{B,1} e^{-j\frac{2\pi}{3}} \right) \\ \bar{i}_S = \frac{1}{3} (\bar{i}_{A,1} + \bar{i}_{B,1}) \end{cases} \quad (5.124)$$

depending on if the faulty inverter is A, B or C respectively.

In terms of additional current space vectors, the fault constraints result from one of the equations in (5.80) as:

$$\begin{cases} \bar{i}_{A,1} = 0 = \bar{i}_M + \bar{i}_N + \bar{i}_S \Leftrightarrow \text{fault } A \\ \bar{i}_{B,1} = 0 = \bar{i}_M e^{-j\frac{2\pi}{3}} + \bar{i}_N e^{j\frac{2\pi}{3}} + \bar{i}_S \Leftrightarrow \text{fault } B \\ \bar{i}_{C,1} = 0 = \bar{i}_M e^{j\frac{2\pi}{3}} + \bar{i}_N e^{-j\frac{2\pi}{3}} + \bar{i}_S \Leftrightarrow \text{fault } C \end{cases} \quad (5.125)$$

Choosing to keep the main current space vector ($\bar{i}_S = \bar{i}_3$) independently controlled from the FTC algorithm, it results that the FTC is defined by a constraint that makes the additional current space vectors \bar{i}_M and \bar{i}_N depend from the main one by the following relationship:

$$\bar{i}_M e^{-j\frac{2\pi}{3}(P-1)} + \bar{i}_N e^{j\frac{2\pi}{3}(P-1)} + \bar{i}_S = 0, \quad \begin{cases} P=1 \Leftrightarrow \text{fault } A \\ P=2 \Leftrightarrow \text{fault } B \\ P=3 \Leftrightarrow \text{fault } C \end{cases} \quad (5.126)$$

The resulting radial force is defined by (5.67) as:

$$\bar{F} = F e^{j\theta_F} = \bar{F}_2 + \bar{F}_4 = K_{PM(3,2)} \bar{i}_2^* e^{j3\theta_m} + K_{PM(3,4)} \bar{i}_4 e^{-j3\theta_m}, \quad (5.127)$$

with:

$$\begin{cases} \bar{i}_2 = \frac{1}{3} (\bar{i}_N c_{m2} + \bar{i}_M^* c_{n2}) \\ \bar{i}_4 = \frac{1}{3} (\bar{i}_M c_{m2} + \bar{i}_N^* c_{n4}) \end{cases} \quad (5.128)$$

Therefore, the force can be written in terms of additional space vectors as:

$$\begin{aligned} \bar{F} &= K_{PM(3,2)} \frac{1}{3} (\bar{i}_N^* c_{m2} + \bar{i}_M c_{n2}) e^{j3\theta_m} + K_{PM(3,4)} \frac{1}{3} (\bar{i}_M c_{m2} + \bar{i}_N^* c_{n4}) e^{-j3\theta_m} = \\ &= \frac{1}{3} [K_{PM(3,2)} c_{n2} e^{j3\theta_m} + K_{PM(3,4)} c_{m2} e^{-j3\theta_m}] \bar{i}_M + \frac{1}{3} [K_{PM(3,2)} c_{m2} e^{j3\theta_m} + K_{PM(3,4)} c_{n4} e^{-j3\theta_m}] \bar{i}_N^*. \end{aligned} \quad (5.129)$$

It results that it is still possible to control the radial force by means of the remaining degrees of freedom resulting by the constraints in (5.126). In particular, in case of two faulty three-phase subsystems (P_1 and P_2), the force equation results by the solution of the following equation system:

$$\begin{cases} \bar{F} = \frac{1}{3} [K_{PM(3,2)} c_{n2} e^{j3\theta_m} + K_{PM(3,4)} c_{m2} e^{-j3\theta_m}] \bar{i}_M + \frac{1}{3} [K_{PM(3,2)} c_{m2} e^{j3\theta_m} + K_{PM(3,4)} c_{n4} e^{-j3\theta_m}] \bar{i}_N^* \\ \bar{i}_M e^{-j\frac{2\pi}{3}(P_1-1)} + \bar{i}_N e^{j\frac{2\pi}{3}(P_1-1)} + \bar{i}_S = 0 \\ \bar{i}_M e^{-j\frac{2\pi}{3}(P_2-1)} + \bar{i}_N e^{j\frac{2\pi}{3}(P_2-1)} + \bar{i}_S = 0 \end{cases} \quad (5.130)$$

However, as already mentioned, this faulty scenario is quite rare and in order to define a force control there are no more enough degrees of freedom for a torque control.

Instead, in case of a single three-phase subsystem (P -th) open fault there are still four available degrees of freedom to control the radial force (2 DoF) and the torque (1 DoF). The equation system to be solved results as:

$$\begin{cases} \bar{F} = \frac{1}{3} [K_{PM(3,2)} c_{n2} e^{j3\theta_m} + K_{PM(3,4)} c_{m2} e^{-j3\theta_m}] \bar{i}_M + \frac{1}{3} [K_{PM(3,2)} c_{m2} e^{j3\theta_m} + K_{PM(3,4)} c_{n4} e^{-j3\theta_m}] \bar{i}_N^* \\ \bar{i}_M e^{-j\frac{2\pi}{3}(P-1)} + \bar{i}_N e^{j\frac{2\pi}{3}(P-1)} + \bar{i}_S = 0 \end{cases} \quad (5.131)$$

The system can be solved by substituting \bar{i}_N from the second equation of (5.131) in the first one as:

$$\begin{aligned} \bar{F} &= \frac{1}{3} \left[K_{PM(3,2)} c_{n2} e^{j3\theta_m} + K_{PM(3,4)} c_{m2} e^{-j3\theta_m} \right] \bar{i}_M + \\ &+ \frac{1}{3} \left[K_{PM(3,2)} c_{m2} e^{j3\theta_m} + K_{PM(3,4)} c_{n4} e^{-j3\theta_m} \right] \left(-\bar{i}_M^* e^{j\frac{4\pi}{3}(P-1)} - \bar{i}_S^* e^{j\frac{2\pi}{3}(P-1)} \right), \end{aligned} \quad (5.132)$$

that is rewritten as:

$$\begin{aligned} \bar{F} &+ \frac{1}{3} \left[K_{PM(3,2)} c_{m2} e^{j3\theta_m} + K_{PM(3,4)} c_{n4} e^{-j3\theta_m} \right] \bar{i}_S^* e^{j\frac{2\pi}{3}(P-1)} = \\ &\frac{1}{3} \left[K_{PM(3,2)} c_{n2} e^{j3\theta_m} + K_{PM(3,4)} c_{m2} e^{-j3\theta_m} \right] \bar{i}_M + \\ &- \frac{1}{3} \left[K_{PM(3,2)} c_{m2} e^{j3\theta_m} + K_{PM(3,4)} c_{n4} e^{-j3\theta_m} \right] e^{j\frac{4\pi}{3}(P-1)} \bar{i}_M^*. \end{aligned} \quad (5.133)$$

Equation (5.133) allows evaluating the reference additional current space vector \bar{i}_M for the definition of the force control equation as follows.

The conjugate of (5.133) is:

$$\begin{aligned} \bar{F}^* &+ \frac{1}{3} \left[K_{PM(3,2)} c_{m2} e^{-j3\theta_m} + K_{PM(3,4)} c_{n4} e^{j3\theta_m} \right] \bar{i}_S e^{-j\frac{2\pi}{3}(P-1)} = \\ &\frac{1}{3} \left[K_{PM(3,2)} c_{n2} e^{-j3\theta_m} + K_{PM(3,4)} c_{m2} e^{j3\theta_m} \right] \bar{i}_M^* + \\ &- \frac{1}{3} \left[K_{PM(3,2)} c_{m2} e^{-j3\theta_m} + K_{PM(3,4)} c_{n4} e^{j3\theta_m} \right] e^{-j\frac{4\pi}{3}(P-1)} \bar{i}_M. \end{aligned} \quad (5.134)$$

Equation (5.134) can be rewritten as:

$$\begin{aligned} \bar{i}_M^* &= \frac{\bar{F}^* + \frac{1}{3} \left[K_{PM(3,2)} c_{m2} e^{-j3\theta_m} + K_{PM(3,4)} c_{n4} e^{j3\theta_m} \right] \bar{i}_S e^{-j\frac{2\pi}{3}(P-1)}}{\frac{1}{3} \left[K_{PM(3,2)} c_{n2} e^{-j3\theta_m} + K_{PM(3,4)} c_{m2} e^{j3\theta_m} \right]} + \\ &+ \frac{\frac{1}{3} \left[K_{PM(3,2)} c_{m2} e^{-j3\theta_m} + K_{PM(3,4)} c_{n4} e^{j3\theta_m} \right] e^{-j\frac{4\pi}{3}(P-1)}}{\frac{1}{3} \left[K_{PM(3,2)} c_{n2} e^{-j3\theta_m} + K_{PM(3,4)} c_{m2} e^{j3\theta_m} \right]} \bar{i}_M. \end{aligned} \quad (5.135)$$

Substituting (5.135) in (5.133) results in the FFTC equation:

$$\begin{aligned}
 & \left[K_{PM(3,2)}c_{n2}e^{j3\vartheta_m} + K_{PM(3,4)}c_{m2}e^{-j3\vartheta_m} \right] \bar{i}_M + \\
 & - \left[K_{PM(3,2)}c_{m2}e^{j3\vartheta_m} + K_{PM(3,4)}c_{n4}e^{-j3\vartheta_m} \right] \frac{\left[K_{PM(3,2)}c_{m2}e^{-j3\vartheta_m} + K_{PM(3,4)}c_{n4}e^{j3\vartheta_m} \right]}{\left[K_{PM(3,2)}c_{n2}e^{-j3\vartheta_m} + K_{PM(3,4)}c_{m2}e^{j3\vartheta_m} \right]} \bar{i}_M = \\
 & = 3\bar{F} + \left[K_{PM(3,2)}c_{m2}e^{j3\vartheta_m} + K_{PM(3,4)}c_{n4}e^{-j3\vartheta_m} \right] \bar{i}_S e^{j\frac{2\pi}{3}(P-1)} + \\
 & + \left[K_{PM(3,2)}c_{m2}e^{j3\vartheta_m} + K_{PM(3,4)}c_{n4}e^{-j3\vartheta_m} \right] \frac{3\bar{F}^* e^{-j\frac{2\pi}{3}(P-1)}}{\left[K_{PM(3,2)}c_{n2}e^{-j3\vartheta_m} + K_{PM(3,4)}c_{m2}e^{j3\vartheta_m} \right]} + \\
 & + \left[K_{PM(3,2)}c_{m2}e^{j3\vartheta_m} + K_{PM(3,4)}c_{n4}e^{-j3\vartheta_m} \right] \frac{\left[K_{PM(3,2)}c_{m2}e^{-j3\vartheta_m} + K_{PM(3,4)}c_{n4}e^{j3\vartheta_m} \right] \bar{i}_S e^{j\frac{2\pi}{3}(P-1)}}{\left[K_{PM(3,2)}c_{n2}e^{-j3\vartheta_m} + K_{PM(3,4)}c_{m2}e^{j3\vartheta_m} \right]}.
 \end{aligned} \tag{5.136}$$

Equation (5.137) can be simplified as:

$$\bar{i}_M = \frac{3\bar{F} + \bar{K}_{F^*}\bar{F}^* + \bar{K}_{S^*}\bar{i}_S^* + \bar{K}_S\bar{i}_S}{\bar{K}_D}, \tag{5.137}$$

introducing the following variables:

$$\begin{aligned}
 \bar{K}_D &= \left[K_{PM(3,2)}c_{n2}e^{j3\vartheta_m} + K_{PM(3,4)}c_{m2}e^{-j3\vartheta_m} \right] + \\
 & - \frac{\left[K_{PM(3,2)}c_{m2}e^{j3\vartheta_m} + K_{PM(3,4)}c_{n4}e^{-j3\vartheta_m} \right] \left[K_{PM(3,2)}c_{m2}e^{-j3\vartheta_m} + K_{PM(3,4)}c_{n4}e^{j3\vartheta_m} \right]}{\left[K_{PM(3,2)}c_{n2}e^{-j3\vartheta_m} + K_{PM(3,4)}c_{m2}e^{j3\vartheta_m} \right]}, \\
 \bar{K}_{F^*} &= \frac{3 \left[K_{PM(3,2)}c_{m2}e^{j3\vartheta_m} + K_{PM(3,4)}c_{n4}e^{-j3\vartheta_m} \right]}{\left[K_{PM(3,2)}c_{n2}e^{-j3\vartheta_m} + K_{PM(3,4)}c_{m2}e^{j3\vartheta_m} \right]} e^{-j\frac{2\pi}{3}(P-1)}, \\
 \bar{K}_{S^*} &= \left[K_{PM(3,2)}c_{m2}e^{j3\vartheta_m} + K_{PM(3,4)}c_{n4}e^{-j3\vartheta_m} \right] e^{j\frac{2\pi}{3}(P-1)}, \\
 \bar{K}_S &= \frac{\left[K_{PM(3,2)}c_{m2}e^{j3\vartheta_m} + K_{PM(3,4)}c_{n4}e^{-j3\vartheta_m} \right] \left[K_{PM(3,2)}c_{m2}e^{-j3\vartheta_m} + K_{PM(3,4)}c_{n4}e^{j3\vartheta_m} \right] e^{j\frac{2\pi}{3}(P-1)}}{\left[K_{PM(3,2)}c_{n2}e^{-j3\vartheta_m} + K_{PM(3,4)}c_{m2}e^{j3\vartheta_m} \right]}.
 \end{aligned}$$

The FFTC control is based on defining the additional space vectors related to the force by (5.137) and (5.131) as:

$$\begin{cases} \bar{i}_M = \frac{3\bar{F} + \bar{K}_{F^*}\bar{F}^* + \bar{K}_{S^*}\bar{i}_S^* + \bar{K}_S\bar{i}_S}{\bar{K}_D} \\ \bar{i}_N = -\bar{i}_M e^{j\frac{2\pi}{3}(P-1)} - \bar{i}_S e^{-j\frac{2\pi}{3}(P-1)} \end{cases} \tag{5.138}$$

This allows controlling the radial force by the two remaining healthy three-phase subsystems considering also the effect of the torque control.

Radial Force Compensation in case of Three-Phase Open Fault (F=0)

If the radial force control is not required, it is possible to just compensate the radial force rising from the torque control of the machine, by an open loop control based on the simplification of (5.138) as:

$$\begin{cases} \bar{i}_M = \frac{\bar{K}_S^* \bar{i}_S^* + \bar{K}_S \bar{i}_S}{\bar{K}_D} \\ \bar{i}_N = -\bar{i}_M e^{j\frac{2\pi}{3}(P-1)} - \bar{i}_S e^{-j\frac{2\pi}{3}(P-1)} \end{cases} \quad (5.139)$$

An improved solution can be found if also the d-axis component of the 3rd current space vector in the rotor reference frame is considered as a variable.

Radial Force FTC in case of Three-Phase Open Fault – optimised algorithm

In the previous analysis, all the degrees of freedom of the current control have been used in the FFTC in order to maintain completely independent the control of the main current space vector from the FFTC. However, the *d*-axis component of the 3rd current space vector might be used to have an additional variable in the FFTC algorithm.

In this subsection, the proposed FTC algorithm exploits also the *d*-axis component of the 3rd space vector with an optimised technique that aims to minimise the stator copper Joule losses in the torque and radial force control in case of one three-phase subsystem open fault.

The equation system that describes the radial force in case of one sector open phase fault (5.131) is rewritten considering as constraint only the q-axis component of the 3rd current space vector in the rotor reference frame (to not affect the torque control with the FFTC):

$$\begin{cases} \bar{F} = \frac{1}{3} [K_{PM(3,2)} c_{n2} e^{j3\theta_m} + K_{PM(3,4)} c_{m2} e^{-j3\theta_m}] \bar{i}_M + \frac{1}{3} [K_{PM(3,2)} c_{m2} e^{j3\theta_m} + K_{PM(3,4)} c_{n4} e^{-j3\theta_m}] \bar{i}_N^* \\ \bar{i}_M e^{-j\frac{2\pi}{3}(P-1)} + \bar{i}_N e^{j\frac{2\pi}{3}(P-1)} + \bar{i}_S = 0 \\ \bar{i}_S = \bar{i}_3 = (\bar{i}_{3d}^+ + j\bar{i}_{3q}^+) e^{j3\theta_m} \end{cases} \quad (5.140)$$

where now the only constraint is that the *q*-axis component of the 3rd current space vector must be equal to its reference value defined by the torque control: $\bar{i}_{3q}^+ = \bar{i}_{3q,ref}^+$.

This constraint can be directly added in the FFTC equation (5.138) as:

$$\bar{i}_M = \frac{3\bar{F} + \bar{K}_{F^*}\bar{F}^* + \bar{K}_{S^*}(i_{3d}^+ - ji_{3q}^+)e^{-j3\theta_m} + \bar{K}_S(i_{3d}^+ + ji_{3q}^+)e^{j3\theta_m}}{\bar{K}_D}, \quad (5.141)$$

resulting as:

$$\bar{i}_M - \frac{\bar{K}_{S^*}e^{-j3\theta_m} + \bar{K}_Se^{j3\theta_m}}{\bar{K}_D}i_{3d}^+ = \frac{3\bar{F} + \bar{K}_{F^*}\bar{F}^* + (j\bar{K}_Se^{j3\theta_m} - j\bar{K}_{S^*}e^{-j3\theta_m})i_{3q}^+}{\bar{K}_D}. \quad (5.142)$$

This means that in order to generate the desired force, considering also the torque control

(i_{3q}^+), it is needed to control the new current vector \bar{i}_{FFTC} defined as:

$$\bar{i}_{FFTC} = \bar{i}_M - \frac{\bar{K}_{S^*}e^{-j3\theta_m} + \bar{K}_Se^{j3\theta_m}}{\bar{K}_D}i_{3d}^+. \quad (5.143)$$

The related three-phase space vectors can be evaluated by (5.80) as:

$$\left\{ \begin{array}{l} \bar{i}_{A,1} = \bar{i}_M + \bar{i}_N + \bar{i}_S \\ \bar{i}_{B,1} = \bar{i}_M e^{-j\frac{2\pi}{3}} + \bar{i}_N e^{j\frac{2\pi}{3}} + \bar{i}_S \\ \bar{i}_{C,1} = \bar{i}_M e^{j\frac{2\pi}{3}} + \bar{i}_N e^{-j\frac{2\pi}{3}} + \bar{i}_S \end{array} \right. \quad \text{with} \quad \left\{ \begin{array}{l} \bar{i}_N = -\bar{i}_S e^{-j\frac{2\pi}{3}(P-1)} - \bar{i}_M e^{j\frac{2\pi}{3}(P-1)} \\ \bar{i}_S = i_{3d}^+ e^{j3\theta_m} + ji_{3q}^+ e^{j3\theta_m} \\ \bar{i}_M = \bar{i}_{FFTC} + \frac{\bar{K}_{S^*}e^{-j3\theta_m} + \bar{K}_Se^{j3\theta_m}}{\bar{K}_D}i_{3d}^+ \end{array} \right. \quad (5.144)$$

Therefore, it is possible to write the following relationship:

$$\left\{ \begin{array}{l} \bar{i}_{A,1} = \left(1 - e^{j\frac{2\pi}{3}(P-1)}\right)\bar{i}_{FFTC} + \\ + \left(\frac{\bar{K}_{S^*}e^{-j3\theta_m} + \bar{K}_Se^{j3\theta_m}}{\bar{K}_D} - e^{j3\theta_m}e^{-j\frac{2\pi}{3}(P-1)} - \frac{\bar{K}_{S^*}e^{-j3\theta_m} + \bar{K}_Se^{j3\theta_m}}{\bar{K}_D}e^{j\frac{2\pi}{3}(P-1)} + e^{j3\theta_m}\right)(i_{3d}^+ + ji_{3q}^+) \\ \bar{i}_{B,1} = \left(e^{-j\frac{2\pi}{3}} - e^{j\frac{2\pi}{3}(P-1)}e^{j\frac{2\pi}{3}}\right)\bar{i}_{FFTC} + \\ + \left(\frac{\bar{K}_{S^*}e^{-j3\theta_m} + \bar{K}_Se^{j3\theta_m}}{\bar{K}_D}e^{-j\frac{2\pi}{3}} - e^{j3\theta_m}e^{-j\frac{2\pi}{3}(P-1)}e^{j\frac{2\pi}{3}} - \frac{\bar{K}_{S^*}e^{-j3\theta_m} + \bar{K}_Se^{j3\theta_m}}{\bar{K}_D}e^{j\frac{2\pi}{3}(P-1)}e^{j\frac{2\pi}{3}} + e^{j3\theta_m}\right)(i_{3d}^+ + ji_{3q}^+) \\ \bar{i}_{C,1} = \left(e^{j\frac{2\pi}{3}} - \bar{i}_{FFTC}e^{j\frac{2\pi}{3}(P-1)}e^{-j\frac{2\pi}{3}}\right)\bar{i}_{FFTC} + \\ + \left(\frac{\bar{K}_{S^*}e^{-j3\theta_m} + \bar{K}_Se^{j3\theta_m}}{\bar{K}_D}e^{j\frac{2\pi}{3}} - e^{j3\theta_m}e^{-j\frac{2\pi}{3}(P-1)}e^{-j\frac{2\pi}{3}} - \frac{\bar{K}_{S^*}e^{-j3\theta_m} + \bar{K}_Se^{j3\theta_m}}{\bar{K}_D}e^{j\frac{2\pi}{3}(P-1)}e^{-j\frac{2\pi}{3}} + e^{j3\theta_m}\right)(i_{3d}^+ + ji_{3q}^+) \end{array} \right. \quad (5.145)$$

The aim of the proposed improved FTC is to control the radial force by minimizing the total stator copper Joule losses defined by (3.48) as:

$$P_J = \frac{3}{2}R_s(i_{A,\alpha}^2 + i_{A,\beta}^2 + i_{B,\alpha}^2 + i_{B,\beta}^2 + i_{C,\alpha}^2 + i_{C,\beta}^2), \quad (5.146)$$

where the equation is now written in the stator reference frame.

The square of the magnitude of the three-phase current space vectors in the Joule losses equation can be rewritten in a suitable way as:

$$P_J = \frac{3}{2} R_s (\bar{i}_{A,1} \bar{i}_{A,1}^* + \bar{i}_{B,1} \bar{i}_{B,1}^* + \bar{i}_{C,1} \bar{i}_{C,1}^*). \quad (5.147)$$

In order to simplify the problem, hereafter the solution is found for the sector A open phase fault. Therefore, the copper losses can be written as:

$$P_J = \frac{3}{2} R_s (\bar{i}_{B,1} \bar{i}_{B,1}^* + \bar{i}_{C,1} \bar{i}_{C,1}^*) = P_{JB} + P_{JC} = \frac{3}{2} R_s (\bar{i}_{B,1} \bar{i}_{B,1}^*) + \frac{3}{2} R_s (\bar{i}_{C,1} \bar{i}_{C,1}^*). \quad (5.148)$$

The space vector relationships (5.145) result as:

$$\left\{ \begin{array}{l} \bar{i}_{B,1} = \left(e^{-j\frac{2\pi}{3}} - e^{j\frac{2\pi}{3}} \right) \bar{i}_{FFTC} + \\ + \left(\frac{\bar{K}_S e^{-j3\vartheta_m} + \bar{K}_S e^{j3\vartheta_m}}{\bar{K}_D} e^{-j\frac{2\pi}{3}} - e^{j3\vartheta_m} e^{j\frac{2\pi}{3}} - \frac{\bar{K}_S e^{-j3\vartheta_m} + \bar{K}_S e^{j3\vartheta_m}}{\bar{K}_D} e^{j\frac{2\pi}{3}} + e^{j3\vartheta_m} \right) (i_{3d}^+ + j i_{3q}^+) \\ \bar{i}_{C,1} = \left(e^{j\frac{2\pi}{3}} - \bar{i}_{FFTC} e^{-j\frac{2\pi}{3}} \right) \bar{i}_{FFTC} + \\ + \left(\frac{\bar{K}_S e^{-j3\vartheta_m} + \bar{K}_S e^{j3\vartheta_m}}{\bar{K}_D} e^{j\frac{2\pi}{3}} - e^{j3\vartheta_m} e^{-j\frac{2\pi}{3}} - \frac{\bar{K}_S e^{-j3\vartheta_m} + \bar{K}_S e^{j3\vartheta_m}}{\bar{K}_D} e^{-j\frac{2\pi}{3}} + e^{j3\vartheta_m} \right) (i_{3d}^+ + j i_{3q}^+) \end{array} \right. \quad (5.149)$$

Written in a reduced shape as:

$$\left\{ \begin{array}{l} \bar{i}_{B,1} = \bar{B}_1 \bar{i}_{FFTC} + \bar{B}_2 (i_{3d}^+ + j i_{3q}^+) \\ \bar{i}_{C,1} = \bar{C}_1 \bar{i}_{FFTC} + \bar{C}_2 (i_{3d}^+ + j i_{3q}^+) \end{array} \right. \quad (5.150)$$

with the new variables:

$$\left\{ \begin{array}{l} \bar{B}_1 = e^{-j\frac{2\pi}{3}} - e^{j\frac{2\pi}{3}} \\ \bar{B}_2 = \frac{\bar{K}_S e^{-j3\vartheta_m} + \bar{K}_S e^{j3\vartheta_m}}{\bar{K}_D} \left(e^{-j\frac{2\pi}{3}} - e^{j\frac{2\pi}{3}} \right) + \left(1 - e^{j\frac{2\pi}{3}} \right) e^{j3\vartheta_m} \\ \bar{C}_1 = e^{j\frac{2\pi}{3}} - e^{-j\frac{2\pi}{3}} \\ \bar{C}_2 = \frac{\bar{K}_S e^{-j3\vartheta_m} + \bar{K}_S e^{j3\vartheta_m}}{\bar{K}_D} \left(e^{j\frac{2\pi}{3}} - e^{-j\frac{2\pi}{3}} \right) + \left(1 - e^{-j\frac{2\pi}{3}} \right) e^{j3\vartheta_m} \end{array} \right. \quad (5.151)$$

Substituting the three-phase current space vectors in the copper losses equation it results:

$$\begin{aligned} \frac{2P_{JB}}{3R_s} &= \bar{B}_1 \bar{i}_{FFTC} \bar{B}_1^* \bar{i}_{FFTC}^* + \bar{B}_1 \bar{i}_{FFTC} \bar{B}_2^* (i_{3d}^+ - j i_{3q}^+) + \\ &+ \bar{B}_2 (i_{3d}^+ + j i_{3q}^+) \bar{B}_1^* \bar{i}_{FFTC}^* + \bar{B}_2 (i_{3d}^+ + j i_{3q}^+) \bar{B}_2^* (i_{3d}^+ - j i_{3q}^+) + \\ &+ \bar{C}_1 \bar{i}_{FFTC} \bar{C}_1^* \bar{i}_{FFTC}^* + \bar{C}_1 \bar{i}_{FFTC} \bar{C}_2^* (i_{3d}^+ - j i_{3q}^+) + \\ &+ \bar{C}_2 (i_{3d}^+ + j i_{3q}^+) \bar{C}_1^* \bar{i}_{FFTC}^* + \bar{C}_2 (i_{3d}^+ + j i_{3q}^+) \bar{C}_2^* (i_{3d}^+ - j i_{3q}^+). \end{aligned} \quad (5.152)$$

The i_{3d}^+ value that minimizes the stator copper Joule losses (being i_{3d}^+ the only variable in (5.152)) can be found as:

$$\begin{aligned} \frac{d}{di_{3d}^+} \left(\frac{2P_{JB}}{3R_s} \right) &= (\bar{B}_1 \bar{i}_{FFTC} \bar{B}_2^* + \bar{B}_2 \bar{B}_1^* \bar{i}_{FFTC} + 2\bar{B}_2 \bar{B}_2^* i_{3d}^+) + \\ &+ (\bar{C}_1 \bar{i}_{FFTC} \bar{C}_2^* + \bar{C}_2 \bar{C}_1^* \bar{i}_{FFTC} + 2\bar{C}_2 \bar{C}_2^* i_{3d}^+) = 0. \end{aligned} \quad (5.153)$$

Resulting in the final FTC equation in case of sector A open phase fault:

$$i_{3d}^+ = - \frac{(\bar{B}_1 \bar{B}_2^* + \bar{C}_1 \bar{C}_2^*) \bar{i}_{FFTC} + (\bar{B}_2 \bar{B}_1^* + \bar{C}_2 \bar{C}_1^*) \bar{i}_{FFTC}^*}{2\bar{B}_2 \bar{B}_2^* + 2\bar{C}_2 \bar{C}_2^*}, \quad (5.154)$$

with:

$$\bar{i}_{FFTC} = \frac{3\bar{F} + \bar{K}_{F^*} \bar{F}^* + (j\bar{K}_S e^{j3\theta_m} - j\bar{K}_S^* e^{-j3\theta_m}) i_{3q}^+}{\bar{K}_D}.$$

Substituting the optimised i_{3d}^+ equation in (5.144) allows defining the optimised control algorithm. It is clear that this solution is more complicated than the previous one where i_{3d}^+ is not considered as a control variable for the FTC.

5.7 Finite Element Simulation Results (Magnet software)

This section shows FE simulation results for the machine prototype in Fig. 5.1. The simulated torque and force are related to the current rating of the machine (about 5 Nm torque or 200N force) or to the force needed to levitate the rotor (about 20-25 N).

A first in-deep FEA is carried out for matching the main control parameters defined in the control equations (5.84):

$$\begin{aligned} \bar{i}_3 &= j i_{3q}^+ e^{j3\theta_m} = j \frac{T_{ref}}{K_T} e^{j3\theta_m}, \\ \bar{i}_2 &= i_{2d}^{+F} e^{j3\theta_m} e^{-j\theta_F} = F \frac{F_{2,pu}}{K_{PM(3,2)}} e^{j3\theta_m} e^{-j\theta_F}, \\ \bar{i}_4 &= i_{4d}^{-F} e^{j3\theta_m} e^{j\theta_F} = F \frac{(1 - F_{2,pu})}{K_{PM(3,4)}} e^{j3\theta_m} e^{j\theta_F}. \end{aligned} \quad (5.155)$$

The force control variable $F_{2,pu}$ is analysed to understand how it affects the performance of the radial force control, and evaluate the machine behaviour at the optimised working point defined by (5.98). Indeed, this working point is found for the machine control considering the minimization of the stator copper Joule losses, but an analytical evaluation of the iron losses,

the force ripples and efficiency has not been done. Therefore, the following FE results aim to clarify the effects of the $F_{2,pu}$ control variable.

Finally, the machine performance in case of one sector open phase fault with and without FTC are presented.

Torque and Radial Force control parameters (K_T , $K_{PM(3,2)}$ and $K_{PM(3,4)}$)

The control parameters K_T , $K_{PM(3,2)}$ and $K_{PM(3,4)}$ have been matched in an open loop current control in FE linear simulations in magnet. In particular, the matching technique is based on an iterative simulation loop for each constant. The rotor is rotated of 360 mechanical degrees and each current space vector, synchronised with its reference system, is controlled in open loop with a fixed amplitude. The resulting torque (for a give i_{3q}^+ value) or the resulting force (for a given i_{2d}^{+F} or i_{4d}^{-F} value) are exported in the simulation post processing and stored. Each control parameter is defined dividing the magnitude of the measured torque (or force) by the magnitude of the controlled space vector.

Table 5.10 shows the three control parameters resulting from the FEA. The skew effect has been considered running three simulations (one for each skew slice) with the rotor rotated of the various skew angles and averaging the obtained results.

The mismatch can be reduced with a better choice of the radius of the airgap used for the evaluation of the machine control parameters. In particular, the torque constant is almost matched if the radius is chosen almost as the radius of the rotor lamination. However, the result shows that the evaluation of the force constants is not as good as the one obtained for the torque main constant. In particular, the mismatch is of about 50% for both the force parameters.

Hereafter, the FEA control parameters are used. Indeed, the FE simulations better represent the machine behaviour than the analytical model.

Table 5.10 – Table of the machine control parameters (FEA)

	Analytical (2D R=0.0243)	Analytical (skew R=0.0243)	Analytical (skew, R=0.02093)	FEA (2D)	FEA (skew)	Units
K_T	0.5246	0.5008	0.4314	0.4337	0.4313	Nm/A
$K_{PM3,2}$	22.71	21.69	18.67	9.60	9.426	N/A
$K_{PM3,4}$	11.36	10.84	9.34	17.85	17.55	N/A

Torque and Radial Force control (optimised control):

According to the FE matched parameters, the $F_{2,pu}$ control variable that allows controlling the radial force minimising the total stator copper losses (5.98) is:

$$F_{2,pu} = -K_{PM(3,2)} \frac{[C_{m2n2}^- (C_{m2n4}^- K_{PM(3,4)} - C_{m2n2}^- K_{PM(3,2)}) + C_{m2n2}^+ (-C_{m2n4}^+ K_{PM(3,4)} - C_{m2n2}^+ K_{PM(3,2)})]}{[(C_{m2n4}^- K_{PM(3,4)} - C_{m2n2}^- K_{PM(3,2)})^2 + (-C_{m2n4}^+ K_{PM(3,4)} - C_{m2n2}^+ K_{PM(3,2)})^2]} = 0.236 \cong 0.25.$$

Therefore, the optimised working point is with a $F_{2,pu}$ value of about 0.25. This means that the optimised radial force control for the stator copper Joule losses is with almost one quarter of the radial force generated exploiting the 4th order field harmonic and three quarter by the 2nd one.

Flux density and slot current density (FEA view)

Fig. 5.5 shows a view of the flux and slot current density for different $F_{2,pu}$ values. The machine is rotating at 3000 rpm at 5 Nm torque in all the views. Except from the left views, the commanded force is 200 N on the y-axis. 200 N is about the rated force of the machine at no load, and it is almost 10 times the rotor weight force. It can be observed that having a $F_{2,pu}$ value equal to about 0.25 results in more uniform current and flux density distributions.

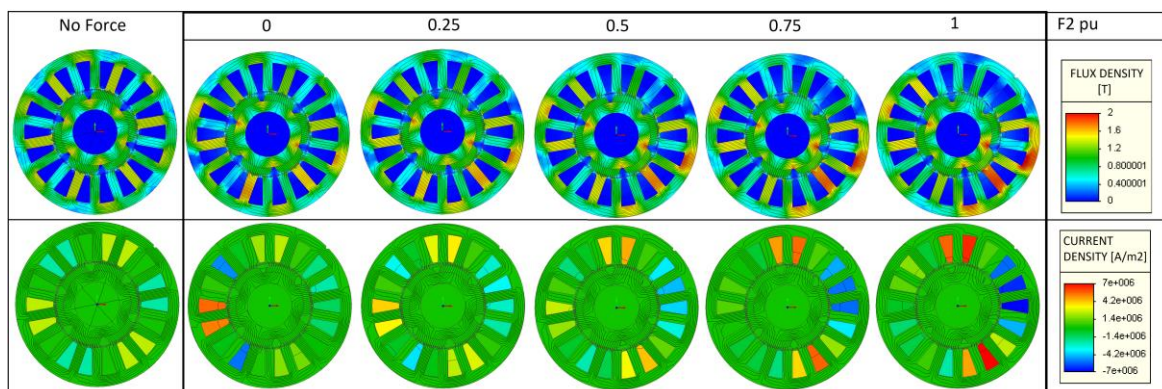


Fig. 5.5 – Flux and slot current density views. Rated torque at no force condition (left) and with 200N force control (right). The F_{2pu} value is increased from zero to 1 (from left to right).

Stator copper Joule losses and distribution

Fig. 5.6 shows the stator copper Joule losses as function of the $F_{2,pu}$ variable at rated torque with and without force control. Fig. 5.7 shows the losses of each three-phase subsystem at rated torque and 200 N force.

The minimum Joule losses are reached for the expected $F_{2,pu}$ value of about 0.25. In particular, this value allows a homogeneous distribution of the copper losses between the inverters, reducing the probability of having localised hot spots and related acceleration of the insulation ageing. In Fig. 5.6 a simplified evaluation of the levitating performance (20 N force) is also highlighted with an asterisk

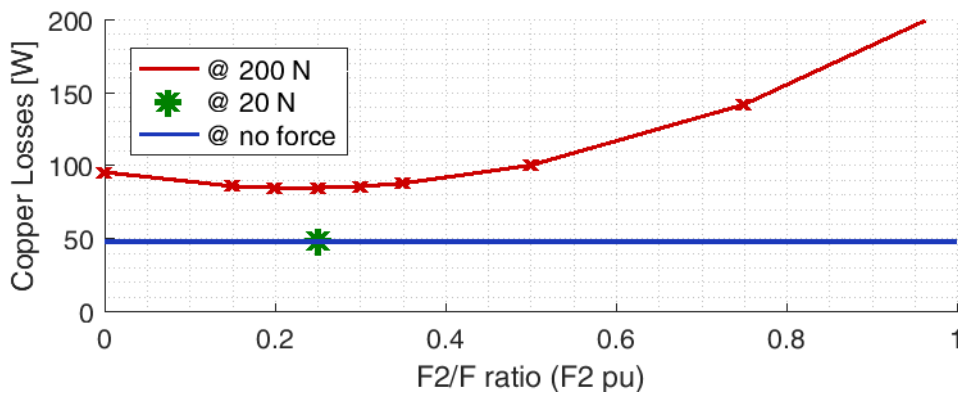


Fig. 5.6 – Stator copper Joule losses as function of the F_{2pu} variable. Rated torque without force (blue), with 20 N (green) and with 200 N (red).

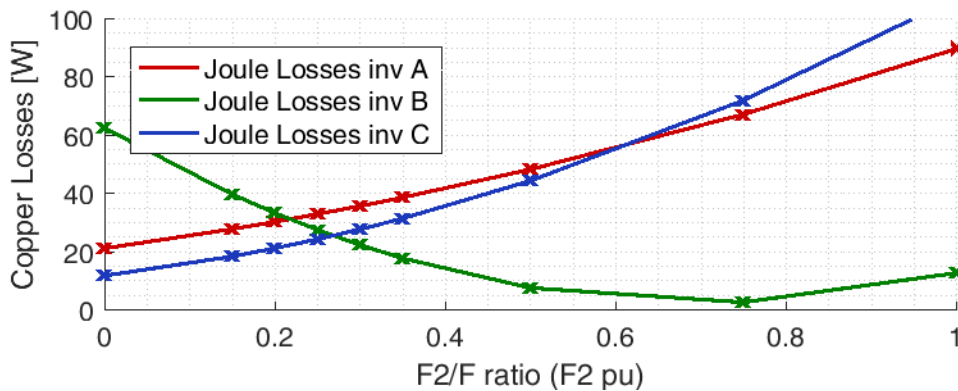


Fig. 5.7 – Stator copper Joule losses in the different three-phase subsystems as function of the F_{2pu} variable. Rated torque with 200 N force.

Iron losses

Fig. 5.8 shows the iron losses as function of the $F_{2,pu}$ variable at rated torque with and without force control. The iron losses at rated torque and 200 N force are also plotted in their different components (eddy and hysteresis) for both the stator and the rotor. The minimum of the losses is still at about $0.25 F_{2,pu}$. Indeed, this can be explained by the more uniform distribution of the stator currents that allows reducing the concentration of the armature flux in reduced areas.

However, the iron losses do not change as much as the copper losses with or without force control. Indeed, in this machine design most of the iron losses are related to the flux generated by the magnets and the armature current effect is a secondary effect. This result significantly depends from the machine topology.

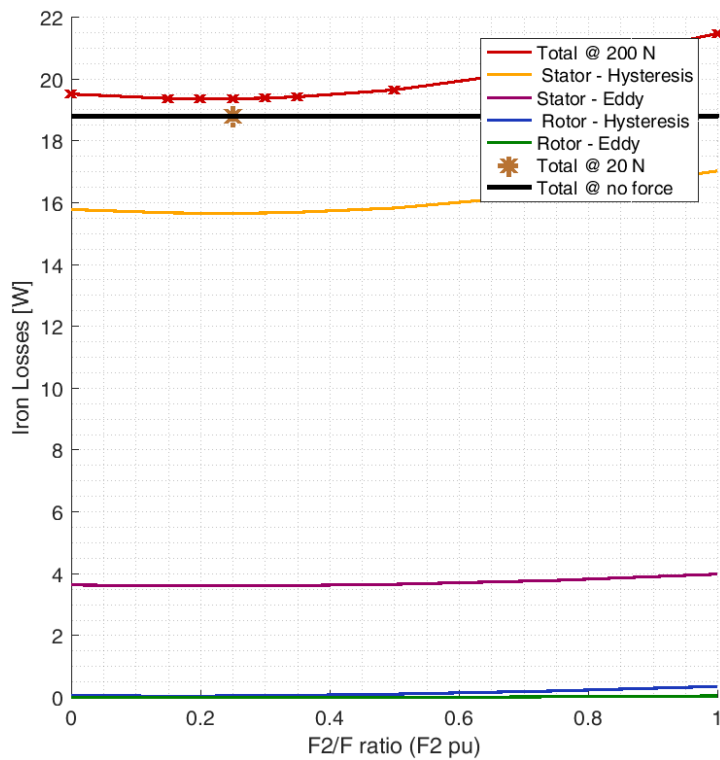


Fig. 5.8 – Iron losses as function of the F2pu variable. Rated torque without force (black), with 20 N (brown asterisk) and with 200 N (red). Iron losses distribution (only for 200 N force t rated torque)

Efficiency

Fig. 5.9 shows the efficiency as function of the $F_{2,pu}$ variable. The efficiency is evaluated considering only the copper and iron losses (the extra-losses as friction and ventilation related ones, are neglected). As in the previous analysis, the efficiencies at rated torque with and without force control are compared. It is worth noticing that the electrical efficiency drop related to the force control needed for the levitation is theoretically negligible for the considered case study. Indeed, in case of a force load of about 10 times the rotor weight the efficiency decreases of about 2.2 percent (from 95.91% to 93.79%). This result can be considered as a benchmark to compare the proposed solution with alternative levitation systems.

Fig. 5.10 summarizes the FEA for the losses and efficiency comparing the rated torque performance with and without radial force control. As already mentioned, the efficiency of the torque and force control for the analysed machine mainly depends from the stator copper Joule losses.

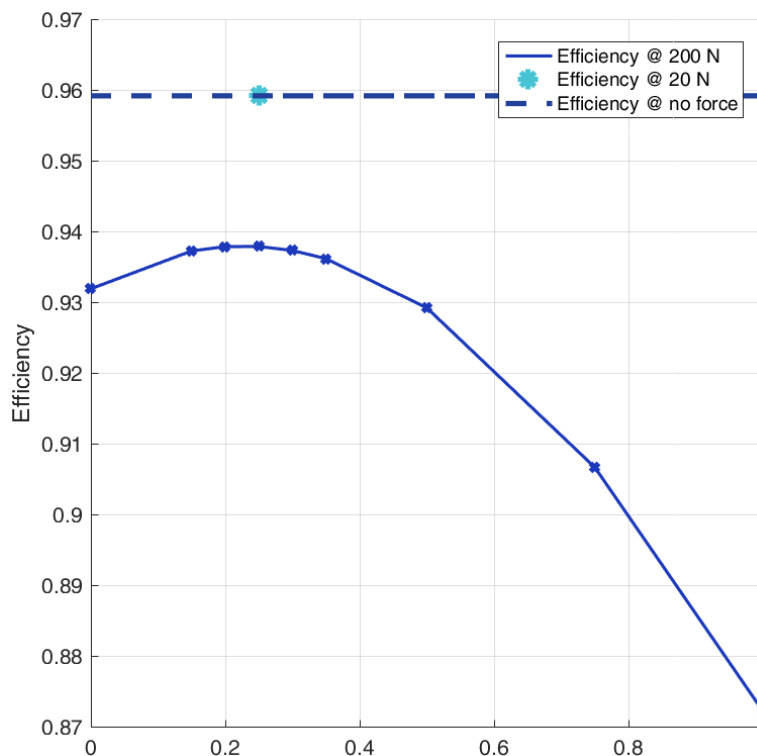


Fig. 5.9 – Efficiency as function of the F_{2pu} variable. Rated torque without force (dashed), with 20 N (light blue asterisk) and with 200 N (continuous).

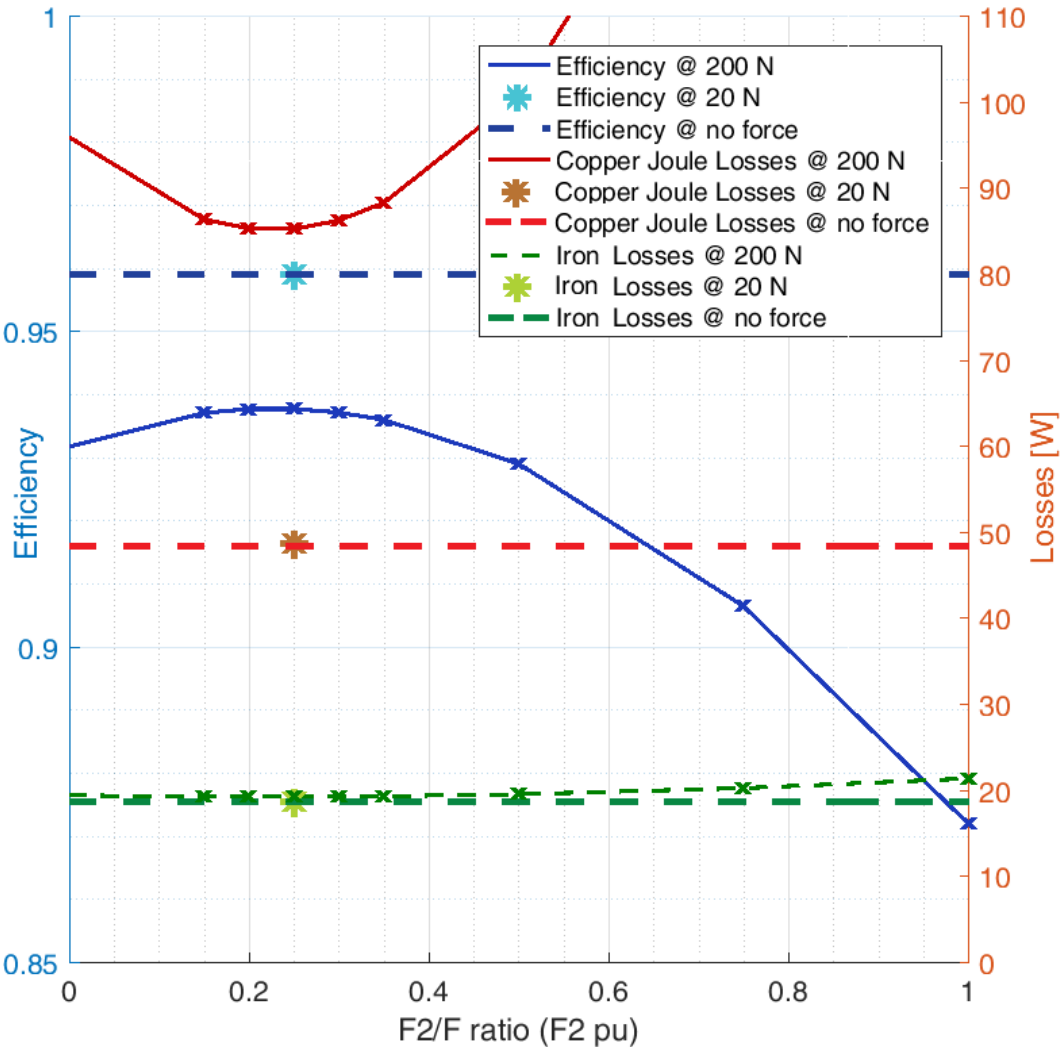


Fig. 5.10 – Losses and efficiency as function of the F2pu variable. Rated torque without force (dashed), with 20 N (asterisk) and with 200 N (continuous). Iron losses (green), copper losses (red) and efficiency (blue).

Torque and Force ripples

In order to understand the open loop torque and force performance, the results of a transient FE simulation are presented here below, where: the machine is controlled at rated torque (5 Nm) and speed (3000 rpm) with a constant force (25 N) and then a force synchronous with the rotor (as in case of dynamic mass unbalance of the shaft). The $F_{2,pu}$ value is 0 (a,d), 0.5 (b,e) and 1 (c,f). Fig. 5.11 shows the resulting force components of the transient simulation. It is clear that higher value of $F_{2,pu}$ result in increased force ripples. Fig. 5.12 shows the open loop control of a 200 N force with the $F_{2,pu}$ variable increasing linearly with the time from 0 to 1 in order to highlight that the optimised 0.25 $F_{2,pu}$ value is still a good working point for the reduction of the force ripple.

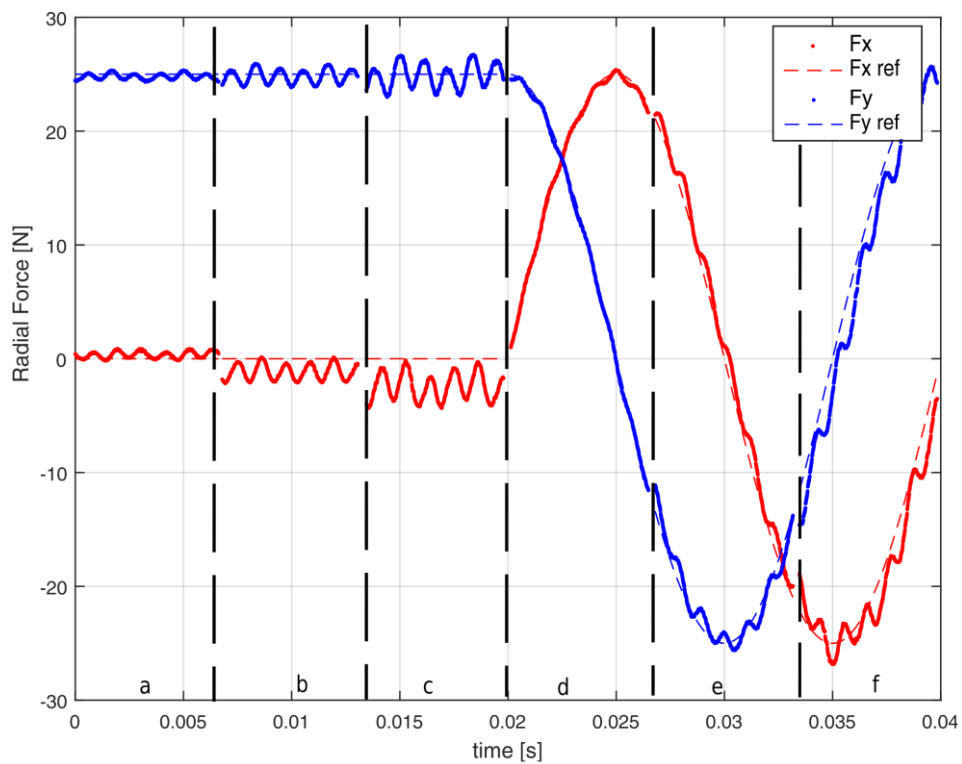


Fig. 5.11 – Machine radial force control at 5 [Nm] torque. The radial force control is 25 [N] static (a, b, c) and 25 [N] dynamic (d, e, f). The ratio F_{2pu} is 0 (a, d), 0.5 (b, e) and 1 (c, f).

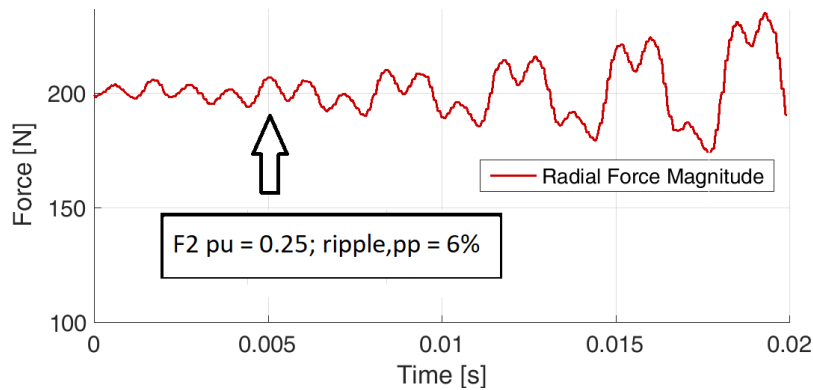


Fig. 5.12 – Radial force ripple at rated torque and speed with 200 N. F_{2pu} varies from 0 ($t = 0$ s) to 1 ($t = 0.02$ s).

Fig. 5.13 and Fig. 5.14 show the resulting torque and phase currents of the same simulation presented in Fig. 5.11. As already investigated, the current distribution in the sectors are more homogeneously distributed with $F_{2,pu}$ values far from 0 or 1 (0.25 is the optimised working point). Instead, the torque performance are completely independent from the radial force control (the iron saturation is not significantly affected by the current control), independently from the $F_{2,pu}$ value.

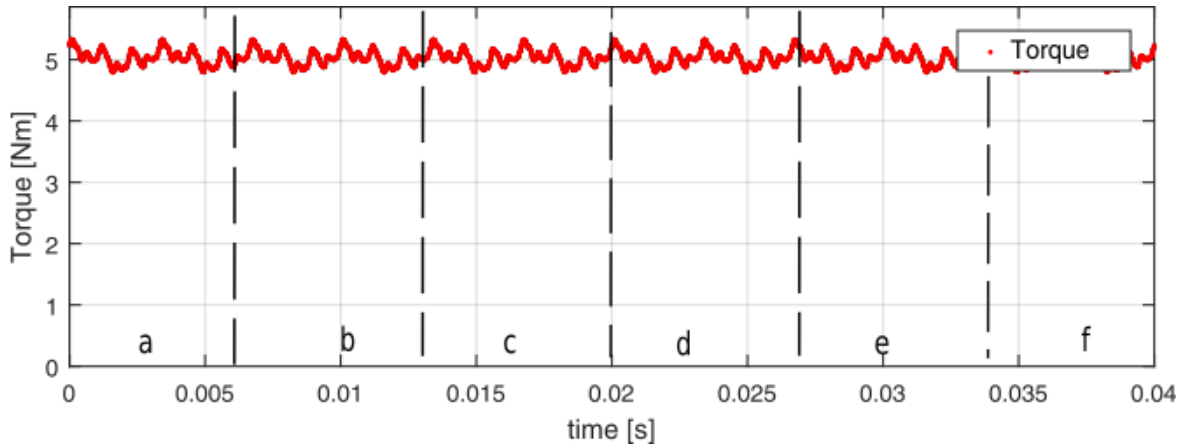


Fig. 5.13 – Machine torque when the reference is 5 Nm and the force is 25 N static (a, b, c) and dynamic (d, e, f). The F_{2pu} value is 0 (a, d), 0.5 (b, e) and 1 (c, f).

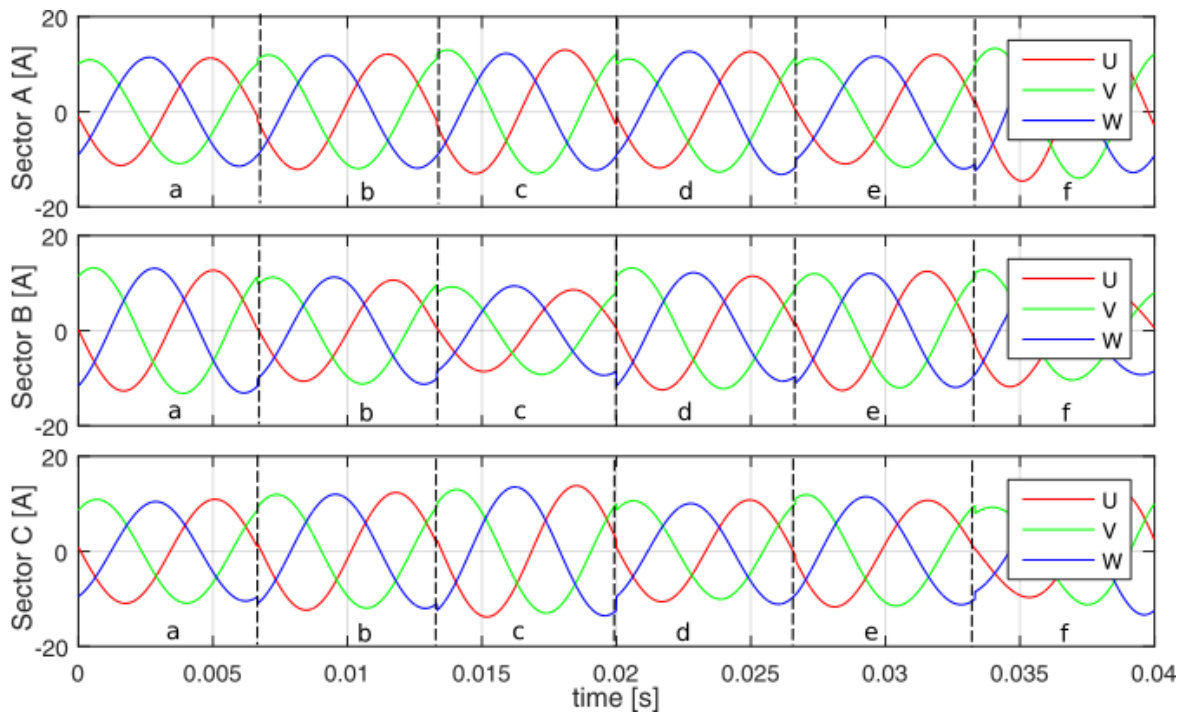


Fig. 5.14 – Machine phase currents when the reference is 5 Nm and the force is 25 N static (a, b, c) and dynamic (d, e, f). The F_{2pu} value is 0 (a, d), 0.5 (b, e) and 1 (c, f).

Radial Force Evaluation in case of Three-Phase Open Fault (standard torque control)

Fig. 5.15 shows the phase currents of a basic control of a multi three-phase machine in case of one inverter fault (the three-inverters remain in faulty condition for 1/3 of the simulation each). The three inverters are independently torque controlled in an equally distributed power sharing approach. In case of fault, the phase currents in the remaining healthy inverters are increased in order to maintain the torque to the reference value (5 Nm). The torque is not shown, because there are not differences from the torque in Fig. 5.14. Instead, as described from (5.105) or (5.107), setting the current sharing coefficient of the faulty inverter equal to zero, the faulty condition results in a radial force acting on the rotor. Fig. 5.16 shows the theoretical and FE force vector trajectory. The force vector is expected to rotate on an elliptical trajectory shifted by an offset in the x-y plane. The ellipsoid is defined by a sum of a direct and an inverse vector rotating at the same speed but in opposite directions and with different phases and amplitudes. The force simplified equation (5.107) is:

$$\bar{F} = j\bar{K}_{ABC3q} i_{3q}^+ F_{3ABCDq,dc}^+ + j\bar{K}_{ABC3q} i_{3q}^+ F_{3ABCDq,direct}^+ e^{j6\theta_m} - j\bar{K}_{ABC3q} i_{3q}^+ F_{3ABCDq,inverse}^+ e^{-j6\theta_m}$$

The mismatch between the theoretical and FE result is represented by the additional force components that have been simplified in the definition of the model, but it seems that for a first analysis of the phenomena the approximation is acceptable.

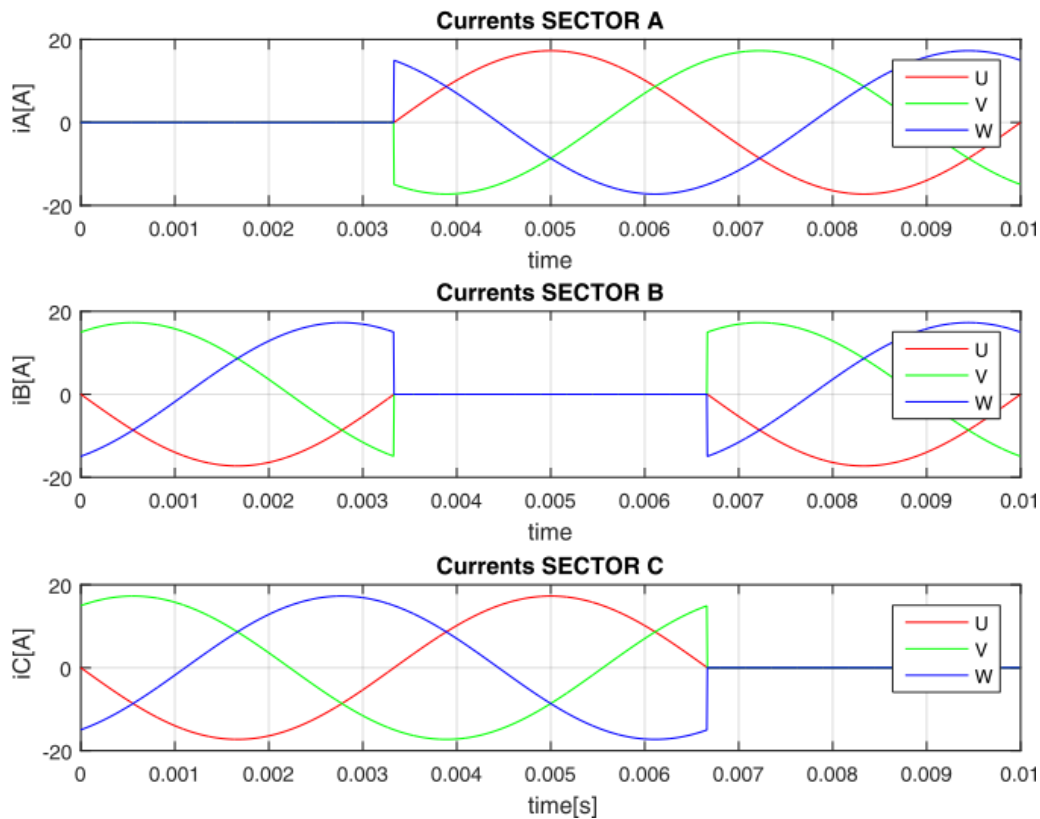


Fig. 5.15 – Currents in one sector open winding configurations with standard redundant symmetrical three-phase current control. The torque is 5 Nm.

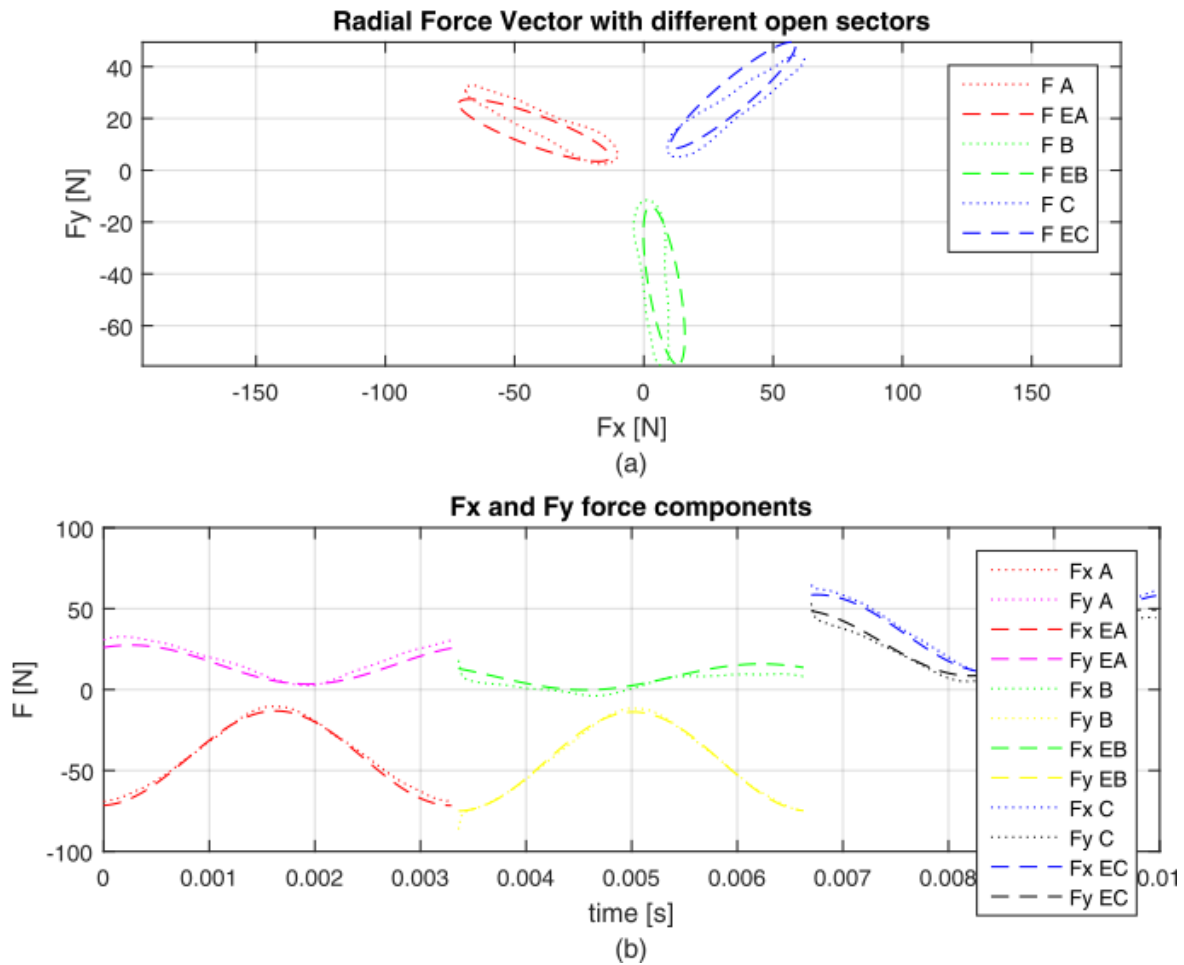


Fig. 5.16 – Simulated radial force (F) and analytical radial force evaluation ($F E$) in one sector open winding configurations with standard redundant three-phase current control. Force vector trajectory (a) and its x - y components (b). The torque is 5 Nm. In the legend, with A, B and C (red-purple, green-yellow and blue-black) the open winding conditions of the respective sectors are identified.

The radial force evaluation is essential to understand how much this fault is critical in the analysed machine, but also to compare the fault tolerant control with the standard one. At rated torque and one missing inverter, the radial force has a mean value of about 44 N and the ripple of about 65 N peak to peak. This can produce bearing damages and rotor vibrations. The maximum phase current in the standard controlled faulty machine, in Fig. 5.15, is 17.3 A, when in healthy conditions it is 11.6 A. As expected from the current sharing theory, the needed current in the faulty machine is $3/2$ times the value of the healthy case.

Radial Force Compensation at Rated Torque ($id3=0$ FTC)

Fig. 5.17 and Fig. 5.18 show the currents and radial force components of a transient FE simulation. The machine is firstly healthy and controlled with the standard torque control (a); then the fault happens in sector A (b); then it is compensated for the radial force due to the

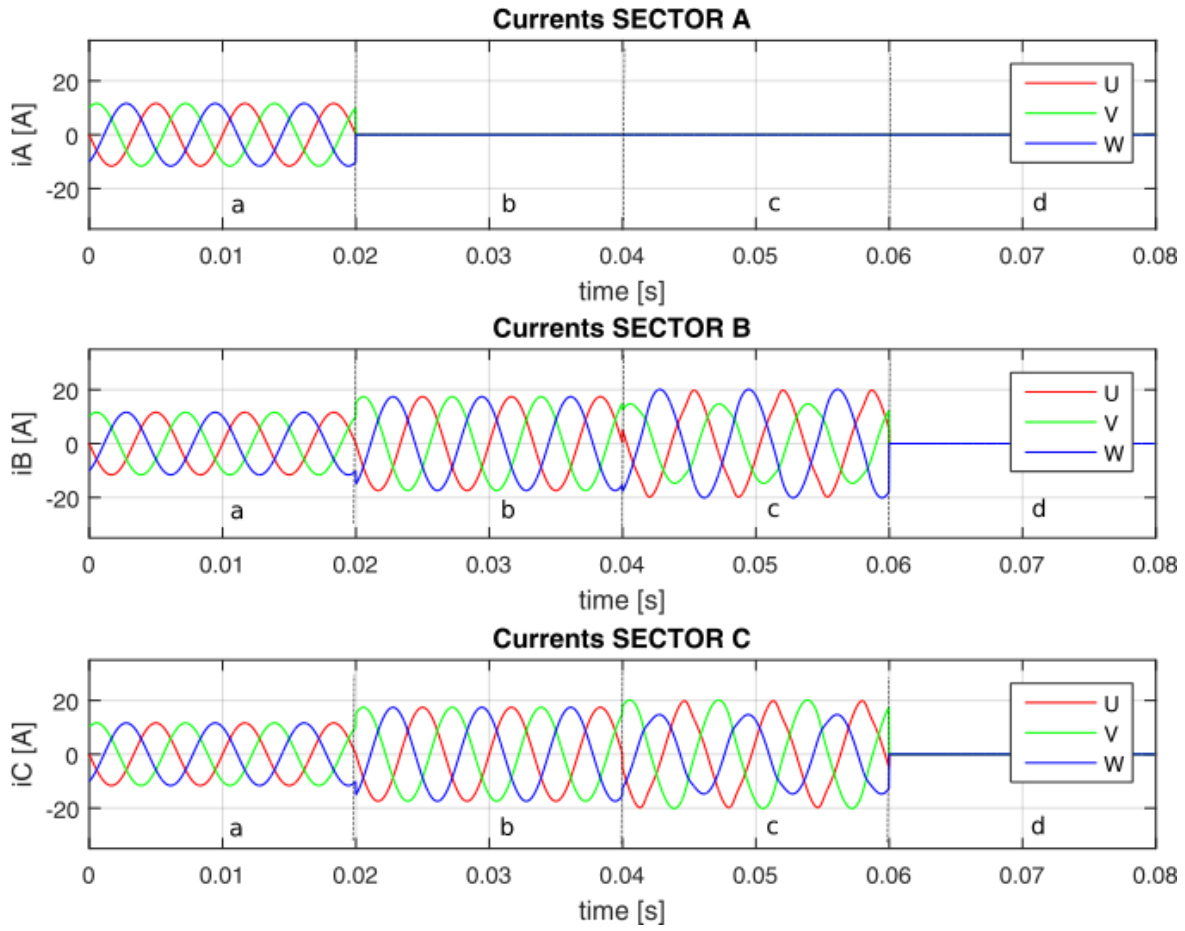


Fig. 5.17 – Currents with 5 Nm torque and 0 N reference radial force. Healthy machine (a), standard open windings control (b), radial force compensation by fault tolerant control (c) and, radial force fault tolerant control at no load (d).

fault in (c); finally, it is compensated for the force in no load conditions (0 Nm) (d). In the first fourth of the reported simulation, the machine is healthy and it is controlled as a three-phase machine (a). As expected, the machine symmetry allows having zero radial force. The only force, which appears, is the rotor weight, but it is neglected in the FE simulation because it is easily evaluable (about 25 N in the simulated machine). Then the machine faulty behaviour is simulated when the standard control is maintained (b). The radial force in case of fault is still the same of Fig. 5.16. Then the machine is compensated for the radial force in an open loop control by the basic fault tolerant algorithm (5.139) (c). The compensation is not complete, due to other radial force contributions neglected in the model. Comparing (b) and (c), the compensation allows reducing the radial force mean value from 44 to 9 N (about 5 times), and the ripple is also significantly reduced from 65 to 11 N (about 6 times). Also if the analysis of the fault tolerant radial force ripple frequencies is not furtherly investigated, it must be noted that, in the standard fault control, the main radial force ripple has a frequency of twice the main electrical frequency, while in the new fault tolerant control there are more and smaller harmonic components with higher frequencies.

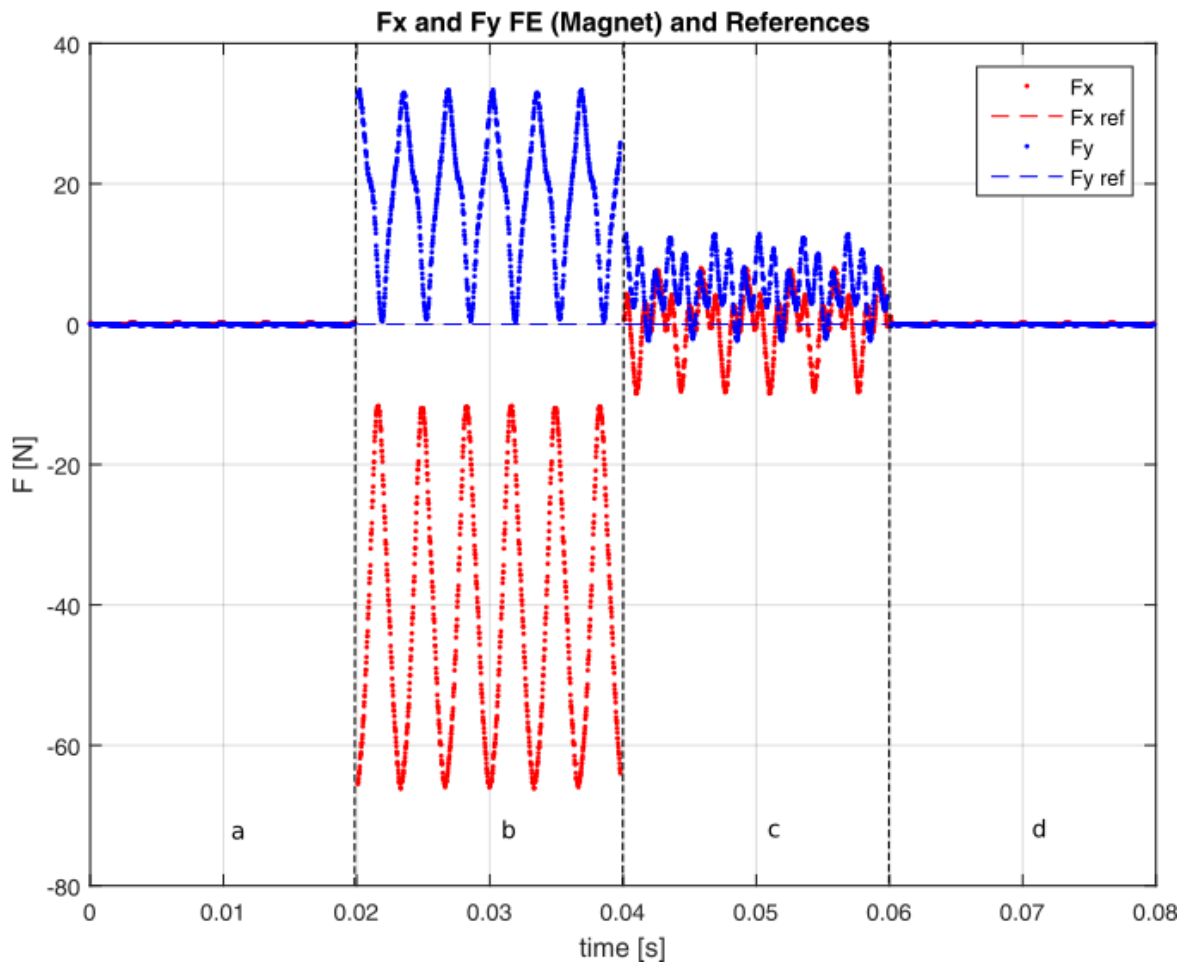


Fig. 5.18 – FE radial force values with 5 Nm torque and 0 N reference radial force. Healthy machine (a), standard open windings control (b), radial force compensation by fault tolerant control (c), radial force fault tolerant control at no load (d).

Radial Force Fault Tolerant Control at Rated Torque ($id3=0$ FTC) – constant force

Fig. 5.19, Fig. 5.20 and Fig. 5.21 show the currents, radial force components and torque of a transient FE simulation similar to the previous one, but in case of a radial force reference value of 25 N in the vertical direction. This value is lightly higher than the force needed to release the bearings from the rotor weight (20 N).

The performance of the fault tolerant radial force control is better at no load (d). This result is in agreement with (5.137), because the presence of a torque control introduces an additional force term that must be compensated in order to control the force to the desired value.

It is also clear that the radial force control performance when the machine is faulty are lower, due to the increase of stator Joule losses and iron losses. Indeed, when the fault happens, also without considering the radial force, the currents increase of $3/2$ to reach the desired torque, as in (b). To compensate for the torque-related radial force there is a further increase (c) that is

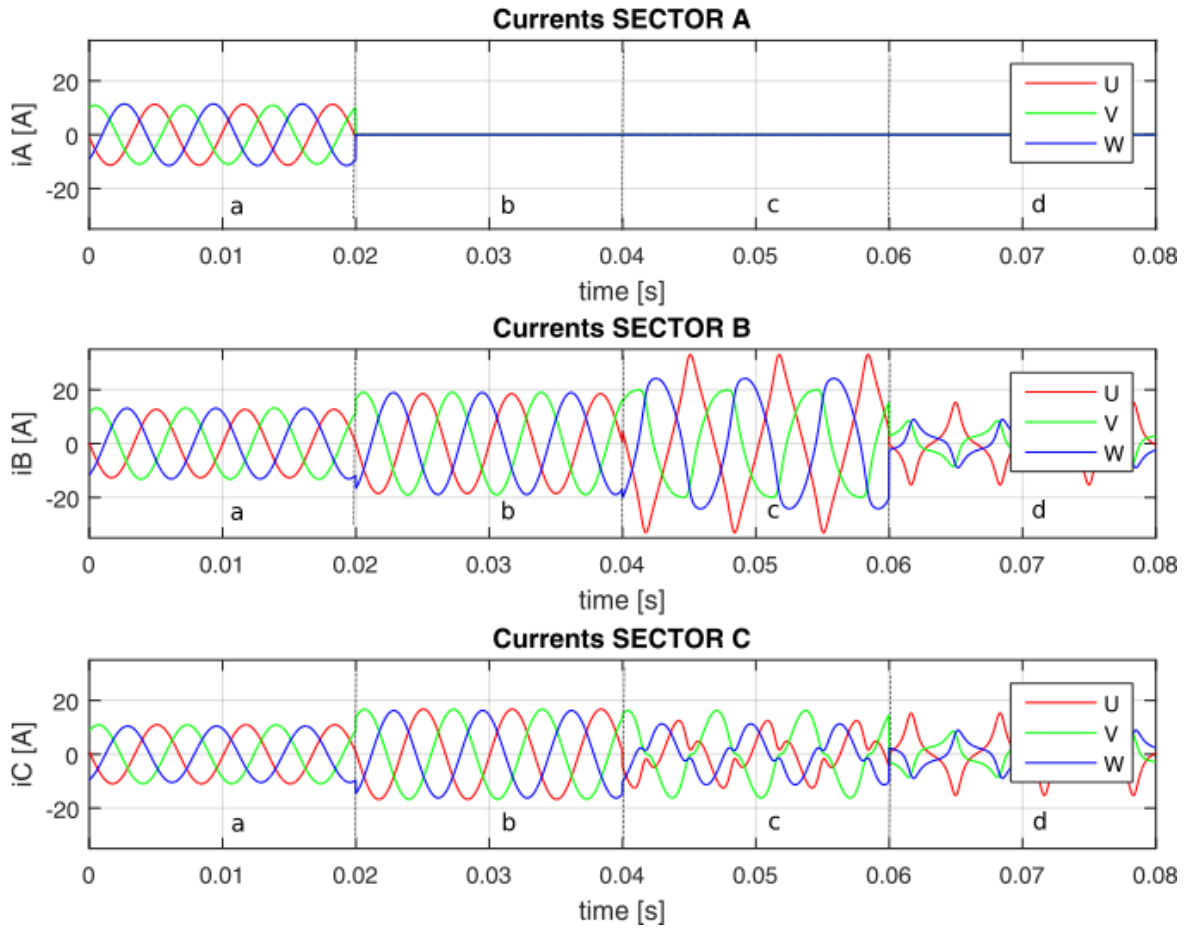


Fig. 5.19 – Currents with 5 Nm torque and 25 N reference radial force. Healthy machine (a), open phase behaviour with standard machine control (b), radial force fault tolerant control (c), fault tolerant radial force control at no load (d).

significantly reduced at no load operation (d). It results that one sector open phase fault makes some of the healthy phases, and the respective VSI, likely work in an overload condition.

The torque performance, presented in Fig. 5.21 is not affected by the force control also in case of one sector open phase fault and radial force FTC. This is an interesting result in term of force and torque control decoupling.

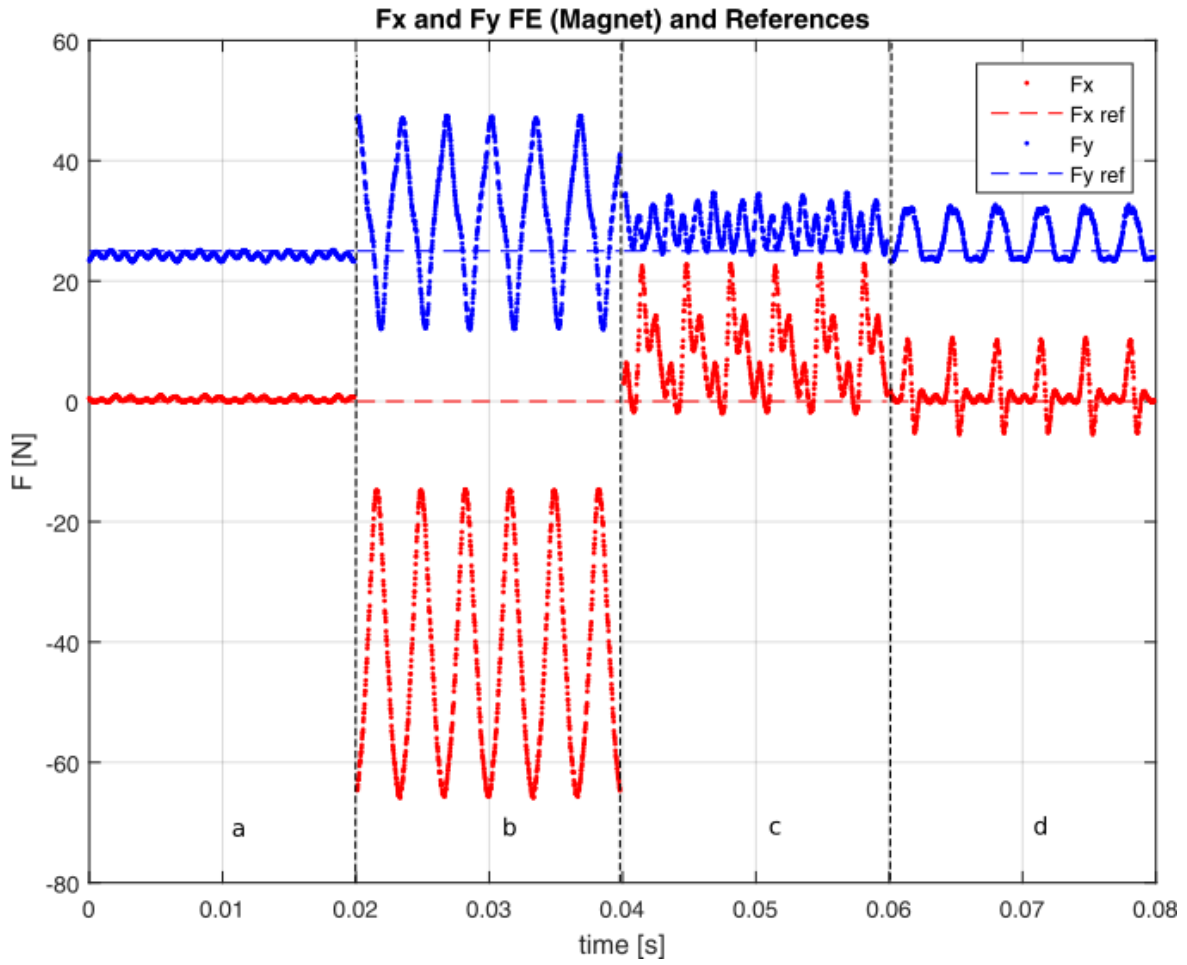


Fig. 5.20 – FE radial force values with 5 Nm torque and 25 N reference radial force. Healthy machine (a), standard open phase control (b), radial force compensation by fault tolerant control (c), radial force fault tolerant control at no load (d).

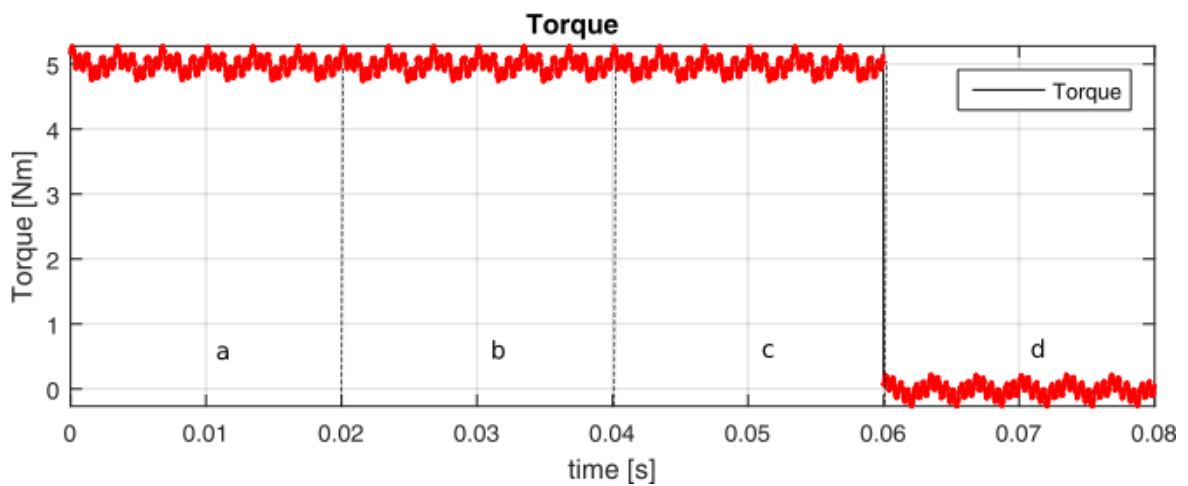


Fig. 5.21 – Machine torque when the reference force is 25 N. The torque is 5 Nm (a,b,c) and 0 Nm (d). Healthy machine (a), faulty machine without fault tolerant control (b), radial force fault tolerant control (c), and radial force fault tolerant control at no load (d).

Radial Force Fault Tolerant Control at Rated Torque ($i_{d3}=0$ FTC) – direction criticality

Fig. 5.22 and Fig. 5.23 show the currents and the radial force components resulting from a radial force FTC commanding a rotating force synchronous with the rotor in case of sector A open phase fault. This simulation is presented in order to highlight the asymmetrical behaviour of the machine. The asymmetrical distribution of the healthy phases results in an increased current request in some critical rotor positions. Therefore, in these positions also the additional force components are more important, resulting in a deterioration of the FTC performance.

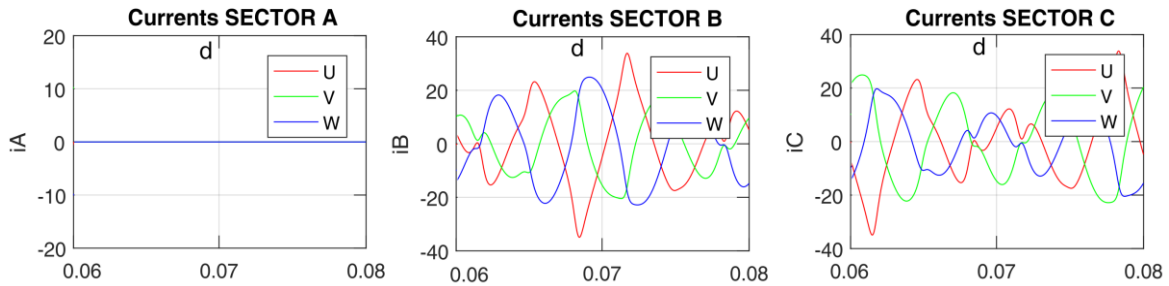


Fig. 5.22 – FE currents values with 5 Nm torque and 25 N rotating reference radial force. Sector A open fault and FTC algorithm.

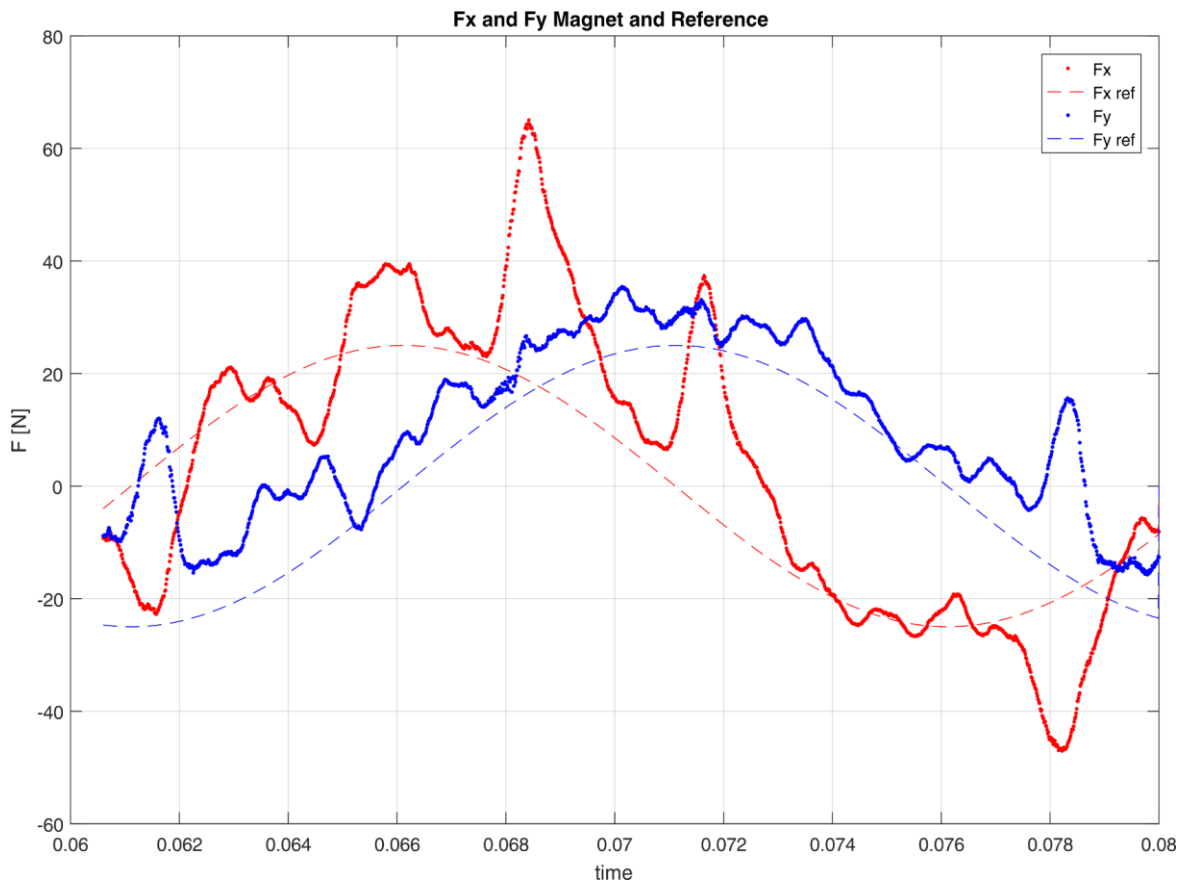


Fig. 5.23 – FE radial force values with 5 Nm torque and 25 N rotating reference radial force. Sector A open fault and FTC algorithm.

5.8 Numerical (Matlab-Simulink) Simulation Results

This section presents the results of numerical simulations done with Matlab-Simulink. The machine model used in the simulation is a FE-based one, developed by Giorgio Valente of Nottingham University. The model is derived by means of multi-static non-linear FE simulations. For each static simulation, the rotor is rotated of a small angle and each sector is fed with current values in the range of operating conditions. The obtained torque and x-y forces are stored in form of lookup table in the Simulink model and a linear method has been used to interpolate the lookup table elements. This model is used for avoiding time-consuming FE co-simulations, meanwhile having a good numerical representation of the system.

The aim of the numerical simulations is to verify the controllability of the system before testing it on the machine prototype, and validate the proposed control algorithms. The machine control scheme is proposed in Fig. 5.24, where two additional PID regulators are introduced to represent the closed loop control for the two DoF bearingless operation. The bearingless operation is simulated considering also the eccentricity effect by a linear effect matched by FEA and the x-y position of the shaft is constrained in a circle of 150 μm radius, simulating the effect of a backup bearing setup (as in the experimental tests).

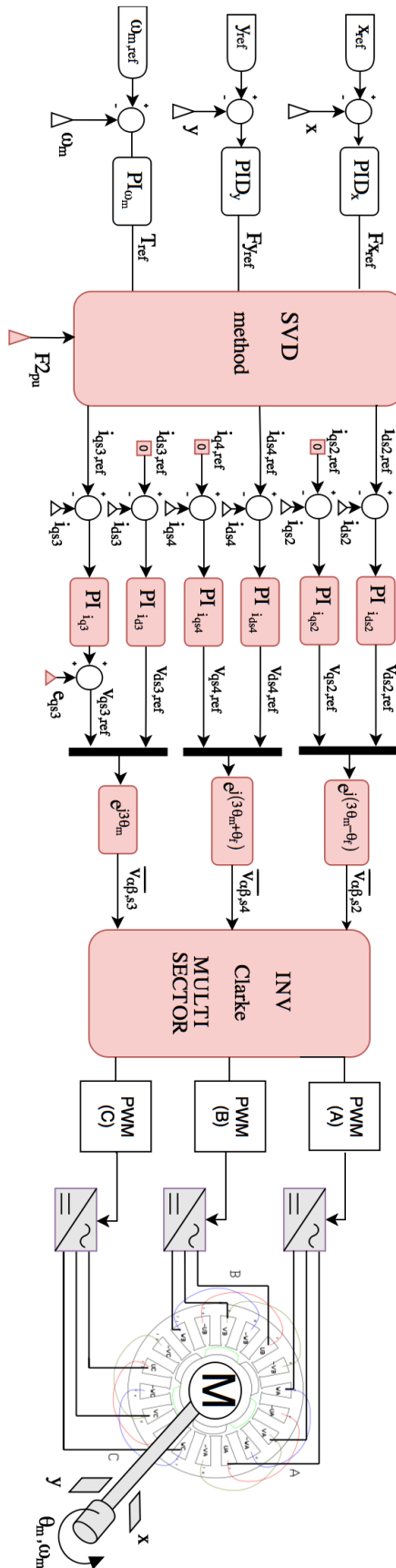


Fig. 5.24 – Control scheme of the prototype for two DoF bearingless operation.

Radial Force Open Loop Control

Fig. 5.25 shows the results of a simulation where the force is open loop controlled. The reference force is rotating at the same speed of the rotor and its magnitude increases with the square of the rotor speed up to the rated force (200 N) at 3000 rpm. This force might represent the needed for compensating a dynamic mass unbalance. It is implicit that, for a proper compensation, the rotor-dynamic behaviour must be well predicted [20]. At first, a speed ramp from 0 to 3000 rpm (rated speed) is commanded. At 0.5 s a load equal to the rated torque is applied. The reference force is finally set to zero at 0.8 s. The simulation is reported only for a 0.25 $F_{2,pu}$ value. The currents are shown in terms of space vectors of the overall machine and three-phase current vectors for each inverter. While the first ones are shown in the synchronised reference frames, the second ones are referred to the rotor reference frame as in a standard machine FOC. This result is particularly interesting, because it verifies the possibility to have zero steady state errors in the current PI regulators owing to the synchronisation of the space vectors in different reference frames. This is no more possible if a control of the standard three-phase current vectors is implemented. The only case where the same result is obtained are the no force control or the case of a constant reference force (as the rotor weight compensation). In these cases, the synchronisation of the three-phase current vector in the rotor reference frame as in a standard FOC allows having constant current reference values as in the space vector algorithm. In all the other cases, the SVD approach results in a better control implementation. Indeed, it is well known that the performance of a PI regulator deteriorates when a sinusoidal input rather than a constant one is applied. The following simulation results are related to the three-phase open fault behaviour with and without FTC.

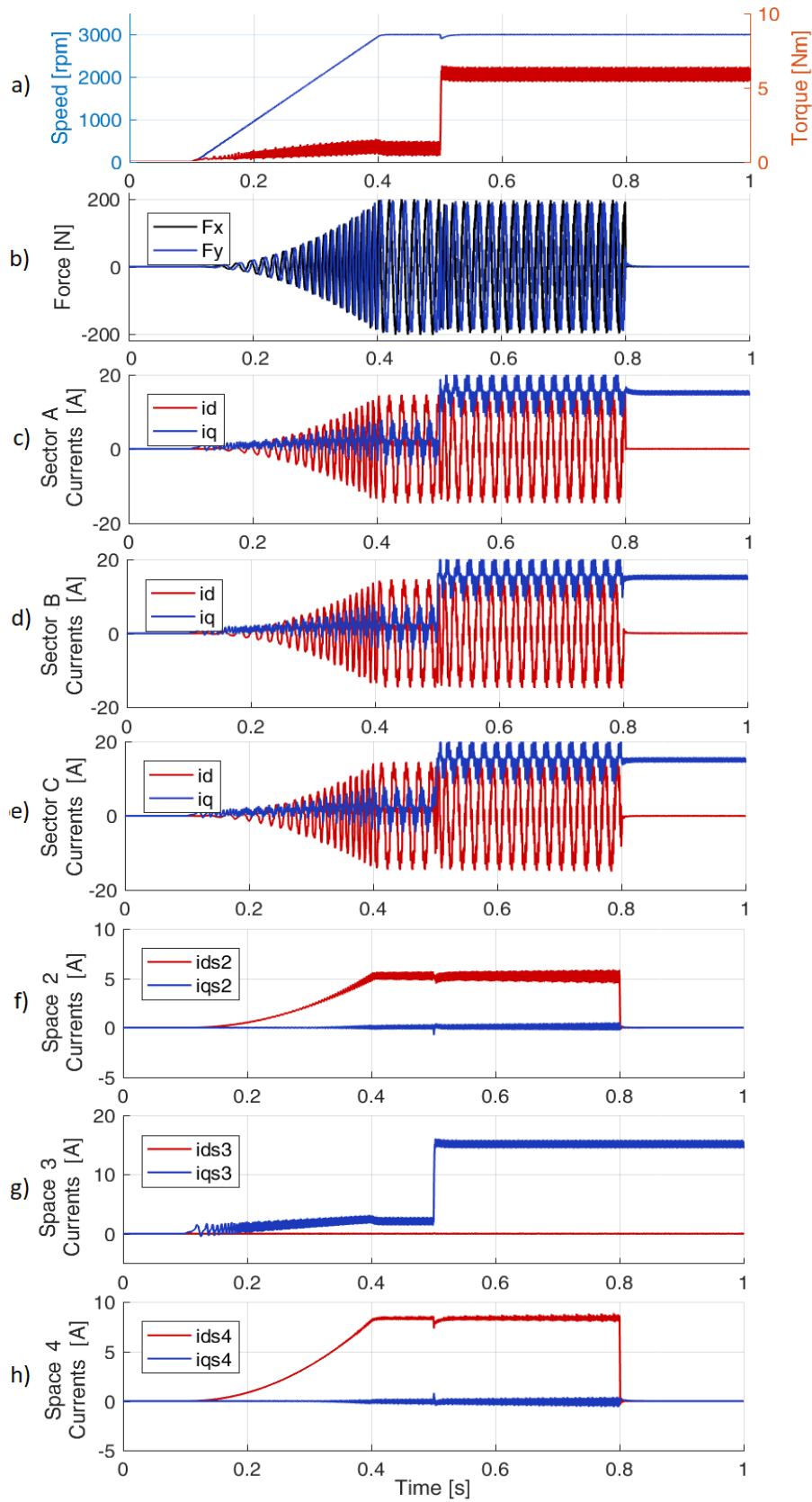


Fig. 5.25 – Numerical simulation of a speed transient at no load from 0 to 3000 rpm, followed by a torque step of 5 Nm (at 0.5 s). The radial force is synchronous with the rotor as in a dynamic mass unbalance until 0.8 s, when the force is set to zero again. The speed, torque (a) and force (b), the d-q currents of each sector (c-e) and the d-q current space vector components (f-h) are plotted.

Radial Force Open Loop Compensation (With detection delay)

Fig. 5.26 and Fig. 5.27 show the result of a standard machine control with a three-phase open fault (at $t = 0.15$ s). At the beginning, the control becomes unstable because the current control algorithm is implemented by the space vector approach. At $t = 0.2$ s the open loop FTC described by (5.139) is implemented for compensating the radial force generated by the torque control in case of fault. Fig. 5.27 shows the currents of the three-phase inverter and the current space vectors of the controlled spaces. It can be noticed that the FTC allows stabilising the machine current control. The force in Fig. 5.26 goes slowly to almost zero with the FTC.

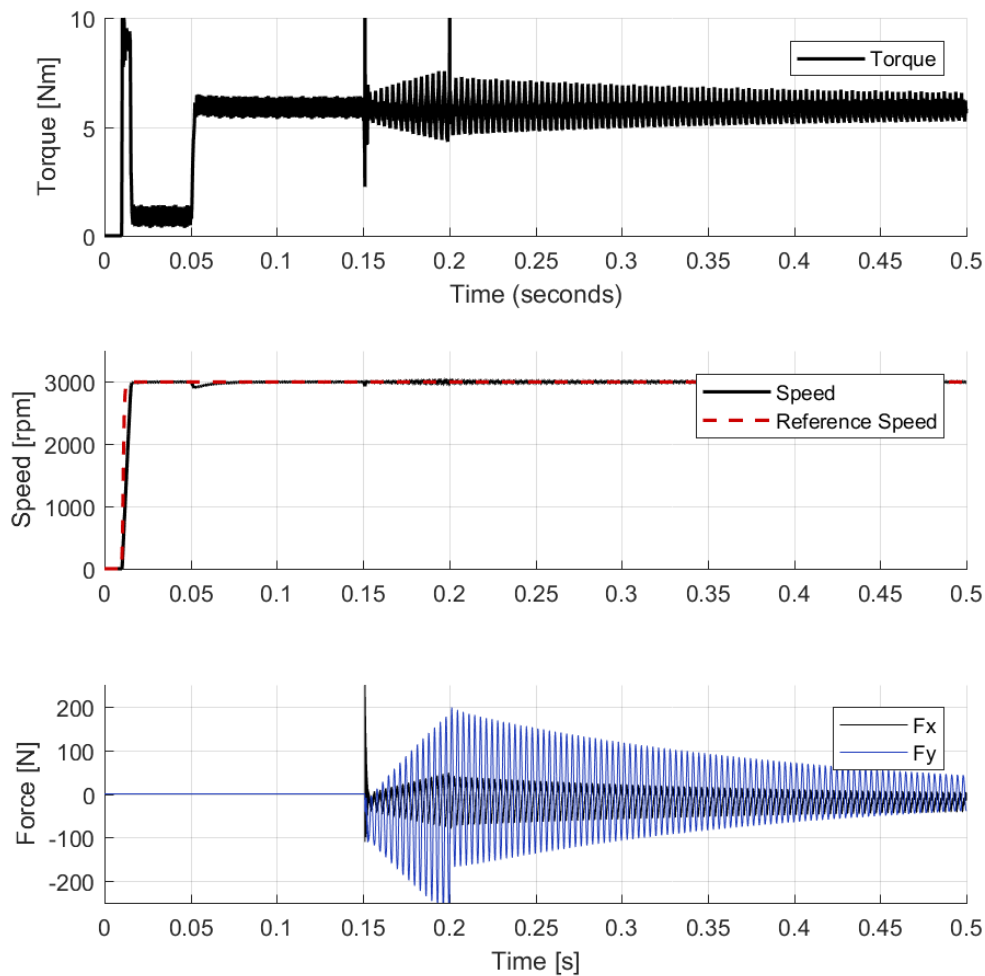


Fig. 5.26 – Machine start up and rated torque step ($t=0.05$ s), followed by sector A open phase fault ($t=0.15$ s) and radial force open loop compensation ($t=0.2$ s).

Modelling of Multi Three-Phase Sectored Machines

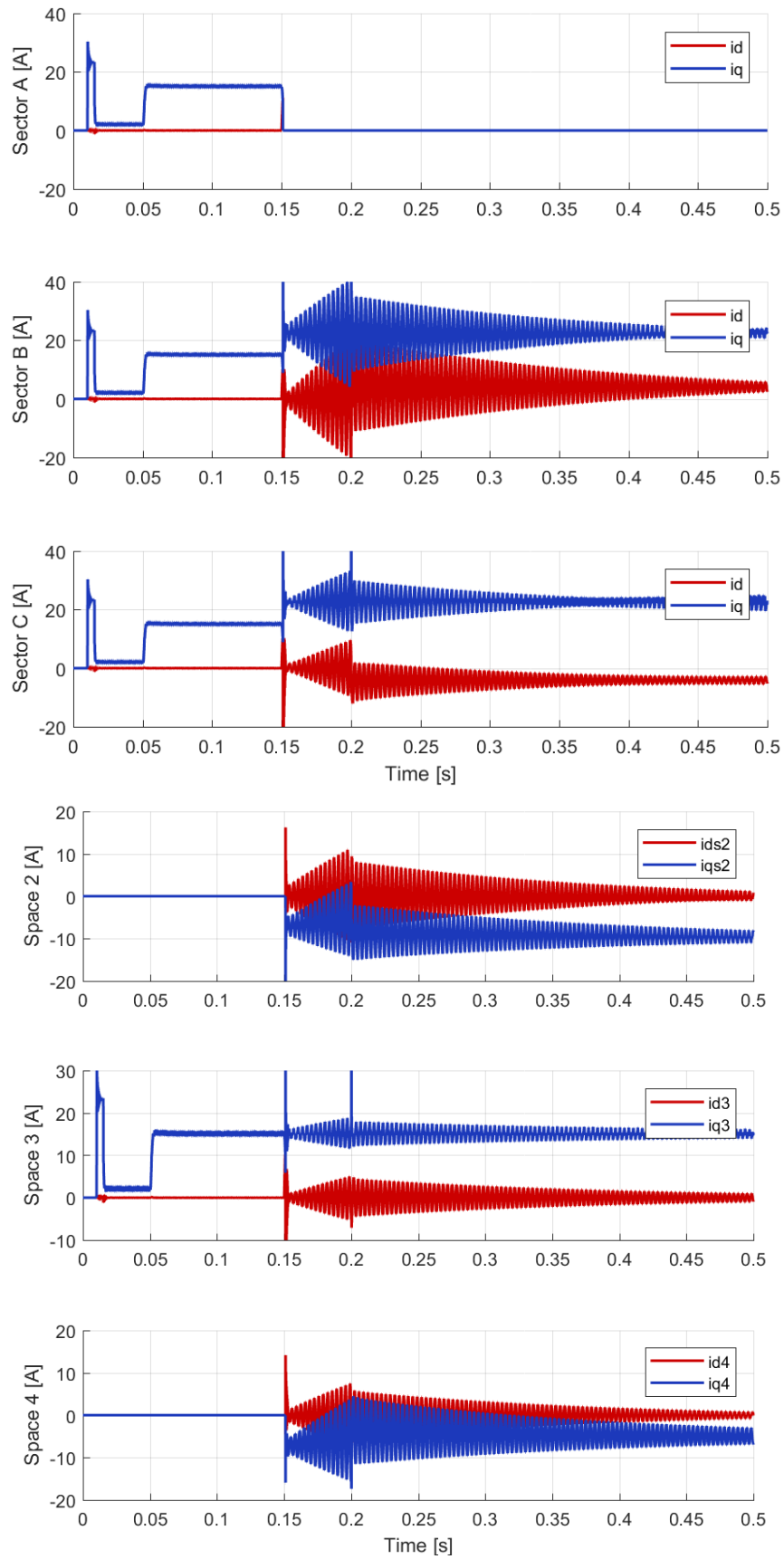


Fig. 5.27 – Machine start up and rated torque step ($t=0.05$ s), followed by sector A open phase fault ($t=0.15$ s) and radial force open loop compensation ($t=0.2$ s). Three-phase d-q currents of the three sectors (top) and synchronised current space vector components (bottom).

Radial Force Open Loop Compensation (instantaneous)

Fig. 5.28 and Fig. 5.29 show the same simulation of the previous subsection, but with the FTC activated at the same time of the fault (at $t = 0.15$ s). In this case, the currents and the force reach the steady state operation in a short time. The q components of the three-phase current vector in Fig. 5.29 increase their average value mainly for the torque production in order to maintain the same 3rd space current vector. This control technique can be used for example in parallel to the converter protections, as the de-sat fault detection, in order to improve the machine behaviour.

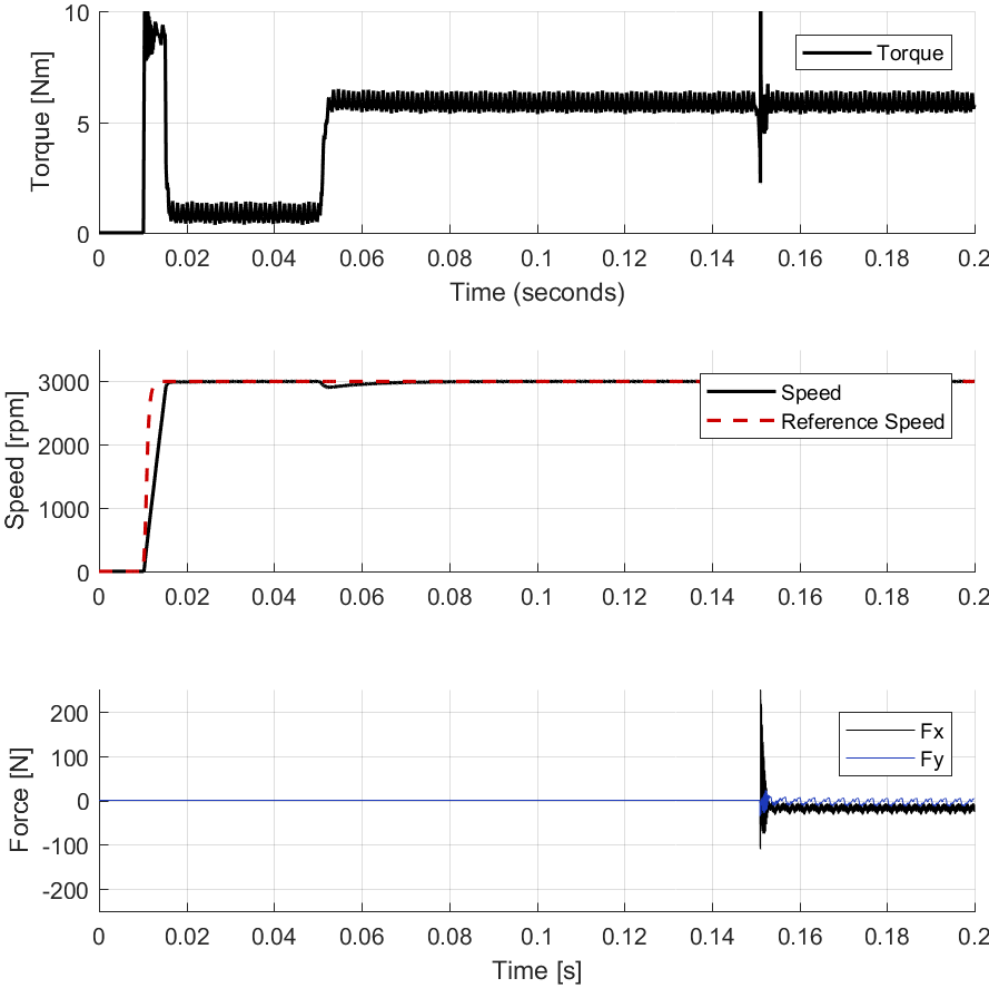


Fig. 5.28 – Machine start up and rated torque step ($t=0.05$ s), followed by sector A open phase fault with instantaneous radial force open loop compensation ($t=0.15$ s).

Modelling of Multi Three-Phase Sectored Machines

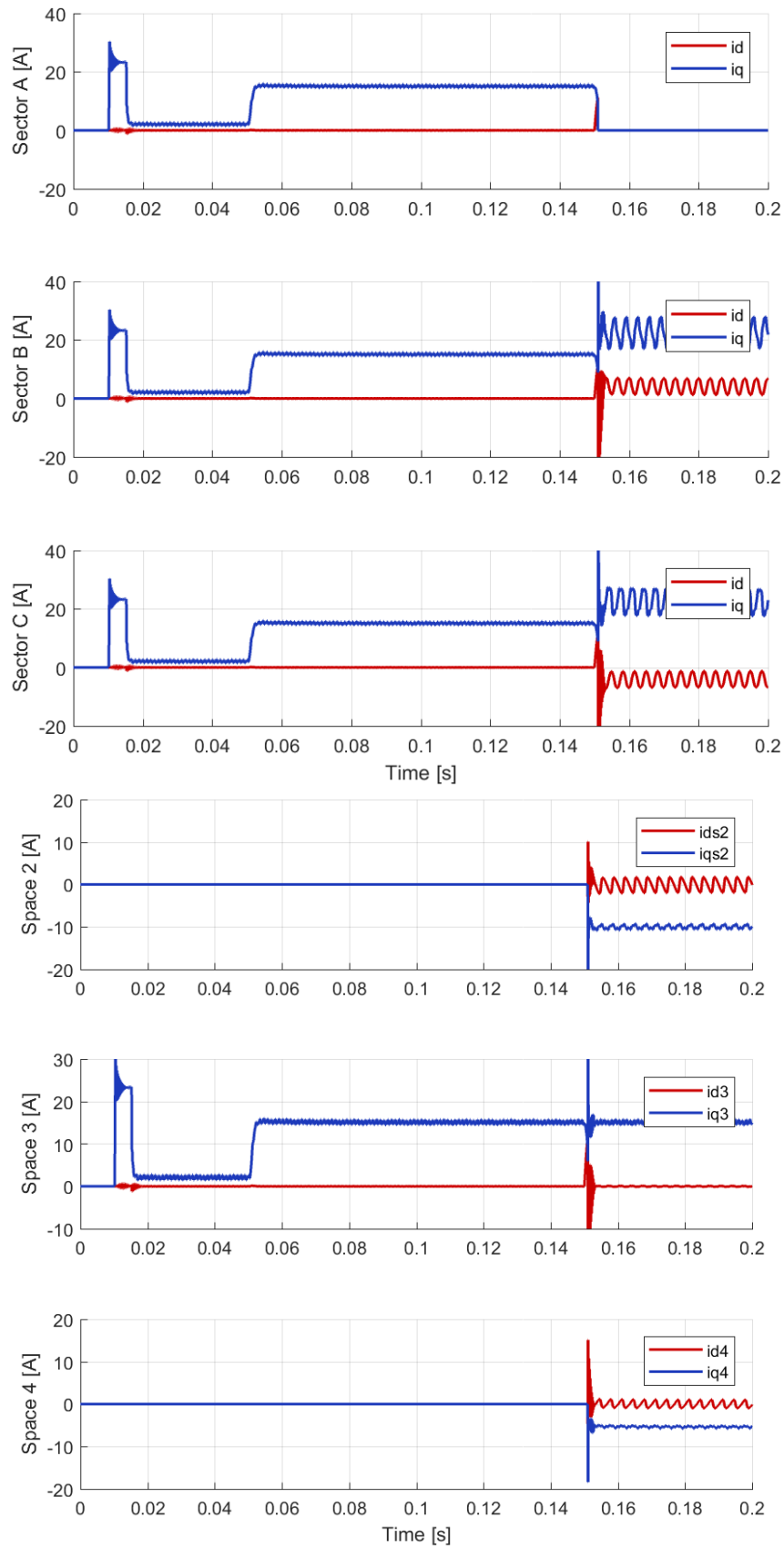


Fig. 5.29 – Machine start up and rated torque step ($t=0.05$ s), followed by sector A open phase fault and instantaneous radial force open loop compensation ($t=0.15$ s). Three-phase d-q currents of the three sectors (top) and synchronised current space vector components (bottom).

Bearingless Operation and FTC (early compensation) – rated torque and rated force

The following simulation is used to summarise the bearingless control with and without three-phase open fault. However, because without a FTC, the machine behaviour becomes unstable and there are huge currents and forces and the bearingless operation results not feasible, the working condition with only the fault is not presented. Instead, to add a possible scenario to the already presented ones, Fig. 5.30, Fig. 5.31 and Fig. 5.32 (top) show the effect of the FTC activation before that the fault happens. The fault can also not happen and the FTC can be used to keep zeroing the currents in one inverter. Only in Fig. 5.32 (bottom) it is shown that also without current or voltage limitations, the control without FTC algorithm does not allow the machine levitation in case of one inverter open fault, and the rotor is pushed in the uncontrolled position defined by the position of the faulty subsystem.

Fig. 5.30 and Fig. 5.31 show a start-up and torque step as in the previous simulations, with the difference that during all the simulation there is an active control of the x-y shaft position in a two degrees of freedom bearingless operation.

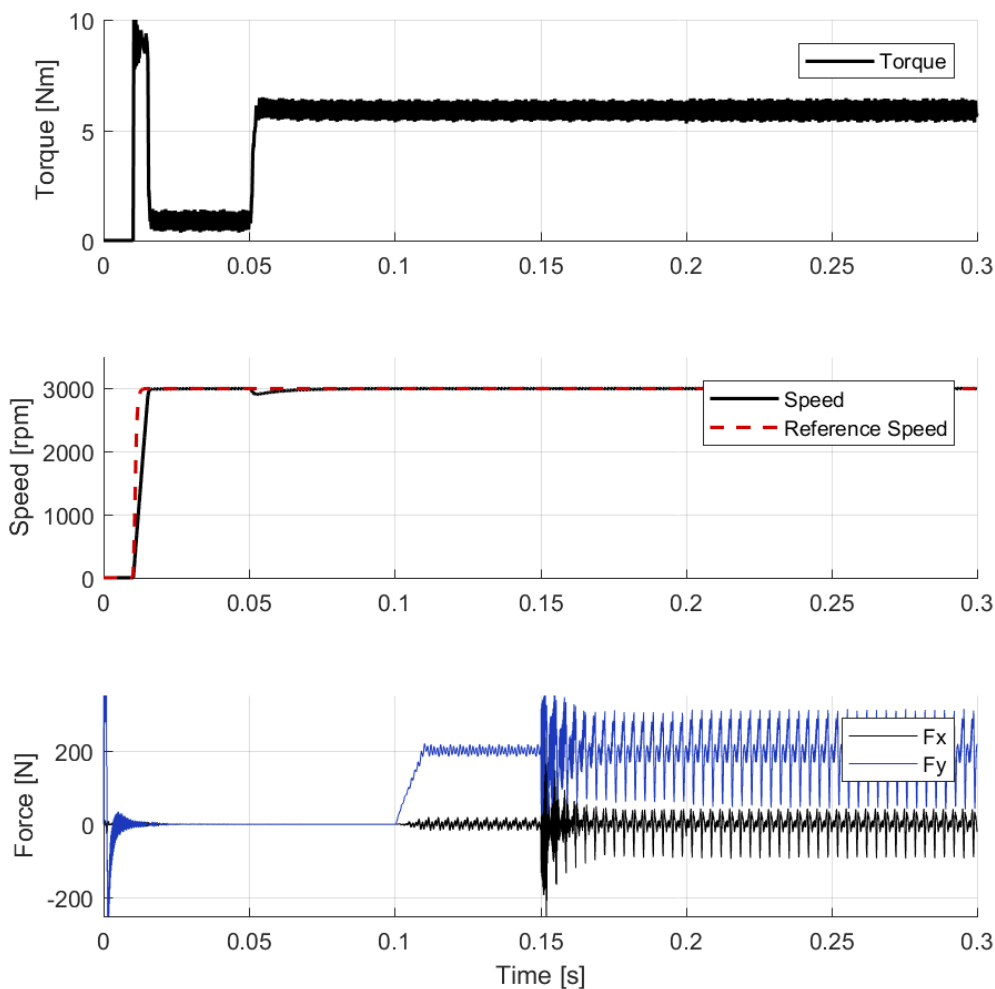


Fig. 5.30 – Machine start up and rated torque step ($t=0.05$ s), followed by rated force step ($t=0.1$ s). FTC operation without fault for zeroing the sector A currents ($t = 0.15$ s) and open phase fault of sector A keeping the FTC active ($t=0.2$ s).

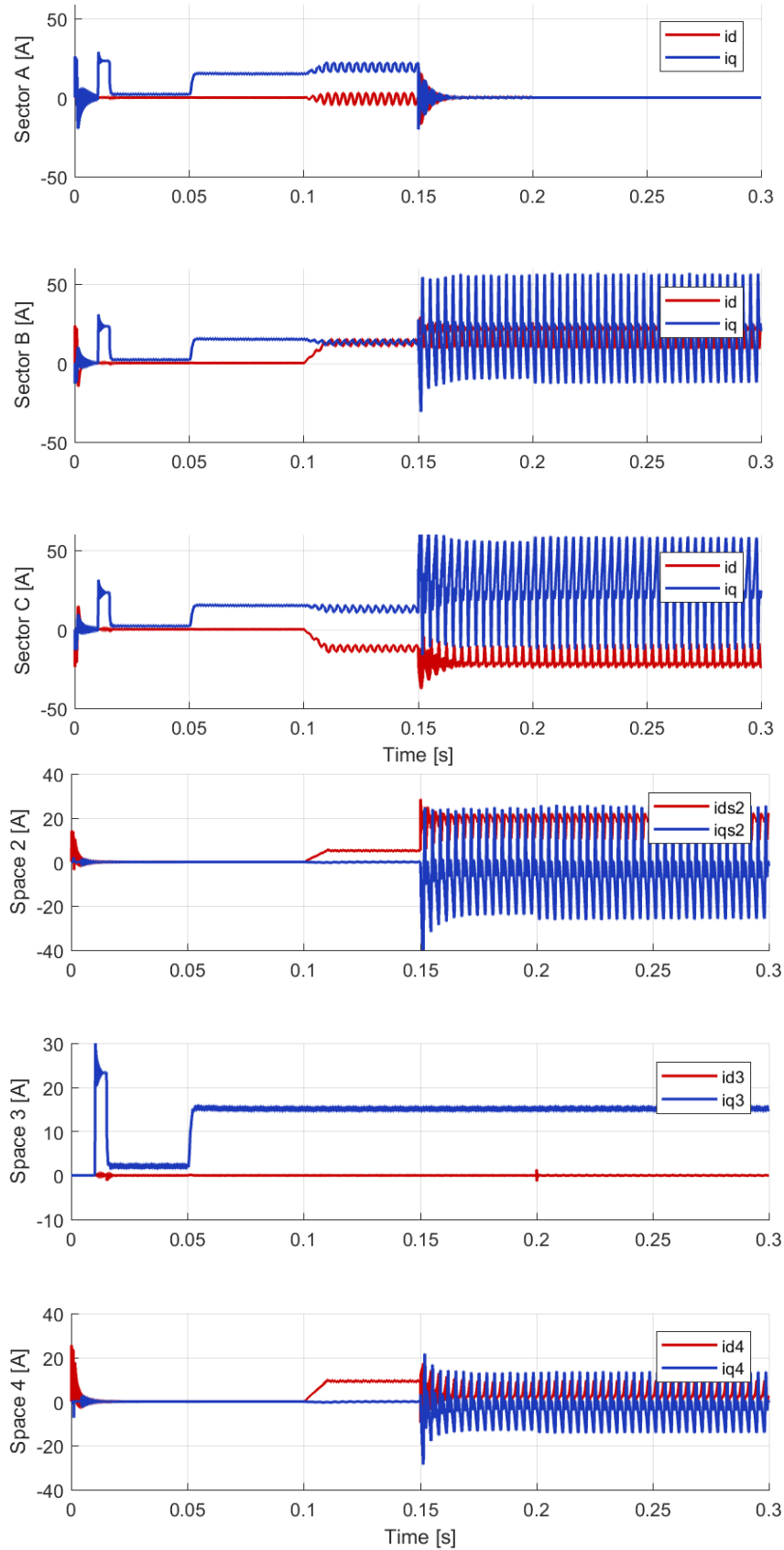


Fig. 5.31 – Machine start up and rated torque step ($t=0.05$ s), followed by rated force step ($t=0.1$ s). FTC operation without fault for zeroing the sector A currents ($t = 0.15$ s) and open phase fault of sector A keeping the FTC active ($t=0.2$ s). Three-phase d-q currents of the three sectors (top) and synchronised current space vector components (bottom).

The x-y position of the shaft is shown in Fig. 5.32 (top), where it is possible to notice that the starting position of the shaft is in the negative y direction and there is a transient to centre the shaft.

Furthermore, at $t = 0.1$ s there is a load force increasing up to the rated force (200 N) which remains until the end of the simulation. At $t = 0.15$ s the FTC is activated in order to bring the currents in the inverter A to zero while controlling the torque and the force simultaneously to their rated values. At $t = 0.2$ s the inverter A is unconnected setting the current exactly equal to zero. It is interesting to note that the machine behaviour before and after the physical open of the inverter A is almost the same, owing to the good performance of the FTC.

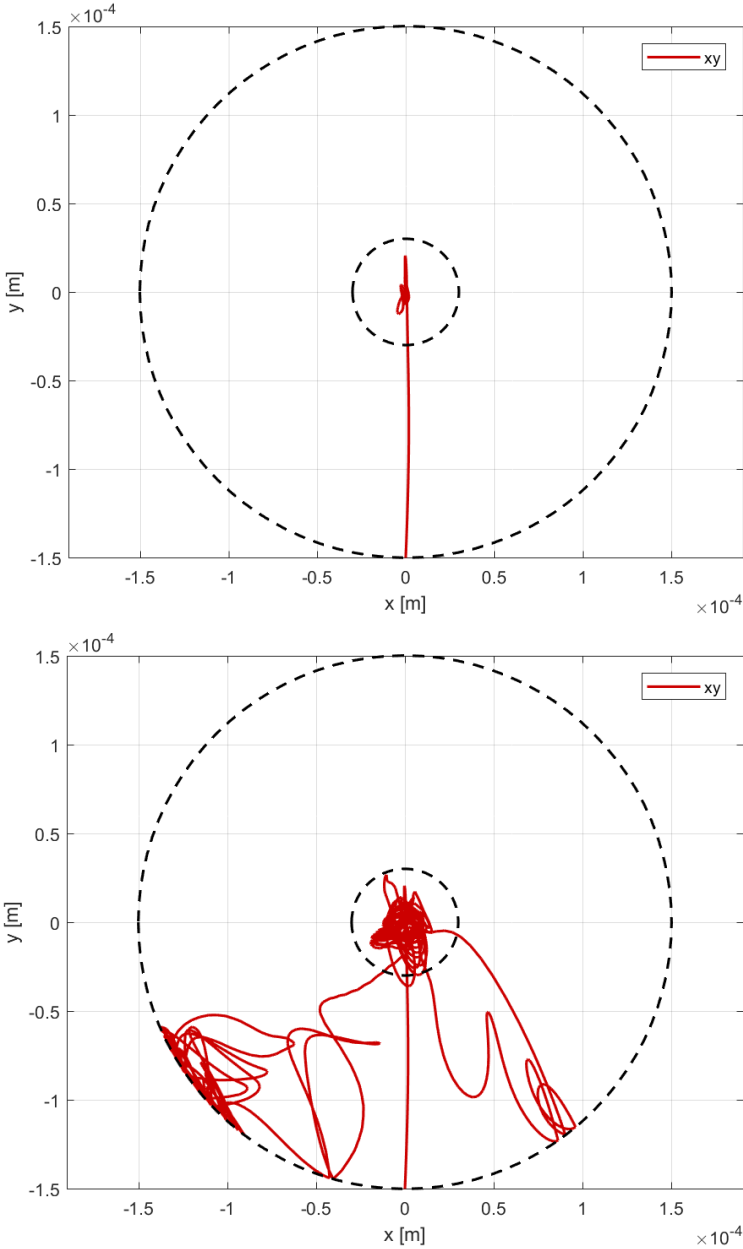


Fig. 5.32 – x-y shaft position in a two DoF bearingless operation with rated force and rated force control at rated speed with sector A open phase fault with FTC (top) and without FTC (bottom).

Bearingless Operation and optimised current sharing control – rated torque and rated force

The following simulation is used to summarise the bearingless control in case of an advanced current sharing of the q-axis component of the three-phase inverters (power sharing) as described in Section 4.5.

Fig. 5.33 and Fig. 5.34 show a start-up and torque step as in the previous simulations, with the x-y shaft position control in a two degrees of freedom bearingless operation. At the beginning the control is an equal power sharing. At $t = 0.05$ s there is a load force increasing up to the rated force (200 N). At $t = 0.1$ s a matryoshka power sharing is commanded. Finally, since $t = 0.15$ s the inverter B is working with a negative power sharing coefficient and the two others with the same positive one. It results that the B inverter is controlled in generating mode, while the A and C converter must provide twice the power if compared to the equal control. Indeed, they have to compensate the power of the B inverter plus producing the power that it generates. The bearingless operation is obtained as in Fig. 5.32 (top), therefore the x-y shaft position is not shown for this simulation.

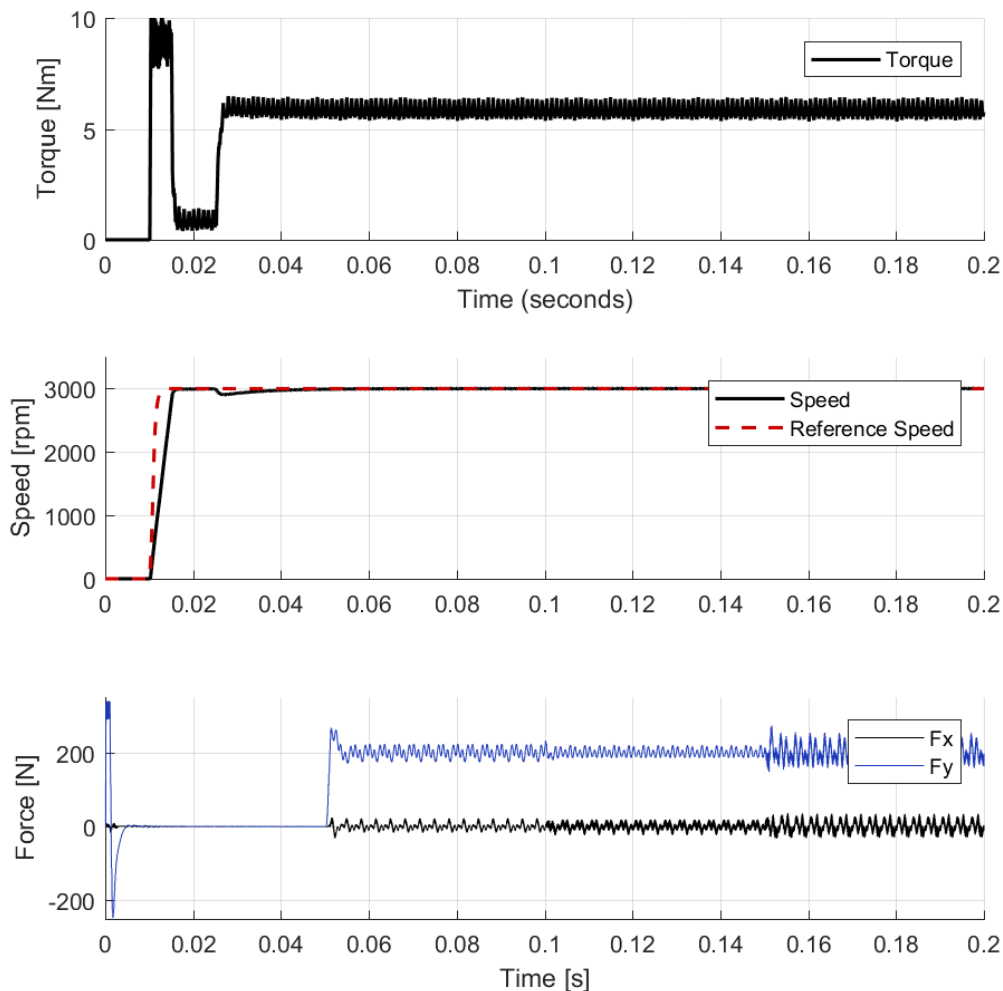


Fig. 5.33 – Start up and rated torque step ($t=0.025$ s), followed by rated force step ($t=0.05$ s). Advanced current sharing control: equal distribution (until $t = 0.1$ s); matryoshka current sharing ($t=0.1-0.15$ s); three-phase subsystem B generating (from $t = 0.15$ s).

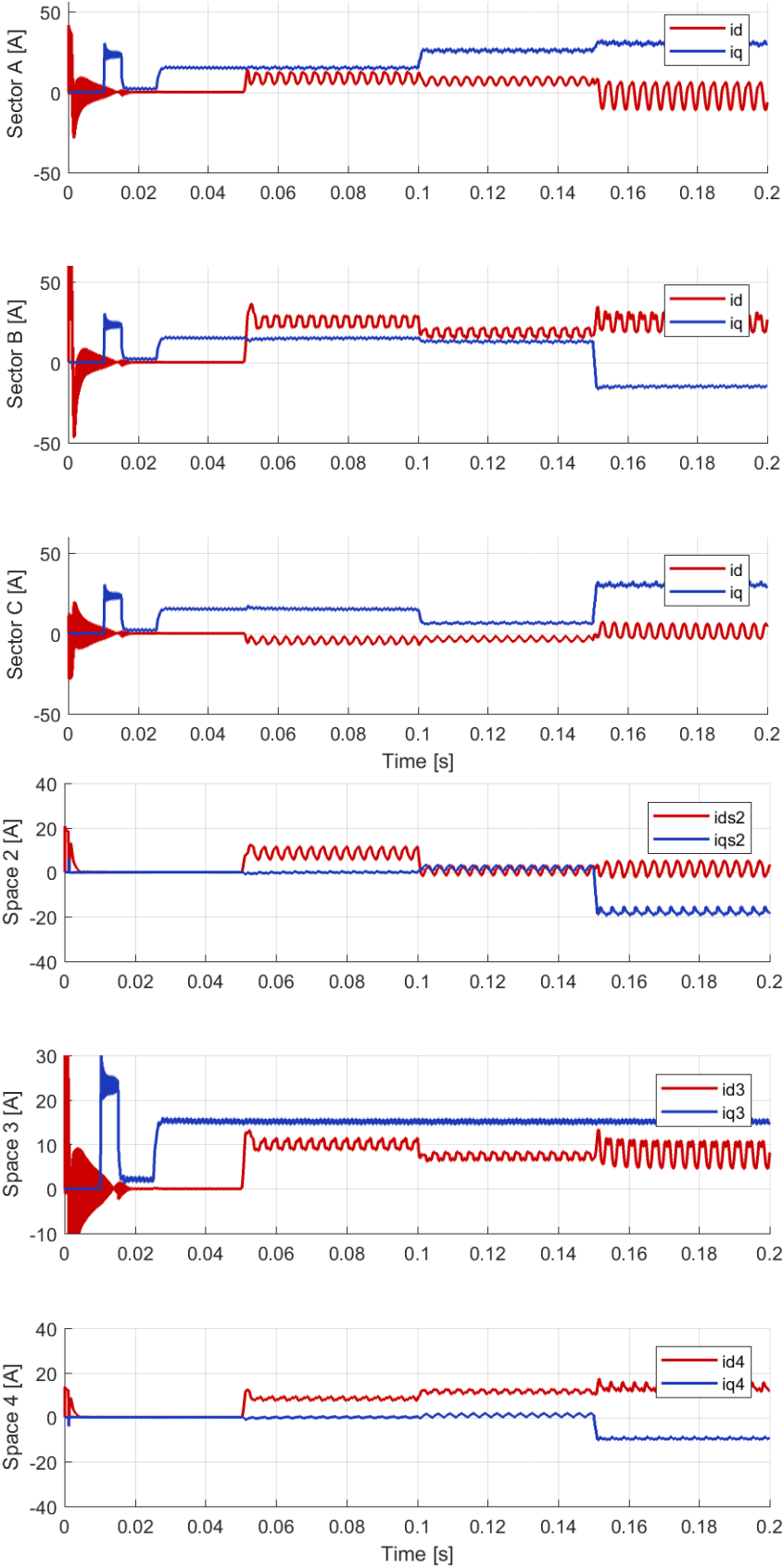


Fig. 5.34 – *d-q* components of the three-phase current space vectors (top) and the general ones (bottom). Start up and rated torque step ($t=0.025$ s), followed by rated force step ($t=0.05$ s). Advanced current sharing control: equal distribution (until $t = 0.1$ s); matryoshka current sharing ($t=0.1-0.15$ s); three-phase subsystem B generating (from $t = 0.15$ s).

Bearingless Operation with Optimised FTC – Minimum copper Joule losses

Fig. 5.35, Fig. 5.36 and Fig. 5.37 compare the basic and optimised FTC described in Section 4.6 for the sector A open phase fault with a bearingless control.

The simulation is divided in two parts. In the first one (until 0.2 s), the machine is working at rated torque (5 Nm). In the second part (from 0.2 s until the end of the simulation) the machine is working at rated torque and rated force (200 N). In both the parts, for half the time the machine is controlled with the basic FTC and for the next half with the optimised FTC.

The bearingless operation is obtained with both the FTC, but as expected the optimised one allows significantly reducing the stator copper Joule losses. Furthermore, the maximum peak phase current is also significantly reduced (as in Fig. 5.37).

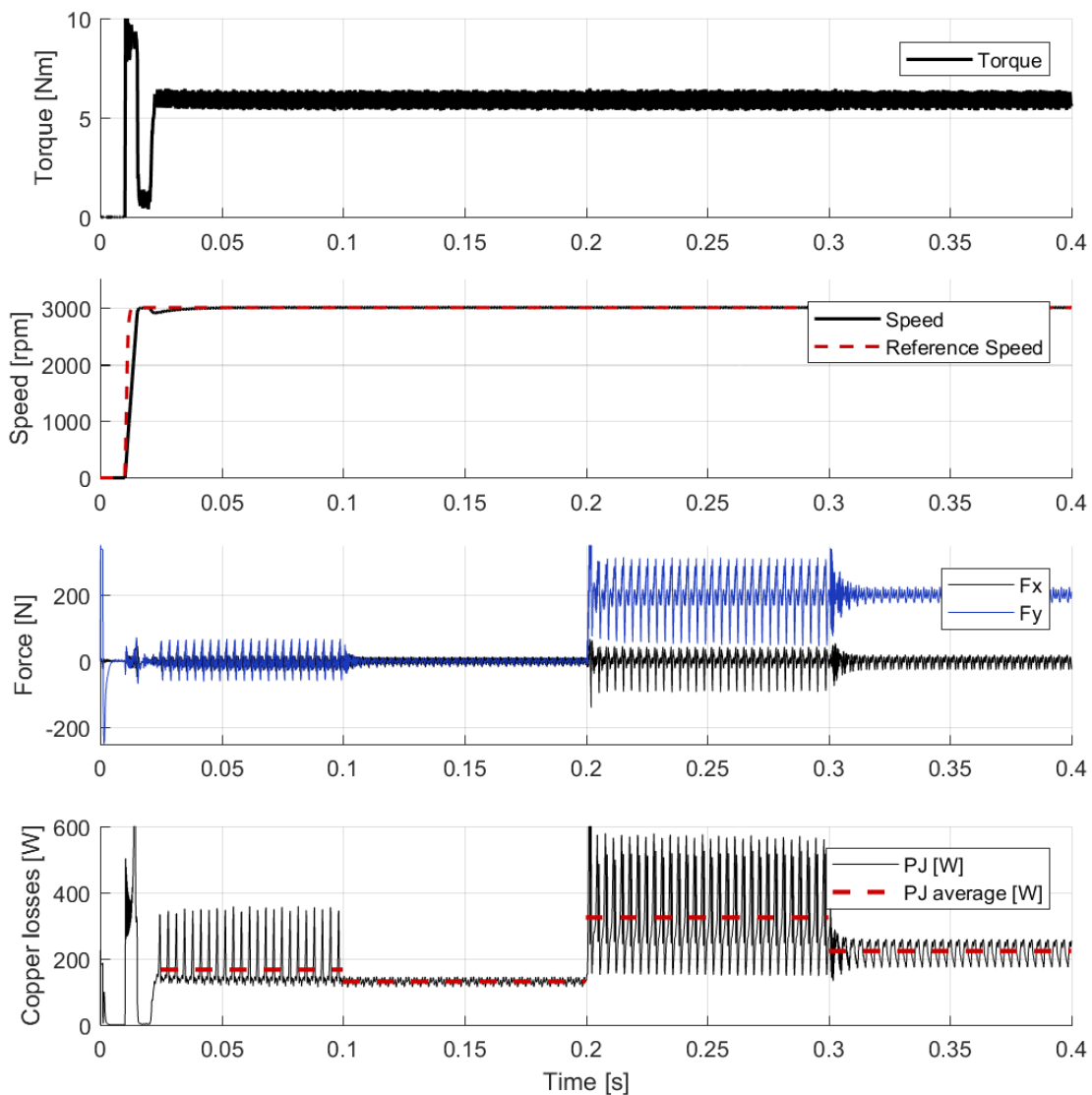


Fig. 5.35 – Start up and rated torque step ($t=0.025$ s), followed by rated force step ($t=0.2$ s) with sector A open phase fault. Basic FTC ($t=0-0.1$ s and $0.2-0.3$ s) and optimised FTC ($t=0.1-0.2$ s and $0.3-0.4$ s).

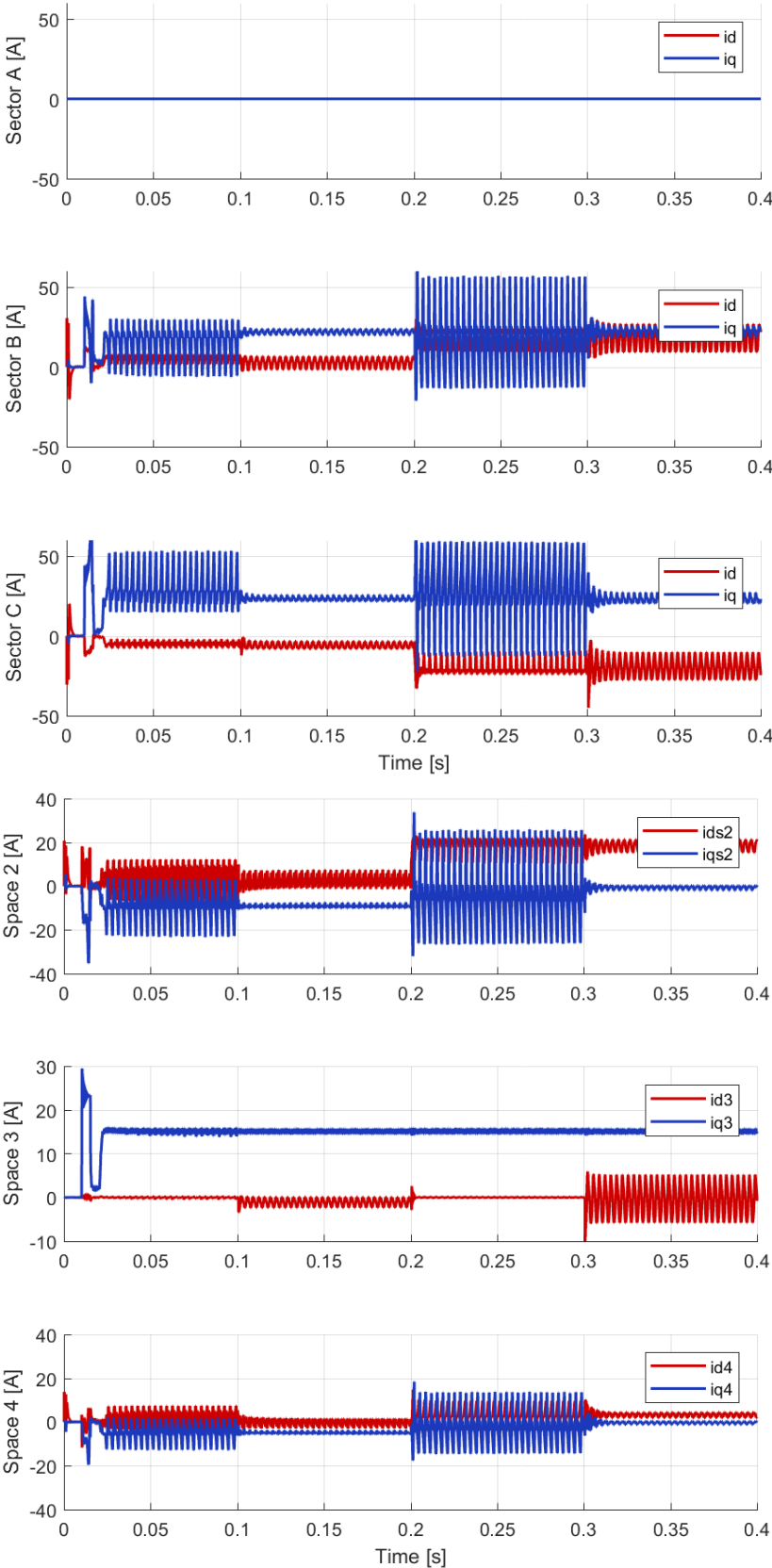


Fig. 5.36 – d-q components of the three-phase current space vectors (top) and the general ones (bottom). Start up and rated torque step ($t=0.025$ s), followed by rated force step ($t=0.2$ s) with sector A open phase fault. Basic FTC ($t=0-0.1$ s and $0.2-0.3$ s) and optimised FTC ($t=0.1-0.2$ s and $0.3-0.4$ s).

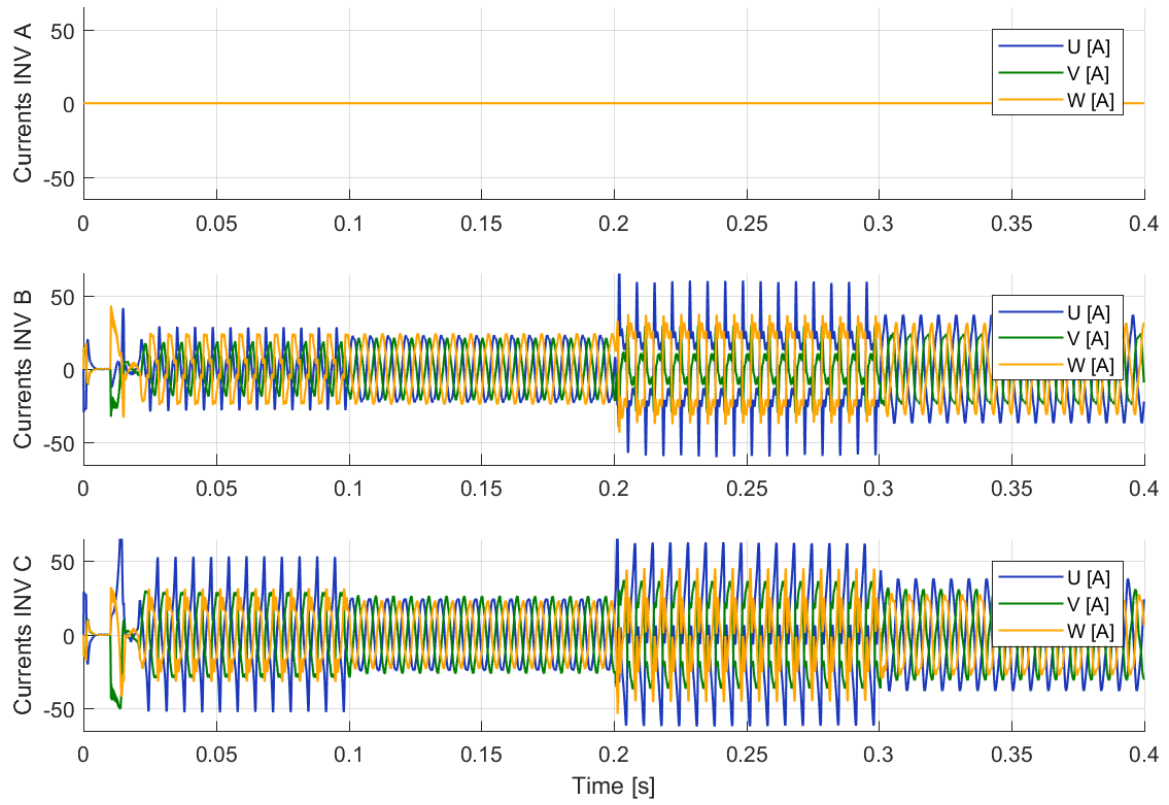


Fig. 5.37 – Phase currents. Start up and rated torque step ($t=0.025$ s), followed by rated force step ($t=0.2$ s) with sector A open phase fault. Basic FTC ($t=0-0.1$ s and $0.2-0.3$ s) and optimised FTC ($t=0.1-0.2$ s and $0.3-0.4$ s).

5.9 Experimental Results

Fig. 5.38 shows the test rig used for the experimental analysis. This rig is available at the University of Nottingham and has been assembled and designed by Giorgio Valente. Other members of the power Electronics, Machine and Control (PEMC) group have designed the various components. I coded the multiphase machine control on the uCube control platform in order to realise the experimental tests summarised in this section.

Fig. 5.38a shows the three three-phase inverters connected to the same dc bus. Each inverter is connected to one of the MSPM motor winding (Fig. 5.38c). The inverters, equipped with a standard IGBT power module with 10 kHz switching frequency, are independently controlled by means of the centralized control platform in Fig. 5.38b [21]. The control platform communicates with the inverter gate drivers by means of fibre optic cables. In order to realize a bearingless drive with two mechanical degrees of freedom, the tilting movement and axial displacement are constrained by a self-alignment bearing mounted on one side of the shaft. The other side is free to only move along the x-y axes within a certain displacement, given by

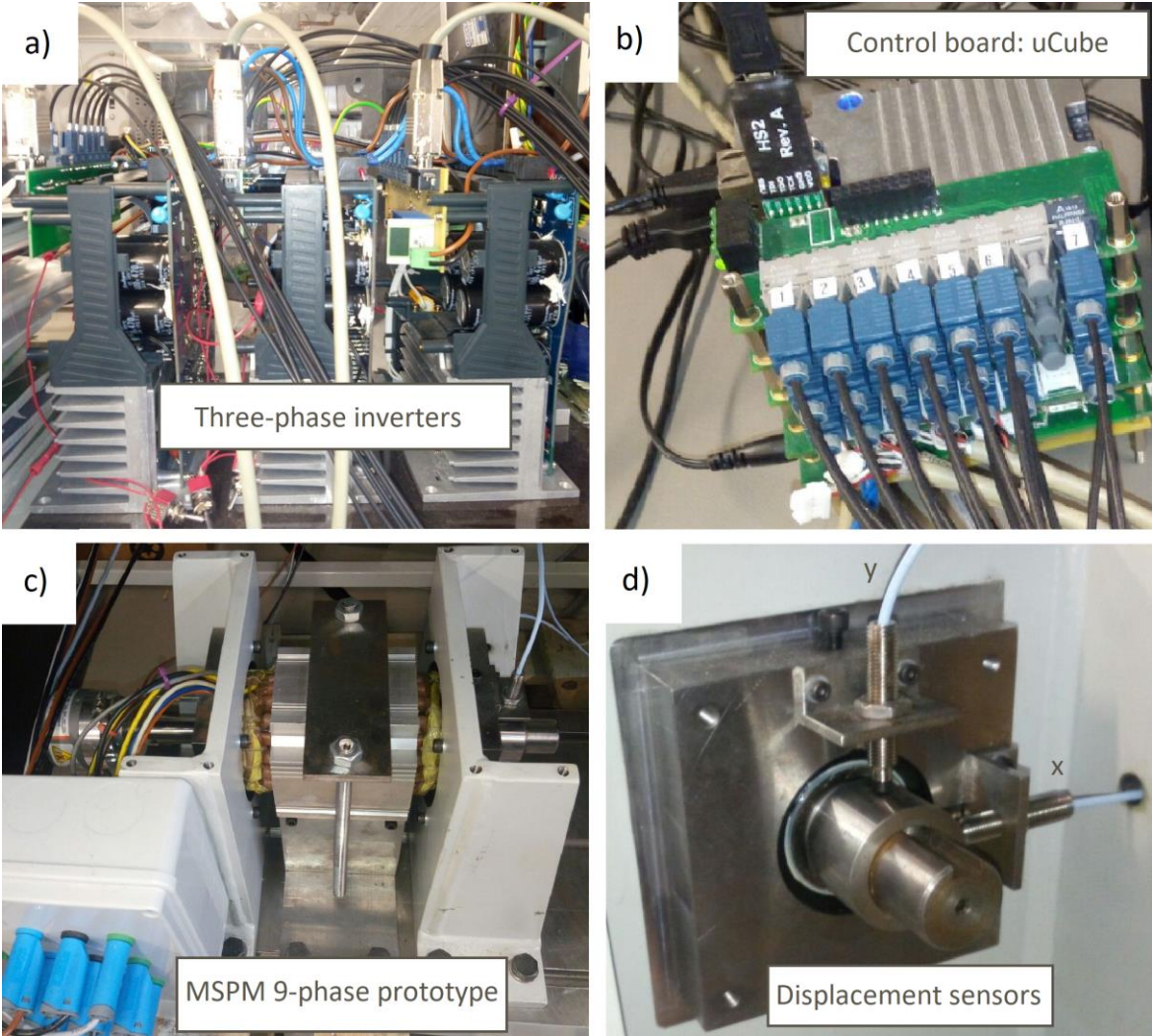


Fig. 5.38 – Experimental test setup. The three three-phase inverters (a), the control board (b), the machine MSPM prototype and test rig (c), and the rotor shaft with the displacement sensors (d).

the clearance of the backup bearing. Fig. 5.38d shows the two displacement probes mounted on the backup bearing housing along the x-y axes. The machine parameters are listed in Table 5.11.

The experimental tests have been performed to validate the radial force control technique in an open loop control and for a two degrees of freedom bearingless operation. The tests are reported only for a $0.25 F_{2,pu}$ value in the control algorithm.

Radial Force Open Loop Control

Fig. 5.39 and Fig. 5.40 show the experimental results for a force open loop control. The reference force is rotating synchronous with the rotor. The aim is to evaluate the possibility to compensate for example a dynamic mass unbalance of the shaft. Similar results have been obtained in the simulation presented in Fig. 5.25. Not having an available force transducer, the force is just supposed to follow the reference value, and only the force direction has been measured by the shaft position on the backup bearing as in Fig. 5.40. It is worth noticing that the initial position of the shaft in all the experimental tests depends on the final position reached in the previous simulation and it is not in the negative y direction (as expected in case of considering only the rotor weight), because of the eccentricity force. The eccentricity effect is easily understandable thinking about the minimization of the system energy principle that generates the reluctance force.

The maximum speed is limited to 600 rpm for avoiding the damage of the backup bearing, being the shaft position constrained only by it. The magnitude of the reference force increases with the square of the rotor speed up to 200 N at 600 rpm (the rated force). As expected in the simulation in Fig. 5.25, the current space vector components in the synchronised reference frames are constant at steady state condition. This allows having theoretically zero steady state error. Instead, Fig. 5.41 shows the phase currents, where it is clear that standard d-q PI regulators for the three-phase current space vectors are not enough to ensure zero steady state error.

Table 5.11 – Main machine parameters.

Parameter	Value
Pole number ($2p$)	6
PM material	NdFeB
Power rating	1.5 [kW]
Rated Speed (ω_m)	3000 [rpm]
Rated torque (T_{rated})	5 [Nm]
Turn/coil	22
Phase resistance (R_s)	0.0808 [Ohm]
Torque constant (K_T)	0.434 [Nm/A]
Space 2 force constant (K_{F2})	9.60 [N/A]
Space 4 force constant (K_{F2})	17.85 [N/A]
Outer Stator diameter	95 [mm]
Inner Stator diameter	49.5 [mm]
Axial length	90 [mm]
Airgap length	1 [mm]
Magnets thickness	4 [mm]

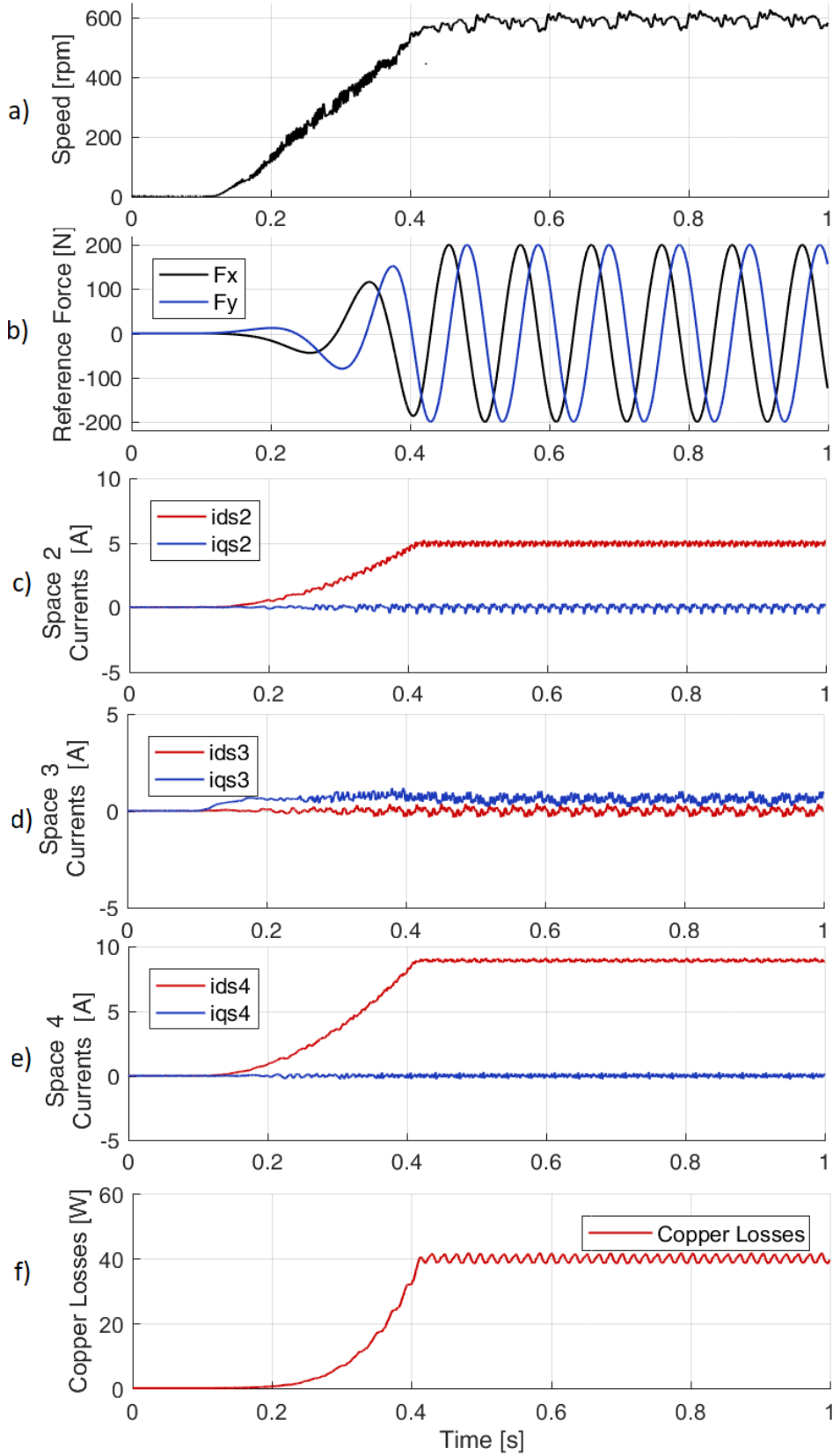


Fig. 5.39 – Experimental results of a speed transient at no load from 0 to 600 rpm. The radial force is synchronous with the rotor as in a dynamic mass unbalance. The speed, torque (a) and force (b), the current space vector components (c-e) and the total stator copper losses are plotted.

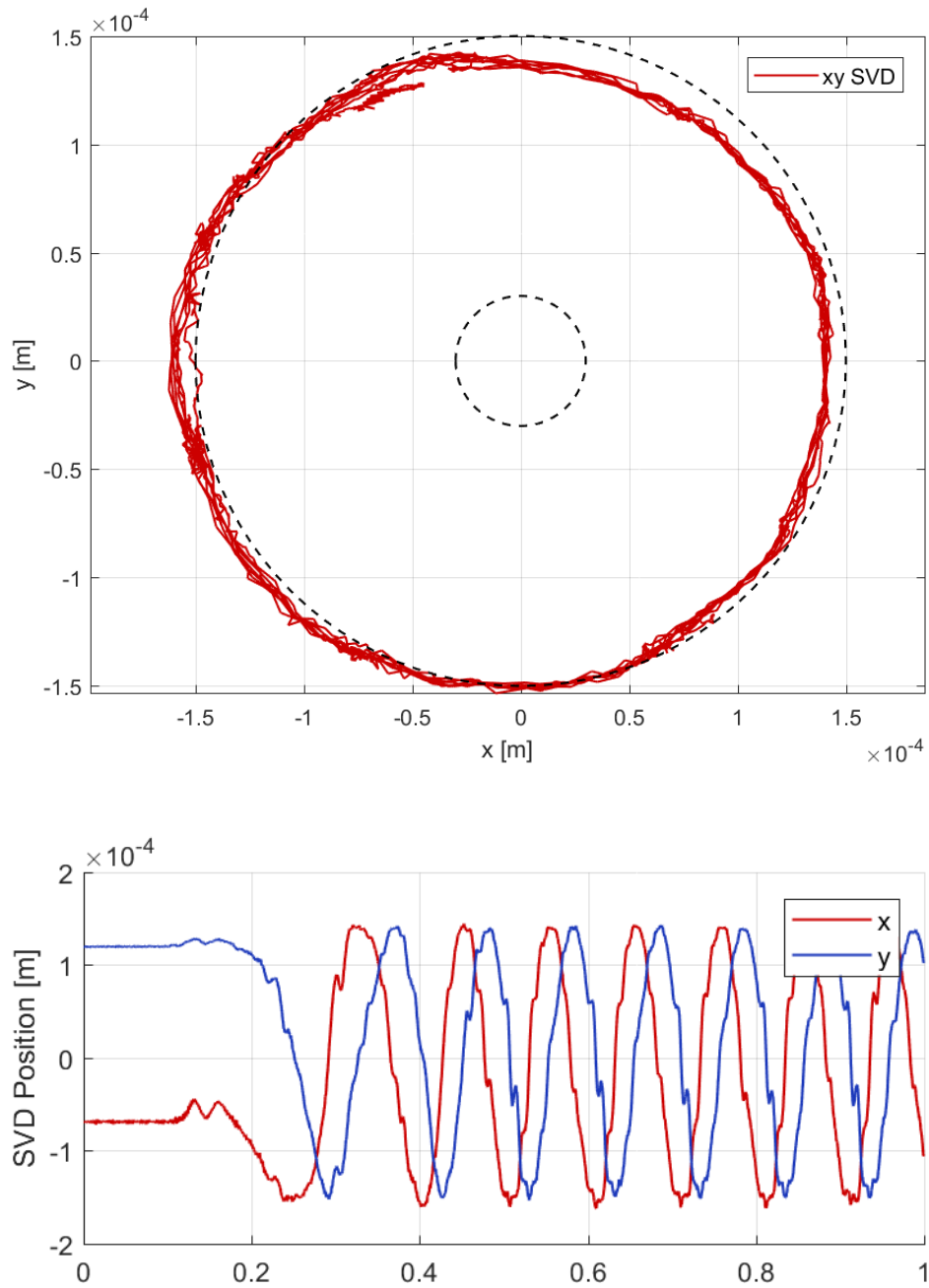


Fig. 5.40 – x-y shaft position. Experimental results of a speed transient at no load from 0 to 600 rpm. The radial force is synchronous with the rotor as in a dynamic mass unbalance. The x-y shaft position is only constrained by a backup bearing with $150\mu\text{m}$ radius.

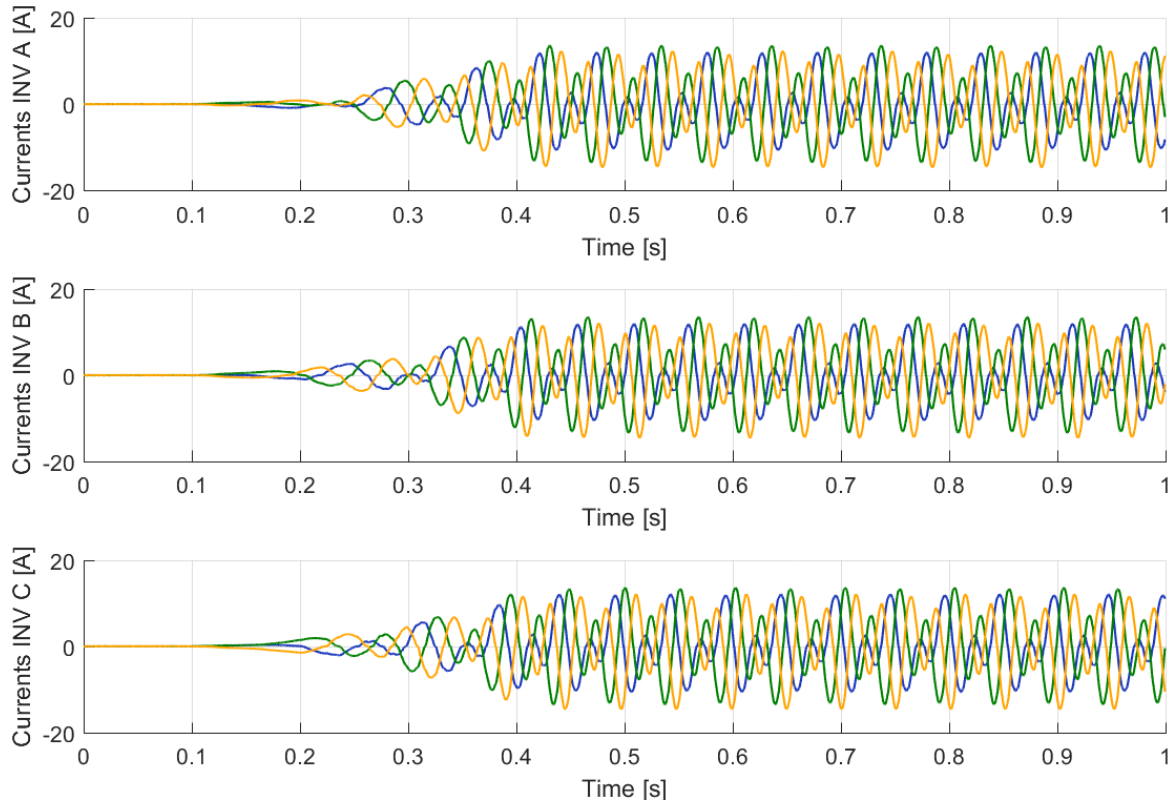


Fig. 5.41 – Phase currents in the three three-phase inverters. Experimental results of a speed transient at no load from 0 to 600 rpm. The radial force is synchronous with the rotor as in a dynamic mass unbalance. The steady state condition is at rated peak currents.

Radial Force Control in Bearingless Closed Loop Operation (stand still)

Fig. 5.42 shows the experimental results of the bearingless operation at stand still. At about 0.22 s the bearingless control of the machine is turned on. After a short transient needed to bring the shaft from the backup bearing boundary to the centre, the steady state operation is reached. As expected from the previous analysis, the copper Joule losses needed to levitate the rotor are negligible.

Fig. 5.43 shows the x-y position of the shaft axis and the backup bearing boundary. Small mismatches of the position of the position sensors makes the starting position be internal to the backup bearing constraint, but this is just an offset in the measure related to a slight imprecision of the position probe placement.

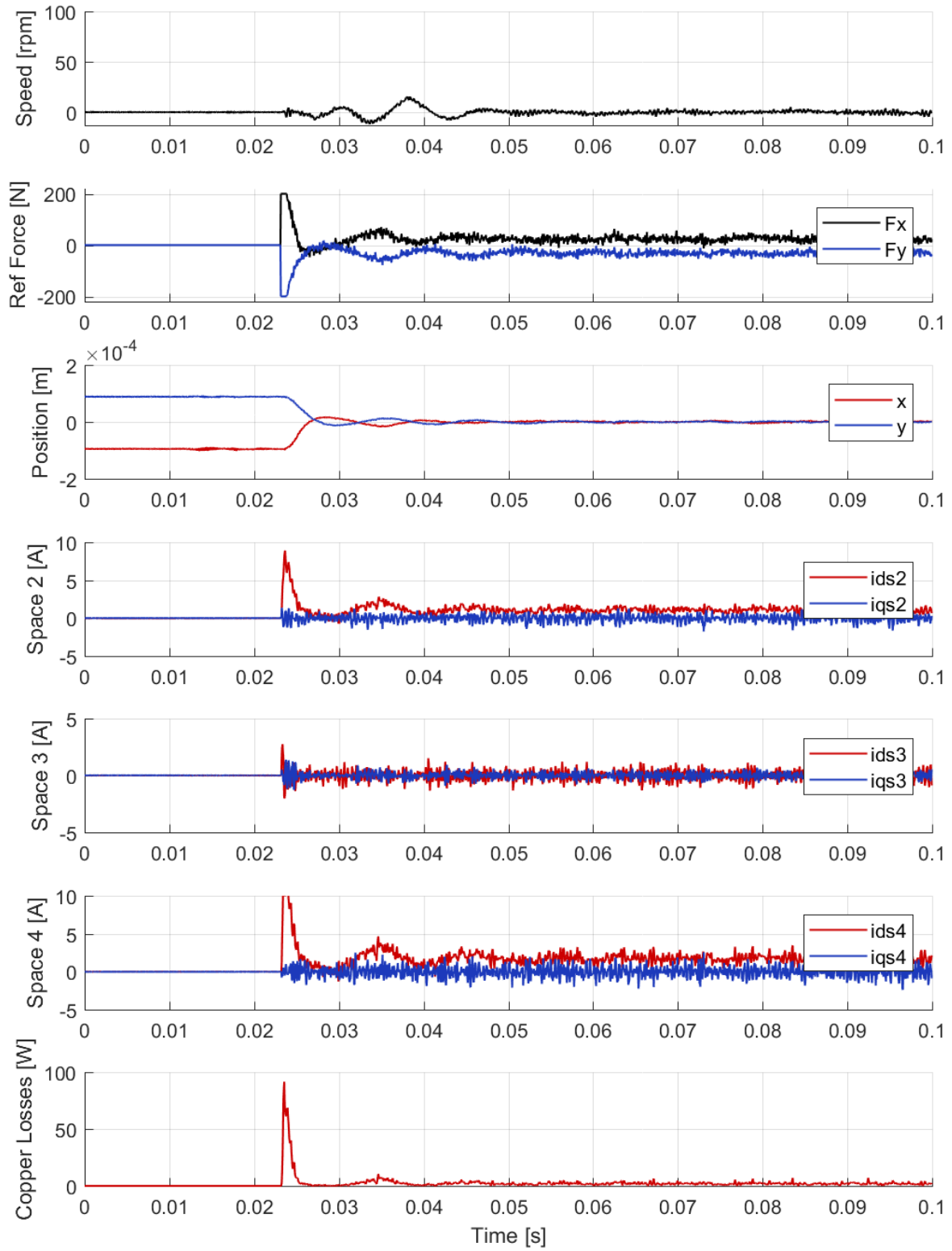


Fig. 5.42 – Stand still bearingless operation experimental results.

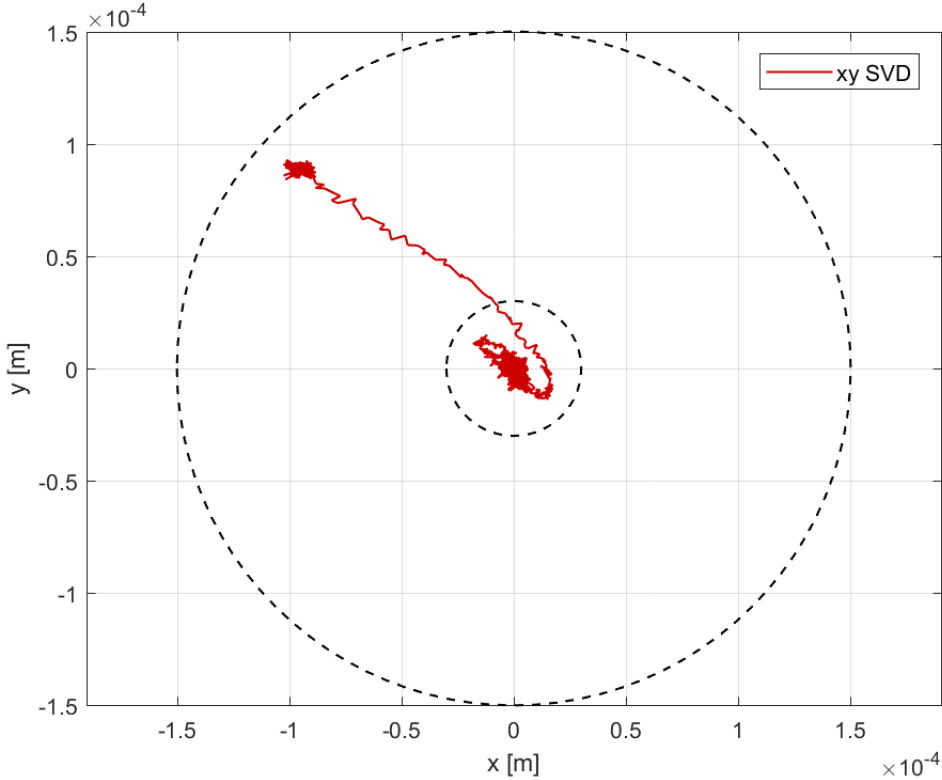


Fig. 5.43 – x-y shaft position: measured. Stand still bearingless experimental results.

Radial Force Control in Bearingless Closed Loop Operation (rated speed - 3000 rpm)

Fig. 5.44 shows the experimental results of the bearingless operation at rated speed in steady state operation. The copper Joule losses needed to levitate the rotor are still small. However, some ripples in the shaft position generate higher work needed to centre the rotor and an increase of the related losses.

Fig. 5.45 shows the x-y position of the shaft axis and the backup bearing boundary. Increasing the speed results in a worse position control, but the performance of the bearingless control is still good. The shaft axis always remains inside a circle of 30 μm radius (highlighted with the internal dashed circumference).

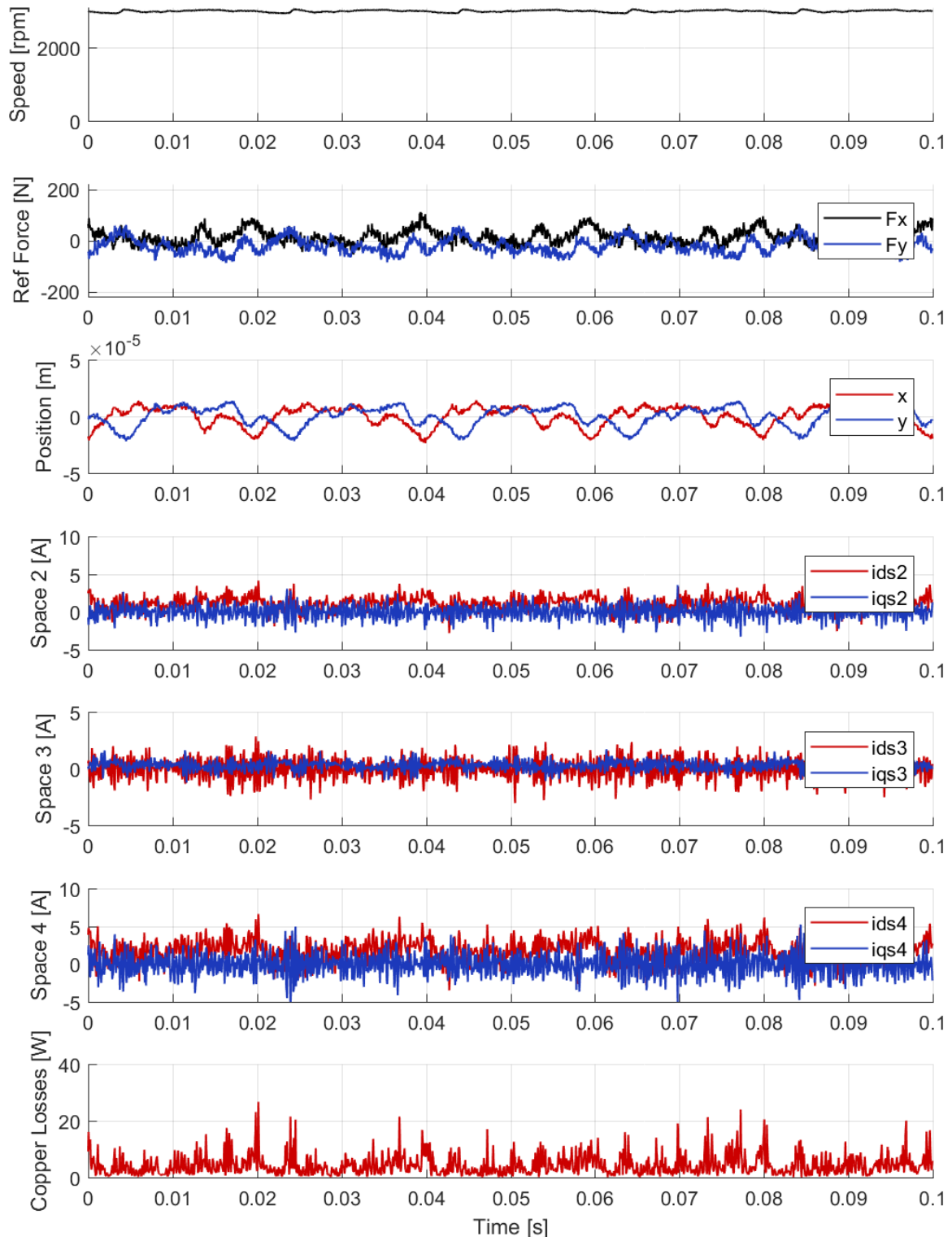


Fig. 5.44 – Bearingless operation at rated speed (3000 rpm): experimental results.

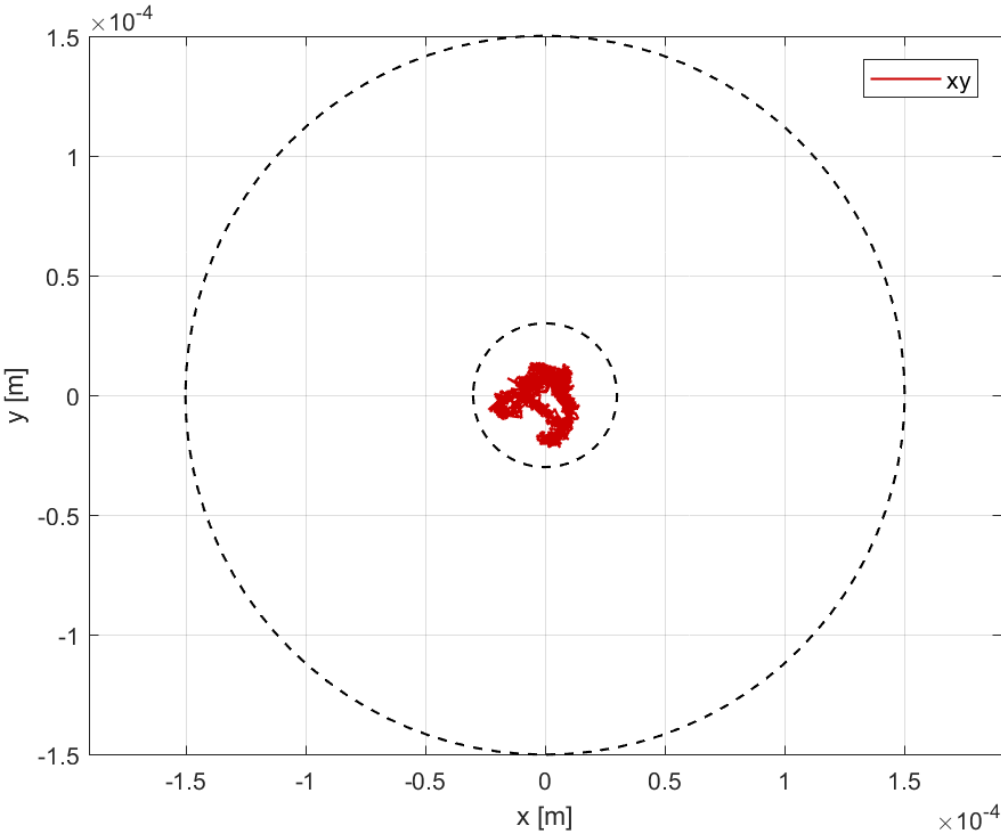


Fig. 5.45 – x-y shaft position: measured. Rated speed bearingless operation (3000 rpm).

Radial Force Control in Bearingless Closed Loop Operation (transient up to 3000 rpm)

Fig. 5.46 and Fig. 5.47 show the speed transient from stand still up to the rated speed in the bearingless operation. After the initial shaft positioning, the rotor position always remains inside the 30 μm radius from the backup bearing centre. Only for a short instant ($t = 0.44 \text{ s}$) the position exceeds this value until almost 50 μm . The copper Joule losses during the transient are almost the same as in steady state operation.

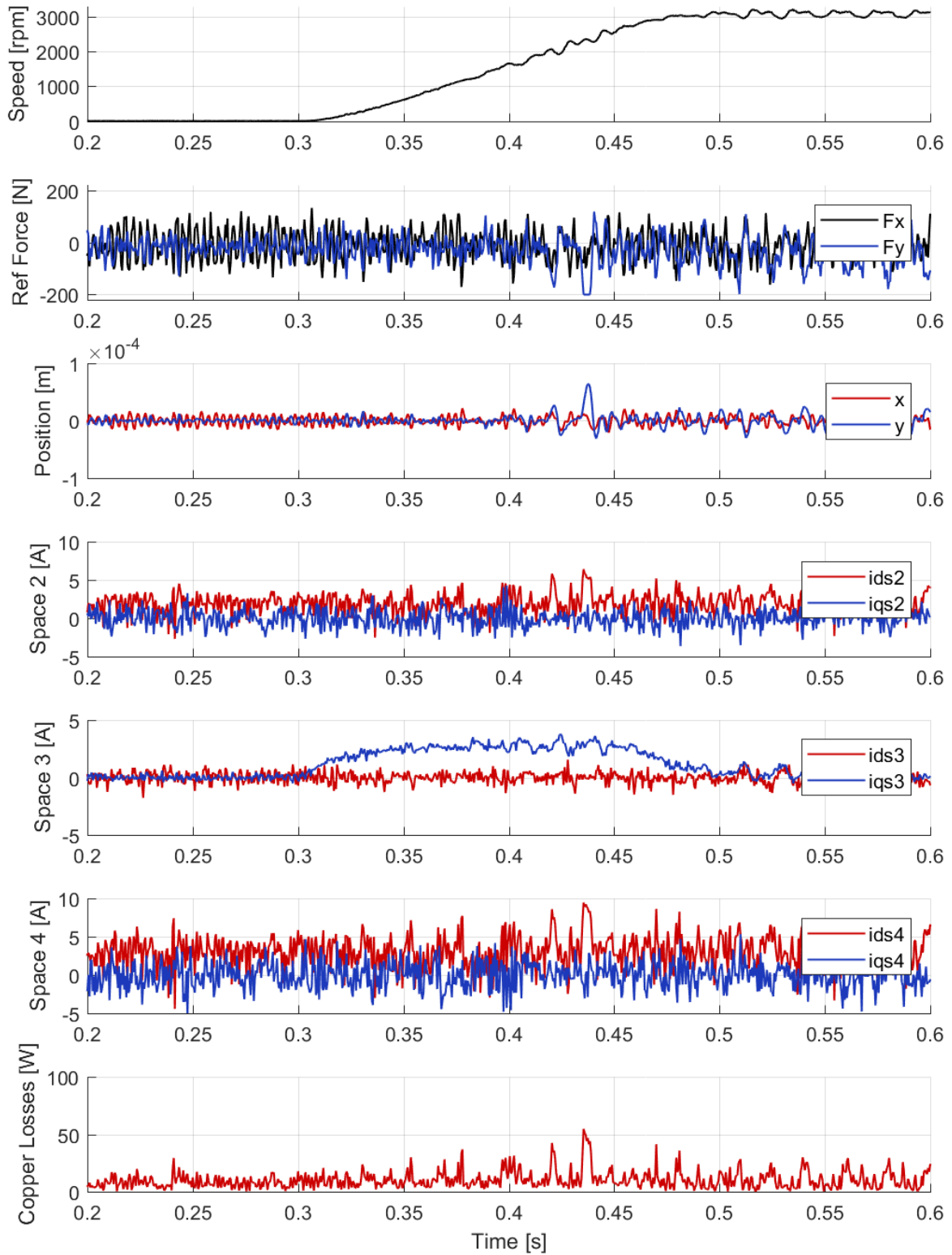


Fig. 5.46 – Bearingless operation for a speed transient from 0 to 3000 rpm: experimental results.

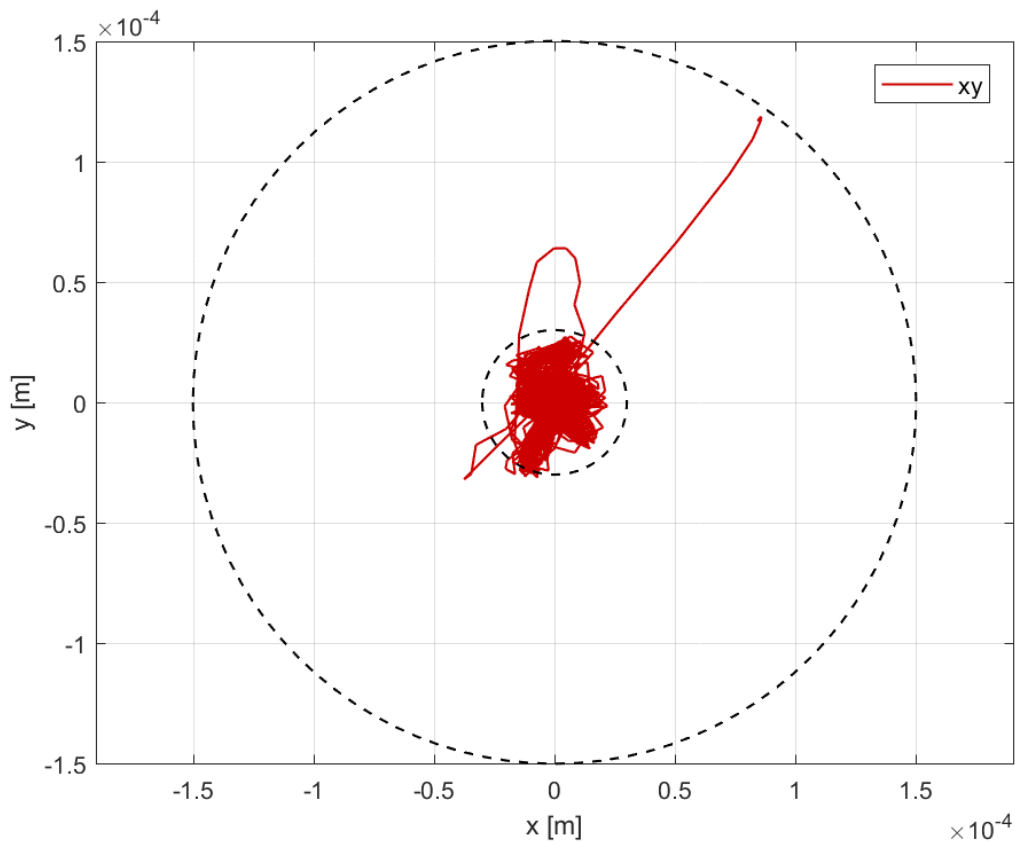


Fig. 5.47 – x - y shaft position: measured. Speed transient from 0 to 3000 rpm in bearingless operation. The initial transient for centring the shaft at stand still is also shown.

Radial Force Control in Bearingless Closed Loop Operation (bearingless control activation at 1000 rpm)

Fig. 5.48 and Fig. 5.49 show the machine behaviour when it is speeded up to 1000 rpm (1/3 the rated speed) without bearingless control, and suddenly the bearingless control is activated ($t = 0.6$ s). Even in this case the steady state bearingless operation is reached in about 0.02 s.

This test might represent the feasibility of a drive with implemented a fault tolerant algorithm that activates a bearingless machine control in case of bearing fault. Of course, this is just a first step for the development of such a technology.

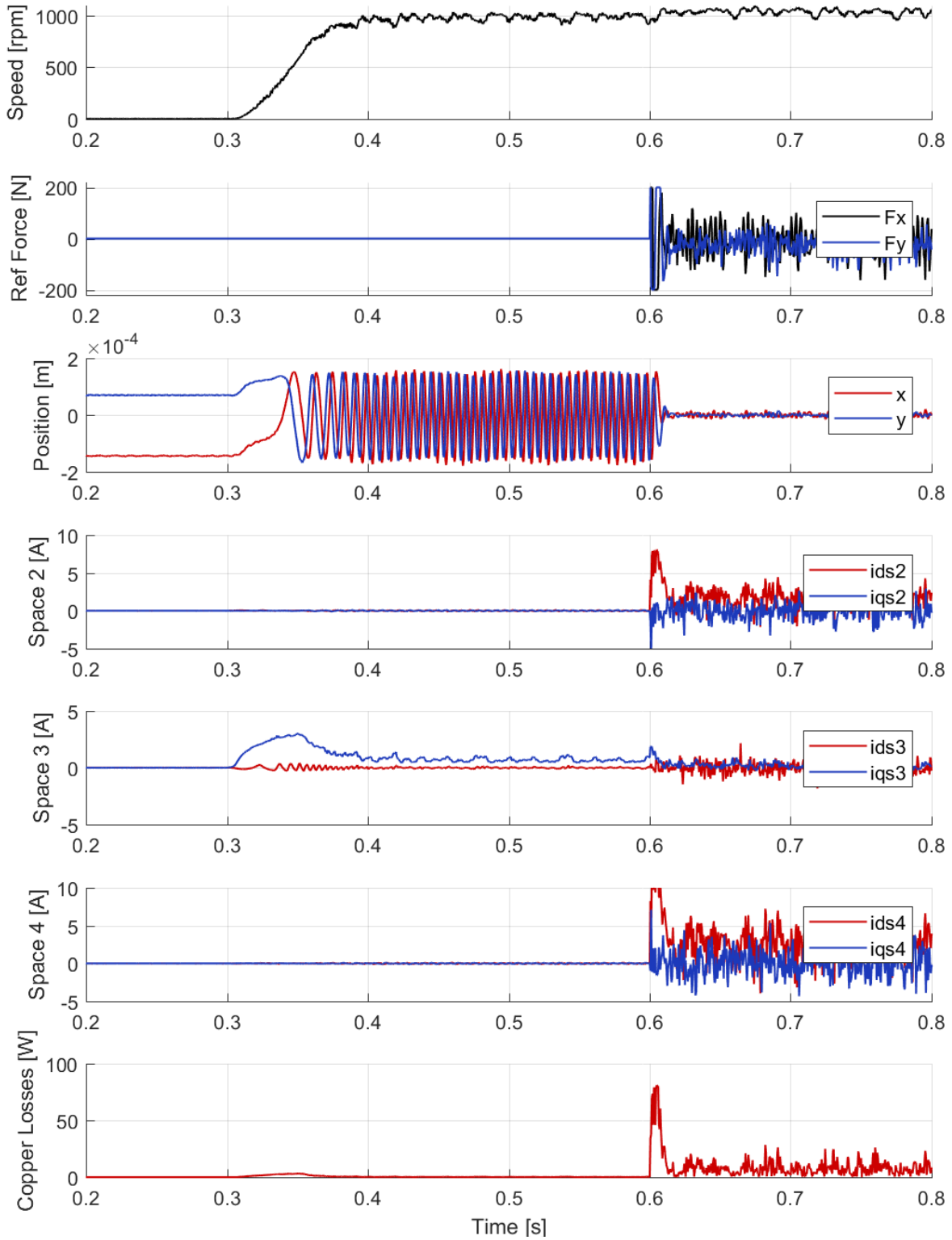


Fig. 5.48 – Speed transient from 0 to 1000 rpm ($t = 0.3$ s), and bearingless control activation ($t = 0.6$ s). Experimental results.

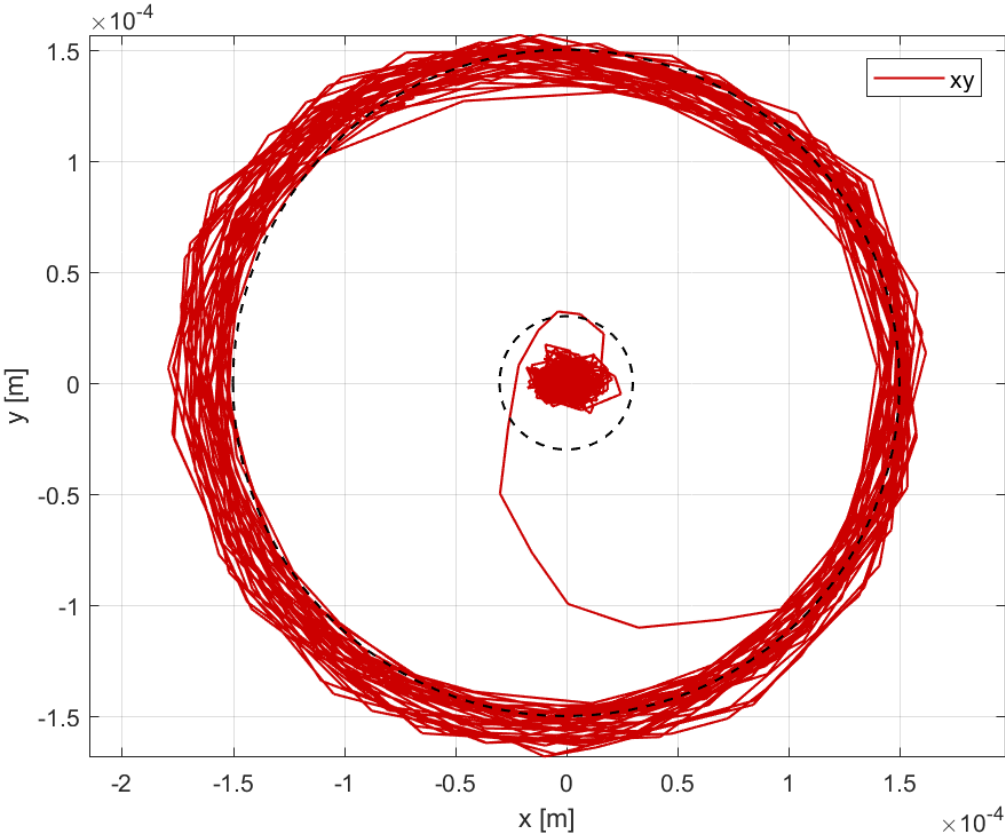


Fig. 5.49 – x-y shaft position: measured. Speed transient from 0 to 1000 rpm ($t = 0.3$ s) without position control, and bearingless control activation ($t = 0.6$ s). Experimental results.

5.10 Conclusions

This chapter presented an in-deep analysis of multi three-phase sectored PM machines (MSPM), taking into account also for the generated radial force. The general MSPM model is simplified for the case of a triple three-phase layout, in order to define a suitable machine control verifiable by the available prototype.

The general control algorithm shows the possibility of using more degrees of freedom for the definition of the radial force control. Therefore, the method is optimised for minimising the machine losses, considering all the degrees of freedom of the machine. The efficiency and performance are presented and compared for different reference values of the force.

The proposed algorithm allows also controlling the torque and the radial force in various working conditions. In particular, different techniques are proposed for managing the power sharing between the three-phase subsystems, and the case of one three-phase open fault.

The performance in open and closed loop of the various control algorithms are compared by means of FEA and Matlab-Simulink simulations.

The theory is verified for a prototype of triple three-phase MSPM machine assembled for a two degrees of freedom bearingless configuration.

Experimental tests validate the model prediction, showing that controlling the radial force and using it for the rotor levitation is feasible.

Further experimental tests will be done in the next future to validate all the other control techniques, providing also radial force measurements for an improved analysis.

To conclude, the radial force space vector control of a multi three-phase sectored machine is feasible. In case of current sharing or open phase faults, the sectored machines show a worse behaviour because of the radial force appearing. However, by means of a reliable machine model, it is possible to compensate these forces. Furthermore, the same techniques used for avoiding the forces in case of asymmetrical machine behaviour can be exploited for the radial force control.

References:

- [1] T. Baumgartner, R. M. Burkart, and J. W. Kolar, "Analysis and Design of a 300-W 500 000 - r/min Slotless Self-Bearing Permanent-Magnet Motor," *IEEE Transactions on Industrial Electronics*, vol. 61, pp. 4326-4336, 2014.
- [2] T. F. A. Chiba, O. Ichikawa, M. Oshima, M. Takemoto, and D. G. Dorrell, *Magnetic bearings and bearingless drives*: Elsevier, 2005.
- [3] A. H. Pesch, A. Smirnov, O. Pyrhönen, and J. T. Sawicki, "Magnetic Bearing Spindle Tool Tracking Through μ -Synthesis Robust Control," *IEEE/ASME Transactions on Mechatronics*, vol. 20, pp. 1448-1457, 2015.
- [4] S. Y. Zhang, C. B. Wei, J. Li, and J. H. Wu, "Robust H - infinity controller based on multi-objective genetic algorithms for active magnetic bearing applied to cryogenic centrifugal compressor," in *2017 29th Chinese Control And Decision Conference (CCDC)*, 2017, pp. 46-51.
- [5] C. Peng, J. Sun, X. Song, and J. Fang, "Frequency-Varying Current Harmonics for Active Magnetic Bearing via Multiple Resonant Controllers," *IEEE Transactions on Industrial Electronics*, vol. 64, pp. 517-526, 2017.
- [6] A. Chiba, M. A. Rahman, and T. Fukao, "Radial force in a bearingless reluctance motor," *IEEE Transactions on Magnetics*, vol. 27, pp. 786-790, 1991.
- [7] T. Schneider and A. Binder, "Design and Evaluation of a 60 000 rpm Permanent Magnet Bearingless High Speed Motor," in *2007 7th International Conference on Power Electronics and Drive Systems*, 2007, pp. 1-8.
- [8] X. Sun, Z. Xue, J. Zhu, Y. Guo, Z. Yang, L. Chen, *et al.*, "Suspension Force Modeling for a Bearingless Permanent Magnet Synchronous Motor Using Maxwell Stress Tensor Method," *IEEE Transactions on Applied Superconductivity*, vol. 26, pp. 1-5, 2016.
- [9] S. Serri, A. Tani, and G. Serra, "A method for non-linear analysis and calculation of torque and radial forces in permanent magnet multiphase bearingless motors," in *International Symposium on Power Electronics Power Electronics, Electrical Drives, Automation and Motion*, 2012, pp. 75-82.
- [10] B. Li, J. Huang, L. He, and H. Zhaowen, "Analysis and control of seven-phase permanent-magnet bearingless motor with single set of half-coiled winding," in *2014 IEEE 23rd International Symposium on Industrial Electronics (ISIE)*, 2014, pp. 2080-2086.
- [11] J. Huang, B. Li, H. Jiang, and M. Kang, "Analysis and Control of Multiphase Permanent-Magnet Bearingless Motor With a Single Set of Half-Coiled Winding," *IEEE Transactions on Industrial Electronics*, vol. 61, pp. 3137-3145, 2014.
- [12] A. Galassini, A. Costabeber, C. Gerada, G. Buticchi, and D. Barater, "A Modular Speed-Drooped System for High Reliability Integrated Modular Motor Drives," *IEEE Transactions on Industry Applications*, vol. 52, pp. 3124-3132, 2016.
- [13] G. Sala, D. Gerada, C. Gerada, and A. Tani, "Radial force control for triple three-phase sector SPM machines. Part II: Open winding fault tolerant control," in *2017 IEEE Workshop on Electrical Machines Design, Control and Diagnosis (WEMDCD)*, 2017, pp. 275-280.
- [14] G. Sala, D. Gerada, C. Gerada, and A. Tani, "Radial force control for triple three-phase sector SPM machines. Part I: Machine model," in *2017 IEEE Workshop on Electrical Machines Design, Control and Diagnosis (WEMDCD)*, 2017, pp. 193-198.

- [15] M. Barcaro, N. Bianchi, and F. Magnussen, "Faulty Operations of a PM Fractional-Slot Machine With a Dual Three-Phase Winding," *IEEE Transactions on Industrial Electronics*, vol. 58, pp. 3825-3832, 2011.
- [16] L. Alberti and N. Bianchi, "Impact of winding arrangement in dual 3-phase induction motor for fault tolerant applications," in *The XIX International Conference on Electrical Machines - ICEM 2010*, 2010, pp. 1-6.
- [17] G. Valente, L. Papini, A. Formentini, C. Gerada, and P. Zanchetta, "Radial force control of multi-sector permanent magnet machines," in *2016 XXII International Conference on Electrical Machines (ICEM)*, 2016, pp. 2595-2601.
- [18] G. Valente, L. Papini, A. Formentini, C. Gerada, and P. Zanchetta, "Radial force control of Multi-Sector Permanent Magnet machines considering radial rotor displacement," in *2017 IEEE Workshop on Electrical Machines Design, Control and Diagnosis (WEMDCD)*, 2017, pp. 140-145.
- [19] L. Alberti and N. Bianchi, "Experimental Tests of Dual Three-Phase Induction Motor Under Faulty Operating Condition," *IEEE Transactions on Industrial Electronics*, vol. 59, pp. 2041-2048, 2012.
- [20] S. Zhou and J. Shi, *Active Balancing and Vibration Control of Rotating Machinery: A Survey* vol. 33, 2001.
- [21] A. Galassini, G. L. Calzo, A. Formentini, C. Gerada, P. Zanchetta, and A. Costabeber, "uCube: Control platform for power electronics," in *2017 IEEE Workshop on Electrical Machines Design, Control and Diagnosis (WEMDCD)*, 2017, pp. 216-221.

CHAPTER 6

Design and Control of Segmented Multi Three-Phase SPM Machines

Multiphase machines, compared to the standard three-phase ones, give more advantages in terms of reliability and efficiency, becoming always more suitable for high performance and fault tolerant applications. Multiphase motors allow exploiting more degrees of freedom in the generation of the armature field, which can be useful to obtain a higher torque density and efficiency, and reduced torque ripples [1]. Furthermore, suitable fault tolerant algorithms might be exploited to overcome fault conditions and/or to detect them [2, 3]. In general, a multiphase drive requires an “extended field oriented control” able to control the air-gap field harmonic components, and a multiphase modulation technique for the inverter can be used to increase the DC-bus exploitation [4]. Among the different multiphase machine topologies, the multi three-phase one has the advantage to use a standard three-phase inverter technology.

The multi three-phase machine can be wound with symmetrical three-phase windings. In this case, each three-phase system winding is shifted from the others of a fixed and defined angle. This winding configuration allows better exploiting the air-gap magnetic field control [5], as described in Chapter 2, 3 and 4. Another possible solution is the sectored one, based on the redundant structure idea. This solution has been analysed in Chapter 5 and other works [6], where two three-phase windings are separately arranged in different stator sectors. This separation of the subsystems results in an asymmetrical magnetomotive force distribution (source of radial force if the sectors are controlled with different current values), but allows also avoiding the subsystems overlapping, achieving higher electromagnetic independence.

In this chapter, a triple three-phase sectored winding configuration is analysed as the one of Chapter 5. The generalisation of the segmentation theory has been limited to some topologies, because of the particular design under study. A sectored machine can be viewed as three machines that are exploded and joined together to realize the triple three-phase design.

To emphasize the decoupling between the three-phase subsystems, the concept of segmentation is introduced. The idea is to increase the sector independence (mechanical, electromagnetic, thermal) without losing in machine performance. Previous works on stator segmentation have been carried out for manufacturing issues [7, 8] or improving the motor performance [9, 10],

but in this thesis this idea is applied for the first time to a distributed winding multi three-phase sectored machine to improve both the performance and the fault tolerant behaviour.

Sectored and Segmented motor design - Concept

The idea of sectorization is used to define an electrical machine in which each three-phase winding is arranged in a different stator area and supplied by a three-phase inverter. On the other hand, the concept of motor segmentation refers to the introduction of an additional material between the machine stator sectors.

Some of the sectored and segmented analysed designs are shown in Fig. 4.1, where the basic sectored winding is the SDa (first design at the top and on the left, the same of Chapter 5).

Hereafter, the most important kind of analysed segmented designs are named as “SDx”, where x is the letter that distinguishes the different topologies as in Fig. 4.1.

Once the segmentation is introduced in the design optimization process, many new degrees of freedom must be taken into account.

The main design variables, shown in Fig. 6.2, can be summarized as:

- segmentation thickness;
- segmentation material and shape;
- sector slots and teeth design.

The rotor, the external stator diameter, the rated torque and the iron area (in order to limit the effects of iron saturation on the design) are chosen as design constraints.

Fig. 6.3 shows the unsegmented design (SDa), which is the starting topology for the segmentation design. Indeed, a sectored design (as SDa) is a particular segmented one with zero segmentation thickness.

Segmentation Thickness

The segmentation thickness is the size of the gap introduced between the machine stator sectors. This gap is represented by the geometrical parameter $\Delta\Psi_{es}$ (named as external segmentation), shown in Fig. 6.2. The segmentation thickness affects the decoupling between the sectors, but also the available space, in each of the three-phase sectors, to design the stator slots and teeth. If this available space decreases, the coil pitch inevitably changes, and this is a new useful degree of freedom for the design. For example, the coil pitch can be exploited to reduce the most relevant armature fields (as the 5th or/and the 7th). Furthermore, the segmented machine control technique (presented in the following sections) strongly depends from the segmentation thickness if standard windings are used.

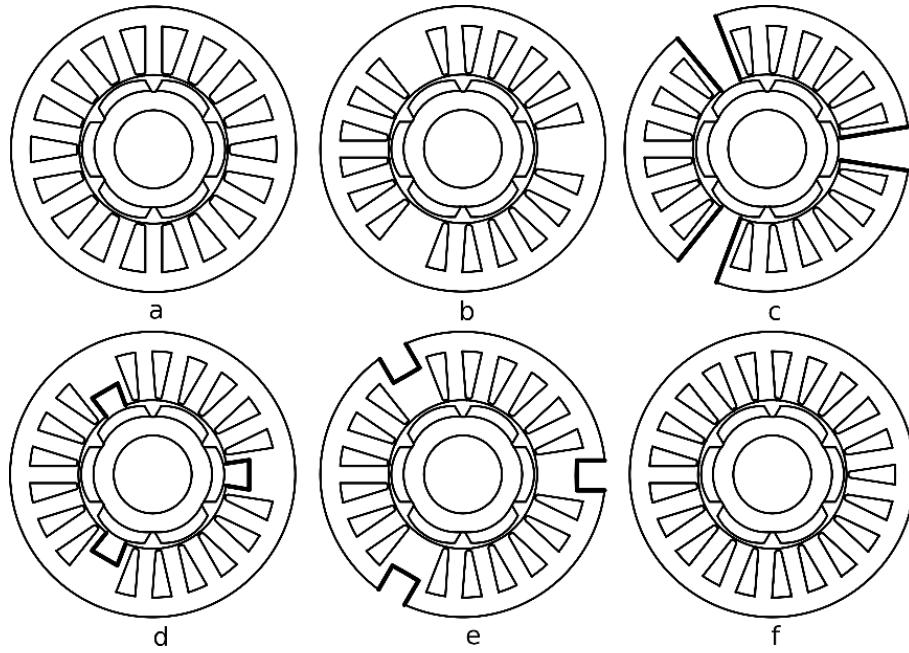


Fig. 6.1 – Triple three-phase sectored designs with different segmentation layouts. The original not segmented design is the a) left top.

Segmentation Material and Shape

Once the segmentation thickness $\Delta\Psi_{es}$ is defined, the resulting available area can be optimized to improve the fault tolerant machine behaviour or to reduce the machine torque ripple. This area can also be exploited for an additional cooling system. It is possible to have a full iron segmentation (as SDb), an air based segmentation (as SDc), or a hybrid segmentation

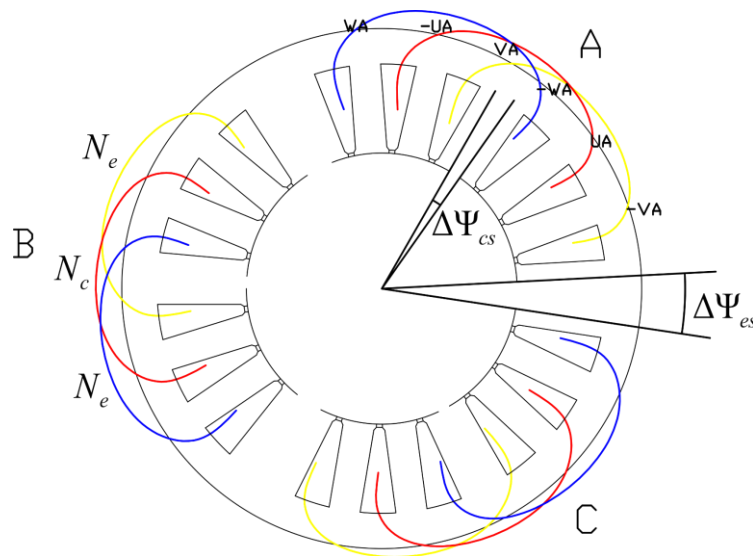


Fig. 6.2 – Triple three-phase sectored design and segmentation concept. The figure also shows the main segmentation parameters.

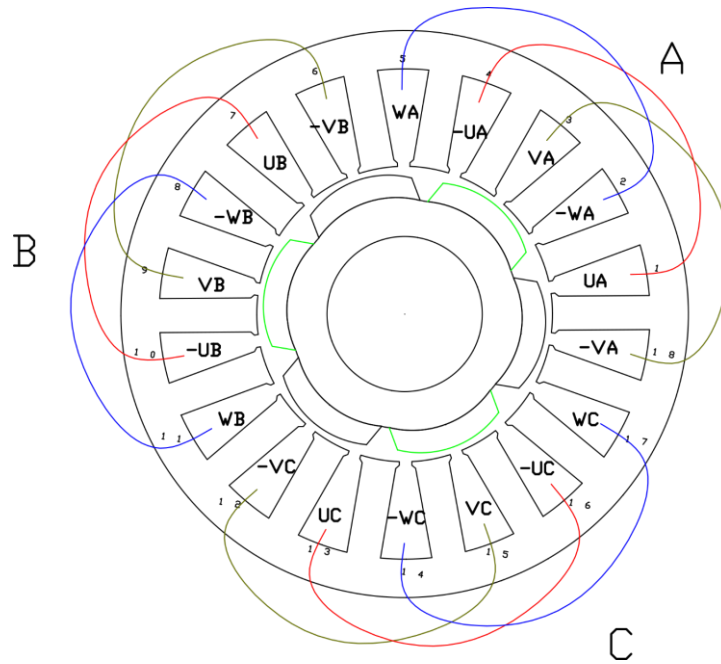


Fig. 6.3 – Triple three-phase sectored design: layout SDa, without segmentation. The turn number is N for each phase.

(as SDd - Sdf). In this area, it is also possible to introduce also a central segmentation $\Delta\Psi_{cs}$ (named as central segmentation), as shown in Fig. 6.2. This further degree of freedom in the design of the sectors has been investigated. The idea is to understand if there might be advantages in distributing the slots in a different position and the design of the central segmentation might be useful to improve the machine performance.

Sector Slots and Teeth Design

The sectors teeth thickness is the same for all the topologies shown in Fig. 6.1 (i.e. they have almost the same iron exploitation). Therefore, the slots area is reduced. The turns per phase number can be maintained the same as the SDa design or can be modified (as described in the following sections) with different turns in the central phase N_c compared to the external ones N_e of each sector. This aims to recreate a more symmetrical magnetomotive force distribution.

Summary of the Segmentation Design Degrees of Freedom

To summarize the approach used for the analysis of the segmentation idea, the list of design variables that has been considered (referring to Fig. 6.2) is:

- $\Delta\Psi_{es}$: external segmentation thickness (angle)
- $\Delta\Psi_{cs}$: central segmentation thickness (angle)
- N_c / N_e : ratio between the turns of the central phases over the external ones

- Material and shape of the areas into the $\Delta\Psi_{es}$ and $\Delta\Psi_{cs}$ arcs.

In order to understand how the segmentation affect the control performance, the next section describes the relationships between the currents and the resulting armature field harmonics in segmented machines.

6.1 Field Analysis of a Triple Three-phase Sectored and Segmented SPM

The electromagnetic model of the machine has been developed considering the segmentation material as full iron and neglecting the slotting effect. Therefore, the machine is analysed with the assumption of isotropic magnetic circuit. This allows significantly simplifying the machine model for understanding how the segmentation affects the magnetomotive force distribution. The effects of the additional segments reluctance has been studied by FEA, as it is usually done for the analysis of the end-effects in linear machines. Indeed, the assumption of considering only the radial component of the magnetic field in a layout such as SDC would result in having a zero flux density under the segmentation angle $\Delta\Psi_{es}$, while in reality the flux in that area is not zero but the flux path depends on the segments geometry, as shown in Fig. 6.4.

In the proposed analysis the time dependence is implicit and the machine equations have been written in mechanical angles, it means that the main harmonic field is the p -th one ($\rho = p$), with p the pole pairs number. The main parameters are defined as: R the average air-gap radius; δ the whole air-gap thickness including the permanent magnets; N the turns per slot number in the SDC machine design (and N_x the actual number in the x -th phase); $\Delta\Psi_y$ the coil

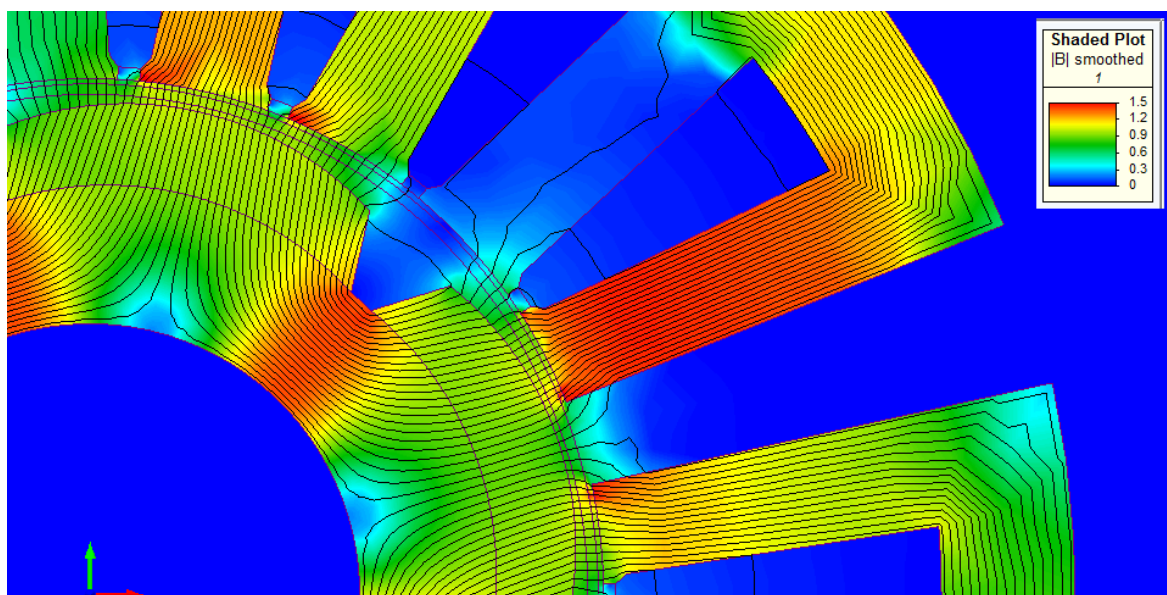


Fig. 6.4 – Zoom of the flux view of the SDC design in the segmentation arc.

pitch angle; i_{xP} the current in the x-phase under the P -sector, identified following the stator anticlockwise (i.e. $P(A)=1, P(B)=2$ and $P(C)=3$ in the triple three-phase layout).

General SV model of a segmented and sectored machine

Each three-phase subsystem of a multi three-phase machine can be completely described by the standard three-phase transformation.

As discussed in Chapter 3 and 5, the currents of each T -th three-phase subsystem are well represented by the following three-phase transformation:

$$\bar{i}_{TP1} = \frac{2}{3} \left(i_{TP,U} + i_{TP,V} e^{j\frac{2\pi}{3}} + i_{TP,W} e^{j\frac{4\pi}{3}} \right), \quad T = 1, 2, \dots, N_T, \quad P = 1, 2, \dots, p, \quad (6.1)$$

and

$$i_{TP0} = \frac{2}{3} (i_{TP,U} + i_{TP,V} + i_{TP,W}), \quad T = 1, 2, \dots, N_T, \quad P = 1, 2, \dots, p, \quad (6.2)$$

where the subscripts T and P are used to represent the T -th three-phase subsystem located in the P -th pole pair. The subscripts U, V and W are used to define the phases of each three-phase subsystem. The multi-space three-phase transformation is:

$$\bar{i}_{TP,h} = \frac{2}{3} \left(i_{TP,U} + i_{TP,V} e^{jh\frac{2\pi}{3}} + i_{TP,W} e^{jh\frac{4\pi}{3}} \right), \quad T = 1, 2, \dots, N_T, \quad P = 1, 2, \dots, p, \quad (6.3)$$

with the relative inverse transformation:

$$i_{TP,k} = \frac{i_{TP,0}}{2} + \Re \left\{ \bar{i}_{TP,1} e^{-j\frac{2\pi}{3}(Z_k-1)} \right\}, \quad k = U, V, W, \quad T = 1, 2, \dots, N_T, \quad P = 1, 2, \dots, p. \quad (6.4)$$

where $Z_U = 1, Z_V = 2$ and $Z_W = 3$ are the indexes that represent the phases of each three-phase subsystem.

The particular geometry of the slot position makes the definition of a suitable symmetrical transformation impossible. Therefore, the h -space current vector \bar{i}_h is defined by the following asymmetrical transformation (similar to (5.6)):

$$\begin{aligned}
 \bar{i}_h = & \frac{2}{3N_T p} \sum_{T=1}^{N_T} \sum_{P=1}^p \left(\frac{N_c}{N} i_{TP,U} e^{jh \left[\frac{2\pi}{p}(P-1) + \left(\frac{2\pi}{6N_T p} \frac{\Delta\Psi_{es} + \Delta\Psi_{cs}}{6N_T} \right) (T-1) \right]} \right) + \\
 & - \frac{2}{3N_T p} \sum_{T=1}^{N_T} \sum_{P=1}^p \left(\frac{N_e}{N} i_{TP,V} e^{jh \left[\frac{2\pi}{p}(P-1) + \left(\frac{2\pi}{6N_T p} \frac{\Delta\Psi_{es} + \Delta\Psi_{cs}}{6N_T} \right) (T-1-N_T) \right]} \right) + \\
 & - \frac{2}{3N_T p} \sum_{T=1}^{N_T} \sum_{P=1}^p \left(\frac{N_e}{N} i_{TP,W} e^{jh \left[\frac{2\pi}{p}(P-1) + \left(\frac{2\pi}{6N_T p} \frac{\Delta\Psi_{es} + \Delta\Psi_{cs}}{6N_T} \right) (T-1+N_T) \right]} \right), \quad (6.5)
 \end{aligned}$$

which can be simplified as:

$$\bar{i}_h = \frac{2}{3N_T p} \sum_{T=1}^{N_T} \sum_{P=1}^p \left(\frac{N_c}{N} i_{TP,U} - \frac{N_e}{N} i_{TP,V} e^{-jh\Delta\Psi_{slot}N_T} - \frac{N_e}{N} i_{TP,W} e^{jh\Delta\Psi_{slot}N_T} \right) e^{jh \left[\frac{2\pi}{p}(P-1) + \Delta\Psi_{slot}(T-1) \right]}, \quad (6.6)$$

with $\Delta\Psi_{slot}$ the angle between two consecutive slots defined as:

$$\Delta\Psi_{slot} = \frac{2\pi - p(\Delta\Psi_{es} + \Delta\Psi_{cs})}{m} = \frac{2\pi}{6N_T p} - \frac{\Delta\Psi_{es} + \Delta\Psi_{cs}}{6N_T}. \quad (6.7)$$

The h -th harmonic of the Fourier series of the armature field (2.47) is:

$$\bar{H}_{cu,h} = \frac{Nmpq}{\pi\delta} \frac{K_{ah}}{h} \bar{i}_h, \quad h=1,2,\dots,\infty. \quad (6.8)$$

For a multi three-phase sectored machine with a single coil per phase, the armature field harmonics can be defined as:

$$\bar{H}_{cu,h} = \frac{N3N_T p}{\pi\delta} \frac{\sin\left(h \frac{\Delta\psi_y}{2}\right)}{h} \bar{i}_h, \quad h=1,2,\dots,\infty, \quad (6.9)$$

with $\Delta\psi_y$ the phase pitch. In the proposed segmented design, the phase pitch is:

$$\Delta\psi_y = \Delta\Psi_{cs} + 3N_T \Delta\Psi_{slot} = \Delta\Psi_{cs} + \frac{2\pi}{2p} - \frac{\Delta\Psi_{es} + \Delta\Psi_{cs}}{2}. \quad (6.10)$$

Assuming that the machine is controlled with the same currents in each three-phase subsystem (standard machine control), the SPM machine can be analysed in the same way under each pole. Therefore, the control technique is defined for the main electrical field harmonic (p -th), while the torque ripple and iron losses are also related to the other electrical field harmonics.

The general torque equation under the assumption of isotropic magnetic circuit and symmetrical SPM rotor (2.250) is:

$$T = 4\mu_0 L R N m p q \frac{B_r \tau_M}{\mu_M \pi \delta} \sum_{h \text{ odd}=1}^{\infty} \Re \left\{ j \bar{i}_{ph}^* \frac{K_{aph}}{h} \sin \left(h \frac{\pi}{2} \right) e^{jph\vartheta_m} K_{skew,ph} \right\}, \quad (6.11)$$

adapted to a sectored and segmented triple three-phase machine (one coil per phase), it results as:

$$T = 4\mu_0 L R N 3 N_T p \frac{B_r \tau_M}{\mu_M \pi \delta} \sum_{h \text{ odd}=1}^{\infty} \Re \left\{ j \bar{i}_{ph}^* \frac{\sin \left(ph \frac{\Delta\psi_y}{2} \right)}{h} \sin \left(h \frac{\pi}{2} \right) e^{jph\vartheta_m} K_{skew,ph} \right\}, \quad (6.12)$$

simplified as:

$$T = \sum_{h \text{ odd}=1}^{\infty} K_{T,ph} \Re \left\{ j \bar{i}_{ph}^* e^{jph\vartheta_m} \right\}, \quad (6.13)$$

with:

$$K_{T,ph} = 4\mu_0 L R N 3 N_T p \frac{B_r \tau_M}{\mu_M \pi \delta} \frac{\sin \left(ph \frac{\Delta\psi_y}{2} \right)}{h} \sin \left(h \frac{\pi}{2} \right) K_{skew,ph}.$$

Because in a segmented design the current space vector \bar{i}_{ph} is defined by an asymmetrical transformation (6.6), the torque equation cannot be simplified as done in Chapter 2, 3 and 4, and each current space vector must be considered as unique (there is not a reasonable N_Z number for which there is a repetition of the current space vectors like $\bar{i}_{N_Z+h} = \bar{i}_h$).

Furthermore, the current space vectors odd multiple of 3 times the pole pair number ($3kp$, with k an odd number) are usually related to the homopolar currents of the three-phase subsystems. Instead, in a segmented design they are related also to the three-phase current space vectors. Indeed, the $3kp$ -order current vectors are defined as:

$$\bar{i}_{3kp} = \frac{2}{3N_T p} \sum_{T=1}^{N_T} \sum_{P=1}^p \left(\frac{N_c}{N} i_{TP,U} - \frac{N_e}{N} i_{TP,V} e^{-j3kp\Delta\Psi_{slot} N_T} - \frac{N_e}{N} i_{TP,W} e^{j3kp\Delta\Psi_{slot} N_T} \right) e^{j3kp \left[\frac{2\pi}{p}(P-1) + \Delta\Psi_{slot}(T-1) \right]},$$

with

$$e^{\pm j3kp\Delta\Psi_{slot} N_T} = e^{\pm j3kp \left(\frac{2\pi}{6N_T p} - \frac{\Delta\Psi_{es} + \Delta\Psi_{cs}}{6N_T} \right) N_T} = e^{\pm jk \left(\frac{2\pi}{2} - p \frac{\Delta\Psi_{es} + \Delta\Psi_{cs}}{2} \right)},$$

resulting in:

$$\bar{i}_{3kp} = \frac{2}{3N_T p} \sum_{T=1}^{N_T} \sum_{P=1}^p \left(\frac{N_c}{N} i_{TP,U} - \frac{N_e}{N} i_{TP,V} e^{-jk \left(\pi - p \frac{\Delta\Psi_{es} + \Delta\Psi_{cs}}{2} \right)} - \frac{N_e}{N} i_{TP,W} e^{jk \left(\pi - p \frac{\Delta\Psi_{es} + \Delta\Psi_{cs}}{2} \right)} \right) e^{j3kp \left[\frac{2\pi}{p}(P-1) + \Delta\Psi_{slot}(T-1) \right]}.$$

If there is not a segmentation ($\Delta\Psi_{es} = \Delta\Psi_{cs} = 0$), remembering that k is an odd number, the equation becomes:

$$\bar{i}_{3kp} = \frac{2}{3N_T p} \sum_{T=1}^{N_T} \sum_{P=1}^p \left(\frac{N_c}{N} i_{TP,U} + \frac{N_e}{N} i_{TP,V} + \frac{N_e}{N} i_{TP,W} \right) e^{j3kp \left[\frac{2\pi}{p} (P-1) + \Delta\Psi_{slot}(T-1) \right]}.$$

Only if also the turn number is the same in all the phases ($N_c = N_e = N$), it results (according to (3.42)):

$$\bar{i}_{3kp} = \frac{2}{3N_T p} \sum_{T=1}^{N_T} \sum_{P=1}^p (i_{TP,U} + i_{TP,V} + i_{TP,W}) e^{j3kp \left[\frac{2\pi}{p} (P-1) + \Delta\Psi_{slot}(T-1) \right]} = \sum_{T=1}^{N_T} \sum_{P=1}^p \left(\frac{e^{j3kp \left[\frac{2\pi}{p} (P-1) + \Delta\Psi_{slot}(T-1) \right]}}{N_T p} \right) i_{TP,0}.$$

If the three-phase subsystems are independently star connected, all these components are zero ($\bar{i}_{3kp} = 0$).

If one of the previous assumption cannot be done, the PM field harmonics of order $3kp$ interacts with the armature field harmonics of the same order generating additional torque ripples.

The model is simplified for a triple three-phase segmented machine in the next subsection, where the design variables are exploited in order to optimise the machine performance.

SV Model of a Triple Three-Phase Segmented and Sectored SPM Machine

Hereafter the equations refer to the studied SPM machine, it means a triple three-phase one ($p = 3$ and $N_T = 1$).

Each independently star connected three-phase subsystem can be completely described by:

$$\bar{i}_{P1} = \frac{2}{3} \left(i_{P,U} + i_{P,V} e^{j\frac{2\pi}{3}} + i_{P,W} e^{j\frac{4\pi}{3}} \right), \quad P = 1(A), 2(B), 3(C), \quad (6.14)$$

with the relative inverse transformation:

$$i_{P,k} = \Re \left\{ \bar{i}_{P,1} e^{-j\frac{2\pi}{3}(Z_k - 1)} \right\}, \quad k = U, V, W, \quad P = 1(A), 2(B), 3(C), \quad (6.15)$$

where $Z_U = 1$, $Z_V = 2$ and $Z_W = 3$ are the indexes that represent the phases of each three-phase subsystem.

The h -space current vector \bar{i}_h is defined as:

$$\bar{i}_h = \frac{2}{9} \sum_{p=1}^3 \left(\frac{N_c}{N} i_{p,U} - \frac{N_e}{N} i_{p,V} e^{-jh\Delta\Psi_{slot}} - \frac{N_e}{N} i_{p,W} e^{jh\Delta\Psi_{slot}} \right) e^{jh\frac{2\pi}{3}(p-1)}, \quad (6.16)$$

with the slot pitch:

$$\Delta\Psi_{slot} = \frac{2\pi}{18} - \frac{\Delta\Psi_{es} + \Delta\Psi_{cs}}{6}. \quad (6.17)$$

The armature field harmonics are defined as:

$$\bar{H}_{cu,h} = \frac{N9}{\pi\delta} \frac{\sin\left(h\frac{\Delta\Psi_y}{2}\right)}{h} \bar{i}_h, \quad h=1,2,\dots,\infty, \quad (6.18)$$

with the phase pitch:

$$\Delta\Psi_y = \frac{2\pi}{6} - \frac{\Delta\Psi_{es}}{2} + \frac{\Delta\Psi_{cs}}{2}. \quad (6.19)$$

The torque equation is:

$$T = \sum_{h=odd=1}^{\infty} K_{T,3h} \Re\{j\bar{i}_{3h}^* e^{j3h\theta_m}\}, \quad (6.20)$$

with:

$$K_{T,3h} = 4\mu_0 L R N 9 \frac{B_r \tau_M}{\mu_M \pi \delta} \frac{\sin\left(3h\frac{\Delta\Psi_y}{2}\right)}{h} \sin\left(h\frac{\pi}{2}\right) K_{skew,3h}.$$

The rotor design is the same of Fig. 6.5. The design analysis has been carried out knowing that the harmonic spectrum of the PM flux density without segmentation and slotting effects has also harmonics that are odd multiples of 3 times the poles number.

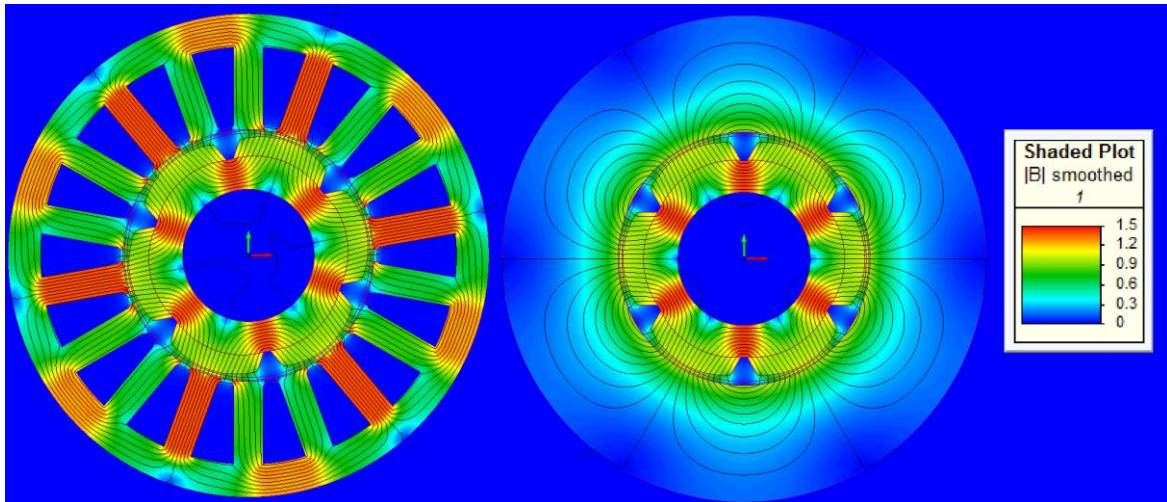


Fig. 6.5 – Permanent magnet flux density with and without slotting effect. FEA view. Machine with and without slots (left and right).

Fig. 6.5 shows the permanent magnet flux view with and without slots (as expected the flux density is different because of the different reluctance of the magnetic circuit, but the analysis is used only to easily filter the slotting related harmonics by the magnet geometry related ones).

Fig. 6.6 and Fig. 6.7 show the waveforms of the radial component of the flux density in the airgap and the relative FFT.

Because the 3rd electrical harmonic of the PM flux is comparable with the 5th and the 7th ones, its effect is taken into account in the analysis of the segmentation geometry performance (mainly for the related torque ripple).

6.2 Machine Control and Winding Design

The machine torque control corresponds to the control of the armature field, which is mainly described by the control of the main harmonic \bar{H}_3 defined by (6.18). To have a constant torque it is needed to maintain the q-axis component of the armature field in the rotor reference frame constant. In a standard control it means to have $|\bar{H}_3|$ constant, and so $|\bar{i}_3|$. If the machine is symmetrically controlled ($\bar{i}_A = \bar{i}_B = \bar{i}_C$), \bar{i}_3 is obtained by (6.16) with $h=3$. In this case, the phase currents can be well represented by the standard three-phase current space vector of one sector by (6.14), below for the sector A, as:

$$\bar{i}_A = \frac{2}{3} (i_{A,U} + i_{A,V} \bar{\alpha} + i_{A,W} \bar{\alpha}^2), \quad \bar{\alpha} = e^{j\frac{2\pi}{3}}. \quad (6.21)$$

Hereafter, the machine is considered with the same current control for each three-phase subsystem ($\bar{i}_A = \bar{i}_B = \bar{i}_C$). Under this assumption, it is easily possible to associate the generic current space vectors with the standard three-phase one.

The connecting relation, substituting (6.15) in (6.16), is:

$$\bar{i}_h = \frac{2}{9} \sum_{p=1}^3 \left(\frac{N_c}{N} \Re\{\bar{i}_A\} - \frac{N_e}{N} \Re\{\bar{i}_A \bar{\alpha}^{-1}\} e^{-jh\Delta\Psi_{slot}} - \frac{N_e}{N} \Re\{\bar{i}_A \bar{\alpha}^{-2}\} e^{jh\Delta\Psi_{slot}} \right) \bar{\alpha}^{h(p-1)}, \quad (6.22)$$

noticing that $\sum_{p=1}^3 \bar{\alpha}^{h(p-1)}$ is always zero for h not multiple of three, otherwise it is equal to 3, (6.22) results as:

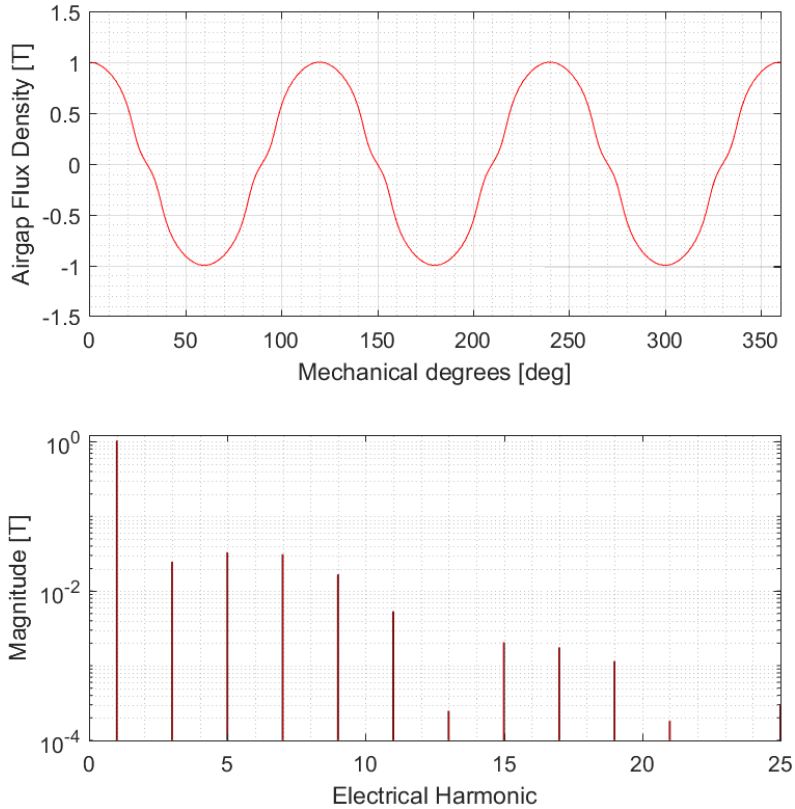


Fig. 6.6 – Permanent magnet flux density without slotting effect.

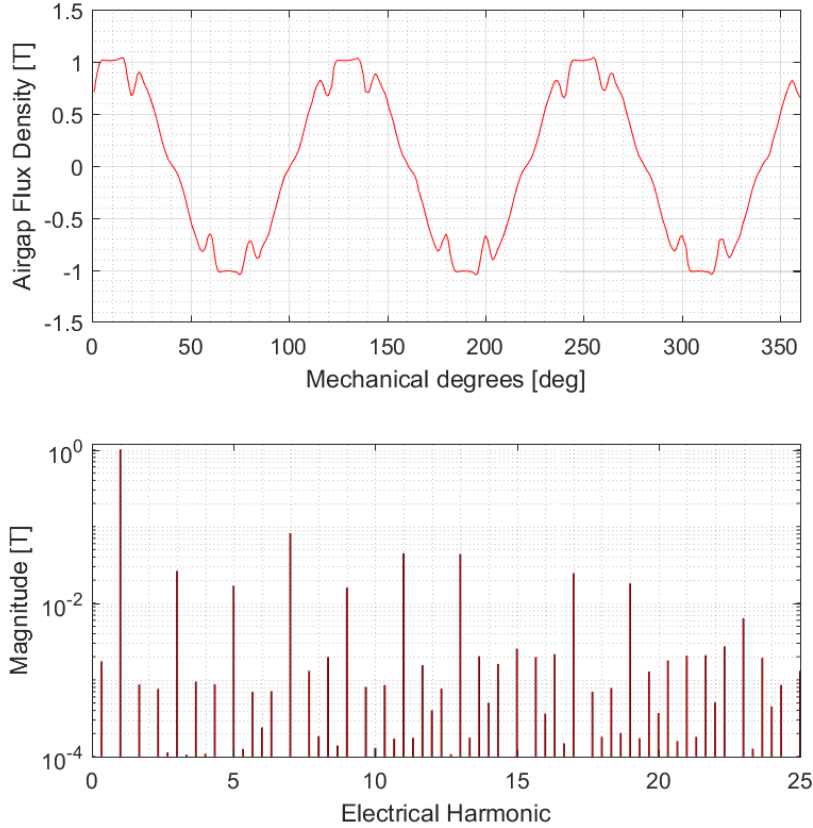


Fig. 6.7 – Permanent magnet flux density with slotting effect.

$$\begin{aligned} \bar{i}_h = & \frac{1}{3} \bar{i}_A \left(\frac{N_c}{N} - \frac{N_e}{N} \bar{\alpha}^{-1} e^{-jh\Delta\Psi_{slot}} - \frac{N_e}{N} \bar{\alpha}^{-2} e^{jh\Delta\Psi_{slot}} \right) + \\ & + \frac{1}{3} \bar{i}_A^* \left(\frac{N_c}{N} - \frac{N_e}{N} \bar{\alpha}^1 e^{-jh\Delta\Psi_{slot}} - \frac{N_e}{N} \bar{\alpha}^2 e^{jh\Delta\Psi_{slot}} \right), \end{aligned} \quad \text{with } h=3k. \quad (6.23)$$

It is worth noticing that in a not segmented design $\Delta\Psi_{slot}$ is equal to $\Delta\Psi_{slot} = \frac{2\pi}{18}$ and $N_c = N_e = N$, therefore, (6.23) is the standard three-phase multi harmonic transformation:

$$\bar{i}_{3k} = \frac{1}{3} \bar{i}_A \left(1 - e^{-j\frac{2\pi}{3}} e^{-jk\frac{2\pi}{6}} - e^{j\frac{2\pi}{3}} e^{jk\frac{2\pi}{6}} \right) + \frac{1}{3} \bar{i}_A^* \left(1 - e^{j\frac{2\pi}{3}} e^{-jk\frac{2\pi}{6}} - e^{-j\frac{2\pi}{3}} e^{jk\frac{2\pi}{6}} \right). \quad (6.24)$$

If k is an odd multiple of 3 (if it is even it does not affect the torque), it results:

$$\bar{i}_{3k} = \frac{1}{3} \bar{i}_A \left(1 + e^{-j\frac{2\pi}{3}} + e^{j\frac{2\pi}{3}} \right) + \frac{1}{3} \bar{i}_A^* \left(1 + e^{j\frac{2\pi}{3}} + e^{-j\frac{2\pi}{3}} \right) = 0. \quad (6.25)$$

If k is a multiple of $3z-1$ with z even (if z is odd the space vector is even and it does not affect the torque), it results:

$$\bar{i}_{3(3z-1)} = \frac{1}{3} \bar{i}_A \left(1 - e^{-j\frac{2\pi}{3}} e^{j\frac{\pi}{3}} - e^{j\frac{2\pi}{3}} e^{-j\frac{\pi}{3}} \right) + \frac{1}{3} \bar{i}_A^* \left(1 - e^{j\frac{2\pi}{3}} e^{j\frac{\pi}{3}} - e^{-j\frac{2\pi}{3}} e^{-j\frac{\pi}{3}} \right) = \bar{i}_A^*. \quad (6.26)$$

If k is a multiple of $3z+1$ with z even (if z is odd the space vector is even and it does not affect the torque), it results:

$$\bar{i}_{3(3z+1)} = \frac{1}{3} \bar{i}_A \left(1 - e^{-j\frac{2\pi}{3}} e^{-j\frac{\pi}{3}} - e^{j\frac{2\pi}{3}} e^{j\frac{\pi}{3}} \right) + \frac{1}{3} \bar{i}_A^* \left(1 - e^{j\frac{2\pi}{3}} e^{-j\frac{\pi}{3}} - e^{-j\frac{2\pi}{3}} e^{j\frac{\pi}{3}} \right) = \bar{i}_A. \quad (6.27)$$

Instead, if there is a segmentation (6.23) can be just rewritten introducing:

$$\Delta\Psi_{slot} = \frac{2\pi}{18} - \frac{\Delta\Psi_{es} + \Delta\Psi_{cs}}{6},$$

as:

$$\begin{aligned} \bar{i}_{3h} = & \frac{1}{3} \bar{i}_A \left(\frac{N_c}{N} - \frac{N_e}{N} e^{-j\frac{2\pi}{3}} e^{-jh\frac{2\pi}{6}} e^{jh\frac{\Delta\Psi_{es} + \Delta\Psi_{cs}}{2}} - \frac{N_e}{N} e^{j\frac{2\pi}{3}} e^{jh\frac{2\pi}{6}} e^{-jh\frac{\Delta\Psi_{es} + \Delta\Psi_{cs}}{2}} \right) + \\ & + \frac{1}{3} \bar{i}_A^* \left(\frac{N_c}{N} - \frac{N_e}{N} e^{j\frac{2\pi}{3}} e^{-jh\frac{2\pi}{6}} e^{jh\frac{\Delta\Psi_{es} + \Delta\Psi_{cs}}{2}} - \frac{N_e}{N} e^{-j\frac{2\pi}{3}} e^{jh\frac{2\pi}{6}} e^{-jh\frac{\Delta\Psi_{es} + \Delta\Psi_{cs}}{2}} \right). \end{aligned} \quad (6.28)$$

Realising that $e^{jh\frac{2\pi}{6}} = -e^{-jh\frac{2\pi}{3}}$ if h is odd (the even harmonics generate only iron losses):

$$\begin{aligned} \bar{i}_{3h} = & \frac{1}{3} \bar{i}_A \left(\frac{N_c}{N} + \frac{N_e}{N} e^{j(h-1)\frac{2\pi}{3}} e^{jh\frac{\Delta\Psi_{es}+\Delta\Psi_{cs}}{2}} + \frac{N_e}{N} e^{-j(h-1)\frac{2\pi}{3}} e^{-jh\frac{\Delta\Psi_{es}+\Delta\Psi_{cs}}{2}} \right) + \\ & + \frac{1}{3} \bar{i}_A^* \left(\frac{N_c}{N} + \frac{N_e}{N} e^{j(h+1)\frac{2\pi}{3}} e^{jh\frac{\Delta\Psi_{es}+\Delta\Psi_{cs}}{2}} + \frac{N_e}{N} e^{-j(h+1)\frac{2\pi}{3}} e^{-jh\frac{\Delta\Psi_{es}+\Delta\Psi_{cs}}{2}} \right). \end{aligned} \quad (6.29)$$

It is useful to introduce the new segmentation parameter:

$$\bar{\beta} = e^{j\frac{\Delta\Psi_{es}+\Delta\Psi_{cs}}{2}}.$$

With the $\bar{\beta}$ parameter, the space vector equation for the field harmonics odd and multiple of the pole pairs number is:

$$\begin{aligned} \bar{i}_{3h} = & \frac{1}{3} \bar{i}_A \left(\frac{N_c}{N} + \frac{N_e}{N} \bar{\alpha}^{(h-1)} \bar{\beta}^h + \frac{N_e}{N} \bar{\alpha}^{-(h-1)} \bar{\beta}^{-h} \right) + \\ & + \frac{1}{3} \bar{i}_A^* \left(\frac{N_c}{N} + \frac{N_e}{N} \bar{\alpha}^{(h+1)} \bar{\beta}^h + \frac{N_e}{N} \bar{\alpha}^{-(h+1)} \bar{\beta}^{-h} \right). \end{aligned} \quad (6.30)$$

Analysing (6.30) it is worth noticing that there are two ways to have a rotating main current space vector $|\bar{i}_3|$ constant: design the phase windings with a different number of turns per phase; maintain the standard winding design and change the control algorithm in order to have the same vector magnitude $|\bar{i}_3|$ for whatever position of the space vector trajectory.

Torque Ripples in Segmented Machines

In a standard machine control, at steady state conditions, the trajectory of the three-phase space vectors \bar{i}_A ($\bar{i}_A = \bar{i}_B = \bar{i}_C$) is a circumference followed at constant speed, as:

$$\bar{i}_A = j \frac{T_{ref}}{K_{T,3}} e^{j3\theta_m}. \quad (6.31)$$

The resulting overall machine space vectors become:

$$\begin{aligned} \bar{i}_{3h} = & j \frac{T_{ref}}{K_{T,3}} \frac{1}{3} \left(\frac{N_c}{N} + \frac{N_e}{N} \bar{\alpha}^{(h-1)} \bar{\beta}^h + \frac{N_e}{N} \bar{\alpha}^{-(h-1)} \bar{\beta}^{-h} \right) e^{j3\theta_m} + \\ & - j \frac{T_{ref}}{K_{T,3}} \frac{1}{3} \left(\frac{N_c}{N} + \frac{N_e}{N} \bar{\alpha}^{(h+1)} \bar{\beta}^h + \frac{N_e}{N} \bar{\alpha}^{-(h+1)} \bar{\beta}^{-h} \right) e^{-j3\theta_m}. \end{aligned} \quad (6.32)$$

The main one result as:

$$\begin{aligned} \bar{i}_3 = & j \frac{T_{ref}}{K_{T,3}} \frac{1}{3} \left(\frac{N_c}{N} + \frac{N_e}{N} \bar{\beta} + \frac{N_e}{N} \bar{\beta}^{-1} \right) e^{j3\theta_m} + \\ & - j \frac{T_{ref}}{K_{T,3}} \frac{1}{3} \left(\frac{N_c}{N} + \frac{N_e}{N} \bar{\alpha}^2 \bar{\beta} + \frac{N_e}{N} \bar{\alpha} \bar{\beta}^{-1} \right) e^{-j3\theta_m}. \end{aligned} \quad (6.33)$$

Therefore, the main current vector in the rotor reference frame ($\bar{i}_3 e^{-j3\theta_m}$) has a reduced direct sequence and presents an inverse sequence. The main current vector can be described as:

$$\bar{i}_3 e^{-j3\theta_m} = \bar{i}_3^+ + \bar{i}_3^- e^{-j6\theta_m}, \quad (6.34)$$

with the direct sequence:

$$\bar{i}_3^+ = j \frac{T_{ref}}{K_{T,3}} \frac{1}{3} \left(\frac{N_c}{N} + \frac{N_e}{N} \bar{\beta} + \frac{N_e}{N} \bar{\beta}^{-1} \right), \quad (6.35)$$

and the inverse sequence:

$$\bar{i}_3^- = -j \frac{T_{ref}}{K_{T,3}} \frac{1}{3} \left(\frac{N_c}{N} + \frac{N_e}{N} \bar{\alpha}^2 \bar{\beta} + \frac{N_e}{N} \bar{\alpha} \bar{\beta}^{-1} \right). \quad (6.36)$$

The resulting main torque contribution results by (6.20) as:

$$T = \frac{T_{ref}}{3} \left(\frac{N_c}{N} + \frac{N_e}{N} \bar{\beta}^{-1} + \frac{N_e}{N} \bar{\beta} \right) - \frac{T_{ref}}{3} \left(\frac{N_c}{N} + \frac{N_e}{N} \bar{\alpha}^1 \bar{\beta}^{-1} + \frac{N_e}{N} \bar{\alpha}^2 \bar{\beta} \right) \cos(6\theta_m). \quad (6.37)$$

Therefore, the segmented design has a reduced torque constant and the standard control generates a torque ripple at six times the rotor frequency (twice the electrical frequency, $f_e = f_m / p$).

The average torque can be increased by a higher value of the phase current. Instead, in order to avoid a huge torque ripple, the second term of (6.37) must be minimised (ideally controlled as zero). In order to obtain this result, in the following section are proposed two techniques that aim to:

- maintain a standard machine control (with the three-phase current space vector having constant steady state magnitude) and compensate the magnetomotive force distribution by a different turn number in the central phase of each sector ($N_c \neq N_e$);
- control the phase currents imposing a control of the overall machine (direct flux control by setting the reference \bar{i}_3 and by it defining the reference three-phase current vectors $\bar{i}_A = \bar{i}_B = \bar{i}_C$).

New Winding Design for Standard Current Control

If a standard three-phase control is used, the steady state torque of a segmented machine is no more constant. Indeed, there is a torque ripple at twice the electrical frequency ($f_e = f_m / p$), related to the second term of (6.37), or as well related to (6.36). However, the ripple can be eliminated by choosing a proper number of turns in the central phase of each sector compared with the turns of the external phases. Indeed, (6.36) is always zero if the following turn number relationship is satisfied:

$$\frac{N_c}{N_e} = -\bar{\alpha}^2 \bar{\beta} - \bar{\alpha} \bar{\beta}^{-1} = -e^{-j\frac{2\pi}{3}} e^{j\frac{\Delta\Psi_{es} + \Delta\Psi_{cs}}{2}} - e^{j\frac{2\pi}{3}} e^{-j\frac{\Delta\Psi_{es} + \Delta\Psi_{cs}}{2}} = -2 \cos\left(\frac{2\pi}{3} - \frac{\Delta\Psi_{es} + \Delta\Psi_{cs}}{2}\right). \quad (6.38)$$

It is interesting to note that (6.38) must be positive and both N_c and N_e must be integer in order to define a feasible winding design. Therefore, the following constraint on the segmentation angles must be verified:

$$\frac{\pi}{2} \leq \frac{2\pi}{3} - \frac{\Delta\Psi_{es} + \Delta\Psi_{cs}}{2} \leq \frac{2\pi}{3}, \quad (6.39)$$

resulting in:

$$0 \leq \Delta\Psi_{es} + \Delta\Psi_{cs} \leq \frac{\pi}{3}, \quad (6.40)$$

while the physical constraint would be:

$$0 \leq \Delta\Psi_{es} + \Delta\Psi_{cs} \leq \frac{2\pi}{3}.$$

Therefore, if the total segmentation is in a range:

$$\frac{\pi}{3} \leq \Delta\Psi_{es} + \Delta\Psi_{cs} \leq \frac{2\pi}{3},$$

it is impossible to define a turn number that allows avoiding the torque ripple defined by the second term of (6.37). However, such a big segmentation would also significantly reduce the average torque described by the first term of (6.37), or in other words, the current control would demand huge reference currents.

Having a winding design with a turn number in agreement with the relationship (6.38) allows defining the reference phase currents as in a standard three-phase machine (or as a standard triple three-phase sector machine as well). However, the control technique is not immediate when this winding solution is used. Indeed, the resistances and the back electromotive forces (for both the magnet flux and the armature one) are not symmetrical in each sector phases. Therefore, there is an inverse voltage sequence request in the machine control, and it is necessary to have an additional regulator to maintain a zero inverse current sequence. This

problem has already been deeply analysed in literature for other control techniques [2, 3], and has been deeply explained in Chapter 3.

Segmented Machine Control Technique for Standard Windings Designs

If the machine is designed with a standard winding layout, a new control technique is needed to have a constant steady state torque (at least for the main torque contribution). The proposed control technique is based on the relationship between the main current space vector \bar{i}_3 and the three-phase one \bar{i}_A , obtained by (6.30) with $h=1$ and its conjugate as:

$$\bar{i}_A^* = \frac{3\bar{i}_3^*}{(1+\bar{\beta}^{-1}+\bar{\beta})} - \bar{i}_A \frac{(1+\bar{\alpha}\bar{\beta}^{-h}+\bar{\alpha}^{-1}\bar{\beta})}{(1+\bar{\beta}^{-1}+\bar{\beta})}, \quad (6.41)$$

and by (6.30) with $h=1$:

$$\bar{i}_A = \frac{3(1+\bar{\beta}^{-1}+\bar{\beta})\bar{i}_3 - 3(1+\bar{\alpha}^{-1}\bar{\beta} + \bar{\alpha}\bar{\beta}^{-1})\bar{i}_3^*}{(1+\bar{\beta} + \bar{\beta}^{-1})^2 - (1+\bar{\alpha}^{-1}\bar{\beta} + \bar{\alpha}\bar{\beta}^{-1})(1+\bar{\alpha}\bar{\beta}^{-h} + \bar{\alpha}^{-1}\bar{\beta})}. \quad (6.42)$$

Therefore, for a given main vector \bar{i}_3 controlled as:

$$\bar{i}_3 = j \frac{T_{ref}}{K_{T,3}} e^{j3\theta_m},$$

the current space vector of each three-phase subsystem $\bar{i}_A = \bar{i}_B = \bar{i}_C$ must be controlled with a direct and inverse sequence as:

$$\bar{i}_A = \bar{i}_{A,dir} + \bar{i}_{A,inv}, \quad (6.43)$$

with:

$$\bar{i}_{A,dir} = j \frac{T_{ref}}{K_{T,3}} \frac{3(1+\bar{\beta}^{-1}+\bar{\beta})}{(1+\bar{\beta} + \bar{\beta}^{-1})^2 - (1+\bar{\alpha}^{-1}\bar{\beta} + \bar{\alpha}\bar{\beta}^{-1})(1+\bar{\alpha}\bar{\beta}^{-h} + \bar{\alpha}^{-1}\bar{\beta})} e^{j3\theta_m}, \quad (6.44)$$

and:

$$\bar{i}_{A,inv} = -j \frac{T_{ref}}{K_{T,3}} \frac{-3(1+\bar{\alpha}^{-1}\bar{\beta} + \bar{\alpha}\bar{\beta}^{-1})}{(1+\bar{\beta} + \bar{\beta}^{-1})^2 - (1+\bar{\alpha}^{-1}\bar{\beta} + \bar{\alpha}\bar{\beta}^{-1})(1+\bar{\alpha}\bar{\beta}^{-h} + \bar{\alpha}^{-1}\bar{\beta})} e^{-j3\theta_m}. \quad (6.45)$$

It results that the control of a segmented machine design needs a direct and inverse current PI regulator as in case of a layout with a different turn number in order to make the resulting \bar{i}_3 vector move on a circumference at constant speed (to generate a constant torque). If this happens, $\bar{i}_A = \bar{i}_B = \bar{i}_C$ are vectors moving on elliptical trajectories.

Fig. 6.8 shows the machine control scheme of a segmented triple three-phase machine, highlighting the necessity of having twice the current regulators for having zero steady state error related to the inverse current or voltage sequences.

6.3 Coil Pitch, End Effect and Cogging Torque in Segmented Sectored Machines

Because the stator segmentation changes the coil pitch, this parameter can be exploited to reduce the most relevant armature fields. On the other hand, this causes an asymmetry in the stator geometry that introduces a torque ripple that can be seen as a machine end effect. This section presents these phenomena in order to show how deal with them.

Coil Pitch

Fig. 6.9 shows the effect of the coil pitch on the armature flux density when only the external segmentation $\Delta\Psi_{es}$ is changed (all the physical range is analysed, $0 \leq \Delta\Psi_{es} \leq \frac{2\pi}{3}$), while the internal segmentation $\Delta\Psi_{cs}$ is zero. The same result is obtained if only the central segmentation is changed maintaining the external segmentation to zero. The reference torque is the same (to be more precise, the main current vector is constant and equal to $\vec{i}_3^+ = j10$ A) and the main torque ripple is compensated by the current control ($\vec{i}_3^- = 0$). The parameters of the analysed unsegmented machine are the one in Table 6.1.

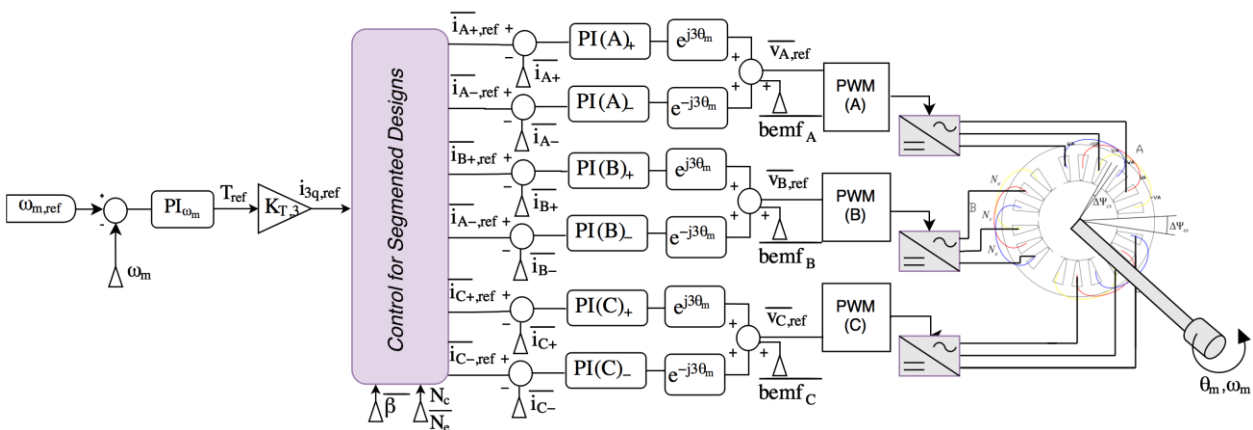


Fig. 6.8 – Control scheme of a triple three-phase segmented machine design.

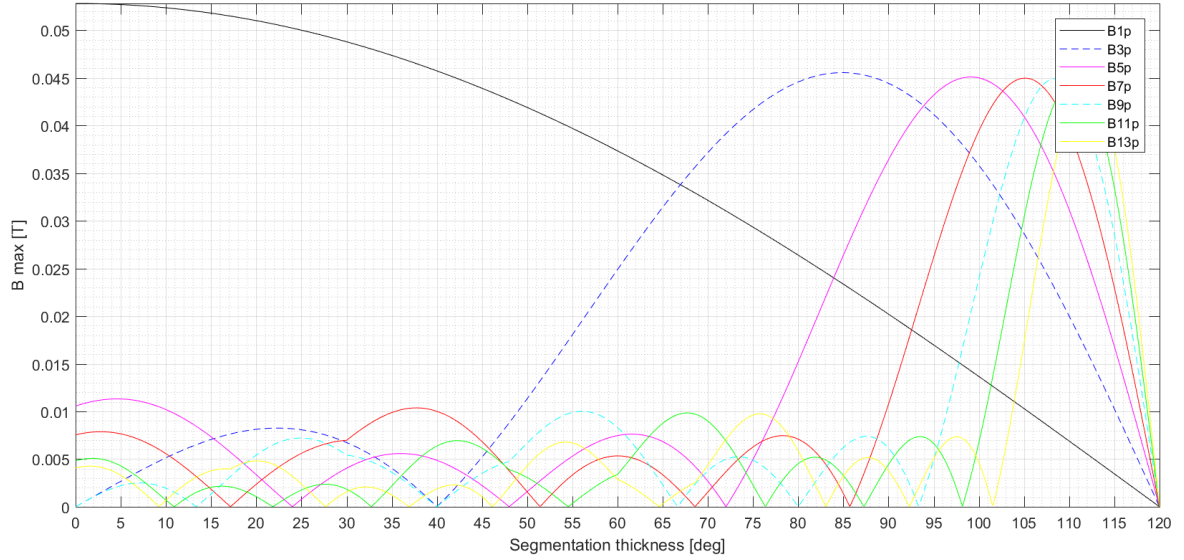


Fig. 6.9 – Coil pitch effect as function of the external (or internal) segmentation thickness.

Table 6.1 - Main machine parameters of SDA design

Parameter	Value
Pole number ($2p$)	6
PM material	NdFeB
Power rating	1.5 [kW]
Rated Speed (ω_m)	3000 [rpm]
Rated torque (T_{rated})	5 [Nm]
Turn/coil	22
Phase resistance (R_s)	0.0808 [Ohm]
Torque constant (K_T)	0.434 [Nm/A]
Space 2 force constant (K_{F2})	9.60 [N/A]
Space 4 force constant (K_{F2})	17.85 [N/A]
Outer Stator diameter	95 [mm]
Inner Stator diameter	49.5 [mm]
Axial length	90 [mm]
Airgap length	1 [mm]
Magnets thickness	4 [mm]

As shown in Fig. 6.9, it is possible to completely eliminate the 5th or the 7th harmonic and the related torque ripples. It must be noticed that a higher segmentation causes a lower main harmonic field and a reduction of the slot areas, so it is preferable to find a solution with a small thickness. Furthermore, the segmentation thickness increases the 3rd harmonic produced by the armature field. Therefore, the analysis of the pitch shortening must consider also the electrical harmonics multiple of three ($3p$), as already discussed.

Fig. 6.10 shows the effect of the coil pitch on the armature flux density when both the central and the external segmentation $\Delta\Psi_{cs}$ and $\Delta\Psi_{es}$ are equally changed (all the physical range is analysed, $0 \leq \Delta\Psi_{es} + \Delta\Psi_{cs} \leq \frac{2\pi}{3}$).

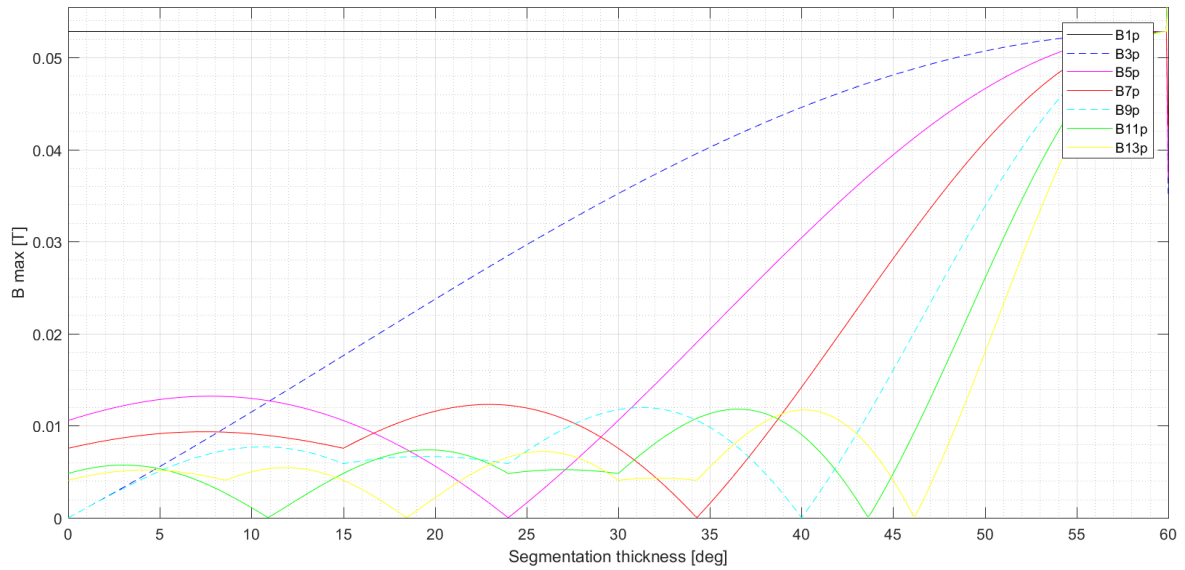


Fig. 6.10 – Coil pitch effect as function of the segmentation thickness. The internal and external segmentation thicknesses are equally increased of the angle shown in the x-axis.

By observing Fig. 6.9 and Fig. 6.10, having both an internal and external segmentation does not significantly help to reduce the higher armature field harmonics. This result makes the exploitation of an internal segmentation not significantly useful for the machine design. Indeed, $\Delta\Psi_{cs}$ affect the harmonic reduction as $\Delta\Psi_{es}$, but it results in reducing the distance between windings of different sectors. Instead, increasing $\Delta\Psi_{es}$ makes the sector phases being located in isolated areas around the stator circumference, improving the sectors decoupling. Because of these observations, the $\Delta\Psi_{cs}$ parameter is no more considered hereafter.

It is interesting to note that in order to generate the reference main vector ($\bar{i}_3^+ = j10$), the needed phase currents increase with the segmentation thickness. The overall thickness values higher than 60 degrees (30 degrees in Fig. 6.10) result in huge required currents. Furthermore, the segmentation reduces the available slots area significantly increasing the current density. Therefore, the analysis focuses on angle up to 30 degrees (15 degrees in Fig. 6.10).

End Effect and Cogging Torque

It is well known that to deal with the end effect in the linear machine design is possible to shape the end geometries by Finite Element Analysis (FEA) and optimization algorithms. Similar solutions can be adopted for the segmented motor design, but with the difference that the machine is still a rotary one. The segmentation end effect depends on the segmentation thickness, and even more on the segmentation material. FEA analysis has been performed to analyse the different design solutions.

On the other hand, an alternative solution has been deduced on the idea of having the smallest polar stator symmetry. It means that it is possible to design a segmented machine adding some

empty slots (without flowing currents) in the gap between two sectors (as in SDf with one added slot between the sectors). This solution allows having a symmetrical stator geometry and, in this way, the torque ripple can be analysed as a cogging torque. This concept comes from the fractional number of slots per pole and per phase machines, where the cogging torque is reduced and its frequency is increased. For the analysed segmented machine, there are two interesting solutions: the 21 slots and the 24 slots. Because of the already described drawbacks of a larger segmentation thickness, the 24 slots design has been discarded.

The mechanical cogging torque frequency in a $2p$ -poles N_s -slots machine, rotating at mechanical frequency f_m , is

$$f_{cogging} = lcm(2p, N_{slots})f_m, \quad (6.46)$$

where lcm is the least common multiple. The relative electrical frequency is $f_{cogging,el} = f_{cogging} / p$. In the analysed machine design, the first solution (adding 1 empty slots between each sector pair) is the one with 21 slots (SDf). The relative cogging torque frequency is $42 f_m$, and it is a lucky design solution, because it corresponds to a segmentation thickness of about 17 degrees. This means, from the analysis shown in Fig. 6.9, that the 7th harmonic armature field is deleted. Because of the high number of possible designs, only the SDb, SDc and SDf layouts (Fig. 6.1) results are presented hereafter. All of them have a segmentation with $\Delta\Psi_{es}$ of about 17 degrees.

6.4 FEA Simulation Results

The analytical and theoretical results have been verified by FEA in Magnet™ (Infolytica). The SDA machine main data are reported in Table 6.1.

Performance - Healthy Machine Behaviour

The torque performance analysis is carried out at about rated current (10 A peak), and in all the following figures the FFT spectra are translated from the SDA FFT spectra (SDa is the design with zero segmentation thickness) for a good comparison between the designs.

Armature Field

The decision of the segmentation thickness has been carried out to delete some harmonic fields in the air-gap, as discussed in Section 6.3. With 10 A peak current and a standard machine control ($\vec{i}_A = \vec{i}_B = \vec{i}_C$ moving on a circular trajectory at constant speed), the armature flux in the

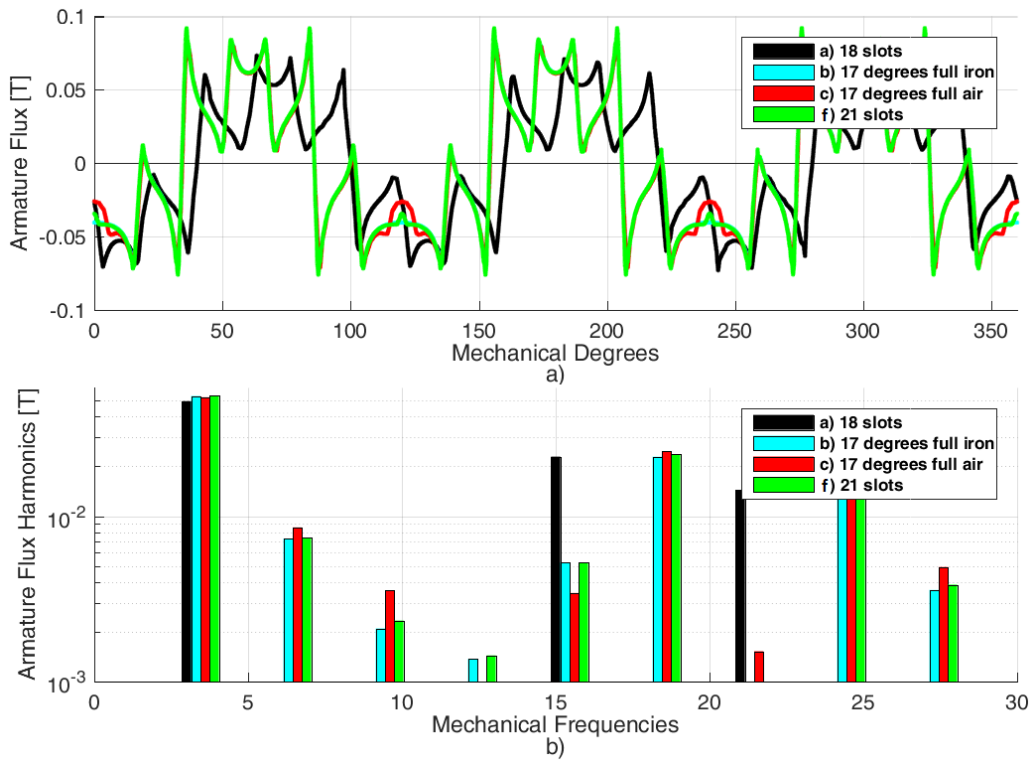


Fig. 6.11 – Coil pitch effect caused by an external segmentation of 17 degrees. Maximum values.

SDa-SDc and SDF designs is as in Fig. 6.11 and Fig. 6.12. The difference between the two figures is that in Fig. 6.11 there are the maximum values obtained when the machine is in the configuration of maximum magnitude of the \vec{i}_3 current space vector (\vec{i}_3 moves on an elliptic trajectory). Instead, in Fig. 6.12 the main vector \vec{i}_3 has its minimum value. The magnitude of \vec{i}_3

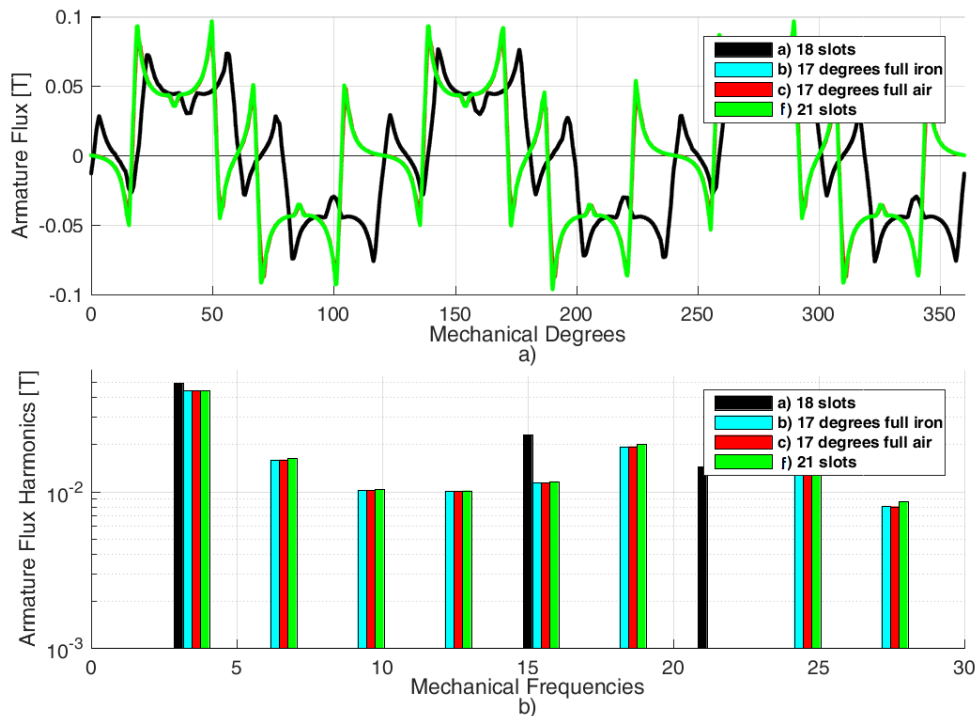


Fig. 6.12 – Coil pitch effect caused by an external segmentation of 17 degrees. Minimum values.

directly affects the magnitude of the armature field \bar{H}_3 (or the flux density \bar{B}_3 as well). Half the difference between the minimum and the maximum value of each flux density harmonic is the inverse sequence of that harmonic, while the average of the two values is the magnitude of the direct sequence. In order to compare the FEA results with the analytical, Fig. 6.13 shows the analytical result, where the negative values are related to the minimum values of the flux density magnitude for a better understanding. The result obtained for a 17 degrees segmentation is highlighted with a vertical red line. There is a good qualitative match with the expected magnitudes given by Fig. 6.11 and Fig. 6.12. The even harmonics multiple of p ($p=3$) are not presented in Fig. 6.13 because they do not affect the torque, while in Fig. 6.11 and Fig. 6.12 they are maintained for highlighting that they exist and they should be considered in the analysis of the iron losses. Instead, they do not affect the torque and neither the radial force (the resulting radial force is always zero in a standard machine control also in case of segmentation).

As predicted by (6.16) and (6.18), the 21st (7th electrical) armature field is almost eliminated in all the new designs and the 15th (5th electrical) is significantly reduced. The 9th (3rd electrical) harmonic is significantly increased by the segmentation, but this is almost inevitable in a segmented design. Other interesting solutions can be founded at about 24 segmentation degrees (the 7th harmonic is eliminated) or at 40 degrees (the 3rd harmonic is eliminated).

However, as already mentioned increasing the segmentation angle reduces the main harmonic, and it affects the machine slot current density caused by the reduction of the available area for the slots. Therefore, in order to avoid a significant reduction of the performance, the 17 degrees segmentation seems a suitable solution for a triple three-phase segmented machine.

The new control technique aims to eliminate the inverse sequence of the main current vector \bar{i}_3 in order to minimise the related torque ripple. Fig. 6.14 shows the analytical effect on the flux harmonics generated by the proposed control. The resulting main harmonic has no more the inverse sequence (the minimum and maximum values are the same). The effect on the other flux harmonics is just a result of the current control and is inevitable.

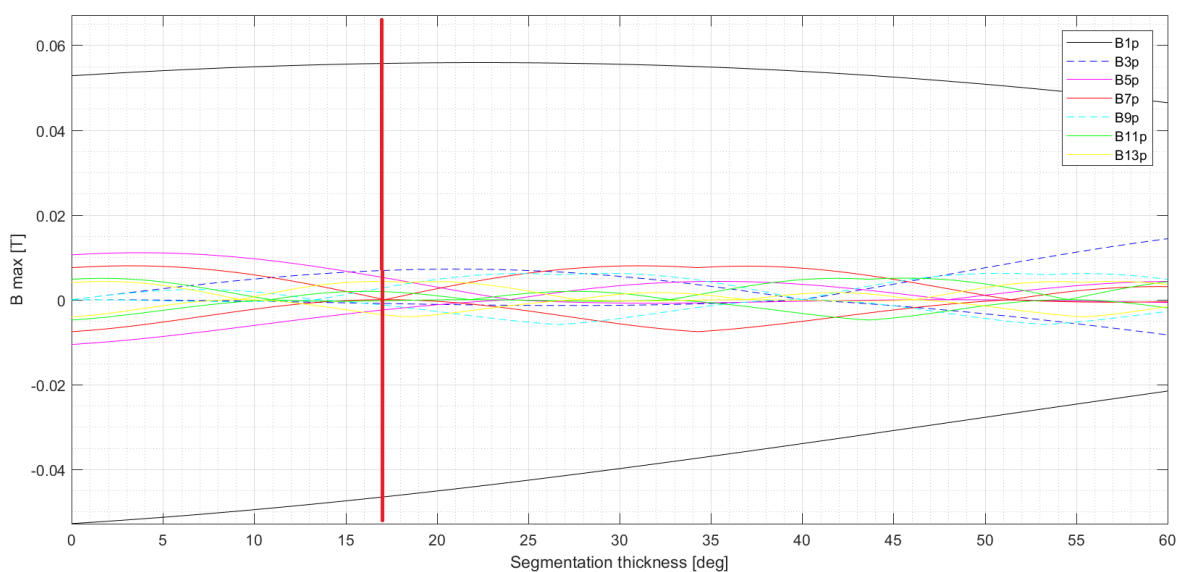


Fig. 6.13 – Coil pitch effect as function of the external segmentation thickness with standard machine control. Maximum flux harmonic values (positive) and minimum flux harmonic values (negative).

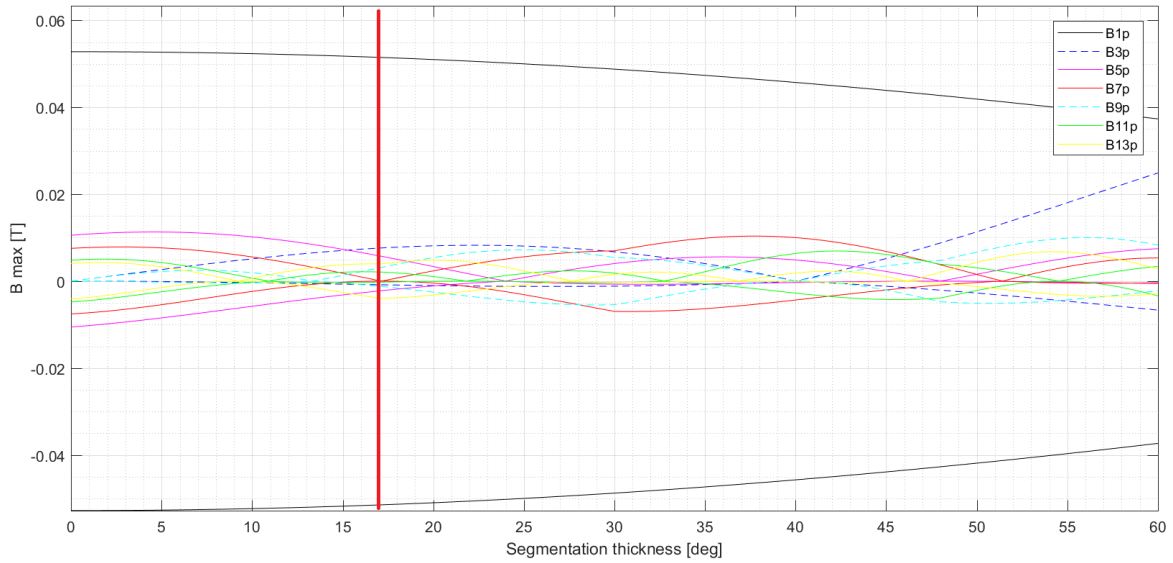


Fig. 6.14 – Coil pitch effect as function of the external segmentation thickness with proposed machine control. Maximum flux harmonic values (positive) and minimum flux harmonic values (negative).

Cogging Torque

Fig. 6.15 shows a comparison between the cogging torques of the investigated designs.

As predicted by (6.46), the cogging torque main harmonic is at $18 f_m$ and $42 f_m$ for the SDa and SDf designs respectively, with a reduced amplitude for the SDf one. Instead, the cogging torque of the SDb and SDc designs is significantly worse. This is because for both there is a stator

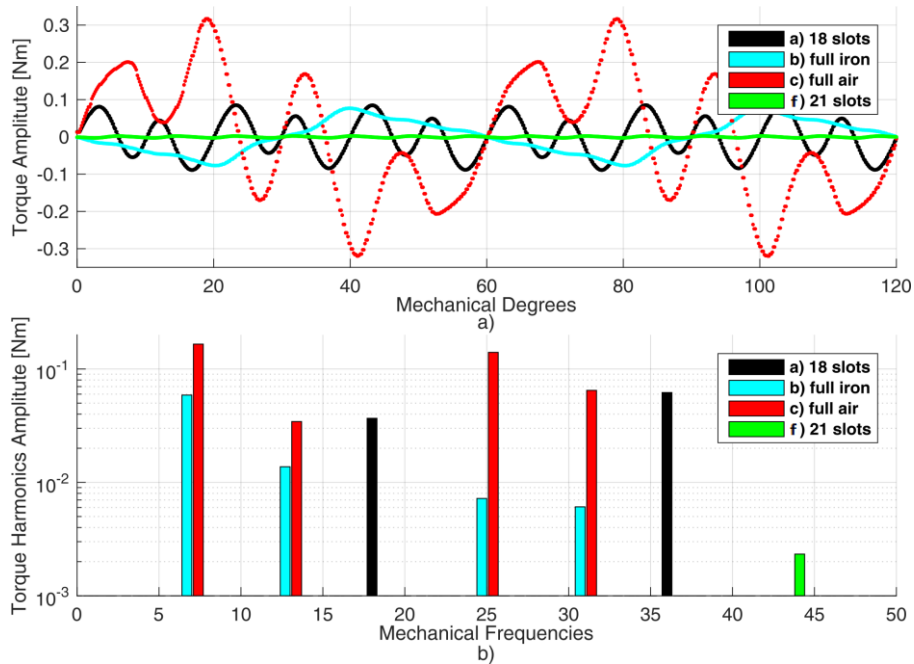


Fig. 6.15 – Cogging Torque (no load torque).

reluctance with periodicity $2p$ ($2p=6$). Therefore, (6.46) results in an additional cogging effect (if it can still called like this) that generates a ripple with the lowest frequency at $6 f_m$.

Fig. 6.16 shows the flux views varying the thickness of the air gap in the segmented design. Moving from a SDb design (full iron) to a SDc one (full air) the end effect of the segmentation changes in terms of related cogging torque, and iron saturation. Even an intermediate design is significantly different from the SDb one. Indeed, the interruption of the back iron generates an important reluctance effect in the magnetic circuit.

Torque – New Control Technique

Fig. 6.17 shows the torque with a standard machine control. From the spectra in Fig. 6.17, it is possible noticing a huge increase of the torque ripple at $6 f_m$ ($2 f_{el}$) at on load conditions.

To overcome this ripple, the new control described by (6.44) and (6.45) is applied. Fig. 6.18 shows the resulting torque. The inverse field of the main harmonic is almost deleted with the new control (with worst results for the SDc design). This control allows having comparable torque performance between the SDb, SDb and SDb designs. It is important to notice that the torque ripple at $6 f_m$ ($2 f_{el}$) is also related to the presence of the 3rd electrical flux harmonic. Indeed, the 3rd harmonic interacts with the permanent magnets generating a torque ripple at $6 f_m$ and another at $12 f_m$ having an inverse sequence with almost the same magnitude of the direct one. part of the ripple at $12 f_m$ is also generated by the 5th harmonic direct sequence, while the ripple at $18 f_m$ is only generated by the 5th harmonic inverse sequence (here it is named

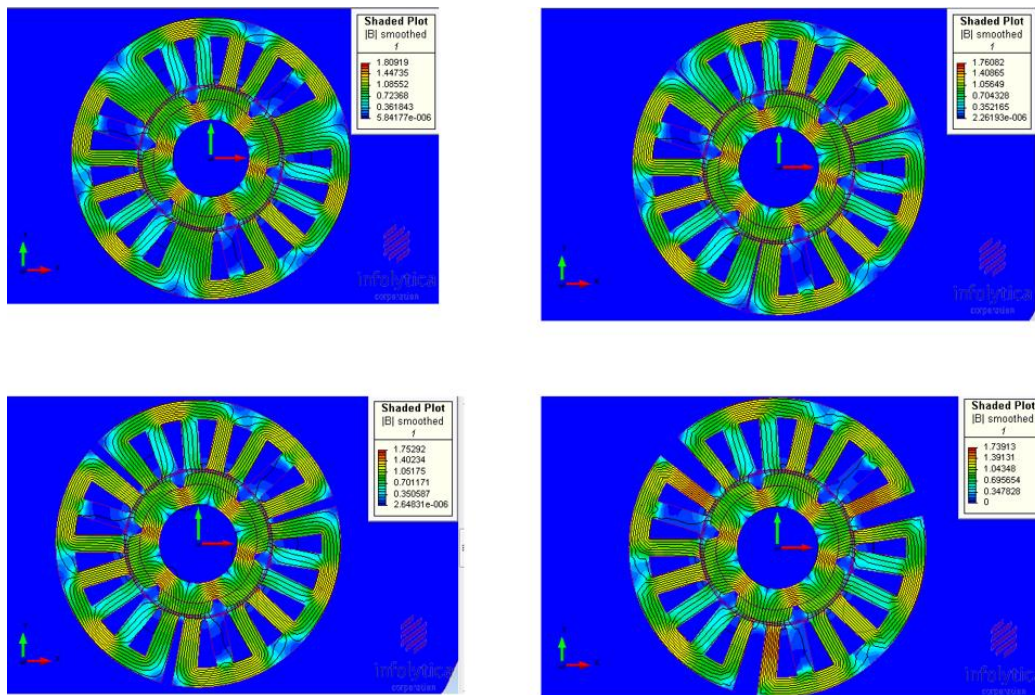


Fig. 6.16 – Flux view depending on the segmented area design moving from an SDb to an SDc design typology.

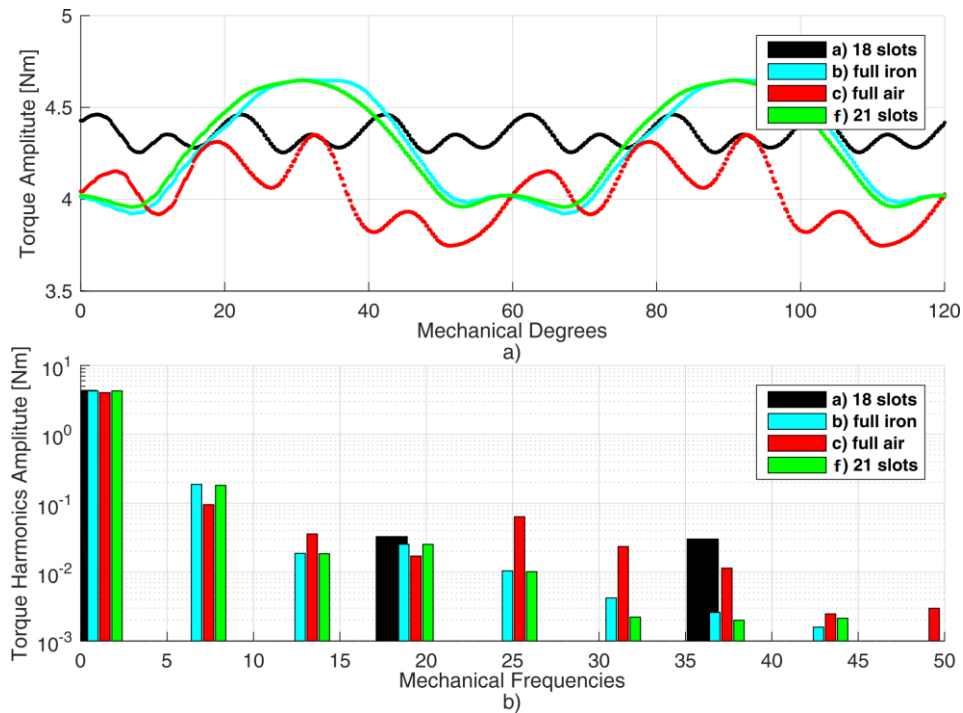


Fig. 6.17 – Torque with 10 A peak current and standard machine control.

inverse sequence the one that appears in all the three-phase machines also without segmentation) because the 7th harmonic is eliminated by the phase pitch shortening. Furthermore, for the SDb and even more for the SDc designs, the segmentation cogging torque acts generating torque ripples at the same frequencies (6, 18, ... f_m). Therefore, the new control technique might be adapted in order to completely eliminate the ripple at $6f_m$ ($2f_{el}$) by a FEA

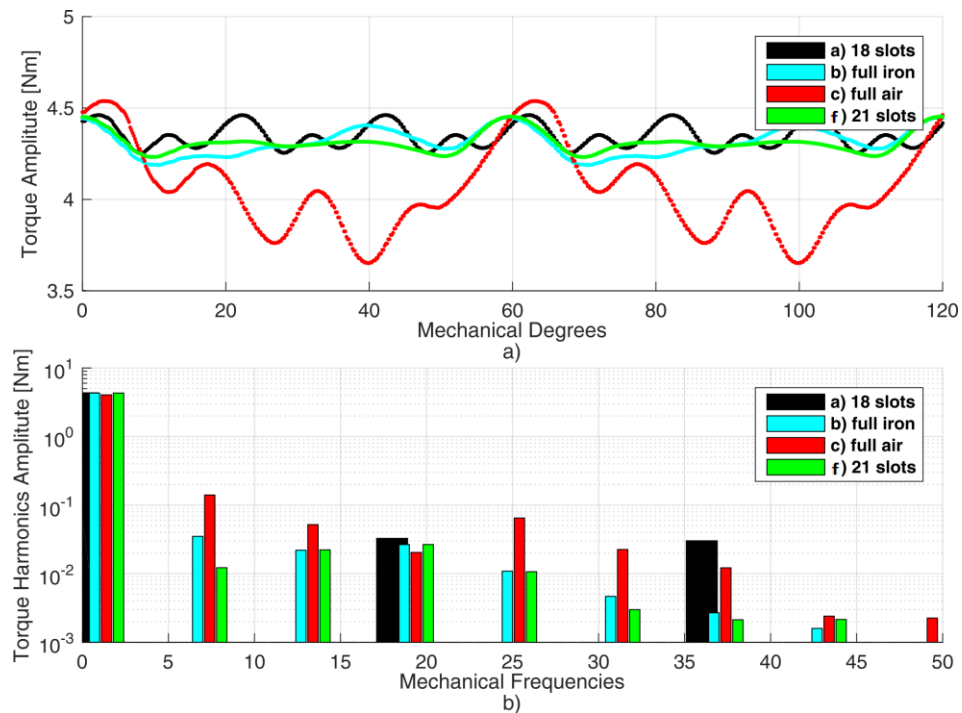


Fig. 6.18 – Torque with 10 A magnitude of the main current space vector (3rd) and new machine control.

approach to consider of all these additional effects. However, the advantages of the new control already help to improve significantly the torque performance of the machine as in Fig. 6.18.

Table 6.2 summarizes the different design performance with the new control technique. The same slot fill factor used to simulate the different designs explains the higher phase resistance and Joule losses values.

SDd Torque – New Winding Design

As mentioned in Section 6.2, it is possible to use a standard current control (in terms of definition of the reference phase currents) by means of a suitable winging layout. In particular, (6.38) defines the ratio of the turns between the central and external phases which allows minimising the torque ripple related to the inverse sequence of the main field harmonic.

The SDf machine is the one with better performance (especially at no load). Therefore, Fig. 6.19 shows the results of the new winding solution with different turns in the different phases only for the SDf design. In this case, the central windings have 16 turns rather than 22. As can be seen from Fig. 6.19, the new winding solution defined by (6.38) results in having almost the same performance of the new control technique in terms of resulting torque. The difference is just related to the approximation owing to the fact that the turn number must be an integer.

It is clear that whatever is the technique used to reduce the main torque ripple, the advantage makes the machine behave in a significantly different way. Indeed, the new control allows reducing the main torque ripple of about 20 times (from about 5% to about 0.25%). The machine torque performance with the new control algorithm becomes comparable with the ones of the original SDa design. Instead, the new design shows significantly better no load performance.

Table 6.2 – Performance with 10 A magnitude of the main current space vector (3rd) with new control technique.

	Sda	SDb	SDc	SDd
Torque [Nm]	4.35	4.31	4.06	4.31
Torque ripple (pp) [Nm]	0.21	0.26	0.89	0.22
R phase [Ohm]	0.08	0.11	0.11	0.11
PJ Copper mean [W]	36.00	51.48	51.48	51.48
I max [A]	10.00	10.65	10.65	10.65
V max [V]	30.31	32.09	30.55	31.82

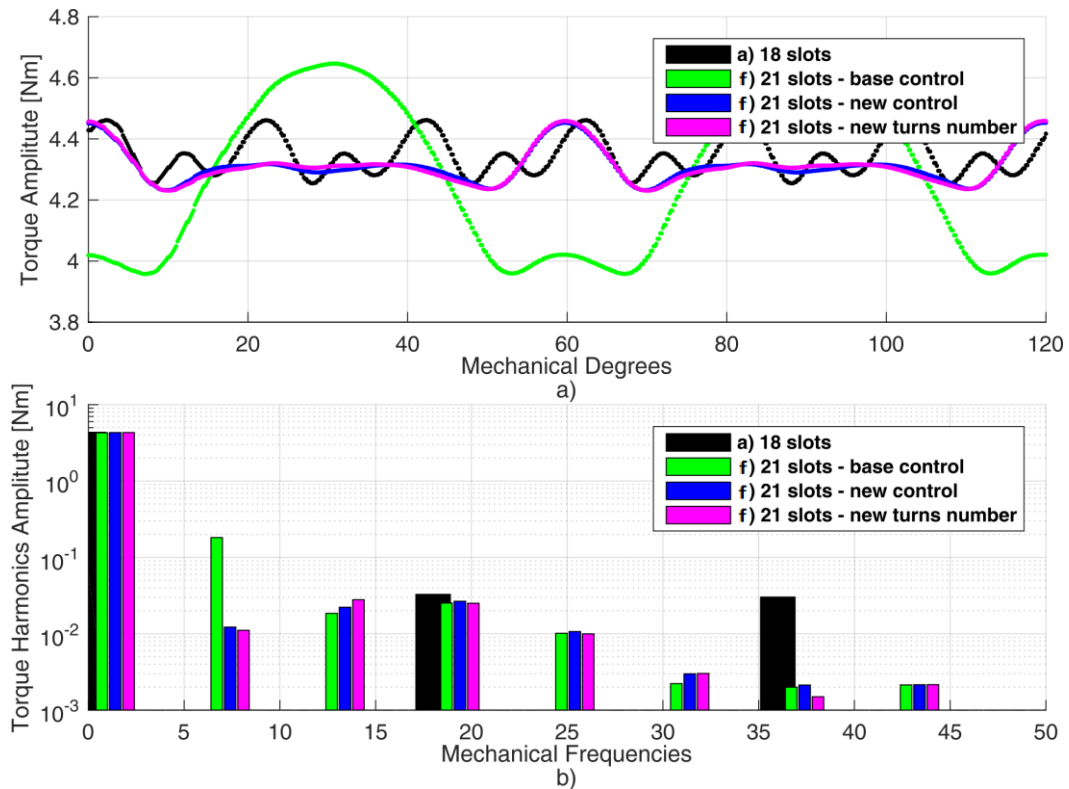


Fig. 6.19 – Torque with 10 A magnitude of the main current space vector (3^{rd}). Comparison of the proposed control techniques and winding design.

6.5 Fault Tolerant Behaviour

In order to have an understanding of the independence between the sectors introduced by the segmentation, the fault tolerant behaviour has been evaluated in terms of sectors decoupling, and for open winding and short circuit faults.

Inductances Analysis

In terms of fault tolerant behaviour, one of the most significant parameter is the ratio between self and mutual phase inductances. In a sectored multi three-phase machine, and even more in a segmented one, the mutual inductance value between phases of different sectors becomes the most important for this analysis [6]. Table 6.3 shows the self and mutual inductances for the designs with 17 degrees of segmentation thickness.

It has been found that the SDb and SDf are the same in terms of self and mutual inductances. As expected, a better solution is obtained with the full air segmented design (SDc).

The geometries with a complete segmentation, as SDc, are the one with higher electromagnetic and thermal insulation between the sectors, but this solution is the one that shows the higher torque reduction and has a more critical mechanical structure than the standard cylindrical one. Having three stator slices rather than one single block means also to change the manufacturing

process and the housing design. This solution is particularly attracting for manufacturing stator processes, for example if a stator open shape is desired for sintered soft magnetic material solutions or for a cheaper and automated windings process. Because this is not the purpose of this study, these additional advantages of a complete segmented solution are not furtherly analysed. However, the possibility to design a multi three-phase machine with a complete insulating segmentation for fault tolerant issues or manufacturing processes has been verified by FEA.

Open Phase and Short Circuits

In terms of one sector open phase behaviour, it is possible to compensate the fault just increasing the reference current amplitudes in the healthy phases of 3/2 times. As deeply analysed in Chapter 5, this control technique is not the only one, and many considerations must be done in terms of radial forces and asymmetrical behaviour. However, for the aim of this chapter, this simplified approach is used to understand the effect of the design segmentation on the machine fault tolerance.

The open phase performance results to be almost the same in all the designs.

Instead, the short circuit machine performance for a one-sector three-phase short circuit fault is increased in the segmented designs, with reduced torque, radial force ripples and short circuit currents. Table 6.4 shows the FEA results of these tests.

6.6 Machine Prototype and Thermal Analysis

The experimental results for the validation of the control and performance analysis have not been carried out yet. However, the prototype has been manufactured, and the drawings of the machine design plus few pictures of the machine are presented here below. Furthermore, it is

Table 6.3 – Inductance matrix components. Self and mutual inductances between phases of the same sector (highlighted) and of different sector (black). The mutual inductances with the phase UA and VA are shown in the top (yellow) and bottom (blue) respectively. The mutual inductances with the phases of the other sectors with UA and VA are shown in the other columns (black)

[mH]	MUCUA	MVCUA	MWCUA	MVAUA	LUA	MWAUA	MVBUA	MUBUA	MWBUA
SDa (18 slots)	0.028	0.028	0.029	0.087	0.310	0.087	0.029	0.028	0.028
SDb (full iron)	0.021	0.021	0.021	0.080	0.404	0.080	0.021	0.021	0.021
SDc (full air)	0.021	0.021	0.021	0.083	0.408	0.083	0.021	0.021	0.021
SDf (21 slots)	0.014	0.014	0.014	0.063	0.386	0.063	0.014	0.014	0.014

[mH]	MUCVA	MVCVA	MWCVA	LVA	MUAVA	MWAVA	MVBUA	MUBUA	MWBUA
SDa (18 slots)	0.029	0.028	0.029	0.310	0.087	0.030	0.028	0.028	0.028
SDb (full iron)	0.021	0.021	0.021	0.406	0.083	0.033	0.021	0.021	0.021
SDc (full air)	0.013	0.013	0.013	0.338	0.065	0.015	0.013	0.013	0.013
SDf (21 slots)	0.021	0.021	0.021	0.402	0.080	0.030	0.021	0.021	0.021

Table 6.4 – Three-phase open phase and short circuit fault (design comparison). In case of open phase fault, the FTC increases the currents in the healthy phases of 3/2 times the reference magnitude of the main current vector (3rd).

	open winding				short circuit			
	Sda	SDb	SDc	SDf	Sda	SDb	SDc	SDf
Torque [Nm]	4.3	4.3	4.0	4.3	1.6	1.9	1.6	1.7
Torque ripple (pp) [Nm]	0.21	0.26	0.85	0.23	4.40	0.74	2.04	0.85
R phase [Ohm]	0.08	0.11	0.11	0.11	0.08	0.11	0.11	0.11
PJ Copper mean [W]	54	78	78	78	476	445	470	442
I max [A]	15.0	16.0	16.0	16.0	74.6	52.6	53.0	52.7
V max [V]	32.0	33.1	31.7	33.1	34.1	33.7	32.0	33.8
V max faulty phases [V]	31.0	30.5	29.0	30.4	2.9	1.2	1.5	1.0
Radial Force [N]	39	63	66	62	491	429	429	426
Force ripple (pp) [N]	52	59	43	58	307	91	106	94

briefly presented an idea for the exploitation of the segmented design for an improved cooling system. The increased thermal decoupling between the sectors in a sectored design is validated.

Machine Design

Fig. 6.20 and Fig. 6.21 show the machine prototype and 3D CAD. The main differences with the original design are in the stator that has now 21 slots rather than 18, and the windings of the central phases that have the possibility to reduce the turn number, as shown in Fig. 6.22.



Fig. 6.20 – Manufactured stator prototype.

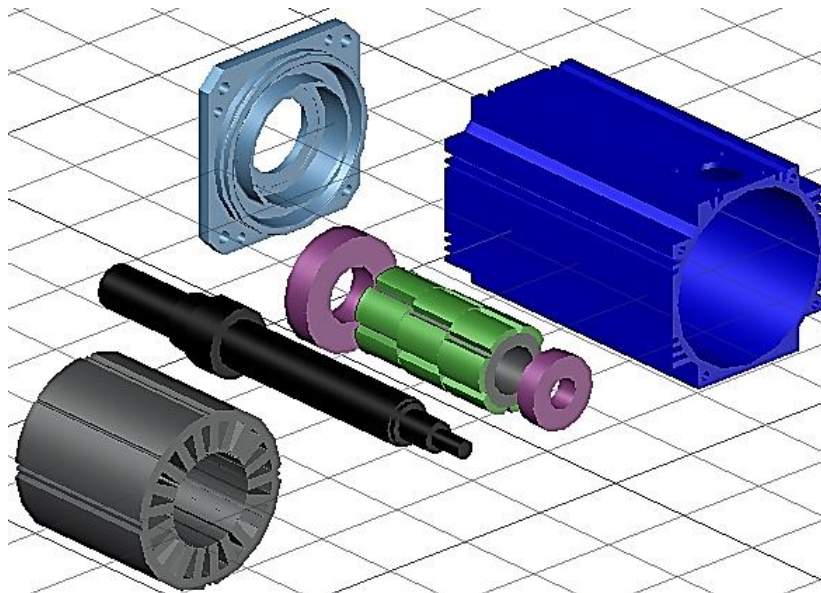


Fig. 6.21 – 3D CAD of the prototype

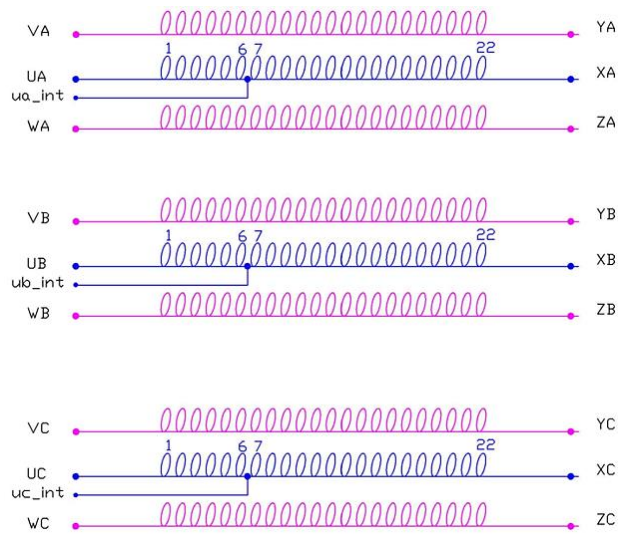


Fig. 6.22 – Winding design for the segmented machine prototype.

Thermal Analysis for Future Developments

A study of the thermal behaviour of the machine has started, with the idea of analysing the possibility of exploiting the empty slots for introducing a thermal cooling of the machine that would allow reducing the thermal coupling between the sectors.

A Matlab-Simscape model has been developed, based on the references used for the developing of the software MotorCad. Indeed, MotorCad does not allow the simulation of a full machine with an asymmetrical thermal behaviour between the different slots. Fig. 6.23 shows the machine thermal behaviour evaluated by the Simscape model when the machine is healthy and working with 10 A phase peak current. In the same figure, it is presented the temperature increase in case of sector A open phase fault (the temperatures are reported in one of the remaining healthy sectors). Fig. 6.24 shows the result given by the MotorCad model. For the limitation of the software, only the healthy case is simulated.

The thermal model has been also compared with some experimental tests done on an available prototype of SDa design. Fig. 6.25 and Fig. 6.26 show the thermocouples arrangement. Fig. 6.28 shows the experimental measurements when the machine is healthy and then one sector is open and the two others are controlled compensating the torque reduction. Fig. 6.27 shows the results given by the Simscape simulation. The model is still not matched in terms of cold plate modelling. Furthermore, for the analysis of the SDF thermal behaviour some data about the effect of the empty slots are needed. Indeed, the thermal behaviour significantly depends on the manufacturing of the end windings and the eventual cooling of the empty slots. Fig. 6.29 shows the idea behind the cooling of the empty slots.

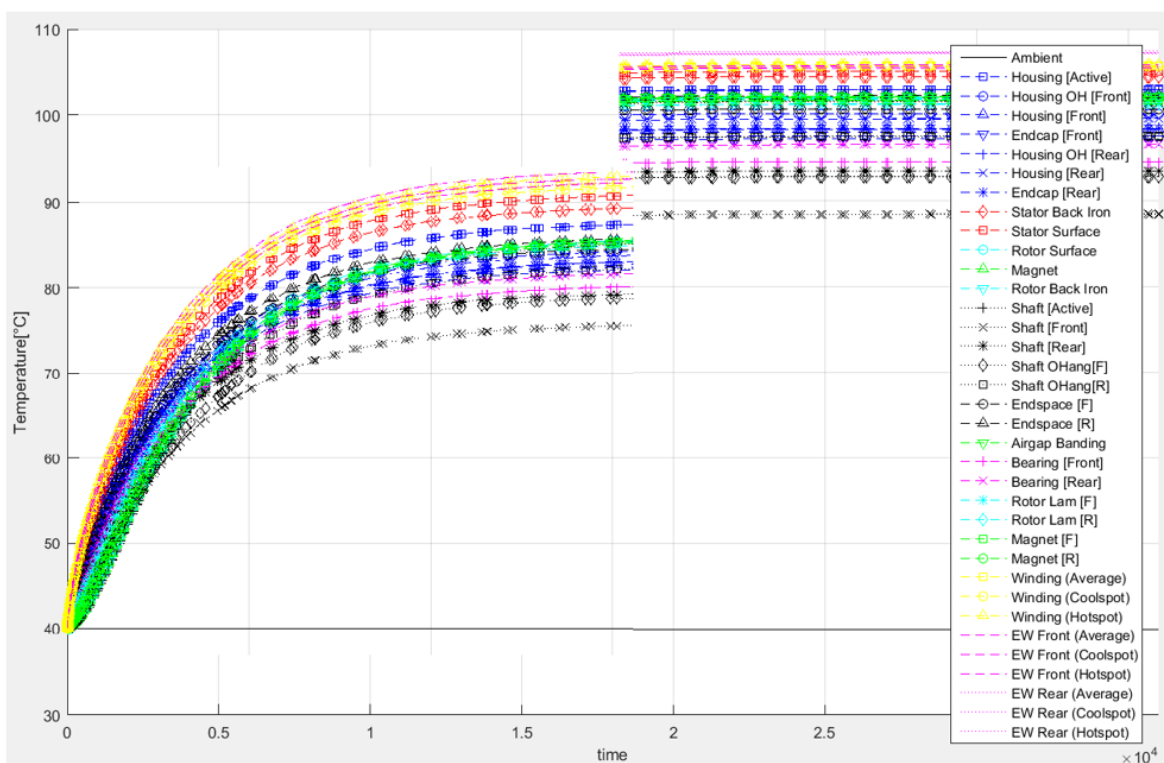


Fig. 6.23 – Evaluated thermal behaviour with Simscape. Healthy machine (left) and one sector open phase fault (right) at rated conditions.

A cooling system between two stator teeth, close to the air-gap and so to the magnets, can be useful for critical applications where the external temperature is high, but also if the housing diameter is restricted and an external cooling system is not allowed. The presence of a cooling system between the stator sectors also follows the idea of thermal insulated three-phase subsystems. With the SDf stator geometry the iron tangential thickness between the sectors is still one tooth. This choice avoids iron saturation, because the main flux flowing through the stator teeth and from the segmentation areas is the permanent magnet one, and that is why having less percentage of iron in the segmentation areas inevitably implicates a higher iron exploitation with more saturated volumes. One of the main drawbacks of the segmented solution is that, if the same iron exploitation is desired and the internal and external stator diameter are not a degree of freedom, the slot area inevitably decreases. A smaller slot area causes higher Joule losses if a standard slot fill factor (for example 0.45) is kept. However, the possible advantages of this new design can also justify a more expensive winding process to increase the slots fill factor (for example 0.60) and maintain the same Joule losses.

The degree of freedom available for the central segmentation $\Delta\Psi_{cs}$ has been neglected because it did not show performance and sector insulation advantages. However, the internal gap might be reintroduced as an alternative solution to improve the cooling system exploiting an additional empty slot in the middle of each sector.

While the thermal advantages related to a segmented design with additional slots (or ducts in general) has still to be validated, the thermal tests and simulations done on the original sectored machine SDa validated the increased thermal decoupling resulting from a sectored design.

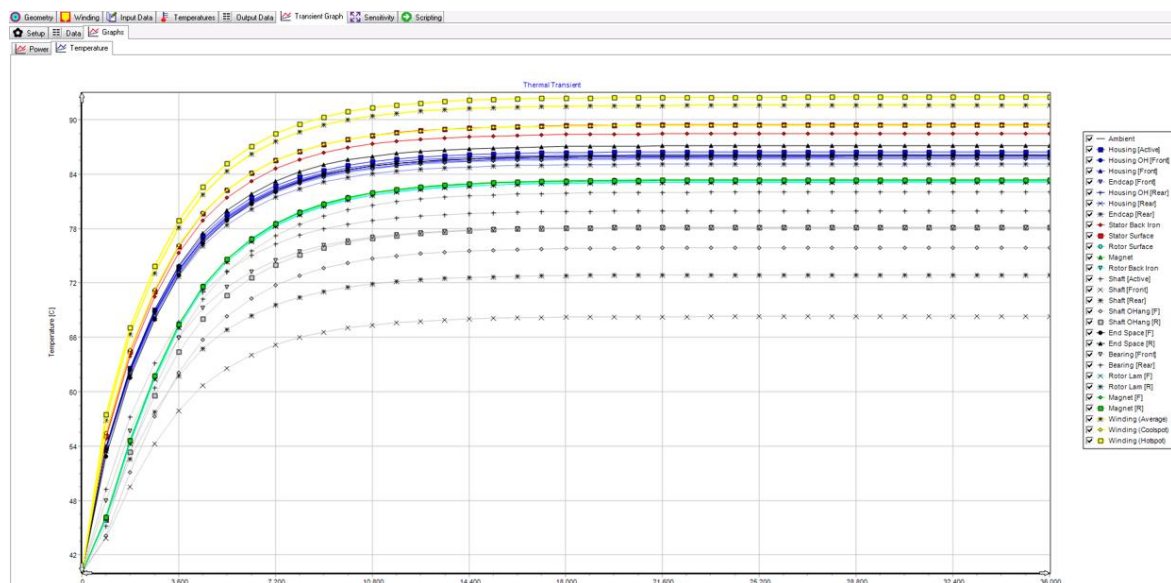


Fig. 6.24 – Evaluated thermal behaviour with MotorCad. Healthy machine.

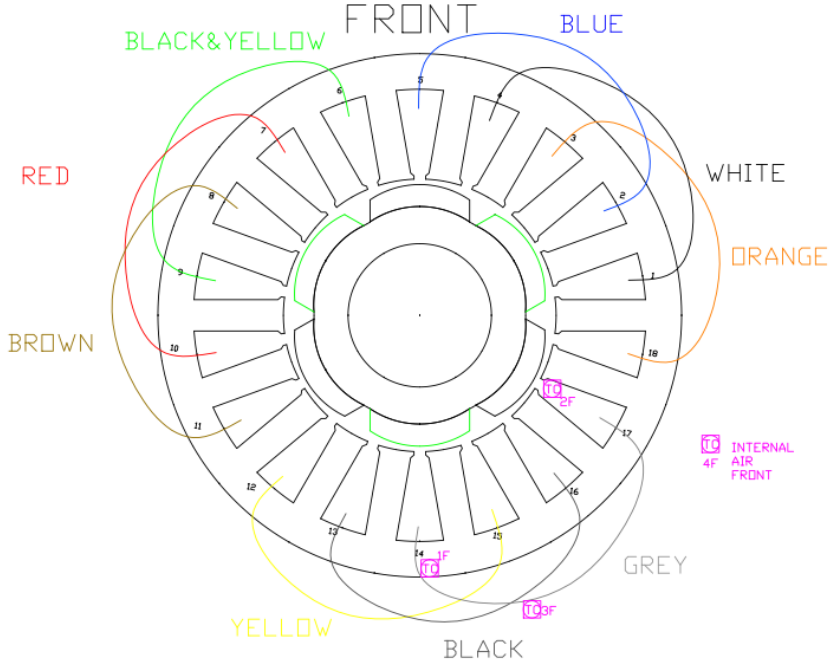


Fig. 6.25 – Thermocouples arrangement: FRONT. The thermocouples are highlighted with the signature [(TC)] in purple.

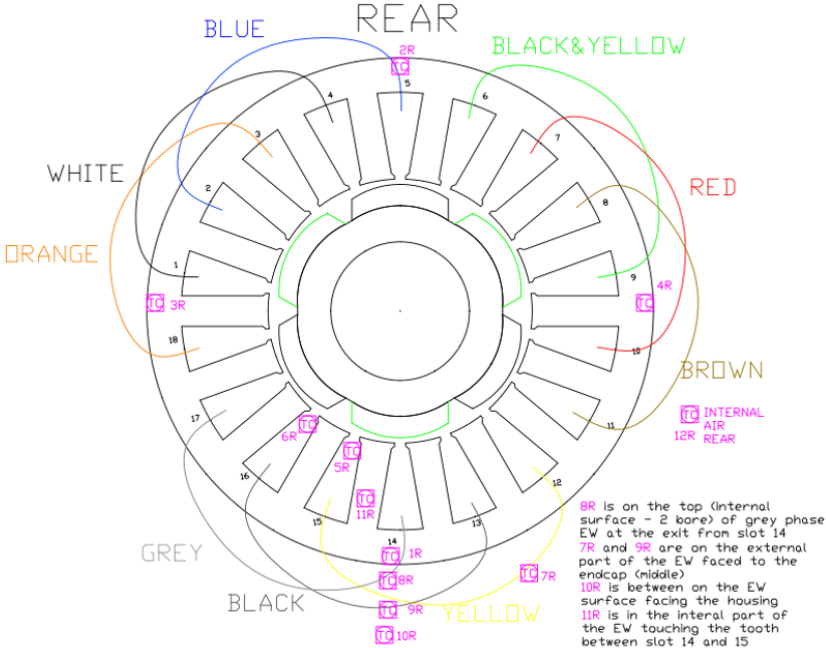


Fig. 6.26 – Thermocouples arrangement: REAR. The thermocouples are highlighted with the signature [(TC)] in purple.

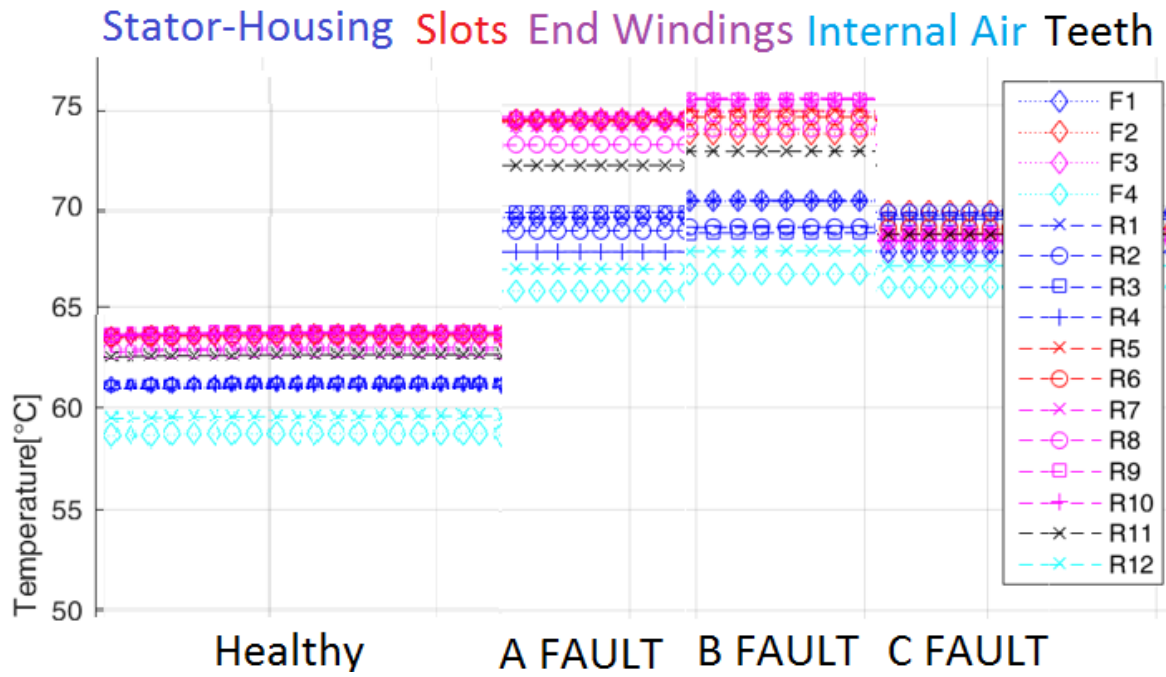


Fig. 6.27 – Simscape simulated results. Healthy machine with 5Arms standard current control (about half the rated current), and with sector A, B and C three-phase open faults with standard fault compensation (the current is increased in the remaining healthy phases up to 7.5 Arms).

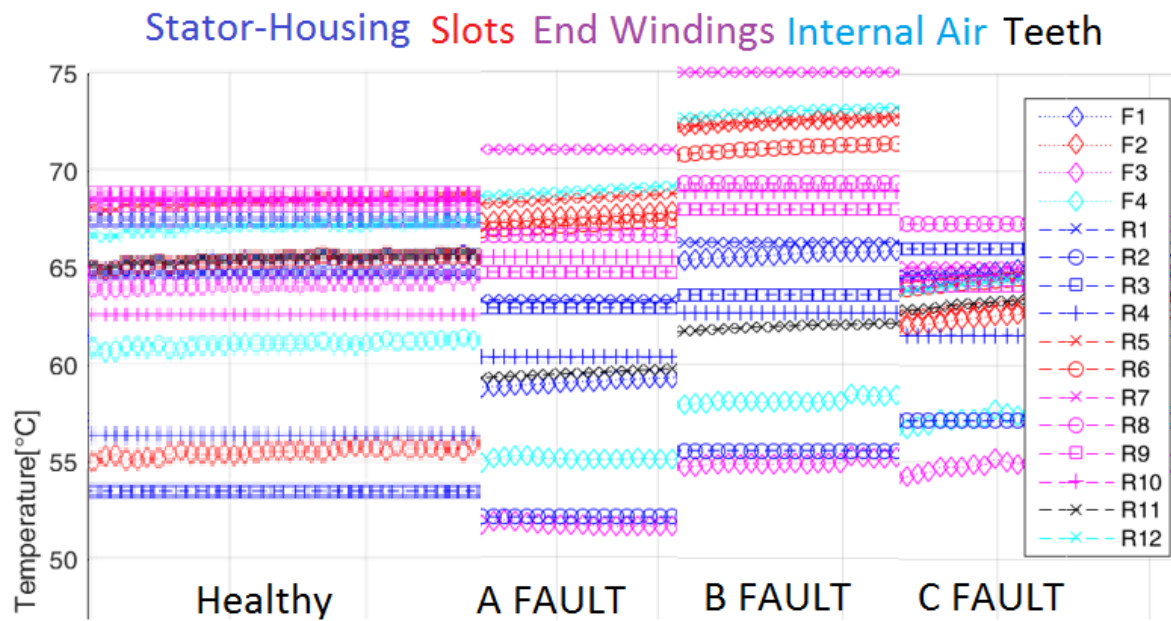


Fig. 6.28 – Experimental results. Healthy machine with 5Arms standard current control (about half the rated current), and with sector A, B and C three-phase open faults with standard fault compensation (the current is increased in the remaining healthy phases up to 7.5 Arms).

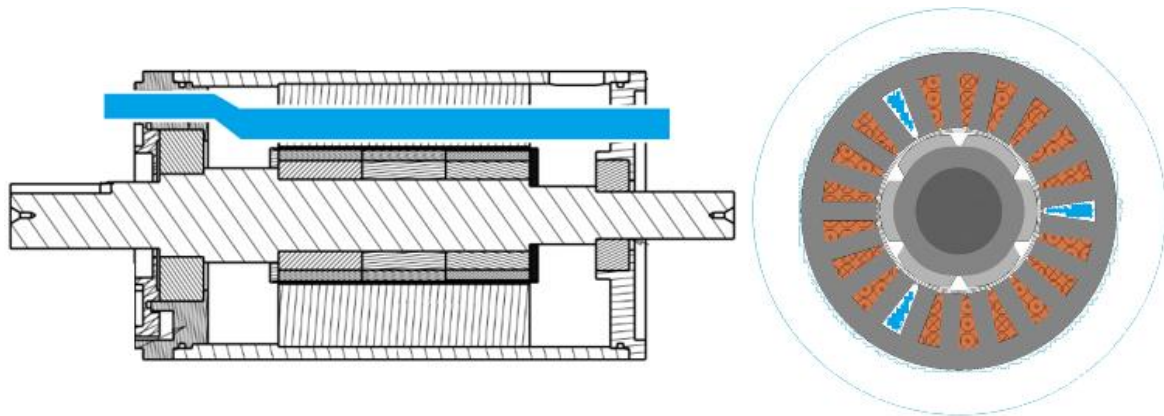


Fig. 6.29 – Exploitation of the empty slots for improving the machine cooling. Concept.

6.7 Conclusion

An overview of the segmentation design for a triple three-phase sectored SPM machine has been presented. A new control technique is proposed to overcome the drawbacks introduced by the stator segmentation. As a possible alternative to the new machine control, a different winding design allows having almost the same machine performance. Both the methods have been validated by FEA. The effect of the segmentation on the coils pitch, the cogging torque, and the segment end effects have been analysed by analytical evaluations and FE transient simulations.

Between the proposed stator geometries, the one with a complete air segmentation, such as SDc, has the higher decoupling between the sectors, but it shows worse performance. Instead, the chosen design (SDf) has significantly better performance. The feasibility to increase the sector decoupling (mechanical, magnetic and thermal) by the stator segmentation has been proven for all the designs, with also advantages in short circuit faults. A prototype of the final design (SDf) has been manufactured in order to verify the control techniques by experimental tests.

This chapter concludes this thesis. All the presented works aim to improve the performance and the reliability of electrical machines. In particular, for the multiphase topology.

Open circuit (Chapter 3), high resistance connections and interturn short circuit (Chapter 4) faults have been deeply analysed. The proposed radial force controls for bearingless control (Chapter 5) might also be useful to prevent bearing faults or eventually compensate a failure of the bearing system, and the segmented machine design (Chapter 6) seems an interesting solution for increasing the machine reliability without significantly affecting the performance.

All the research work, carried out during the doctorate and presented in this thesis, aims to give a contribution to the state of the art of multiphase electrical machines for the development of high performance drives with improved reliability.

References:

- [1] L. Parsa and H. A. Toliyat, "Five-phase permanent-magnet motor drives," *IEEE Transactions on Industry Applications*, vol. 41, pp. 30-37, 2005.
- [2] A. Tani, M. Mengoni, L. Zarri, G. Serra, and D. Casadei, "Control of Multiphase Induction Motors With an Odd Number of Phases Under Open-Circuit Phase Faults," *IEEE Transactions on Power Electronics*, vol. 27, pp. 565-577, 2012.
- [3] A. Tani, Y. Gritli, M. Mengoni, L. Zarri, G. Sala, A. Bellini, *et al.*, "Detection of magnet demagnetization and high-resistance connections in five-phase surface-mounted permanent magnet generators," in *2015 IEEE 10th International Symposium on Diagnostics for Electrical Machines, Power Electronics and Drives (SDEMPED)*, 2015, pp. 487-493.
- [4] D. Casadei, D. Dujic, E. Levi, G. Serra, A. Tani, and L. Zarri, "General Modulation Strategy for Seven-Phase Inverters With Independent Control of Multiple Voltage Space Vectors," *IEEE Transactions on Industrial Electronics*, vol. 55, pp. 1921-1932, 2008.
- [5] A. Tani, G. Serra, M. Mengoni, L. Zarri, G. Rini, and D. Casadei, "Dynamic stator current sharing in quadruple three-phase induction motor drives," in *IECON 2013 - 39th Annual Conference of the IEEE Industrial Electronics Society*, 2013, pp. 5173-5178.
- [6] M. Barcaro, N. Bianchi, and F. Magnussen, "Analysis and Tests of a Dual Three-Phase 12-Slot 10-Pole Permanent-Magnet Motor," *IEEE Transactions on Industry Applications*, vol. 46, pp. 2355-2362, 2010.
- [7] B. Bickel, J. Franke, and T. Albrecht, "Manufacturing cell for winding and assembling a segmented stator of PM-synchronous machines for hybrid vehicles," in *2012 2nd International Electric Drives Production Conference (EDPC)*, 2012, pp. 1-5.
- [8] J. Brettschneider, R. Spitzner, and R. Boehm, "Flexible mass production concept for segmented BLDC stators," in *2013 3rd International Electric Drives Production Conference (EDPC)*, 2013, pp. 1-8.
- [9] G. J. Li, Z. Q. Zhu, W. Q. Chu, M. P. Foster, and D. A. Stone, "Influence of Flux Gaps on Electromagnetic Performance of Novel Modular PM Machines," *IEEE Transactions on Energy Conversion*, vol. 29, pp. 716-726, 2014.
- [10] N. S. Lobo, E. Swint, and R. Krishnan, "M-Phase N-Segment Flux-Reversal-Free Stator Switched Reluctance Machines," in *2008 IEEE Industry Applications Society Annual Meeting*, 2008, pp. 1-8.

Abstract

Advances in power electronic and machine control techniques are making the inverter-fed drives an always more attractive solution. Because of the number of inverter legs is arbitrary, also the number of phases results as a further degree of freedom for the machine design. Therefore, the multiphase winding is often a possible solution.

Due to the increasing demand for high performance and high power variable speed drives, the research on multiphase machines has experienced a significant growth in the last two decades. Indeed, one of the main advantages of the multiphase technology is the possibility of splitting the power of the system across a higher number of power electronic devices with a reduced rating. A similar result can be obtained by using multi-level converters. However, the redundancy of the phases leads to an increased reliability of the machine and to the introduction of additional degrees of freedom in the current control and the machine design.

This work aims to study and analyze the highly reliable and fault tolerant machines. It proposes innovative solutions for multiphase machine design and control to meet the safety-critical requirements in “More-Electric Aircraft” (MEA) and “More Electric Engine” (MEE) in which thermal, pneumatic or hydraulic drives in aerospace applications are replaced with electric ones.

Open phase, high resistance and short circuit faults are investigated. Fault tolerant controls and fault detection algorithms are presented. Radial force control techniques and bearingless operation are verified and improved for various working scenarios. Fault tolerant designs of multiphase machines are also proposed.

Academic activities

Summary of the research activity

The aim of the research program was to study and analyze the highly reliable and fault tolerant AC machines and to propose innovative solutions for multiphase machines. In particular, to develop new control algorithms to meet the safety-critical requirements in “More-Electric Aircraft” (MEA) and “More Electric Engine” (MEE), in which thermal, pneumatic or hydraulic drives in aerospace applications are replaced with electric ones.

This first year I’ve been involved on the faults diagnosis in electrical drives, specifically on the multiphase ones. The research activity focused on high resistance and interturn short circuit faults. I designed a new winding for an induction machine and I realized suitable prototype (in collaboration with the company Elettromeccanica Lucchi, Rimini). In particular, the prototype is has a nine-phase winding with the possibility to test many short circuit conditions. Meanwhile, I started analyzing the control of power flows in multi three-phase drives. The aim was to verify the possibility for a multi three phase drive to supply different and independent systems or lines (battery, ups, different voltage lines).

In the second year, I started developing new control algorithms for the compensation of open phase faults and I worked on the short circuit diagnosis for the induction machine prototype manufactured in the first year. New fault tolerant controls have been developed to compensate the open phase faults in quadruple three-phase induction machines. These controls have been tested on a scaled down prototype of Starter-Generator for MEA applications. In the same year, I spent six months at the Department of Electrical and Electronic Engineering - University of Nottingham, United Kingdom, in cooperation with Prof. Christopher Gerada. The main proposed goal of the project was to study and analyze the feasibility of the stator segmentation of a nine-phase permanent magnet machine to improve its performance and fault-tolerant behavior in case of fault. In the period abroad, I started analyzing also the possibility to control the radial force in multiphase machines. In particular, with the aim of developing two degrees of freedom bearingless control.

The third year has been focused on the improvement of the models and control techniques developed in the previous ones, and to verify some of the theoretical results by simulations and experimental tests both in Bologna and Nottingham Universities.

During the doctorate, I developed a general model of multiphase machine able to model it in healthy conditions and also in case of faults. I developed innovative control algorithms based on the definition of "extended" field oriented control, namely an algorithm that is able to control not only the fundamental component of the air-gap field but also other harmonic components.

I simulated the models and the control algorithms by means of numerical simulations (mainly in Matlab-Simulink) and finite element analysis (in Flux v.12 and Magnet-Infolytica).

I used and programmed three different DSPs (Digital Signal Processor) to control the different drives needed to carry out the experimental tests.

Seminars

1. Plect Workshop: Advanced Modeling and Simulation of Power Electronic System;
 2. Introduction to fault diagnosis for dynamic system (Prof. Paolo Castaldi);
 3. Lightning induced disturbances on distribution electricity networks (Prof. Carlo Alberto Nucci);
 4. Fundamentals of design and testing for EMC (Prof. Leonardo Sandrolini);
 5. Fundamental properties of superconductive materials and devices (Prof. Marco Breschi);
 6. Keysight – Debug avanzato mediante l’uso di Oscilloscopi Ad Alta Risoluzione;
 7. Keysight – Caratterizzazione e Modeling dei Dispositivi a Semiconduttore;
 8. Corso di aggiornamento per versione v12 del programma software FLUX;
 9. Feed your knowledge of Electromagnetic Design;
 10. ‘Finite Element Analysis in the electrical machine design’ and ‘Real time electrical and mechanical power measurement in electrical machines and drives’;
 11. LabView Core 1 and 2 seminars.
- Courses
 1. Metodologie di progettazione delle macchine elettriche M (Prof. Giovanni Serra).
 - Conferences
 1. Workshop WEMDCD 2015;
 2. Annual Conference of the IEEE Industrial Electronics Society IECON 2016;
 3. Workshop WEMDCD 2017.
 - Summer school
 1. European PhD School 16th Edition Gaeta.

Research period abroad

Foreign tutor:	Prof. Christopher Gerada
Foreign institute:	Department of Electrical and Electronic Engineering - University of Nottingham, Nottingham, United Kingdom
Exchange periods:	From February 10 th 2016 to August 10 th 2016 From May 1 st 2017 to November 1 st 2017

Assistant Supervisor

Luca Ianni, “Controllo tollerante ai guasti di uno starter generator multi trifase per applicazioni aeronautiche“. (M.Sc.)

Filippo Ciccola, “Analisi dei guasti negli avvolgimenti di statore delle macchine asincrone“. (M.Sc.)

Mattia Mantellini, “Realizzazione di uno strumento didattico per la simulazione del collegamento di un alternatore in parallelo alla rete“. (B.Sc.)

Pietro Girardini, “Analisi teorica e sperimentale della compensazione dei guasti nelle macchine asincrone multifase per applicazioni aeronautiche“. (M.Sc.)

Antonio Gualtieri, “Analisi teorica e sperimentale di macchine asincrone multifase con numero di fasi dispari e rotore a gabbia di scoiattolo“. (M.Sc.)

Publications

Tani, Y. Gritli, M. Mengoni, L. Zarri, G. Sala, A. Bellini, G. Serra, “Detection of Magnet Demagnetization and High-Resistance Connections in Five-Phase Surface-Mounted Permanent Magnet Generators,” in Proc. 10th IEEE International Symposium on Diagnostics for Electric Machines, Power Electronics and Drives (SDEMPED 2015), Guarda, 2015, pp. 487-493.

M. Mengoni, G. Sala, L. Zarri, A. Tani, G. Serra, Y. Gritli, M. Duran, “Control of a Fault-Tolerant Quadruple Three-phase Induction Machine for More Electric Aircrafts,” IECON 2016 - 42nd Annual Conference of IEEE Industrial Electronic Society, Florence, 2016, pp. 5747-5753.

G. Sala, D. Gerada, C. Gerada, and A. Tani, "Design and control of segmented triple three-phase SPM machines for fault tolerant drives," in 2017 IEEE Workshop on Electrical Machines Design, Control and Diagnosis (WEMDCD), Nottingham, 2017, pp. 63-68.

G. Sala, D. Gerada, C. Gerada, and A. Tani, "Radial force control for triple three-phase sectored SPM machines. Part II: Open winding fault tolerant control," in 2017 IEEE Workshop on Electrical Machines Design, Control and Diagnosis (WEMDCD), Nottingham, 2017, pp. 275-280.

G. Sala, D. Gerada, C. Gerada, and A. Tani, "Radial force control for triple three-phase sectored SPM machines. Part I: Machine model," in 2017 IEEE Workshop on Electrical Machines Design, Control and Diagnosis (WEMDCD), Nottingham, 2017, pp. 193-198.

G. Sala, P. Girardini, M. Mengoni, L. Zarri, A. Tani and G. Serra, "Comparison of fault tolerant control techniques for quadruple three-phase induction machines under open-circuit fault," 2017 IEEE 11th International Symposium on Diagnostics for Electrical Machines, Power Electronics and Drives (SDEMPED), Tinos, 2017, pp. 213-219.

G. Sala, G. Valente, A. Formentini, L. Papini, D. Gerada, P. Zanchetta, A. Tani, C. Gerada, "Space Vectors and Pseudo Inverse Matrix Methods for the Radial Force Control in Bearingless Multi-Sector Permanent Magnet Machines," in *IEEE Transactions on Industrial Electronics*, vol. PP, no. 99, pp. 1-11, 2018.